Advanced self-lubricating surfaces based on carbon nanoparticles

Dissertation

zur Erlangung des Grades
des Doktors der Ingenieurswissenschaften
der Naturwissenschaftlich-Technischen Fakultät
der Universität des Saarlandes

von

Leander Reinert

Saarbrücken

Juli 2018

Tag des Kolloquiums:	17.12.2018
Dekan:	Prof. Dr. Guido Kickelbick
Berichterstatter:	Prof. Dr. Frank Mücklich
	Prof. Dr. Dirk Bähre
	Prof. Dr. Gerhard Hirt
Vorsitz:	Prof. Dr. Guido Kickelbick
Akad. Mittelbau:	Dr. Frank Aubertin

„Willst du dich am Ganzen erquicken, so musst du das Ganze im Kleinsten erblicken“

(Johann Wolfgang von Goethe)

„Willst du dich am Ganzen erquicken, so musst du das Ganze im Kleinsten erblicken“

(Johann Wolfgang von Goethe)

TABLE OF CONTENTS

ACKNOWLEDGEMENTS

Thinking back to the time at the beginning of my PhD thesis, the overwhelming feeling of having finally graduated was linked to a motivated, but strange popular belief: I thought that a PhD thesis was the scientific output of a single person, based on their individual capabilities, with the aim of investigating something completely new. Hence, with the basic knowledge in material science and engineering from my studies, my plan was to find a "scientific gap" in literature and to develop a systematic and straightforward research plan with a tight schedule. Then, I would work on this plan until understanding the given problem in every little detail, presenting the final solution and complete my doctorate.

…I was so wrong and have learned so much since then, including what a PhD thesis is truly about. However, one of the things that I learned the quickest, I owe to all the members of the chair of functional materials (FuWe): teamwork. This, among other things, is why I consider it my duty to thank and dedicate this section to several people who have supported and helped me stay on track and finally create a manuscript, which combines the findings of our research from the last years.

First and foremost, I would like to thank my supervisor, Prof. Dr. Frank Mücklich, for providing the possibility to work at his institute, but also for his permanent support and his everlasting confidence in me. It was he who drew my attention to the field of materials science when I was still a pupil. I still remember his words during a visit to my former school: "If you can't decide whether to study physics, chemistry or mathematics, you should come and study materials science". Since then, he accompanied me on my way from being a scientific assistant at his institute to becoming a doctoral candidate. Due to his open-mindedness, aside from my position as a PhD student, I also got the opportunity to work at the Material Engineering Center Saarland (MECS), gathering valuable experience working together with industry. I am proud to be a part of his research group.

Also, I want to thank Prof. Dr. Dirk Bähre for being my scientific guide, for our fruitful discussions during my yearly progress reports and for his role as second reviewer of my thesis.

Thinking about my colleagues, I am very lucky to be part of such a highly motivated and supportive team of researchers. Certainly, one of the persons that I owe the most to is Dr. Sebastian Suárez. The process of being a PhD student involves phases, which are dominated by self-doubt and the question "why am I doing all this". I had never met a person as optimistic, motivating, idealistic and enthusiastic about scientific research as Seba. He helped me with almost daily motivating discussions, shared his experience as a post-doctoral researcher, assisted in countless experiments, gave me trust and friendship. I would like to express my deepest gratitude to you, Seba.

Furthermore, I would like to thank the following people who have guided me on my way as a PhD student not only as colleagues, but also as friends, making everyday work a place to feel at home: Philipp Grützmacher, Prof. Dr. Andreas Rosenkranz, Prof. Dr. Carsten Gachot, Dominik Britz, Federico

Lasserre, Christian Schäfer, Dr. Nicolas Souza, Daniel Müller, Timothy MacLucas and Sebastian Slawik. Prof. Dr. Rosenkranz, Dr. Suarez, Dr. Souza and Mr Grützmacher are especially appreciated for proofreading this dissertation.

Additionally, my thanks go to all my other colleagues from FuWe as well as researchers of other institutes who gave me the opportunity to use their experimental equipment or to benefit from their knowledge in various experimental or simulation tasks. In this context, I would like to mention Prof. Dr. Volker Presser, Prof. Dr. Itzhak Green, Prof. Dr. Michael Varenberg, Dr. Frank Müller and Dr. Marco Zeiger amongst others.

Almost half way through my PhD, my better half named Belinda came into my life. It was and still is such a good feeling to be supported and understood not only scientifically, but also emotionally. You are my daily constant and motivation, that makes even the worst day look better and I am very grateful for every single moment with you.

Last but not least, I also want to thank my family, especially my mom and dad for their endless support, open ears and understanding during the last years. My family always encouraged and believed in me and I will treasure their support forever.

ZUSAMMENFASSUNG

Diese Dissertation setzt sich zum Ziel, mittels neuartiger Festschmierstoffe (Kohlenstoff-Nanopartikel (CNP)), deren Einsatz in einer geeigneten Materialklasse (Metall Matrix Komposite (MMC)) und der Entwicklung eines spezifischen Oberflächendesigns (mittels Laser-Oberflächenstrukturierung) selbstschmierende Oberflächen herzustellen sowie die involvierten Mechanismen zu verstehen. Dies umfasst die vollständige Prozessentwicklung von der Synthese und Verarbeitung über die experimentelle Analyse und theoretische Modellierung, der Diskussion und dem Verständnis der Mechanismen bis hin zur Herstellung eines Prototyps.

Von drei untersuchten CNP (zwiebelartiger Kohlenstoff, Nanodiamanten und Kohlenstoff-Nanoröhrchen (CNT)) konnten CNT als geeigneter Festschmierstoff identifiziert werden. Dies ist auf ihr hohes Aspektverhältnis, Flexibilität sowie ihren Degradationsmechanismus zurückzuführen. Die kontinuierliche Versorgung des Kontaktes mit CNT ist durch deren elastische Kompression und Rückstellvermögen gewährleistet. Der entsprechende Degradationsmechanismus erlaubt eine effiziente Schmierung unabhängig von vorherrschender Luftfeuchtigkeit, Oberflächenrauheit, dem Belastungskollektiv und der Kontaktmechanik, was auf die Anpassungsfähigkeit der Schmierungsmechanismen (Rollen, Gleiten und Scheren) zurückzuführen ist.

So konnten permanent selbstschmierende Oberflächen hergestellt werden, welche eine maximale Reduzierung von Reibung und Verschleiß um den Faktor 4 bzw. 115 ermöglichen.

ABSTRACT

This dissertation deals with a new branch of solid lubricants (carbon nanoparticles (CNP)), their use in a suitable base-material (Metal Matrix Composites (MMC)) and the investigation of a specific surface design (processed by laser surface structuring) to create and understand self-lubricating surfaces. The dissertation covers the complete process development from the synthesis and processing, experimental analysis and theoretical modeling, discussion and understanding of involved mechanisms up to the production of a prototype.

Out of three investigated CNP (onion-like carbon, nanodiamonds and carbon nanotubes (CNT)), CNT are identified as the most suitable solid lubricant for self-lubricating surfaces. In this regard, their large aspect ratio, flexibility as well as degradation mechanism are the most important aspects to consider. Being stored in a surface, CNT are continuously pulled into the contact by elastic compression and restoration. Due to their degradation mechanism, their lubrication activity is insensitive to variations in humidity, surface roughness, loading conditions and contact mechanics. The lubrication mechanisms of CNT adapt to the given situation by effectively combining different solid lubricant working principles, namely: rolling, sliding and shearing.

As a result, permanent self-lubricating surfaces are successfully produced, allowing for a maximum reduction in friction and wear by a factor of 4 and 115, respectively.

ABBREVATIONS AND SYMBOLS

a_1, a_2	Unit vectors	I_G	Intensity of G-band
a-C	Amorphous carbon	$I_{G'}$	Intensity of G'-band
a-C:H	Amorphous, hydrogenated DLC	LA	Raman mode
a-Si:O	Quartz-like network	LO	Raman mode
A_r	Real area of contact	L	Normal load
AFM	Atomic force microscopy	LST	Laser surface texturing
α	Pressure dependent shear strength	λ	Wavelength
bcc	Body centered cubic	MEMS	Micro-electro mechanical systems
CPS	Cold pressed sintering	MWCNT	Multi-wall carbon nanotube/-s
CSA	Chlorosulfonic acid	MMC	Metal matrix composite/-s
CNP	Carbon nanoparticle/-s	μ	Friction coefficient
CNT	Carbon nanotube/-s	ND	Nanodiamond/-s
COF	Coefficient of friction	NC-graphite	Nanocrystalline graphite
CVD	Chemical vapor deposition	OLC	Onion-like carbon
C_h	Chiral vector	P	Contact pressure
DMF	Dimethylformamid	p	Structural periodicity
DC	Direct current	PTFE	Polytetrafluorethylene
DLN	Diamond-like nanocomposite/-s	PE	Polyethylene
D-band	A Raman mode	RBM	Radial breathing mode
D'-band	A Raman mode	R_k	Core roughness
DLIP	Direct laser interference patterning	SEM	Scanning electron microscopy
DLW	Direct laser writing	SPS	Spark plasma sintering
d_t	Tube diameter	SWCNT	Single-wall carbon nanotubes
DLC	Diamond-like carbon	σ	Normal stress
0-D	0-Dimensional	ta-C	Tetragonal amorphous carbon
EPD	Electrophoretic deposition	ta-c:H	Hydrogenated ta-C
fcc	Face centered cubic	TEM	Transmission electron microscopy
F	Friction force	TNT	Trinitrotoluol
FIB	Focused ion beam	TMD	Transition metal dichalcogenide/-s
FWHM	Full width at half maximum	T	Tube-axis
G-band	A Raman mode	τ_S	Shear strength
G'-band	A Raman mode	τ_0	Interfacial shear strength
HUP	Hot uniaxial pressing (HUP)	τ	Shear stress
HPT	High pressure torsion	UV	Ultraviolet
HIP	Hot isostatic pressing	vol.-%	Volume-%
IF	Inorganic fullerene/-s	X_{CG}	G-band center position
I_D	Intensity of D-band	XPS	X-ray photoelectron spectroscopy

1. MOTIVATION AND OBJECTIVES

Tribology is defined as the science of interacting surfaces in relative motion and all practices related thereto. It includes the study of wear, friction and lubrication and ranges from spacecraft to household appliances or even the human body [1,2]. Thus, understanding and tailoring the tribological properties of mechanical systems has been and still is a vastly studied field of research.

Nowadays, friction and wear are recognized as having a major influence on the efficiency and lifetime of machinery and thus, determine the economic viability of a product to a great extent [3–6]. This fact is clearly exemplified by an average passenger car spending about one third of its total fuel energy on friction and wear [3]. In nearly every technical application, transmitting kinetic/mechanical energy from its source to the desired application area is realized by the interaction of at least two surfaces. Aside from certain applications where high friction is desirable (e.g. for automotive brakes or clutches[7,8]), the intention is to reduce friction and wear to a minimal level (e.g. for bearings). This can be accomplished by tribological optimization of the lubrication [9], surface design [10] and base materials [11].

Certainly, the simplest and most effective way to reduce friction and wear is to use a suitable lubricant. For a wide range of applications, a liquid lubricant is used (e.g. oil), which tunes the separation of the contacting surfaces as a function of the applied normal load, sliding speed as well as oil viscosity, thus affecting friction and wear [12]. However, for some applications, the use of solid instead of liquid lubricants can be advantageous or unavoidable, for example, in cases of harsh environmental conditions such as high temperature ranges (e.g. kiln truck bearings) or high vacuum (e.g. spaceflight applications) [13–15]. There is a variety of different solid lubricants such as MoS_2, WS_2, graphite, lubricious oxides, diamond-like carbon (DLC), certain polymers or soft metal coatings, all of which are limited in their range of application [13]. Even though they can be very effective under certain conditions, they typically fail in one or several of the following requirements, namely: insensitivity to operational environments including low chemical reactivity (oxidation or formation of unwanted by-products), easy replenishment, capability to dissipate generated heat, constant lubrication, aging stability or adhesion [13,16]. For example, MoS_2 is often used in applications working under vacuum or inert gas, since it reacts with oxygen in atmospheric environments thus losing its ability to lubricate [13]. In contrast, graphite particularly shows efficient lubrication under moderate to high relative humidity. In the case of low relative humidity or vacuum, a high coefficient of friction (COF > 0.5) is observed as its lubrication mechanism relies on the intercalation of water molecules between consecutive graphene layers [17].

Nevertheless, today's technical applications demand an ever greater degree of robustness and insensitivity with regard to environmental and loading conditions in the use of solid lubricants [18,19]. For example in spacecraft, satellites or satellite launch vehicles wait for extended periods of time in

humid environments before starting, after which they must work under vacuum conditions. For this reason, solid lubricants must be developed that adapt to changing environmental or loading conditions while still reliably lubricating the mechanical components of a system [20].

Regarding the used base material, especially in the field of dry friction, the mechanical and chemical properties of the contacting surfaces are of utmost importance. One way to tailor these is by using metal matrix composites (MMC), with the metal matrix most often being reinforced by a non-metallic phase. The properties of MMC can be designed to fit the requirements of an intended application (e.g. light weight but high strength). They are often employed as structural and functional materials such as fiber-reinforced pistons, aluminum crankcases with strengthened cylinder surfaces or particle-strengthened brake discs, in the automotive or aerospace sectors. MMC are also broadly found in wear-resistant or friction-reducing sliding contact materials in bearings and pistons or cylinder liners in engines [21–26]. This is not only due to the fact that the microstructure of MMC, and thus their mechanical properties, can be controlled by the processing parameters and the reinforcement phase, but also because lubricants (such as graphite) can be used as reinforcement phase in order to obtain self-lubricating materials [22].

In this regard, using a solid lubricant as reinforcement phase can overcome some drawbacks of solid lubricant coatings, such as limited lifetime, difficult replenishment, oxidation, aging-related degradation or poor adhesion [16]. Not only can MMC be used as a bulk self-lubricating material but there are also several ways to apply MMC as surface coating, rendering this method to create self-lubricating materials a very versatile technique, which could be used for many different substrate materials and applications [27–30]. However, a significant disadvantage arises when using rather soft, easy to shear solid lubricants such as graphite in MMC, namely poor mechanical properties. These composites sometimes have even lower mechanical properties than the unreinforced alloy [16]. In this regard, the tendency is to reduce the reinforcement material's size to the nano range, allowing for a fine and homogeneous reinforcement distribution. This could possibly resolve some of the limitations such as poor ductility, machinability and reduced fracture toughness [16].

In recent years, carbon nanoparticles (CNP) have arisen as promising candidates to reduce friction and wear under various operational environments, which is ascribed to their intrinsic mechanical properties, chemical inertness, thermal stability as well as atomic structure and morphology [31–36]. Several works report on the friction and wear-reducing effects of the particles when used as solid lubricant coating or as reinforcement phase in composite materials [29,35–47]. However, the underlying lubrication mechanisms of the particles are still a matter of debate and thus the potential lubricating effects may not be fully exploited. The present thesis focuses on three CNP in particular: Multi-wall carbon nanotubes (MWCNT), onion-like carbon (OLC) and nanodiamonds (ND). MWCNT consist of multiple, hollow graphitic shells (sp^2-hybridized carbon atoms), providing a tube-like form with a very high aspect ratio[48,49]. OLC, also known as carbon onions, show the same hybridization and a similar graphitic shell-like structure, but with a spheroidal particle morphology[50]. Finally, with a

particle morphology similar to OLC, ND provide a diamond atomic structure with sp^3-hybridized carbon atoms [33]. These three different types of CNP are chosen intentionally since they can be systematically distinguished. A systematic investigation of the lubrication mechanisms of different CNP and lubrication requirements in the same tribological system has not been done before in literature, although it would allow for a more in depth understanding of the mechanisms involved.

When designing self-lubricating surfaces and addressing the used lubricant and base material, the impact of the surface design should also be explored, since surface topography and chemistry have a major influence on the contact mechanics, and consequently, the occurring wear mechanisms. From various techniques to create well-defined surface designs such as honing, blasting, micro coining or lithography, laser surface texturing (LST) and in particular Direct Laser Interference Patterning (DLIP) have shown to be suitable, cost and time-efficient approaches [10,51]. In addition to reducing the real contact area and trapping abrasive wear debris, created surface depressions can act as storage for liquid and solid lubricants, thus continuously supplying the contact region with lubricant [52,53]. Additionally, the ability to systematically vary the surface design allows for a more in-depth understanding of the occurring lubrication mechanisms. For this reason, laser surface texturing is proposed in the present dissertation as a tool to create self-lubricating surfaces and to understand the influence of the surface design on the lubrication mechanism of CNP.

The development route of the present dissertation is schematically presented in ***Fig. 1***.

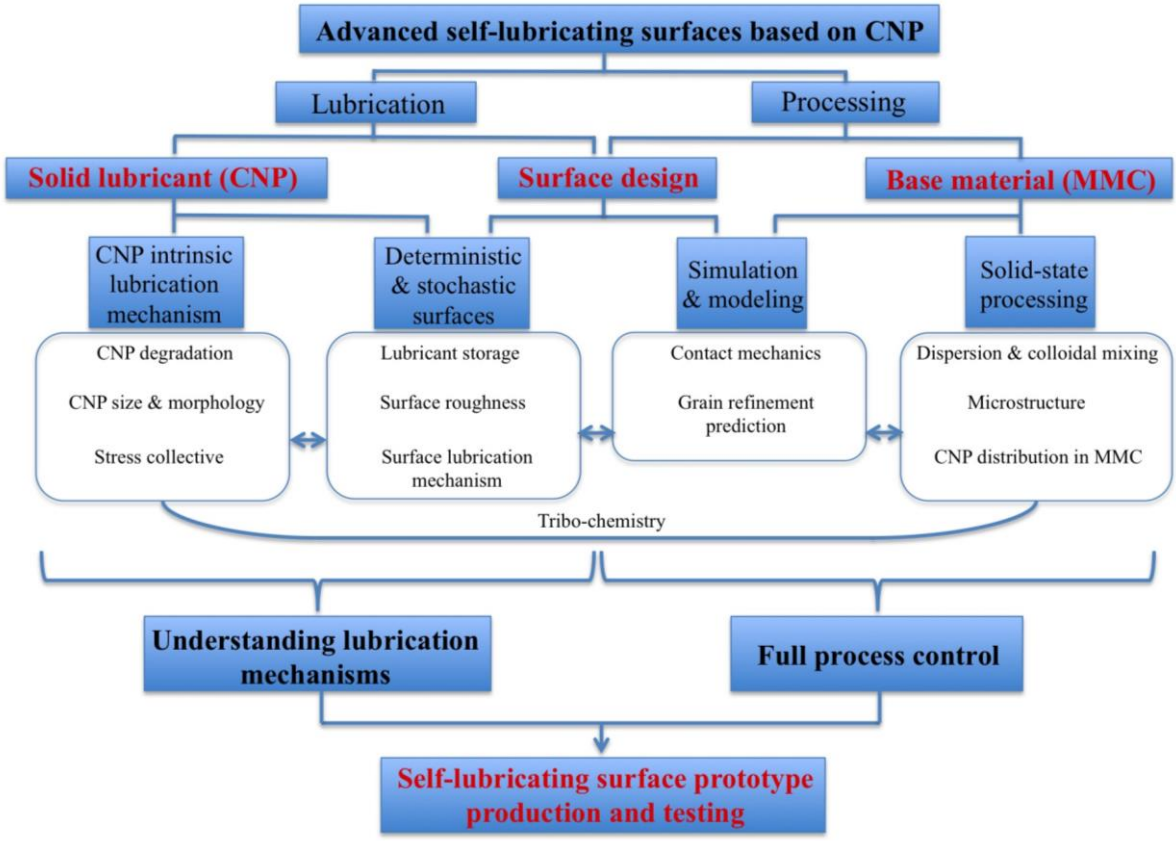

Figure 1: Schematic of the development route of the present dissertation

In summary, the present dissertation deals with an emerging branch of solid lubricants (CNP), their use in a suitable base material (MMC) with a specific surface design (using LST), thus addressing the three most important points for the development and understanding of self-lubricating surfaces based on CNP. The dissertation covers the complete process development to create these surfaces from the synthesis and processing, experimental and theoretical modeling, discussion and understanding of effects and mechanisms up to the production of a prototypical component, which should be suitable for permanent self-lubricating unidirectional sliding. In particular and based on the schematic in ***Fig. 1***, the following three objectives should be met:

OBJECTIVE 1

The first objective of this dissertation is to find a CNP dispersion and MMC processing method that enables a uniform production of CNP-reinforced MMC. This method should avoid particle functionalization, minimize particle degradation and enable a fine and homogeneous particle distribution within the resulting MMC. In addition, the method must allow for full process control so that a model can be established, which predicts the final microstructure of the manufactured composites.

OBJECTIVE 2

The second objective is to understand the intrinsic lubrication mechanisms of CNP and the different tribological influences involved when using them as a lubricant in MMC or as a coating. For this purpose, the tribological properties of CNP-coated surfaces must be investigated and compared to CNP-reinforced surfaces. In this regard, influences of the microstructure, lubricant storage, surface roughness and design, degradation mechanisms, size/morphology of CNP and stress collective have to be carefully evaluated, compared and discussed. Based on these findings and the resulting contact mechanics, the question must finally be answered as to which CNP is best suited for the intended purpose of the self-lubricating surfaces.

OBJECTIVE 3

A prototypical component must be produced and tailored to combine all the positive findings of objective 1 and 2. The prototype should be tested under conformal contact situation, comparable to the situation of a bearing subjected to unidirectional sliding, providing a constantly decreased friction and wear under steady-state conditions.

2. STATE OF THE ART

2.1 Carbon nanoparticles (CNP)

Carbon is a very versatile element and can be found in great abundance on our planet. With an atomic electron configuration of six electrons (two in the 1s orbital, two in the 2s orbital and two in the 2p orbital), carbon materials can be classified into two main groups, depending on the energetic state of the carbon bonding, called hybridization. The first and most stable carbon allotrope is graphite, possessing an sp^2-hybridization, the ground state phase of carbon under standard temperature and pressure. Under high pressure (several GPa), graphite transforms to diamond, resulting in sp^3-hybridization of the carbon atoms [54].

In the case of graphite, each carbon atom is covalently bonded to three other carbon atoms, through its three coplanar sp^2 orbitals, forming σ-bonds, and orthogonal p orbital, forming a π-bond. The latter produces what is considered as an electron cloud (delocalized electrons), similar to what is observed in metals. Structurally, graphite presents a layered structure consisting of several stacked planar single layers (called graphene) that are interconnected by weak Van-der-Waals interactions. In contrast, the diamond structure is characterized by a fourfold covalent bonding (four sp^3 orbitals) of the carbon atoms with a tetrahedral symmetry (109.5°) [54,55]. The graphite and diamond bonding structure is depicted in ***Fig. 2***.

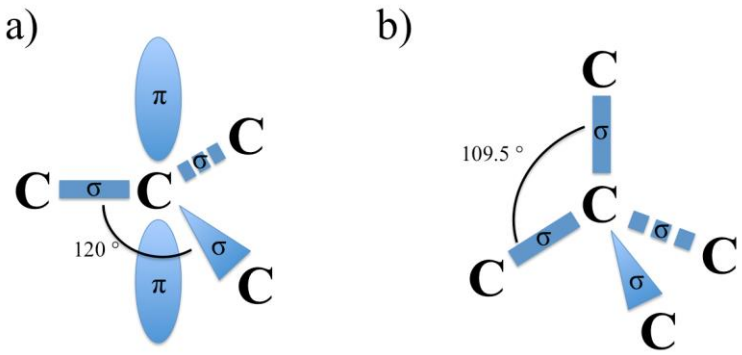

Figure 2: a) Bonding structure of graphite and b) diamond.

Based on these two principal carbon modifications, a large variety of carbon materials and recently carbon nanomaterials have been developed. A material is generally considered a nanomaterial if at least one internal or external spatial dimension is in the nm scale (up to 100 nm) [56]. In addition of being distinguished by their carbon hybridization, carbon nanomaterials are usually classified as 0-D, 1-D, 2D and 3-D materials according to their properties and their morphology (flatness, sphericity). ***Fig. 3*** gives a brief overview of a selection of currently known sp^2-hybridized carbon nanomaterials [57].

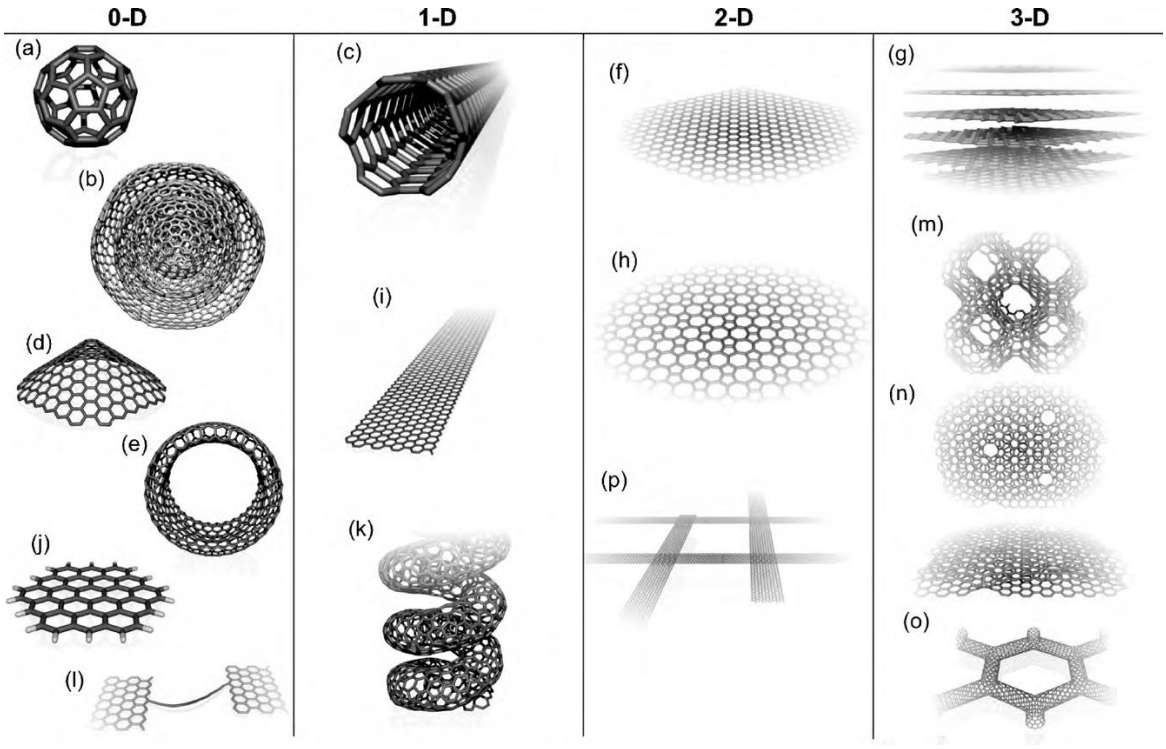

Figure 3: Selection of currently known forms of sp^2-hybridized carbon nanomaterials.
a) C_{60}: Buckmisterfullerene, b) carbon onion, c) carbon nanotube, d) nanocone/horn, e) nanotoroid, f) graphene, g) graphite, h) haeckelite surface, i) graphene nanoribbon, j) graphene cluster, k) helicoidal carbon nanotube, l) short carbon chain, m) schwarzite crystal, n) carbon nanofoam, o) nanotube network, p) nanoribbon network [57].

In this context, dimensionality determines the number of principal directions in which the nanomaterials are expanded. Thus, spheroidal nanoparticles (e.g. carbon onions in ***Fig. 3 b***) are often referred to as 0-D nanoparticles, whereas cylindrical nanoparticles (e.g. carbon nanotubes in ***Fig. 3 c***) are denoted as 1-D nanoparticles. Especially in the cases of 0-D and 1-D carbon nanomaterials, a defect formation in the atomic structure is often observed since the curvature of these structures is extremely high. For example, a possible defect in a sp^2-hybridized carbon nanomaterial could be a pentagonal carbon bonding (instead of hexagonal), a crystal boundary in polycrystalline graphite or simply dangling bonds of the aromatic system [58]. Specifically, the pentagonal defects are often needed in order to form closed spherical or tube-like morphologies in the nanometer scale.

Since carbon can exist in a vast variety of different configurations, new nano-carbon modifications are constantly being discovered and the same modification is sometimes given different names by different works for different applications, which indeed makes it hard to compare the modifications in an objective way [59]. A general overview about carbon nanomaterials is given by Gogotsi and Presser [31].

However, for tribological applications and thus the intended use in this dissertation, 0-D or 1-D carbon nanoparticles (CNP) in particular have been highlighted in recent years, providing promising

properties to act as solid lubricants in mechanically loaded contacts. This fact is mainly due to their morphology (spheroidal or tubular shape) and their high chemical and mechanical stability, which is why they are often said to potentially act as nano ball- or roller bearings [31,34,60]. Nonetheless, since this hypothesis has not yet been thoroughly verified and the potential lubrication mechanisms of the particles are not yet understood, one objective of the present dissertation is the systematic investigation and analysis of these mechanisms.

For this purpose, three different CNP were chosen in order to represent 0-D and 1-D CNP as well as both carbon hybridization states (sp^2 and sp^3). These are nanodiamonds, carbon onions and carbon nanotubes, described in more detail in the following sections.

2.1.1 Nanodiamonds (ND)

Nanodiamonds (ND) are spherical nanoparticles (diameter of typically 2-10 nm) with a predominant sp^3 carbon hybridization and a diamond lattice constant of 0.35 nm. Within their most interesting characteristics, they have shown remarkable biocompatibility, chemical stability, mechanical and optical properties [33]. Although already discovered in the 1960s by a detonation reaction, the interest in these particles did not grow until the beginning of the 1990s [61]. Since then, they have received increasing attention in numerous research fields such as: tribology [62], drug delivery [63], bioimaging [64] or tissue engineering [65].

Nowadays, an abundance of methods is available for their production, including laser ablation [66], high energy ball milling of high pressure, high temperature diamond microcrystals [67] as well as the detonation technique [68]. Since the ND used in this dissertation were synthesized via detonation, this method is described in more detail in the following. The basic atomic structure of a common single nanodiamond particle is shown schematically in ***Fig. 4***.

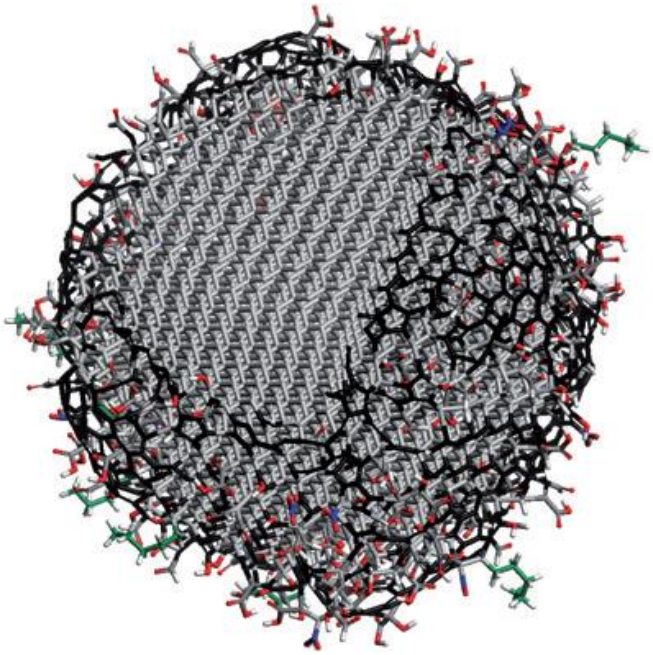

Figure 4: Schematic representation of the most common atomic structure of a single nanodiamond particle. The grey-colored, highly ordered structures correspond to the sp^3-hybridized, diamond carbon bonding. In black, aromatic structures of sp^2-hybridized carbon are visible which terminate the surface of the nanodiamond. Additionally, oxygen- and nitrogen-containing functional groups are depicted (red and blue, respectively) as well as hydrocarbon chains (green) or hydrogen terminations (white) [33].

The grey-colored, highly ordered structures represent the sp^3-hybridized carbon bonding and form the core of the particle. In order to remain stable under ambient conditions, the outer shell of the particle must either be terminated by functional groups (e.g. oxygen- or nitrogen-containing groups) or sp^2-hybridized carbon structures of graphitic or amorphous nature. This becomes evident when looking at the phase diagram of nano-carbon in ***Fig. 5 (a)***, which can also be used as starting point for explaining the basic principle of detonation synthesis.

The phase diagram shows that the most stable phase of carbon under standard pressure and temperature is graphite, which becomes even more significant for nanoscale carbon as indicated with the blue lines. For detonation synthesis, explosives with a negative oxygen balance (e.g. a mixture of trinitrotoluol (TNT) and hexogen) are detonated within a closed chamber containing N_2, CO_2 and H_2O. The generated shock wave leads to a raise in pressure and temperature, reaching the *Jouguet* point (point A in ***Fig. 5 (a)*** or red dashed line in ***Fig. 5 (b)***) and to the formation of liquid nano-carbon as also schematically illustrated in areas III to VI of ***Fig. 5 (b)*** [69].

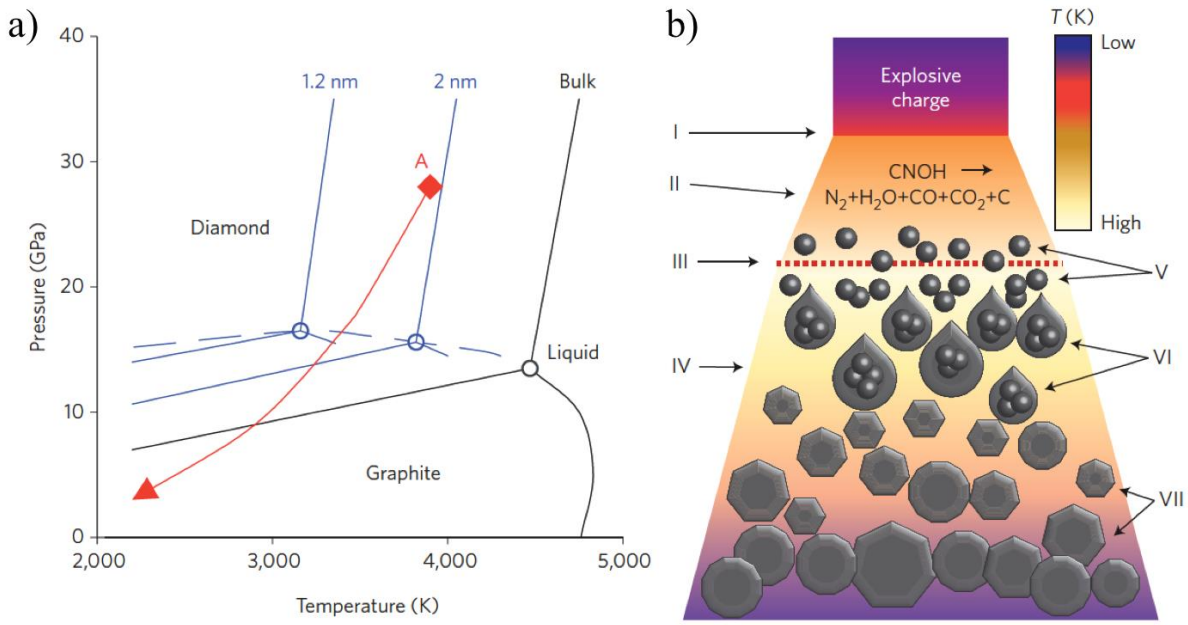

Figure 5: a) Phase diagram of carbon as a function of pressure and temperature with blue lines inserted for nanomaterials. b) Scheme of the shock wave evolution in the detonation synthesis of nanodiamonds, showing (I) shock wave front, (II) zone of chemical reaction, (III) *Chapman-Jougout* plane (corresponding to point A in the phase diagram, (IV and V) detonation products, (VI) formation of liquid droplets and finally, (VII) crystallization process towards the formation of nanodiamonds [33].

With decreasing temperature and pressure, the liquid carbon solidifies and crystallizes into highly ordered diamond structures until reaching the diamond-graphite equilibrium line, from which the termination of the diamond shell with graphitic structures starts to occur [33]. Subsequently, the formed detonation soot must be purified by liquid oxidants (e.g. HNO_3, HCl) or oxidized in air at elevated temperatures in order to remove non-carbonaceous impurities [69,70].

With regard to the predominant sp^3 carbon core hybridization, ND inherits most of its properties from the well-known macroscale diamond with a Young's modulus of 1000 GPa, a Vickers hardness of 10000 HV and a thermal conductivity of 2200 W m^{-1} K^{-1} [71]. Nevertheless, the surface of a ND, which is enclosed by sp^2-hybridized carbon and functional groups, can be further chemically functionalized in several different ways, resulting in a wide range of potential applications for ND [72]. For further information, an extensive overview of the structure, properties and applications of ND is given by Mochalin et al. [33].

2.1.2 Onion-like carbon (OLC)

Onion-like carbon, also called carbon onions, are spheroidal, fullerene-like carbon nanoparticles (diameter of typically 5-10 nm), possessing a concentric, multi-shell configuration with an equilibrium interlayer spacing of 0.34 nm and predominant sp^2 carbon hybridization (***Fig. 6***) [73,74]. Typically, these structures are highly defective, since hexagonal (aromatic) carbon bonding is not

enough to build a closed, spherical carbon shell. Main features of OLC are their high mechanical stability [31], very large surface area as well as high electrical conductivity (2-4 S cm^{-1}) [73,75].

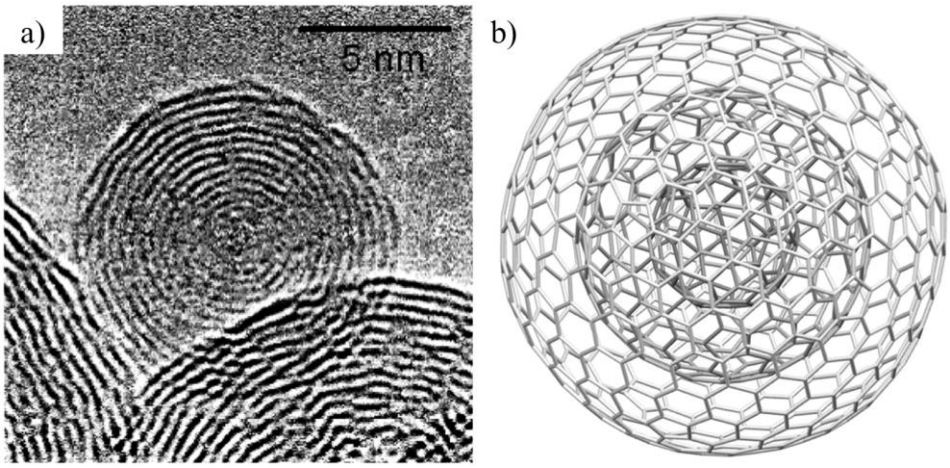

Figure 6: a) Transmission electron micrograph of OLC, presenting the layered, onion-like morphology of the particle. b) Schematic of a defect-free, single OLC particle, showing the typical aromatic carbon multi-shell structure of sp^2-hybridized carbon rings [74].

S. Iijima first discovered carbon onions in 1980 as a byproduct of carbon black synthesis [76]. 12 years later, D. Ugarte was able to observe and understand the formation of OLC in situ by focusing an electron beam on carbon soot [77]. Since then, OLC were investigated for various potential applications ranging from tribology [36], over bioimaging [78] to batteries [79] and supercapacitors [73]. Despite other methods for OLC synthesis (e.g. arc discharge of graphite in liquids [80] or combustion of naphthalene [81] and many more), vacuum and inert gas annealing of nanodiamond precursors have turned out to be the most extended approaches of large scale OLC production nowadays [75,82]. Generally, the type of precursor and the synthesis conditions strongly influence the final OLC morphology and size (up to 100 nm in diameter possible). However, using the thermal annealing technique, very high purity OLC with typical sizes between 5 to 10 nm (high material homogeneity) are achieved at a relatively low price [73]. Since the OLC used in this dissertation were produced using this technique, the basic thermally induced transformation process of ND towards OLC is depicted in ***Fig. 7***.

The annealing process of ND allows for the precise tuning of the carbon sp^2 to sp^3-hybridization ratio as a function of the temperature. The transformation of a ND begins at the outer shell of the particle and continues stepwise to the particle core. At first, desorption of water and detachment of oxygen-containing functional groups on the ND surface are observed for temperatures up to 200°C [83]. This is followed by the detachment of surface functional groups and the subsequent emission of CO and CO_2, which leads to the formation and subsequent recombination of dangling bonds, thus starting to form the typical sp^2 related π-bonds at around 700-800°C.

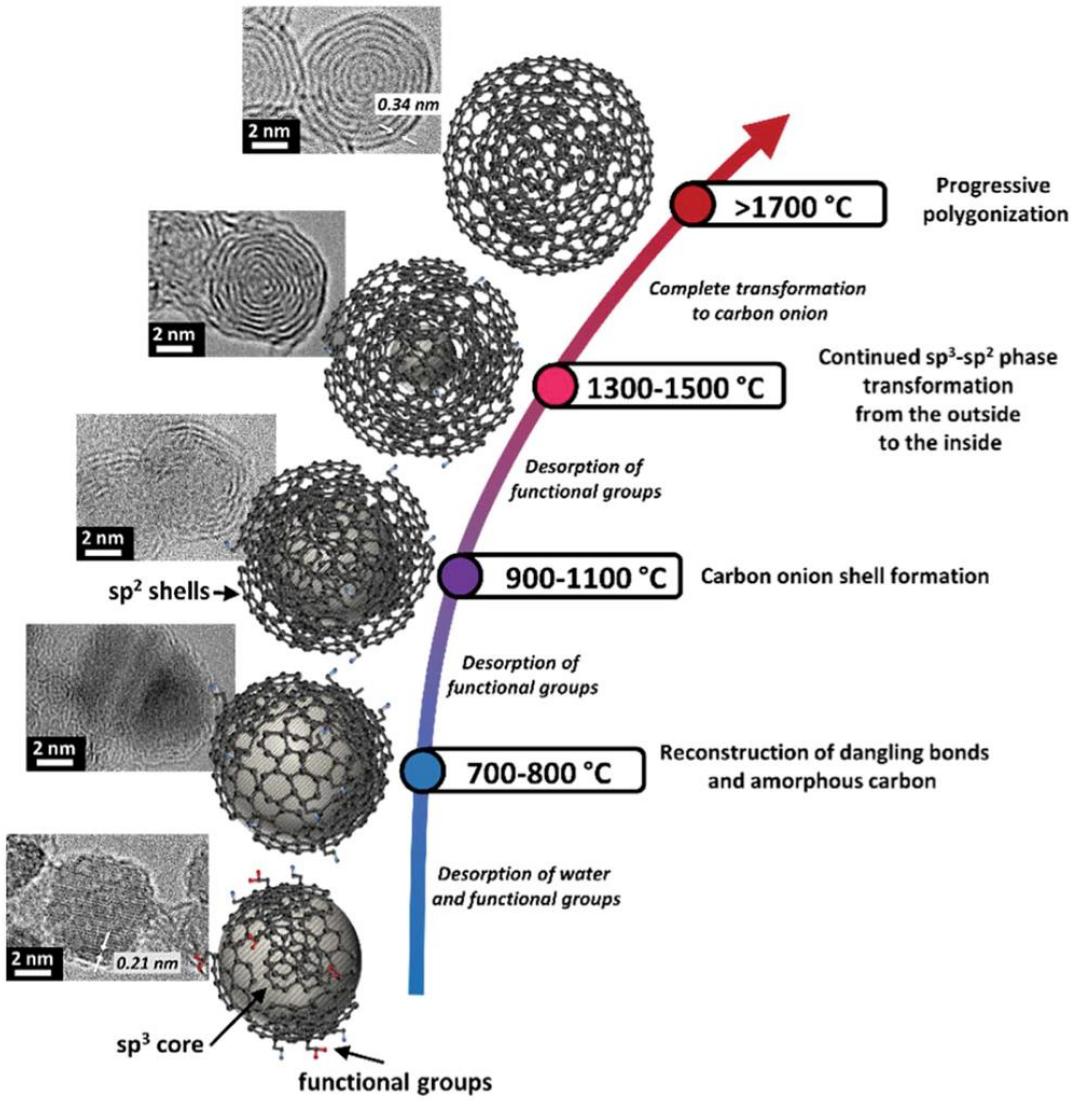

Figure 7: Schematic transformation process of ND to OLC as a function of temperature with corresponding TEM micrographs exemplifying the transformation stages. Variations in the individual stages can occur since the transformation process also depends on the used environmental conditions (inert gas or vacuum) and the nanodiamond precursor size [73,84].

Graphitization of the ND proceeds with increasing temperature, still providing a diamond inner core, until finally fully transformed and highly ordered carbon onions are built at temperatures higher than 1700°C [85,86]. This is due to the fact that the high stability of the inner diamond core is usually associated to the buildup of internal pressure, as a consequence of the atomic rearrangement of the outer shell. During this process, the volume of the particles is enlarged with ND and OLC providing a density of 3.3 g cm^{-3} and 1.9 g cm^{-3}, respectively. Since OLC are closed, mainly sp^2-hybridized carbon structures, it is believed that they possess very high mechanical strength [31,36]. For more detailed information on OLC synthesis and applications, please refer to the review articles of Bartelmess et al. [75] or Zeiger et al. [73].

2.1.3 Carbon nanotubes (CNT)

Carbon nanotubes were discovered by Iijima [48] in 1991 and have experienced an increasing interest in research since then. CNTs are tube-like CNP with a very high aspect ratio (tube length to diameter ratio, roughly in the range of 1000/1), consisting of highly crystalline sp^2-hybridized aromatic carbon rings. Morphologically, a CNT can be imagined as a rolled graphene layer forming a hollow cylinder with half fullerenes capping the ends [87]. Theoretically, the particles possess superior mechanical, thermal, and electrical properties and found numerous potential applications such as in tribology, for structural composites, energy transfer and storage [31,88–91].

Generally, one can distinguish between a single-wall CNT (SWCNT) and a multi-wall CNT (MWCNT). A schematic is given in ***Fig. 8***.

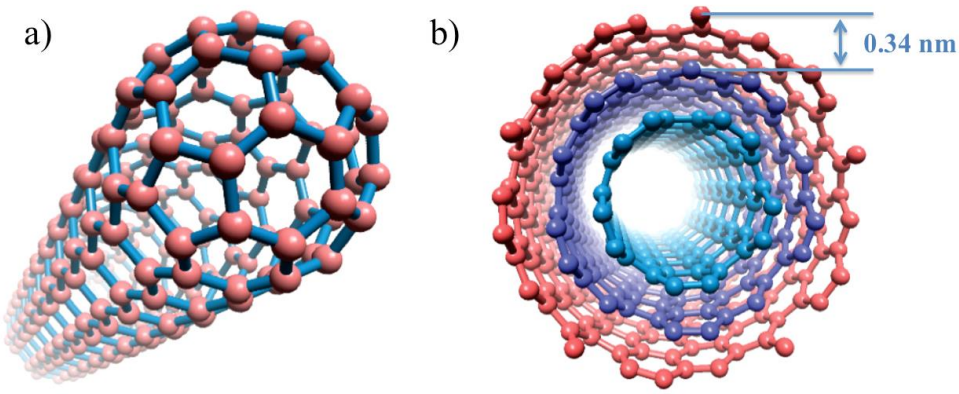

Figure 8: Schematic of a) single-wall CNT and b) multi-wall CNT with an intertubular lattice spacing of 0.34 nm. Modified from [92].

MWCNT consist of several concentrically arranged SWCNT with an equilibrium interlayer distance of around 0.34 nm [93]. The resulting diameter of a MWCNT is a function of the number of walls and typically ranges from 5-100 nm [94]. The physical properties of different CNT can vary significantly, which is why their atomic structure has to be considered in more detail. A graphene layer could be "rolled" in different ways, resulting in a wide variety of CNT chiralities. The chirality map (**Fig. 9**) is based on a planar graphene sheet with hexagonally bonded carbon atoms. Due to the system's symmetry, a 30° wedge of possible different rolling directions can be defined. Within this wedge, a chiral vector C_h is given as a multiple (n,m) of two unit directions (a_1, a_2) of the hexagonal cells. It connects the origin atom with another atom, defining the connection point of the rolled graphene sheet and thus the chirality of the CNT. With its vector norm, the circumference of the tube is given as well. The normal of this vector is the tube-axis T and the tube diameter d_t can be geometrically calculated, assuming that the tube is perfectly round [87].

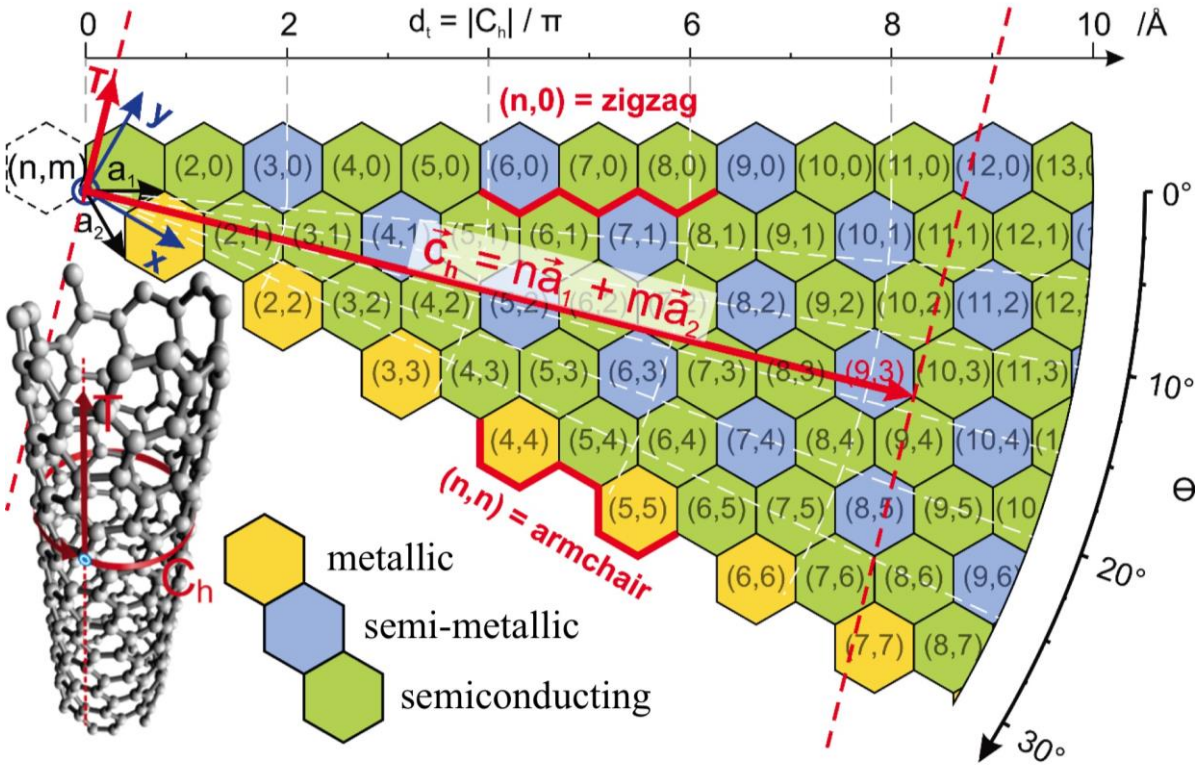

Figure 9: A chirality map is shown, presenting a 30° wedge of a graphene sheet. The chiral vector C_h with the coordinate system being described by the unit vectors (a_1, a_2), the tube axis T and the tube diameter d_t are presented and schematically illustrated. A color coding describes the electrical behavior of the SWCNT as a function of the integers of C_h [92].

Derived from this chirality map, three principal configurations can be distinguished: A "zigzag" configuration is given for (n, 0), an n=m configuration is called "armchair" and anything in between the two is denoted "chiral". It is found that the properties of the SWCNT, for example the electronic properties (metallic, semi-metallic or semiconducting) are strongly related to their chiral vector [95].

The physical properties of SWCNT compared to MWCNT also differ significantly. Although no consensus has been reported in the literature, both can show a remarkable Young's modulus of up to 1 TPa [96]. However, the axial tensile strength or thermal conductivity, for example, reach values of 20-30 GPa and 6600 W m^{-1} K^{-1} for SWCNT and 150 GPa and 3000 W m^{-1} K^{-1} for MWCNT, respectively [97–100]. In this context, CNT are known to provide extraordinarily high specific stiffness and strength (Young's modulus or strength normalized by the density, respectively), resulting in a lightweight material, but possessing better mechanical properties than any structural material used nowadays. This is related to the presence of axial σ-bonds, regarded as the strongest bonds in nature [101]. Furthermore, a CNT can be bent and coiled without breaking, additionally allowing for almost full elastic restoration [102]. These properties make CNT particularly attractive as a reinforcing phase in composite materials with the aim of transferring their intrinsic properties to a macroscopic material.

Nevertheless, these outstanding physical properties described in literature would only be realizable for CNT in a "perfect" structural s well as deagglomerated state. This means that no structural defects in the carbon lattice and no exo- or endohedral contaminants should be present. Furthermore, it is well known that CNT tend to form large agglomerates of multiple entangled tubes due to their large aspect ratio and strong electromagnetic interactions. These interactions are caused by the delocalized π electron clouds, which allow for the spontaneous formation of dipoles and thus attractive Van der Waals forces. All of these requirements have been very challenging in CNT synthesis and processing during the last decades [103].

Regarding the CNT synthesis, the most commonly used methods are chemical vapor deposition (CVD), arc discharge and laser ablation [104,105]. Among those, CVD synthesis can be easily scaled to industrial quantities and provides good control over the morphology of the obtained CNT. The MWCNT that have been used in the present dissertation were produced by CVD, and thus this specific synthesis method is described in more detail. The CNT growth mechanisms in a CVD synthesis process are presented schematically in ***Fig. 10***.

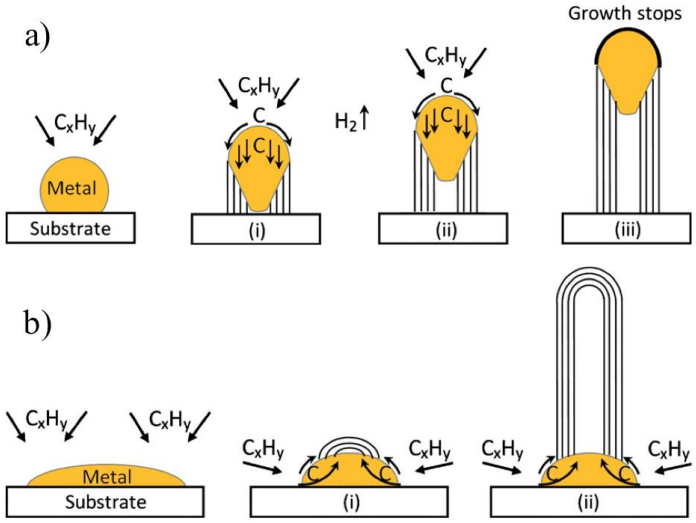

Figure 10: Growth mechanism of CNT in a CVD process showing a) the tip-growth model and b) the base growth model at different stages [106].

CVD, particularly catalytic CVD, is usually done in a fluidized bed with organometallics as catalysts (e.g. ferrocene) [107–109] or by thermal decomposition of a hydrocarbon gas (e.g. methane, ethylene, benzene) in the presence of a metal catalyst (e.g. Ni, Co, Fe). In the second case, a hydrocarbon gas (C_xH_x in ***Fig. 10***) is passed through a reactor containing a heated metal catalyst (600-1200°C) on which CNT start to grow. As soon as the hydrocarbon vapor gets in contact with the hot metal catalyst, it decomposes into carbon and hydrogen with carbon subsequently being dissolved into the metal. After reaching the carbon solubility limit (or even beyond that limit), carbon precipitates are formed, crystallizing to a cylindrical network with no dangling bonds. The interplay of exothermal decomposition of hydrocarbon and endothermal carbon crystallization keeps the process running.

Two basic models are distinguished, depending on the metal catalyst to substrate material interaction. If the interaction is weak, carbon diffuses to the bottom of the catalyst where it crystallizes and pushes the metal particle off the substrate. This process continues until the top surface of the particle is fully covered with excess carbon. This model is called "tip-growth model" and is schematically presented in ***Fig 10 (a)***. In the case of the second model, the "base growth model" (***Fig. 10 (b)***), the catalyst-substrate interaction is strong, thus the crystallizing carbon growth on top of the metal particle, first forming a hemispherical dome which is then extended with the form of a graphitic cylinder. Both, SWCNT as well as MWCNT can be produced using this method, mainly depending on the metal catalyst particle size and type. For example, for very small particles (few tens of nm in diameter), SWCNT formation is expected whereas for larger particles, MWCNT formation is favored. However, CNT synthesis depends on many more parameters such as the used hydrocarbon, catalyst, pressure, temperature, gas-flow rate, deposition time and reactor geometry. A good overview of CVD synthesis of CNT is given by Kumar et al. [106], whereas a general introduction towards other synthesis methods is provided by Mubarak et al [110].

2.1.4 Raman spectroscopy characterization of CNP

After having introduced different CNP, it becomes evident that their atomic structure and morphology is the key to their physical properties. Hence, characterizing these features is essential when processing the particles to use them for a specific application. Various techniques have been proposed to characterize CNP (e.g. X-ray photoelectron spectroscopy (XPS), transmission electron microscopy (TEM), etc.) [87]. Even though all of these methods are very useful and irreplaceable tools in their particular way, one quick but still precise method for advanced CNP characterization stands out: Raman spectroscopy [111]. However, the intention of the following section is not to introduce Raman spectroscopy as a method, but rather to give a short introduction to the state of the art in using this technique for characterization of sp^2 and sp^3 carbon structures. For a more general approach and an introduction to Raman spectroscopy, please refer to Gardiner and Graves [112].

In Raman spectroscopy, excitation of the atomic structures is typically done with a monochromatic light source (laser) of specific known energy (wavelength). This being said, the first difference between sp^2- and sp^3-hybridized carbon structures must be discussed, which is that sp^2 domains with their characteristic π-bonding are up to 230 times more sensitive to visible light excitation compared to those with sp^3 hybridization [113–115]. This has been related to differences in the Raman cross-sections based on calculations of Loudon [116]. An ultraviolet (UV)-laser with a wavelength of 244 nm produces a radiation energy of 5.08 eV, which is close to the energy band gap between electronic states of the σ bonds, for example in diamond (5.47 eV). This fact allows for near-resonance conditions, which enhance the Raman signal [114]. In contrast, green laser light (wavelength of 514.5 nm) produces a radiation energy of only 2.41 eV, being far from resonance.

Analyzing an sp^2-hybridized nano-graphite sample using a green laser and looking at its typical Raman spectrum in ***Fig. 11***, the main characteristic bands of graphitic carbon can be found. These Raman bands are the so-called D, G, D' and G' band [117].

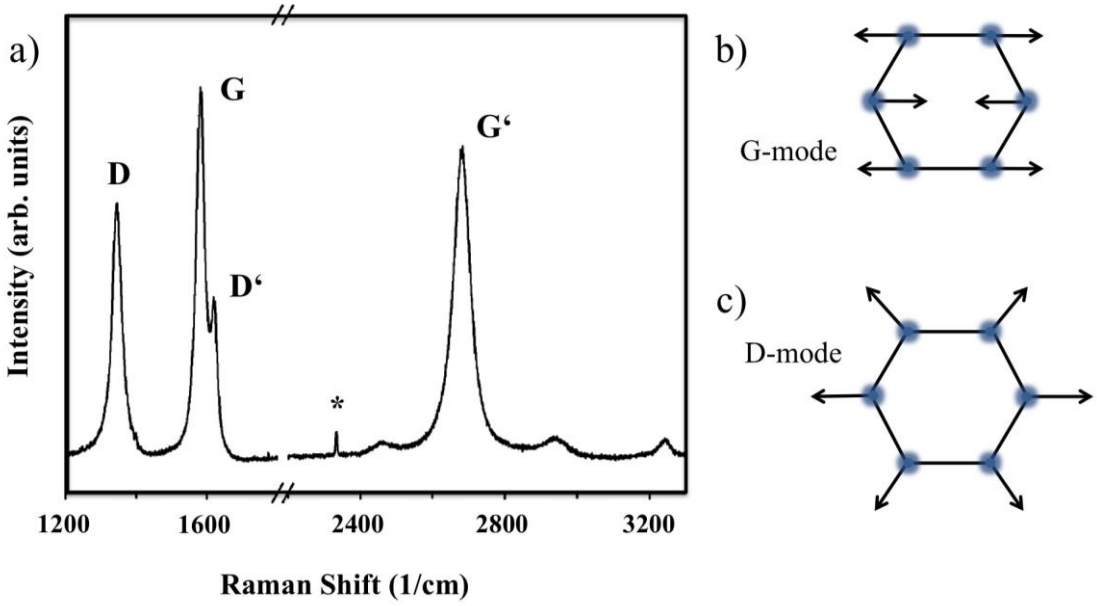

Figure 11: a) Raman spectrum of a nano-graphite sample including the main characteristic peaks for a Raman analysis of graphitic carbon (except for *, which is a Raman mode of N_2 gas and was present recording the spectrum). The excitation wavelength was 514.5 nm. Furthermore, schematics illustrating the vibrational modes of the carbon lattice corresponding to b) the G-mode and c) the D-mode are added. Modified from [115,117].

Starting off with the most pronounced peak in ***Fig. 11 (a)***, the **G-band** at around 1580 cm^{-1} is the most representative band for sp^2-hybridized carbon structures. If this peak is observed, sp^2 carbon networks are present. The G-band is generated by tangential vibrations of sp^2 carbon atom chains, not requiring the presence of six fold carbon rings (***Fig. 11 (b)***) and its width can be used to describe the degree of crystallinity of the sample [58,118]. However, nearly all graphite materials show some defects. Thus, the **D-band** (1350 cm^{-1}) as well as the **D'-band** (1620 cm^{-1}) are assigned to the presence of disorder. The intensity of the D-peak can be attributed to the number of defects or impurities whereas its width is correlated to the variety of impurities present [119]. The D-band arises by radial breathing of the hexagonal carbon lattice (***Fig. 11 (c)***), which is forbidden in a perfect single crystal graphitic lattice and only becomes active in the presence of disorder [115].

The peak with the second highest intensity in ***Fig. 11 (a)*** corresponds to the **G'-band** and is found at around 2700 cm^{-1}. It originates from a two-phonon, second order scattering process, the name being misleading as it is not related to the G band, but is a harmonic of the D-band [120]. Although related to the D-band, it is insensitive to defects of the graphitic structure and indicative for the long-range order of the structures. This is evident as with less ordering of the structure, coupling of the atoms

ceases, which would be necessary for a two-phonon process [120]. Thus, highly crystalline carbon structures with long-range order typically show a very pronounced G'-band intensity.

Other peaks (e.g. RBM, LA, LO etc.) also contribute to the Raman spectra of certain graphitic structures and allow for their distinction [119]. However, the above-mentioned are present for sp^2 carbon structures and are thus commonly used for their structural integrity assessment (quality control). For a more in-depth analysis of all the bands and modes involved in the Raman spectrum of graphitic carbon, please refer to Dresselhaus et al. [119] and Pimenta et al. [117]

Since Raman spectroscopy is a volume-sensitive technique, absolute intensities must not be used for a quantitative comparison. Instead, intensity ratios, such as the I_D/I_G, or the $I_{G'}/I_D$ ratio are widely accepted with the first one known as the defect index and the latter one as purity index. In this regard, the intensity ratios of the maximum peak intensities or the ratios of the integral peak intensity may be used. In the case of using the integral peak intensity, the full width at half maximum (FWHM) of the peaks, being related to the crystallinity of the analyzed graphitic carbon structure [85], is included in the analysis. A lower FWHM typically means that a higher crystallinity of the carbon structure is present, since the energy differences of the resonance are small [121]. However, both approaches regarding the evaluation of intensity ratios for a Raman analysis of carbon structures are accepted in literature and provide the same tendencies [50].

The defect index (whether determined by maximum intensity or integral intensity ratio) is associated with the amount and density of structural defects in the graphitic lattice. The early work of Tuinstra and König [122] in 1970 already noticed the inverse proportional correlation of the defect index and the crystal domain size L_a. However, 36 years later, it was the work of Cançado et al. [123] providing a general equation for a quantitative correlation of these parameters as a function of the used laser excitation wavelength (see equation 1). Using this equation, the coherent diffraction domain size/mean defect-to-defect distance can be calculated.

$$L_a = (2.4 \cdot 10^{-10})\lambda_{laser}^4 \cdot \left(\frac{I_D}{I_G}\right)^{-1} \quad (1)$$

Regarding the purity index, DiLeo et al. [120] were the first to come up with a quantification of the purity of MWCNT based on the $I_{G'}/I_D$ intensity ratio. They used Raman spectroscopy to measure previously prepared MWCNT containing varying, known amounts of carbonaceous by-products, successively decreasing the MWCNT purity. The correlation of the intensity ratios I_D/I_G, $I_{G'}/I_G$ and $I_{G'}/I_D$ showed, that the $I_{G'}/I_D$ ratio is in very close correlation to the purity level of the measured MWCNT and thus, a purity quantification using this ratio became possible. Other works also refer to the mentioned intensity ratios, such as the work of Ferrari and Robertson [115]. They proposed a three-stage phenomenological amorphization trajectory model, describing the degradation of highly crystalline graphitic carbon towards amorphous carbon. The model is based on an interpretation of the defect index but also on the wavenumber of the G-band position (X_{CG}), as shown in ***Fig. 12***.

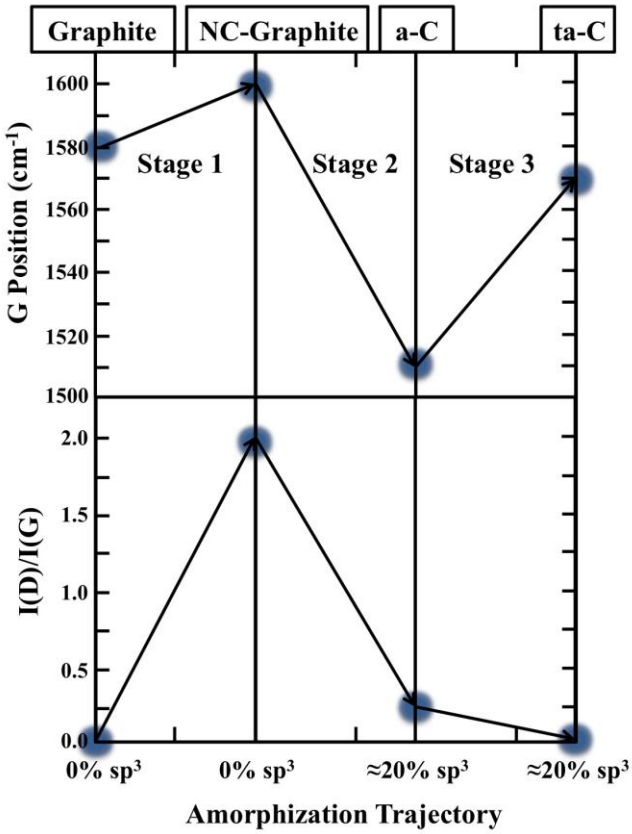

Figure 12: Phenomenological three-stage amorphization model of crystalline graphite towards tetrahedral amorphous carbon. The model also allows for a quantification of sp^3 carbon as a function of the defect index and the G-band position. First, nanocrystalline graphite is formed before the amorphization towards amorphous carbon (a-C) and finally tetragonal amorphous carbon (ta-C) proceeds. Modified from [115].

It was observed, that the G-band shift in highly crystalline graphite derives from the appearance of the disorder-induced D'-band at 1620 cm^{-1}, which convolutes with the G peak for small crystallites. Fitting of the G-peak thus results in a net increase in the G-band position. With the defect index vastly increasing at the same time, it is concluded, that a transition from monocrystalline to polycrystalline structures occurs [115].

In stage two, X_{CG} decreases from 1600 cm^{-1} to 1510 cm^{-1} with the defect index approaching a value of 0 at the same time, indicating strongly distortional carbon structures providing no long-range order. Hence this stage represents the transition from nanocrystalline graphite to amorphous, mainly sp^2 carbon structures. In stage 3, passing from a-C (amorphous carbon) to ta-C (tetragonal amorphous carbon) involves a rise in sp^3 content from 10–20 % to 85 % and a gradual change of carbon hexagonal rings to tetragonal chains [115].

With regard to CNP, for high purity, highly crystalline CNT, the above-described methods can be used for a structural characterization. Detailed analysis and explanation of all the Raman peaks in the spectrum of CNT can be found in Dresselhaus et al. [119]. In contrast to CNT, OLC are already highly

defective in their pristine state. Additionally, with the particles being only 5 – 10 nm in size, analyzing long-range order of graphitic carbon networks indeed becomes non-trivial. Nonetheless, since OLC are derived from ND, large amounts of information can be derived when analyzing the structural transformation process of ND to OLC using Raman spectroscopy [33].

The transformation process was analyzed using Raman spectroscopy by Cebik et al. [50] and is found in ***Fig. 13***.

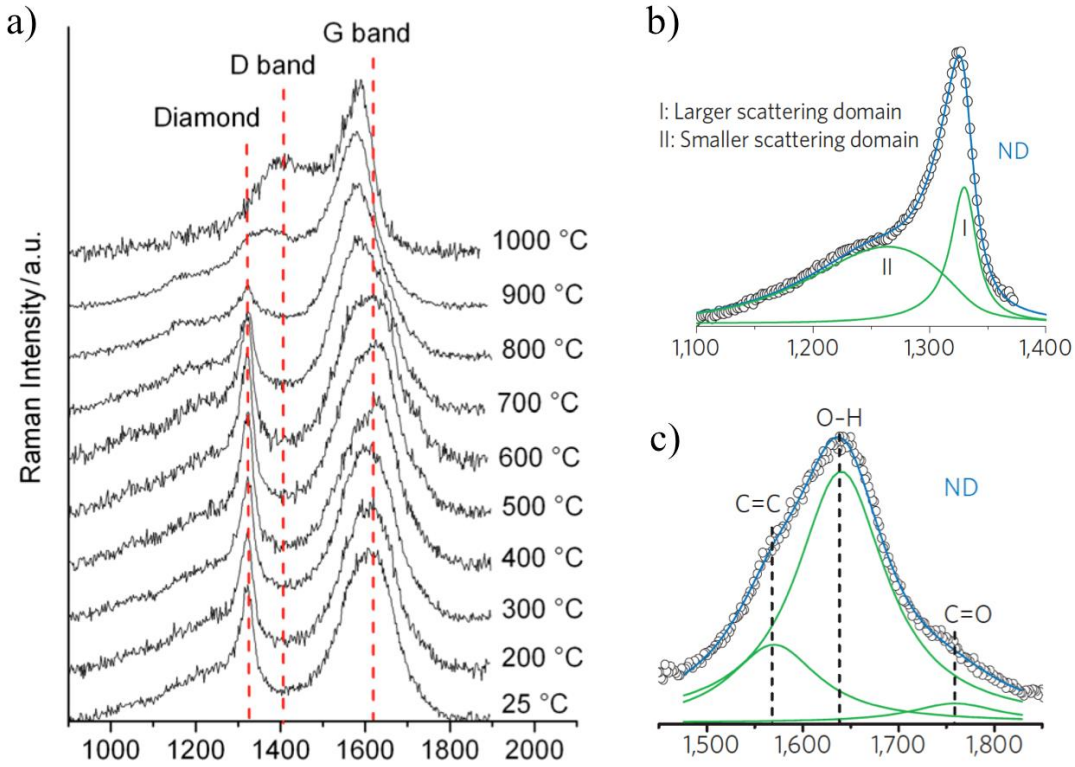

Figure 13: a) Raman spectra of the transformation process from ND to OLC as a function of the annealing temperature from room temperature to 1000°C (recorded with a UV laser excitation of 325 nm). b) Diamond-band and c) G-band deconvolution for ND particles [33,50].

The typical Raman spectrum of ND (measured using UV-excitation) as well as a deconvolution of its peaks is shown in ***Fig. 13 (b)*** and ***(c)***. The diamond peak is found at around 1330 cm^{-1} and is derived from large domain scattering. It is overlapped with a second broad peak at 1250 cm^{-1}, which is assigned to partially crystalline or even amorphous diamond, concurring with a short-range order scattering type of Raman mode [124–126]. Thus, the peaks are related to a signal combination of large and small domain scattering, respectively [33]. Due to this convolution, the absolute position of the diamond peak can be used to estimate diamond crystal sizes [50]. Furthermore, with decreasing crystallite size and increasing content of non-diamond phases, the full width at half maximum (FWHM) of the diamond peak increases [127].

Generally, Raman features above 1360 cm^{-1} cannot be due to C-C sp^3 vibrations [50]. The shifted G-band position at 1640 cm^{-1} in ***Fig. 13 (c)*** is explained by the combination of three peaks. The first one can be identified as the sp^2 carbon derived G-band at 1580 cm^{-1}. The higher wavenumber peaks

are usually observed in UV Raman spectra of amorphous carbon containing a high concentration of carbon atoms with tetrahedral bonding [114]. These two bands provide wavenumbers too high for one-phonon scattering in carbon materials, thus they are assigned to functional O-H groups and to stretching vibrations of carbonyl C=O groups, which are attached to the ND surface, derived from detonation synthesis [33,114,128]. Further smaller peaks in the Raman spectrum of ND can be observed and are discussed in more detail in Cebik et al [50].

With increasing annealing temperature up to 1000 °C, a transformation from sp^3 to sp^2 carbon hybridization is noticeable in the Raman spectra in ***Fig 13 (a)***. The number of atoms of a 0-D particle increases strongly with its diameter. Hence, the Raman signal coming from the outer shell should be the strongest and dominate the spectrum. As the transformation of ND to OLC starts at the outer shell of the particle, this results in a high sensitivity for the transformation process using Raman spectroscopy. At 600-1000 °C, the described up-shifted G-peak of ND starts to decrease to lower wavenumbers and an additional peak at around 1400 cm^{-1} is formed. This peak can be assigned to an up-shifted defect-induced D-band of OLC. Annealing ND at higher temperature involves purification of the particles, which explains the decreasing wavenumber of the G-band, since surface functional groups are detached and the typical sp^2 carbon G-band at around 1580-1600 cm^{-1} is obtained.

All the discussed information in this chapter is useful to understand the degradation mechanisms of CNP in a tribological contact and thus, Raman spectroscopy is considered a key technique of the present dissertation.

2.2 Metal matrix composites (MMC)

Composite materials are defined as a combination of at least two materials that exhibit chemical, physical or morphological differences. The combined materials must not dissolve into each other and thus form an interface. Furthermore, it is expected that their combination results in a synergetic effect, named the composite effect [129].

In MMC, the matrix is usually the phase with the largest volume content, providing ductility as well as load transfer to the reinforcement phase. The reinforcement phase usually has certain desirable physical properties (e.g. stiffness, electrical conductivity etc.), which, however, cannot be taken advantage of separately. By introducing this phase into the matrix, these properties can at least partially be transferred to the composite and thus be integrated into a technically usable system [129].

The material class of MMC can be sub-classified, considering the type and contribution of reinforcement components, into particle-, fiber- and layer composite materials (***Fig. 14***). With regard to fiber composite materials a distinction between continuous fiber composite materials (multi- and monofilament) and short fibers or whisker composite materials is made [23].

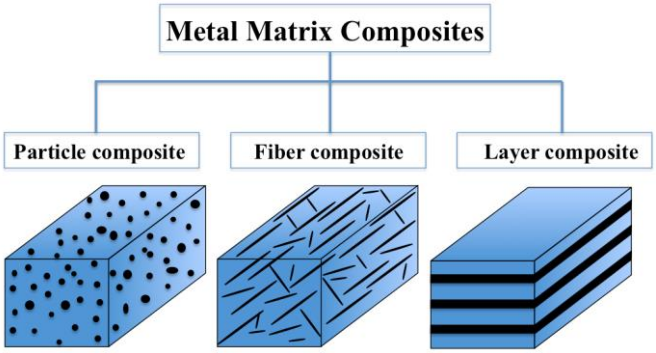

Figure 14: Basic classification of MMC

The properties of MMC can be designed so as to fit the requirements of the intended application (e.g. light weight but high strength). They are often employed as structural and functional materials such as fiber reinforced pistons, aluminum crankcases with strengthened cylinder surfaces or particle strengthened brake discs, in the automotive or aerospace sectors. MMC are also broadly found in other application fields such as magnetic materials, electronics or wear-resistant sliding contact materials [23–25].

The latter was chosen in the present thesis, as it offers the possibility to transfer promising physical properties of the reinforcement phase to a machineable, macroscopic material [130]. Since CNP provide promising properties to act as solid lubricant, their use as reinforcement phase in MMC in order to produce a self-lubricating system is a logical consequence. Self-lubricating composites in general have been around for many years and find applications for example in bearings and piston or cylinder liners in engines. These composites are developing into an important class of tribological

materials and offer new ways to combat friction and wear under extreme conditions [21]. However, despite the selection of a matrix and reinforcing material, processing parameters must also be chosen carefully so as to achieve the desired composite properties. This is due to the fact that the properties strongly depend on the microstructure and density of the composite as well as the formation of interphases, partially tunable by simple variables. The typical methods involved in MMC production will therefore be discussed in the following section.

2.2.1 Blending, processing and microstructural tailoring

There is an overwhelming wealth of literature and publications on the processing of MMC with different reinforcement phases and matrix materials. So, to keep the focus on the present dissertation, only the blending and processing of CNP-reinforced MMC are considered in this chapter. In this regard, only solid-state processing (powder metallurgy) has to be covered, since liquid-state processing is typically not used to produce CNP-reinforced MMC.

CNP are typically present in agglomerated form when purchased or produced, resulting from molecular, electrostatic interdependencies such as Van-der-Waals or dipole-dipole interactions. Hence, the CNP must be dispersed before being blended with the metal powder, which can be done in different ways. Those methods include dipping, nanoscale dispersion processing, magnetic stirring, layer stacking, colloidal mixing, molecular-level mixing, friction stir processing, ball milling, roller mixing and others [121,131–140]. Out of those, the three most common can be described in more detail: molecular level mixing, ball milling and colloidal mixing.

Molecular level mixing

This method involves functionalizing the CNP with surface functional groups (e.g. –OH, -COOH etc.) in order to be able to decorate them with metal ions. This is typically done by acid treatment of the particles [141]. Subsequently, CNP are dispersed in a solvent and a metal salt as well as reducing agent is added so as to form metal oxides on the CNP surface, with the functional surface groups acting as nucleation centers (***Fig 15 (a)*** and ***(b)***). After this, the powder is calcinated and reduced (e.g. in a hydrogen atmosphere), leading to a full encapsulation of the CNP by the reduced metal (***Fig 15 (c)*** and ***(d)***).

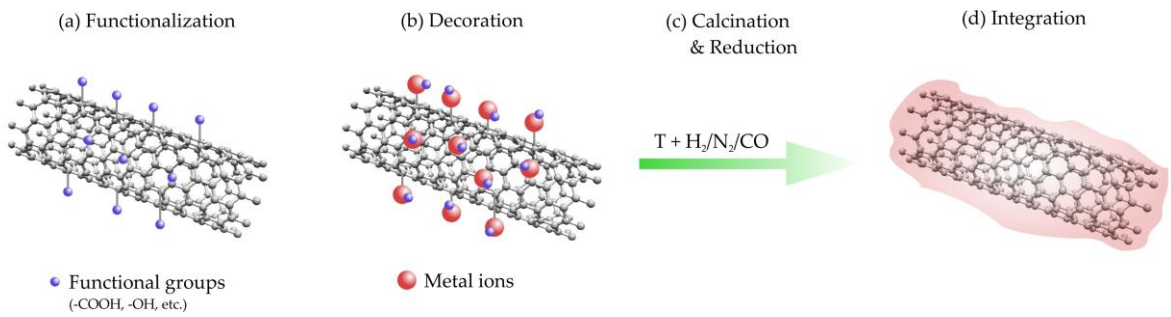

Figure 15: Schematic of the molecular-level mixing method in the case of CNT. a) Functionalization and b) metal oxide decoration followed by c) calcination and reduction leading to metal encapsulated CNT in d) [103].

Due to the full encapsulation of the particles, a very homogeneous interface is formed and CNP reagglomeration is prevented, resulting in a very good mixing of the metallic phase and the CNP. This method is often used in applications where a good interfacial bonding is critical. However, since the method involves particle functionalization, covalent bonds of the CNP are broken, significantly diminishing their outstanding physical properties[37,103,142–146].

Ball milling

In this method, CNP, the metal powder and hard balls (e.g. hardened steel) are filled in a planetary or attrition ball mill, rotating with a defined speed (***Fig. 16 (a)***).

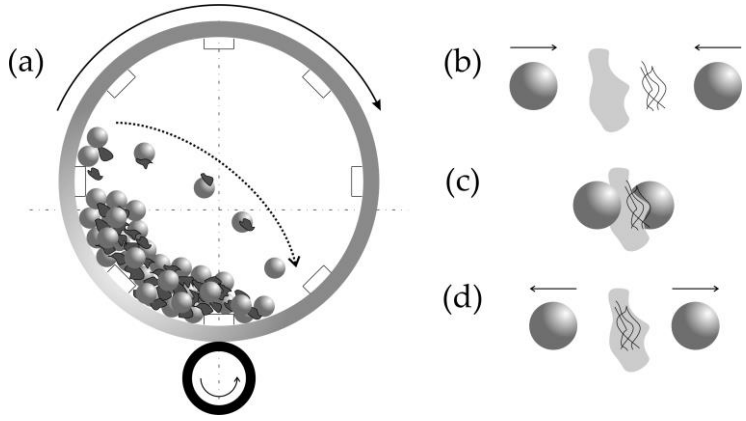

Figure 16: a) Schematic of ball milling. Integration process of CNP into the metal particles is shown in b), c) and d) [103].

By rotating the mill, the inserted hard balls collide with the powder, leading to comminution, welding and integration of CNP into the metal particles, as schematically presented in ***Fig. 16 (b) – (d)***. The processing parameters of this method range from the rotational speed, over different balls and powder ratios, ball diameters, atmosphere, and reducing agents, to the mixing time, and determine if the process is considered as high- or low energy ball milling. This difference is made due to the main drawback of this method, which is the degradation of the CNP. Since high pressures (up to 30 GPa [147]) are attained when two balls collide, the CNP can be degraded thus losing their

intrinsic properties to some extent. Nonetheless, this method is widely used and provides a homogeneous distribution of CNP in a metal matrix [103,148–153].

Colloidal mixing

Disaggregated CNP can be mixed with the metal particles in a solvent, usually with ultrasonic agitation or shear mixing as illustrated in ***Fig. 17 (a)*** and ***(b)***. The used solvent (e.g. ethylene glycol or Dimethylformamid (DMF)) as well as the CNP surface plays a critical role in the dispersion and stability of the mixture. The surface of CNP is sometimes functionalized in order to stabilize the obtained dispersions, which, however, leads to a deterioration of their intrinsic, physical particle properties. Further information about different solvents, their advantages and limitations regarding this process can be found in Cheng et al. [154].

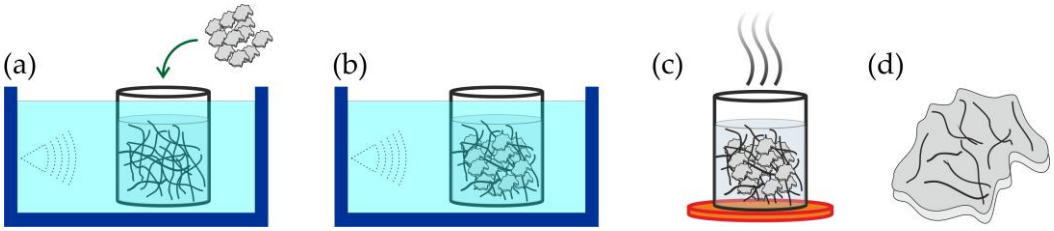

Figure 17: Schema of colloidal mixing. Ultrasonication is used to disaggregate the CNP and metal particles are added (a), followed by a merging of the two phases in the solvent (b). The solvent is evaporated (c) yielding a mixture of CNP and metal powder (d) [103].

Concerning ultrasonication or shear mixing, various works in literature disagree on its positive or negative influence on the structural integrity of the particles. For example, Hilding et al. [155] report about the breaking and shortening of CNT as a function of time in an ultrasonic bath. Hence, using this method, a careful evaluation of the time and power of the particle dispersion method has to be done in order to avoid damaging the CNP. After disaggregating and mixing the particles, the solvent is usually evaporated and a mixed powder of CNP and metal particles is left [103,156–163].

In contrast to molecular level mixing, colloidal mixing can be done avoiding a functionalization of the particles. Additionally, a lower degradation compared to ball milling is expected thus possibly preserving the physical properties of the particles. For this reason, this colloidal mixing was selected in the present dissertation for mixing CNP and metal particles and a systematic investigation of the dispersion process is provided.

The merged powder, obtained using the methods described above, is then further processed into dense, solid composite materials. This bottom-up process is known as sintering and involves the application of heat and often pressure, for a certain time under a vacuum or inert gas atmosphere. However, a large variety of methods exist and sintering is done by one or a combination of methods,

such as spark plasma sintering (SPS), friction stir processing, hot extrusion, hot uniaxial pressing (HUP), cold pressed sintering (CPS), high pressure torsion (HPT), hot isostatic pressing (HIP) microwave sintering, mechanical alloying or laser engineered net shaping [103]. Before further discussing these methods, a short introduction to the basic sintering mechanisms is given in the following.

The driving force of sintering is the reduction of the total interfacial energy, which is a function of the specific interfacial energy and the total interfacial area, both changing during the sintering process due to the replacement of solid/vapor interfaces with solid/solid interfaces. The sintering process can be divided into three stages, shown in ***Fig. 18***. In general, the sintering rate (densification rate) increases with decreasing particle size and with increasing sintering temperature, pressure and time, among other factors. All of these however, share some general sintering stages.

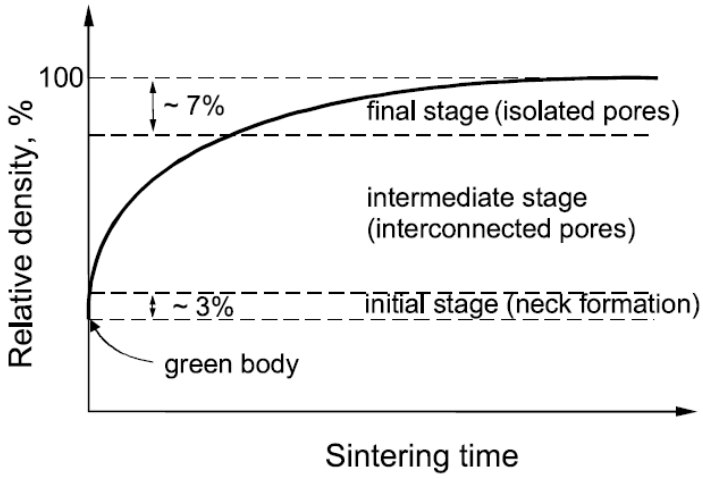

Figure 18: Densification curve of a powder compact, showing the three sintering stages [164].

The first preparation step of the sintering process is often a pre-compaction of the powder at room temperature. During this process, a so-called green body is obtained, providing a geometrical shape close to that of the final composite. As soon as the green body is exposed to a certain threshold temperature (which depends on the melting point of the used metal matrix), the first stage of sintering is reached with the typical "neck formation" observed. This process involves the connection (neck) of the metal particles and is dominated by a lattice diffusion of atoms to the grain boundaries and from the grain boundaries to the neck, thus forming a diffusion path for the material to connect. During this stage, only a 3% increase in relative density of the composite is noted [164].

With the necks being formed, interconnected pores are built, initializing the intermediate sintering stage. During this stage, grain growth is induced and the channel sizes, connecting the individual pores, are reduced, leading to a significant compaction of the composite up to a relative density of 93%.

The final 7 % of densification must be achieved in the final sintering stage. However, it is very hard and time consuming to achieve almost full densification. During this stage, the interconnecting pore channels are closed, resulting in isolation of the pores and the appearance of pressure when pore size shrinking occurs as a consequence of adsorbed gas evaporation at the solid/air interfaces. Thus, the final densification of powder compacts is strongly affected by the sintering atmosphere, since gas is entrapped within the pores. Applying external pressure during this stage significantly helps in achieving higher relative densities of the final sintered composite due to an enhanced creep activity and plastic deformation. Hence, a general distinction is made between pressureless and pressure-assisted sintering techniques. For further information on occurring mechanisms and sintering models, please refer to the book of Kang [164]. Among others, three of the most used techniques, CPS, SPS and HUP, will be discussed in more detail in the following.

Cold Pressed Sintering (CPS)

The CPS process can be easily up scaled, allowing for the production of large quantities of materials. After the powder is filled in a die, the powder is pre-compacted using a cold uniaxial press, producing the green pellet. This pellet is subsequently sintered in a furnace under vacuum or inert atmosphere (***Fig. 19***).

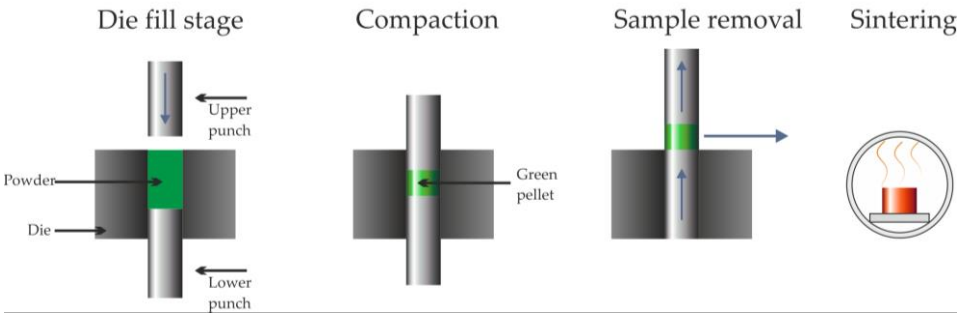

Figure 19: Schematic of CPS, visualizing cold pressing of the green pellet and subsequent pressureless sintering in a furnace [103].

The main drawback of this method is the obtained low densification (usually not more than 93% relative densification). The mechanism is based mainly on lattice and grain boundary diffusion, which does not allow for full densification without the presence of additional pressure or very long sintering times. If pressure is applied, plastic deformation and creeping are added as additional sintering mechanisms thus increasing the driving forces and kinetics of the sintering mechanism. Hence, the sintering temperature and time can be reduced to a significant degree [164].

Spark Plasma Sintering (SPS)

One of the methods involving the use of pressure is SPS. The mixed powder is pre-compressed to a green pellet using graphite punches, whereupon a pulsed DC voltage is applied inducing a high electric current flow, heating and thus sintering the green pellet by Joule heating. During this process, a constant pressure is held. A schematic of this process can be found in ***Fig. 20.***

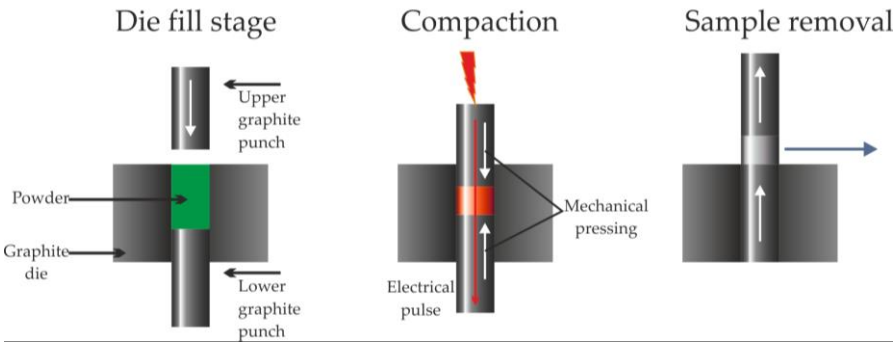

Figure 20: Schematic of SPS, showing pre-compaction of the powder by cold pressing using graphite punches, followed by applying a high current (pulsed electric DC) but keeping the applied pressure. Thus, sintering is performed by electrical resistance heating [103].

The method allows for very fast heating rates (several hundred °C/min) and thus a high sample throughput. However, the maximum pressure that can be generated is limited by the mechanical properties of the graphite punches, typically not withstanding a normal pressure of much more than 80 MPa. Considering the resistance heating used in this technique, large differences in the electric conductivity of reinforcement phase and metal matrix can be a problem and possibly lead to the formation of large pores and no full densification [103]. Despite this, high quality composite materials with very high densification can be produced very quickly.

Hot Uniaxial Pressing (HUP)

In the case of the HUP method, a pre-compacted green pellet is inserted in a steel die and alumina punches are used to apply a uniaxial pressure. This technique allows for a pressure of several hundreds of MPa during the sintering process. Heating is achieved by induction, which limits the possible heating rate and renders HUP a very time-consuming sintering process. The basic principle is illustrated in ***Fig. 21***.

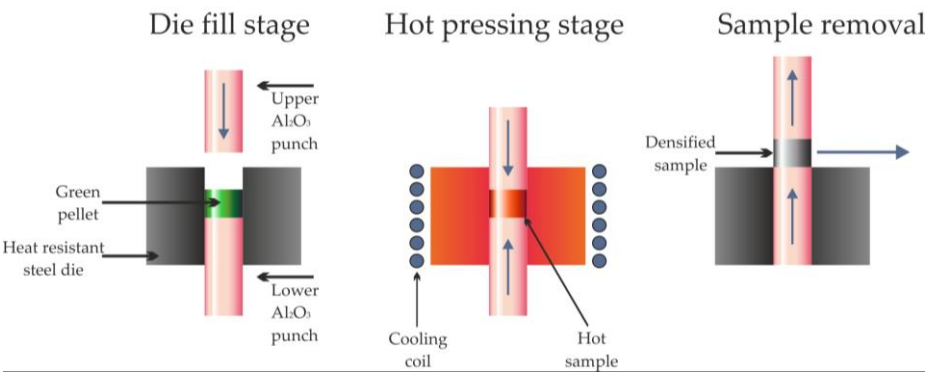

Figure 21: Schematic process of HUP, demonstrating the pre-compaction process by cold pressing using alumina punches which is then followed by inductive heating while keeping a constant pressure to sinter the sample [103].

Although a slow technique, very high quality composites with almost full densification can be produced [103].

Compared to SPS, HUP is not very sensitive to differences in physical properties (such as electrical conductivity) of the reinforcing phase and matrix material. Nonetheless and in contrast to CPS, it allows for the production of high quality, low porosity composites. Hence, for the present dissertation, this technique is chosen for the production of CNP-reinforced MMC.

Solid state sintering allows for microstructural tailoring of the final composite, affecting final grain size, density, distribution and interface of the reinforcement phase. In addition to the possibility to control the microstructure of the composite by the aforementioned sintering parameters [165], it has been demonstrated that the addition of CNP acts on the grain boundary mobility by hindering their displacement during grain growth [41,166–169]. This effect refines the final grain size of the obtained composite and thus influences the mechanical behavior by grain boundary strengthening according to the well-known Hall-Petch effect [170]. The mechanism of a hindered grain growth can be explained by the Zener-pinning effect, based on the equilibrium of the pinning pressure of the CNP on the grain boundaries (exerted by the drag force of all the CNP on the grain boundaries) and the driving pressure for grain growth [171]. The extent of the grain refinement effect largely depends on the reinforcement phase distribution and interface [172]. The factors affecting the distribution of the CNP in the metal matrix are still not fully understood and are therefore subject of research of the present dissertation.

2.2.1 CNP reinforced MMC

Typically, MMC reinforced by large particles are prone to defect formation such as cracks during mechanical testing which can result in the ultimate failure of the composites. Reducing the reinforcement particle size in MMC to the nano-size range could possibly resolve some of the limitations such as poor ductility and elongation, poor machinability, and reduced fracture toughness of MMC [16]. In this chapter, a short overview is given regarding the reinforcing mechanisms involved specifically in CNT-, OLC- and ND-reinforced MMC as well as the challenges associated to their processing. Since the research progress in CNP-reinforced MMC differs significantly depending on the CNP used, a discussion for each of the three CNP is provided in the following.

CNT reinforced MMC

CNT-reinforced MMC have so far shown great potential in load bearing applications, which is mainly due to the interesting mechanical properties of CNT. In this field, CNT-reinforced Al, Mg or Ti matrix composites are used to obtain lightweight materials with high specific strength [173–177]. CNT reinforcement provides the ability to induce a grain refinement effect based on Zener-pinning. In addition, a proper distribution of CNT acts as an obstacle for dislocation movement, activating another strengthening mechanism known as particle dispersion strengthening or Orowan-strengthening [169,173,178]. The CNT might hinder dislocation movement during plastic deformation thus strengthening the composite. Furthermore, CNT possess a very low or even negative coefficient of thermal expansion in a wide temperature range [179,180]. Thus, the combination with a metal (high coefficient of thermal expansion) can result in a strengthening due to thermal expansion mismatch. For one part, the strengthening depends on the volume content of the CNT in the metal matrix [177]. For the other part, however, it has been reported that the strengthening effect strongly depends on a homogeneous, fine dispersion of the particles, which is often difficult to achieve [131,173].

This being said, enormous efforts have been put into the development of a method to produce a fine dispersion of CNT within a metal matrix, all involving either particle functionalization (covalent or non-covalent) or high energy merging techniques (e.g. ball milling) [141,181–184]. As already discussed, these techniques result in the breaking of covalent bonds or include a molecular wrapping of the particles, which would induce chemical modification of the composite. In any case, it influences the interfacial bond between the CNT and the metal matrix by allowing the carbon to diffuse to the metal, especially at degraded sites, thereby allowing for the formation of metal carbides, or by preventing a seamless interface between the CNT and the metal matrix in the case of molecular wrapping.

With regard to the interface between CNT and a metal matrix as well as their cohesiveness, it is evident that it plays a decisive role with regard to the load transfer from metal to CNT, also known as the shear lag model [140,178,185]. In this model, the stress is transferred from the matrix to the CNT

through the interface and is related to the shear stress τ between CNT and the matrix material, as can be seen in ***Fig. 22***.

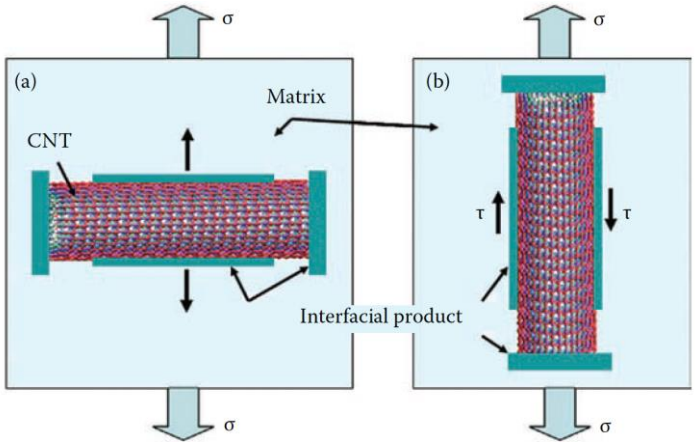

Figure 22: Schematic illustration of the influence of CNT orientation relative to the external applied load σ on the load transfer of metal to CNT [140].

However, the formation of a carbide interphase between metal matrix and CNT also depends on the used matrix and is a matter of debate in the literature. There are contradictory statements as to whether an interphase is formed at all when CNT are embedded in a metallic matrix or in which matrix systems this occurs (especially in the case of Al with its tendency to form the Al_4C_3 phase) [173,185,186]. Further, it is rather unclear, if the formation of an interphase would help in load transfer or not, since a carbide phase is usually brittle. Also, interphase formation involves degradation of the CNT and thus, diminishes their intrinsic mechanical properties [140,187,188]. Additionally, it has been discussed, that the orientation of the CNT and the respective interphase relative to the applied external stress is crucial, as it is also schematically demonstrated in ***Fig. 22.***

Due to the variability of processing methods and parameters used and the lack of characterization methods that are able to identify an interphase formation of probably 1-2 nm in size, this discussion is indeed non-trivial.

Despite mechanical reinforcement, electrical or thermal transport properties have also been in the scope of research, predominantly in the case of CNT-reinforced Cu matrix composites. Regarding the excellent thermal and electrical conductivity of CNT, this is evident with CNT expected to present a ballistic-type of electrical conduction [175,189]. It has been reported that obtaining individual CNT after dispersion in the metal matrix as well as avoiding CNT functionalization is critical for an improvement in this sector [159,190–192]. This explains why improvements were only obtained for low concentrations of CNT, which is due to their tendency to agglomerate at higher concentrations [159,192].

Although impressive effects of metal matrix reinforcement by CNT have been demonstrated in the past, chemical modification of the particles, interphase formation with the metal matrix (e.g. a

carbide formation) or degradation of the particles in various studies have made it hard to systematically investigate or compare the reported effects. Thus, in order to understand the impact of CNT as a reinforcement phase for different applications, these particle modifications should be avoided. In this regard, nickel has appeared to be a suitable candidate for a fundamental investigation of these effects since the only carbides formed by Ni are of metastable nature within a wide temperature range, as can be seen in ***Fig. 23.***

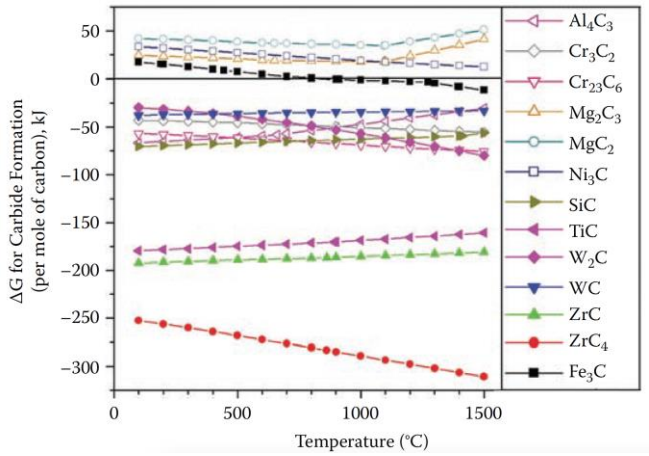

Figure 23: Gibbs free energy of formation of several carbides in different metal systems as a function of temperature [140].

Ni_3C is, among all possible carbides, the one with the lowest formation energy (26.36 kJ/mol) and was reported not to form an interphase when CNT are used as reinforcement phase [193,194].

For this reason, nickel is chosen as metal matrix material to be reinforced with CNP in the present dissertation. This is done in order to prevent influences of a carbide phase formation on the studied tribological effects of CNP as reinforcement phase in MMC.

Good overview on the topic of CNT-reinforced MMC are also provided by Bakshi et al. [32] or Tjong [195]. The state of the art related to CNT reinforcement of MMC for tribological applications will be discussed in detail in section 2.4.2 of the present dissertation.

ND reinforced MMC

In the case of ND, research is mainly focusing on ND-reinforced Al, Ni or Cu as metal matrix. Popov et al. [196,197] discussed the effect of nanodiamond addition to aluminum composites on the stabilization of the microstructure for different annealing temperatures. He observed, that the recrystallization process is delayed compared to the unreinforced Al and higher temperatures are needed in order to induce grain growth. Furthermore, they have shown that also for ND-reinforced Al composites, the formation of a carbide interphase (ND particle-size-dependent) might be critical for the reinforcement effect. In this regard, it has been shown recently, that a carbide formation can be observed already at 400-450°C for very small ND, whereas up to 800°C is needed in the case of larger ND particles [198].

Further works used ND as reinforcement phase for Al in conjunction with CNT [199]. Highly increased hardness and strength of the composite were measured, explained similarly to the CNT-reinforced composites by the Hall-Petch effect, Orowan strengthening, thermal mismatch and shear lag [199,200]. The higher intrinsic hardness of the particles surely assists in the hardening process of the composite with very homogeneous dispersions of ND being obtained in these studies. Further research regarding structural materials has been done by Livramento et al. [167] or Nunes et al. [201,202], processing ND-reinforced nano-Cu or -Ni by mechanical alloying, SPS and hot extrusion, in order to improve hardness. This was argued to be a consequence of hindered dislocation mobility and the resulting difficulty in plastic deformation of the material. However, the work also highlights ND-reinforced Cu matrix composites as a valid material for thermal management applications for example in electronics, since ND provide a very high thermal conductivity. In contrast, Yu et al. [203] have investigated ND-reinforced Zinc composites for biodegradable implants, which exhibit lower hardness and strength compared to the unreinforced Zinc while corrosion resistance is improved.

However, much of the research in the field of ND-reinforced MMC is done with spray or electrochemical coatings in order to improve the mechanical or tribological behavior of surfaces [41,42,204–206]. In this regard, tribological properties of ND as reinforcement material will be discussed further in chapter 2.4.2 of the present dissertation.

OLC-reinforced MMC

So far, there is no literature on OLC-reinforced MMC. However, some of the reinforcement mechanisms of CNT and ND such as grain refinement due to the Zener-pinning effect, Orowan strengthening or shear lag are expected to also occur with OLC. Their properties as a reinforcement phase in MMC for tribological applications are yet unexplored.

2.3 Strategies to control friction and wear of surfaces

In general, friction and wear can be altered through lubrication, surface design and the base materials [21,207]. Of course, despite these three points, the stress collective, which includes the applied normal stresses, the velocity, the runtime, the kinematics and environmental conditions, has to be considered [207]. Although these parameters can sometimes be selected individually in order to optimize a tribological system, they are often predefined due to the intended field of application (e.g. spacecraft, high-temperature applications etc.). Thus, lubrication, surface design and base material have to be chosen carefully in order to fit the given requirements. This is briefly discussed in the following [207].

Lubrication

When it comes to lubrication, a general distinction between liquid and solid lubrication is made. In most applications nowadays, liquid lubricants such as oils or greases are used. For liquid lubrication, different operating regimes have to be distinguished depending on the viscosity, the velocity and the contact pressure, which is described by the Stribeck curve (***Fig 24***).

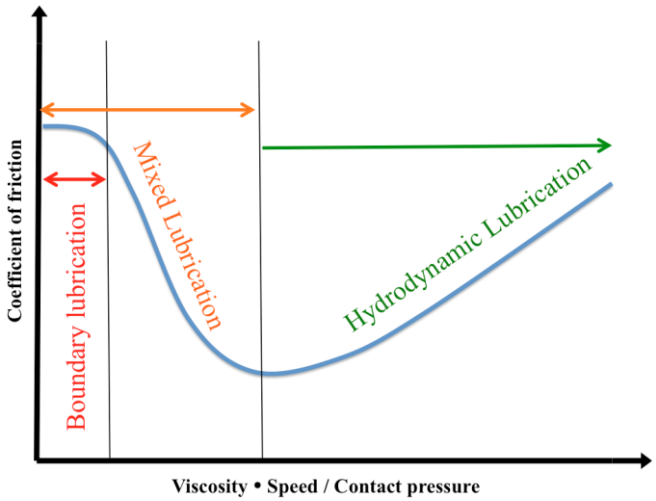

Figure 24: Schematic illustration of the Stribeck curve for liquid lubrication, showing the three main lubrication regimes: boundary, mixed and hydrodynamic lubrication.

This curve determines the lubrication regime, subdivided into boundary, mixed and hydrodynamic lubrication. For example under hydrodynamic lubrication, the physical properties of the liquid lubricant, such as viscosity and traction, determine the performance of the system. What is special about this regime compared to the others, however, is that it completely separates the two surfaces in relative movement and thus reduces wear to a minimum, allowing for very long service lifetimes of the lubricated components. Liquid lubrication further provides many more advantageous properties, such as the ability to dampen or cool the tribological system. Nevertheless and despite all the advantages over solid lubricants, liquid lubricants also have their limits, which justify the use of solid

lubricants for certain applications [21,208]. In the present dissertation, only solid lubrication and thus "dry friction" is considered, which is why liquid lubricants are not discussed further.

Solid lubricants are mainly used to control friction and wear under harsh operating conditions (e.g. high vacuum, high speeds, high loads and very low or high temperatures) where conventional materials and liquid lubricants cannot provide the desired performance or durability [21,185,208]. Solid lubricants work similar to their liquid counterparts, in particular, they typically shear or slide easily to ensure low friction and wear between the surfaces in relative motion. With the focus of the present dissertation being put on this type of lubrication, a short overview on solid lubricants will be provided in section 2.3.1.

Surface design

Regarding the impact of the surface design on dry friction, surface topography and also surface chemistry have to be considered, both significantly influencing friction and wear of a surface. In the case of surface chemistry, surface contaminants, adsorption layers, oxide layers or formed tribolayers can change the behavior of a tribological system [207]. For example, the adhesion of two contacting surfaces plays a crucial role when it comes to friction, but also wear mechanisms. Adhesion is usually high for two contacting surfaces providing a similar chemical composition (e.g. steel on steel). This could result in micro-welding of the surface, producing severe adhesive wear and high friction, since microwelds have to be broken in order to allow the two surfaces to perform a relative motion. For this particular example, if surface contaminations, adhesion layers or oxide layers prevent the direct metallic contact, adhesion is highly reduced and so are friction and wear [21,207]. Therefore, when tuning surface topography and trying to understand its influence on a tribological system, it is always highly recommended to characterize and identify changes in surface chemistry as well, since they are often interrelated. For example a change in the surface topography of a steel surface by laser irradiation could lead to a thermally induced oxide formation [209]. Hence, and although focusing on a systematical topographical surface modification, the present dissertation also investigates possible changes in surface chemistry and their influence on the measured tribological effects. For more information on the influence of surface chemistry on tribology of surfaces, please refer to Gellman et al. [210] or Bhushan [21].

When considering the surface topographies of two contacting surfaces, an important distinction between apparent contact area and real contact area must be made. The apparent contact area can easily be calculated by the macroscopic, geometrical shape of the two contacting bodies, and, according to the law of Amonton [211], friction is independent of this apparent contact area. In contrast, the real contact area, being the sum of individual surface asperity contacts and much smaller than the apparent contact area, is directly proportional to friction [207]. A schematic is given in ***Fig. 25*** in order to visualize the difference between those two perspectives.

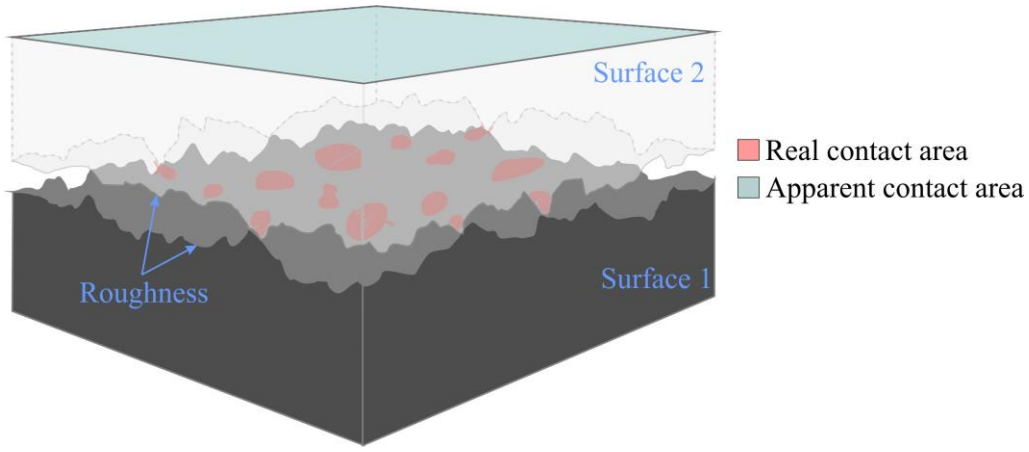

Figure 25: Schematic illustration of the contact between two rough surfaces, visualizing the apparent and real contact areas. The apparent contact area is determined by the geometry of the contacting bodies, whereas the real area is the sum of the individual surface roughness asperity contacts.

Characterization of the surface roughness/morphology provides important information to understand its tribological performance. Nowadays, an abundance of parameters is available, describing certain surface features, which are used to compare the surface topographies of different tribological systems [207]. A well-known and widely accepted surface description is done using the Abbott-Firestone curve [212]. The geometry of the curve defines different parameters, such as the core roughness R_k, which is often used to estimate the load bearing capacity of a surface.

However, surface roughness parameters can also be used to estimate the real contact area of a tribological system. This research area has always been and still is a very busy topic, involving numerous approaches and models in the field of contact mechanics. One of the earliest contact models, assuming perfectly flat surfaces (without roughness), which was used as a starting point in many other models, is the Hertzian contact model [213]. Since then, numerous other models appeared, trying to consider fully elastic or elasto-plastic contact conditions, with surfaces possessing stochastic roughness or intentionally altered surface topographies with or without a given anisotropy. A few examples are the Greenwood Williamson model [214], the Kogut-Etsion model [215], the Chang-Etsion-Bogy model [216], the Jackson-Green model [217] or the Persson model [218]. These models are always a function of the given surface topography and the mechanical properties of the base material. Hence, numerous experimental works have addressed this fact, trying to tune the surface topography and thus the real contact area by using a variety of different methods, including honing[219], micro-coining[220], lithography[221], laser surface texturing[222] or others. The focus of the present dissertation being also set on surface topography tailoring in conjunction with solid lubricant surface coating, this topic is covered in more detail in section 2.3.2.

Base materials

With regard to the base materials under dry friction, first and foremost, their mechanical properties have to be put in the limelight. The mechanical properties together with the surface topography and a given loading condition determine whether the contact situation is fully elastic or elasto-plastic (for example by calculating the plasticity index [223]) and also how large the real area of contact is. It also influences friction and wear mechanisms. For example, if a hard material is in contact with a softer material, abrasion and ploughing can often be detected, whereas adhesion rather occurs for materials with similar chemical composition. In this regard, it always has to be kept in mind, that wear is not directly proportional to friction. More specifically, a soft metal coating, which is in contact with a hard counterpart, can show significant wear due to easy plastic deformation and shearing of the surface, resulting in relatively low friction at the same time [20,224].

Another important feature of the base material is its microstructure. First, it influences the mechanical properties of a material to a great extent [170,225]. For example, a lower mean grain size of a base material significantly increases its hardness due to grain boundary strengthening according to the well-known Hall-Petch effect [170]. Furthermore, the connectivity of different phases inside the bulk material also plays an important role. A 3-D connection of hard, but brittle phases in a ductile matrix can reduce the strength of the material, whereas a fine non-connected distribution of the same phase in the same matrix can significantly increase its strength [226]. Additionally, the microstructure strongly affects the surface oxidation behavior during the tribological contact. In particular, smaller grain sizes mean more grain boundaries, which typically can act as diffusion paths for oxygen, thus inducing stronger surface oxidation with the oxide layer acting beneficially as a hard, protective film against wear or detrimentally by increasing the abrasive component of the system and forming oxidic wear particles [227,228]. Still, although a material with a specific microstructure is chosen for a certain tribological application, the microstructure can change during the experiment due to plastic deformation or recrystallization [229]. In addition, from a crystallographic point of view, the grain orientation and thus the texture of a material contributes significantly to its tribological behavior. Depending on the crystallography (e.g. fcc, bcc) and the grain orientation, different slip-planes are activated as a function of the external stress collective, creating anisotropy in yield and plastic deformation of the material surface and thus affecting the tribological behavior [230,231]. Whether a slip-plane is activated or not can be calculated by the critical shear stress using Schmid's law [232]. Combining this knowledge with a grain orientation map (e.g. obtained by electron backscatter diffraction) allows for the identification of easy or hard sliding directions on the surface of a material (if a texture is present).

The microstructure of a base material can be altered in many different ways (e.g. annealing, quenching, cold forming etc.). However, tailoring the microstructure of a MMC using the reinforcement phase provides one of the most interesting ways. This is because the processing

parameters are simple and the reinforcement phase may also have a stabilizing effect on the microstructure during the tribological contact due to the Zener-Pinning effect. Hence, this approach has been chosen in the present dissertation.

2.3.1 Solid lubricants

The need for solid lubricants is motivated by many particularities. The low vapor pressure of solid lubricants compared to liquid lubricants still allows for their use under vacuum conditions, with some of them providing excellent lubricating properties specifically under these conditions (such as MoS_2). Furthermore, for liquid lubricants, extreme pressures can lead to severe lubrication problems, as liquid lubricants may not support these, resulting in a boundary lubrication regime. Additionally, very low or very high temperatures may lead to solidification or decomposition of the liquid lubricants, respectively. On the other hand, strong temperature changes during service can lead to drastic variations in viscosity and thus a change in the lubrication regime. Likewise, most liquid lubricants are not well suited for applications where electrical conductivity is important, since they possess rather insulating characteristics. Regarding storage of liquid lubricants, problems often occur as they evaporate, drain, creep or migrate over time. These and further limitations could be overcome by their replacement with solid lubricants [13,14,21].

Certainly, not only liquid but also solid lubricants show significant shortcomings. Some, for example, are rather poor thermal conductors and lack of the ability to conduct heat out of the contact. In addition, supplying a contact with solid lubricants is more difficult than with liquid lubricants and most solid lubricants have very limited wear lives, which sometimes leads to failure in lubrication behavior over time. Oxidation can significantly influence the properties of some solid lubricants, which may result in structural or chemical changes or generation of unwanted by-products [21].

A general distinction between solid lubricants regarding carbon based materials (e.g. graphite, graphene Diamond-like-Carbon (DLC)), transition metal dichalcogenides (TMD) (e.g. MoS_2, WS_2), polymers (e.g. PTFE), lubricious oxides (e.g. Cs based oxides) and soft metals (e.g. Ag, Sn) can be made [13,14,20]. For most of the solid lubricants, their working principle is explained simply by the theory of Bowden and Tabor [233]. The coefficient of friction (COF) μ of a solid lubricant can be expressed as a function of the interfacial shear strength of the solid lubricant τ_0, the contact pressure P and the pressure dependence of the shear strength α (which is the lowest attainable friction coefficient for the specific tribological system) using the following equation [20,233]:

$$\mu = \frac{F}{L} = \frac{A_r \cdot \tau_S}{L} = \frac{\tau_S}{P} = \frac{\tau_0}{P} + \alpha \qquad (2)$$

In equation (2), F corresponds to the friction force, L to the normal load, A_r to the real area of contact and τ_S to the shear strength [20]. Thus, with a low interfacial shear strength of the solid lubricant in

combination with a hard substrate and thus a high pressure, efficient lubrication and thus a low COF might be achieved.

However, the individual lubrication mechanisms of the various solid lubricants slightly differ from each other and a brief explanation of the mechanisms and limitations of the most important solid lubricants is given in the following.

Graphite

Graphite has long been known for its good lubrication properties and has been used in industrial applications as solid lubricant for several decades [234]. Graphite possesses a highly crystalline structure of stacked hexagonal carbon lattices (stacked graphene sheets) with an sp^2 carbon hybridization and a strong, covalent, in-plane bonding of the carbon atoms. A schematic of the atomic structure is given in ***Fig. 26***.

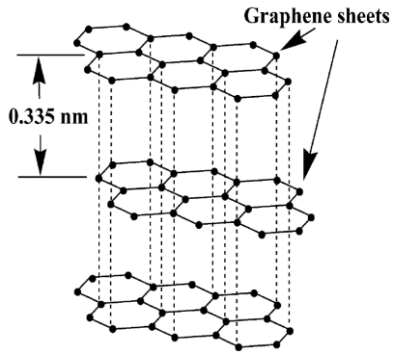

Figure 26: Schematic illustration of the atomic structure of graphite, consisting of stacked graphene sheets with an interlayer distance of 0.335 nm [235].

With the sheets only being interconnected by weak Van-der-Waals forces, they become relatively easy to shear. However, graphite lubrication is strongly dependent on the presence of water or adsorbed gas molecules, since the shearing of graphene sheets works only based on intercalation of these molecules between the individual graphene sheets, leading to an increase in the interlayer spacing between near-surface basal planes [17]. In the case of low relative humidity or vacuum, high friction and wear occurs and a process called “dusting” sets in [20].

Graphene

Recently, it has been found that besides its thermal, electrical, optical, and mechanical properties, graphene can serve as a solid lubricant [17]. Its high impermeability to liquids and gases [236], extreme strength [237], and easy shear capability on atomically smooth surfaces are the major favorable attributes for its high potential as a solid lubricant [238,239].

In particular, it was shown that in contrast to graphite, graphene provides efficient lubrication under dry or inert gas environments, as can be seen in ***Fig. 27***. Furthermore, wear reduction by four orders of magnitude was observed on steel surfaces, when coated by solution-processed graphene [239]. One accepted explanation of the lubricating effect is based on low adhesion based on the nearly perfect single, hexagonal lattice providing a low surface energy. A stacking of several layers would result in easy shearing ability of the surfaces. However, other studies contradict this explanation by introducing fluorinated graphene, providing even lower adhesion but higher friction at the same time. However, it is accepted that, graphene is able to conformally coat surfaces and is mechanically stable, preventing the direct tribological contact of the surfaces. Additionally, the protection of the surface against oxidation due to the high impermeability to liquids and gases contributes significantly to an efficient wear reduction. There is still an on-going discussion about the lubrication mechanism of graphene [17].

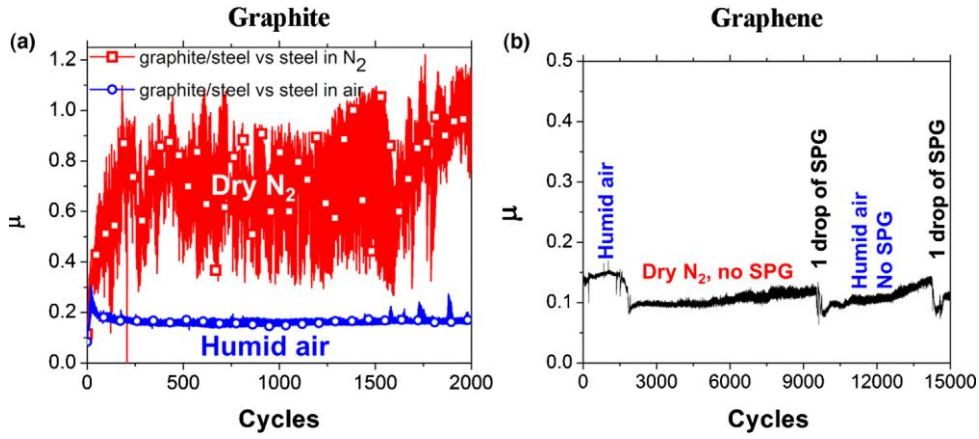

Figure 27: COF (μ) measured against the number of cycles for a graphite (a) or solution processed graphene (SPG) (b) lubricated steel surface under dry nitrogen or humid air conditions. A ball on disc tribometer was used with a steel ball of 9.5 mm in diameter and a normal load of 1 N was applied [17]. In c) a simulation with an AFM tip contacting and shearing a graphene layer is performed, resulting in an out-of-plane deformation of graphene [17].

Unfortunately, the promising lubrication properties of graphene decrease significantly when large contact pressures are applied. For the same configuration as shown in ***Fig. 27***, it has been reported that when increasing the load to 3 N (inducing 0.7 GPa of pressure for the given configuration), the lubrication vanishes after only 200 cycles [17,239]. Furthermore, differences are obtained regarding monolayer graphene coatings, few-layer graphene coatings and multi-layer graphene coatings [240]. It is often concluded that the friction force is higher for a monolayer of graphene and decreases with increasing number of layers. However, the strong interaction between graphene, the substrate material, the surface roughness, the interaction between the graphene layers, and the graphene-substrate separation distance all have to be considered for a proper analysis [240].

Thus, it is clear that further research needs to be carried out in this field in order to fully understand the mechanisms and to exploit the full potential of this material for its use in technical applications. A good overview on this topic is given by Berman et al. [17].

Diamond-like-Carbon (DLC)

DLC coatings are typically hard and wear resistant, but they can also provide low friction and chemical inertness under certain conditions. The DLC structure consists of disordered carbon, providing only a short-range order of a mixture of sp^3 and sp^2-hybridized carbon atoms. In order to induce high toughness and beneficial tribological properties, pure DLC is doped with metals or lightweight elements, like H, N, Si, Cr, W or Ti [20]. The ternary phase diagram of carbon-hydrogenated alloys is depicted in ***Fig. 28***.

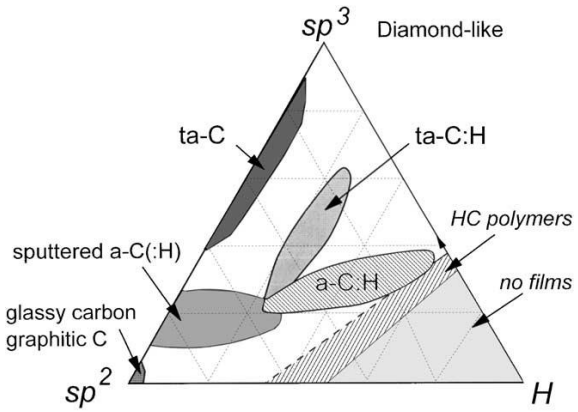

Figure 28: ternary phase diagram of bonding in amorphous carbon-hydrogen alloys [241].

Hydrogen doping is widely used and corresponds to the phase a-C:H (amorphous, hydrogenated DLC) or ta-c:H (tetragonal, amorphous, hydrogenated DLC) in the phase diagram. Depending on the deposition techniques, such as sputtering, ion or plasma beams, the different phases can be obtained, providing different mechanical and tribological properties. A detailed description of this can be found in the work of J. Robertson [241].

The friction coefficients of DLC coatings vary widely from 0.01 to 0.5 and depend upon the testing conditions (e.g. contact pressure, velocity or temperature), the environment as well as the hybridization ratio and hydrogen content [20]. This is also true for the wear rates, which can get as low as 10^{-7}-10^{-9} $mm^3/N{\cdot}m$ [242]. As an example, hydrogen-free DLC provides the lowest COF under humid conditions whereas hydrogenated coatings perform better in dry or inert gas environments. Under specific conditions, COF values as low as 0.005 (superlubricated state) can be reached in self-mated sliding contacts, which is attributed to a passivation of the contacting surfaces due to hydrogenated carbon [243].

However, synthesizing DLC possessing low friction and wear in both dry and humid environments is a challenging task. Research is currently focused on the investigation of diamond-like nanocomposite (DLN) coatings, consisting of two amorphous interpenetrating networks, a diamond-like (a-C:H) network and a quartz-like (a-Si:O) network with minimal bonding between the two networks, yielding very promising results in this regard [244]. Also ultrananocrystalline diamond structures have been found to provide promising tribological properties under varying environmental conditions [245]. However, the research topic of DLC is a broadly studied field and cannot be covered in a small summary in the present dissertation. Thus, please refer to the book of Donnet and Erdemir [242] for a general overview and introduction to the topic. Finally, and in contrast to other solid lubricants such as graphite, it has to be mentioned that DLC is always used as a coating for surfaces and not as, for example, a reinforcement phase in a MMC.

Transition Metal Dichalcogenides (TMD)

The lubricating properties of TMD, such as MoS_2 or WS_2 are derived from the inter-mechanical weakness of those structures, which is related to their crystal structure [246]. MoS_2 crystallizes in the hexagonal structure where a sheet of molybdenum atoms is sandwiched between two hexagonally packed sulfur layers. Similar to graphite, they present a strong interplanar bonding of the Sulfur atoms as well as a covalent Sulfur-Molybdenum bonding, whereas only week Van-der-Waals bonding is observed between the individual sandwich layers as well as between the stacked Sulfur layers, which allows for easy shearing (***Fig 29***).

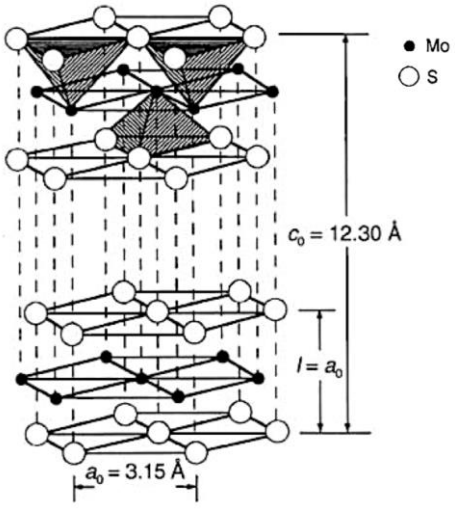

Figure 29: Atomic structure of MoS_2 with interatomic distances [246].

The lubrication mechanism of MoS_2 is based on the development of a transfer film on the counter-material to support interfacial sliding. Due to the ability of TMD to form a transfer film and to orient its crystal structure beneficially to the sliding direction ((0002) planes parallel to the sliding direction), they are not only used as sputtered surface coating, but also as inorganic fullerene (IF)

nanoparticles or as additive in oils or greases [247,248]. Both, MoS_2 and WS_2 can provide a very low COF of only 0.05 or lower and also very low wear rates, typically being the lowest for steady state conditions of the system. However, this is only true for either dry inert gas atmospheres or in ultrahigh vacuum. When TMDs are used under humid conditions, the formation of MoO_3 and WO_3 at the edges of the basal planes has been observed, hindering the planes from easy gliding [249–251]. This problem also occurs for higher temperatures (300 °C and above) [249–251]. One approach to overcome these limitations is the doping of TMD with various metal or oxide dopants (e.g. Ti, Al, Ni, Au, Pb, PbO, and Sb_2O_3) [20,252]. The presence of these dopants or alloying of TMD with amorphous carbon can lead to a higher oxidation resistance in humid environments compared to pure TMD [253]. Due to their high lubrication capabilities under vacuum conditions, TMDs are often used for spacecraft applications. A short and comprehensive introduction to the field of tribological properties of TMD is provided by Polcar and Cavaleiro [253].

Polymers

In the case of polymers, their low intermolecular cohesion is responsible for their rather low friction properties. For example, this could be due to easy extraction of molecular chains out of the crystalline fraction (e.g. for PTFE, PE or Polyimide) [208,254]. Thus, polymers can be used as solid lubricant coatings, for example, on metallic materials. In addition, they offer a low coefficient of friction both in vacuum and under atmospheric conditions, as the lubrication mechanism does not depend on adsorbed molecules and chemical reactivity is low. Generally, polymers are not suited for high temperature applications due to melting or degradation. Furthermore, the low thermal conductivity inhibits heat dissipation, which can also cause premature failure due to melting under room temperature. Therefore, polymers are typically used for low sliding speed applications. Finally, the low intermolecular cohesion causes a further severe limitation, as it results in unacceptable amounts of wear [254]. This limitation can be partially overcome by adding fillers to the polymers, which is why polymers are most often used as matrix material in conjunction with other solid lubricants [20].

Lubricious oxides

Oxide based materials most often are hard to shear at room temperature. However, some of them (e.g. Cs, Re, Ti, Mo, Zn, V, W, B) develop easy-to-shear characteristics at higher temperatures, which is why they are often referred to as lubricious oxides [208,255,256]. It has been shown that the crystal chemistry of oxides is linked to their shear rheology and thus to their ability to act as a high-temperature solid lubricant. An intense study on the lubrication behavior of different oxides as a function of the temperature has been provided by A. Erdemir [255]. Lubricious oxides are not very widespread and limited in their usage exclusively for high temperature applications. Most of them

only become an interesting solid lubricant for temperatures higher than 500°C [255]. A very good overview of the topic is provided by Aouadi et al. [14].

Soft metals

Soft metals, such as Pb, Sn, Ag or Au are able to provide a low COF when applied onto relatively hard substrates. In contrast to solid lubricants, whose function mechanism is based on the development of a transfer film on the opposite surface, soft metal film lubrication is initiated by shearing in the film. Unfortunately, this results in significantly higher friction, rendering soft metal coatings not the most efficient among the solid lubricants. In any case, the thickness of the coating determines the efficiency of the soft metal coating and most metal coatings have an optimum thickness. This optimum thickness results from the fact that very thick layers lead to a larger real contact area and thus to higher friction, whereas very thin layers can cause an abrupt increase in friction if they cannot prevent the direct interaction of the two substrates [20,224].

Summarizing, all of the above-described solid lubricants can possess good lubrication properties for specific conditions. However, they are also limited in their range of applications with regard to their environmental conditions and the prevailing stress collective. The increasing demands on tribological applications set the need to develop solid lubricants, which provide a higher environment robustness and independence from the stress situation [18,19]. This might be given for CNP as solid lubricants and will be discussed further in section 2.4 of the present dissertation. A very comprehensive and general introduction into the field of solid lubricants, its advantages, limitations and working principles is given by Scharf and Prasad [20] as well as Donnet and Erdemir [208].

2.3.2 Surface topography designing

Surfaces of real machine elements in tribological contact are not atomically flat and generally exhibit a certain surface roughness. In this regard, the early work of Bowden and Tabor investigated the interaction between asperities of a rough surface with regard to the influence on the frictional behavior [257]. They correlated the frictional behavior of a surface with adhesion/welding of asperities of the real contact area and their subsequent releasing (when a critical shear stress is applied). Since then, great efforts have been undertaken for various lubricated and non-lubricated tribological systems in order to measure, characterize and understand the influence of surface roughness on the tribological behavior and to correlate surface roughness with the real contact area of two contacting surfaces [21,214–217,258–262]. Despite the real contact area, a lot of different surface interactions have to

be considered, including plastic deformation and consequently deformation energies, contact angles between asperities or simply the mechanical properties of the contacting materials [207].

However, the roughness of a system is often connected to the end application, as this determines how much effort can be invested in the design or processing of a surface (e.g. surfaces of Micro-Electro Mechanical Systems (MEMS) [263] compared to large scale machine elements [262]). Thus, regarding larger scale tribological systems such as machine elements, numerous experimental works have tried to develop a fast and economic method to alter the real contact area by specifically varying the surface topography [219–222,264–267]. In these works, it has also been shown, that surface topography alteration affects more than just the real contact area. For example, the formation of a hydrodynamic pressure under lubricated conditions can be controlled by a defined surface topography [53]. Additionally, the surface depressions have been observed to trap and store generated wear particles as well as lubricants [52,53]. Furthermore, the creation of topographical structures providing an anisotropy typically also results in anisotropic effects on friction and wear of the surfaces. Thus, considering all those effects, it is sufficiently proven that surface topography designing is a powerful tool for the systematic manipulation of the tribological properties of a system.

Out of various techniques to create well-defined surface patterns such as honing, micro coining or lithography, laser surface texturing (LST) has shown to be suitable, cost and time-efficient approach [10,51]. *Hence laser surface processing has been chosen in the present dissertation for surface topography designing.*

Due to this fact, the focus in the following is put on LST as a method to tune surface topography. Generally, when it comes to LST using pulsed laser systems, different laser-material interactions have to be distinguished based on the laser pulse length ranging from short (microsecond- to nanosecond-pulses) to ultra-short (picosecond- to femtosecond-pulses) [268]. In the case that a metallic surface is processed using a short-pulsed laser system, the laser-material interaction is based on melting and heat conduction, resulting in shifting of the molten material according to temperature- and surface tension gradients. In contrast, an ultra-short pulsed laser system induces direct metal ablation, not allowing the metal to melt and generating a shock wave, which ejects evaporated or overheated liquid (***Fig. 30***). Ultra-short-pulsed laser surface structuring normally results in the creation of sharp topographical edges, whereas short-pulsed laser structuring provides rather smooth surface structures [268].

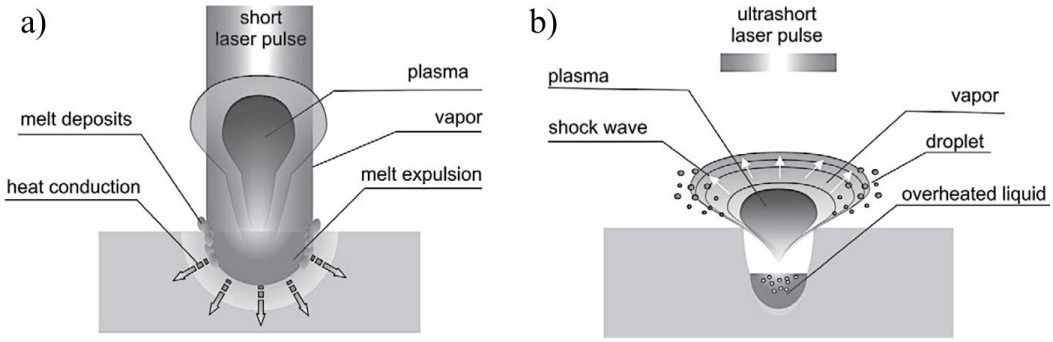

Figure 30: Schematic of the laser material interaction for a) a short-pulsed laser system and b) an ultra-short-pulsed laser system [268].

Another significant difference is the possibility to create higher surface aspect ratios for ultra-short pulsed laser systems compared to short-pulsed laser systems. Ultra-short laser pulses ablate the material with each individual pulse, resulting in successive material removal and thus deeper structures compared to a simple redistribution of molten material in the case of short laser pulses.

The pulsed laser systems can be used to create interference fields, producing a periodical laser intensity distribution on the material surface. This distribution causes a precise distribution of energy at places of high laser intensity, while the material remains almost unaffected in zones of low intensity. The interference field is generated by splitting up the main beam into two or more coherent sub-beams, subsequently overlapping at the surface. Depending on the laser pulse length, a redistribution of molten material (short-pulsed) or precise metal ablation (ultra-short-pulsed) occurs, resulting in the development of a defined surface topography. This process is called DLIP [51,269]. Different interference geometries can be obtained, such as line-, dot- or even lattice-like patterns with typical feature sizes in the micron to sub-micron range, depending on the used laser system, the laser wavelength and the angle of the overlapping sub-beams. A schematic of the DLIP process for a nanosecond laser system is given in ***Fig. 31***.

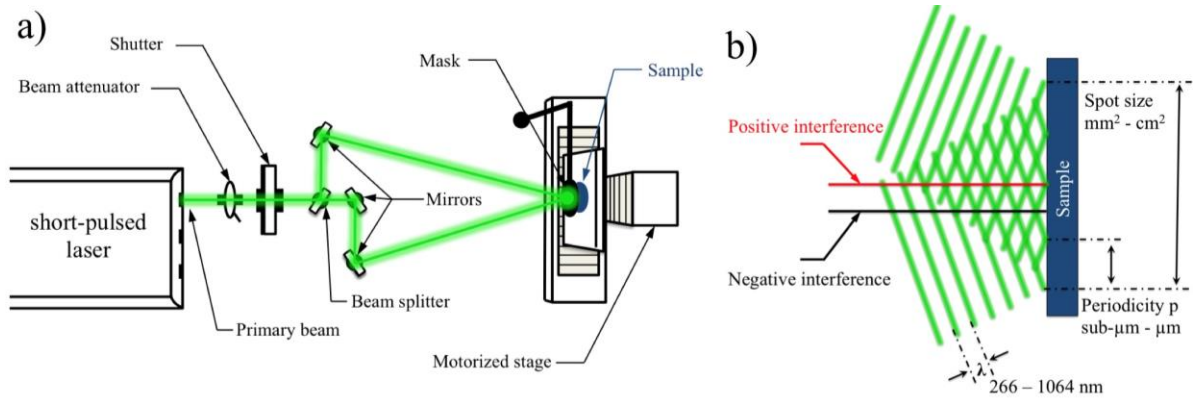

Figure 31: a) Schematic of the equipment and optics needed for the beam guidance in order to overlap the sub-beams on the sample surface according to the DLIP principle using a nanosecond laser. b) Schematic of the interference principle, creating regions of high intensity (positive interference) and low intensity (negative interference). The distance from one positive interference position to the next depends on the interfering angle of the sub-beams and the wavelength λ of the laser beam.

Besides the possibility to laser structure surfaces using DLIP, direct laser writing (DLW) can also be used [270]. For this technique, the laser beam is highly focused, and a sequential, automated surface processing is performed. It allows for larger surface structures (several micrometers to millimeter scale) and provides a highly controllable way to create different surface aspect ratios.

Studies on the tribological behavior of laser-structured metallic surfaces have shown a significant reduction in friction and wear under lubricated and non-lubricated conditions [53,266,271–273]. In addition to the effects caused by a reduced contact area and trapping of wear debris, the surface depressions can act as storage for liquid and solid lubricants, thus continuously supplying the contact region with the lubricant [52,53]. This can avoid premature failure of machine components by significantly enhancing the longevity of the lubrication effect.

Hence, in the present dissertation, laser structured surfaces were used in combination with the new solid lubricant (CNP) in order to create enhanced self-lubricating surfaces. Furthermore, specifically designed surfaces may allow for a more detailed understanding of the lubrication mechanisms of CNP. An in-depth discussion of the state of the art of CNP lubrication mechanisms and their usage in the field of tribology is therefore given in the next sections.

2.4 Tribological application of CNP

In recent years, CNP have risen as promising candidates to reduce friction and wear under various operational environments, which is ascribed to their outstanding mechanical properties, chemical inertness, thermal stability as well as atomic structure and geometrical shape [31–36,240]. Various works report on the friction and wear reducing effects of the particles when used as solid lubricant coating or as reinforcement phase in composite materials [29,35–47]. There are also numerous works using CNP as an additive in oils in order to achieve enhanced lubrication effects [60,62,274–280]. However, with the focus of the present dissertation being put on dry friction, these works are not considered in the following, since the lubrication mechanism of additives in oils strongly differ from the mechanisms present under dry friction.

The underlying lubrication mechanisms of the particles under dry friction conditions are still not fully understood and thus the potential lubricating effects may not be fully exploited [240]. The present thesis focuses on three CNP in particular, namely MWCNT, OLC and ND. These three different types of CNP are chosen intentionally since they can be systematically distinguished, representing sp^2 as well as sp^3-hybridized, 0-D (low aspect ratio) and also 1-D (high aspect ratio) carbon nanoparticles, and thus cover a wide range of CNP allotropes. Due to this fact, a systematic investigation is possible, allowing for an understanding of the governing lubrication mechanisms in more detail. Hence, in the following sections, only the above-mentioned three CNP are considered.

2.4.1 CNP as solid lubricant

There are various theories on the intrinsic lubrication mechanisms of CNP. However, the state of the art regarding the three particles differs. Hence, they are discussed separately in the following.

MWCNT

In many research works, friction and wear reduction are experimentally observed, when MWCNT are added to the tribological contact. It was stated that MWCNT are able to efficiently lubricate the contact in either air or vacuum conditions [281], for low and high temperatures [282] and under various relative humidity [35,283]. Regarding the occurring lubrication mechanisms, different explanations are found in literature. A common reason is that MWCNT would form a lubricious layer on the surface of the contacting materials [16,44,45]. However, it is often not further specified what this lubricious layer is composed of. There are studies, observing the formation of a “carbonaceous layer”, of which the lubrication mechanism would be similar to the known graphite lubrication. This would imply the structural degradation of MWCNT within a tribological contact [16,44,283]. This statement contradicts what was found by Dickrell et al., who showed a frictional anisotropy effect for quartz surfaces coated with MWCNT studied under a low load of 2 mN [35,91]. MWCNT that are aligned horizontally

(transversely) to a surface show a much lower coefficient of friction than MWCNT aligned perpendicularly (vertically) to the surface ("CNT forest") (***Fig. 32***). It was concluded that MWCNT might possess the ability to efficiently separate the sliding surfaces, which would also explain their ability to reduce wear of the contacting partners [32,38]. Additionally, it was assumed that MWCNT are able to slide and/or roll on the surfaces, being the logical consequence from their tube-like morphology and their relatively low physical interaction with surfaces due to their closed, curved shell and low concentration of dangling bonds [284]. In this regard, by measuring the lateral forces involved and observing the rotation of a single MWCNT on the surface, earlier studies of Falvo et al. using atomic force microscopy (AFM) proved that MWCNT are able to perform a defined sliding and/or rolling motion on top of a graphitic surface [34]. Still, so far, the rolling and/or sliding ability of MWCNT has not yet been proven for macroscopic tribological testing conditions. Regarding their potential ability to roll, simulations of CNT bundles in a tribological contact were performed by Ni and Sinnott [47], observing what is called the "tank-belt" effect and describing the CNT rolling motion similar to that of a deformed chain rolling between two contacting diamond surfaces under shear as can be seen in ***Fig. 32 (b)*** [45,47,285].

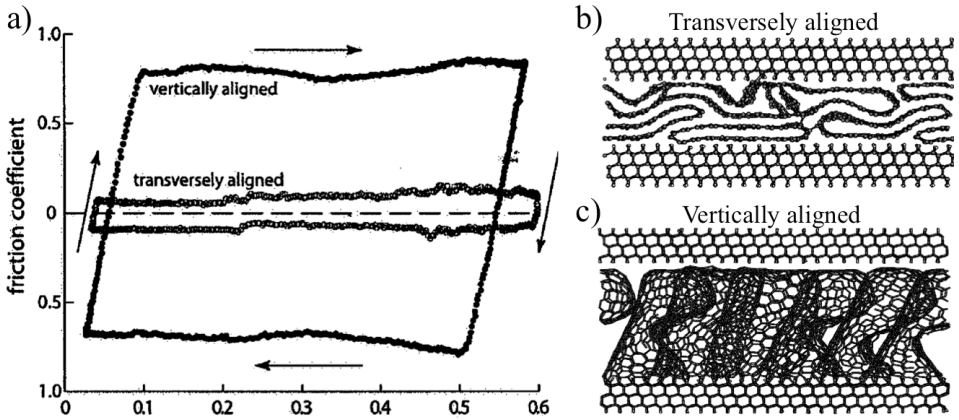

Figure 32: a) Mean value of 60 cycles of a pin on disc friction coefficient measurement of MWCNT on a quartz surface measured using a borosilicate pin and a normal load of 2 mN [35]. b) Schematic of the tank-belt model, showing transversely oriented CNT and c) vertically oriented CNT in between two diamond surfaces [47].

In this regard, Mylvaganam et al. [286] performed simulations on the sliding direction on agglomerated, transversely aligned CNT against a diamond tip under very low loads (several nN). It was shown that a sliding of 90° to the longitudinal axis of the CNT caused "spinning" of CNT that were situated below the top CNT layer, which is not the case when sliding is performed in parallel the CNT longitudinal axis. However, in terms of the friction coefficient, no change was observed and thus it was concluded that the lubrication effect of CNT is derived by their atomically smooth surface without dangling atoms (which is true in theory, but hardly ever obtained for synthesized CNT). Interestingly, further simulations of CNT under high temperature conditions (1500-2000 K) by Colonna et al. [287] showed, that for pressures above 1.5 GPa, a structural degradation towards graphite can be expected.

It becomes thus evident, that the lubrication mechanism is a function of the given tribological system and a wide span of parameters like relative humidity, contact mechanics, the contacting material properties and their surfaces as well as the distribution, structural integrity and agglomeration of MWCNT [240,288]. Thus, all those influences have to be considered in order to learn more about the lubrication mechanisms of these particles, which, so far, has not yet been done for one specific tribological system.

ND

Regarding the intrinsic lubrication mechanism of ND, there is not yet much literature in the field of dry friction. This could be due to the fact that an sp^3 hybridization is usually associated with a hard material, which does not provide the basic requirements of a solid lubricant (according to Bowden and Tabor) [233]. However, due to their spherical shape, there is literature that assumes a possible function as nano-roller bearings, separating the two contacting surfaces thus preventing the occurrence of severe wear and reducing the COF [41,289]. Yet, this assumption was not proven and in contrast, other studies contradict this assumption [62]. Especially under ambient conditions, ND are rather connected to act as an abrasive rather than a solid lubricant [290]. A beneficial effect on friction and wear could be observed mainly under vacuum conditions. It is argued, that low adhesion between the diamond surface and the substrate surface (due to adsorbed oxygen-containing species on the surface) can cause this frictional and wear reduction [290]. Studies by Berman et al. further reported about the possibility to reach "superlubricity" with friction coefficients as low as 0.004 if ND are combined with graphene as solid lubricants in the contact area of a DLC sphere and SiO_2 substrate [291,292]. The effect was only observed for dry environments. In the case of an increase in relative humidity to 30%, the effect vanishes as can be seen in ***Fig. 33 (a)*** and ***(b)***. It is argued, that ND particles are wrapped by graphene nanoscrolls as depicted in ***Fig. 33 (c-f)***. In this respect, ND would provide the mechanical stability of the nano-bearing, whereas atomic incommensurability, and thus superlubricity (which was first discovered by Shinjo and Hirano for muscovite mica crystal [230]), is given by the direct contact of the DLC surface with the graphene sheet [291,292]. If humidity were present, the adsorption of water molecules would prevent the formation of graphene nano-scrolls and therefore would show detrimental frictional effects. It is still an open question, whether these promising lubrication effects could be transferred to technically relevant materials with rough surfaces.

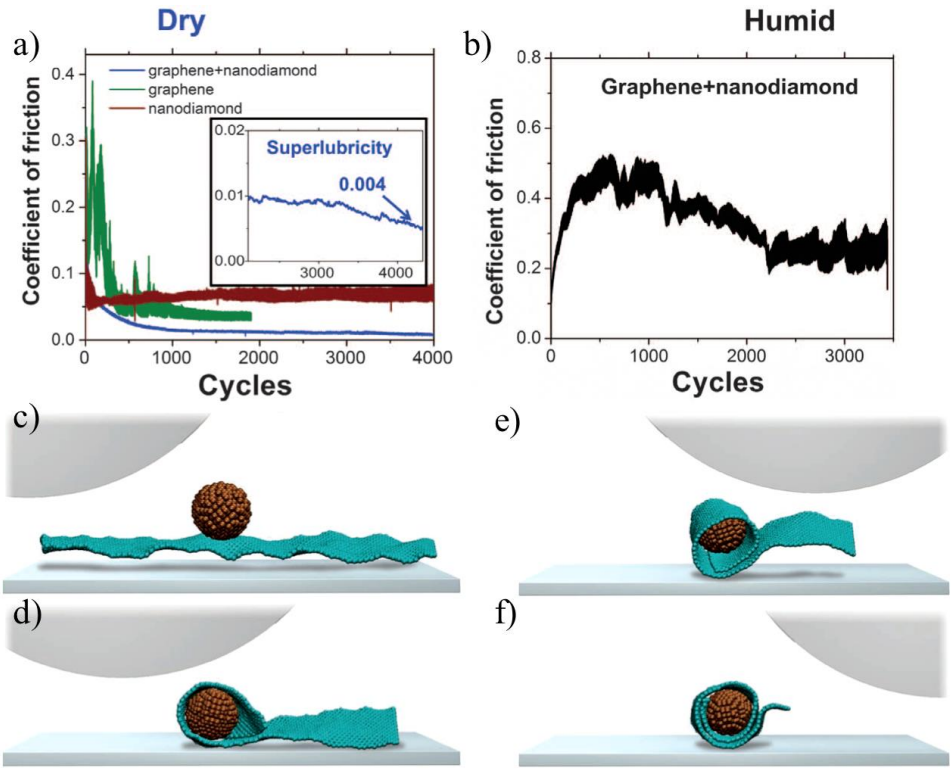

Figure 33: a) Friction coefficient measurement of nanodiamond, graphene and nanodiamond+graphene for a DLC against SiO_2 contact under dry ambient conditions and b) humid (30% relative humidity) conditions. c) – f) shows a schematic of the mechanism of graphene nanoscroll wrapping of nanodiamonds in the mentioned tribological contact [291,292].

However, the reported observations also give rise to the promising lubrication properties of OLC (being similar to a wrapped graphene scroll), which is discussed in the next paragraph. Generally, research using ND for tribological applications is rather focused on their usage as additives in liquid lubricants or as reinforcement phase in composites, where beneficial tribological effects are obtained due to a change in the rheological behavior of oils, an embedding of ND in the surfaces or a hardening/strengthening effect of the composite [33,62,197,277,279,293,294].

OLC

The polyhedral or spherical structure of OLC suggests that they could also function as nano-bearings in tribological systems [31]. Since there are almost no free valence electrons on the curved surface of OLC, only weak intermolecular interactions with other materials are assumed [31,280]. As a result, OLC have a high degree of freedom, as only a few bonds are formed on the surface of the friction partners. In the case of atmospheric conditions or even under vacuum, OLC provide a significantly lower COF than graphite, as can be seen in ***Fig. 34 (a)*** and ***(b)***, respectively [36].

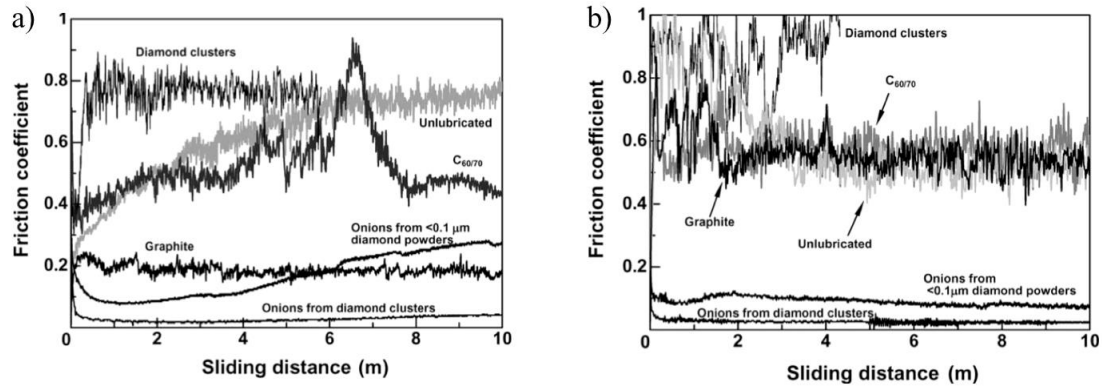

Figure 34: Friction coefficient measurement of OLC, graphite, C60 fullerene and diamond clusters under a) ambient conditions and b) under vacuum [36].

OLC particles are apparently not dependent on the presence of water molecules or oxygen for solid lubrication. Furthermore, using OLC compared to graphite, the wear rate could be reduced by 3 to 6 orders of magnitude, which is attributed to surface separation by OLC. Hirata et al. [36] further produced OLC using diamond powder and others using diamond clusters. In ***Fig. 34***, a clear difference in the tribological behavior of these two OLC variations is observed. This is explained by the different number of defects on the surface. OLC derived from diamond powder has significantly more defects, therefore resulting in a lower binding stability and being more prone to chemical reactions with the contacting surfaces. Additionally, the lubrication effect of OLC might be strongly dependent on the provided surface roughness of the substrate material. If the roughness is too high, the particles may not provide an efficient surface separation anymore. When OLC are in direct contact, they can be damaged and thus restricted in their freedom of movement. However, although being damaged or pinned, AFM experiments reported a deformed OLC layer found on steel surfaces, still providing a very low COF [295].

Despite these experimental findings, various simulations have been performed in order to understand the lubrication mechanism of OLC. These have shown, that the capability of OLC to perform a rolling movement on a surface could be prevented by exceeding a certain contact pressure. This has been justified by the formation of bonds with the contacting materials, pinning the OLC particles. In the case of two OLC-lubricated DLC layers, a maximum contact pressure of 5 GPa was simulated at which the coefficient of friction increases from 0.024 to 0.151, and thus, the mechanism changes from rolling to sliding [296]. In general, the lubrication mechanism of OLC is referred to as a rolling or sliding movement on top of the surfaces rather than a structural modification (for example exfoliation) [45,46].

2.4.2 CNPs as protective coating

Due to the promising physical properties of CNP, various coating methods were deployed so as to use CNP as surface coatings. Again, the state of the art of the particles strongly varies, and thus, they are described individually. Not all of the presented methods were applied in order to use the coating for tribological applications. However, a brief overview of all the methods capable of coating surfaces with CNP is provided in the following.

MWCNT

In the specific case of MWCNT, it must be distinguished between dry and wet coating routes. The dry coating route involves drawing films directly from MWCNT forest arrays [297,298]. These methods are easily scalable. However, they were not used in the field of tribology since they are normally not suitable to coat complex geometries such as a journal bearing or surface textures. In this regard, wet coating techniques are rather deployed, which always involve the dispersion of the MWCNT in a suitable solvent (for example by using ultrasonic agitation) with or without prior particle surface functionalization. One of those methods is dip coating [299–301]. In this regard, Mirri et al. [300] have performed experiments using Chlorosulfonic acid (CSA) to produce thin conductive, transparent MWCNT films on glass substrates. Other techniques are drop casting, spray coating or rod coating. The methods basically work by individually placing or randomly spraying droplets of dispersed CNT in a solvent onto a surface or by drawing a rod to spread a CNT dispersion over the surface, respectively. Subsequently the solvent is evaporated and the CNT remain on the surface [281,302–304]. One of the main drawbacks of these techniques is the so-called “coffee stain” formation due to Marangoni convection during evaporation of the solvent, resulting in inhomogeneous distribution of the CNT coating. In order to reduce this effect, surface heating is often performed so as to speed up the evaporation process of the solvent, or it is attempted to change the rheological parameters of the colloidal suspension (being described by the “Ohnesorge number”) [302]. Alternatively, the technique can be combined with spin-coating or techniques like vacuum filtration [302,305,306]. All of these techniques have disadvantages in terms of layer quality, homogeneity or the possibility of process up-scaling. Another technique to coat surfaces homogeneously with CNT is CVD [307–309]. However, due to its working principle, this process only produces CNT, which are vertically aligned to the surface (CNT forests) and it was shown, that horizontally aligned CNT provide a much higher frictional reduction compared to CNT forests deposited by CVD [91]. Thus, although this technique allows for a homogeneous coating, other techniques should be favored [281,286].

A very promising technique to produce horizontally arranged, homogeneous CNT coatings is electrophoretic deposition (EPD) [310–313]. EPD is based on the motion of charged particles in an electric field and their subsequent adhesion/physisorption onto an electrically conductive substrate material as illustrated in ***Fig. 35***.

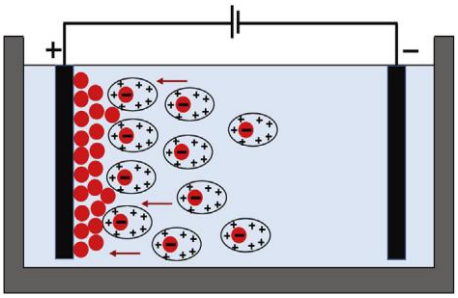

Figure 35: Schematic of the electrophoresis principle. Electrodes provide a specific voltage so that charged, dispersed particles (colored in red) are deposited on the cathode (+) or anode (-) depending on their surface charge [314].

The process allows for a more homogeneous deposition of CNT compared to drop casting or spin coating, has short processing times and is easily up-scalable. In addition, the possibility of coating complex surface topographies with a well-defined layer thickness is an important advantage over other processes. More theoretical information on the general working principle of EPD can be found in Besra et al. [315].

For these reasons and since MWCNT coating of substrates is combined with laser surface structuring in the present dissertation, EPD is chosen as coating technique in order to homogeneously cover surfaces with horizontally arranged CNT. The application of CNT coatings using EPD in the field of tribology is a new approach and has not been investigated before.

Another approach to coat surfaces with CNT is to produce composite coatings, using CNT as reinforcement phase in a polymeric or metallic matrix that is then deposited on a surface (e.g. electroless plating [316]). This method is extensively deployed in tribology, yielding good results in frictional and wear reduction [28,317–322]. However, the effects of a composite coating on the tribological behavior are often due to the combination of intrinsic lubrication properties of the CNT and their reinforcing effect on the matrix material, which is therefore discussed in general for CNT-reinforced MMC in section 2.4.3 of the present dissertation.

ND

In the literature, a nanodiamond coating is often referred to as nanocrystalline diamond coating [240,323,324]. Regarding this, for example, microwave plasma enhanced CVD was used to grow a nanocrystalline diamond coating on a silicon substrate, providing low friction and wear [325]. However, the literature has to be carefully evaluated when it comes to coatings using ND particles or nanocrystalline diamond (nanodiamond film growth), since the latter provides a closed, interconnected diamond layer and not individual ND particles.

Regarding the deposition of individual ND particles, argon gas spraying of ND with a diameter of 75 nm onto a steel surfaces has been performed by Gubarevich et al. [290], subsequently performing tribological measurements against SiC and Al_2O_3 balls. It is reported, that low friction and wear could be obtained under vacuum as well as ambient conditions. For vacuum, this is explained with the assumption of ND being able to form a stable, densely packed layer with low roughness, which is covered by oxygen-containing functional groups providing an inert, low adhesion surface. However, a more detailed analysis is not given.

Other than that, EPD is found to be the most important, if not the only technique to mention that has been carried out on various substrate materials [326–332]. Not much research has been done in the field of tribology with respect to these coatings. Tribological experiments using electrophoretically deposited ND on aluminum alloys have been conducted by Kalyanasundaran et al. [331], who found an improvement in wear resistance compared to the uncoated surfaces. Despite that, ND are only deployed as additive in metallic or polymeric surface coatings [42,333,334]. The beneficial tribological properties of these coatings are rather due to the reinforcement of the metallic or polymeric phase with ND and will thus be discussed in section 2.4.3 of the present dissertation in the case of ND-reinforced MMC.

OLC

When it comes to OLC-coated surfaces, there is not much literature either. Hirata et al. [36] reported on the tribological properties of OLC (see section 2.4.1) that have been spread over a silicon wafer without giving further specifications on how the particles were deposited. In contrast, Gubarevich et al. [335] describe an OLC coating process by plasma spraying of ND. In this process, high temperatures (2700-4500 K) of the ND particles are reached, leading to a transformation to OLC. Immediately after transformation, the particles are deposited on a stainless-steel substrate. The authors emphasize the use of this coating for solid lubrication. However, the tribological properties of the produced coatings are not evaluated. The potential of OLC coatings to function as solid lubricant was also postulated by Cabioc'h et al. [336], who developed a process to coat silica substrates by synthesizing OLC into silver thin films. This has been done by carbon ion implantation into the silver films at 500°C. The subsequent annealing of the silver layer at 850°C is described to lead to a silver evaporation, leaving a pure OLC coating on the surface. Nonetheless, a tribological evaluation of the coating is not provided. There are also further studies about OLC coatings of substrates, which are not related to the field of tribology, such as Pech et al. [337], who investigated the possibility to deposit OLC on Si/SiO_2 substrates by EPD, forming homogeneous OLC coatings. Generally, OLC coatings are fairly unexplored in the field of tribology.

2.4.3 CNP as reinforcing phase in tribology of MMC

Generally, the disadvantages of solid lubricant coatings are limited lifetime, difficulty in replenishment, oxidation or aging-related degradation as well as poor adhesion. Hence, in order to overcome these drawbacks, embedding solid lubricants in MMC seems to be an interesting alternative approach to create self-lubricating materials [16,21]. Self-lubricating composites in general have been already available for many years and find applications for example in bearings, piston or cylinder liners in engines [21]. These composites are developing into an important class of tribological materials and offer new ways to combat friction and wear under extreme conditions [21]. In this regard, the choice of CNP as solid lubricant is not only due to their interesting intrinsic lubrication properties, but, as already discussed in section 2.2.1, also provides numerous possibilities and mechanisms to act as reinforcement phase in MMC, especially in the field of mechanical reinforcement. For these reasons, CNP are used as reinforcement phase for MMC in the field of tribology. In the following, a short overview of the state of the art of this research area is provided for each of the three CNP used in the present dissertation.

MWCNT

Research in this field has been conducted mainly for CNT reinforced Al, Cu, Cr, Mg and Ni based MMC as bulk materials or coatings [27,29,37–40,44,156,160,338–347]. Although many studies have been performed on this topic, all providing promising results regarding friction and wear reduction irrespective of the used matrix material, not much is known about the occurring tribological mechanisms in these systems. Typically, the reinforcement for most tribological applications is done with concentrations of up to 20 vol.-% of MWCNT. For one part, the mechanical reinforcement effects (which were discussed already in section 2.2.1 of the present dissertation) can lead to an increased hardness and strength of the composite, which is usually connected to a reduced occurrence of wear [37,38]. Therefore, a fine and homogeneous distribution of CNT in the matrix material is what is typically aimed at in order to maximize the grain refinement effect through Zener-pinning or the Hall-Petch effect as well as the Orowan-strengthening mechanism [16]. For example, CNT could hinder the dislocation movement and therefore reduce plastic deformation of the surfaces during wear, significantly influencing the predominant wear mechanisms. Accordingly, it has been reported, that the wear rate but also the COF decreases with increasing MWCNT content as can be seen in the case of Al MWCNT composites in ***Fig. 36*** [160,338,343].

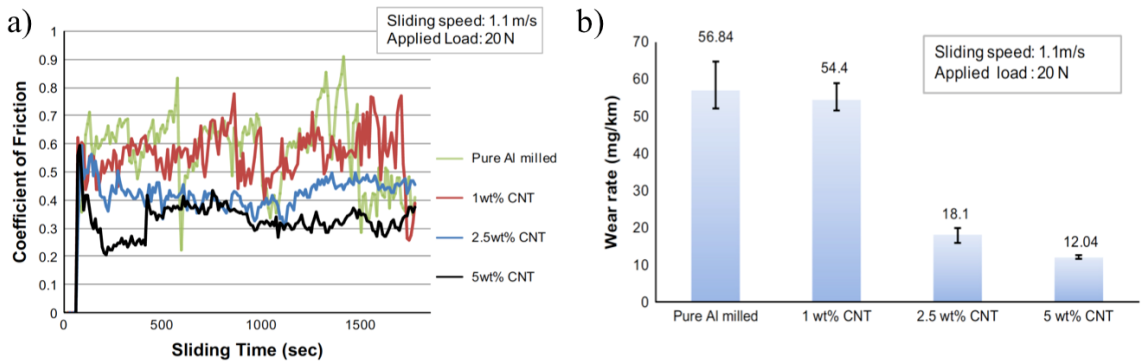

Figure 36: a) COF measurements of MWCNT-reinforced Al composites for different MWCNT concentrations and b) the corresponding wear rate measurements [338].

The authors also reported that the wear rate and the COF would decrease with increasing sliding speed, whereas an increased normal load would also increase the wear rate but lower the COF. Those findings are in good agreement with other studies, working with MWCNT-reinforced Ni or Cu [27,160,346]. The mentioned works further correlated the results with the formation of a lubricating carbon film on the surface and thus degraded MWCNT. However, other studies that reported on similar results, conclude that the used MWCNT were fully intact after tribological testing and argue that the beneficial tribological properties were obtained due to the possibility of CNT to perform a rolling movement and to act as nano-bearings [322,342]. Again, other works report on the dependence of the number of walls of MWCNT deciding on whether the particles degrade or not [156]. Hence, although different works came to similar tribological results, different explanations regarding the lubrication mechanisms of MWCNT were reported [240].

Regarding a possible rolling or sliding mechanism of MWCNT, it must be noted that what is unfavorable for mechanical reinforcement of composites may be advantageous for a tribological optimization. A weak bonding of MWCNT to the metal phase is certainly not beneficial for a mechanical load transfer from the matrix to the reinforcement phase (considering the shear-lag model). However, it could lead to a free movement and thus easy sliding or rolling of MWCNT between the contacting surfaces [16]. In this context, the metallic matrix would function as a solid lubricant reservoir that continuously supplies the surface with the lubricant. In the event that a strong bonding exists, a rolling or sliding may not occur, while structural degradation of the CNT may arise with the formation of a lubricating carbonaceous layer. This may explain why different researchers observe beneficial tribological effects for the same composites but provide contradicting explanations and findings.

For this reason, choosing a metal matrix with a low tendency to form a stable interphase with MWCNT might be of great importance for an improvement in tribological behavior of the surface regarding a possible rolling/sliding mechanism of MWCNT. Thus, also for this reason, nickel is chosen as matrix material in the present dissertation due to its low tendency to form carbides.

With respect to this and despite the possibility of CNT to form a lubricious layer, the improvement in wear resistance is also often attributed to the role of CNT to act as spacers between the contacting surfaces [38,44]. Scharf et al. [44] have performed interesting studies with MWCNT-reinforced nickel metal matrix composites (Ni-MMC). The observed frictional results are shown in ***Fig. 37***, measuring the COF of the composite against 440C steel balls (***Fig. 37 (a)***) or against Si_3N_4 balls (***Fig. 37 (b)***). The corresponding distribution of the MWCNT reinforcement phase is shown in ***Fig. 37 (c)*** using scanning electron microscopy (SEM) and a chemical verification by Auger electron spectroscopy showing Ni (green) and carbon (red) is provided in ***Fig. 37 (d)***. It can be noticed that MWCNT are present in agglomerated form. Nonetheless, a clear, long-term reduction in the COF is achieved by the reinforcement using MWCNT. In addition, it has been found that the formation of a lubricious MWCNT layer could act as an oxidation barrier, as oxygen first reacts with carbon and thus hinders the formation of NiO. This could reduce the formation of abrasive, oxidic third bodies in the tribological contact [44]. Furthermore, the fact that MWCNT are present on the surface of the worn composites significantly changes the surface chemistry compared to the unreinforced materials, strongly affecting the occurring wear mechanisms of the surfaces regarding effects based on adhesion [343].

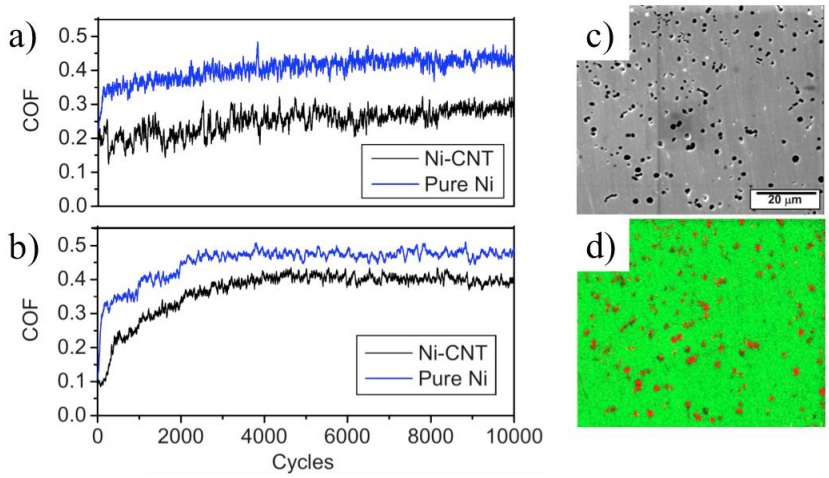

Figure 37: COF measurements of unreinforced Ni reference and the MWCNT reinforced Ni composite measured with a ball-on-disc tribometer using a) 440C steel balls and b) Si_3N_4 balls as counterparts. The distribution of the MWCNT reinforcement phase in the composite is shown c), which is also validated by auger electron spectroscopy in d), with the color green representing the nickel matrix and red representing carbon. [44]

Scharf et al. [44] further reported on a structural degradation of the MWCNT under tribological contact. The formed lubricious layer is still not further investigated. It is still rather unclear what the lubricating layer consists of and how the MWCNT degradation affects the tribological properties of the composites. The forming layer is sometimes said to be similar to graphite. However, a comparison of MWCNT-reinforced Ni with graphite-reinforced Ni has shown, that the MWCNT

reinforcement provides lower COF and wear [345]. Thus, the lubrication mechanism of MWCNT must be different from that of pure graphite lubrication.

Furthermore, Suarez et al [40] have reported about similar friction and wear reducing effects of MWCNT-reinforced Ni (processed by HUP and CPS) in the case of short-term tribological experiments (200 sliding cycles). They found, that the measured friction and wear reduction could be correlated with a formation of an interfacial lubricating carbon layer, which is, however, not further specified. Additionally, they referred to the grain refinement effect of the CNT, leading to a higher hardness and lower indentation depth of the used alumina ball into the HUP-processed composite surface for low loads (up to 100 mN). For higher loads, surface oxidation would play a crucial role for the lubricating effect of these composites. In this regard, the samples with a lower mean grain size (HUP samples) lost their lubrication effect when measured using 300 mN of normal load due to the formation of a closed NiO layer (acting as a high shear strength layer and increasing the COF). In contrast, the CPS samples, with a higher mean grain size, showed less oxidation (due to fewer grain boundaries and thus less diffusion paths for oxygen) and stayed lubricated under 300 mN of normal load.

In summary, it should be noted that the tribological effects regarding self-lubricating properties of MWCNT-reinforced MMC of all the studies in literature vary significantly, due to the different measuring conditions (humidity, load, temperature, conformal or non-conformal contact conditions, elastic or elasto-plastic contact conditions, etc.), processing parameters (sintering method, dispersion method, etc.), and materials (matrix material, mechanical properties, surface roughness, microstructure, counter-material, etc.) used, which makes it difficult to fully understand the lubrication mechanisms of these composites and to improve the measured promising effects. In this regard, Zhang et al. [322] stated in their review paper: "*It is hard to ascribe the positive tribological role of CNT to any sole cause, as for most cases, if not all, more than one mechanism may work simultaneously*".

ND

ND have been used as reinforcement phase for various MMC (Al, Ti, Ni, Cu, W etc.) in the field of tribology mainly for anti-wear purposes [42,43,348–351]. Generally, the wear reduction is correlated with a significant increase in the hardness of ND-reinforced MMC. With increasing amounts of ND (typically up to 10 vol.-%), wear resistance is typically improved. These findings can be correlated with the strengthening mechanisms of ND as reinforcement phase in MMC that are described in section 2.2.1 of the present dissertation as well as the intrinsic high particles hardness. An improved wear resistance can also be correlated with the formation of a tribofilm [352]. In this regard, the high thermal conductivity of ND can increase heat transfer and thus promote a tribofilm formation, for example in the case of ND-reinforced WC-Co or Al composites [351,352]. Thus, the presence of ND particles as reinforcement phase can affect chemistry, microstructural evolution as well as the

mechanical behavior of the composites [352]. Certain conditions, such as increased temperature or nanocrystalline microstructures of the matrix phase have also resulted in increased wear if ND are added [42,353]. This increased wear could be explained by the removal of the ND from the matrix material, leading to an increased abrasive wear component due to the hard ND particles acting as third body or a thermally induced degradation of ND, resulting in a reduction of the hardness of the composite [353][42]. A significant frictional reduction, if any, is usually not observed in literature. However and in contrast, Kaftelen et al. [351] reported a frictional reduction of up to 50% compared to the unreinforced Al reference. This frictional reduction, however, is attributed to the ND-induced formation of a lubricious oxide layer on the ND-reinforced Al composites.

OLC

So far, there is no literature on OLC-reinforced MMC for tribological applications. However, some of the reinforcement mechanisms of CNT and ND are also expected to occur in OLC-reinforced MMC. The lubricating properties of OLC as reinforcement phase in MMC are not yet investigated.

Summarizing, since a mechanical reinforcement effect is expected to occur for all the CNP-reinforced MMC, a systematic tribological comparison of these composites provides more information on the occurring intrinsic lubrication mechanisms of the individual particles. A systematic investigation and correlation of the lubrication effects of similar CNP under the same conditions has not yet been done in literature and is therefore performed in the present dissertation.

3. OVERVIEW

In the following, the main objectives are linked to the new findings of this dissertation. Subsequently, chapter four presents nine self-contained papers, all of which have been published in international, peer-reviewed journals and provide a detailed discussion of all results of this dissertation. The necessity of the following chapter is to provide a connection of the aforementioned publications to the proposed objectives and thus, to give a comprehensive overview and a concise summary of the most important results. For a more detailed presentation of the results, combined with an in-depth discussion as well as information about the used materials and methods, please refer to the attached publications.

OBJECTIVE 1

Colloidal mixing appears to be a well-suited approach to satisfy the requirements of objective 1. In **Fig. 38**, a short overview about the research areas addressed in objective 1 is given, which will be discussed in the following sections.

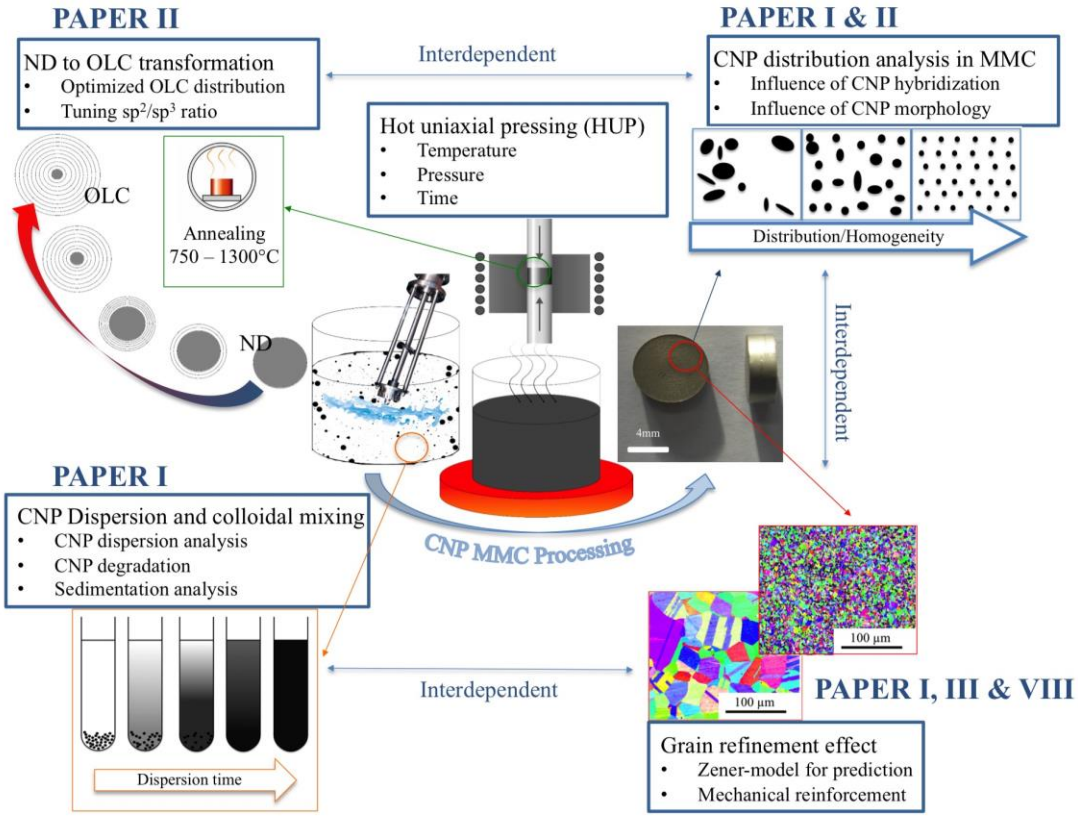

Figure 38: Schematic overview of the addressed areas regarding objective 1 of the present dissertation, which allow for a full process control and comparative production of CNP-reinforced Ni-MMC. The papers, dealing with the respective topics are indicated.

CNP DISPERSION AND COLLOIDAL MIXING

A detailed dispersion analysis and the investigation of the colloidal mixing method are provided in **PAPER I**. In their initial state (as-received), the CNP consist of large particle agglomerates (agglomerate diameters of up to 1 mm), which therefore must be de-agglomerated to be processed further. De-agglomeration is done by dispersion in ethylene glycol using a shear mixer followed by ultrasonic agitation. **PAPER I** provides a thorough study on this process avoiding particle functionalization and investigating the time needed to obtain the finest possible dispersion of CNP in the solvent. It is found that there is no difference between the dispersion grade of CNT, OLC and ND using the described method. A saturation value of the agglomerate radius is found to settle in at 40-70 nm after 5 min of shear mixing, followed by 20 min in the ultrasonic bath. Longer treatment times do not allow for finer dispersions.

The dispersed particles are analyzed by Raman spectroscopy with the aim of tracing a possible degradation caused by strong shear forces produced by the shear mixer and/or the ultrasonic agitation. In this regard, it is shown that even after 2 hours of ultrasonic agitation, no CNP degradation is observed. Once the dispersions are taken out of the ultrasonic bath, re-agglomeration of the particles starts to occur. Hence, the dispersion stability is further analyzed by sedimentation analysis and zeta-potential measurements. From these experiments, it is concluded that ND provide the highest dispersion stability over time, followed by OLC and finally CNT. For one part, this is explained by the different bonding types in CNT and OLC, compared to ND. The π-bonding with a delocalized electron cloud in the case of the sp^2-hybridized CNT and OLC translates into a higher electrostatic interaction of the particles (e.g. Van-der-Waals forces), resulting in a stronger agglomeration tendency. Although CNT and OLC dispersions show a similar zeta-potential (resulting from the similar electronic configuration), the sedimentation behavior differs strongly, which is related to the high aspect ratio of the CNT, inducing an additional mechanical interlocking effect, aiding the re-agglomeration.

GRAIN REFINEMENT EFFECT AND CNP DISTRIBUTION ANALYSIS IN MMC

After determining the proper dispersion and blending route, composite samples are processed by HUP and the distribution of CNP in the metal matrix as well as the microstructure and mechanical reinforcement effect are analyzed. Regarding the CNP distribution and agglomerate sizes, the findings of the sedimentation analysis are verified, with ND providing the smallest agglomerates within MMC, followed by OLC and finally CNT. However, even though ND provide smaller agglomerates, both, OLC as well as ND agglomerates are distributed homogeneously, compared to CNT. This fact translates into a more pronounced grain refinement effect in the case of ND and OLC. The similar grain size distribution for ND and OLC is reasonable, since the grain refinement effect is rather dependent on the agglomerate distribution (as well as morphology) within the material than the

absolute agglomerate size. In contrast, the agglomerate size determines the development of the particle dispersion strengthening mechanism and thus the mechanical reinforcement effect. For this reason, the highest hardness increase (compared to the unreinforced Ni reference) is achieved for ND, followed by OLC and finally CNT reinforcement. From **PAPER I**, it is finally concluded that a low aspect ratio (0-D) and an sp^3 carbon hybridization is beneficial for a homogeneous, fine distribution of CNP within MMC, leading to strongly pronounced grain refinement and an improved mechanical reinforcement effects.

PAPER III provides further analysis regarding the manufacturing of CNP-reinforced MMC with different CNP concentrations, ranging from 0.5 vol.-% up to 10 vol.-%. This is done in order to investigate the evolution of the grain refinement effect as a function of the used CNP type and concentration, and thus to predict and control the microstructure of the resulting composites. With increasing CNP concentration, the mean grain size of the composites decreases. However, it is confirmed that the strongest grain refinement effect can be observed for ND and the weakest for CNT, when comparing the same particle concentrations. Furthermore, different saturation concentrations are found. If the saturation concentrations are exceeded, the grains become coarser again due to the higher tendency of the particles to form larger agglomerates (due to a shorter mean re-agglomeration free path). In the case of CNT, this concentration is 3 vol.-%, whereas up to 6.5 vol.-% and 10 vol.-% are achievable for OLC and ND, respectively. This behavior is explained by the same facts and findings from **PAPER I**. However, the acquired experimental data is additionally used to adapt a modified Zener model, predicting the mean grain sizes of the composites as a function of the CNP type and concentration for concentrations lower than the individual saturation concentration.

Despite a process control based on the particle type and concentration, a way has been found allowing for the production of CNP reinforced MMC featuring the same mean grain size and hardness irrespective of the used CNP type and concentration in **PAPER VIII**. This is achieved by choosing a lower sintering temperature (700°C instead of 750°C), which results in a reduced driving force of grain growth and thus prevents differences in the extent of the Zener pinning effect when using different CNP types, concentrations and distributions. This finding is very important in order to be able to compare the composites tribologically, excluding any effect of differences in their microstructure or mechanical reinforcement.

ND TO OLC TRANSFORMATION

In **PAPER II**, a way is found to take advantage of the beneficial homogeneous distribution and small agglomerate sizes of ND in MMC, and apply it to OLC-reinforced composites. This is done by first manufacturing ND-reinforced Ni-MMC and subsequently transforming ND to OLC within the already sintered composite by annealing.

The ND reinforced sintered composites are annealed at different temperatures from 750°C up to 1300°C and the ND agglomerates are analyzed by UV Raman spectroscopy. With increasing

annealing temperature, the diamond band of the Raman spectrum vanishes and the disorder-induced D-band starts to be observed. At the same time, the wavenumber of the upshifted G-band of sp^2-hybridized carbon (from the outer shell of the ND particles) is reduced until reaching 1588 cm^{-1} after annealing at 1300°C. This observation clearly agrees with the transformation of ND powder towards OLC, reported in literature. The findings are supported by TEM analysis, verifying the presence of OLC within the MMC after annealing at 1300°C. Additionally, XPS measurements of the samples annealed at 750 °C and 1300°C confirm a change of the sp^2-hybridized carbon content from 31.1 % to 84.2 %, respectively. Comparing these results to the Raman analysis, it becomes clear, that the sp^2 to sp^3 carbon hybridization ratio can be tuned as a function of the annealing temperature of the composite. It is the first time in literature that the transformation process of ND to OLC within an MMC has been investigated and reported.

All these findings allow for full process control of CNP Ni-MMC manufacturing by colloidal mixing and HUP, avoiding particle functionalization, minimizing particle degradation and enabling a fine and homogeneous particle distribution as well as a microstructure prediction of the produced MMC.

OBJECTIVE 2

In order to achieve objective 2, an extensive tribological characterization of the composites is necessary. In this regard, ***Fig. 39*** provides an overview of which areas are addressed in the present dissertation in order to understand the tribological behavior of the composites and to create self-lubricating surfaces.

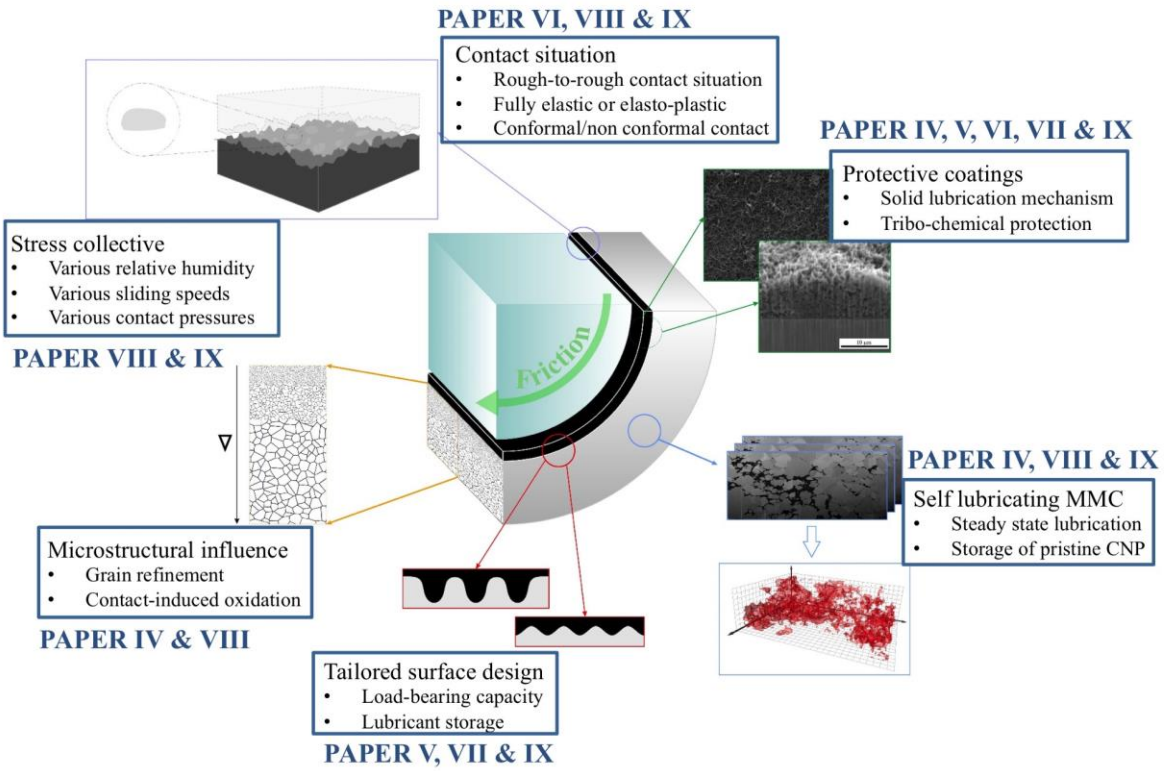

Figure 39: Schematic overview of the addressed areas of the present dissertation, which enable for the understanding of the lubrication mechanisms involved in self-lubricating surfaces based on CNP. The papers, dealing with the respective topics are indicated

MICROSTRUCTURAL INFLUENCE

As a first step, a tribological comparison of CNT-reinforced Ni-MMC and CNT-coated Ni is performed in **PAPER IV**. The coating is done by drop casting a CNT dispersion on a Ni surface. Compared to the unreinforced CNT-coated Ni, the CNT-reinforced MMC provides a refined microstructure with CNT stored within the composite. In both approaches, CNT are present in the direct tribological contact area and thus, the investigation allows for the analysis of the influence of a refined microstructure on the tribological behavior of these surfaces. For the CNT-coated and the CNT-reinforced surface, the same frictional reduction is observed for the first 200 sliding cycles. Due to this, it is concluded that the frictional behavior is dominated by the presence or absence of CNT in the tribological contact and not by the microstructure. This observation is supported by the findings of the long-term experiments (20000 sliding cycles), where a frictional reduction is noticed exclusively

for the CNT-reinforced samples. For the CNT-coated surfaces, the breakdown in lubrication can be explained by the CNT being removed from the contact zone, which is verified by SEM analysis of the wear tracks. In the case of the CNT-reinforced composites, a continuous supply of CNT allows for a long-term lubrication of the contact.

However, as discussed earlier, a smaller mean grain size of CNP-reinforced samples leads to a higher amount of grain boundaries, acting as diffusion paths for oxygen and thus favoring surface oxidation during a tribological experiment. This is shown in **PAPER VIII**. For high, non-conformal loading conditions (8N) and medium relative humidity (45%), a refined microstructure of a CNP-reinforced composite tends to form a homogenous oxide layer during the tribological experiment, whereas this is not observed for the coarse grained, unreinforced Ni reference. When choosing the MMC processing parameters to produce CNP-reinforced MMC with the same mean grain size, irrespective of the CNP type and concentration, a frictional reduction is only possible for the CNT-reinforced composites. For the reference, ND and OLC reinforced samples, the same tribological behavior is observed under various experimental conditions. These findings underline the statement that the microstructure affects the frictional behavior of CNP-reinforced composites to a rather minor degree and only due to induced differences in the surface oxidation behavior.

PROTECTIVE COATINGS AND TAILORED SURFACE DESIGN

Aiming towards a more detailed understanding of the lubrication mechanism of CNP-containing surfaces, the influence of the surface roughness as well as deterministic surface designs on the lubrication activity of CNP is investigated in **PAPER V, VI, VII and IX**. For this purpose, the different surfaces are coated using EPD in order to create homogeneous coatings with a defined thickness, allowing for copying of the generated surface topographies.

- *Surface roughness:*

It is found in **PAPER VI**, that the high aspect ratio and flexibility of 1-D CNT particles is beneficial for a constant lubrication, irrespective of the given surface roughness, since the particles can be dragged into the direct tribological contact region thus efficiently separating the contacting surfaces. Even though 0-D particles can separate the contacting surfaces and lubricate the contact by sliding/rolling, they lose this ability when interacting with a surface roughness higher than the particle diameter. Hence, with a particle diameter of 10 nm (at maximum) for OLC, the lubrication of technical surfaces or wear-subjected composite surfaces is not possible, which is also confirmed in **PAPER VIII**. The intrinsic lubrication mechanism of CNT is further found to be a mixture of two mechanisms. For one part, CNT are found oriented perpendicular to the sliding direction of the surfaces, separating the surfaces and being able to perform a sliding/rolling movement. For the other part, degraded CNT are found oriented parallel to the sliding direction of the surfaces, forming a lubricating graphitic carbon layer.

- *Surface design:*

Since the surface topography plays an important role for the lubrication activity of the CNP, a deterministic surface topography is created on a steel surface by DLIP using a nanosecond laser or by DLW using a femtosecond laser, which is thoroughly analyzed in **PAPER V, VII and IX**. Because of the aforementioned reasons, the as-produced line-like surface structures are coated exclusively with CNT and not OLC or ND. Using EPD as a coating technique, it is shown by focused ion beam (FIB) cross-sections and SEM, that the laser patterning-induced surface topography is copied homogeneously by the CNT coating. The coating of these surfaces with CNT is done for two reasons: First, the possibility to create self-lubricating surfaces throughout versatile structuring and coating techniques using CNT should be evaluated. Second, the surface state of a composite-type surface should be imitated and simplified by a periodic surface design in order to allow for a more detailed understanding of the lubricating mechanism of CNP reinforced composites. In this regard, a large amount of CNT agglomerates in CNT-reinforced MMC feature a diameter of 1 µm or more (similar to the produced line-like surface structures with a depth of 1 µm). Furthermore, since the CNT are not chemically or physically bonded to the surrounding Ni matrix, the created laser-patterned, CNT-coated surfaces can be considered similar to the CNT-reinforced composite surfaces.

It is found, that the CNT coating and laser patterning act synergetically. Although bare patterning or coating fails in terms of continuous friction reduction, long-lasting lubrication is achieved by combining both approaches (frictional reduction of up to a factor of 4 compared to the reference). The CNT coating is further found to act as a tribo-chemical protection layer, efficiently separating the surfaces, hindering the surfaces from strong oxidation (by acting as an oxygen diffusion barrier) and reducing the formation of oxidic wear particles. Hence, wear of the laser patterning induced surface topography is slowed down due to the CNT coating. Nevertheless, oxidic wear particles do form, but they are trapped in the surface depressions of the laser structure and thus are transferred out of the tribological contact. Additionally, the created surface depressions of the laser patterns act as solid lubricant storage, supplying the surface continuously with pristine CNT (as in the case of CNT-MMC surfaces) thus prolonging the longevity of the lubrication effect significantly (more than five times compared to the CNT-coated, unpatterned surface).

In this regard, a schematic model of the lubrication mechanism of the surfaces is provided in **PAPER V**. The general lubrication mechanism of the surface is based on elastic compression and restoration of CNT bundles, stored inside of the surface depressions and being continuously dragged into the direct tribological contact due to their high aspect ratio and flexibility. Raman analysis of the CNT in the wear tracks provides further insights onto their degradation mechanism, which is correlated to a three-stage amorphization trajectory model (see section 2.1.4). According to this model, nanocrystalline graphite is formed when CNT are tribologically stressed. In **PAPER IX**, the lubrication effect of CNT is discussed further and is found to act on a mixture of rolling/sliding of

CNT and graphitic lubrication by degraded CNT, which is presented in detail in a schematic model within this paper. In this regard, the degradation process of CNT, forming nanocrystalline graphite is very important, since pristine CNT can slide/role on top of formed graphitic layers, reducing the friction to COF values lower than what would be expected for a pure graphite-based lubrication.

Comparing the surface structures achieved using a nanosecond or femtosecond laser, a different laser-material interaction is observed. The ablation process of the femtosecond laser translates into the creation of surfaces with a higher load-bearing capacity. Hence, surfaces can be produced, which resemble even more the surfaces of CNT reinforced composite. In order to investigate the effect of the stored solid lubricant volume on the longevity of the lubrication effect, two different structural depths (1µm and 3µm) are chosen. Unexpectedly, the surfaces with less deep structures provide longer lubrication compared to the surfaces with deeper structures. Despite other influencing aspects discussed in **PAPER VII**, the steeper slope of the surface depressions of the deeper structures is found to be too high to allow for an elastic compression and restoration of the CNT bundles and thus the efficient supply of the contact with the solid lubricant.

Since the CNT-coated surfaces are similar to the CNT-reinforced composite surfaces, the presented lubrication mechanism models of **PAPER V, VII and IX** can be transferred to composite-type surfaces as well.

SELF-LUBRICATING MMC, STRESS COLLECTIVE AND CONTACT SITUATION

For a detailed investigation of the tribological behavior of CNP-reinforced MMC, the composites are reinforced with different concentrations of CNP (5, 10 and 20 vol%) and exposed to different geometrical contact situations (conformal and non-conformal), different relative humidities (4% and 45%) and different loads (in order to achieve fully elastic or elasto-plastic contact conditions) in **PAPER IV, VIII and IX**.

- *CNP concentration:*

In **PAPER VIII**, it can be seen that effective lubrication is observed only for CNT. The lubrication effect is more pronounced for higher concentrations, which is in good agreement with the findings of **PAPER IV**. Neither for ND nor for OLC, is a significant lubrication effect observable, which is explained by the particles being too small to be successfully brought into the tribological contact in order to separate the surfaces.

- *Relative humidity:*

The composites are investigated under different relative humidity in **PAPER IV, VIII and IX**, actively avoiding (in low humidity) or allowing (in medium humidity) for a graphite-based (intercalation/delamination) lubrication, respectively. Exclusively for CNT-reinforced composites, effective and constant lubrication is given under all tested conditions and particle concentrations. This

is explained with the high versatility of the lubrication mechanism of CNT. In the case of low humidity, lubrication is based on sliding/rolling of CNT on top of graphitic layers (which were formed by degraded CNT). For higher relative humidity, the lubrication is a mixture between sliding/rolling of CNT and a graphite-based lubrication.

- *Geometrical contact situation:*

Both, non-conformal and conformal contact conditions are analyzed in **PAPER VIII and IX**, respectively. In both cases, an effective lubrication is given for CNT. The lubrication is even more pronounced for conformal contact conditions, since a higher amount of CNT is present, lower contact pressures are applied and the surfaces can be separated more easily by CNT.

- *Loading condition:*

The contact loading is chosen based on contact mechanics simulations using the Jackson-Green model (using an Al_2O_3 ball as counter material) in **PAPER VIII**. In this simulation, the mechanical properties as well as the measured surface topographies of the contacting surfaces are taken into account. For a normal load of 100 mN, the composite bulk material behaves fully elastic whereas an elasto-plastic contact regime is reached at 8 N normal load. For low loads and relative humidity, the presence of CNT decreases a tribologically-induced surface oxidation as it has already been shown for the CNT coatings in **PAPER IV, V and VII**, which is not given for OLC- or ND-reinforced MMC. The lubrication mechanism of CNT in these composites is found to be based on the same mechanisms as in the laser-structured, CNT-coated surfaces, whereas the lubrication mechanism of the surfaces exposed to higher loads slightly differs. This is due to the formation of a homogeneous tribo-layer in all the CNP-reinforced composites, consisting of homogeneously intermixed Ni, NiO and carbon, which is investigated using TEM and EDS analysis. It is further observed, that cracks are formed within this layer, leading to the formation of individual, loosely-bonded sheets, which can freely move on top of each other or the substrate surface. The lubricating effects for CNT-reinforced composites is explained with the high aspect ratio and the possibility of CNT to be dragged in between the formed surface sheets, allowing the sheets to slide upon each other or the substrate due to the already described, intrinsic lubrication mechanism of CNT.

- *Sliding speed:*

Different linear sliding speeds are used in **PAPER IV, V, VI, VII, VIII and IX** from 1 mm/s, over 1 cm/s up to 1 m/s. Regardless of whether the surfaces are coated with CNT or reinforced with CNT, effective lubrication is provided in all cases, rendering the general lubrication effect insensitive to sliding speeds within these ranges.

All this highlights CNT as a very versatile solid lubricant, which can be used under various contact situations and environmental conditions in order to successfully create self-lubricating surfaces.

Even though they have shown homogeneous distribution, a high mechanical reinforcement effect and also potential lubrication effects, ND and OLC are not suited for self-lubricating surfaces.

Summarizing, a continuous supply of CNP into the tribological contact is the most important thing to consider for CNP based self-lubricating surfaces, which can be achieved by CNP coated surfaces with a deterministic surface topography and/or CNP reinforced-MMC. Only for CNT, an effective lubrication is given irrespective of all tested loads, speeds, surfaces, materials, relative humidity or contact mechanics. This can be explained with the high aspect ratio of CNT, allowing them to be dragged into the tribological contact. Lubrication is achieved for all conditions due to the different possibilities of CNT to lubricate the contact (particle sliding/rolling and/or graphite-based lubrication).

OBJECTIVE 3

The findings of **ALL PREVIOUS PAPERS** are combined in this final objective in order to create application-oriented advanced self-lubricating surfaces based on CNP in **PAPER IX**. This is achieved by manufacturing CNT-reinforced composites with a volume concentration of 20% based on the performance shown in **PAPER VIII**, laser structuring the composite surfaces using the femtosecond laser with a structural depth of 1 µm found in **PAPER VII** and subsequently coating the surface structures homogeneously by EPD with CNT in order to protect the surface and to reduce surface oxidation, as developed in **PAPER V, VI and VII**. Based on this development, a prototypical self-lubricating material has been processed and machined to be tested in a macroscopically loaded (20 N) conformal contact situation (similar to real testing conditions of a technical journal-type bearing). Continuously self-lubricating surfaces are produced, allowing for a maximum permanent reduction in friction and wear by a factor of 4 and 115, respectively, compared to a pure Ni surface with the lubrication mechanisms being fully understood.

4. INCLUDED PAPERS

4.0 Outline

I

Colloidal mixing is found to be a suitable technique for the processing of CNP-reinforced Ni-MMC with the dispersion process and the distribution of CNP in MMC being extensively analyzed. A functionalization or degradation of CNP can be avoided, still allowing for homogeneous particle distributions within the MMC. 0-D CNP and an sp^3-hybridization allow for the most homogeneous distributions, the smallest mean grain size and highest mechanical reinforcement effect.

II

The homogeneous distribution of ND in **PAPER I** is transferred to OLC by first manufacturing ND reinforced Ni-MMC and subsequently transforming ND to OLC within the already sintered composite by annealing. It is the first time in literature that the transformation process of ND to OLC within an MMC has been investigated.

III

The influence of CNP concentration on their distribution as well as the grain refinement effect is analyzed based on the processing method of **PAPER I**. Using the acquired experimental data, a modified Zener-model is introduced, predicting the mean grain sizes of the composites as a function of the CNP type and concentration and allowing for full process control of CNP Ni-MMC manufacturing.

IV

With the findings of **PAPER I and III**, a tribological comparison of CNT reinforced Ni-MMC and CNT-coated Ni (by drop casting CNT on a pure Ni sample) is conducted. It is found that a refined microstructure plays only a minor role regarding its effect on a frictional reduction. Much more important is the general presence or absence of CNP in the tribological contact. A continuous supply of CNP into the tribological contact is the most important thing to consider for CNP-based self-lubricating surfaces.

V

Based on **PAPER IV**, a simplified surface situation, comparable to CNT-reinforced composites, is reproduced, allowing for a more detailed understanding of the lubrication mechanism. This is achieved by creating a deterministic surface topography on steel surfaces using DLIP, subsequently coating these surfaces by electrophoretic deposition with CNT, copying the surface topography by the CNT coating. A schematic model, describing the lubrication mechanism of these surfaces is presented and the longevity of the lubrication is significantly extended (factor of 5) compared to unpatterned surfaces.

VI

The influence of surface roughness on the lubrication activity of 0-D and 1-D CNP is investigated. It is found that the high aspect ratio of 1-D particles is beneficial for a constant lubrication irrespective of the given surface roughness, since the particles can be dragged into the direct tribological contact region thus efficiently separating the contacting surfaces. 0-D particles lose their ability to lubricate the contact if a surface roughness higher than the particle diameter is reached.

VII

Based on the findings of **PAPER V and VI**, different surface designs are created by DLW using a femtosecond pulsed laser system. The created surfaces provide a higher load bearing capability than the surface of **PAPER V**. However, only for a specific surface design an efficient lubrication and a further prolongation of the lubrication effect up to almost 100 000 sliding cycles under the given loading conditions is achieved.

VIII

Based on the findings of **PAPER I, III and IV**, CNP reinforced Ni-MMC are produced with different CNP concentrations, all having the same microstructure. Using contact mechanics simulations and taking into account the mechanical properties and the surface topographies of the composites, tribological measurements under fully elastic and elasto-plastic contact conditions are conducted. Additionally, the composites are investigated under different relative humidity, actively avoiding (in low humidity) or allowing (in medium humidity) for a graphite-based lubrication. Exclusively for CNT reinforced composites, effective and constant lubrication is given under all tested conditions and the lubrication and wear mechanisms of the individual composites are investigated and discussed in detail using various high-resolution characterization methods.

IX

The findings of **ALL PREVIOUS PAPERS** are combined in this final work in order to create advanced self-lubricating surfaces based on CNP. This is achieved by manufacturing the most promising CNT reinforced composites of **PAPER VIII**, laser structuring the composite surfaces using the surface design of **PAPER VII** and subsequently coating the surface structures by EPD with CNT, which was developed in **PAPER V, VI and VII**. This way, constantly self-lubricating surfaces are produced, allowing for a maximum reduction in friction and wear by a factor of 4 and 115, respectively, compared to a pure Ni surface. Additionally, the lubrication and degradation mechanism of CNT in a tribological contact is investigated and presented in detail by Raman analysis in a schematic model.

I Dispersion analysis of carbon nanotubes, carbon onions, and nanodiamonds for their application as reinforcement phase in nickel matrix composites

Leander Reinert[1], Marco Zeiger[2], Sebastian Suárez[1], Volker Presser[2] and Frank Mücklich[1]

[1] Department of Material Science and Engineering, Saarland University, 66123 Saarbrücken, Germany
[2] INM – Leibniz Institute for New Materials, 66123 Saarbrücken, Germany

*Published in **"RSC Advances" (Impact factor (2018): 3.108)***
Reproduced by permission of The Royal Society of Chemistry.
Accessible online at: https://doi.org/10.1039/C5RA14310A

Own contribution:

Sample processing including particle dispersion and sintering; Dynamic light scattering; Zeta Potential measurement; Raman spectroscopy analysis; Scanning electron microscopy and particle distribution analysis; Electron backscatter diffraction; Vickers micro-hardness measurement; Writing; Discussion; Planning.

Abstract:

Dispersions of multi-wall carbon nanotubes, onion-like carbon, and nanodiamonds in ethylene glycol are produced using a homogenizer and an ultrasonic bath, altering the treatment time. The dispersed particles are then used as reinforcement phase for nickel matrix composites. These nanoparticles are chosen to represent different carbon hybridization states (sp^2 vs. sp^3) or a different particle geometry (0D vs. 1D). This allows for a systematic investigation of the effect of named differences on the dispersibility in the solvent and in the composite, as well as the mechanical reinforcement effect. A comprehensive suite of complementary analytical methods are employed, including transmission electron microscopy, Raman spectroscopy, dynamic light scattering, sedimentation analysis, zeta-potential measurements, scanning electron microscopy, electron back scatter diffraction, and Vickers microhardness measurements. It can be concluded that the maximum achievable dispersion grade in the solvent is similar, not altering the structural integrity of the particles. However, nanodiamonds show the best dispersion stability, followed by onion-like carbon, and finally multi-walled carbon nanotubes. The distribution and agglomerate sizes of the particles within the composites are in good agreement with the dispersion analysis, which is finally correlated with a maximum grain refinement by a factor of 3 and a maximum mechanical reinforcement effect for nanodiamonds.

Cite this as:
L. Reinert, M. Zeiger, S. Suárez, V. Presser, F. Mücklich, Dispersion analysis of carbon nanotubes, carbon onions and nanodiamonds for their application as reinforcement phase in nickel matrix composites. *RSC Advances* **2015**, 5, 95149-95159. (*https://doi.org/10.1039/C5RA14310A*)

II In-situ nanodiamond to carbon onion transformation in metal matrix composites

Sebastian Suarez[1], **Leander Reinert[1]**, Marco Zeiger[2], Patrice Miska[3], Samuel Grandthyll[4], Frank Müller[4], Volker Presser[2] and Frank Mücklich[1]

[1] Department of Material Science and Engineering, Saarland University, 66123 Saarbrücken, Germany
[2] INM – Leibniz Institute for New Materials, 66123 Saarbrücken, Germany
[3] Institue Jean Lamour, CNRS UMR 7198, Université de Lorraine, Nancy, F-54000, France
[4] Experimental Physics, Saarland University, Campus E2 9, 66123 Saarbrücken, Germany

Published in ***"Carbon" (Impact factor (2018): 7,082)***
Accessible online at: *https://doi.org/10.1016/j.carbon.2017.12.072*

Own contribution:

Sample processing including particle dispersion and sintering; UV-Raman spectroscopy analysis; Scanning electron microscopy and particle distribution analysis; Writing; Discussion; Planning.

Abstract:

In the present study, nickel matrix composites reinforced with a fine distribution of nanodiamonds (6.5 vol%) as reinforcement phase are annealed in vacuum at different temperatures ranging from 750 °C to 1300 °C. This is carried out to evaluate the in-situ transformation of nanodiamonds to carbon onions within a previously densified composite. The resulting materials are thoroughly analyzed by complementary analytical methods, including Raman spectroscopy, transmission electron microscopy, scanning electron microscopy, energy dispersive X-ray spectroscopy and X-ray photoelectron spectroscopy. The proposed in-situ transformation method presents two main benefits. On one hand, since the particle distribution of a nanodiamond-reinforced composite is significantly more homogenous than in the case of the carbon onions, it is expected that the transformed particles will preserve the initial distribution features of nanodiamonds. On the other hand, the proposed process allows for the tuning of the sp^3/sp^2 carbon ratio by applying a single straightforward post-processing step.

Cite this as:
S. Suárez, L. Reinert, M. Zeiger, P. Miska, S. Grandthyll, F. Müller, V. Presser, F. Mücklich, In-situ nanodiamond to carbon onion transformation in metal matrix composites. *Carbon* **2017**, 129, 631-636. (*https://doi.org/10.1016/j.carbon.2017.12.072*)

III Carbon Nanoparticle-Reinforced Metal Matrix Composites: Microstructural Tailoring and Predictive Modeling

Leander Reinert, Sebastian Suárez, Thomas Müller and Frank Mücklich

Department of Material Science and Engineering, Saarland University, 66123 Saarbrücken, Germany

*Published in **"Advanced Engineering Materials" (Impact factor (2017): 2.319)***
Accessible online at: https://doi.org/10.1002/adem.201600750

Own contribution:

Sample processing including particle dispersion and sintering; Scanning electron microscopy and particle distribution analysis; Electron backscatter diffraction; Writing; Discussion; Planning.

Abstract:

Nickel matrix composites are produced with concentrations of 0.5–10 vol% of carbon nanotubes (CNT), onion-like carbon (OLC), or nanodiamonds (nD) as reinforcement phase by hot pressing. The effect of the carbon nanoparticle (CNP) type and concentration on the microstructure is analyzed. Grain sizes are measured and a model is adapted to predict the observed grain refinement for all CNP. The individual saturation concentration and maximum achievable grain refinement differs (for CNT: 3 vol%, OLC: 6.5 vol% and nD: 10 vol%), which is correlated to the agglomerate diameter distribution. This can be traced back to different hybridization states and different particle geometries, therefore providing valuable information for CNP-reinforced Metal matrix composites to a general extent.

Cite this as:
L. Reinert, S. Suárez, T. Müller, F. Mücklich, Carbon Nanoparticle-Reinforced Metal Matrix Composites: Microstructural Tailoring and Predictive Modeling. *AEM* **2017**, 19, 1600750. (*https://doi.org/10.1002/adem.201600750*)

IV Tribo-Mechanisms of Carbon Nanotubes: Friction and Wear Behavior of CNT-Reinforced Nickel Matrix Composites and CNT-Coated Bulk Nickel

Leander Reinert[1], Sebastian Suárez[1] and Andreas Rosenkranz[1,2]

[1] Department of Material Science and Engineering, Saarland University, 66123 Saarbrücken, Germany
[2] Institute of Experimental Physics, Pontificia Universidad Católica de Chile, Santiago 7820436, Chile

*Published in **"Lubricants" (Impact factor: not applicable)***

Accessible online at: https://doi.org/10.3390/lubricants4020011

Own contribution:

Sample processing including particle dispersion and drop casting of particles; Tribological experiments and friction coefficient analysis; Scanning electron microscopy and wear track analysis; Raman Spectroscopy; Writing; Discussion; Planning.

Abstract:

In this study, nickel matrix composites reinforced by carbon nanotubes (CNTs) are compared to unreinforced CNT-coated (by drop-casting) bulk nickel samples in terms of their friction and wear behavior, thus gaining significant knowledge regarding the tribological influence of CNTs and the underlying tribo-mechanism. It has been shown that the frictional behavior is mainly influenced by the CNTs present in the contact zone, as just minor differences in the coefficient of friction between the examined samples can be observed during run-in. Consequently, the known effect of a refined microstructure, thus leading to an increased hardness of the CNT reinforced samples, seems to play a minor role in friction reduction compared to the solid lubrication effect induced by the CNTs. Additionally, a continuous supply of CNTs to the tribo-contact can be considered isolated for the reinforced composites, which provides a long-term friction reduction compared to the CNT-coated sample. Finally, it can be stated that CNTs can withstand the accumulated stress retaining to some extent their structural state for the given strain. A comprehensive study performed by complementary analytical methods is employed, including Raman spectroscopy and scanning electron microscopy tounderstand the involved friction and wear mechanisms.

Cite this as:
L. Reinert, S. Suárez, A. Rosenkranz, Tribo-Mechanisms of Carbon Nanotubes: Friction and Wear Behavior of CNT-Reinforced Nickel Matrix Composites and CNT-Coated Bulk Nickel. *Lubricants* **2016**, 4, 11. (*https://doi.org/10.3390/lubricants4020011*)

V Long-lasting solid lubrication by CNT-coated patterned surfaces

Leander Reinert, Federico Lasserre, Carsten Gachot, Philipp Grützmacher, Timothy MacLucas, Nicolas Souza, Frank Mücklich and Sebastian Suárez

Department of Material Science and Engineering, Saarland University, 66123 Saarbrücken, Germany

*Published in **"Nature – Scientific Reports" (Impact factor (2017): 4.609)***

Accessible online at: https://doi.org/10.1038/srep42873

Own contribution:

Laser texturing; Tribological experiments and friction coefficient analysis; Scanning electron microscopy and wear track analysis; Raman Spectroscopy; Writing; Discussion; Planning.

Abstract:

The use of lubricants (solid or liquid) is a well-known and suitable approach to reduce friction and wear of moving machine components. Another possibility to influence the tribological behaviour is the formation of well-defined surface topographies such as dimples, bumps or lattice-like pattern geometries by laser surface texturing. However, both methods are limited in their effect: surface textures may be gradually destroyed by plastic deformation and lubricants may be removed from the contact area, therefore no longer properly protecting the contacting surfaces. The present study focuses on the combination of both methods as an integral solution, overcoming individual limitations of each method. Multiwall carbon nanotubes (MWCNT), a known solid lubricant, are deposited onto laser surface textured samples by electrophoretic deposition. The frictional behaviour is recorded
by a tribometer and resulting wear tracks are analysed by scanning electron microscopy and Raman spectroscopy in order to reveal the acting tribological mechanisms. The combined approach shows an extended, minimum fivefold longevity of the lubrication and a significantly reduced degradation of the laser textures. Raman spectroscopy proves decelerated MWCNT degradation and oxide formation in the contact. Finally, a lubricant entrapping model based on surface texturing is proposed and demonstrated.

Cite this as:
L. Reinert, F. Lasserre, C. Gachot, P. Grützmacher, T. MacLucas, N. Souza, F. Mücklich, S. Suárez, Long-lasting solid lubrication by CNT-coated patterned surfaces. *Scientific Reports* **2017**, 7, 42873. (*https://doi.org/10.1038/srep42873*)

VI Influence of surface roughness on the lubrication effect of carbon nanoparticle-coated steel surfaces

Leander Reinert, Silas Schütz, Sebastian Suárez and Frank Mücklich

Department of Material Science and Engineering, Saarland University, 66123 Saarbrücken, Germany

*Published in **"Tribology letters" (Impact factor (2018): 2.182)***
The final publication is available at link.springer.com
Accessible online at: https://doi.org/10.1007/s11249-018-1001-6

Own contribution:

Planning of tribological experiments; Friction coefficient analysis; Scanning electron microscopy and wear track analysis; Writing; Discussion; Planning.

Abstract:

In the present study, a systematic evaluation of the influence of the surface roughness on the lubrication activity of multiwall carbon nanotubes (MWCNT) and onion-like carbon (OLC) is performed. MWCNT and OLC are chosen as they both present an sp^2-hybridization of carbon atoms, show a similar layered atomic structure and exhibit the potential to roll on top of a surface. However, their morphology (size and aspect ratio) clearly differs, allowing for a methodical study of these differences on the lubrication effect on systematically varied surface roughness. Stainless steel platelets with different surface finishing were produced and coated by electrophoretic deposition with OLC or MWCNT. The frictional behavior is recorded using a ball-on-disc tribometer and the resulting wear tracks are analyzed by scanning electron microscopy in order to reveal the acting tribological mechanisms. It is found, that the lubrication mechanism of both types of particles is traced back to a mixture between a rolling motion on the surfaces and particle degradation, including the formation of nanocrystalline graphitic layers. This investigation further highlights, that choosing the suitable surface finish for a tribological application is crucial for achieving beneficial tribological effects of carbon nanoparticle lubricated surfaces.

Cite this as:
L. Reinert, S. Schütz, S. Suárez, F. Mücklich, Influence of surface roughness on the lubrication effect of carbon nanoparticle-coated steel surfaces. *Tribology letters* **2018**, 66 (*https://doi.org/10.1007/s11249-018-1001-6*)

VII Influence of surface design on the solid lubricity of carbon nanotubes-coated steel surfaces

Christian Schäfer[1], **Leander Reinert[1]**, Timothy MacLucas[1], Philipp Grützmacher[1], Rolf Merz[2], Frank Mücklich[1] and Sebastian Suárez[1]

[1] Department of Material Science and Engineering, Saarland University, 66123 Saarbrücken, Germany
[2] Institut für Oberflächen-und Schichtanalytik GmbH, Trippstadter Straße 120, 67663 Kaiserslautern, Germany

*Published in **"Tribology letters" (Impact factor (2018): 2.182)***
The final publication is available at link.springer.com
Accessible online at: https://doi.org/10.1007/s11249-018-1044-8

Own contribution:

Planning and coordination of tribological experiments; Friction coefficient analysis; Scanning electron microscopy and wear track analysis; Raman spectroscopy analysis; Writing; Discussion; Planning.

Abstract:

Topographically designed surfaces are able to store solid lubricants, preventing their removal out of the tribological contact and thus significantly prolonging the lubrication lifetime of a surface. The present study provides a systematic evaluation of the influence of surface structure design on the solid lubrication effect of multi-walled carbon nanotubes (MWCNT) coated steel surfaces. For this purpose, direct laser writing using a femtosecond pulsed laser system is deployed to create surface structures, which are subsequently coated with MWCNT by electrophoretic deposition. The structural depth or aspect ratio of the structures and thus the lubricant storage volume of the solid lubricant is varied. The frictional behavior of the surfaces is recorded using a ball-on-disc tribometer and the surfaces are thoroughly characterized by complementary characterization techniques. Efficient lubrication is achieved for all MWCNT coated surfaces. However, and in contrast to what would be expected, it is shown that deeper structures with larger lubricant storage volume do not lead to an extended lubrication lifetime and behave almost equally to the coated unstructured surfaces. This can be attributed, among other things, to differences in the final surface roughness of the structures and the slope steepness of the structures, which prevent efficient lubricant supply into the contact.

Cite this as:
C. Schäfer, L. Reinert, T. MacLucas, P. Grützmacher, R. Merz, F. Mücklich and S. Suárez, Influence of surface design on the solid lubricity of carbon nanotubes-coated steel surfaces, *Tribology letters* **2018,** 66:89 (*https://doi.org/10.1007/s11249-018-1044-8*)

VIII Tribological behavior of self-lubricating carbon nanoparticle reinforced metal matrix composites

Leander Reinert[1], Itzhak Green[2], Steffen Gimmler[1], Björn Lechthaler[1], Frank Mücklich[1] and Sebastian Suárez[1]

[1] Department of Material Science and Engineering, Saarland University, 66123 Saarbrücken, Germany
[2] George W. Woodruff-School of Mechanical Engineering, Georgia Institute of Technology, Atlanta, USA

*Published in **"Wear" (Impact factor (2018): 2.960)***
Accessible online at: https://doi.org/10.1016/j.wear.2018.05.003

Own contribution:

Planning and coordination of tribological experiments; Friction coefficient analysis; Surface analysis by laser scanning microscopy; Scanning electron microscopy and wear track analysis; Electron backscatter diffraction analysis; Electron dispersive spectroscopy analysis; Raman spectroscopy analysis; Writing; Discussion; Planning.

Abstract:

The present study focuses on investigating the dominant friction and wear mechanisms in the case of dry sliding of carbon nanoparticle reinforced nickel matrix composites under elastic and elasto-plastic contact conditions. For this purpose, multi-wall carbon nanotubes (CNT), onion-like carbon (OLC) and nanodiamonds (nD) were chosen to represent a large variety of carbon nanoparticles as they can be systematically distinguished regarding their carbon hybridization state (sp^2 vs. sp^3) as well as their morphology and size ("0D" vs. "1D"). Contact simulations based on the Greenwood-Williamson model are conducted in order to calculate the required contact loads. Friction and wear analysis is supported by complementary characterization techniques, including scanning electron microscopy, transmission electron microscopy, energy dispersive spectroscopy, Raman spectroscopy, light microscopy as well as laser scanning microscopy. It is found, that only CNT provide efficient lubrication as reinforcement phase in composites, presenting different lubrication mechanisms for the tested contact conditions. The high aspect ratio of CNT is found to be essential for the lubrication mechanisms, allowing the particles to be dragged into the direct tribological contact. The lubrication effect increases with increasing volume content of CNT, reaching a maximum steady state frictional reduction of 50% compared to the unreinforced nickel reference.

Cite this as:
L. Reinert, I. Green, S. Gimmler, B. Lechthaler, F. Mücklich and S. Suárez, Tribological behavior of self-lubricating carbon nanoparticle reinforced metal matrix composites. *Wear* **2018**, 408-409, 72-85 (*https://doi.org/10.1016/j.wear.2018.05.003*)

IX Dry friction and wear of self-lubricating carbon nanotube-containing surfaces

Leander Reinert[1], Michael Varenberg[2], Frank Mücklich[1] and Sebastian Suárez[1]

[1] Department of Material Science and Engineering, Saarland University, 66123 Saarbrücken, Germany
[2] George W. Woodruff-School of Mechanical Engineering, Georgia Institute of Technology, Atlanta, USA

Published in ***"Wear" (Impact factor (2018): 2.960)***
Accessible online at: https://doi.org/10.1016/j.wear.2018.03.021

Own contribution:

Planning and coordination of sample processing, Surface analysis by laser scanning microscopy; Tribological experiments including friction coefficient and quantitative wear analysis; Scanning electron microscopy including particle distribution and wear track analysis; Raman spectroscopy; Electron backscatter diffraction analysis; Electron dispersive spectroscopy analysis; Writing; Discussion; Planning.

Abstract:

The unfavorable environmental conditions of certain tribological systems, such as operation at high temperatures or under vacuum, set the need to replace liquid with solid lubricants. Multi-Wall-Carbon Nanotubes (MWCNTs) have been emphasized as a very effective solid lubricant. The particles have been used to create self-lubricating materials by acting as reinforcement phase in composites or as solid-lubricant coating that works in conjunction with textured surfaces to prevent the removal of particles from the contact. However, both approaches are restricted to some extent. In the case of composites, the solid lubricant concentration is limited so as not to influence the mechanical stability of the final component. For coated surface structures, the textured surfaces can degrade during the experiment. The present study focuses on the combination of these approaches in order to create enhanced self-lubricating surfaces with MWCNTs as the solid lubricant. A custom-made ring on block tribometer is used to study the behavior of laser textured MWCNT-coated and MWCNT-reinforced nickel matrix composites under the conditions of unidirectional sliding in conformal contact. It is shown that the combination of both approaches allows for a maximum 4-fold reduction in friction and a 115-fold reduction in wear rate compared to the reference. Additionally, the lubrication mechanism of the MWCNTs is investigated in more detail and a structural degradation model of the mechanically stressed MWCNTs is proposed. Our results highlight the integrated solution as a suitable approach for self-lubricating surfaces subjected to unidirectional sliding

.Cite this as:
L. Reinert, M. Varenberg, F. Mücklich, S. Suarez, Dry friction and wear of self-lubricating carbon nanotube-containing surfaces. *Wear* **2018**, 406-407, 33-42. (*https://doi.org/10.1016/j.wear.2018.03.021*)

5. CONCLUSIONS AND OUTLOOK

The dissertation addresses the development of self-lubricating surfaces using a new and emerging field of solid lubricants (CNP). Hence, a method must be found, providing full process control and allowing for a comparable and reproducible way to produce CNP-containing surfaces without changing the CNP properties (**Objective 1**). Secondly, the lubrication activity and mechanism of the chosen CNP, providing systematically distinguishable morphology and carbon hybridization, must be evaluated and understood under varying stress collective, surface designs and contact situations (**Objective 2**). Based on these findings, a prototypical, constantly self-lubricating surface should be manufactured, combining the most efficient approaches (**Objective 3**). In the following, the most important findings of the dissertation are briefly summarized.

OBJECTIVE 1

CNP containing surfaces can be produced through CNP reinforcement of MMC. Regarding its processing, colloidal mixing followed by hot uniaxial pressing is chosen, since a functionalization or degradation of the CNP is avoided, still allowing for homogeneous particle distributions within the MMC. It is found that 0-D CNP and an sp^3-hybridization present the most homogeneous distributions, the smallest mean grain size and highest mechanical reinforcement effect. The best achievable particle distribution for sp^3-hybridized particles (ND) was successfully transferred to sp^2-hybridized particles (OLC) by annealing a pre-sintered ND-reinforced MMC. Even though the transformation process of ND to OLC is well known, it is the first time that it has been successfully conducted and characterized within a pre-sintered composite. Additionally, a model, based on the Zener-boundary drag effect, has been adapted, predicting the final mean grain size as a function of the type and concentration of the used CNP when the proposed optimum processing parameters are used. However, the processing parameters can also be chosen so as to produce CNP-reinforced MMC with various concentrations, all providing the same microstructure and thus allowing for a tribological comparison. Considering all these points, it can be stated that all challenges regarding the development of a reproducible and fully controllable processing method have been met.

OBJECTIVE 2

A continuous supply of CNP into the direct tribological contact is the most important thing to consider for CNP-based self-lubricating surfaces. A high aspect ratio and flexibility of the particles are beneficial to achieve a permanent lubrication, regardless of the given surface roughness, since the particles can be pulled into the direct tribological contact region thus efficiently separating the contacting surfaces. These conditions are met for 1-D CNT particles. Even though 0-D particles can separate the contacting surfaces and lubricate the contact by sliding/rolling, they lose this ability when interacting with a surface roughness higher than the particle diameter, which is given for most technical surfaces. A specifically designed deterministic surface (using DLIP or DLW) has been

introduced and is subsequently coated with CNT. It is found that the surface design and CNT coating interact synergetically with CNT being stored within the created surface depressions, which continuously supply the surface with the solid lubricant, achieving a 9-fold extension in the longevity of the lubrication effect. The surface lubrication mechanism acts on compression and elastic restoration of CNT bundles and the ability of CNT to be dragged inside of the contact region irrespective of the given topographical contact situation. Since the designed surface is comparable to a CNT-reinforced MMC surface, the lubrication mechanism can be transferred to CNP-reinforced MMC as well.

Particle degradation is observed for all CNP in a tribological contact. However, specifically for CNT, the degradation is directly related to its intrinsic lubrication mechanism. It is the first time that a tribologically induced CNT degradation has been quantified and correlated to an amorphization trajectory model. With on-going CNT degradation, nanocrystalline graphite is formed. This is very important so as to allow pristine CNT to perform a sliding/rolling movement on top of these graphitic surfaces, reducing the COF to values below what would be expected for a pure graphite-based lubrication. Based on contact mechanics simulations (using the Jackson-Green model), the composites are also tested under elastic or elaso-plastic contact situations, with only CNT reinforced MMC presenting constant lubrication. For low loads and low relative humidity, surface oxidation is reduced with CNT acting as an oxidation barrier, effectively separating the contacting surfaces and diminishing the occurrence of wear. Since graphite-based lubrication can be excluded for low relative humidity, lubrication is mainly associated with sliding/rolling of pristine CNT on top of the formed graphitic layer. For higher loads and relative humidity, strong oxidation is observed. However, the formed carbonaceous oxidic layer breaks into sheets, which can freely move on the surface being lubricated by CNT. In this case, lubrication acts on a mixture of sliding/rolling of CNT and shearing based graphite lubrication. Regarding conformal or non-conformal contact situations or different sliding speeds (1 mm/s – 1 m/s) for CNT coated or reinforced composites, efficient and constant lubrication is always given. This qualifies CNT as a versatile solid lubricant, adapting to the given contact situations and environmental conditions by effectively combining different solid lubricant working principles, namely: rolling, sliding and shearing.

OBJECTIVE 3

The combination of CNT-reinforced MMC, specific surface designing by laser structuring and subsequent CNT coating finally results in the production of advanced self-lubricating surfaces. A prototypical self-lubricating surface has been successfully manufactured and is tested in a macroscopically loaded (20 N) conformal contact situation (similar to real testing conditions of a journal-type bearing component), allowing for a maximum reduction in friction and wear by a factor of 4 and 115, respectively (compared to a pure Ni surface) with the lubrication mechanisms being fully understood.

Summarizing, out of the three studied CNP types, CNT are identified as a nano-scale, multi-purpose solid lubricant, which can be effectively applied to create self-lubricating surfaces. Being stored in a nickel matrix or a specifically designed surface, CNT are continuously transferred into the contact and are thus easy to replenish. The effectiveness of the lubrication is comparable to other currently used solid lubricants but is more robust regarding the stress collective or environmental conditions. With sp^2-hybridized graphitic carbon being the most stable carbon configuration under standard pressure and temperature, CNT are expected to provide a very good aging stability. CNT are further known to be thermally stable under atmospheric conditions at temperatures of up to 600-700°C, rendering CNT a promising solid lubricant candidate for higher temperature applications [354]. Additionally, CNT are able to carry away generated heat due to their high thermal conductivity and also provide a high electrical conductivity, rendering them an interesting reinforcement material for tribo-electrical applications (for example plug connectors or contact brushes). Due to their nano-scale size, low density and high mechanical strength, CNT further offer the possibility to mechanically reinforce structural components, which are subjected to friction and wear, thus also being usable for lightweight construction of machine elements. Finally, and together with all the mentioned points, the suitability of CNT as a lubricant under vacuum as well as under atmospheric conditions proves its advantage in terms of applicability and robustness compared to other solid lubricants.

OUTLOOK

The identification of the requirements needed to create self-lubricating surfaces based on CNT and the detailed understanding of their lubrication mechanism are a stepping-stone in the state of the art of this research field. The choice of laser patterning as a very versatile and flexible tool allows for the transfer of the chosen surface design to nearly any material surface. Additionally, the chosen coating technique (electrophoretic deposition) is suited for every electrically conductive substrate material. Hence, the findings presented in this dissertation could be easily transferred to almost any metallic surface, which highlights its wide span of applicability.

The utilization of CNT as solid lubricant in MMC requires the chemical inertness of the matrix material with regards to a potential carbide formation. Thus, with elements such as Cu and Sn showing no tendency to form carbides, the presented method could be transferred to sintered bronze slider bearings, which already find application in almost every sector of tribological importance (general mechanical engineering, automotive, power tools, sports and leisure equipment, office-, textile- or agricultural machinery, etc.). So far, these sintered slider bearings are soaked with a liquid lubricant (e.g. oil) or other solid lubricants such as MoS_2 are embedded. However, regarding the processing of CNT-reinforced sintered bronze slider bearings, research still needs to be carried out.

Regarding other technically applicable materials, such as steel or other alloys, they typically contain elements like Cr, Al, Ti or V, all showing a strong tendency to form thermodynamically-stable

carbides. Hence, when sintering a CNT powder mixture including these elements, CNT would be fully dissolved in the metal phase forming carbides and no lubrication can be expected. One way to overcome this limitation could be a protective coating of the CNT before sintering the composite material, with the coating acting as a diffusion barrier between the metal matrix and the CNT. In this regard, a full CNT encapsulation using the molecular level mixing method could be an interesting approach, although the CNT would be covalently functionalized and thus degraded to some extent. An alternative could be a galvanic coating of the CNT (e.g. with Ni). However, since the coating would form a metallic bond to the matrix material, the mobility of the encapsulated CNT could be reduced, diminishing the lubrication effect. Hence, further research should be carried out in this area.

Another promising approach to expand the field of application of CNT-reinforced Ni-MMC is its use as surface coating using electroless or electro deposition, which is currently studied in literature. These techniques allow applying the self-lubricating MMC onto technically more relevant alloys acting as a friction- and wear-reducing surface protection layer. Also, additive manufacturing, e.g. using laser-cladding, could be very promising in order to coat technically usable components. In this regard, the presented CNT Ni powder processing method could be used to manufacture a precursor powder for this processing route. However, both mentioned coating methods would involve a new process development and full material characterization, since the involved temperatures, microstructure or phase formations could differ significantly from the system presented in this dissertation. Therefore, it would be a complete study in itself.

6. NOT INCLUDED PAPERS

Within the framework of the present dissertation, further research sectors were addressed which are not directly correlated to the topic of the dissertation. Nonetheless, several papers have been published, which are mentioned in the following:

[1] C. Gachot, A. Rosenkranz, **L. Reinert**, E. Ramos-Moore, N. Souza, M. H. Müser, and F. Mücklich, "Dry Friction Between Laser-Patterned Surfaces: Role of Alignment, Structural Wavelength and Surface Chemistry," Tribol. Lett., vol. 9, 2013, doi: 10.1007/s11249-012-0057-y

[2] A. Rosenkranz, **L. Reinert**, C. Gachot, and F. Mücklich, "Alignment and wear debris effects between laser-patterned steel surfaces under dry sliding conditions," Wear, vol. 318, 2014, doi: 10.1016/j.wear.2014.06.016

[3] A. Rosenkranz, **L. Reinert**, C. Gachot, H. Aboufadl, S. Grandthyll, K. Jacobs, F. Müller, and F. Mücklich, "Oxide Formation, Morphology, and Nanohardness of Laser-Patterned Steel Surfaces," Adv. Eng. Mater., 2015, doi 10.1002/adem.201400487

[4] A. Rosenkranz, F. Krupp, **L. Reinert**, F. Mücklich, and B. Sauer, "Tribological performance of laser-patterned chain links – Influence of pattern geometry and periodicity," Wear, vol. 370, 2016, doi: 10.1016/j.wear.2016.11.006

[5] S. Suarez, **L. Reinert**, and F. Mücklich, "Carbon Nanotube (CNT)-Reinforced Metal Matrix Bulk Composites: Manufacturing and Evaluation," in Diamond and Carbon Composites and Nanocomposites, 2016. doi: 10.5772/63886

[6] M. Leidner, S. Thoss, H. Schmidt, **L. Reinert**, K. Trinh, C. Schäfer and F. Mücklich, "Verbesserung der tribologischen und elektrischen Eigenschaften von Zinn-Kontaktoberflächen durch Partikel/Schmierstoff-Einbettung mittels Laser-Texturierung" , 6th Symposium Connectors, 2017, pp. 59-67, Lemgo, Germany

[7] M. Leidner, S. Thoss, H. Schmidt, J. C. Poliseno, **L. Reinert**, C. Schäfer and F. Mücklich, "Verbesserung der tribologischen und elektrischen Eigenschaften von zinnbeschichteten Steckverbindern mittels Laser-Texturierung" , Albert-Keil Seminar of Connectors, 2017, Karlsruhe, Germany

REFERENCES

[1] B. Bhushan, *Principles and Applications of Tribology*, John Wiley & Sons, **1999**.

[2] A. Kamali, in *McMinn D.J.W. Mod. Hip Resurfacing*, Springer, **2009**, pp. 79–89.

[3] K. Holmberg, P. Andersson, A. Erdemir, *Tribol. Int.* **2012**, *47*, 221.

[4] M. Urbakh, J. Klafter, D. Gourdon, J. Israelachvili, *Nature* **2004**, *430*, 525.

[5] C. M. Taylor, *Wear* **1998**, *221*, 1.

[6] B. Zhmud, *Tribol. Lubr. Technol.* **2011**, *67*, 42.

[7] M. Eriksson, F. Bergman, S. Jacobson, *Wear* **2002**, *252*, 26.

[8] A. Khamlichi, M. Bezzazi, A. Jabbouri, R. P., J. P. Davim, *Int. J. Phys. Sci.* **2008**, *3*, 65.

[9] M. M. Khonsari, E. R. Booser, *Applied Tribology: Bearing Design and Lubrication*, John Wiley & Sons Ltd., **2008**.

[10] I. Etsion, *J. Tribol. Trans. ASME* **2005**, *127*, 248.

[11] H. K. D. H. Bhadeshia, *Prog. Mater. Sci.* **2012**, *57*, 268.

[12] M. Woydt, R. Wäsche, *Wear* **2010**, *268*, 1542.

[13] C.Donnet, Ali Erdemir, *Tribol. Lett.* **2004**, *17*, 389.

[14] S. M. Aouadi, H. Gao, A. Martine, T. W. Scharf, C. Muratore, *Surf. Coatings Technol.* **2014**, *257*, 266.

[15] J. R. Jones, M. J. Jansen, *Proc. Inst. Mech. Eng. Part J J. Eng. Tribol.* **2008**, *222*, 997.

[16] A. Dorri Moghadam, E. Omrani, P. L. Menezes, P. K. Rohatgi, *Compos. Part B Eng.* **2015**, *77*, 402.

[17] D. Berman, A. Erdemir, A. V. Sumant, *Mater. Today* **2014**, *17*, 31.

[18] T. W. Scharf, P. G. Kotula, S. V. Prasad, *Acta Mata.* **2010**, *58*, 4100.

[19] C. Muratore, A. A. Voevodin, *Annu. Rev. Mater. Res.* **2009**, *39*, 297.

[20] T. W. Scharf, S. V. Prasad, *J. Mater. Sci.* **2013**, *48*, 511.

[21] B. Bhushan, *Modern Tribology Handook*, CRC Press LLC, **2001**.

[22] S. V. Prasad, R. Asthana, *Tribol. Lett.* **2004**, *17*, 445.

[23] K. U. Kainer, in *Met. Matrix Compos. Cust. Mater. Automot. Aerosp. Eng.*, Wiley-VCH Verlag GmbH, **2006**.

[24] D. Miracle, *Compos. Sci. Technol.* **2005**, *65*, 2526.

[25] P. K. Rohatgi, M. Tabandeh-Khorshid, E. Omrani, M. R. Lovell, P. L. Menezes, in *Tribol. Sci. Eng. From Basics to Adv. Concepts*, Springer New York, **2013**, pp. 233–268.

[26] E. Omrani, A. Moghadam, P. L. Menezes, P. K. Rohatgi, in *Mater. Forming, Mach. Tribol.*, **2016**, pp. 63–103.

[27] G. Hatipoglu, M. Kartal, M. Uysal, T. Cetinkaya, H. Akbulut, *Tribol. Int.* **2016**, *98*, 59.

[28] W. X. Chen, J. P. Tu, L. Y. Wang, H. Y. Gan, Z. D. Xu, X. B. Zhang, *Carbon* **2003**, *41*, 215.

[29] X. H. Chen, J. Peng, F. Deng, J. Wang, W. Li, *J. Mater. Sci. Lett.* **2001**, *20*, 2057.

[30] J. Tan, T. Yu, B. Xu, Q. Yao, *Tribol. Lett.* **2006**, *21*, 107.

[31] Y. Gogotsi, V. Presser, *Carbon Nanomaterials*, CRC Press, **2014**.

[32] S. R. Bakshi, D. Lahiri, A. Agarwal, *Int. Mater. Rev.* **2010**, *55*, 41.

[33] V. N. Mochalin, O. Shenderova, D. Ho, Y. Gogotsi, *Nat. Nanotechnol.* **2012**, *7*, 11.

[34] M. R. Falvo, R. M. T. Ii, A. Helser, V. Chi, *Nature* **1999**, *397*, 1.

[35] P. L. Dickrell, S. B. Sinnott, D. W. Hahn, N. R. Raravikar, L. S. Schadler, P. M. Ajayan, W. G.

Sawyer, *Tribol. Lett.* **2005**, *18*, 59.

[36] A. Hirata, M. Igarashi, T. Kaito, *Tribol. Int.* **2004**, *37*, 899.

[37] K. T. Kim, S. Il Cha, S. H. Hong, *Mater. Sci. Eng. A* **2007**, *449–451*, 46.

[38] X. H. Chen, C. S. Chen, H. N. Xiao, H. B. Liu, L. P. Zhou, S. L. Li, G. Zhang, *Tribol. Int.* **2006**, *39*, 22.

[39] S. Arai, A. Fujimori, M. Murai, M. Endo, *Mater. Lett.* **2008**, *62*, 3545.

[40] S. Suárez, A. Rosenkranz, C. Gachot, F. Mücklich, *Carbon* **2014**, *66*, 164.

[41] Y. Li, B. X. Li, W. J. Zou, *Appl. Mech. Mater.* **2011**, *80–81*, 683.

[42] L. Wang, Y. Gao, Q. Xue, H. Liu, T. Xu, *Mater. Sci. Eng. A* **2005**, *390*, 313.

[43] V. Y. Dolmatov, T. Fujimura, G. K. Burkat, E. A. Orlova, M. V Veretennikova, *Powder Metall. Met. Ceram.* **2003**, *42*, 55.

[44] T. W. Scharf, A. Neira, J. Y. Hwang, J. Tiley, R. Banerjee, *J. Appl. Phys.* **2009**, *106*, 13508.

[45] J. M. Martin, N. Ohmae, *Nanolubricants*, John Wiley & Sons Ltd., **2008**.

[46] L. Joly-Pottuz, E. W. Bucholz, N. Matsumoto, S. R. Phillpot, S. B. Sinnott, N. Ohmae, J. M. Martin, *Tribol. Lett.* **2010**, *37*, 75.

[47] B. Ni, S. B. Sinnott, *Surf. Sci.* **2001**, *487*, 87.

[48] S. Iijima, *Nature* **1991**, *354*, 56.

[49] M. F. L. De Volder, S. H. Tawfick, R. H. Baughman, A. J. Hart, *Science* **2013**, *339*, 535.

[50] J. Cebik, J. K. McDonough, F. Peerally, R. Medrano, I. Neitzel, Y. Gogotsi, S. Osswald, *Nanotechnology* **2013**, *24*, 1.

[51] F. Mücklich, A. Lasagni, C. Daniel, *Int. J. Mat. Res.* **2006**, *97*, 1337.

[52] T. Hu, Y. Zhang, L. Hu, *Wear* **2012**, *278–279*, 77.

[53] A. Rosenkranz, T. Heib, C. Gachot, F. Mücklich, *Wear* **2015**, *334–335*, 1.

[54] H. O. Pierson, *Handbook of Carbon, Graphite, Diamonds and Fullerenes*, Noyes Publications, **1994**.

[55] M. S. Dresselhaus, G. Dresselhaus, P. Avouris, *Carbon Nanotubes*, Springer Verlag, **2003**.

[56] C. Buzea, I. I. Pacheco, K. Robbie, *Biointerphases* **2007**, *2*, 17.

[57] M. Terrones, A. R. Botello-Méndez, J. Campos-Delgado, F. López-Urías, Y. I. Vega-Cantú, F. J. Rodríguez-Macías, A. L. Elías, E. Muñoz-Sandoval, A. G. Cano-Márquez, J. C. Charlier, H. Terrones, *Nano Today* **2010**, *5*, 351.

[58] J. H. Lehman, M. Terrones, E. Mansfield, K. E. Hurst, V. Meunier, *Carbon* **2011**, *49*, 2581.

[59] I. Suarez-Martinez, N. Grobert, C. P. Ewels, *Carbon* **2012**, *50*, 741.

[60] L. Joly-pottuz, N. Matsumoto, H. Kinoshita, B. Vacher, M. Belin, G. Montagnac, *Tribol. Int.* **2008**, *41*, 69.

[61] V. V. Danilenko, *Phys. Solid State* **2004**, *46*, 595.

[62] C.-C. Chou, S.-H. Lee, *Wear* **2010**, *269*, 757.

[63] K. V. Purtov, A. I. Petunin, A. E. Burov, A. P. Puzyr, V. S. Bondar, *Nanoscale Res. Lett.* **2010**, *5*, 631.

[64] Y. R. Chang, H. Y. Lee, K. Chen, C. C. Chang, D. S. Tsai, C. C. Fu, T. S. Lim, Y. K. Tzeng, C. Y. Fang, C. C. Han, H. C. Chang, W. Fann, *Nat. Nanotechnol.* **2008**, *3*, 284.

[65] Q. Zhang, V. N. Mochalin, I. Neitzel, I. Y. Knoke, J. Han, C. A. Klug, J. G. Zhou, P. I. Lelkes, Y. Gogotsi, *Biomaterials* **2011**, *32*, 87.

[66] G.-W. Yang, J.-B. Wang, Q.-X. Liu, *J. Phys. Condens. Matter* **1998**, *10*, 7923.

[67] J.-P. Boudou, P. a Curmi, F. Jelezko, J. Wrachtrup, P. Aubert, M. Sennour, G. Balasubramanian, R. Reuter, A. Thorel, E. Gaffet, *Nanotechnology* **2009**, *20*, 1.

[68] N. R. Greiner, D. S. Phillips, J. D. Johnson, F. Volk, *Nature* **1988**, *333*, 440.

[69] D. M. Gruen, O. A. Shenderova, A. Y. Vul, *Synthesis, Properties and Applications of Ultrananocrystalline Diamond*, Springer Verlag, **2005**.

[70] S. Osswald, G. Yushin, V. Mochalin, S. O. Kucheyev, Y. Gogotsi, *J. Am. Chem. Soc.* **2006**, *128*, 11635.

[71] S. V Kidalov, F. M. Shakhov, A. Y. Vul, *Diam. Relat. Mater.* **2007**, *16*, 2063.

[72] K. M. El-Say, *J. Appl. Pharm. Sci.* **2011**, *1*, 29.

[73] M. Zeiger, N. Jäckel, V. N. Mochalin, V. Presser, *J. Mater. Chem. A* **2016**, *4*, 3172.

[74] A. Camisasca, S. Giordani, *Inorganica Chim. Acta* **2017**, *468*, 67.

[75] J. Bartelmess, S. Giordani, *Beilstein J. Nanotechnol.* **2014**, *5*, 1980.

[76] S. Iijima, *J. Cryst. Growth* **1980**, *50*, 675.

[77] D. Ugarte, *Nature* **1992**, *359*, 707.

[78] M. Ghosh, S. K. Sonkar, M. Saxena, S. Sarkar, *Small* **2011**, *7*, 3170.

[79] F. D. Han, B. Yao, Y. J. Bai, *J. Phys. Chem. C* **2011**, *115*, 8923.

[80] I. Alexandrou, H. Wang, N. Sano, G. A. J. Amaratunga, *J. Chem. Phys.* **2004**, *120*, 1055.

[81] M. Choucair, J. A. Stride, *Carbon* **2012**, *50*, 1109.

[82] L. Echegoyen, A. Ortiz, M. N. Chaur, A. J. Palkar, in *Chem. Nanocarbons*, **2010**, pp. 463–483.

[83] B. J. M. Etzold, I. Neitzel, M. Kett, F. Strobl, V. N. Mochalin, Y. Gogotsi, *Chem. Mater.* **2014**, *26*, 3479.

[84] P. Ganesh, P. R. C. Kent, V. Mochalin, *J. Appl. Phys.* **2011**, *110*, DOI 10.1063/1.3641984.

[85] M. Zeiger, N. Jäckel, M. Aslan, D. Weingarth, V. Presser, *Carbon* **2015**, *84*, 584.

[86] A. Rosenkranz, L. Freeman, S. Fleischmann, F. Lasserre, Y. Fainman, F. E. Talke, *Carbon* **2018**, *132*, 495.

[87] T. Belin, F. Epron, *Mater. Sci. Eng. B Solid-State Mater. Adv. Technol.* **2005**, *119*, 105.

[88] H. Dai, *Surf. Sci.* **2002**, *500*, 218.

[89] I. Kang, Y. Y. Heung, J. H. Kim, J. W. Lee, R. Gollapudi, S. Subramaniam, S. Narasimhadevara, D. Hurd, G. R. Kirikera, V. Shanov, M. J. Schulz, D. Shi, J. Boerio, S. Mall, M. Ruggles-Wren, *Compos. Part B Eng.* **2006**, *37*, 382.

[90] J. P. Salvetat-Delmotte, A. Rubio, *Carbon* **2002**, *40*, 1729.

[91] P. L. Dickrell, S. K. Pal, G. R. Bourne, C. Muratore, A. A. Voevodin, P. M. Ajayan, L. S. Schadler, W. G. Sawyer, *Tribol. Lett.* **2006**, *24*, 85.

[92] N. Souza, Laser and Carbon : Nanotube Synthesis and Annealing, Saarland university, **2017**.

[93] Y. Gogotsi, *Nanotubes and Nanofibers*, CRC Press, Taylor And Francis Group, **2006**.

[94] S. Reich, C. Thomsen, J. Maultzsch, *Carbon Nanotubes: Basic Concepts and Physical Properties*, Wiley-VCH Verlag GmbH, **2004**.

[95] R. Saito, M. Fujita, G. Dresselhaus, M. S. Dresselhaus, *Phys. Rev. B* **1992**, *46*, 1804.

[96] M. Yu, *Science (80-.).* **2000**, *287*, 637.

[97] P. Kim, L. Shi, A. Majumdar, P. McEuen, *Phys. Rev. Lett.* **2001**, *87*, 215502.

[98] S. Berber, Y. Kwon, D. Tomanek, *Phys. Rev. Lett.* **2000**, *84*, 4613.

[99] B. G. Demczyk, Y. M. Wang, J. Cumings, M. Hetman, W. Han, A. Zettl, R. O. Ritchie, *Mater. Sci. Eng. A* **2002**, *334*, 173.

[100] F. Li, H. M. Cheng, S. Bai, G. Su, M. S. Dresselhaus, *Appl. Phys. Lett.* **2000**, *77*, 3161.

[101] Y. Lu, P. K. Liaw, *JOM* **2001**, 31.

[102] M. R. Falvo, G. J. Clary, R. M. Taylor, V. Chi, F. P. Brooks, S. Washburn, R. Superfine, *Nature* **1997**, *389*, 582.

[103] S. Suarez, L. Reinert, F. Mücklich, in *Diam. Carbon Compos. Nanocomposites*, IntechOpen, **2016**.

[104] M. M. A. Rafique, J. Iqbal, *J. Encapsulation Adsorpt. Sci.* **2011**, *1*, 29.

[105] M. Paradise, T. Goswami, *Mater. Des.* **2007**, *28*, 1477.

[106] M. Kumar, Y. Ando, *J. Nanosci. Nanotechnol.* **2010**, *10*, 3739.

[107] K. E. Kim, K. J. Kim, W. S. Jung, S. Y. Bae, J. Park, J. Choi, J. Choo, *Chem. Phys. Lett.* **2005**, *401*, 459.

[108] H. Hou, A. K. Schaper, F. Weller, A. Greiner, *Chem. Mater.* **2002**, *14*, 3990.

[109] C. H. See, A. T. Harris, *Ind. Eng. Chem. Res.* **2007**, *46*, 997.

[110] N. M. Mubarak, E. C. Abdullah, N. S. Jayakumar, J. N. Sahu, *J. Ind. Eng. Chem.* **2014**, *20*, 1186.

[111] C. V. Raman, K. S. Krishan, *Nature* **1928**, *121*, 501.

[112] D. J. Gardiner, P. R. Graves, *Practical Raman Spectroscopy*, Springer Verlag Berlin Heidelberg, **1989**.

[113] S. R. Sails, D. J. Gardiner, M. Bowden, J. Savage, D. Rodway, *Diam. Relat. Mater.* **1996**, *5*, 589.

[114] O. O. Mykhaylyk, Y. M. Solonin, D. N. Batchelder, R. Brydson, *J. Appl. Phys.* **2005**, *97*, 1.

[115] A. Ferrari, J. Robertson, *Phys. Rev. B* **2000**, *61*, 14095.

[116] R. Loudon, in *Adv. Phys.*, **1964**, pp. 423–482.

[117] M. a Pimenta, G. Dresselhaus, M. S. Dresselhaus, L. G. Cançado, A. Jorio, R. Saito, *Phys. Chem. Chem. Phys.* **2007**, *9*, 1276.

[118] A. C. Ferrari, *Solid State Commun.* **2007**, *143*, 47.

[119] M. S. Dresselhaus, G. Dresselhaus, R. Saito, A. Jorio, *Phys. Rep.* **2005**, *409*, 47.

[120] R. A. DiLeo, B. J. Landi, R. P. Raffaelle, *J. Appl. Phys.* **2007**, *101*, DOI 10.1063/1.2712152.

[121] S. Suarez, F. Lasserre, O. Prat, F. Mücklich, *Phys. Status Solidi* **2014**, *211*, 1555.

[122] F. Tuinstra, *J. Chem. Phys.* **1970**, *53*, 1126.

[123] L. G. Caṇado, K. Takai, T. Enoki, M. Endo, Y. A. Kim, H. Mizusaki, A. Jorio, L. N. Coelho, R. Magalhães-Paniago, M. A. Pimenta, *Appl. Phys. Lett.* **2006**, *88*, 2.

[124] S. Prawer, K. W. Nugent, D. N. Jamieson, J. O. Orwa, L. A. Bursill, J. L. Peng, *Chem. Phys. Leters* **2000**, *332*, 93.

[125] G. N. Yushin, S. Osswald, V. I. Padalko, G. P. Bogatyreva, Y. Gogotsi, *Diam. Relat. Mater.* **2005**, *14*, 1721.

[126] G. Morell, O. Quifiones, Y. Diaz, I. M. Vargas, B. R. Weiner, R. S. Katiyar, *Diam. Relat. Mater.* **1998**, *7*, 1029.

[127] L. C. Nistor, V. Landuyt, V. G. Ralchenko, E. D. Obraztsova, A. A. Smolin, *Diam. Carbon Compos. Nanocomposites* **1997**, *6*, 159.

[128] V. Mochalin, S. Osswald, Y. Gogotsi, *Chem. Mater* **2009**, *21*, 273.

[129] D. B. Miracle, S. L. Donaldson, V. Chairs, S. D. Henry, P. Editor, C. Moosbrugger, T. Editor, G. J. Anton, E. Assistant, B. R. Sanders, M. Production, N. Hrivnak, C. Terman, C. Editors, J. Brown, E. J.

Kubel, M. Park, *ASM Handbook - Composites*, ASM International, **2001**.

[130] A. D. Moghadam, B. F. Schultz, J. B. Ferguson, E. Omrani, P. K. Rohatgi, N. Gupta, *Jom* **2014**, *66*, 872.

[131] T. Kuzumaki, K. Miyazawa, H. Ichinose, k. Ito, *J. Mater. Res.* **1998**, *13*, 2445.

[132] H. Kwon, M. Takamichi, A. Kawasaki, M. Leparoux, *Mater. Chem. Phys.* **2013**, *138*, 787.

[133] T. Borkar, J. Hwang, J. Y. Hwang, T. W. Scharf, J. Tiley, S. H. Hong, R. Banerjee, *J. Mater. Res.* **2014**, *29*, 761.

[134] B. Lim, C. Kim, B. Kim, U. Shim, S. Oh, B. Sung, J. Choi, S. Baik, *Nanotechnology* **2006**, *17*, 5759.

[135] Q. Liu, L. Ke, F. Liu, C. Huang, L. Xing, *Mater. Des.* **2013**, *45*, 343.

[136] C. A. Isaza Merino, J. M. Meza Meza, G. A. Sierra Gallego, *J. Manuf. Sci. Eng.* **2016**, *138*, 1.

[137] W. Xu, R. Hu, J. Li, H. Fu, *Trans. Nonferrous Met. Soc. China* **2011**, *21*, 2237.

[138] H. Imai, K. Kondoh, S. Li, J. Umeda, B. Fugetsu, M. Takahashi, *Mater. Trans.* **2014**, *55*, 522.

[139] J. Y. Hwang, A. Neira, T. W. Scharf, J. Tiley, R. Banerjee, *Scr. Mater.* **2008**, *59*, 487.

[140] A. Agarwal, S. Bakshi, D. Lahiri, *Carbon Nanotubes - Reinforced Metal Matrix Composites*, CRC Press, Taylor And Francis Group, **2011**.

[141] F. Avilés, J. V. Cauich-Rodríguez, L. Moo-Tah, A. May-Pat, R. Vargas-Coronado, *Carbon* **2009**, *47*, 2970.

[142] D. H. Nam, Y. K. Kim, S. I. Cha, S. H. Hong, *Carbon* **2012**, *50*, 4809.

[143] K. T. Kim, J. Eckert, G. Liu, J. M. Park, B. K. Limd, S. H. Hong, *Scr. Mater.* **2011**, *64*, 181.

[144] M. Lal, S. K. Singhal, I. Sharma, R. B. Mathur, *Appl. Nanosci.* **2012**, *3*, 29.

[145] P.-C. Tsai, Y.-R. Jeng, *Compos. Sci. Technol.* **2013**, *79*, 28.

[146] J. Y. Hwang, B. K. Lim, J. Tiley, R. Banerjee, S. H. Hong, *Carbon* **2013**, *57*, 282.

[147] H. J. Choi, J. H. Shin, D. H. Bae, *Compos. Part A Appl. Sci. Manuf.* **2012**, *43*, 1061.

[148] H. J. Choi, B. H. Min, J. H. Shin, D. H. Bae, *Compos. Part A Appl. Sci. Manuf.* **2011**, *42*, 1438.

[149] H. J. Choi, J. H. Shin, D. H. Bae, *Compos. Sci. Technol.* **2011**, *71*, 1699.

[150] H. Asgharzadeh, S.-H. Joo, H. S. Kim, *Metall. Mater. Trans. A* **2014**, *45*, 4129.

[151] O. Carvalho, G. Miranda, D. Soares, F. S. Silva, *Mech. Adv. Mater. Struct.* **2016**, *23*, 66.

[152] J. P. Tu, Y. Z. Yang, L. Y. Wang, X. C. Ma, X. B. Zhang, *Tribol. Lett.* **2001**, *10*, 225.

[153] Z. W. Xue, L. D. Wang, P. T. Zhao, S. C. Xu, J. L. Qi, W. D. Fei, *Mater. Des.* **2012**, *34*, 298.

[154] Q. Cheng, S. Debnath, E. Gregan, H. J. Byrne, *J. Phys. Chem. C* **2010**, *114*, 8821.

[155] J. Hilding, E. A. Grulke, Z. George Zhang, F. Lockwood, *J. Dispers. Sci. Technol.* **2003**, *24*, 1.

[156] C. Guiderdoni, E. Pavlenko, V. Turq, A. Weibel, P. Puech, C. Estournès, A. Peigney, W. Bacsa, C. Laurent, *Carbon* **2013**, *58*, 185.

[157] R. Sule, P. A. Olubambi, I. Sigalas, J. K. O. Asante, J. C. Garrett, W. D. Roos, *Synth. Met.* **2015**, *202*, 123.

[158] T. Tokunaga, K. Kaneko, Z. Horita, *Mater. Sci. Eng. A* **2008**, *490*, 300.

[159] S. Cho, K. Kikuchi, T. Miyazaki, K. Takagi, A. Kawasaki, T. Tsukada, *Scr. Mater.* **2010**, *63*, 375.

[160] K. Rajkumar, S. Aravindan, *Wear* **2011**, *270*, 613.

[161] C. Guiderdoni, C. Estournès, A. Peigney, A. Weibel, V. Turq, C. Laurent, *Carbon* **2011**, *49*, 4535.

[162] D. D. Phuong, P. Van Trinh, N. Van An, N. Van Luan, P. N. Minh, R. K. Khisamov, K. S. Nazarov, L. R. Zubairov, R. R. Mulyukov, A. A. Nazarov, *J. Alloys Compd.* **2014**, *613*, 68.

[163] U. Maitra, A. Gomathi, C. N. R. Rao, *J. Exp. Nanosci.* **2008**, *3*, 271.

[164] Suk-Joong L.Kang, *Sintering, Densification,Grain Growth,and Microstructure*, Elsevier Butterworth Heinemann, **2005**.

[165] C. Li, X. Liu, J. Yi, L. Teng, R. Bao, J. Tan, C. Yang, Z. Zou, *J. Mater. Res.* **2016**, *31*, 3757.

[166] Q. Huang, L. Gao, Y. Liu, J. Sun, *J. Mater. Chem.* **2005**, *15*, 1995.

[167] V. Livramento, J. B. Correia, N. Shohoji, E. Õsawa, *Diam. Relat. Mater.* **2007**, *16*, 202.

[168] G.-D. Zhan, J. D. Kuntz, J. Wan, A. K. Mukherjee, *Nat. Mater.* **2003**, *2*, 38.

[169] S. Suárez, E. Ramos-Moore, B. Lechthaler, F. Mücklich, *Carbon* **2014**, *70*, 173.

[170] N. Hansen, *Scr. Mater.* **2004**, *51*, 801.

[171] P. A. Manohar, M. Ferry, T. Chandra, *ISIJ Int.* **1998**, *38*, 913.

[172] A. Sanaty-Zadeh, *Mater. Sci. Eng. A* **2012**, *531*, 112.

[173] S. R. Bakshi, A. Agarwal, *Carbon* **2011**, *49*, 533.

[174] M. Paramsothy, J. Chan, R. Kwok, M. Gupta, *Compos. Part A Appl. Sci. Manuf.* **2011**, *42*, 180.

[175] S. M. Uddin, T. Mahmud, C. Wolf, C. Glanz, I. Kolaric, C. Volkmer, H. Höller, U. Wienecke, S. Roth, H.-J. Fecht, *Compos. Sci. Technol.* **2010**, *70*, 2253.

[176] K. S. Munir, P. Kingshott, C. Wen, *Crit. Rev. Solid State Mater. Sci.* **2015**, *40*, 38.

[177] A. M. K. Esawi, K. Morsi, A. Sayed, M. Taher, S. Lanka, *Compos. Sci. Technol.* **2010**, *70*, 2237.

[178] R. George, K. T. Kashyap, R. Rahul, S. Yamdagni, *Scr. Mater.* **2005**, *53*, 1159.

[179] N. Hu, B. Jia, M. Arai, C. Yan, J. Li, Y. Liu, S. Atobe, H. Fukunaga, *Comput. Mater. Sci.* **2012**, *54*, 249.

[180] Y.-K. Kwon, S. Berber, D. Tománek, *Phys. Rev. Lett.* **2004**, *92*, 15901.

[181] N. Karousis, N. Tagmatarchis, D. Tasis, *Chem. Rev.* **2010**, *110*, 5366.

[182] Y.-L. Zhao, J. F. Stoddart, *Acc. Chem. Res.* **2009**, *42*, 1161.

[183] L. Vaisman, H. D. Wagner, G. Marom, *Adv. Colloid Interface Sci.* **2006**, *128–130*, 37.

[184] N. Pierard, a Fonseca, J.-F. Colomer, C. Bossuot, J.-M. Benoit, G. Van Tendeloo, J.-P. Pirard, J. . Nagy, *Carbon* **2004**, *42*, 1691.

[185] S. C. Tjong, *Mater. Sci. Eng. R Reports* **2013**, *74*, 281.

[186] R. Pérez-Bustamante, I. Estrada-Guel, W. Antúnez-Flores, M. Miki-Yoshida, P. J. Ferreira, R. Martínez-Sánchez, *J. Alloys Compd.* **2008**, *450*, 323.

[187] M. . Vidal-Sétif, M. Lancin, C. Marhic, R. Valle, J.-L. Raviart, J.-C. Daux, M. Rabinovitch, *Mater. Sci. Eng. A* **1999**, *272*, 321.

[188] L. M. Tham, L. Cheng, *Acta Mata.* **2001**, *49*, 3243.

[189] P. Poncharal, C. Berger, Y. Yi, Z. Wang, W. de Heer, *J. Phys. Chem. B* **2002**, *106*, 12104.

[190] I. Firkowska, A. Boden, A.-M. Vogt, S. Reich, *J. Mater. Chem.* **2011**, *21*, 17541.

[191] J. Hone, M. C. Llaguno, N. M. Nemes, A. T. Johnson, J. E. Fischer, D. A. Walters, M. J. Casavant, J. Schmidt, R. E. Smalley, J. Hone, M. C. Llaguno, N. M. Nemes, A. T. Johnson, *Appl. Phys. Lett.* **2004**, *77*, 666.

[192] S. Yamanaka, R. Gonda, A. Kawasaki, H. Sakamoto, Y. Mekuchi, M. Kun, T. Tsukada, *Mater. Trans.* **2007**, *48*, 2506.

[193] J. S. Gibson, J. Uddin, T. R. Cundari, N. K. Bodiford, A. K. Wilson, *J. Phys. Condens. Matter* **2010**, *22*, 445503.

[194] S. Suarez, F. Lasserre, F. Mücklich, *Mater. Sci. Eng. A* **2013**, *587*, 381.

[195] S. C. Tjong, *Carbon Nanotube Reinforced Composites*, Wiley-VCH Verlag GmbH, **2009**.

[196] V. A. Popov, E. V Vershinina, *Eur. J. Inorg. Chem.* **2016**, 2122.

[197] V. A. Popov, in *Nanocomposites*, Nova Science Publishers, Inc., **2013**, pp. 369–401.

[198] V. Popov, *Surf. Interface Anal.* **2018**, 1.

[199] H. Kwon, G. Lee, S. Kim, B. Lee, W. Seo, M. Leparoux, *Mater. Sci. Eng. A* **2015**, *632*, 72.

[200] F. Zhang, S. Liu, P. Zhao, T. Liu, J. Sun, *Mater. Des.* **2017**, *131*, 144.

[201] D. Nunes, V. Livramento, J. B. Correia, K. Hanada, *Mater. Sci. Forum* **2010**, *636–637*, 682.

[202] D. Nunes, M. Vilarigues, J. B. Correia, P. A. Carvalho, *Acta Mata.* **2012**, *60*, 737.

[203] M. Yu, C. George, Y. Cao, *J Mater Sci* **2014**, *49*, 3629.

[204] S. Yin, Y. Xie, J. Cizek, E. J. Ekoi, T. Hussain, D. P. Dowling, R. Lupoi, *Compos. Part B* **2017**, *113*, 44.

[205] D. J. Woo, B. Sneed, F. Peerally, F. C. Heer, L. N. Brewer, J. P. Hooper, S. Osswald, *Carbon* **2013**, *63*, 404.

[206] V. P. Isakov, A. I. Lyamkin, D. N. Nikitin, A. S. Shalimova, A. V Solntsev, *Prot. Met. Phys. Chem. surfaces* **2010**, *46*, 578.

[207] H. Czichos, K. Habig, *Tribologie-Handbuch*, Vieweg+Teubner, **2010**.

[208] C. Donnet, A. Erdemir, *Tribol. Lett.* **2004**, *17*, 389.

[209] A. Rosenkranz, L. Reinert, C. Gachot, H. Aboufadl, S. Grandthyll, K. Jacobs, F. Müller, F. Mücklich, *Adv. Eng. Mater.* **2015**, *17*, 1234.

[210] A. J. Gellman, N. D. Spencer, *J. Eng. Tribol.* **2002**, *216*, 443.

[211] P. J. Blau, in *Encycl. Tribol.*, Springer, Boston, **2013**.

[212] E. J. Abbott, F. A. Firestone, *Mech. Eng.* **1933**, *55*, 569.

[213] H. Hertz, *J. für die reine und Angew. Math. 92* **1881**.

[214] J. Greenwood, J. Williamson, *Proc. R. Soc. London* **1966**, *295*, 300.

[215] L. Kogut, I. Etsion, *J. Tribol.* **2004**, *126*, 34.

[216] W. R. Chang, I. Etsion, D. B. Bogy, *J. Tribol.* **1987**, *109*, 257.

[217] R. Jackson, I. Green, *Tribol. Trans.* **2011**, *54*, 300.

[218] B. N. J. Persson, *Surf. Sci. Rep.* **2006**, *61*, 201.

[219] W. Grabon, P. Pawlus, J. Sep, *Tribiology Int.* **2010**, *43*, 1882.

[220] A. Rosenkranz, A. Szurdak, C. Gachot, G. Hirt, F. Mücklich, *Tribiology Int.* **2016**, *95*, 290.

[221] R. A. Singh, E.-S. Yoon, H. J. Kim, H. Kong, S. Park, H. E. Jeong, K. Y. Suh, *Surf. Eng.* **2007**, *23*, 161.

[222] I. Etsion, *Tribol. Lett.* **2004**, *17*, 733.

[223] R. L. Jackson, I. Green, *Tribol. Int.* **2006**, *39*, 906.

[224] F. P. Bowden, D. Tabor, *The Friction and Lubrication of Solids*, Clarendon Press - Oxford, **2001**.

[225] R. Mishra, B. Basu, R. Balasubramaniam, *Mater. Sci. Eng. A* **2004**, *373*, 370.

[226] A. Kruglova, M. Engstler, G. Gaiselmann, O. Stenzel, V. Schmidt, M. Roland, S. Diebels, F. Mücklich, *Comput. Mater. Sci.* **2016**, *120*, 99.

[227] F. H. Stott, G. C. Wood, *Tribol. Int.* **1978**, 211.

[228] R. K. Singh Raman, A. S. Khanna, R. K. Tiwari, J. B. Gnanamoorthy, *Oxid. Met.* **1992**, *37*, 1.

[229] N. Argibay, M. Chandross, S. Cheng, J. R. Michael, *J. Mater. Sci.* **2017**, *52*, 2780.

[230] M. Hirano, K. Shinjo, R. Kaneko, Y. Murata, *Phys. Rev. Lett.* **1991**, *67*, 2642.

[231] W. F. Hosford, *Textures Microstruct.* **1996**, *26*, 479.

[232] G. Gottstein, *Physical Foundations of Materials Science*, Springer Verlag, **2004**.

[233] F. P. Bowden, D. Tabor, *Br. J. Appl. Phys.* **1966**, *17*, 1521.

[234] D. H. Buckley, W. A. Brainard, *Carbon* **1975**, *13*, 501.

[235] R. Sengupta, M. Bhattacharya, S. Bandyopadhyay, A. K. Bhowmick, *Prog. Polym. Sci.* **2011**, *36*, 638.

[236] J. S. Bunch, S. S. Verbridge, J. S. Alden, A. M. Van Der, J. M. Parpia, H. G. Craighead, P. L. Mceuen, J. S. Bunch, S. S. Verbridge, J. S. Alden, A. M. Van Der Zande, J. M. Parpia, H. G. Craighead, P. L. Mceuen, *Nano Lett.* **2008**, *8*, 2458.

[237] C. Lee, Q. Li, W. Kalb, X. Z. Liu, H. Berger, R. W. Carpick, J. Hone, *Science (80-.).* **2010**, *328*, 76.

[238] D. Berman, A. Erdemir, A. V. Sumant, *Carbon* **2013**, *54*, 454.

[239] D. Berman, A. Erdemir, A. V. Sumant, *Carbon* **2013**, *59*, 167.

[240] W. Zhai, N. Srikanth, L. B. Kong, K. Zhou, *Carbon* **2017**, *119*, 150.

[241] J. Robertson, *Mater. Sci. Eng. Reports* **2002**, *37*, 129.

[242] C. Donnet, A. Erdemir, *Tribology of Diamond-Like Carbon Films*, Springer, **2007**.

[243] A. Erdemir, O. L. Eryilmaz, G. Frenske, *J. Vac. Sci. Technol. A Vacuum, Surfaces, Film.* **2000**, *18*, 1982.

[244] T. W. Scharf, J. A. Ohlhausen, D. R. Tallant, S. V. Prasad, *J. Appl. Phys.* **2007**, *101*, DOI 10.1063/1.2711147.

[245] A. R. Konicek, D. S. Grierson, P. U. P. A. Gilbert, W. G. Sawyer, A. V. Sumant, R. W. Carpick, *Phys. Rev. Lett.* **2008**, *100*, 1.

[246] A. Savan, E. Pflüger, P. Voumard, A. Schröer, M. S. Paul, *Lubr. Sci.* **2000**, *12*, 185.

[247] L. Cizaire, B. Vacher, T. Le Mogne, J. M. Martin, L. Rapoport, A. Margolin, R. Tenne, *Surf. coatings Technol.* **2002**, *160*, 282.

[248] L. Rapoport, N. Fleischer, R. Tenne, *Adv. Mater.* **2003**, *15*, 651.

[249] H. E. Sliney, *Tribol. Int.* **1982**, *15*, 303.

[250] S. V. Prasad, J. S. Zabinski, *J. Mater. Sci. Lett.* **1993**, *12*, 1413.

[251] B. C. Windom, W. G. Sawyer, D. W. Hahn, *Tribol. Lett.* **2011**, *42*, 301.

[252] J. S. Zabinski, M. S. Donley, S. D. Walck, T. R. Schneider, N. T. McDevitt, *Tribol. Trans.* **1995**, *38*, 894.

[253] T. Polcar, A. Cavaleiro, *Surf. Coatings Technol.* **2011**, *206*, 686.

[254] B. J. Briscoe, D. Tabor, *Wear* **1975**, *34*, 29.

[255] A. Erdemir, *Tribol. Lett.* **2000**, *8*, 97.

[256] T. Aizawa, A. Mitsuo, S. Yamamoto, T. Sumitomo, S. Muraishi, *Wear* **2005**, *259*, 708.

[257] F. P. Bowden, D. Tabor, *Nature* **1942**, *150*, 197.

[258] J. Kogovšek, M. Remškar, A. Mrzel, M. Kalin, *Tribol. Int.* **2013**, *61*, 40.

[259] B. N. J. Persson, O. Albohr, U. Tartaglino, A. I. Volokitin, E. Tosatti, *J. Phys. Condens. Matter* **2005**, *17*, DOI 10.1088/0953-8984/17/1/R01.

[260] H. Lee, B. Bhushan, *J. Colloid Interface Sci.* **2011**, *353*, 574.

[261] M. Sahin, C. S. Çetinarslan, H. E. Akata, *Mater. Des.* **2007**, *28*, 633.

[262] F. Svahn, Å. Kassman-Rudolphi, E. Wallén, *Wear* **2003**, *254*, 1092.

[263] K. Komvopoulos, *J. Adhes. Sci. Technol.* **2003**, *17*, 477.

[264] J. Sondhauß, H. Fuchs, A. Schirmeisen, *Tribol. Lett.* **2011**, *42*, 319.

[265] S. Yuan, W. Huang, X. Wang, *Tribol. Int.* **2011**, *44*, 1047.

[266] A. Rosenkranz, L. Reinert, C. Gachot, F. Mücklich, *Wear* **2014**, *318*, 49.

[267] A. A. Voevodin, J. S. Zabinski, *Wear* **2006**, *261*, 1285.

[268] K. H. Leitz, B. Redlingshöer, Y. Reg, A. Otto, M. Schmidt, *Phys. Procedia* **2011**, *12*, 230.

[269] A. Lasagni, Advanced Design of Periodical Structures by Laser Interference Metallurgy in the Micro/nano Scale on Macroscopic Areas, Saarland university, **2006**.

[270] P. Grützmacher, A. Rosenkranz, C. Gachot, *Appl. Surf. Sci.* **2016**, *370*, 59.

[271] A. Rosenkranz, Tribologie an Oberflächen Mit Maßgeschneidertem Topographischem Design, Saarland university, **2014**.

[272] C. Gachot, A. Rosenkranz, L. Reinert, E. Ramos-Moore, N. Souza, M. H. Müser, F. Mücklich, *Tribol. Lett.* **2013**, *9*, 193.

[273] J. Li, D. Xiong, J. Dai, Z. Huang, R. Tyagi, *Tribol. Int.* **2010**, *43*, 1193.

[274] J. Kałużny, A. Merkisz-Guranowska, M. Giersig, K. Kempa, *Int. J. Automot. Technol.* **2017**, *18*, 1047.

[275] Y. Peng, Y. Hu, H. Wang, *Tribol. Lett.* **2006**, *25*, 247.

[276] Y. Yao, X. Wang, J. Guo, X. Yang, B. Xu, *Mater. Lett.* **2008**, *62*, 2524.

[277] M. G. Ivanov, D. M. Ivanov, S. V. Pavlyshko, I. Petrov, A. Vargas, G. McGuire, O. Shenderova, *Fullerenes, Nanotub. Carbon Nanostructures* **2012**, *20*, 606.

[278] A. P. Puzyr, A. E. Burov, G. E. Selyutin, V. Voroshilov, V. S. Bondar, *Tribol. Trans.* **2012**, *55*, 149.

[279] V. Y. Dolmatov, *J. Superhard Mater.* **2010**, *32*, 14.

[280] K. W. Street, M. Marchetti, R. L. Vander Wal, A. J. Tomasek, *Tribol. Lett.* **2004**, *16*, 143.

[281] K. Miyoshi, K. W. S. Jr., R. L. Vander Wal, R. Andrews, A. Sayir, *Tribol. Lett.* **2005**, *19*, 191.

[282] X. Zhang, B. Luster, A. Church, C. Muratore, A. a Voevodin, P. Kohli, S. Aouadi, S. Talapatra, *ACS Appl. Mater. Interfaces* **2009**, *1*, 735.

[283] J. J. Hu, S. H. Jo, Z. F. Ren, A. Voevodin, J. S. Zabinski, *Tribol. Lett.* **2005**, *19*, 119.

[284] S. Park, D. Srivastava, K. Cho, *Nano Lett.* **2003**, *3*, 1273.

[285] S. Heo, S. B. Sinnott, *J. Appl. Phys.* **2007**, *102*, DOI 10.1063/1.2784007.

[286] K. Mylvaganam, L. C. Zhang, K. Q. Xiao, *Carbon* **2009**, *47*, 1693.

[287] F. Colonna, A. Fasolino, E. J. Meijer, *Phys. Rev. B* **2013**, *88*, 165416.

[288] L. Rui, *AIP Adv.* **2014**, *4*, DOI 10.1063/1.4867087.

[289] Q. Ouyang, K. Okada, *Appl. Surf. Sci.* **1994**, *78*, 309.

[290] A. V. Gubarevich, S. Usuba, Y. Kakudate, A. Tanaka, O. Odawara, *Diam. Relat. Mater.* **2005**, *14*, 1549.

[291] D. Berman, S. A. Deshmukh, S. K. R. S. Sankaranarayanan, A. Erdemir, A. V. Sumant, *Science (80-.).* **2015**, *348*, 1118.

[292] J. Hone, R. W. Carpick, *Science (80-.).* **2015**, *348*, 1087.

[293] C. C. Chou, S. H. Lee, *J. Mater. Process. Technol.* **2008**, *201*, 542.

[294] O. Elomaa, T. J. Hakala, V. Myllymäki, J. Oksanen, H. Ronkainen, V. K. Singh, J. Koskinen, *Diam. Relat. Mater.* **2013**, *34*, 89.

[295] N. Matsumoto, L. Joly-Pottuz, H. Kinoshita, N. Ohmae, *Diam. Relat. Mater.* **2007**, *16*, 1227.

[296] E. W. Bucholz, S. R. Phillpot, S. B. Sinnott, *Comput. Mater. Sci.* **2012**, *54*, 91.

[297] M. Zhang, S. Fang, A. A. Zakhidov, S. B. Lee, R. H. Baughman, *Science (80-.).* **2005**, *309*, 1215.

[298] C. Feng, K. Liu, J. S. Wu, L. Liu, J. S. Cheng, Y. Zhang, Y. Sun, Q. Li, S. Fan, K. Jiang, *Adv. Funct. Mater.* **2010**, *20*, 885.

[299] M. E. Spotnitz, D. Ryan, H. A. Stone, *J. Mater. Chem.* **2004**, *14*, 1299.

[300] F. Mirri, A. W. K. Ma, T. T. Hsu, N. Behabtu, S. L. Eichmann, C. C. Young, D. E. Tsentalovich, M. Pasquali, *ACS Nano* **2012**, *6*, 9737.

[301] E. Y. Jang, T. J. Kang, H. W. Im, D. W. Kim, Y. H. Kim, *Small* **2008**, *4*, 2255.

[302] M. Majumder, C. Rendall, M. Li, N. Behabtu, J. A. Eukel, R. H. Hauge, H. K. Schmidt, M. Pasquali, *Chem. Eng. Sci.* **2010**, *65*, 2000.

[303] B. Dan, G. Irvin, M. Pasquali, *ACS Nano* **2009**, *3*, 835.

[304] T. V. Sreekumar, T. Liu, S. Kumar, L. M. Ericson, R. H. Hauge, R. E. Smalley, *Chem. Mater.* **2003**, *15*, 175.

[305] M. A. Meitl, Y. Zhou, A. Gaur, S. Jeon, M. L. Usrey, M. S. Strano, J. A. Rogers, *Nano Lett.* **2004**, *4*, 1643.

[306] L. Hu, D. S. Hecht, G. Gruner, *Nano Lett.* **2004**, *4*, 2513.

[307] F. De Nicola, P. Castrucci, M. Scarselli, F. Nanni, I. Cacciotti, M. De Crescenzi, *Nanotechnology* **2015**, *26*, 145701.

[308] A. Hirata, N. Yoshioka, *Tribol. Int.* **2004**, *37*, 893.

[309] M. D. Abad, J. C. Sánchez-López, A. Berenguer-Murcia, V. B. Golovko, M. Cantoro, A. E. H. Wheatley, A. Fernández, B. F. G. Johnson, J. Robertson, *Diam. Relat. Mater.* **2008**, *17*, 1853.

[310] A. R. Boccaccini, J. Cho, J. A. Roether, B. J. C. Thomas, E. Jane Minay, M. S. P. Shaffer, *Carbon* **2006**, *44*, 3149.

[311] B. J. C. Thomas, M. S. P. Shaffer, S. Freeman, M. Koopman, K. K. Chawla, A. R. Boccaccini, *Key Eng. Mater.* **2006**, *314*, 141.

[312] B. J. C. Thomas, A. R. Boccaccini, M. S. P. Shaffer, *J. Am. Ceram. Soc.* **2005**, *88*, 980.

[313] J. Cho, S. Schaab, J. A. Roether, A. R. Boccaccini, *J. Nanoparticle Res.* **2008**, *10*, 99.

[314] Y. Ma, J. Han, M. Wang, X. Chen, S. Jia, *J. Mater.* **2018**, *4*, 108.

[315] L. Besra, M. Liu, *Prog. Mater. Sci.* **2007**, *52*, 1.

[316] Y. Zhu, Y. Chen, C. Zhu, X. Shen, **2010**, *23*, 409.

[317] K. Balani, Y. Chen, S. P. Harimkar, N. B. Dahotre, A. Agarwal, *Acta Biomater.* **2007**, *3*, 944.

[318] M. Alishahi, S. M. Monirvaghefi, A. Saatchi, S. M. Hosseini, *Appl. Surf. Sci.* **2012**, *258*, 2439.

[319] W. X. Chen, F. Li, G. Han, J. B. Xia, L. Y. Wang, J. P. Tu, Z. D. Xu, *Tribol. Lett.* **2003**, *15*, 275.

[320] W. X. Chen, J. P. Tu, Z. D. Xu, W. L. Chen, X. B. Zhang, D. H. Cheng, *Mater. Lett.* **2003**, *57*, 1256.

[321] H. D. Lee, O. V. Penkov, D. E. Kim, *Thin Solid Films* **2013**, *534*, 410.

[322] W. Zhang, G. J. Ma, C. W. Wu, *Rev. Adv. Mater. Sci* **2014**, *36*, 75.

[323] R. Velázquez, V. Neto, K. Uppireddi, B. Weiner, G. Morell, *Coatings* **2013**, *3*, 243.

[324] K. Tsugawa, C. Technologies, A. Indu, A. Indu, *New Diam. Front. Carbon Technol.* **2006**, *16*, 337.

[325] N. Sharma, N. Kumar, B. Sundaravel, K. Panda, W. David, M. Kamarrudin, S. Dash, B. K. Panigrahi, A. K. Tyagi, I. N. Lin, B. Raj, *Tribol. Int.* **2011**, *44*, 980.

[326] A. M. Affoune, B. L. V. Prasad, H. Sato, T. Enoki, *Langmuir* **2001**, *17*, 547.

[327] L. La Torre Riveros, D. A. Tryk, C. R. Cabrera, *Rev. Adv. Mater. Sci.* **2005**, *10*, 256.

[328] L. La-Torre-Riveros, K. Soto, M. A. Scibioh, C. R. Cabrera, *J. Electrochem. Soc.* **2010**, *157*, B831.

[329] L. Schmidlin, V. Pichot, S. Josset, R. Pawlak, T. Glatzel, S. Kawai, E. Meyer, D. Spitzer, *Appl. Phys. Lett.* **2012**, *101*, DOI 10.1063/1.4772983.

[330] G. L. Bilbro, *Diam. Relat. Mater.* **2002**, *11*, 1572.

[331] D. Katyanasundaran, P. Molian, *Micro Nano Lett.* **2008**, *3*, 110.

[332] E. Maillard-Schaller, O. M. Kuettel, L. Diederich, L. Schlapbach, V. V. Zhirnov, P. I. Belobrov, *Diam. Relat. Mater.* **1999**, *8*, 805.

[333] I. Petrov, P. Detkov, A. Drovosekov, M. V. Ivanov, T. Tyler, O. Shenderova, N. P. Voznecova, Y. P. Toporov, D. Schulz, *Diam. Relat. Mater.* **2006**, *15*, 2035.

[334] H. Mazaheri, S. R. Allahkaram, *Appl. Surf. Sci.* **2012**, *258*, 4574.

[335] A. Valeryevna, J. Kitamura, S. Usuba, H. Yokoi, *Carbon* **2003**, *41*, 2601.

[336] T. Cabioc'h, E. Thune, M. Jaouen, *Chem. Phys. Lett.* **2000**, *320*, 202.

[337] D. Pech, M. Brunet, H. Durou, P. Huang, V. Mochalin, Y. Gogotsi, P.-L. Taberna, P. Simon, *Nat. Nanotechnol.* **2010**, *5*, 651.

[338] M. M. H. Bastwros, A. M. K. Esawi, A. Wifi, *Wear* **2013**, *307*, 164.

[339] B. Liu, Z. Zeng, Y. Lin, *Surf. Coatings Technol.* **2009**, *203*, 3610.

[340] S. T. Selvamani, S. Premkumar, M. Vigneshwar, P. Hariprasath, K. Palanikumar, *J. Magnes. Alloy.* **2017**, *5*, 326.

[341] M. Mansoor, M. Shahid, *Adv. Mater. Res.* **2015**, *1101*, 62.

[342] J.-W. An, D.-H. You, D.-S. Lim, *Wear* **2003**, *255*, 677.

[343] U. Abdullahi, M. A. Maleque, U. Nirmal, *Procedia Eng.* **2013**, *68*, 736.

[344] D. G. Liu, J. Sun, Z. X. Gui, K. J. Song, L. M. Luo, Y. C. Wu, *Diam. Relat. Mater.* **2017**, *74*, 229.

[345] W. X. Chen, J. P. Tu, L. Y. Wang, H. Y. Gan, Z. D. Xu, X. B. Zhang, *Carbon* **2003**, *41*, 215.

[346] Z. H. Li, X. Q. Wang, M. Wang, F. F. Wang, H. L. Ge, *Tribol. Int.* **2006**, *39*, 953.

[347] L. Zhang, Q. Wang, G. Liu, W. Guo, B. Ye, W. Li, H. Jiang, W. Ding, *Tribol. Lett.* **2018**, *66*, 1.

[348] Y. Li, B. X. Li, W. J. Zou, *Appl. Mech. Mater.* **2011**, *80–81*, 683.

[349] A. L. D. Skury, G. S. Bobrovinichii, S. N. Monteiro, *Mater. Sci. Forum* **2012**, *727–728*, 320.

[350] M. Bao, C. Zhang, D. Lahiri, A. Agarwal, *Jom* **2012**, *64*, 702.

[351] H. Kaftelen, M. L. Öveçoğlu, *J. Compos. Mater.* **2012**, *46*, 1521.

[352] A. Nieto, L. Jiang, J. Kim, D. E. Kim, J. M. Schoenung, *Sci. Rep.* **2017**, *7*, 1.

[353] A. Nieto, J. Kim, O. V. Penkov, D. E. Kim, J. M. Schoenung, *Surf. Coatings Technol.* **2017**, *315*, 283.

[354] L. S. K. Pang, J. D. Saxby, S. P. Chatfield, *J. Phys. Chem.* **1993**, *97*, 6941.

FIGURES

TABLE OF CONTENTS

ACKNOWLEDGEMENTS

Thinking back to the time at the beginning of my PhD thesis, the overwhelming feeling of having finally graduated was linked to a motivated, but strange popular belief: I thought that a PhD thesis was the scientific output of a single person, based on their individual capabilities, with the aim of investigating something completely new. Hence, with the basic knowledge in material science and engineering from my studies, my plan was to find a "scientific gap" in literature and to develop a systematic and straightforward research plan with a tight schedule. Then, I would work on this plan until understanding the given problem in every little detail, presenting the final solution and complete my doctorate.

…I was so wrong and have learned so much since then, including what a PhD thesis is truly about. However, one of the things that I learned the quickest, I owe to all the members of the chair of functional materials (FuWe): teamwork. This, among other things, is why I consider it my duty to thank and dedicate this section to several people who have supported and helped me stay on track and finally create a manuscript, which combines the findings of our research from the last years.

First and foremost, I would like to thank my supervisor, Prof. Dr. Frank Mücklich, for providing the possibility to work at his institute, but also for his permanent support and his everlasting confidence in me. It was he who drew my attention to the field of materials science when I was still a pupil. I still remember his words during a visit to my former school: "If you can't decide whether to study physics, chemistry or mathematics, you should come and study materials science". Since then, he accompanied me on my way from being a scientific assistant at his institute to becoming a doctoral candidate. Due to his open-mindedness, aside from my position as a PhD student, I also got the opportunity to work at the Material Engineering Center Saarland (MECS), gathering valuable experience working together with industry. I am proud to be a part of his research group.

Also, I want to thank Prof. Dr. Dirk Bähre for being my scientific guide, for our fruitful discussions during my yearly progress reports and for his role as second reviewer of my thesis.

Thinking about my colleagues, I am very lucky to be part of such a highly motivated and supportive team of researchers. Certainly, one of the persons that I owe the most to is Dr. Sebastian Suárez. The process of being a PhD student involves phases, which are dominated by self-doubt and the question "why am I doing all this". I had never met a person as optimistic, motivating, idealistic and enthusiastic about scientific research as Seba. He helped me with almost daily motivating discussions, shared his experience as a post-doctoral researcher, assisted in countless experiments, gave me trust and friendship. I would like to express my deepest gratitude to you, Seba.

Furthermore, I would like to thank the following people who have guided me on my way as a PhD student not only as colleagues, but also as friends, making everyday work a place to feel at home: Philipp Grützmacher, Prof. Dr. Andreas Rosenkranz, Prof. Dr. Carsten Gachot, Dominik Britz, Federico

Lasserre, Christian Schäfer, Dr. Nicolas Souza, Daniel Müller, Timothy MacLucas and Sebastian Slawik. Prof. Dr. Rosenkranz, Dr. Suarez, Dr. Souza and Mr Grützmacher are especially appreciated for proofreading this dissertation.

Additionally, my thanks go to all my other colleagues from FuWe as well as researchers of other institutes who gave me the opportunity to use their experimental equipment or to benefit from their knowledge in various experimental or simulation tasks. In this context, I would like to mention Prof. Dr. Volker Presser, Prof. Dr. Itzhak Green, Prof. Dr. Michael Varenberg, Dr. Frank Müller and Dr. Marco Zeiger amongst others.

Almost half way through my PhD, my better half named Belinda came into my life. It was and still is such a good feeling to be supported and understood not only scientifically, but also emotionally. You are my daily constant and motivation, that makes even the worst day look better and I am very grateful for every single moment with you.

Last but not least, I also want to thank my family, especially my mom and dad for their endless support, open ears and understanding during the last years. My family always encouraged and believed in me and I will treasure their support forever.

ZUSAMMENFASSUNG

Diese Dissertation setzt sich zum Ziel, mittels neuartiger Festschmierstoffe (Kohlenstoff-Nanopartikel (CNP)), deren Einsatz in einer geeigneten Materialklasse (Metall Matrix Komposite (MMC)) und der Entwicklung eines spezifischen Oberflächendesigns (mittels Laser-Oberflächenstrukturierung) selbstschmierende Oberflächen herzustellen sowie die involvierten Mechanismen zu verstehen. Dies umfasst die vollständige Prozessentwicklung von der Synthese und Verarbeitung über die experimentelle Analyse und theoretische Modellierung, der Diskussion und dem Verständnis der Mechanismen bis hin zur Herstellung eines Prototyps.

Von drei untersuchten CNP (zwiebelartiger Kohlenstoff, Nanodiamanten und Kohlenstoff-Nanoröhrchen (CNT)) konnten CNT als geeigneter Festschmierstoff identifiziert werden. Dies ist auf ihr hohes Aspektverhältnis, Flexibilität sowie ihren Degradationsmechanismus zurückzuführen. Die kontinuierliche Versorgung des Kontaktes mit CNT ist durch deren elastische Kompression und Rückstellvermögen gewährleistet. Der entsprechende Degradationsmechanismus erlaubt eine effiziente Schmierung unabhängig von vorherrschender Luftfeuchtigkeit, Oberflächenrauheit, dem Belastungskollektiv und der Kontaktmechanik, was auf die Anpassungsfähigkeit der Schmierungsmechanismen (Rollen, Gleiten und Scheren) zurückzuführen ist.

So konnten permanent selbstschmierende Oberflächen hergestellt werden, welche eine maximale Reduzierung von Reibung und Verschleiß um den Faktor 4 bzw. 115 ermöglichen.

ABSTRACT

This dissertation deals with a new branch of solid lubricants (carbon nanoparticles (CNP)), their use in a suitable base-material (Metal Matrix Composites (MMC)) and the investigation of a specific surface design (processed by laser surface structuring) to create and understand self-lubricating surfaces. The dissertation covers the complete process development from the synthesis and processing, experimental analysis and theoretical modeling, discussion and understanding of involved mechanisms up to the production of a prototype.

Out of three investigated CNP (onion-like carbon, nanodiamonds and carbon nanotubes (CNT)), CNT are identified as the most suitable solid lubricant for self-lubricating surfaces. In this regard, their large aspect ratio, flexibility as well as degradation mechanism are the most important aspects to consider. Being stored in a surface, CNT are continuously pulled into the contact by elastic compression and restoration. Due to their degradation mechanism, their lubrication activity is insensitive to variations in humidity, surface roughness, loading conditions and contact mechanics. The lubrication mechanisms of CNT adapt to the given situation by effectively combining different solid lubricant working principles, namely: rolling, sliding and shearing.

As a result, permanent self-lubricating surfaces are successfully produced, allowing for a maximum reduction in friction and wear by a factor of 4 and 115, respectively.

ABBREVATIONS AND SYMBOLS

a_1, a_2	Unit vectors	I_G	Intensity of G-band
a-C	Amorphous carbon	$I_{G'}$	Intensity of G'-band
a-C:H	Amorphous, hydrogenated DLC	LA	Raman mode
a-Si:O	Quartz-like network	LO	Raman mode
A_r	Real area of contact	L	Normal load
AFM	Atomic force microscopy	LST	Laser surface texturing
α	Pressure dependent shear strength	λ	Wavelength
bcc	Body centered cubic	MEMS	Micro-electro mechanical systems
CPS	Cold pressed sintering	MWCNT	Multi-wall carbon nanotube/-s
CSA	Chlorosulfonic acid	MMC	Metal matrix composite/-s
CNP	Carbon nanoparticle/-s	μ	Friction coefficient
CNT	Carbon nanotube/-s	ND	Nanodiamond/-s
COF	Coefficient of friction	NC-graphite	Nanocrystalline graphite
CVD	Chemical vapor deposition	OLC	Onion-like carbon
C_h	Chiral vector	P	Contact pressure
DMF	Dimethylformamid	p	Structural periodicity
DC	Direct current	PTFE	Polytetrafluorethylene
DLN	Diamond-like nanocomposite/-s	PE	Polyethylene
D-band	A Raman mode	RBM	Radial breathing mode
D'-band	A Raman mode	R_k	Core roughness
DLIP	Direct laser interference patterning	SEM	Scanning electron microscopy
DLW	Direct laser writing	SPS	Spark plasma sintering
d_t	Tube diameter	SWCNT	Single-wall carbon nanotubes
DLC	Diamond-like carbon	σ	Normal stress
0-D	0-Dimensional	ta-C	Tetragonal amorphous carbon
EPD	Electrophoretic deposition	ta-c:H	Hydrogenated ta-C
fcc	Face centered cubic	TEM	Transmission electron microscopy
F	Friction force	TNT	Trinitrotoluol
FIB	Focused ion beam	TMD	Transition metal dichalcogenide/-s
FWHM	Full width at half maximum	T	Tube-axis
G-band	A Raman mode	τ_S	Shear strength
G'-band	A Raman mode	τ_0	Interfacial shear strength
HUP	Hot uniaxial pressing (HUP)	τ	Shear stress
HPT	High pressure torsion	UV	Ultraviolet
HIP	Hot isostatic pressing	vol.-%	Volume-%
IF	Inorganic fullerene/-s	X_{CG}	G-band center position
I_D	Intensity of D-band	XPS	X-ray photoelectron spectroscopy

1. MOTIVATION AND OBJECTIVES

Tribology is defined as the science of interacting surfaces in relative motion and all practices related thereto. It includes the study of wear, friction and lubrication and ranges from spacecraft to household appliances or even the human body [1,2]. Thus, understanding and tailoring the tribological properties of mechanical systems has been and still is a vastly studied field of research.

Nowadays, friction and wear are recognized as having a major influence on the efficiency and lifetime of machinery and thus, determine the economic viability of a product to a great extent [3–6]. This fact is clearly exemplified by an average passenger car spending about one third of its total fuel energy on friction and wear [3]. In nearly every technical application, transmitting kinetic/mechanical energy from its source to the desired application area is realized by the interaction of at least two surfaces. Aside from certain applications where high friction is desirable (e.g. for automotive brakes or clutches[7,8]), the intention is to reduce friction and wear to a minimal level (e.g. for bearings). This can be accomplished by tribological optimization of the lubrication [9], surface design [10] and base materials [11].

Certainly, the simplest and most effective way to reduce friction and wear is to use a suitable lubricant. For a wide range of applications, a liquid lubricant is used (e.g. oil), which tunes the separation of the contacting surfaces as a function of the applied normal load, sliding speed as well as oil viscosity, thus affecting friction and wear [12]. However, for some applications, the use of solid instead of liquid lubricants can be advantageous or unavoidable, for example, in cases of harsh environmental conditions such as high temperature ranges (e.g. kiln truck bearings) or high vacuum (e.g. spaceflight applications) [13–15]. There is a variety of different solid lubricants such as MoS_2, WS_2, graphite, lubricious oxides, diamond-like carbon (DLC), certain polymers or soft metal coatings, all of which are limited in their range of application [13]. Even though they can be very effective under certain conditions, they typically fail in one or several of the following requirements, namely: insensitivity to operational environments including low chemical reactivity (oxidation or formation of unwanted by-products), easy replenishment, capability to dissipate generated heat, constant lubrication, aging stability or adhesion [13,16]. For example, MoS_2 is often used in applications working under vacuum or inert gas, since it reacts with oxygen in atmospheric environments thus losing its ability to lubricate [13]. In contrast, graphite particularly shows efficient lubrication under moderate to high relative humidity. In the case of low relative humidity or vacuum, a high coefficient of friction (COF > 0.5) is observed as its lubrication mechanism relies on the intercalation of water molecules between consecutive graphene layers [17].

Nevertheless, today's technical applications demand an ever greater degree of robustness and insensitivity with regard to environmental and loading conditions in the use of solid lubricants [18,19]. For example in spacecraft, satellites or satellite launch vehicles wait for extended periods of time in

humid environments before starting, after which they must work under vacuum conditions. For this reason, solid lubricants must be developed that adapt to changing environmental or loading conditions while still reliably lubricating the mechanical components of a system [20].

Regarding the used base material, especially in the field of dry friction, the mechanical and chemical properties of the contacting surfaces are of utmost importance. One way to tailor these is by using metal matrix composites (MMC), with the metal matrix most often being reinforced by a non-metallic phase. The properties of MMC can be designed to fit the requirements of an intended application (e.g. light weight but high strength). They are often employed as structural and functional materials such as fiber-reinforced pistons, aluminum crankcases with strengthened cylinder surfaces or particle-strengthened brake discs, in the automotive or aerospace sectors. MMC are also broadly found in wear-resistant or friction-reducing sliding contact materials in bearings and pistons or cylinder liners in engines [21–26]. This is not only due to the fact that the microstructure of MMC, and thus their mechanical properties, can be controlled by the processing parameters and the reinforcement phase, but also because lubricants (such as graphite) can be used as reinforcement phase in order to obtain self-lubricating materials [22].

In this regard, using a solid lubricant as reinforcement phase can overcome some drawbacks of solid lubricant coatings, such as limited lifetime, difficult replenishment, oxidation, aging-related degradation or poor adhesion [16]. Not only can MMC be used as a bulk self-lubricating material but there are also several ways to apply MMC as surface coating, rendering this method to create self-lubricating materials a very versatile technique, which could be used for many different substrate materials and applications [27–30]. However, a significant disadvantage arises when using rather soft, easy to shear solid lubricants such as graphite in MMC, namely poor mechanical properties. These composites sometimes have even lower mechanical properties than the unreinforced alloy [16]. In this regard, the tendency is to reduce the reinforcement material's size to the nano range, allowing for a fine and homogeneous reinforcement distribution. This could possibly resolve some of the limitations such as poor ductility, machinability and reduced fracture toughness [16].

In recent years, carbon nanoparticles (CNP) have arisen as promising candidates to reduce friction and wear under various operational environments, which is ascribed to their intrinsic mechanical properties, chemical inertness, thermal stability as well as atomic structure and morphology [31–36]. Several works report on the friction and wear-reducing effects of the particles when used as solid lubricant coating or as reinforcement phase in composite materials [29,35–47]. However, the underlying lubrication mechanisms of the particles are still a matter of debate and thus the potential lubricating effects may not be fully exploited. The present thesis focuses on three CNP in particular: Multi-wall carbon nanotubes (MWCNT), onion-like carbon (OLC) and nanodiamonds (ND). MWCNT consist of multiple, hollow graphitic shells (sp^2-hybridized carbon atoms), providing a tube-like form with a very high aspect ratio[48,49]. OLC, also known as carbon onions, show the same hybridization and a similar graphitic shell-like structure, but with a spheroidal particle morphology[50]. Finally, with a

particle morphology similar to OLC, ND provide a diamond atomic structure with sp^3-hybridized carbon atoms [33]. These three different types of CNP are chosen intentionally since they can be systematically distinguished. A systematic investigation of the lubrication mechanisms of different CNP and lubrication requirements in the same tribological system has not been done before in literature, although it would allow for a more in depth understanding of the mechanisms involved.

When designing self-lubricating surfaces and addressing the used lubricant and base material, the impact of the surface design should also be explored, since surface topography and chemistry have a major influence on the contact mechanics, and consequently, the occurring wear mechanisms. From various techniques to create well-defined surface designs such as honing, blasting, micro coining or lithography, laser surface texturing (LST) and in particular Direct Laser Interference Patterning (DLIP) have shown to be suitable, cost and time-efficient approaches [10,51]. In addition to reducing the real contact area and trapping abrasive wear debris, created surface depressions can act as storage for liquid and solid lubricants, thus continuously supplying the contact region with lubricant [52,53]. Additionally, the ability to systematically vary the surface design allows for a more in-depth understanding of the occurring lubrication mechanisms. For this reason, laser surface texturing is proposed in the present dissertation as a tool to create self-lubricating surfaces and to understand the influence of the surface design on the lubrication mechanism of CNP.

The development route of the present dissertation is schematically presented in ***Fig. 1***.

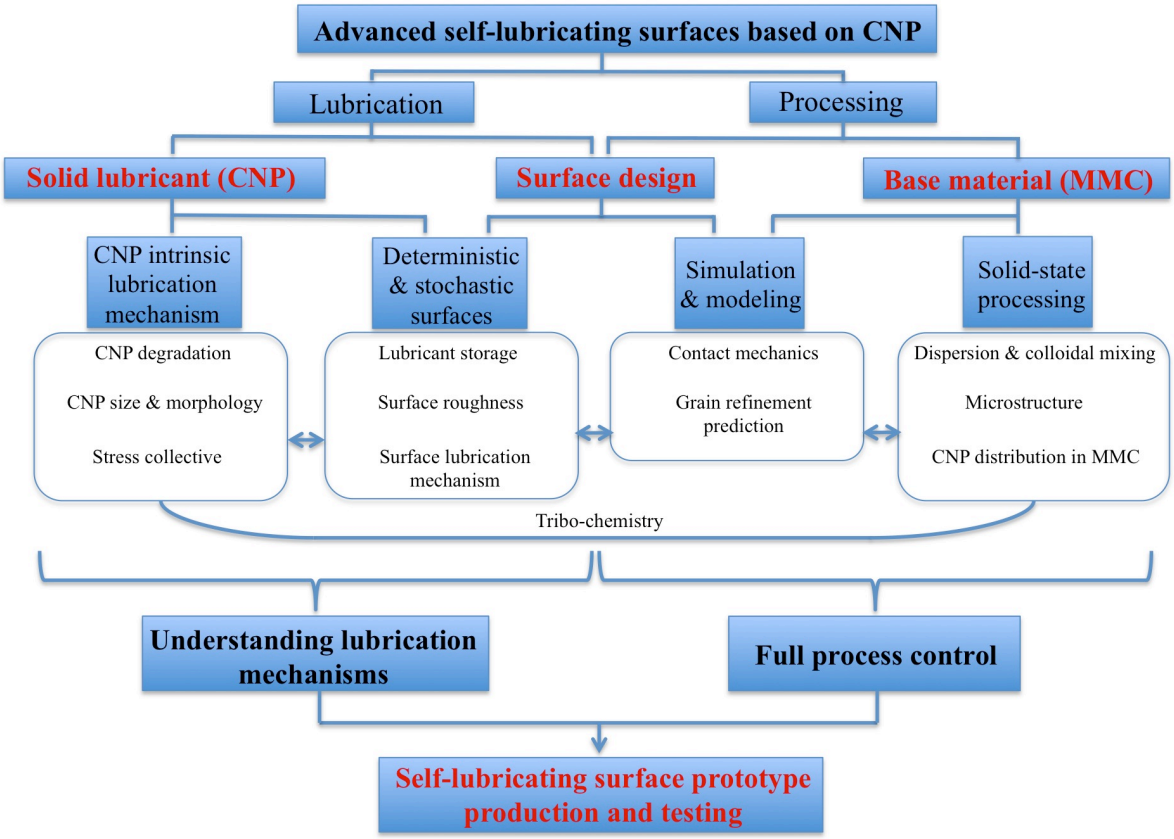

Figure 1: Schematic of the development route of the present dissertation

In summary, the present dissertation deals with an emerging branch of solid lubricants (CNP), their use in a suitable base material (MMC) with a specific surface design (using LST), thus addressing the three most important points for the development and understanding of self-lubricating surfaces based on CNP. The dissertation covers the complete process development to create these surfaces from the synthesis and processing, experimental and theoretical modeling, discussion and understanding of effects and mechanisms up to the production of a prototypical component, which should be suitable for permanent self-lubricating unidirectional sliding. In particular and based on the schematic in ***Fig. 1***, the following three objectives should be met:

OBJECTIVE 1

The first objective of this dissertation is to find a CNP dispersion and MMC processing method that enables a uniform production of CNP-reinforced MMC. This method should avoid particle functionalization, minimize particle degradation and enable a fine and homogeneous particle distribution within the resulting MMC. In addition, the method must allow for full process control so that a model can be established, which predicts the final microstructure of the manufactured composites.

OBJECTIVE 2

The second objective is to understand the intrinsic lubrication mechanisms of CNP and the different tribological influences involved when using them as a lubricant in MMC or as a coating. For this purpose, the tribological properties of CNP-coated surfaces must be investigated and compared to CNP-reinforced surfaces. In this regard, influences of the microstructure, lubricant storage, surface roughness and design, degradation mechanisms, size/morphology of CNP and stress collective have to be carefully evaluated, compared and discussed. Based on these findings and the resulting contact mechanics, the question must finally be answered as to which CNP is best suited for the intended purpose of the self-lubricating surfaces.

OBJECTIVE 3

A prototypical component must be produced and tailored to combine all the positive findings of objective 1 and 2. The prototype should be tested under conformal contact situation, comparable to the situation of a bearing subjected to unidirectional sliding, providing a constantly decreased friction and wear under steady-state conditions.

2. STATE OF THE ART

2.1 Carbon nanoparticles (CNP)

Carbon is a very versatile element and can be found in great abundance on our planet. With an atomic electron configuration of six electrons (two in the 1s orbital, two in the 2s orbital and two in the 2p orbital), carbon materials can be classified into two main groups, depending on the energetic state of the carbon bonding, called hybridization. The first and most stable carbon allotrope is graphite, possessing an sp^2-hybridization, the ground state phase of carbon under standard temperature and pressure. Under high pressure (several GPa), graphite transforms to diamond, resulting in sp^3-hybridization of the carbon atoms [54].

In the case of graphite, each carbon atom is covalently bonded to three other carbon atoms, through its three coplanar sp^2 orbitals, forming σ-bonds, and orthogonal p orbital, forming a π-bond. The latter produces what is considered as an electron cloud (delocalized electrons), similar to what is observed in metals. Structurally, graphite presents a layered structure consisting of several stacked planar single layers (called graphene) that are interconnected by weak Van-der-Waals interactions. In contrast, the diamond structure is characterized by a fourfold covalent bonding (four sp^3 orbitals) of the carbon atoms with a tetrahedral symmetry (109.5°) [54,55]. The graphite and diamond bonding structure is depicted in ***Fig. 2***.

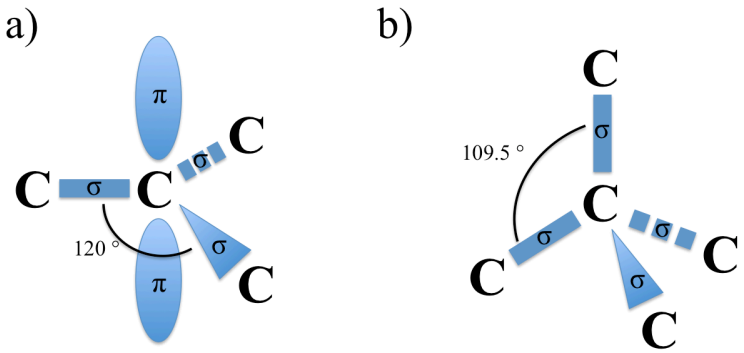

Figure 2: a) Bonding structure of graphite and b) diamond.

Based on these two principal carbon modifications, a large variety of carbon materials and recently carbon nanomaterials have been developed. A material is generally considered a nanomaterial if at least one internal or external spatial dimension is in the nm scale (up to 100 nm) [56]. In addition of being distinguished by their carbon hybridization, carbon nanomaterials are usually classified as 0-D, 1-D, 2D and 3-D materials according to their properties and their morphology (flatness, sphericity). ***Fig. 3*** gives a brief overview of a selection of currently known sp^2-hybridized carbon nanomaterials [57].

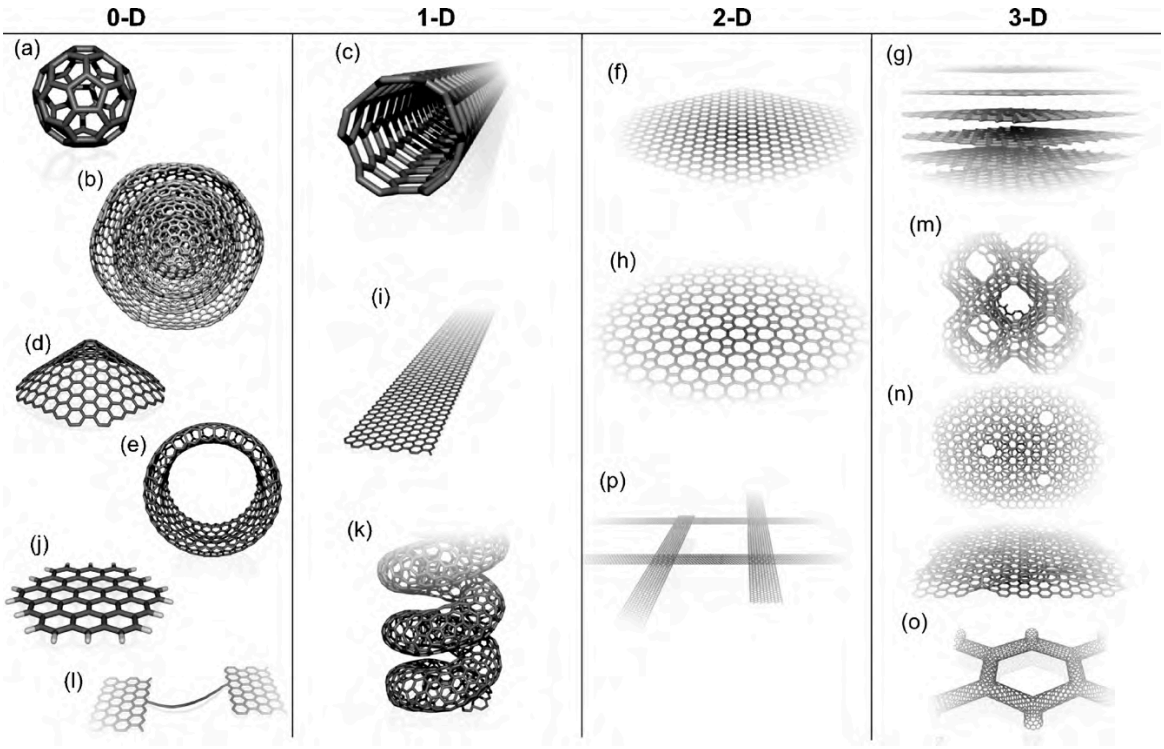

Figure 3: Selection of currently known forms of sp^2-hybridized carbon nanomaterials. a) C_{60}: Buckmisterfullerene, b) carbon onion, c) carbon nanotube, d) nanocone/horn, e) nanotoroid, f) graphene, g) graphite, h) haeckelite surface, i) graphene nanoribbon, j) graphene cluster, k) helicoidal carbon nanotube, l) short carbon chain, m) schwarzite crystal, n) carbon nanofoam, o) nanotube network, p) nanoribbon network [57].

In this context, dimensionality determines the number of principal directions in which the nanomaterials are expanded. Thus, spheroidal nanoparticles (e.g. carbon onions in ***Fig. 3 b***) are often referred to as 0-D nanoparticles, whereas cylindrical nanoparticles (e.g. carbon nanotubes in ***Fig. 3 c***) are denoted as 1-D nanoparticles. Especially in the cases of 0-D and 1-D carbon nanomaterials, a defect formation in the atomic structure is often observed since the curvature of these structures is extremely high. For example, a possible defect in a sp^2-hybridized carbon nanomaterial could be a pentagonal carbon bonding (instead of hexagonal), a crystal boundary in polycrystalline graphite or simply dangling bonds of the aromatic system [58]. Specifically, the pentagonal defects are often needed in order to form closed spherical or tube-like morphologies in the nanometer scale.

Since carbon can exist in a vast variety of different configurations, new nano-carbon modifications are constantly being discovered and the same modification is sometimes given different names by different works for different applications, which indeed makes it hard to compare the modifications in an objective way [59]. A general overview about carbon nanomaterials is given by Gogotsi and Presser [31].

However, for tribological applications and thus the intended use in this dissertation, 0-D or 1-D carbon nanoparticles (CNP) in particular have been highlighted in recent years, providing promising

properties to act as solid lubricants in mechanically loaded contacts. This fact is mainly due to their morphology (spheroidal or tubular shape) and their high chemical and mechanical stability, which is why they are often said to potentially act as nano ball- or roller bearings [31,34,60]. Nonetheless, since this hypothesis has not yet been thoroughly verified and the potential lubrication mechanisms of the particles are not yet understood, one objective of the present dissertation is the systematic investigation and analysis of these mechanisms.

For this purpose, three different CNP were chosen in order to represent 0-D and 1-D CNP as well as both carbon hybridization states (sp^2 and sp^3). These are nanodiamonds, carbon onions and carbon nanotubes, described in more detail in the following sections.

2.1.1 Nanodiamonds (ND)

Nanodiamonds (ND) are spherical nanoparticles (diameter of typically 2-10 nm) with a predominant sp^3 carbon hybridization and a diamond lattice constant of 0.35 nm. Within their most interesting characteristics, they have shown remarkable biocompatibility, chemical stability, mechanical and optical properties [33]. Although already discovered in the 1960s by a detonation reaction, the interest in these particles did not grow until the beginning of the 1990s [61]. Since then, they have received increasing attention in numerous research fields such as: tribology [62], drug delivery [63], bioimaging [64] or tissue engineering [65].

Nowadays, an abundance of methods is available for their production, including laser ablation [66], high energy ball milling of high pressure, high temperature diamond microcrystals [67] as well as the detonation technique [68]. Since the ND used in this dissertation were synthesized via detonation, this method is described in more detail in the following. The basic atomic structure of a common single nanodiamond particle is shown schematically in ***Fig. 4***.

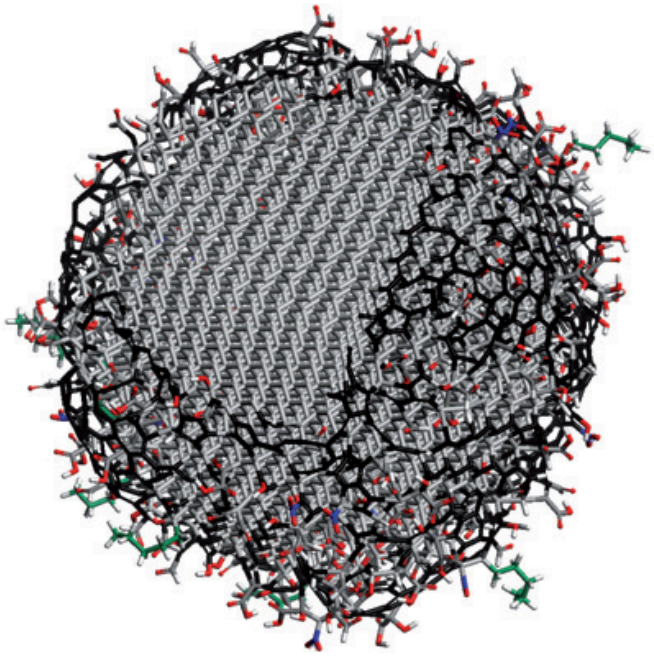

Figure 4: Schematic representation of the most common atomic structure of a single nanodiamond particle. The grey-colored, highly ordered structures correspond to the sp^3-hybridized, diamond carbon bonding. In black, aromatic structures of sp^2-hybridized carbon are visible which terminate the surface of the nanodiamond. Additionally, oxygen- and nitrogen-containing functional groups are depicted (red and blue, respectively) as well as hydrocarbon chains (green) or hydrogen terminations (white) [33].

The grey-colored, highly ordered structures represent the sp^3-hybridized carbon bonding and form the core of the particle. In order to remain stable under ambient conditions, the outer shell of the particle must either be terminated by functional groups (e.g. oxygen- or nitrogen-containing groups) or sp^2-hybridized carbon structures of graphitic or amorphous nature. This becomes evident when looking at the phase diagram of nano-carbon in ***Fig. 5 (a)***, which can also be used as starting point for explaining the basic principle of detonation synthesis.

The phase diagram shows that the most stable phase of carbon under standard pressure and temperature is graphite, which becomes even more significant for nanoscale carbon as indicated with the blue lines. For detonation synthesis, explosives with a negative oxygen balance (e.g. a mixture of trinitrotoluol (TNT) and hexogen) are detonated within a closed chamber containing N_2, CO_2 and H_2O. The generated shock wave leads to a raise in pressure and temperature, reaching the *Jouguet* point (point A in ***Fig. 5 (a)*** or red dashed line in ***Fig. 5 (b)***) and to the formation of liquid nano-carbon as also schematically illustrated in areas III to VI of ***Fig. 5 (b)*** [69].

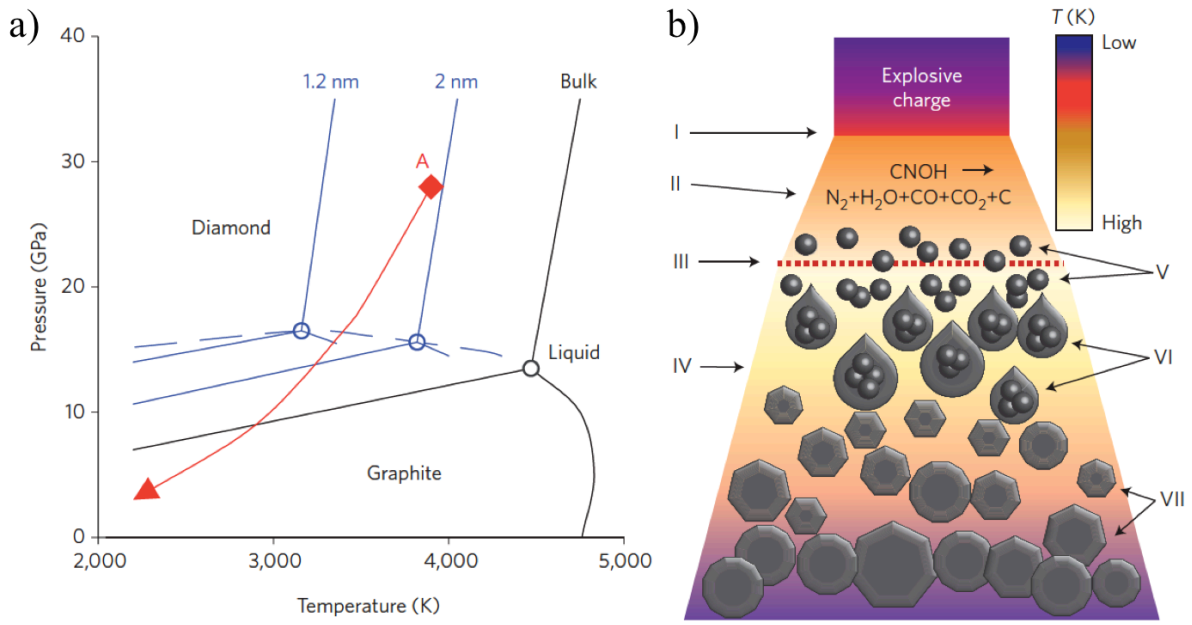

Figure 5: a) Phase diagram of carbon as a function of pressure and temperature with blue lines inserted for nanomaterials. b) Scheme of the shock wave evolution in the detonation synthesis of nanodiamonds, showing (I) shock wave front, (II) zone of chemical reaction, (III) *Chapman-Jougout* plane (corresponding to point A in the phase diagram, (IV and V) detonation products, (VI) formation of liquid droplets and finally, (VII) crystallization process towards the formation of nanodiamonds [33].

With decreasing temperature and pressure, the liquid carbon solidifies and crystallizes into highly ordered diamond structures until reaching the diamond-graphite equilibrium line, from which the termination of the diamond shell with graphitic structures starts to occur [33]. Subsequently, the formed detonation soot must be purified by liquid oxidants (e.g. HNO_3, HCl) or oxidized in air at elevated temperatures in order to remove non-carbonaceous impurities [69,70].

With regard to the predominant sp^3 carbon core hybridization, ND inherits most of its properties from the well-known macroscale diamond with a Young's modulus of 1000 GPa, a Vickers hardness of 10000 HV and a thermal conductivity of 2200 W m^{-1} K^{-1} [71]. Nevertheless, the surface of a ND, which is enclosed by sp^2-hybridized carbon and functional groups, can be further chemically functionalized in several different ways, resulting in a wide range of potential applications for ND [72]. For further information, an extensive overview of the structure, properties and applications of ND is given by Mochalin et al. [33].

2.1.2 Onion-like carbon (OLC)

Onion-like carbon, also called carbon onions, are spheroidal, fullerene-like carbon nanoparticles (diameter of typically 5-10 nm), possessing a concentric, multi-shell configuration with an equilibrium interlayer spacing of 0.34 nm and predominant sp^2 carbon hybridization (***Fig. 6***) [73,74]. Typically, these structures are highly defective, since hexagonal (aromatic) carbon bonding is not

enough to build a closed, spherical carbon shell. Main features of OLC are their high mechanical stability [31], very large surface area as well as high electrical conductivity (2-4 S cm^{-1}) [73,75].

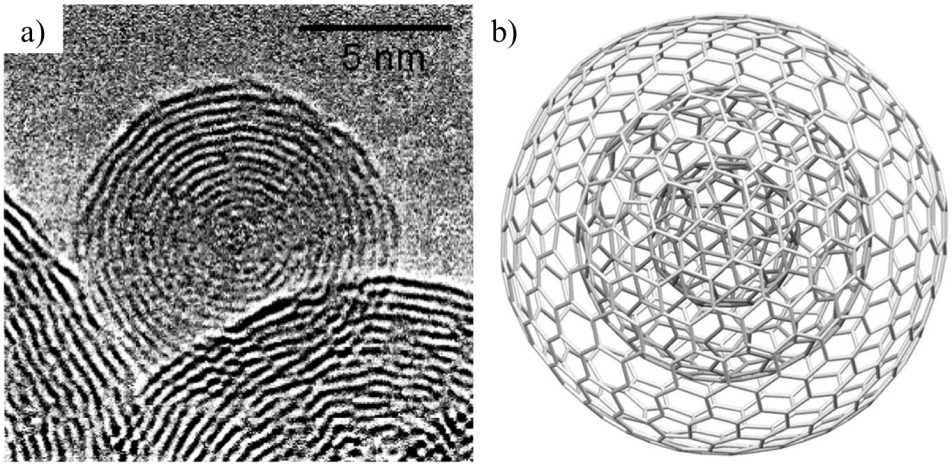

Figure 6: a) Transmission electron micrograph of OLC, presenting the layered, onion-like morphology of the particle. b) Schematic of a defect-free, single OLC particle, showing the typical aromatic carbon multi-shell structure of sp^2-hybridized carbon rings [74].

S. Iijima first discovered carbon onions in 1980 as a byproduct of carbon black synthesis [76]. 12 years later, D. Ugarte was able to observe and understand the formation of OLC in situ by focusing an electron beam on carbon soot [77]. Since then, OLC were investigated for various potential applications ranging from tribology [36], over bioimaging [78] to batteries [79] and supercapacitors [73]. Despite other methods for OLC synthesis (e.g. arc discharge of graphite in liquids [80] or combustion of naphthalene [81] and many more), vacuum and inert gas annealing of nanodiamond precursors have turned out to be the most extended approaches of large scale OLC production nowadays [75,82]. Generally, the type of precursor and the synthesis conditions strongly influence the final OLC morphology and size (up to 100 nm in diameter possible). However, using the thermal annealing technique, very high purity OLC with typical sizes between 5 to 10 nm (high material homogeneity) are achieved at a relatively low price [73]. Since the OLC used in this dissertation were produced using this technique, the basic thermally induced transformation process of ND towards OLC is depicted in ***Fig. 7***.

The annealing process of ND allows for the precise tuning of the carbon sp^2 to sp^3-hybridization ratio as a function of the temperature. The transformation of a ND begins at the outer shell of the particle and continues stepwise to the particle core. At first, desorption of water and detachment of oxygen-containing functional groups on the ND surface are observed for temperatures up to 200°C [83]. This is followed by the detachment of surface functional groups and the subsequent emission of CO and CO_2, which leads to the formation and subsequent recombination of dangling bonds, thus starting to form the typical sp^2 related π-bonds at around 700-800°C.

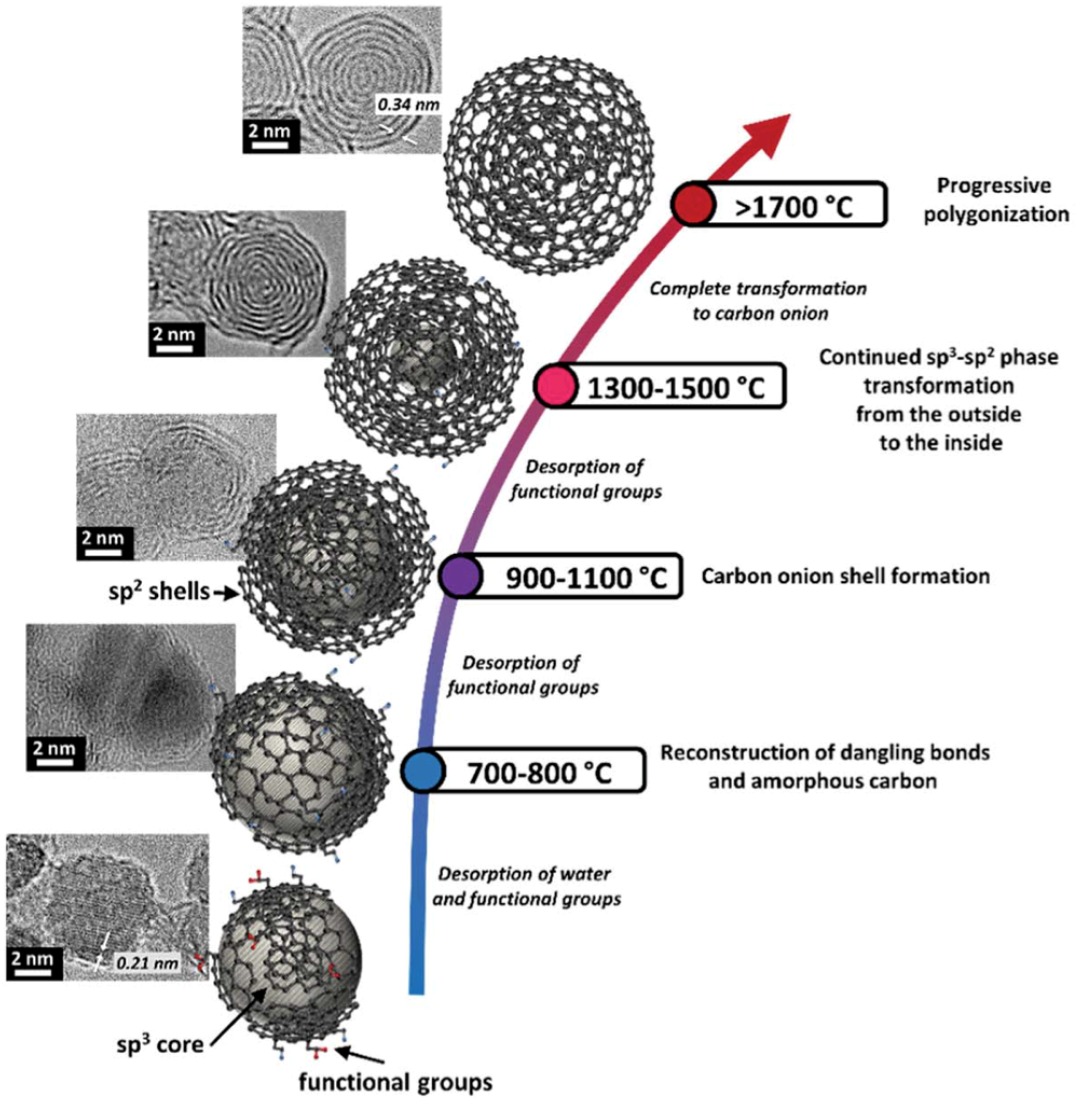

Figure 7: Schematic transformation process of ND to OLC as a function of temperature with corresponding TEM micrographs exemplifying the transformation stages. Variations in the individual stages can occur since the transformation process also depends on the used environmental conditions (inert gas or vacuum) and the nanodiamond precursor size [73,84].

Graphitization of the ND proceeds with increasing temperature, still providing a diamond inner core, until finally fully transformed and highly ordered carbon onions are built at temperatures higher than 1700°C [85,86]. This is due to the fact that the high stability of the inner diamond core is usually associated to the buildup of internal pressure, as a consequence of the atomic rearrangement of the outer shell. During this process, the volume of the particles is enlarged with ND and OLC providing a density of 3.3 g cm^{-3} and 1.9 g cm^{-3}, respectively. Since OLC are closed, mainly sp^2-hybridized carbon structures, it is believed that they possess very high mechanical strength [31,36]. For more detailed information on OLC synthesis and applications, please refer to the review articles of Bartelmess et al. [75] or Zeiger et al. [73].

2.1.3 Carbon nanotubes (CNT)

Carbon nanotubes were discovered by Iijima [48] in 1991 and have experienced an increasing interest in research since then. CNTs are tube-like CNP with a very high aspect ratio (tube length to diameter ratio, roughly in the range of 1000/1), consisting of highly crystalline sp^2-hybridized aromatic carbon rings. Morphologically, a CNT can be imagined as a rolled graphene layer forming a hollow cylinder with half fullerenes capping the ends [87]. Theoretically, the particles possess superior mechanical, thermal, and electrical properties and found numerous potential applications such as in tribology, for structural composites, energy transfer and storage [31,88–91].

Generally, one can distinguish between a single-wall CNT (SWCNT) and a multi-wall CNT (MWCNT). A schematic is given in ***Fig. 8***.

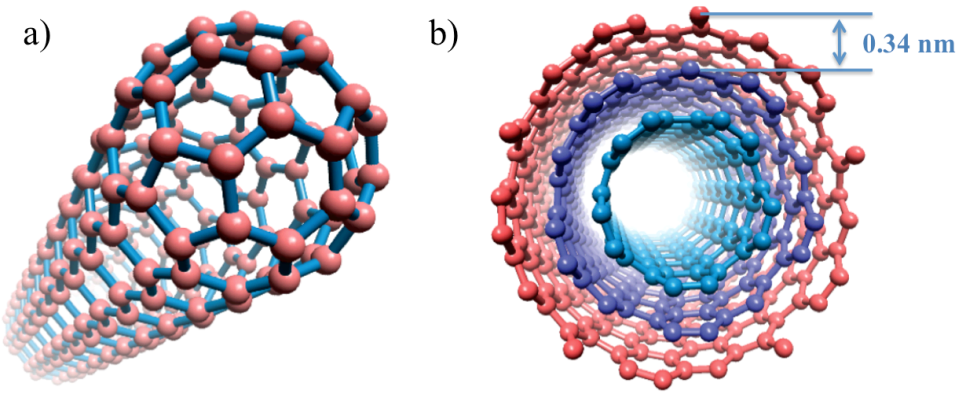

Figure 8: Schematic of a) single-wall CNT and b) multi-wall CNT with an intertubular lattice spacing of 0.34 nm. Modified from [92].

MWCNT consist of several concentrically arranged SWCNT with an equilibrium interlayer distance of around 0.34 nm [93]. The resulting diameter of a MWCNT is a function of the number of walls and typically ranges from 5-100 nm [94]. The physical properties of different CNT can vary significantly, which is why their atomic structure has to be considered in more detail. A graphene layer could be "rolled" in different ways, resulting in a wide variety of CNT chiralities. The chirality map (**Fig. 9**) is based on a planar graphene sheet with hexagonally bonded carbon atoms. Due to the system's symmetry, a 30° wedge of possible different rolling directions can be defined. Within this wedge, a chiral vector C_h is given as a multiple (n,m) of two unit directions (a_1, a_2) of the hexagonal cells. It connects the origin atom with another atom, defining the connection point of the rolled graphene sheet and thus the chirality of the CNT. With its vector norm, the circumference of the tube is given as well. The normal of this vector is the tube-axis T and the tube diameter d_t can be geometrically calculated, assuming that the tube is perfectly round [87].

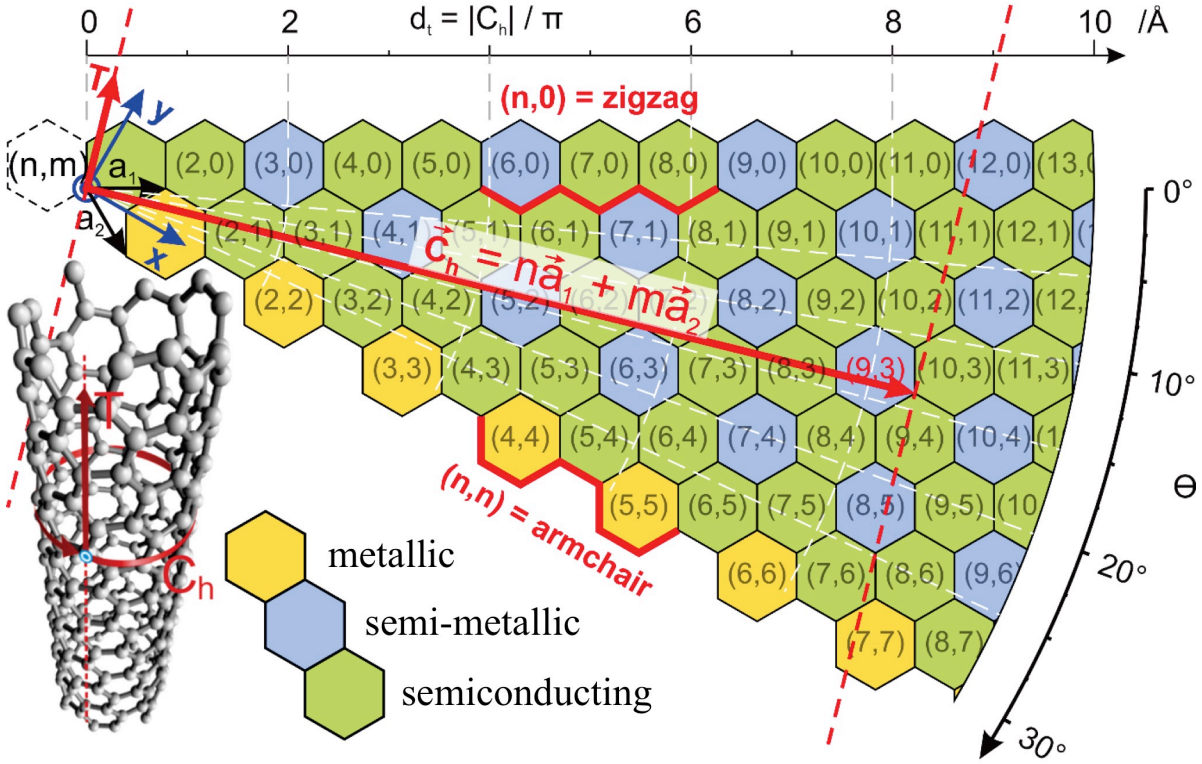

Figure 9: A chirality map is shown, presenting a 30° wedge of a graphene sheet. The chiral vector C_h with the coordinate system being described by the unit vectors (a_1, a_2), the tube axis T and the tube diameter d_t are presented and schematically illustrated. A color coding describes the electrical behavior of the SWCNT as a function of the integers of C_h [92].

Derived from this chirality map, three principal configurations can be distinguished: A “zigzag” configuration is given for (n, 0), an n=m configuration is called “armchair” and anything in between the two is denoted “chiral”. It is found that the properties of the SWCNT, for example the electronic properties (metallic, semi-metallic or semiconducting) are strongly related to their chiral vector [95].

The physical properties of SWCNT compared to MWCNT also differ significantly. Although no consensus has been reported in the literature, both can show a remarkable Young’s modulus of up to 1 TPa [96]. However, the axial tensile strength or thermal conductivity, for example, reach values of 20-30 GPa and 6600 W m^{-1} K^{-1} for SWCNT and 150 GPa and 3000 W m^{-1} K^{-1} for MWCNT, respectively [97–100]. In this context, CNT are known to provide extraordinarily high specific stiffness and strength (Young’s modulus or strength normalized by the density, respectively), resulting in a lightweight material, but possessing better mechanical properties than any structural material used nowadays. This is related to the presence of axial σ-bonds, regarded as the strongest bonds in nature [101]. Furthermore, a CNT can be bent and coiled without breaking, additionally allowing for almost full elastic restoration [102]. These properties make CNT particularly attractive as a reinforcing phase in composite materials with the aim of transferring their intrinsic properties to a macroscopic material.

Nevertheless, these outstanding physical properties described in literature would only be realizable for CNT in a "perfect" structural s well as deagglomerated state. This means that no structural defects in the carbon lattice and no exo- or endohedral contaminants should be present. Furthermore, it is well known that CNT tend to form large agglomerates of multiple entangled tubes due to their large aspect ratio and strong electromagnetic interactions. These interactions are caused by the delocalized π electron clouds, which allow for the spontaneous formation of dipoles and thus attractive Van der Waals forces. All of these requirements have been very challenging in CNT synthesis and processing during the last decades [103].

Regarding the CNT synthesis, the most commonly used methods are chemical vapor deposition (CVD), arc discharge and laser ablation [104,105]. Among those, CVD synthesis can be easily scaled to industrial quantities and provides good control over the morphology of the obtained CNT. The MWCNT that have been used in the present dissertation were produced by CVD, and thus this specific synthesis method is described in more detail. The CNT growth mechanisms in a CVD synthesis process are presented schematically in ***Fig. 10***.

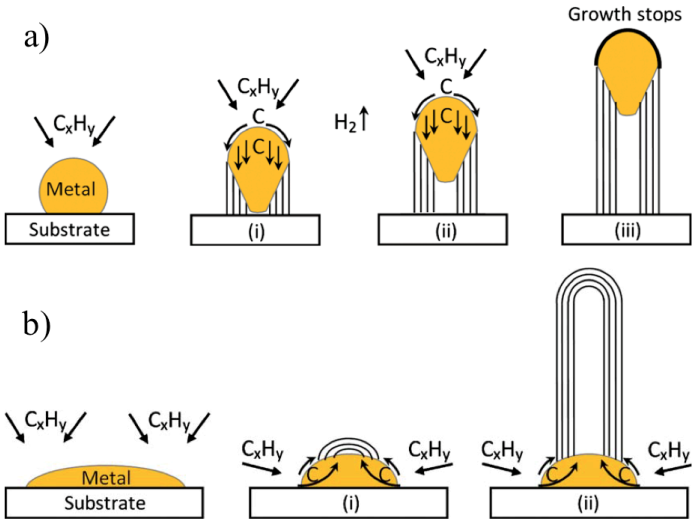

Figure 10: Growth mechanism of CNT in a CVD process showing a) the tip-growth model and b) the base growth model at different stages [106].

CVD, particularly catalytic CVD, is usually done in a fluidized bed with organometallics as catalysts (e.g. ferrocene) [107–109] or by thermal decomposition of a hydrocarbon gas (e.g. methane, ethylene, benzene) in the presence of a metal catalyst (e.g. Ni, Co, Fe). In the second case, a hydrocarbon gas (C_xH_x in ***Fig. 10***) is passed through a reactor containing a heated metal catalyst (600-1200°C) on which CNT start to grow. As soon as the hydrocarbon vapor gets in contact with the hot metal catalyst, it decomposes into carbon and hydrogen with carbon subsequently being dissolved into the metal. After reaching the carbon solubility limit (or even beyond that limit), carbon precipitates are formed, crystallizing to a cylindrical network with no dangling bonds. The interplay of exothermal decomposition of hydrocarbon and endothermal carbon crystallization keeps the process running.

Two basic models are distinguished, depending on the metal catalyst to substrate material interaction. If the interaction is weak, carbon diffuses to the bottom of the catalyst where it crystallizes and pushes the metal particle off the substrate. This process continues until the top surface of the particle is fully covered with excess carbon. This model is called "tip-growth model" and is schematically presented in ***Fig 10 (a)***. In the case of the second model, the "base growth model" (***Fig. 10 (b)***), the catalyst-substrate interaction is strong, thus the crystallizing carbon growth on top of the metal particle, first forming a hemispherical dome which is then extended with the form of a graphitic cylinder. Both, SWCNT as well as MWCNT can be produced using this method, mainly depending on the metal catalyst particle size and type. For example, for very small particles (few tens of nm in diameter), SWCNT formation is expected whereas for larger particles, MWCNT formation is favored. However, CNT synthesis depends on many more parameters such as the used hydrocarbon, catalyst, pressure, temperature, gas-flow rate, deposition time and reactor geometry. A good overview of CVD synthesis of CNT is given by Kumar et al. [106], whereas a general introduction towards other synthesis methods is provided by Mubarak et al [110].

2.1.4 Raman spectroscopy characterization of CNP

After having introduced different CNP, it becomes evident that their atomic structure and morphology is the key to their physical properties. Hence, characterizing these features is essential when processing the particles to use them for a specific application. Various techniques have been proposed to characterize CNP (e.g. X-ray photoelectron spectroscopy (XPS), transmission electron microscopy (TEM), etc.) [87]. Even though all of these methods are very useful and irreplaceable tools in their particular way, one quick but still precise method for advanced CNP characterization stands out: Raman spectroscopy [111]. However, the intention of the following section is not to introduce Raman spectroscopy as a method, but rather to give a short introduction to the state of the art in using this technique for characterization of sp^2 and sp^3 carbon structures. For a more general approach and an introduction to Raman spectroscopy, please refer to Gardiner and Graves [112].

In Raman spectroscopy, excitation of the atomic structures is typically done with a monochromatic light source (laser) of specific known energy (wavelength). This being said, the first difference between sp^2- and sp^3-hybridized carbon structures must be discussed, which is that sp^2 domains with their characteristic π-bonding are up to 230 times more sensitive to visible light excitation compared to those with sp^3 hybridization [113–115]. This has been related to differences in the Raman cross-sections based on calculations of Loudon [116]. An ultraviolet (UV)-laser with a wavelength of 244 nm produces a radiation energy of 5.08 eV, which is close to the energy band gap between electronic states of the σ bonds, for example in diamond (5.47 eV). This fact allows for near-resonance conditions, which enhance the Raman signal [114]. In contrast, green laser light (wavelength of 514.5 nm) produces a radiation energy of only 2.41 eV, being far from resonance.

Analyzing an sp^2-hybridized nano-graphite sample using a green laser and looking at its typical Raman spectrum in ***Fig. 11***, the main characteristic bands of graphitic carbon can be found. These Raman bands are the so-called D, G, D' and G' band [117].

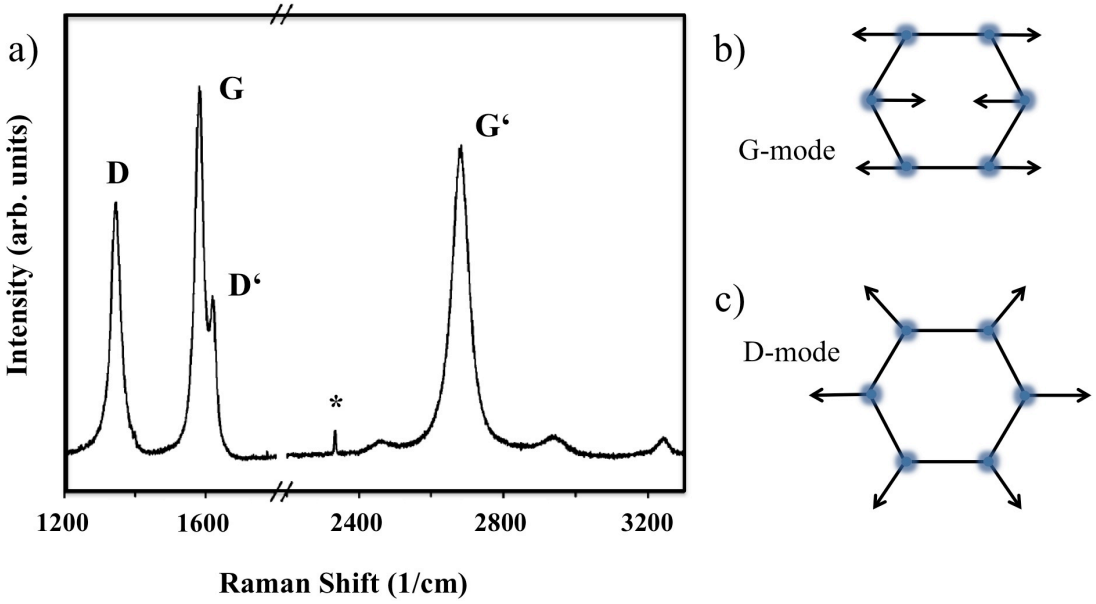

Figure 11: a) Raman spectrum of a nano-graphite sample including the main characteristic peaks for a Raman analysis of graphitic carbon (except for *, which is a Raman mode of N_2 gas and was present recording the spectrum). The excitation wavelength was 514.5 nm. Furthermore, schematics illustrating the vibrational modes of the carbon lattice corresponding to b) the G-mode and c) the D-mode are added. Modified from [115,117].

Starting off with the most pronounced peak in ***Fig. 11 (a)***, the **G-band** at around 1580 cm^{-1} is the most representative band for sp^2-hybridized carbon structures. If this peak is observed, sp^2 carbon networks are present. The G-band is generated by tangential vibrations of sp^2 carbon atom chains, not requiring the presence of six fold carbon rings (***Fig. 11 (b)***) and its width can be used to describe the degree of crystallinity of the sample [58,118]. However, nearly all graphite materials show some defects. Thus, the **D-band** (1350 cm^{-1}) as well as the **D'-band** (1620 cm^{-1}) are assigned to the presence of disorder. The intensity of the D-peak can be attributed to the number of defects or impurities whereas its width is correlated to the variety of impurities present [119]. The D-band arises by radial breathing of the hexagonal carbon lattice (***Fig. 11 (c)***), which is forbidden in a perfect single crystal graphitic lattice and only becomes active in the presence of disorder [115].

The peak with the second highest intensity in ***Fig. 11 (a)*** corresponds to the **G'-band** and is found at around 2700 cm^{-1}. It originates from a two-phonon, second order scattering process, the name being misleading as it is not related to the G band, but is a harmonic of the D-band [120]. Although related to the D-band, it is insensitive to defects of the graphitic structure and indicative for the long-range order of the structures. This is evident as with less ordering of the structure, coupling of the atoms

ceases, which would be necessary for a two-phonon process [120]. Thus, highly crystalline carbon structures with long-range order typically show a very pronounced G'-band intensity.

Other peaks (e.g. RBM, LA, LO etc.) also contribute to the Raman spectra of certain graphitic structures and allow for their distinction [119]. However, the above-mentioned are present for sp^2 carbon structures and are thus commonly used for their structural integrity assessment (quality control). For a more in-depth analysis of all the bands and modes involved in the Raman spectrum of graphitic carbon, please refer to Dresselhaus et al. [119] and Pimenta et al. [117]

Since Raman spectroscopy is a volume-sensitive technique, absolute intensities must not be used for a quantitative comparison. Instead, intensity ratios, such as the I_D/I_G, or the $I_{G'}/I_D$ ratio are widely accepted with the first one known as the defect index and the latter one as purity index. In this regard, the intensity ratios of the maximum peak intensities or the ratios of the integral peak intensity may be used. In the case of using the integral peak intensity, the full width at half maximum (FWHM) of the peaks, being related to the crystallinity of the analyzed graphitic carbon structure [85], is included in the analysis. A lower FWHM typically means that a higher crystallinity of the carbon structure is present, since the energy differences of the resonance are small [121]. However, both approaches regarding the evaluation of intensity ratios for a Raman analysis of carbon structures are accepted in literature and provide the same tendencies [50].

The defect index (whether determined by maximum intensity or integral intensity ratio) is associated with the amount and density of structural defects in the graphitic lattice. The early work of Tuinstra and König [122] in 1970 already noticed the inverse proportional correlation of the defect index and the crystal domain size L_a. However, 36 years later, it was the work of Cançado et al. [123] providing a general equation for a quantitative correlation of these parameters as a function of the used laser excitation wavelength (see equation 1). Using this equation, the coherent diffraction domain size/mean defect-to-defect distance can be calculated.

$$L_a = (2.4 \cdot 10^{-10})\lambda_{laser}^4 \cdot \left(\frac{I_D}{I_G}\right)^{-1} \quad (1)$$

Regarding the purity index, DiLeo et al. [120] were the first to come up with a quantification of the purity of MWCNT based on the $I_{G'}/I_D$ intensity ratio. They used Raman spectroscopy to measure previously prepared MWCNT containing varying, known amounts of carbonaceous by-products, successively decreasing the MWCNT purity. The correlation of the intensity ratios I_D/I_G, $I_{G'}/I_G$ and $I_{G'}/I_D$ showed, that the $I_{G'}/I_D$ ratio is in very close correlation to the purity level of the measured MWCNT and thus, a purity quantification using this ratio became possible. Other works also refer to the mentioned intensity ratios, such as the work of Ferrari and Robertson [115]. They proposed a three-stage phenomenological amorphization trajectory model, describing the degradation of highly crystalline graphitic carbon towards amorphous carbon. The model is based on an interpretation of the defect index but also on the wavenumber of the G-band position (X_{CG}), as shown in ***Fig. 12***.

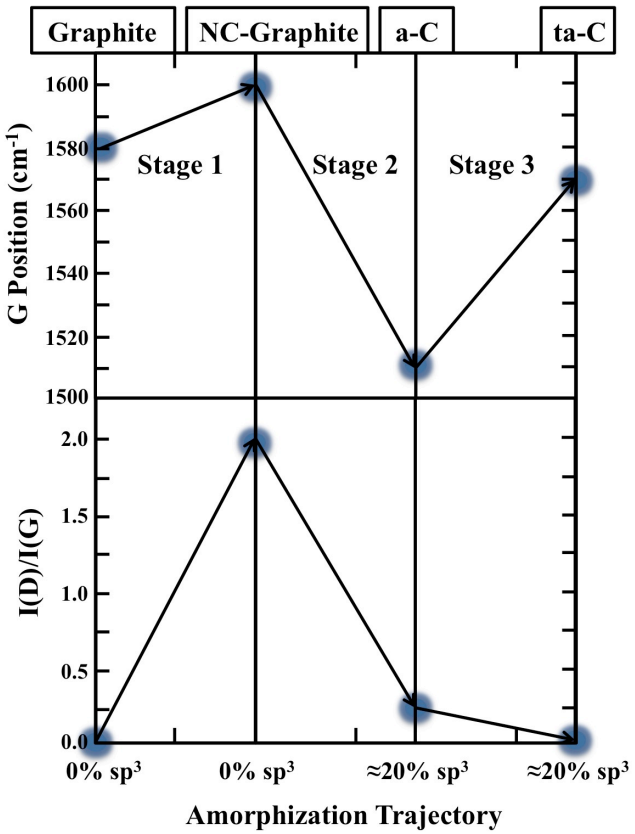

Figure 12: Phenomenological three-stage amorphization model of crystalline graphite towards tetrahedral amorphous carbon. The model also allows for a quantification of sp^3 carbon as a function of the defect index and the G-band position. First, nanocrystalline graphite is formed before the amorphization towards amorphous carbon (a-C) and finally tetragonal amorphous carbon (ta-C) proceeds. Modified from [115].

It was observed, that the G-band shift in highly crystalline graphite derives from the appearance of the disorder-induced D'-band at 1620 cm^{-1}, which convolutes with the G peak for small crystallites. Fitting of the G-peak thus results in a net increase in the G-band position. With the defect index vastly increasing at the same time, it is concluded, that a transition from monocrystalline to polycrystalline structures occurs [115].

In stage two, X_{CG} decreases from 1600 cm^{-1} to 1510 cm^{-1} with the defect index approaching a value of 0 at the same time, indicating strongly distortional carbon structures providing no long-range order. Hence this stage represents the transition from nanocrystalline graphite to amorphous, mainly sp^2 carbon structures. In stage 3, passing from a-C (amorphous carbon) to ta-C (tetragonal amorphous carbon) involves a rise in sp^3 content from 10–20 % to 85 % and a gradual change of carbon hexagonal rings to tetragonal chains [115].

With regard to CNP, for high purity, highly crystalline CNT, the above-described methods can be used for a structural characterization. Detailed analysis and explanation of all the Raman peaks in the spectrum of CNT can be found in Dresselhaus et al. [119]. In contrast to CNT, OLC are already highly

defective in their pristine state. Additionally, with the particles being only 5 – 10 nm in size, analyzing long-range order of graphitic carbon networks indeed becomes non-trivial. Nonetheless, since OLC are derived from ND, large amounts of information can be derived when analyzing the structural transformation process of ND to OLC using Raman spectroscopy [33].

The transformation process was analyzed using Raman spectroscopy by Cebik et al. [50] and is found in ***Fig. 13***.

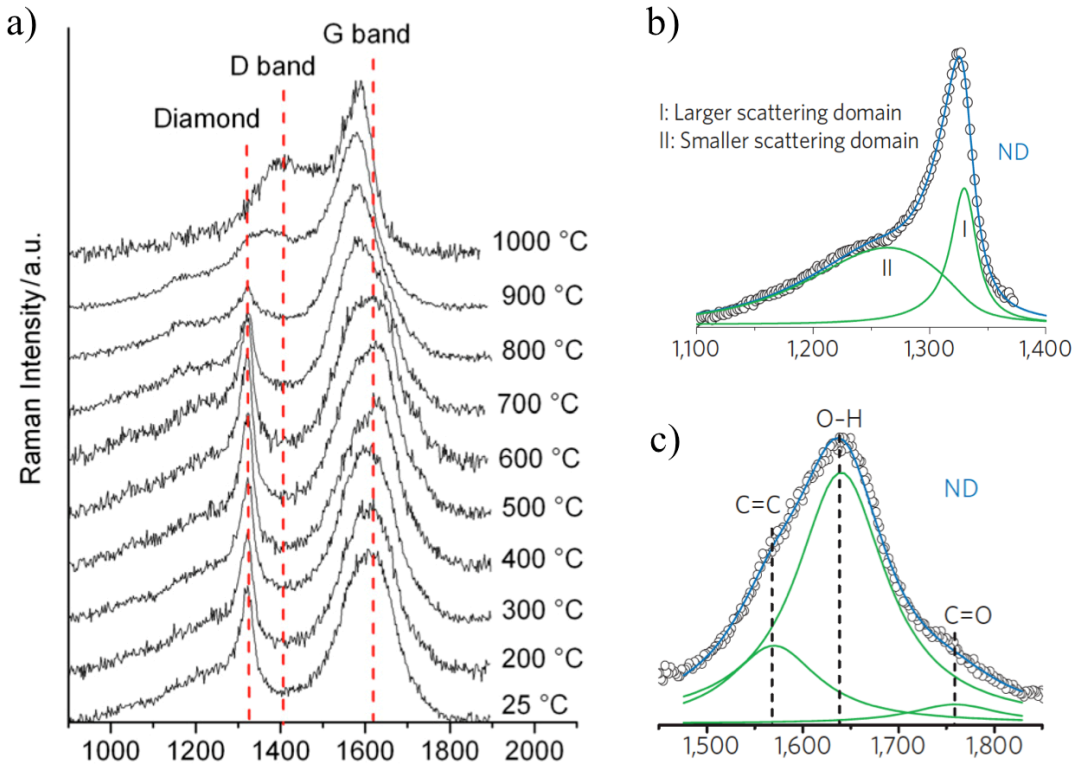

Figure 13: a) Raman spectra of the transformation process from ND to OLC as a function of the annealing temperature from room temperature to 1000°C (recorded with a UV laser excitation of 325 nm). b) Diamond-band and c) G-band deconvolution for ND particles [33,50].

The typical Raman spectrum of ND (measured using UV-excitation) as well as a deconvolution of its peaks is shown in ***Fig. 13 (b)*** and ***(c)***. The diamond peak is found at around 1330 cm^{-1} and is derived from large domain scattering. It is overlapped with a second broad peak at 1250 cm^{-1}, which is assigned to partially crystalline or even amorphous diamond, concurring with a short-range order scattering type of Raman mode [124–126]. Thus, the peaks are related to a signal combination of large and small domain scattering, respectively [33]. Due to this convolution, the absolute position of the diamond peak can be used to estimate diamond crystal sizes [50]. Furthermore, with decreasing crystallite size and increasing content of non-diamond phases, the full width at half maximum (FWHM) of the diamond peak increases [127].

Generally, Raman features above 1360 cm^{-1} cannot be due to C-C sp^3 vibrations [50]. The shifted G-band position at 1640 cm^{-1} in ***Fig. 13 (c)*** is explained by the combination of three peaks. The first one can be identified as the sp^2 carbon derived G-band at 1580 cm^{-1}. The higher wavenumber peaks

are usually observed in UV Raman spectra of amorphous carbon containing a high concentration of carbon atoms with tetrahedral bonding [114]. These two bands provide wavenumbers too high for one-phonon scattering in carbon materials, thus they are assigned to functional O-H groups and to stretching vibrations of carbonyl C=O groups, which are attached to the ND surface, derived from detonation synthesis [33,114,128]. Further smaller peaks in the Raman spectrum of ND can be observed and are discussed in more detail in Cebik et al [50].

With increasing annealing temperature up to 1000 °C, a transformation from sp^3 to sp^2 carbon hybridization is noticeable in the Raman spectra in ***Fig 13 (a)***. The number of atoms of a 0-D particle increases strongly with its diameter. Hence, the Raman signal coming from the outer shell should be the strongest and dominate the spectrum. As the transformation of ND to OLC starts at the outer shell of the particle, this results in a high sensitivity for the transformation process using Raman spectroscopy. At 600-1000 °C, the described up-shifted G-peak of ND starts to decrease to lower wavenumbers and an additional peak at around 1400 cm^{-1} is formed. This peak can be assigned to an up-shifted defect-induced D-band of OLC. Annealing ND at higher temperature involves purification of the particles, which explains the decreasing wavenumber of the G-band, since surface functional groups are detached and the typical sp^2 carbon G-band at around 1580-1600 cm^{-1} is obtained.

All the discussed information in this chapter is useful to understand the degradation mechanisms of CNP in a tribological contact and thus, Raman spectroscopy is considered a key technique of the present dissertation.

2.2 Metal matrix composites (MMC)

Composite materials are defined as a combination of at least two materials that exhibit chemical, physical or morphological differences. The combined materials must not dissolve into each other and thus form an interface. Furthermore, it is expected that their combination results in a synergetic effect, named the composite effect [129].

In MMC, the matrix is usually the phase with the largest volume content, providing ductility as well as load transfer to the reinforcement phase. The reinforcement phase usually has certain desirable physical properties (e.g. stiffness, electrical conductivity etc.), which, however, cannot be taken advantage of separately. By introducing this phase into the matrix, these properties can at least partially be transferred to the composite and thus be integrated into a technically usable system [129].

The material class of MMC can be sub-classified, considering the type and contribution of reinforcement components, into particle-, fiber- and layer composite materials (***Fig. 14***). With regard to fiber composite materials a distinction between continuous fiber composite materials (multi- and monofilament) and short fibers or whisker composite materials is made [23].

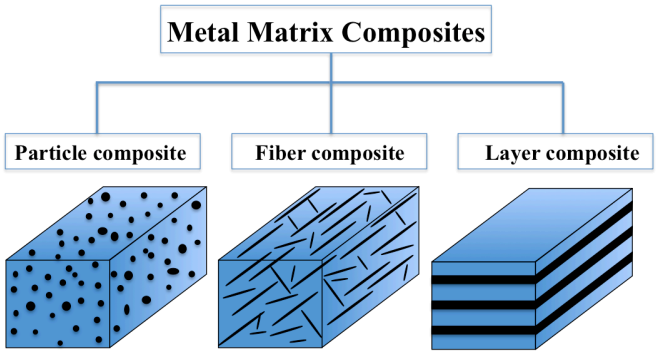

Figure 14: Basic classification of MMC

The properties of MMC can be designed so as to fit the requirements of the intended application (e.g. light weight but high strength). They are often employed as structural and functional materials such as fiber reinforced pistons, aluminum crankcases with strengthened cylinder surfaces or particle strengthened brake discs, in the automotive or aerospace sectors. MMC are also broadly found in other application fields such as magnetic materials, electronics or wear-resistant sliding contact materials [23–25].

The latter was chosen in the present thesis, as it offers the possibility to transfer promising physical properties of the reinforcement phase to a machineable, macroscopic material [130]. Since CNP provide promising properties to act as solid lubricant, their use as reinforcement phase in MMC in order to produce a self-lubricating system is a logical consequence. Self-lubricating composites in general have been around for many years and find applications for example in bearings and piston or cylinder liners in engines. These composites are developing into an important class of tribological

materials and offer new ways to combat friction and wear under extreme conditions [21]. However, despite the selection of a matrix and reinforcing material, processing parameters must also be chosen carefully so as to achieve the desired composite properties. This is due to the fact that the properties strongly depend on the microstructure and density of the composite as well as the formation of interphases, partially tunable by simple variables. The typical methods involved in MMC production will therefore be discussed in the following section.

2.2.1 Blending, processing and microstructural tailoring

There is an overwhelming wealth of literature and publications on the processing of MMC with different reinforcement phases and matrix materials. So, to keep the focus on the present dissertation, only the blending and processing of CNP-reinforced MMC are considered in this chapter. In this regard, only solid-state processing (powder metallurgy) has to be covered, since liquid-state processing is typically not used to produce CNP-reinforced MMC.

CNP are typically present in agglomerated form when purchased or produced, resulting from molecular, electrostatic interdependencies such as Van-der-Waals or dipole-dipole interactions. Hence, the CNP must be dispersed before being blended with the metal powder, which can be done in different ways. Those methods include dipping, nanoscale dispersion processing, magnetic stirring, layer stacking, colloidal mixing, molecular-level mixing, friction stir processing, ball milling, roller mixing and others [121,131–140]. Out of those, the three most common can be described in more detail: molecular level mixing, ball milling and colloidal mixing.

Molecular level mixing

This method involves functionalizing the CNP with surface functional groups (e.g. –OH, -COOH etc.) in order to be able to decorate them with metal ions. This is typically done by acid treatment of the particles [141]. Subsequently, CNP are dispersed in a solvent and a metal salt as well as reducing agent is added so as to form metal oxides on the CNP surface, with the functional surface groups acting as nucleation centers (***Fig 15 (a)*** and ***(b)***). After this, the powder is calcinated and reduced (e.g. in a hydrogen atmosphere), leading to a full encapsulation of the CNP by the reduced metal (***Fig 15 (c)*** and ***(d)***).

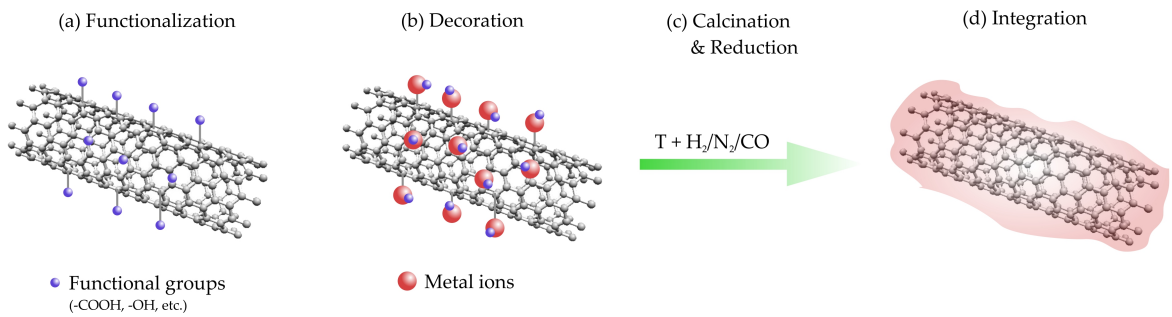

Figure 15: Schematic of the molecular-level mixing method in the case of CNT. a) Functionalization and b) metal oxide decoration followed by c) calcination and reduction leading to metal encapsulated CNT in d) [103].

Due to the full encapsulation of the particles, a very homogeneous interface is formed and CNP reagglomeration is prevented, resulting in a very good mixing of the metallic phase and the CNP. This method is often used in applications where a good interfacial bonding is critical. However, since the method involves particle functionalization, covalent bonds of the CNP are broken, significantly diminishing their outstanding physical properties[37,103,142–146].

Ball milling

In this method, CNP, the metal powder and hard balls (e.g. hardened steel) are filled in a planetary or attrition ball mill, rotating with a defined speed (***Fig. 16 (a)***).

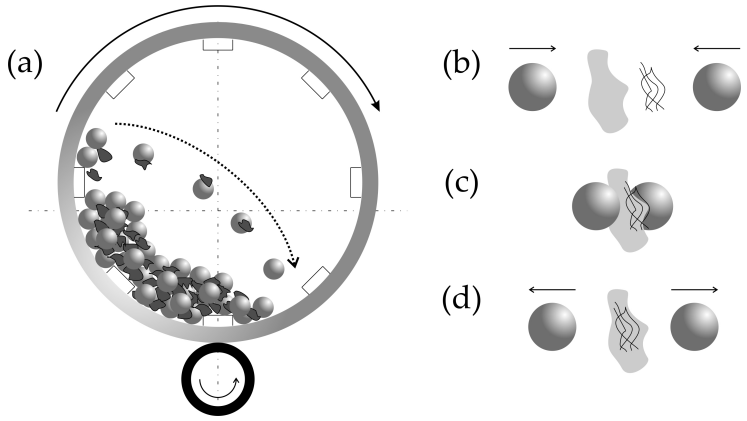

Figure 16: a) Schematic of ball milling. Integration process of CNP into the metal particles is shown in b), c) and d) [103].

By rotating the mill, the inserted hard balls collide with the powder, leading to comminution, welding and integration of CNP into the metal particles, as schematically presented in ***Fig. 16 (b) – (d)***. The processing parameters of this method range from the rotational speed, over different balls and powder ratios, ball diameters, atmosphere, and reducing agents, to the mixing time, and determine if the process is considered as high- or low energy ball milling. This difference is made due to the main drawback of this method, which is the degradation of the CNP. Since high pressures (up to 30 GPa [147]) are attained when two balls collide, the CNP can be degraded thus losing their

intrinsic properties to some extent. Nonetheless, this method is widely used and provides a homogeneous distribution of CNP in a metal matrix [103,148–153].

Colloidal mixing

Disaggregated CNP can be mixed with the metal particles in a solvent, usually with ultrasonic agitation or shear mixing as illustrated in ***Fig. 17 (a)*** and ***(b)***. The used solvent (e.g. ethylene glycol or Dimethylformamid (DMF)) as well as the CNP surface plays a critical role in the dispersion and stability of the mixture. The surface of CNP is sometimes functionalized in order to stabilize the obtained dispersions, which, however, leads to a deterioration of their intrinsic, physical particle properties. Further information about different solvents, their advantages and limitations regarding this process can be found in Cheng et al. [154].

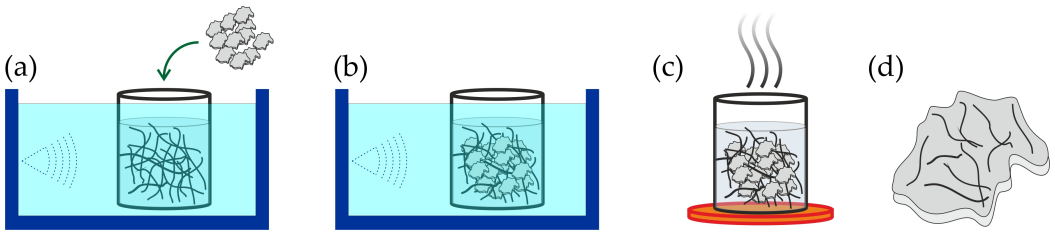

Figure 17: Schema of colloidal mixing. Ultrasonication is used to disaggregate the CNP and metal particles are added (a), followed by a merging of the two phases in the solvent (b). The solvent is evaporated (c) yielding a mixture of CNP and metal powder (d) [103].

Concerning ultrasonication or shear mixing, various works in literature disagree on its positive or negative influence on the structural integrity of the particles. For example, Hilding et al. [155] report about the breaking and shortening of CNT as a function of time in an ultrasonic bath. Hence, using this method, a careful evaluation of the time and power of the particle dispersion method has to be done in order to avoid damaging the CNP. After disaggregating and mixing the particles, the solvent is usually evaporated and a mixed powder of CNP and metal particles is left [103,156–163].

In contrast to molecular level mixing, colloidal mixing can be done avoiding a functionalization of the particles. Additionally, a lower degradation compared to ball milling is expected thus possibly preserving the physical properties of the particles. For this reason, this colloidal mixing was selected in the present dissertation for mixing CNP and metal particles and a systematic investigation of the dispersion process is provided.

The merged powder, obtained using the methods described above, is then further processed into dense, solid composite materials. This bottom-up process is known as sintering and involves the application of heat and often pressure, for a certain time under a vacuum or inert gas atmosphere. However, a large variety of methods exist and sintering is done by one or a combination of methods,

such as spark plasma sintering (SPS), friction stir processing, hot extrusion, hot uniaxial pressing (HUP), cold pressed sintering (CPS), high pressure torsion (HPT), hot isostatic pressing (HIP) microwave sintering, mechanical alloying or laser engineered net shaping [103]. Before further discussing these methods, a short introduction to the basic sintering mechanisms is given in the following.

The driving force of sintering is the reduction of the total interfacial energy, which is a function of the specific interfacial energy and the total interfacial area, both changing during the sintering process due to the replacement of solid/vapor interfaces with solid/solid interfaces. The sintering process can be divided into three stages, shown in ***Fig. 18***. In general, the sintering rate (densification rate) increases with decreasing particle size and with increasing sintering temperature, pressure and time, among other factors. All of these however, share some general sintering stages.

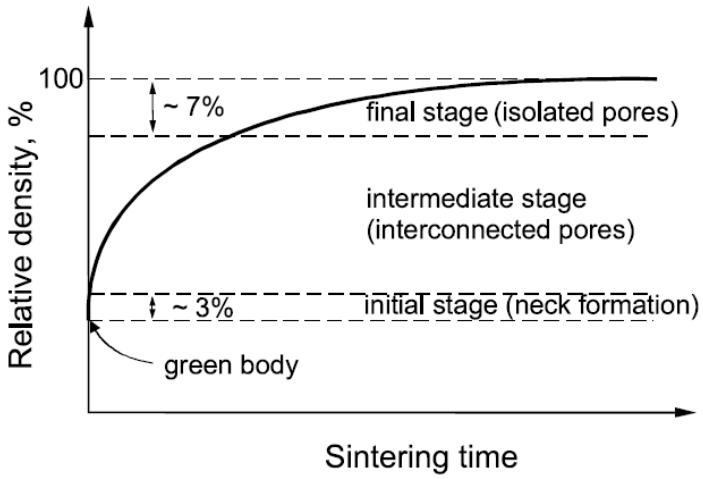

Figure 18: Densification curve of a powder compact, showing the three sintering stages [164].

The first preparation step of the sintering process is often a pre-compaction of the powder at room temperature. During this process, a so-called green body is obtained, providing a geometrical shape close to that of the final composite. As soon as the green body is exposed to a certain threshold temperature (which depends on the melting point of the used metal matrix), the first stage of sintering is reached with the typical "neck formation" observed. This process involves the connection (neck) of the metal particles and is dominated by a lattice diffusion of atoms to the grain boundaries and from the grain boundaries to the neck, thus forming a diffusion path for the material to connect. During this stage, only a 3% increase in relative density of the composite is noted [164].

With the necks being formed, interconnected pores are built, initializing the intermediate sintering stage. During this stage, grain growth is induced and the channel sizes, connecting the individual pores, are reduced, leading to a significant compaction of the composite up to a relative density of 93%.

The final 7 % of densification must be achieved in the final sintering stage. However, it is very hard and time consuming to achieve almost full densification. During this stage, the interconnecting pore channels are closed, resulting in isolation of the pores and the appearance of pressure when pore size shrinking occurs as a consequence of adsorbed gas evaporation at the solid/air interfaces. Thus, the final densification of powder compacts is strongly affected by the sintering atmosphere, since gas is entrapped within the pores. Applying external pressure during this stage significantly helps in achieving higher relative densities of the final sintered composite due to an enhanced creep activity and plastic deformation. Hence, a general distinction is made between pressureless and pressure-assisted sintering techniques. For further information on occurring mechanisms and sintering models, please refer to the book of Kang [164]. Among others, three of the most used techniques, CPS, SPS and HUP, will be discussed in more detail in the following.

Cold Pressed Sintering (CPS)

The CPS process can be easily up scaled, allowing for the production of large quantities of materials. After the powder is filled in a die, the powder is pre-compacted using a cold uniaxial press, producing the green pellet. This pellet is subsequently sintered in a furnace under vacuum or inert atmosphere (***Fig. 19***).

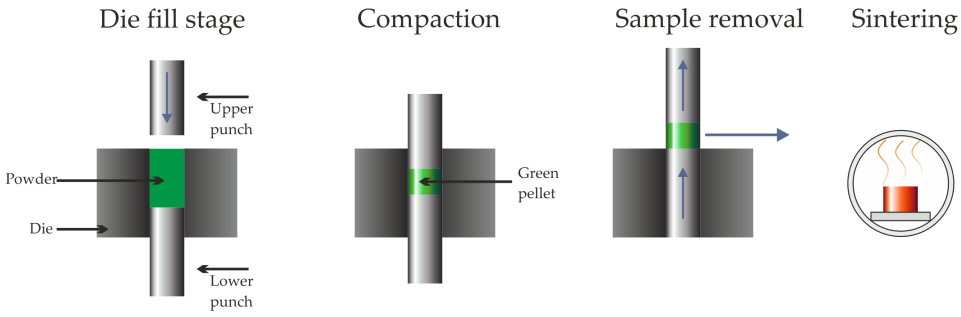

Figure 19: Schematic of CPS, visualizing cold pressing of the green pellet and subsequent pressureless sintering in a furnace [103].

The main drawback of this method is the obtained low densification (usually not more than 93% relative densification). The mechanism is based mainly on lattice and grain boundary diffusion, which does not allow for full densification without the presence of additional pressure or very long sintering times. If pressure is applied, plastic deformation and creeping are added as additional sintering mechanisms thus increasing the driving forces and kinetics of the sintering mechanism. Hence, the sintering temperature and time can be reduced to a significant degree [164].

Spark Plasma Sintering (SPS)

One of the methods involving the use of pressure is SPS. The mixed powder is pre-compressed to a green pellet using graphite punches, whereupon a pulsed DC voltage is applied inducing a high electric current flow, heating and thus sintering the green pellet by Joule heating. During this process, a constant pressure is held. A schematic of this process can be found in ***Fig. 20.***

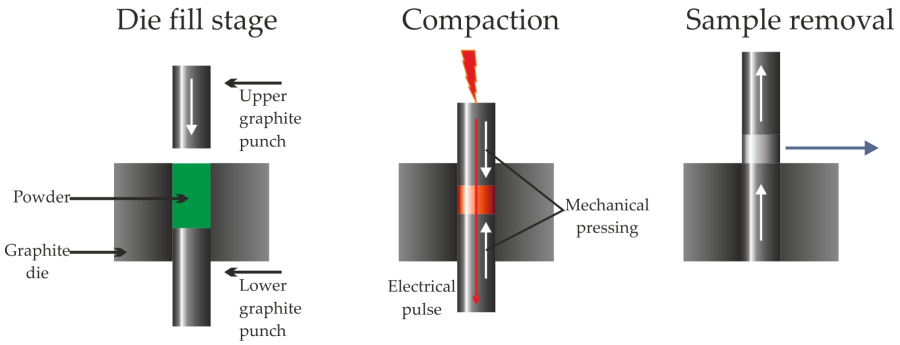

Figure 20: Schematic of SPS, showing pre-compaction of the powder by cold pressing using graphite punches, followed by applying a high current (pulsed electric DC) but keeping the applied pressure. Thus, sintering is performed by electrical resistance heating [103].

The method allows for very fast heating rates (several hundred °C/min) and thus a high sample throughput. However, the maximum pressure that can be generated is limited by the mechanical properties of the graphite punches, typically not withstanding a normal pressure of much more than 80 MPa. Considering the resistance heating used in this technique, large differences in the electric conductivity of reinforcement phase and metal matrix can be a problem and possibly lead to the formation of large pores and no full densification [103]. Despite this, high quality composite materials with very high densification can be produced very quickly.

Hot Uniaxial Pressing (HUP)

In the case of the HUP method, a pre-compacted green pellet is inserted in a steel die and alumina punches are used to apply a uniaxial pressure. This technique allows for a pressure of several hundreds of MPa during the sintering process. Heating is achieved by induction, which limits the possible heating rate and renders HUP a very time-consuming sintering process. The basic principle is illustrated in ***Fig. 21***.

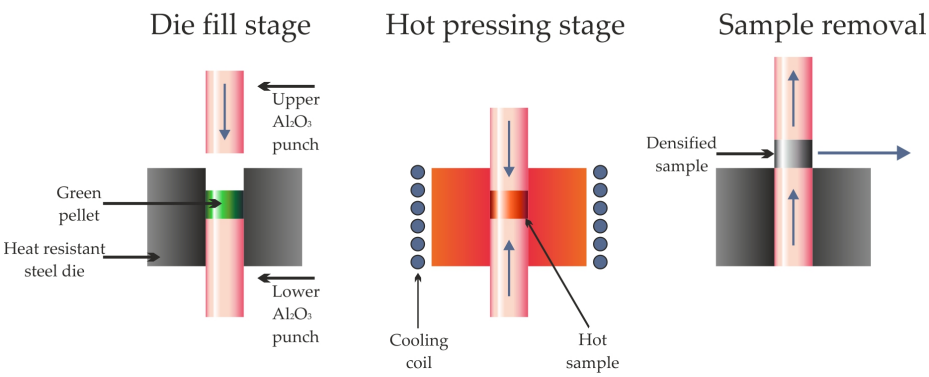

Figure 21: Schematic process of HUP, demonstrating the pre-compaction process by cold pressing using alumina punches which is then followed by inductive heating while keeping a constant pressure to sinter the sample [103].

Although a slow technique, very high quality composites with almost full densification can be produced [103].

Compared to SPS, HUP is not very sensitive to differences in physical properties (such as electrical conductivity) of the reinforcing phase and matrix material. Nonetheless and in contrast to CPS, it allows for the production of high quality, low porosity composites. Hence, for the present dissertation, this technique is chosen for the production of CNP-reinforced MMC.

Solid state sintering allows for microstructural tailoring of the final composite, affecting final grain size, density, distribution and interface of the reinforcement phase. In addition to the possibility to control the microstructure of the composite by the aforementioned sintering parameters [165], it has been demonstrated that the addition of CNP acts on the grain boundary mobility by hindering their displacement during grain growth [41,166–169]. This effect refines the final grain size of the obtained composite and thus influences the mechanical behavior by grain boundary strengthening according to the well-known Hall-Petch effect [170]. The mechanism of a hindered grain growth can be explained by the Zener-pinning effect, based on the equilibrium of the pinning pressure of the CNP on the grain boundaries (exerted by the drag force of all the CNP on the grain boundaries) and the driving pressure for grain growth [171]. The extent of the grain refinement effect largely depends on the reinforcement phase distribution and interface [172]. The factors affecting the distribution of the CNP in the metal matrix are still not fully understood and are therefore subject of research of the present dissertation.

2.2.1 CNP reinforced MMC

Typically, MMC reinforced by large particles are prone to defect formation such as cracks during mechanical testing which can result in the ultimate failure of the composites. Reducing the reinforcement particle size in MMC to the nano-size range could possibly resolve some of the limitations such as poor ductility and elongation, poor machinability, and reduced fracture toughness of MMC [16]. In this chapter, a short overview is given regarding the reinforcing mechanisms involved specifically in CNT-, OLC- and ND-reinforced MMC as well as the challenges associated to their processing. Since the research progress in CNP-reinforced MMC differs significantly depending on the CNP used, a discussion for each of the three CNP is provided in the following.

CNT reinforced MMC

CNT-reinforced MMC have so far shown great potential in load bearing applications, which is mainly due to the interesting mechanical properties of CNT. In this field, CNT-reinforced Al, Mg or Ti matrix composites are used to obtain lightweight materials with high specific strength [173–177]. CNT reinforcement provides the ability to induce a grain refinement effect based on Zener-pinning. In addition, a proper distribution of CNT acts as an obstacle for dislocation movement, activating another strengthening mechanism known as particle dispersion strengthening or Orowan-strengthening [169,173,178]. The CNT might hinder dislocation movement during plastic deformation thus strengthening the composite. Furthermore, CNT possess a very low or even negative coefficient of thermal expansion in a wide temperature range [179,180]. Thus, the combination with a metal (high coefficient of thermal expansion) can result in a strengthening due to thermal expansion mismatch. For one part, the strengthening depends on the volume content of the CNT in the metal matrix [177]. For the other part, however, it has been reported that the strengthening effect strongly depends on a homogeneous, fine dispersion of the particles, which is often difficult to achieve [131,173].

This being said, enormous efforts have been put into the development of a method to produce a fine dispersion of CNT within a metal matrix, all involving either particle functionalization (covalent or non-covalent) or high energy merging techniques (e.g. ball milling) [141,181–184]. As already discussed, these techniques result in the breaking of covalent bonds or include a molecular wrapping of the particles, which would induce chemical modification of the composite. In any case, it influences the interfacial bond between the CNT and the metal matrix by allowing the carbon to diffuse to the metal, especially at degraded sites, thereby allowing for the formation of metal carbides, or by preventing a seamless interface between the CNT and the metal matrix in the case of molecular wrapping.

With regard to the interface between CNT and a metal matrix as well as their cohesiveness, it is evident that it plays a decisive role with regard to the load transfer from metal to CNT, also known as the shear lag model [140,178,185]. In this model, the stress is transferred from the matrix to the CNT

through the interface and is related to the shear stress τ between CNT and the matrix material, as can be seen in ***Fig. 22***.

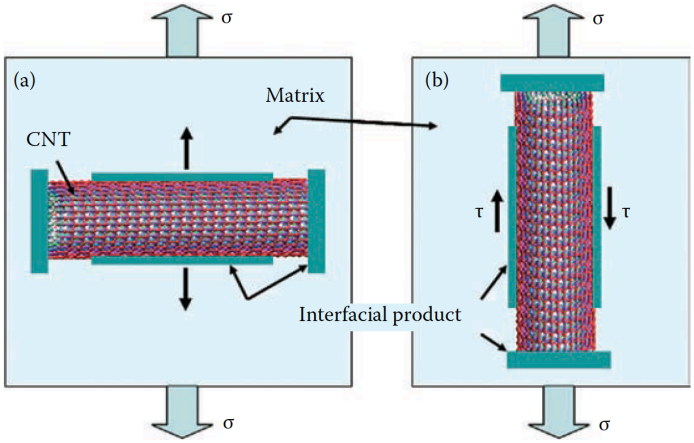

Figure 22: Schematic illustration of the influence of CNT orientation relative to the external applied load σ on the load transfer of metal to CNT [140].

However, the formation of a carbide interphase between metal matrix and CNT also depends on the used matrix and is a matter of debate in the literature. There are contradictory statements as to whether an interphase is formed at all when CNT are embedded in a metallic matrix or in which matrix systems this occurs (especially in the case of Al with its tendency to form the Al_4C_3 phase) [173,185,186]. Further, it is rather unclear, if the formation of an interphase would help in load transfer or not, since a carbide phase is usually brittle. Also, interphase formation involves degradation of the CNT and thus, diminishes their intrinsic mechanical properties [140,187,188]. Additionally, it has been discussed, that the orientation of the CNT and the respective interphase relative to the applied external stress is crucial, as it is also schematically demonstrated in ***Fig. 22.***

Due to the variability of processing methods and parameters used and the lack of characterization methods that are able to identify an interphase formation of probably 1-2 nm in size, this discussion is indeed non-trivial.

Despite mechanical reinforcement, electrical or thermal transport properties have also been in the scope of research, predominantly in the case of CNT-reinforced Cu matrix composites. Regarding the excellent thermal and electrical conductivity of CNT, this is evident with CNT expected to present a ballistic-type of electrical conduction [175,189]. It has been reported that obtaining individual CNT after dispersion in the metal matrix as well as avoiding CNT functionalization is critical for an improvement in this sector [159,190–192]. This explains why improvements were only obtained for low concentrations of CNT, which is due to their tendency to agglomerate at higher concentrations [159,192].

Although impressive effects of metal matrix reinforcement by CNT have been demonstrated in the past, chemical modification of the particles, interphase formation with the metal matrix (e.g. a

carbide formation) or degradation of the particles in various studies have made it hard to systematically investigate or compare the reported effects. Thus, in order to understand the impact of CNT as a reinforcement phase for different applications, these particle modifications should be avoided. In this regard, nickel has appeared to be a suitable candidate for a fundamental investigation of these effects since the only carbides formed by Ni are of metastable nature within a wide temperature range, as can be seen in ***Fig. 23.***

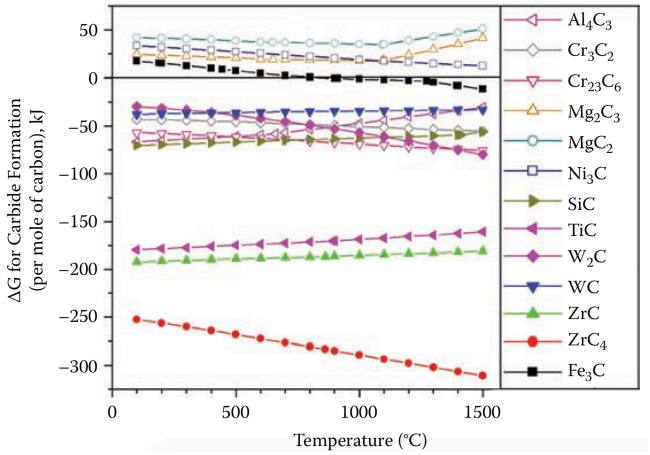

Figure 23: Gibbs free energy of formation of several carbides in different metal systems as a function of temperature [140].

Ni_3C is, among all possible carbides, the one with the lowest formation energy (26.36 kJ/mol) and was reported not to form an interphase when CNT are used as reinforcement phase [193,194].

For this reason, nickel is chosen as metal matrix material to be reinforced with CNP in the present dissertation. This is done in order to prevent influences of a carbide phase formation on the studied tribological effects of CNP as reinforcement phase in MMC.

Good overview on the topic of CNT-reinforced MMC are also provided by Bakshi et al. [32] or Tjong [195]. The state of the art related to CNT reinforcement of MMC for tribological applications will be discussed in detail in section 2.4.2 of the present dissertation.

ND reinforced MMC

In the case of ND, research is mainly focusing on ND-reinforced Al, Ni or Cu as metal matrix. Popov et al. [196,197] discussed the effect of nanodiamond addition to aluminum composites on the stabilization of the microstructure for different annealing temperatures. He observed, that the recrystallization process is delayed compared to the unreinforced Al and higher temperatures are needed in order to induce grain growth. Furthermore, they have shown that also for ND-reinforced Al composites, the formation of a carbide interphase (ND particle-size-dependent) might be critical for the reinforcement effect. In this regard, it has been shown recently, that a carbide formation can be observed already at 400-450°C for very small ND, whereas up to 800°C is needed in the case of larger ND particles [198].

Further works used ND as reinforcement phase for Al in conjunction with CNT [199]. Highly increased hardness and strength of the composite were measured, explained similarly to the CNT-reinforced composites by the Hall-Petch effect, Orowan strengthening, thermal mismatch and shear lag [199,200]. The higher intrinsic hardness of the particles surely assists in the hardening process of the composite with very homogeneous dispersions of ND being obtained in these studies. Further research regarding structural materials has been done by Livramento et al. [167] or Nunes et al. [201,202], processing ND-reinforced nano-Cu or -Ni by mechanical alloying, SPS and hot extrusion, in order to improve hardness. This was argued to be a consequence of hindered dislocation mobility and the resulting difficulty in plastic deformation of the material. However, the work also highlights ND-reinforced Cu matrix composites as a valid material for thermal management applications for example in electronics, since ND provide a very high thermal conductivity. In contrast, Yu et al. [203] have investigated ND-reinforced Zinc composites for biodegradable implants, which exhibit lower hardness and strength compared to the unreinforced Zinc while corrosion resistance is improved.

However, much of the research in the field of ND-reinforced MMC is done with spray or electrochemical coatings in order to improve the mechanical or tribological behavior of surfaces [41,42,204–206]. In this regard, tribological properties of ND as reinforcement material will be discussed further in chapter 2.4.2 of the present dissertation.

OLC-reinforced MMC

So far, there is no literature on OLC-reinforced MMC. However, some of the reinforcement mechanisms of CNT and ND such as grain refinement due to the Zener-pinning effect, Orowan strengthening or shear lag are expected to also occur with OLC. Their properties as a reinforcement phase in MMC for tribological applications are yet unexplored.

2.3 Strategies to control friction and wear of surfaces

In general, friction and wear can be altered through lubrication, surface design and the base materials [21,207]. Of course, despite these three points, the stress collective, which includes the applied normal stresses, the velocity, the runtime, the kinematics and environmental conditions, has to be considered [207]. Although these parameters can sometimes be selected individually in order to optimize a tribological system, they are often predefined due to the intended field of application (e.g. spacecraft, high-temperature applications etc.). Thus, lubrication, surface design and base material have to be chosen carefully in order to fit the given requirements. This is briefly discussed in the following [207].

Lubrication

When it comes to lubrication, a general distinction between liquid and solid lubrication is made. In most applications nowadays, liquid lubricants such as oils or greases are used. For liquid lubrication, different operating regimes have to be distinguished depending on the viscosity, the velocity and the contact pressure, which is described by the Stribeck curve (***Fig 24***).

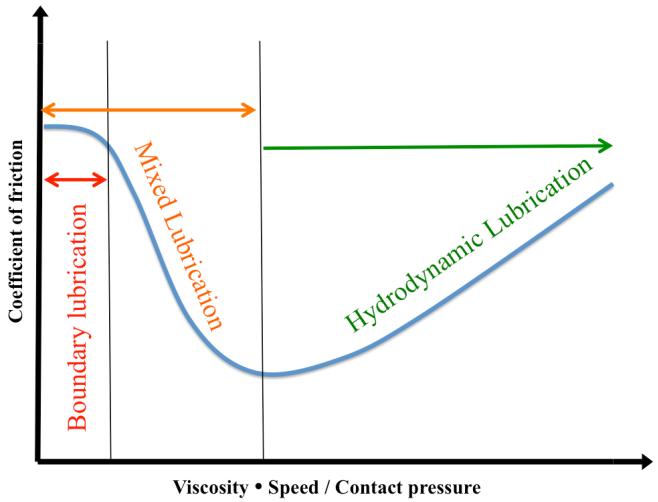

Figure 24: Schematic illustration of the Stribeck curve for liquid lubrication, showing the three main lubrication regimes: boundary, mixed and hydrodynamic lubrication.

This curve determines the lubrication regime, subdivided into boundary, mixed and hydrodynamic lubrication. For example under hydrodynamic lubrication, the physical properties of the liquid lubricant, such as viscosity and traction, determine the performance of the system. What is special about this regime compared to the others, however, is that it completely separates the two surfaces in relative movement and thus reduces wear to a minimum, allowing for very long service lifetimes of the lubricated components. Liquid lubrication further provides many more advantageous properties, such as the ability to dampen or cool the tribological system. Nevertheless and despite all the advantages over solid lubricants, liquid lubricants also have their limits, which justify the use of solid

lubricants for certain applications [21,208]. In the present dissertation, only solid lubrication and thus "dry friction" is considered, which is why liquid lubricants are not discussed further.

Solid lubricants are mainly used to control friction and wear under harsh operating conditions (e.g. high vacuum, high speeds, high loads and very low or high temperatures) where conventional materials and liquid lubricants cannot provide the desired performance or durability [21,185,208]. Solid lubricants work similar to their liquid counterparts, in particular, they typically shear or slide easily to ensure low friction and wear between the surfaces in relative motion. With the focus of the present dissertation being put on this type of lubrication, a short overview on solid lubricants will be provided in section 2.3.1.

Surface design

Regarding the impact of the surface design on dry friction, surface topography and also surface chemistry have to be considered, both significantly influencing friction and wear of a surface. In the case of surface chemistry, surface contaminants, adsorption layers, oxide layers or formed tribolayers can change the behavior of a tribological system [207]. For example, the adhesion of two contacting surfaces plays a crucial role when it comes to friction, but also wear mechanisms. Adhesion is usually high for two contacting surfaces providing a similar chemical composition (e.g. steel on steel). This could result in micro-welding of the surface, producing severe adhesive wear and high friction, since microwelds have to be broken in order to allow the two surfaces to perform a relative motion. For this particular example, if surface contaminations, adhesion layers or oxide layers prevent the direct metallic contact, adhesion is highly reduced and so are friction and wear [21,207]. Therefore, when tuning surface topography and trying to understand its influence on a tribological system, it is always highly recommended to characterize and identify changes in surface chemistry as well, since they are often interrelated. For example a change in the surface topography of a steel surface by laser irradiation could lead to a thermally induced oxide formation [209]. Hence, and although focusing on a systematical topographical surface modification, the present dissertation also investigates possible changes in surface chemistry and their influence on the measured tribological effects. For more information on the influence of surface chemistry on tribology of surfaces, please refer to Gellman et al. [210] or Bhushan [21].

When considering the surface topographies of two contacting surfaces, an important distinction between apparent contact area and real contact area must be made. The apparent contact area can easily be calculated by the macroscopic, geometrical shape of the two contacting bodies, and, according to the law of Amonton [211], friction is independent of this apparent contact area. In contrast, the real contact area, being the sum of individual surface asperity contacts and much smaller than the apparent contact area, is directly proportional to friction [207]. A schematic is given in ***Fig. 25*** in order to visualize the difference between those two perspectives.

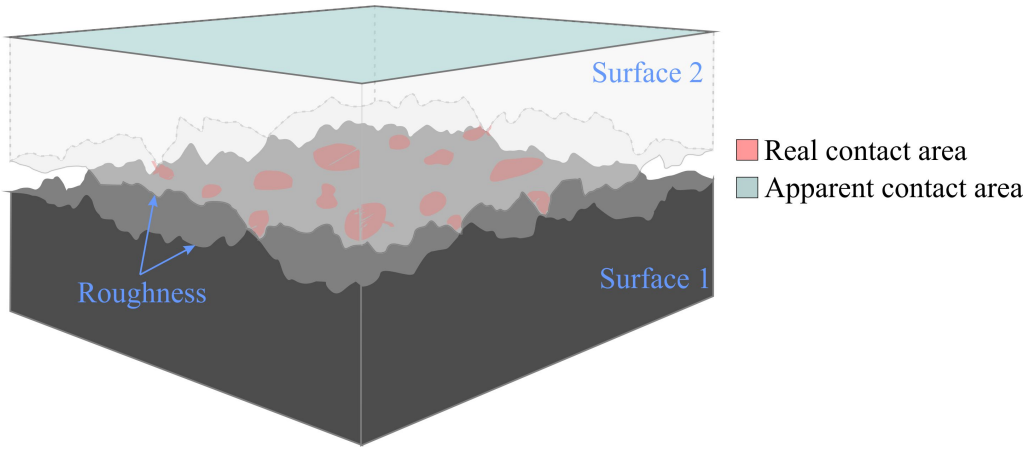

Figure 25: Schematic illustration of the contact between two rough surfaces, visualizing the apparent and real contact areas. The apparent contact area is determined by the geometry of the contacting bodies, whereas the real area is the sum of the individual surface roughness asperity contacts.

Characterization of the surface roughness/morphology provides important information to understand its tribological performance. Nowadays, an abundance of parameters is available, describing certain surface features, which are used to compare the surface topographies of different tribological systems [207]. A well-known and widely accepted surface description is done using the Abbott-Firestone curve [212]. The geometry of the curve defines different parameters, such as the core roughness R_k, which is often used to estimate the load bearing capacity of a surface.

However, surface roughness parameters can also be used to estimate the real contact area of a tribological system. This research area has always been and still is a very busy topic, involving numerous approaches and models in the field of contact mechanics. One of the earliest contact models, assuming perfectly flat surfaces (without roughness), which was used as a starting point in many other models, is the Hertzian contact model [213]. Since then, numerous other models appeared, trying to consider fully elastic or elasto-plastic contact conditions, with surfaces possessing stochastic roughness or intentionally altered surface topographies with or without a given anisotropy. A few examples are the Greenwood Williamson model [214], the Kogut-Etsion model [215], the Chang-Etsion-Bogy model [216], the Jackson-Green model [217] or the Persson model [218]. These models are always a function of the given surface topography and the mechanical properties of the base material. Hence, numerous experimental works have addressed this fact, trying to tune the surface topography and thus the real contact area by using a variety of different methods, including honing[219], micro-coining[220], lithography[221], laser surface texturing[222] or others. The focus of the present dissertation being also set on surface topography tailoring in conjunction with solid lubricant surface coating, this topic is covered in more detail in section 2.3.2.

Base materials

With regard to the base materials under dry friction, first and foremost, their mechanical properties have to be put in the limelight. The mechanical properties together with the surface topography and a given loading condition determine whether the contact situation is fully elastic or elasto-plastic (for example by calculating the plasticity index [223]) and also how large the real area of contact is. It also influences friction and wear mechanisms. For example, if a hard material is in contact with a softer material, abrasion and ploughing can often be detected, whereas adhesion rather occurs for materials with similar chemical composition. In this regard, it always has to be kept in mind, that wear is not directly proportional to friction. More specifically, a soft metal coating, which is in contact with a hard counterpart, can show significant wear due to easy plastic deformation and shearing of the surface, resulting in relatively low friction at the same time [20,224].

Another important feature of the base material is its microstructure. First, it influences the mechanical properties of a material to a great extent [170,225]. For example, a lower mean grain size of a base material significantly increases its hardness due to grain boundary strengthening according to the well-known Hall-Petch effect [170]. Furthermore, the connectivity of different phases inside the bulk material also plays an important role. A 3-D connection of hard, but brittle phases in a ductile matrix can reduce the strength of the material, whereas a fine non-connected distribution of the same phase in the same matrix can significantly increase its strength [226]. Additionally, the microstructure strongly affects the surface oxidation behavior during the tribological contact. In particular, smaller grain sizes mean more grain boundaries, which typically can act as diffusion paths for oxygen, thus inducing stronger surface oxidation with the oxide layer acting beneficially as a hard, protective film against wear or detrimentally by increasing the abrasive component of the system and forming oxidic wear particles [227,228]. Still, although a material with a specific microstructure is chosen for a certain tribological application, the microstructure can change during the experiment due to plastic deformation or recrystallization [229]. In addition, from a crystallographic point of view, the grain orientation and thus the texture of a material contributes significantly to its tribological behavior. Depending on the crystallography (e.g. fcc, bcc) and the grain orientation, different slip-planes are activated as a function of the external stress collective, creating anisotropy in yield and plastic deformation of the material surface and thus affecting the tribological behavior [230,231]. Whether a slip-plane is activated or not can be calculated by the critical shear stress using Schmid's law [232]. Combining this knowledge with a grain orientation map (e.g. obtained by electron backscatter diffraction) allows for the identification of easy or hard sliding directions on the surface of a material (if a texture is present).

The microstructure of a base material can be altered in many different ways (e.g. annealing, quenching, cold forming etc.). However, tailoring the microstructure of a MMC using the reinforcement phase provides one of the most interesting ways. This is because the processing

parameters are simple and the reinforcement phase may also have a stabilizing effect on the microstructure during the tribological contact due to the Zener-Pinning effect. Hence, this approach has been chosen in the present dissertation.

2.3.1 Solid lubricants

The need for solid lubricants is motivated by many particularities. The low vapor pressure of solid lubricants compared to liquid lubricants still allows for their use under vacuum conditions, with some of them providing excellent lubricating properties specifically under these conditions (such as MoS_2). Furthermore, for liquid lubricants, extreme pressures can lead to severe lubrication problems, as liquid lubricants may not support these, resulting in a boundary lubrication regime. Additionally, very low or very high temperatures may lead to solidification or decomposition of the liquid lubricants, respectively. On the other hand, strong temperature changes during service can lead to drastic variations in viscosity and thus a change in the lubrication regime. Likewise, most liquid lubricants are not well suited for applications where electrical conductivity is important, since they possess rather insulating characteristics. Regarding storage of liquid lubricants, problems often occur as they evaporate, drain, creep or migrate over time. These and further limitations could be overcome by their replacement with solid lubricants [13,14,21].

Certainly, not only liquid but also solid lubricants show significant shortcomings. Some, for example, are rather poor thermal conductors and lack of the ability to conduct heat out of the contact. In addition, supplying a contact with solid lubricants is more difficult than with liquid lubricants and most solid lubricants have very limited wear lives, which sometimes leads to failure in lubrication behavior over time. Oxidation can significantly influence the properties of some solid lubricants, which may result in structural or chemical changes or generation of unwanted by-products [21].

A general distinction between solid lubricants regarding carbon based materials (e.g. graphite, graphene Diamond-like-Carbon (DLC)), transition metal dichalcogenides (TMD) (e.g. MoS_2, WS_2), polymers (e.g. PTFE), lubricious oxides (e.g. Cs based oxides) and soft metals (e.g. Ag, Sn) can be made [13,14,20]. For most of the solid lubricants, their working principle is explained simply by the theory of Bowden and Tabor [233]. The coefficient of friction (COF) μ of a solid lubricant can be expressed as a function of the interfacial shear strength of the solid lubricant τ_0, the contact pressure P and the pressure dependence of the shear strength α (which is the lowest attainable friction coefficient for the specific tribological system) using the following equation [20,233]:

$$\mu = \frac{F}{L} = \frac{A_r \cdot \tau_S}{L} = \frac{\tau_S}{P} = \frac{\tau_0}{P} + \alpha \qquad (2)$$

In equation (2), F corresponds to the friction force, L to the normal load, A_r to the real area of contact and τ_S to the shear strength [20]. Thus, with a low interfacial shear strength of the solid lubricant in

combination with a hard substrate and thus a high pressure, efficient lubrication and thus a low COF might be achieved.

However, the individual lubrication mechanisms of the various solid lubricants slightly differ from each other and a brief explanation of the mechanisms and limitations of the most important solid lubricants is given in the following.

Graphite

Graphite has long been known for its good lubrication properties and has been used in industrial applications as solid lubricant for several decades [234]. Graphite possesses a highly crystalline structure of stacked hexagonal carbon lattices (stacked graphene sheets) with an sp^2 carbon hybridization and a strong, covalent, in-plane bonding of the carbon atoms. A schematic of the atomic structure is given in ***Fig. 26***.

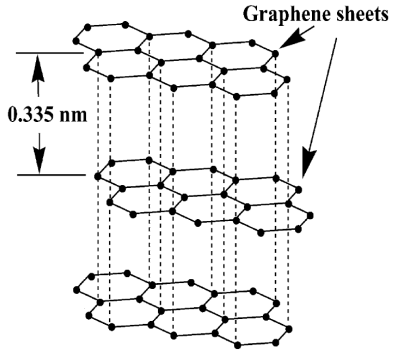

Figure 26: Schematic illustration of the atomic structure of graphite, consisting of stacked graphene sheets with an interlayer distance of 0.335 nm [235].

With the sheets only being interconnected by weak Van-der-Waals forces, they become relatively easy to shear. However, graphite lubrication is strongly dependent on the presence of water or adsorbed gas molecules, since the shearing of graphene sheets works only based on intercalation of these molecules between the individual graphene sheets, leading to an increase in the interlayer spacing between near-surface basal planes [17]. In the case of low relative humidity or vacuum, high friction and wear occurs and a process called “dusting” sets in [20].

Graphene

Recently, it has been found that besides its thermal, electrical, optical, and mechanical properties, graphene can serve as a solid lubricant [17]. Its high impermeability to liquids and gases [236], extreme strength [237], and easy shear capability on atomically smooth surfaces are the major favorable attributes for its high potential as a solid lubricant [238,239].

In particular, it was shown that in contrast to graphite, graphene provides efficient lubrication under dry or inert gas environments, as can be seen in ***Fig. 27***. Furthermore, wear reduction by four orders of magnitude was observed on steel surfaces, when coated by solution-processed graphene [239]. One accepted explanation of the lubricating effect is based on low adhesion based on the nearly perfect single, hexagonal lattice providing a low surface energy. A stacking of several layers would result in easy shearing ability of the surfaces. However, other studies contradict this explanation by introducing fluorinated graphene, providing even lower adhesion but higher friction at the same time. However, it is accepted that, graphene is able to conformally coat surfaces and is mechanically stable, preventing the direct tribological contact of the surfaces. Additionally, the protection of the surface against oxidation due to the high impermeability to liquids and gases contributes significantly to an efficient wear reduction. There is still an on-going discussion about the lubrication mechanism of graphene [17].

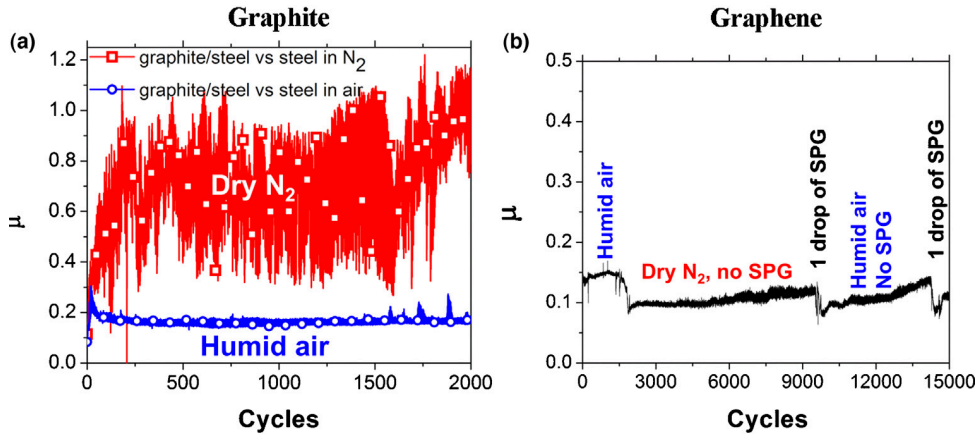

Figure 27: COF (μ) measured against the number of cycles for a graphite (a) or solution processed graphene (SPG) (b) lubricated steel surface under dry nitrogen or humid air conditions. A ball on disc tribometer was used with a steel ball of 9.5 mm in diameter and a normal load of 1 N was applied [17]. In c) a simulation with an AFM tip contacting and shearing a graphene layer is performed, resulting in an out-of-plane deformation of graphene [17].

Unfortunately, the promising lubrication properties of graphene decrease significantly when large contact pressures are applied. For the same configuration as shown in ***Fig. 27***, it has been reported that when increasing the load to 3 N (inducing 0.7 GPa of pressure for the given configuration), the lubrication vanishes after only 200 cycles [17,239]. Furthermore, differences are obtained regarding monolayer graphene coatings, few-layer graphene coatings and multi-layer graphene coatings [240]. It is often concluded that the friction force is higher for a monolayer of graphene and decreases with increasing number of layers. However, the strong interaction between graphene, the substrate material, the surface roughness, the interaction between the graphene layers, and the graphene-substrate separation distance all have to be considered for a proper analysis [240].

Thus, it is clear that further research needs to be carried out in this field in order to fully understand the mechanisms and to exploit the full potential of this material for its use in technical applications. A good overview on this topic is given by Berman et al. [17].

Diamond-like-Carbon (DLC)

DLC coatings are typically hard and wear resistant, but they can also provide low friction and chemical inertness under certain conditions. The DLC structure consists of disordered carbon, providing only a short-range order of a mixture of sp^3 and sp^2-hybridized carbon atoms. In order to induce high toughness and beneficial tribological properties, pure DLC is doped with metals or lightweight elements, like H, N, Si, Cr, W or Ti [20]. The ternary phase diagram of carbon-hydrogenated alloys is depicted in ***Fig. 28***.

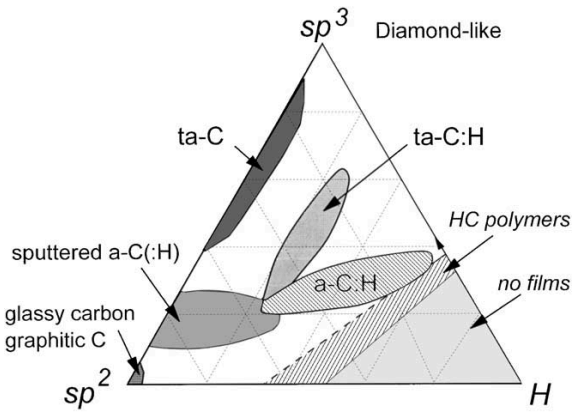

Figure 28: ternary phase diagram of bonding in amorphous carbon-hydrogen alloys [241].

Hydrogen doping is widely used and corresponds to the phase a-C:H (amorphous, hydrogenated DLC) or ta-c:H (tetragonal, amorphous, hydrogenated DLC) in the phase diagram. Depending on the deposition techniques, such as sputtering, ion or plasma beams, the different phases can be obtained, providing different mechanical and tribological properties. A detailed description of this can be found in the work of J. Robertson [241].

The friction coefficients of DLC coatings vary widely from 0.01 to 0.5 and depend upon the testing conditions (e.g. contact pressure, velocity or temperature), the environment as well as the hybridization ratio and hydrogen content [20]. This is also true for the wear rates, which can get as low as 10^{-7}-10^{-9} $mm^3/N{\cdot}m$ [242]. As an example, hydrogen-free DLC provides the lowest COF under humid conditions whereas hydrogenated coatings perform better in dry or inert gas environments. Under specific conditions, COF values as low as 0.005 (superlubricated state) can be reached in self-mated sliding contacts, which is attributed to a passivation of the contacting surfaces due to hydrogenated carbon [243].

However, synthesizing DLC possessing low friction and wear in both dry and humid environments is a challenging task. Research is currently focused on the investigation of diamond-like nanocomposite (DLN) coatings, consisting of two amorphous interpenetrating networks, a diamond-like (a-C:H) network and a quartz-like (a-Si:O) network with minimal bonding between the two networks, yielding very promising results in this regard [244]. Also ultrananocrystalline diamond structures have been found to provide promising tribological properties under varying environmental conditions [245]. However, the research topic of DLC is a broadly studied field and cannot be covered in a small summary in the present dissertation. Thus, please refer to the book of Donnet and Erdemir [242] for a general overview and introduction to the topic. Finally, and in contrast to other solid lubricants such as graphite, it has to be mentioned that DLC is always used as a coating for surfaces and not as, for example, a reinforcement phase in a MMC.

Transition Metal Dichalcogenides (TMD)

The lubricating properties of TMD, such as MoS_2 or WS_2 are derived from the inter-mechanical weakness of those structures, which is related to their crystal structure [246]. MoS_2 crystallizes in the hexagonal structure where a sheet of molybdenum atoms is sandwiched between two hexagonally packed sulfur layers. Similar to graphite, they present a strong interplanar bonding of the Sulfur atoms as well as a covalent Sulfur-Molybdenum bonding, whereas only week Van-der-Waals bonding is observed between the individual sandwich layers as well as between the stacked Sulfur layers, which allows for easy shearing (***Fig 29***).

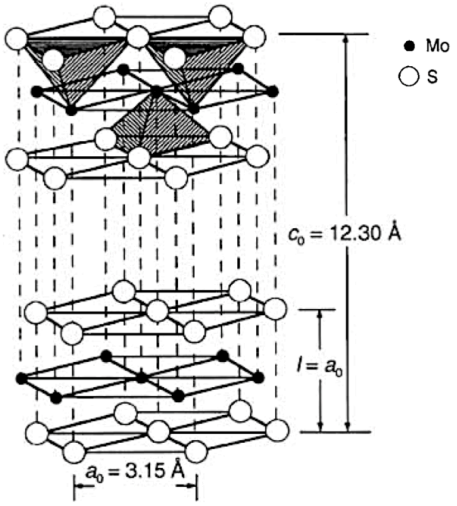

Figure 29: Atomic structure of MoS_2 with interatomic distances [246].

The lubrication mechanism of MoS_2 is based on the development of a transfer film on the counter-material to support interfacial sliding. Due to the ability of TMD to form a transfer film and to orient its crystal structure beneficially to the sliding direction ((0002) planes parallel to the sliding direction), they are not only used as sputtered surface coating, but also as inorganic fullerene (IF)

nanoparticles or as additive in oils or greases [247,248]. Both, MoS_2 and WS_2 can provide a very low COF of only 0.05 or lower and also very low wear rates, typically being the lowest for steady state conditions of the system. However, this is only true for either dry inert gas atmospheres or in ultrahigh vacuum. When TMDs are used under humid conditions, the formation of MoO_3 and WO_3 at the edges of the basal planes has been observed, hindering the planes from easy gliding [249–251]. This problem also occurs for higher temperatures (300 °C and above) [249–251]. One approach to overcome these limitations is the doping of TMD with various metal or oxide dopants (e.g. Ti, Al, Ni, Au, Pb, PbO, and Sb_2O_3) [20,252]. The presence of these dopants or alloying of TMD with amorphous carbon can lead to a higher oxidation resistance in humid environments compared to pure TMD [253]. Due to their high lubrication capabilities under vacuum conditions, TMDs are often used for spacecraft applications. A short and comprehensive introduction to the field of tribological properties of TMD is provided by Polcar and Cavaleiro [253].

Polymers

In the case of polymers, their low intermolecular cohesion is responsible for their rather low friction properties. For example, this could be due to easy extraction of molecular chains out of the crystalline fraction (e.g. for PTFE, PE or Polyimide) [208,254]. Thus, polymers can be used as solid lubricant coatings, for example, on metallic materials. In addition, they offer a low coefficient of friction both in vacuum and under atmospheric conditions, as the lubrication mechanism does not depend on adsorbed molecules and chemical reactivity is low. Generally, polymers are not suited for high temperature applications due to melting or degradation. Furthermore, the low thermal conductivity inhibits heat dissipation, which can also cause premature failure due to melting under room temperature. Therefore, polymers are typically used for low sliding speed applications. Finally, the low intermolecular cohesion causes a further severe limitation, as it results in unacceptable amounts of wear [254]. This limitation can be partially overcome by adding fillers to the polymers, which is why polymers are most often used as matrix material in conjunction with other solid lubricants [20].

Lubricious oxides

Oxide based materials most often are hard to shear at room temperature. However, some of them (e.g. Cs, Re, Ti, Mo, Zn, V, W, B) develop easy-to-shear characteristics at higher temperatures, which is why they are often referred to as lubricious oxides [208,255,256]. It has been shown that the crystal chemistry of oxides is linked to their shear rheology and thus to their ability to act as a high-temperature solid lubricant. An intense study on the lubrication behavior of different oxides as a function of the temperature has been provided by A. Erdemir [255]. Lubricious oxides are not very widespread and limited in their usage exclusively for high temperature applications. Most of them

only become an interesting solid lubricant for temperatures higher than 500°C [255]. A very good overview of the topic is provided by Aouadi et al. [14].

Soft metals

Soft metals, such as Pb, Sn, Ag or Au are able to provide a low COF when applied onto relatively hard substrates. In contrast to solid lubricants, whose function mechanism is based on the development of a transfer film on the opposite surface, soft metal film lubrication is initiated by shearing in the film. Unfortunately, this results in significantly higher friction, rendering soft metal coatings not the most efficient among the solid lubricants. In any case, the thickness of the coating determines the efficiency of the soft metal coating and most metal coatings have an optimum thickness. This optimum thickness results from the fact that very thick layers lead to a larger real contact area and thus to higher friction, whereas very thin layers can cause an abrupt increase in friction if they cannot prevent the direct interaction of the two substrates [20,224].

Summarizing, all of the above-described solid lubricants can possess good lubrication properties for specific conditions. However, they are also limited in their range of applications with regard to their environmental conditions and the prevailing stress collective. The increasing demands on tribological applications set the need to develop solid lubricants, which provide a higher environment robustness and independence from the stress situation [18,19]. This might be given for CNP as solid lubricants and will be discussed further in section 2.4 of the present dissertation. A very comprehensive and general introduction into the field of solid lubricants, its advantages, limitations and working principles is given by Scharf and Prasad [20] as well as Donnet and Erdemir [208].

2.3.2 Surface topography designing

Surfaces of real machine elements in tribological contact are not atomically flat and generally exhibit a certain surface roughness. In this regard, the early work of Bowden and Tabor investigated the interaction between asperities of a rough surface with regard to the influence on the frictional behavior [257]. They correlated the frictional behavior of a surface with adhesion/welding of asperities of the real contact area and their subsequent releasing (when a critical shear stress is applied). Since then, great efforts have been undertaken for various lubricated and non-lubricated tribological systems in order to measure, characterize and understand the influence of surface roughness on the tribological behavior and to correlate surface roughness with the real contact area of two contacting surfaces [21,214–217,258–262]. Despite the real contact area, a lot of different surface interactions have to

be considered, including plastic deformation and consequently deformation energies, contact angles between asperities or simply the mechanical properties of the contacting materials [207].

However, the roughness of a system is often connected to the end application, as this determines how much effort can be invested in the design or processing of a surface (e.g. surfaces of Micro-Electro Mechanical Systems (MEMS) [263] compared to large scale machine elements [262]). Thus, regarding larger scale tribological systems such as machine elements, numerous experimental works have tried to develop a fast and economic method to alter the real contact area by specifically varying the surface topography [219–222,264–267]. In these works, it has also been shown, that surface topography alteration affects more than just the real contact area. For example, the formation of a hydrodynamic pressure under lubricated conditions can be controlled by a defined surface topography [53]. Additionally, the surface depressions have been observed to trap and store generated wear particles as well as lubricants [52,53]. Furthermore, the creation of topographical structures providing an anisotropy typically also results in anisotropic effects on friction and wear of the surfaces. Thus, considering all those effects, it is sufficiently proven that surface topography designing is a powerful tool for the systematic manipulation of the tribological properties of a system.

Out of various techniques to create well-defined surface patterns such as honing, micro coining or lithography, laser surface texturing (LST) has shown to be suitable, cost and time-efficient approach [10,51]*. Hence laser surface processing has been chosen in the present dissertation for surface topography designing.*

Due to this fact, the focus in the following is put on LST as a method to tune surface topography. Generally, when it comes to LST using pulsed laser systems, different laser-material interactions have to be distinguished based on the laser pulse length ranging from short (microsecond- to nanosecond-pulses) to ultra-short (picosecond- to femtosecond-pulses) [268]. In the case that a metallic surface is processed using a short-pulsed laser system, the laser-material interaction is based on melting and heat conduction, resulting in shifting of the molten material according to temperature- and surface tension gradients. In contrast, an ultra-short pulsed laser system induces direct metal ablation, not allowing the metal to melt and generating a shock wave, which ejects evaporated or overheated liquid (***Fig. 30***). Ultra-short-pulsed laser surface structuring normally results in the creation of sharp topographical edges, whereas short-pulsed laser structuring provides rather smooth surface structures [268].

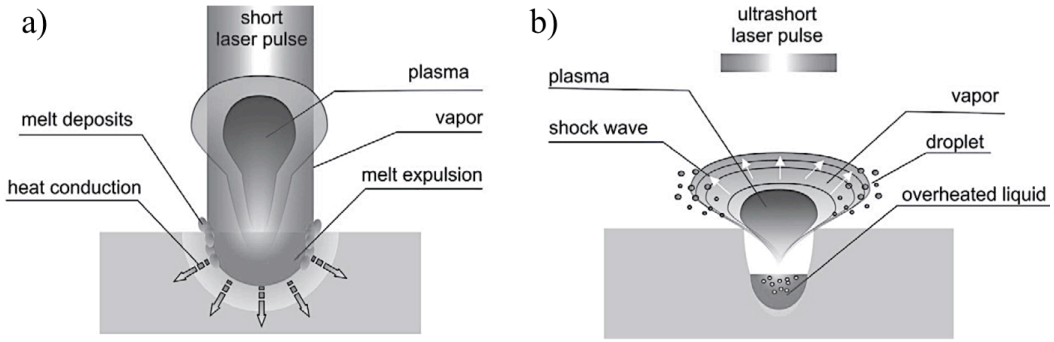

Figure 30: Schematic of the laser material interaction for a) a short-pulsed laser system and b) an ultra-short-pulsed laser system [268].

Another significant difference is the possibility to create higher surface aspect ratios for ultra-short pulsed laser systems compared to short-pulsed laser systems. Ultra-short laser pulses ablate the material with each individual pulse, resulting in successive material removal and thus deeper structures compared to a simple redistribution of molten material in the case of short laser pulses.

The pulsed laser systems can be used to create interference fields, producing a periodical laser intensity distribution on the material surface. This distribution causes a precise distribution of energy at places of high laser intensity, while the material remains almost unaffected in zones of low intensity. The interference field is generated by splitting up the main beam into two or more coherent sub-beams, subsequently overlapping at the surface. Depending on the laser pulse length, a redistribution of molten material (short-pulsed) or precise metal ablation (ultra-short-pulsed) occurs, resulting in the development of a defined surface topography. This process is called DLIP [51,269]. Different interference geometries can be obtained, such as line-, dot- or even lattice-like patterns with typical feature sizes in the micron to sub-micron range, depending on the used laser system, the laser wavelength and the angle of the overlapping sub-beams. A schematic of the DLIP process for a nanosecond laser system is given in ***Fig. 31***.

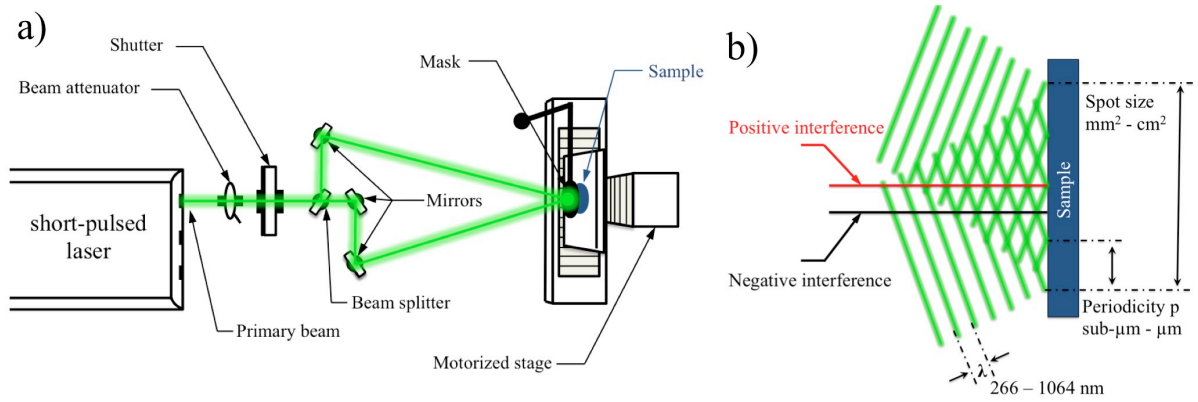

Figure 31: a) Schematic of the equipment and optics needed for the beam guidance in order to overlap the sub-beams on the sample surface according to the DLIP principle using a nanosecond laser. b) Schematic of the interference principle, creating regions of high intensity (positive interference) and low intensity (negative interference). The distance from one positive interference position to the next depends on the interfering angle of the sub-beams and the wavelength λ of the laser beam.

Besides the possibility to laser structure surfaces using DLIP, direct laser writing (DLW) can also be used [270]. For this technique, the laser beam is highly focused, and a sequential, automated surface processing is performed. It allows for larger surface structures (several micrometers to millimeter scale) and provides a highly controllable way to create different surface aspect ratios.

Studies on the tribological behavior of laser-structured metallic surfaces have shown a significant reduction in friction and wear under lubricated and non-lubricated conditions [53,266,271–273]. In addition to the effects caused by a reduced contact area and trapping of wear debris, the surface depressions can act as storage for liquid and solid lubricants, thus continuously supplying the contact region with the lubricant [52,53]. This can avoid premature failure of machine components by significantly enhancing the longevity of the lubrication effect.

Hence, in the present dissertation, laser structured surfaces were used in combination with the new solid lubricant (CNP) in order to create enhanced self-lubricating surfaces. Furthermore, specifically designed surfaces may allow for a more detailed understanding of the lubrication mechanisms of CNP. An in-depth discussion of the state of the art of CNP lubrication mechanisms and their usage in the field of tribology is therefore given in the next sections.

2.4 Tribological application of CNP

In recent years, CNP have risen as promising candidates to reduce friction and wear under various operational environments, which is ascribed to their outstanding mechanical properties, chemical inertness, thermal stability as well as atomic structure and geometrical shape [31–36,240]. Various works report on the friction and wear reducing effects of the particles when used as solid lubricant coating or as reinforcement phase in composite materials [29,35–47]. There are also numerous works using CNP as an additive in oils in order to achieve enhanced lubrication effects [60,62,274–280]. However, with the focus of the present dissertation being put on dry friction, these works are not considered in the following, since the lubrication mechanism of additives in oils strongly differ from the mechanisms present under dry friction.

The underlying lubrication mechanisms of the particles under dry friction conditions are still not fully understood and thus the potential lubricating effects may not be fully exploited [240]. The present thesis focuses on three CNP in particular, namely MWCNT, OLC and ND. These three different types of CNP are chosen intentionally since they can be systematically distinguished, representing sp^2 as well as sp^3-hybridized, 0-D (low aspect ratio) and also 1-D (high aspect ratio) carbon nanoparticles, and thus cover a wide range of CNP allotropes. Due to this fact, a systematic investigation is possible, allowing for an understanding of the governing lubrication mechanisms in more detail. Hence, in the following sections, only the above-mentioned three CNP are considered.

2.4.1 CNP as solid lubricant

There are various theories on the intrinsic lubrication mechanisms of CNP. However, the state of the art regarding the three particles differs. Hence, they are discussed separately in the following.

MWCNT

In many research works, friction and wear reduction are experimentally observed, when MWCNT are added to the tribological contact. It was stated that MWCNT are able to efficiently lubricate the contact in either air or vacuum conditions [281], for low and high temperatures [282] and under various relative humidity [35,283]. Regarding the occurring lubrication mechanisms, different explanations are found in literature. A common reason is that MWCNT would form a lubricious layer on the surface of the contacting materials [16,44,45]. However, it is often not further specified what this lubricious layer is composed of. There are studies, observing the formation of a “carbonaceous layer”, of which the lubrication mechanism would be similar to the known graphite lubrication. This would imply the structural degradation of MWCNT within a tribological contact [16,44,283]. This statement contradicts what was found by Dickrell et al., who showed a frictional anisotropy effect for quartz surfaces coated with MWCNT studied under a low load of 2 mN [35,91]. MWCNT that are aligned horizontally

(transversely) to a surface show a much lower coefficient of friction than MWCNT aligned perpendicularly (vertically) to the surface ("CNT forest") (***Fig. 32***). It was concluded that MWCNT might possess the ability to efficiently separate the sliding surfaces, which would also explain their ability to reduce wear of the contacting partners [32,38]. Additionally, it was assumed that MWCNT are able to slide and/or roll on the surfaces, being the logical consequence from their tube-like morphology and their relatively low physical interaction with surfaces due to their closed, curved shell and low concentration of dangling bonds [284]. In this regard, by measuring the lateral forces involved and observing the rotation of a single MWCNT on the surface, earlier studies of Falvo et al. using atomic force microscopy (AFM) proved that MWCNT are able to perform a defined sliding and/or rolling motion on top of a graphitic surface [34]. Still, so far, the rolling and/or sliding ability of MWCNT has not yet been proven for macroscopic tribological testing conditions. Regarding their potential ability to roll, simulations of CNT bundles in a tribological contact were performed by Ni and Sinnott [47], observing what is called the "tank-belt" effect and describing the CNT rolling motion similar to that of a deformed chain rolling between two contacting diamond surfaces under shear as can be seen in ***Fig. 32 (b)*** [45,47,285].

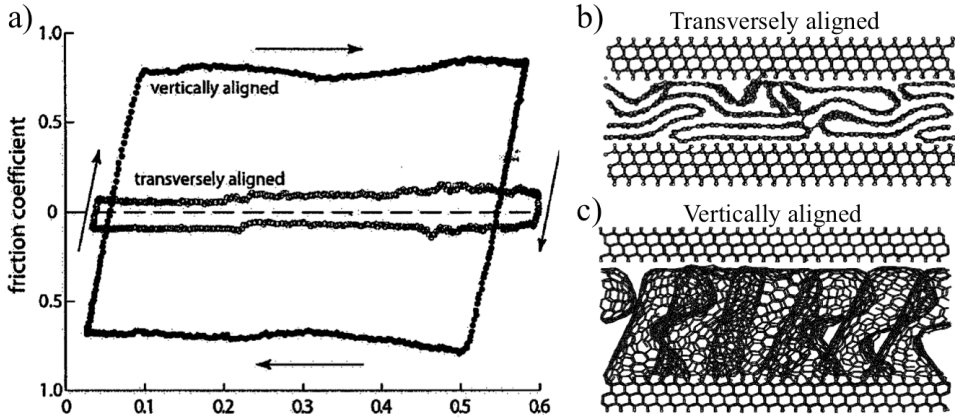

Figure 32: a) Mean value of 60 cycles of a pin on disc friction coefficient measurement of MWCNT on a quartz surface measured using a borosilicate pin and a normal load of 2 mN [35]. b) Schematic of the tank-belt model, showing transversely oriented CNT and c) vertically oriented CNT in between two diamond surfaces [47].

In this regard, Mylvaganam et al. [286] performed simulations on the sliding direction on agglomerated, transversely aligned CNT against a diamond tip under very low loads (several nN). It was shown that a sliding of 90° to the longitudinal axis of the CNT caused "spinning" of CNT that were situated below the top CNT layer, which is not the case when sliding is performed in parallel the CNT longitudinal axis. However, in terms of the friction coefficient, no change was observed and thus it was concluded that the lubrication effect of CNT is derived by their atomically smooth surface without dangling atoms (which is true in theory, but hardly ever obtained for synthesized CNT). Interestingly, further simulations of CNT under high temperature conditions (1500-2000 K) by Colonna et al. [287] showed, that for pressures above 1.5 GPa, a structural degradation towards graphite can be expected.

It becomes thus evident, that the lubrication mechanism is a function of the given tribological system and a wide span of parameters like relative humidity, contact mechanics, the contacting material properties and their surfaces as well as the distribution, structural integrity and agglomeration of MWCNT [240,288]. Thus, all those influences have to be considered in order to learn more about the lubrication mechanisms of these particles, which, so far, has not yet been done for one specific tribological system.

ND

Regarding the intrinsic lubrication mechanism of ND, there is not yet much literature in the field of dry friction. This could be due to the fact that an sp^3 hybridization is usually associated with a hard material, which does not provide the basic requirements of a solid lubricant (according to Bowden and Tabor) [233]. However, due to their spherical shape, there is literature that assumes a possible function as nano-roller bearings, separating the two contacting surfaces thus preventing the occurrence of severe wear and reducing the COF [41,289]. Yet, this assumption was not proven and in contrast, other studies contradict this assumption [62]. Especially under ambient conditions, ND are rather connected to act as an abrasive rather than a solid lubricant [290]. A beneficial effect on friction and wear could be observed mainly under vacuum conditions. It is argued, that low adhesion between the diamond surface and the substrate surface (due to adsorbed oxygen-containing species on the surface) can cause this frictional and wear reduction [290]. Studies by Berman et al. further reported about the possibility to reach "superlubricity" with friction coefficients as low as 0.004 if ND are combined with graphene as solid lubricants in the contact area of a DLC sphere and SiO_2 substrate [291,292]. The effect was only observed for dry environments. In the case of an increase in relative humidity to 30%, the effect vanishes as can be seen in ***Fig. 33 (a)*** and ***(b)***. It is argued, that ND particles are wrapped by graphene nanoscrolls as depicted in ***Fig. 33 (c-f)***. In this respect, ND would provide the mechanical stability of the nano-bearing, whereas atomic incommensurability, and thus superlubricity (which was first discovered by Shinjo and Hirano for muscovite mica crystal [230]), is given by the direct contact of the DLC surface with the graphene sheet [291,292]. If humidity were present, the adsorption of water molecules would prevent the formation of graphene nano-scrolls and therefore would show detrimental frictional effects. It is still an open question, whether these promising lubrication effects could be transferred to technically relevant materials with rough surfaces.

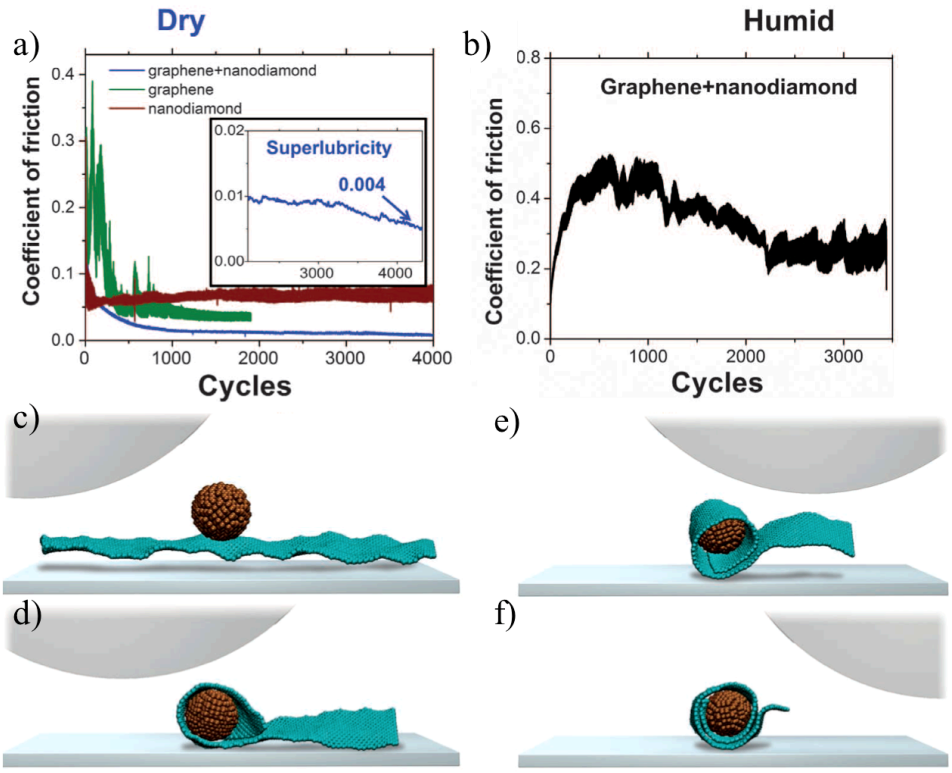

Figure 33: a) Friction coefficient measurement of nanodiamond, graphene and nanodiamond+graphene for a DLC against SiO_2 contact under dry ambient conditions and b) humid (30% relative humidity) conditions. c) – f) shows a schematic of the mechanism of graphene nanoscroll wrapping of nanodiamonds in the mentioned tribological contact [291,292].

However, the reported observations also give rise to the promising lubrication properties of OLC (being similar to a wrapped graphene scroll), which is discussed in the next paragraph. Generally, research using ND for tribological applications is rather focused on their usage as additives in liquid lubricants or as reinforcement phase in composites, where beneficial tribological effects are obtained due to a change in the rheological behavior of oils, an embedding of ND in the surfaces or a hardening/strengthening effect of the composite [33,62,197,277,279,293,294].

OLC

The polyhedral or spherical structure of OLC suggests that they could also function as nano-bearings in tribological systems [31]. Since there are almost no free valence electrons on the curved surface of OLC, only weak intermolecular interactions with other materials are assumed [31,280]. As a result, OLC have a high degree of freedom, as only a few bonds are formed on the surface of the friction partners. In the case of atmospheric conditions or even under vacuum, OLC provide a significantly lower COF than graphite, as can be seen in ***Fig. 34 (a)*** and ***(b)***, respectively [36].

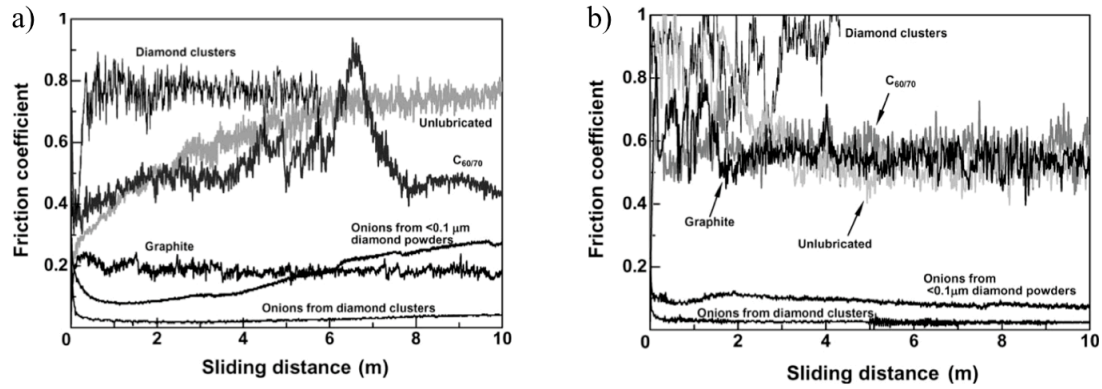

Figure 34: Friction coefficient measurement of OLC, graphite, C60 fullerene and diamond clusters under a) ambient conditions and b) under vacuum [36].

OLC particles are apparently not dependent on the presence of water molecules or oxygen for solid lubrication. Furthermore, using OLC compared to graphite, the wear rate could be reduced by 3 to 6 orders of magnitude, which is attributed to surface separation by OLC. Hirata et al. [36] further produced OLC using diamond powder and others using diamond clusters. In ***Fig. 34***, a clear difference in the tribological behavior of these two OLC variations is observed. This is explained by the different number of defects on the surface. OLC derived from diamond powder has significantly more defects, therefore resulting in a lower binding stability and being more prone to chemical reactions with the contacting surfaces. Additionally, the lubrication effect of OLC might be strongly dependent on the provided surface roughness of the substrate material. If the roughness is too high, the particles may not provide an efficient surface separation anymore. When OLC are in direct contact, they can be damaged and thus restricted in their freedom of movement. However, although being damaged or pinned, AFM experiments reported a deformed OLC layer found on steel surfaces, still providing a very low COF [295].

Despite these experimental findings, various simulations have been performed in order to understand the lubrication mechanism of OLC. These have shown, that the capability of OLC to perform a rolling movement on a surface could be prevented by exceeding a certain contact pressure. This has been justified by the formation of bonds with the contacting materials, pinning the OLC particles. In the case of two OLC-lubricated DLC layers, a maximum contact pressure of 5 GPa was simulated at which the coefficient of friction increases from 0.024 to 0.151, and thus, the mechanism changes from rolling to sliding [296]. In general, the lubrication mechanism of OLC is referred to as a rolling or sliding movement on top of the surfaces rather than a structural modification (for example exfoliation) [45,46].

2.4.2 CNPs as protective coating

Due to the promising physical properties of CNP, various coating methods were deployed so as to use CNP as surface coatings. Again, the state of the art of the particles strongly varies, and thus, they are described individually. Not all of the presented methods were applied in order to use the coating for tribological applications. However, a brief overview of all the methods capable of coating surfaces with CNP is provided in the following.

MWCNT

In the specific case of MWCNT, it must be distinguished between dry and wet coating routes. The dry coating route involves drawing films directly from MWCNT forest arrays [297,298]. These methods are easily scalable. However, they were not used in the field of tribology since they are normally not suitable to coat complex geometries such as a journal bearing or surface textures. In this regard, wet coating techniques are rather deployed, which always involve the dispersion of the MWCNT in a suitable solvent (for example by using ultrasonic agitation) with or without prior particle surface functionalization. One of those methods is dip coating [299–301]. In this regard, Mirri et al. [300] have performed experiments using Chlorosulfonic acid (CSA) to produce thin conductive, transparent MWCNT films on glass substrates. Other techniques are drop casting, spray coating or rod coating. The methods basically work by individually placing or randomly spraying droplets of dispersed CNT in a solvent onto a surface or by drawing a rod to spread a CNT dispersion over the surface, respectively. Subsequently the solvent is evaporated and the CNT remain on the surface [281,302–304]. One of the main drawbacks of these techniques is the so-called “coffee stain” formation due to Marangoni convection during evaporation of the solvent, resulting in inhomogeneous distribution of the CNT coating. In order to reduce this effect, surface heating is often performed so as to speed up the evaporation process of the solvent, or it is attempted to change the rheological parameters of the colloidal suspension (being described by the “Ohnesorge number”) [302]. Alternatively, the technique can be combined with spin-coating or techniques like vacuum filtration [302,305,306]. All of these techniques have disadvantages in terms of layer quality, homogeneity or the possibility of process up-scaling. Another technique to coat surfaces homogeneously with CNT is CVD [307–309]. However, due to its working principle, this process only produces CNT, which are vertically aligned to the surface (CNT forests) and it was shown, that horizontally aligned CNT provide a much higher frictional reduction compared to CNT forests deposited by CVD [91]. Thus, although this technique allows for a homogeneous coating, other techniques should be favored [281,286].

A very promising technique to produce horizontally arranged, homogeneous CNT coatings is electrophoretic deposition (EPD) [310–313]. EPD is based on the motion of charged particles in an electric field and their subsequent adhesion/physisorption onto an electrically conductive substrate material as illustrated in ***Fig. 35***.

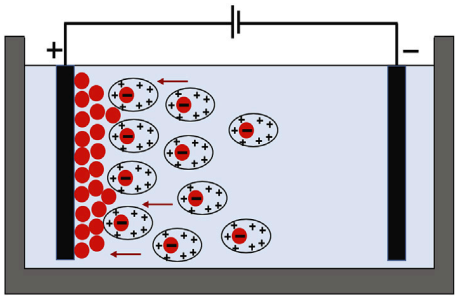

Figure 35: Schematic of the electrophoresis principle. Electrodes provide a specific voltage so that charged, dispersed particles (colored in red) are deposited on the cathode (+) or anode (-) depending on their surface charge [314].

The process allows for a more homogeneous deposition of CNT compared to drop casting or spin coating, has short processing times and is easily up-scalable. In addition, the possibility of coating complex surface topographies with a well-defined layer thickness is an important advantage over other processes. More theoretical information on the general working principle of EPD can be found in Besra et al. [315].

For these reasons and since MWCNT coating of substrates is combined with laser surface structuring in the present dissertation, EPD is chosen as coating technique in order to homogeneously cover surfaces with horizontally arranged CNT. The application of CNT coatings using EPD in the field of tribology is a new approach and has not been investigated before.

Another approach to coat surfaces with CNT is to produce composite coatings, using CNT as reinforcement phase in a polymeric or metallic matrix that is then deposited on a surface (e.g. electroless plating [316]). This method is extensively deployed in tribology, yielding good results in frictional and wear reduction [28,317–322]. However, the effects of a composite coating on the tribological behavior are often due to the combination of intrinsic lubrication properties of the CNT and their reinforcing effect on the matrix material, which is therefore discussed in general for CNT-reinforced MMC in section 2.4.3 of the present dissertation.

ND

In the literature, a nanodiamond coating is often referred to as nanocrystalline diamond coating [240,323,324]. Regarding this, for example, microwave plasma enhanced CVD was used to grow a nanocrystalline diamond coating on a silicon substrate, providing low friction and wear [325]. However, the literature has to be carefully evaluated when it comes to coatings using ND particles or nanocrystalline diamond (nanodiamond film growth), since the latter provides a closed, interconnected diamond layer and not individual ND particles.

Regarding the deposition of individual ND particles, argon gas spraying of ND with a diameter of 75 nm onto a steel surfaces has been performed by Gubarevich et al. [290], subsequently performing tribological measurements against SiC and Al_2O_3 balls. It is reported, that low friction and wear could be obtained under vacuum as well as ambient conditions. For vacuum, this is explained with the assumption of ND being able to form a stable, densely packed layer with low roughness, which is covered by oxygen-containing functional groups providing an inert, low adhesion surface. However, a more detailed analysis is not given.

Other than that, EPD is found to be the most important, if not the only technique to mention that has been carried out on various substrate materials [326–332]. Not much research has been done in the field of tribology with respect to these coatings. Tribological experiments using electrophoretically deposited ND on aluminum alloys have been conducted by Kalyanasundaran et al. [331], who found an improvement in wear resistance compared to the uncoated surfaces. Despite that, ND are only deployed as additive in metallic or polymeric surface coatings [42,333,334]. The beneficial tribological properties of these coatings are rather due to the reinforcement of the metallic or polymeric phase with ND and will thus be discussed in section 2.4.3 of the present dissertation in the case of ND-reinforced MMC.

OLC

When it comes to OLC-coated surfaces, there is not much literature either. Hirata et al. [36] reported on the tribological properties of OLC (see section 2.4.1) that have been spread over a silicon wafer without giving further specifications on how the particles were deposited. In contrast, Gubarevich et al. [335] describe an OLC coating process by plasma spraying of ND. In this process, high temperatures (2700-4500 K) of the ND particles are reached, leading to a transformation to OLC. Immediately after transformation, the particles are deposited on a stainless-steel substrate. The authors emphasize the use of this coating for solid lubrication. However, the tribological properties of the produced coatings are not evaluated. The potential of OLC coatings to function as solid lubricant was also postulated by Cabioc'h et al. [336], who developed a process to coat silica substrates by synthesizing OLC into silver thin films. This has been done by carbon ion implantation into the silver films at 500°C. The subsequent annealing of the silver layer at 850°C is described to lead to a silver evaporation, leaving a pure OLC coating on the surface. Nonetheless, a tribological evaluation of the coating is not provided. There are also further studies about OLC coatings of substrates, which are not related to the field of tribology, such as Pech et al. [337], who investigated the possibility to deposit OLC on Si/SiO_2 substrates by EPD, forming homogeneous OLC coatings. Generally, OLC coatings are fairly unexplored in the field of tribology.

2.4.3 CNP as reinforcing phase in tribology of MMC

Generally, the disadvantages of solid lubricant coatings are limited lifetime, difficulty in replenishment, oxidation or aging-related degradation as well as poor adhesion. Hence, in order to overcome these drawbacks, embedding solid lubricants in MMC seems to be an interesting alternative approach to create self-lubricating materials [16,21]. Self-lubricating composites in general have been already available for many years and find applications for example in bearings, piston or cylinder liners in engines [21]. These composites are developing into an important class of tribological materials and offer new ways to combat friction and wear under extreme conditions [21]. In this regard, the choice of CNP as solid lubricant is not only due to their interesting intrinsic lubrication properties, but, as already discussed in section 2.2.1, also provides numerous possibilities and mechanisms to act as reinforcement phase in MMC, especially in the field of mechanical reinforcement. For these reasons, CNP are used as reinforcement phase for MMC in the field of tribology. In the following, a short overview of the state of the art of this research area is provided for each of the three CNP used in the present dissertation.

MWCNT

Research in this field has been conducted mainly for CNT reinforced Al, Cu, Cr, Mg and Ni based MMC as bulk materials or coatings [27,29,37–40,44,156,160,338–347]. Although many studies have been performed on this topic, all providing promising results regarding friction and wear reduction irrespective of the used matrix material, not much is known about the occurring tribological mechanisms in these systems. Typically, the reinforcement for most tribological applications is done with concentrations of up to 20 vol.-% of MWCNT. For one part, the mechanical reinforcement effects (which were discussed already in section 2.2.1 of the present dissertation) can lead to an increased hardness and strength of the composite, which is usually connected to a reduced occurrence of wear [37,38]. Therefore, a fine and homogeneous distribution of CNT in the matrix material is what is typically aimed at in order to maximize the grain refinement effect through Zener-pinning or the Hall-Petch effect as well as the Orowan-strengthening mechanism [16]. For example, CNT could hinder the dislocation movement and therefore reduce plastic deformation of the surfaces during wear, significantly influencing the predominant wear mechanisms. Accordingly, it has been reported, that the wear rate but also the COF decreases with increasing MWCNT content as can be seen in the case of Al MWCNT composites in ***Fig. 36*** [160,338,343].

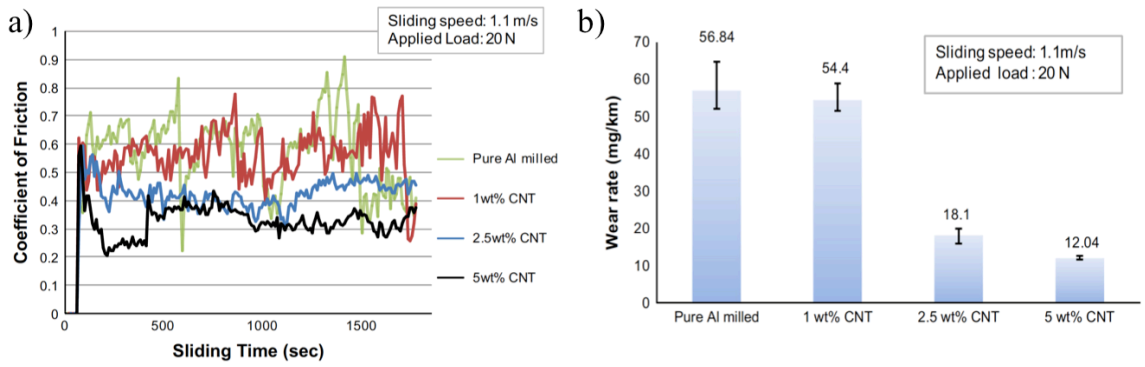

Figure 36: a) COF measurements of MWCNT-reinforced Al composites for different MWCNT concentrations and b) the corresponding wear rate measurements [338].

The authors also reported that the wear rate and the COF would decrease with increasing sliding speed, whereas an increased normal load would also increase the wear rate but lower the COF. Those findings are in good agreement with other studies, working with MWCNT-reinforced Ni or Cu [27,160,346]. The mentioned works further correlated the results with the formation of a lubricating carbon film on the surface and thus degraded MWCNT. However, other studies that reported on similar results, conclude that the used MWCNT were fully intact after tribological testing and argue that the beneficial tribological properties were obtained due to the possibility of CNT to perform a rolling movement and to act as nano-bearings [322,342]. Again, other works report on the dependence of the number of walls of MWCNT deciding on whether the particles degrade or not [156]. Hence, although different works came to similar tribological results, different explanations regarding the lubrication mechanisms of MWCNT were reported [240].

Regarding a possible rolling or sliding mechanism of MWCNT, it must be noted that what is unfavorable for mechanical reinforcement of composites may be advantageous for a tribological optimization. A weak bonding of MWCNT to the metal phase is certainly not beneficial for a mechanical load transfer from the matrix to the reinforcement phase (considering the shear-lag model). However, it could lead to a free movement and thus easy sliding or rolling of MWCNT between the contacting surfaces [16]. In this context, the metallic matrix would function as a solid lubricant reservoir that continuously supplies the surface with the lubricant. In the event that a strong bonding exists, a rolling or sliding may not occur, while structural degradation of the CNT may arise with the formation of a lubricating carbonaceous layer. This may explain why different researchers observe beneficial tribological effects for the same composites but provide contradicting explanations and findings.

For this reason, choosing a metal matrix with a low tendency to form a stable interphase with MWCNT might be of great importance for an improvement in tribological behavior of the surface regarding a possible rolling/sliding mechanism of MWCNT. Thus, also for this reason, nickel is chosen as matrix material in the present dissertation due to its low tendency to form carbides.

With respect to this and despite the possibility of CNT to form a lubricious layer, the improvement in wear resistance is also often attributed to the role of CNT to act as spacers between the contacting surfaces [38,44]. Scharf et al. [44] have performed interesting studies with MWCNT-reinforced nickel metal matrix composites (Ni-MMC). The observed frictional results are shown in ***Fig. 37***, measuring the COF of the composite against 440C steel balls (***Fig. 37 (a)***) or against Si_3N_4 balls (***Fig. 37 (b)***). The corresponding distribution of the MWCNT reinforcement phase is shown in ***Fig. 37 (c)*** using scanning electron microscopy (SEM) and a chemical verification by Auger electron spectroscopy showing Ni (green) and carbon (red) is provided in ***Fig. 37 (d)***. It can be noticed that MWCNT are present in agglomerated form. Nonetheless, a clear, long-term reduction in the COF is achieved by the reinforcement using MWCNT. In addition, it has been found that the formation of a lubricious MWCNT layer could act as an oxidation barrier, as oxygen first reacts with carbon and thus hinders the formation of NiO. This could reduce the formation of abrasive, oxidic third bodies in the tribological contact [44]. Furthermore, the fact that MWCNT are present on the surface of the worn composites significantly changes the surface chemistry compared to the unreinforced materials, strongly affecting the occurring wear mechanisms of the surfaces regarding effects based on adhesion [343].

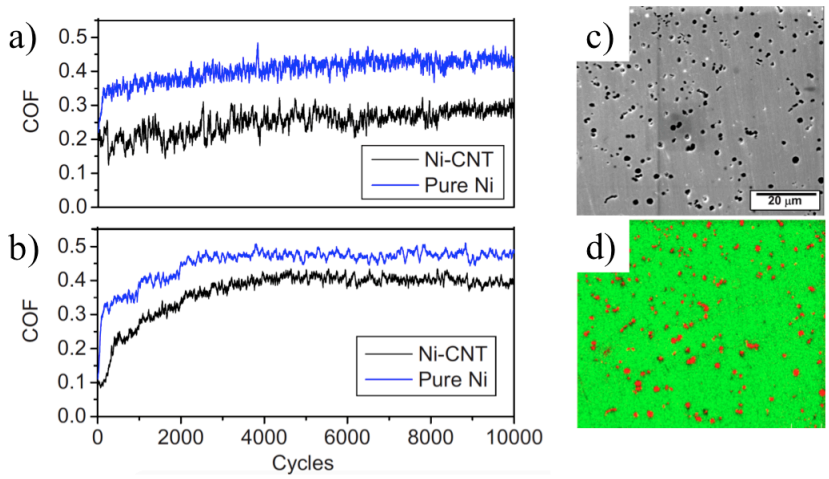

Figure 37: COF measurements of unreinforced Ni reference and the MWCNT reinforced Ni composite measured with a ball-on-disc tribometer using a) 440C steel balls and b) Si_3N_4 balls as counterparts. The distribution of the MWCNT reinforcement phase in the composite is shown c), which is also validated by auger electron spectroscopy in d), with the color green representing the nickel matrix and red representing carbon. [44]

Scharf et al. [44] further reported on a structural degradation of the MWCNT under tribological contact. The formed lubricious layer is still not further investigated. It is still rather unclear what the lubricating layer consists of and how the MWCNT degradation affects the tribological properties of the composites. The forming layer is sometimes said to be similar to graphite. However, a comparison of MWCNT-reinforced Ni with graphite-reinforced Ni has shown, that the MWCNT

reinforcement provides lower COF and wear [345]. Thus, the lubrication mechanism of MWCNT must be different from that of pure graphite lubrication.

Furthermore, Suarez et al [40] have reported about similar friction and wear reducing effects of MWCNT-reinforced Ni (processed by HUP and CPS) in the case of short-term tribological experiments (200 sliding cycles). They found, that the measured friction and wear reduction could be correlated with a formation of an interfacial lubricating carbon layer, which is, however, not further specified. Additionally, they referred to the grain refinement effect of the CNT, leading to a higher hardness and lower indentation depth of the used alumina ball into the HUP-processed composite surface for low loads (up to 100 mN). For higher loads, surface oxidation would play a crucial role for the lubricating effect of these composites. In this regard, the samples with a lower mean grain size (HUP samples) lost their lubrication effect when measured using 300 mN of normal load due to the formation of a closed NiO layer (acting as a high shear strength layer and increasing the COF). In contrast, the CPS samples, with a higher mean grain size, showed less oxidation (due to fewer grain boundaries and thus less diffusion paths for oxygen) and stayed lubricated under 300 mN of normal load.

In summary, it should be noted that the tribological effects regarding self-lubricating properties of MWCNT-reinforced MMC of all the studies in literature vary significantly, due to the different measuring conditions (humidity, load, temperature, conformal or non-conformal contact conditions, elastic or elasto-plastic contact conditions, etc.), processing parameters (sintering method, dispersion method, etc.), and materials (matrix material, mechanical properties, surface roughness, microstructure, counter-material, etc.) used, which makes it difficult to fully understand the lubrication mechanisms of these composites and to improve the measured promising effects. In this regard, Zhang et al. [322] stated in their review paper: "*It is hard to ascribe the positive tribological role of CNT to any sole cause, as for most cases, if not all, more than one mechanism may work simultaneously*".

ND

ND have been used as reinforcement phase for various MMC (Al, Ti, Ni, Cu, W etc.) in the field of tribology mainly for anti-wear purposes [42,43,348–351]. Generally, the wear reduction is correlated with a significant increase in the hardness of ND-reinforced MMC. With increasing amounts of ND (typically up to 10 vol.-%), wear resistance is typically improved. These findings can be correlated with the strengthening mechanisms of ND as reinforcement phase in MMC that are described in section 2.2.1 of the present dissertation as well as the intrinsic high particles hardness. An improved wear resistance can also be correlated with the formation of a tribofilm [352]. In this regard, the high thermal conductivity of ND can increase heat transfer and thus promote a tribofilm formation, for example in the case of ND-reinforced WC-Co or Al composites [351,352]. Thus, the presence of ND particles as reinforcement phase can affect chemistry, microstructural evolution as well as the

mechanical behavior of the composites [352]. Certain conditions, such as increased temperature or nanocrystalline microstructures of the matrix phase have also resulted in increased wear if ND are added [42,353]. This increased wear could be explained by the removal of the ND from the matrix material, leading to an increased abrasive wear component due to the hard ND particles acting as third body or a thermally induced degradation of ND, resulting in a reduction of the hardness of the composite [353][42]. A significant frictional reduction, if any, is usually not observed in literature. However and in contrast, Kaftelen et al. [351] reported a frictional reduction of up to 50% compared to the unreinforced Al reference. This frictional reduction, however, is attributed to the ND-induced formation of a lubricious oxide layer on the ND-reinforced Al composites.

OLC

So far, there is no literature on OLC-reinforced MMC for tribological applications. However, some of the reinforcement mechanisms of CNT and ND are also expected to occur in OLC-reinforced MMC. The lubricating properties of OLC as reinforcement phase in MMC are not yet investigated.

Summarizing, since a mechanical reinforcement effect is expected to occur for all the CNP-reinforced MMC, a systematic tribological comparison of these composites provides more information on the occurring intrinsic lubrication mechanisms of the individual particles. A systematic investigation and correlation of the lubrication effects of similar CNP under the same conditions has not yet been done in literature and is therefore performed in the present dissertation.

3. OVERVIEW

In the following, the main objectives are linked to the new findings of this dissertation. Subsequently, chapter four presents nine self-contained papers, all of which have been published in international, peer-reviewed journals and provide a detailed discussion of all results of this dissertation. The necessity of the following chapter is to provide a connection of the aforementioned publications to the proposed objectives and thus, to give a comprehensive overview and a concise summary of the most important results. For a more detailed presentation of the results, combined with an in-depth discussion as well as information about the used materials and methods, please refer to the attached publications.

OBJECTIVE 1

Colloidal mixing appears to be a well-suited approach to satisfy the requirements of objective 1. In **Fig. 38**, a short overview about the research areas addressed in objective 1 is given, which will be discussed in the following sections.

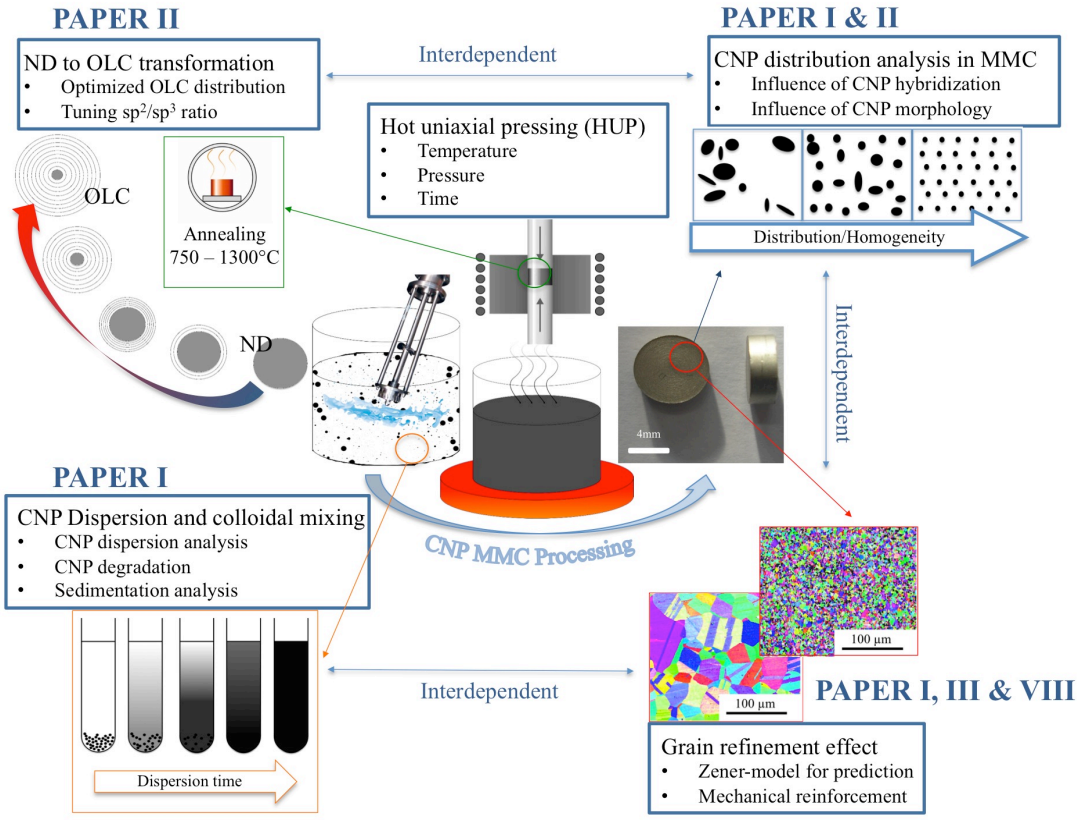

Figure 38: Schematic overview of the addressed areas regarding objective 1 of the present dissertation, which allow for a full process control and comparative production of CNP-reinforced Ni-MMC. The papers, dealing with the respective topics are indicated.

CNP DISPERSION AND COLLOIDAL MIXING

A detailed dispersion analysis and the investigation of the colloidal mixing method are provided in **PAPER I**. In their initial state (as-received), the CNP consist of large particle agglomerates (agglomerate diameters of up to 1 mm), which therefore must be de-agglomerated to be processed further. De-agglomeration is done by dispersion in ethylene glycol using a shear mixer followed by ultrasonic agitation. **PAPER I** provides a thorough study on this process avoiding particle functionalization and investigating the time needed to obtain the finest possible dispersion of CNP in the solvent. It is found that there is no difference between the dispersion grade of CNT, OLC and ND using the described method. A saturation value of the agglomerate radius is found to settle in at 40-70 nm after 5 min of shear mixing, followed by 20 min in the ultrasonic bath. Longer treatment times do not allow for finer dispersions.

The dispersed particles are analyzed by Raman spectroscopy with the aim of tracing a possible degradation caused by strong shear forces produced by the shear mixer and/or the ultrasonic agitation. In this regard, it is shown that even after 2 hours of ultrasonic agitation, no CNP degradation is observed. Once the dispersions are taken out of the ultrasonic bath, re-agglomeration of the particles starts to occur. Hence, the dispersion stability is further analyzed by sedimentation analysis and zeta-potential measurements. From these experiments, it is concluded that ND provide the highest dispersion stability over time, followed by OLC and finally CNT. For one part, this is explained by the different bonding types in CNT and OLC, compared to ND. The π-bonding with a delocalized electron cloud in the case of the sp^2-hybridized CNT and OLC translates into a higher electrostatic interaction of the particles (e.g. Van-der-Waals forces), resulting in a stronger agglomeration tendency. Although CNT and OLC dispersions show a similar zeta-potential (resulting from the similar electronic configuration), the sedimentation behavior differs strongly, which is related to the high aspect ratio of the CNT, inducing an additional mechanical interlocking effect, aiding the re-agglomeration.

GRAIN REFINEMENT EFFECT AND CNP DISTRIBUTION ANALYSIS IN MMC

After determining the proper dispersion and blending route, composite samples are processed by HUP and the distribution of CNP in the metal matrix as well as the microstructure and mechanical reinforcement effect are analyzed. Regarding the CNP distribution and agglomerate sizes, the findings of the sedimentation analysis are verified, with ND providing the smallest agglomerates within MMC, followed by OLC and finally CNT. However, even though ND provide smaller agglomerates, both, OLC as well as ND agglomerates are distributed homogeneously, compared to CNT. This fact translates into a more pronounced grain refinement effect in the case of ND and OLC. The similar grain size distribution for ND and OLC is reasonable, since the grain refinement effect is rather dependent on the agglomerate distribution (as well as morphology) within the material than the

absolute agglomerate size. In contrast, the agglomerate size determines the development of the particle dispersion strengthening mechanism and thus the mechanical reinforcement effect. For this reason, the highest hardness increase (compared to the unreinforced Ni reference) is achieved for ND, followed by OLC and finally CNT reinforcement. From **PAPER I**, it is finally concluded that a low aspect ratio (0-D) and an sp^3 carbon hybridization is beneficial for a homogeneous, fine distribution of CNP within MMC, leading to strongly pronounced grain refinement and an improved mechanical reinforcement effects.

PAPER III provides further analysis regarding the manufacturing of CNP-reinforced MMC with different CNP concentrations, ranging from 0.5 vol.-% up to 10 vol.-%. This is done in order to investigate the evolution of the grain refinement effect as a function of the used CNP type and concentration, and thus to predict and control the microstructure of the resulting composites. With increasing CNP concentration, the mean grain size of the composites decreases. However, it is confirmed that the strongest grain refinement effect can be observed for ND and the weakest for CNT, when comparing the same particle concentrations. Furthermore, different saturation concentrations are found. If the saturation concentrations are exceeded, the grains become coarser again due to the higher tendency of the particles to form larger agglomerates (due to a shorter mean re-agglomeration free path). In the case of CNT, this concentration is 3 vol.-%, whereas up to 6.5 vol.-% and 10 vol.-% are achievable for OLC and ND, respectively. This behavior is explained by the same facts and findings from **PAPER I**. However, the acquired experimental data is additionally used to adapt a modified Zener model, predicting the mean grain sizes of the composites as a function of the CNP type and concentration for concentrations lower than the individual saturation concentration.
Despite a process control based on the particle type and concentration, a way has been found allowing for the production of CNP reinforced MMC featuring the same mean grain size and hardness irrespective of the used CNP type and concentration in **PAPER VIII**. This is achieved by choosing a lower sintering temperature (700°C instead of 750°C), which results in a reduced driving force of grain growth and thus prevents differences in the extent of the Zener pinning effect when using different CNP types, concentrations and distributions. This finding is very important in order to be able to compare the composites tribologically, excluding any effect of differences in their microstructure or mechanical reinforcement.

ND TO OLC TRANSFORMATION

In **PAPER II**, a way is found to take advantage of the beneficial homogeneous distribution and small agglomerate sizes of ND in MMC, and apply it to OLC-reinforced composites. This is done by first manufacturing ND-reinforced Ni-MMC and subsequently transforming ND to OLC within the already sintered composite by annealing.
The ND reinforced sintered composites are annealed at different temperatures from 750°C up to 1300°C and the ND agglomerates are analyzed by UV Raman spectroscopy. With increasing

annealing temperature, the diamond band of the Raman spectrum vanishes and the disorder-induced D-band starts to be observed. At the same time, the wavenumber of the upshifted G-band of sp^2-hybridized carbon (from the outer shell of the ND particles) is reduced until reaching 1588 cm^{-1} after annealing at 1300°C. This observation clearly agrees with the transformation of ND powder towards OLC, reported in literature. The findings are supported by TEM analysis, verifying the presence of OLC within the MMC after annealing at 1300°C. Additionally, XPS measurements of the samples annealed at 750 °C and 1300°C confirm a change of the sp^2-hybridized carbon content from 31.1 % to 84.2 %, respectively. Comparing these results to the Raman analysis, it becomes clear, that the sp^2 to sp^3 carbon hybridization ratio can be tuned as a function of the annealing temperature of the composite. It is the first time in literature that the transformation process of ND to OLC within an MMC has been investigated and reported.

All these findings allow for full process control of CNP Ni-MMC manufacturing by colloidal mixing and HUP, avoiding particle functionalization, minimizing particle degradation and enabling a fine and homogeneous particle distribution as well as a microstructure prediction of the produced MMC.

OBJECTIVE 2

In order to achieve objective 2, an extensive tribological characterization of the composites is necessary. In this regard, ***Fig. 39*** provides an overview of which areas are addressed in the present dissertation in order to understand the tribological behavior of the composites and to create self-lubricating surfaces.

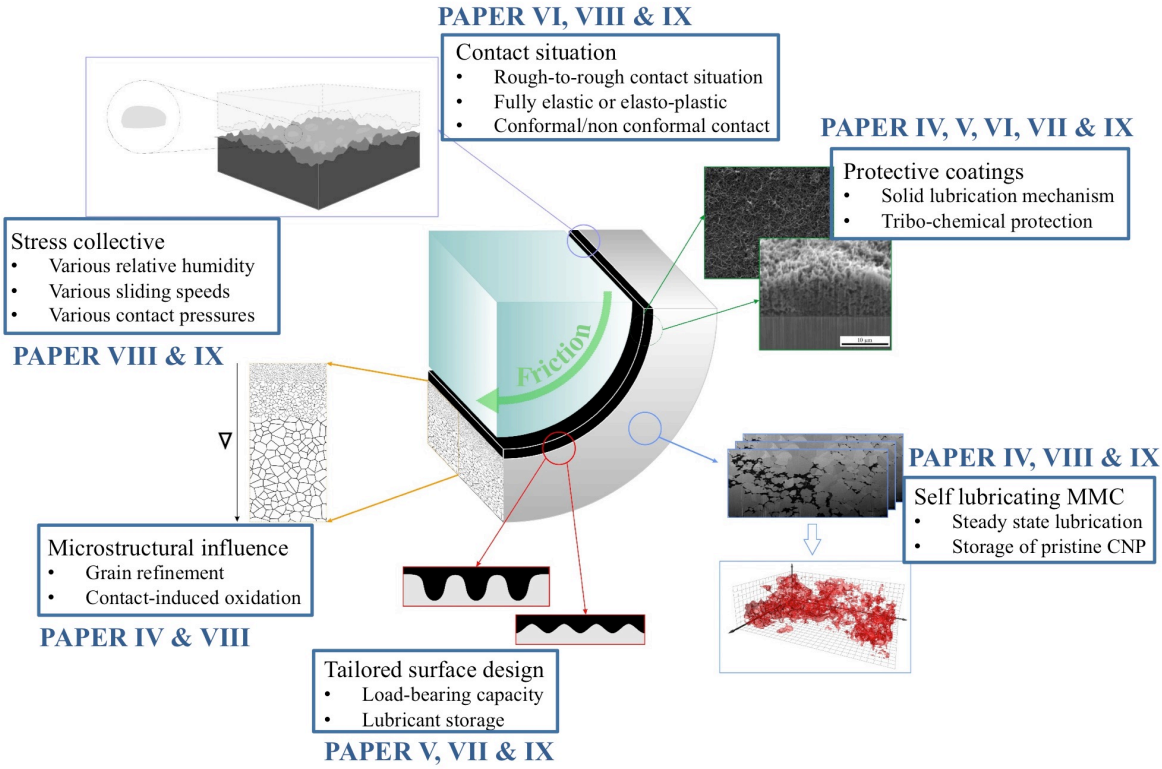

Figure 39: Schematic overview of the addressed areas of the present dissertation, which enable for the understanding of the lubrication mechanisms involved in self-lubricating surfaces based on CNP. The papers, dealing with the respective topics are indicated

MICROSTRUCTURAL INFLUENCE

As a first step, a tribological comparison of CNT-reinforced Ni-MMC and CNT-coated Ni is performed in **PAPER IV**. The coating is done by drop casting a CNT dispersion on a Ni surface. Compared to the unreinforced CNT-coated Ni, the CNT-reinforced MMC provides a refined microstructure with CNT stored within the composite. In both approaches, CNT are present in the direct tribological contact area and thus, the investigation allows for the analysis of the influence of a refined microstructure on the tribological behavior of these surfaces. For the CNT-coated and the CNT-reinforced surface, the same frictional reduction is observed for the first 200 sliding cycles. Due to this, it is concluded that the frictional behavior is dominated by the presence or absence of CNT in the tribological contact and not by the microstructure. This observation is supported by the findings of the long-term experiments (20000 sliding cycles), where a frictional reduction is noticed exclusively

for the CNT-reinforced samples. For the CNT-coated surfaces, the breakdown in lubrication can be explained by the CNT being removed from the contact zone, which is verified by SEM analysis of the wear tracks. In the case of the CNT-reinforced composites, a continuous supply of CNT allows for a long-term lubrication of the contact.

However, as discussed earlier, a smaller mean grain size of CNP-reinforced samples leads to a higher amount of grain boundaries, acting as diffusion paths for oxygen and thus favoring surface oxidation during a tribological experiment. This is shown in **PAPER VIII**. For high, non-conformal loading conditions (8N) and medium relative humidity (45%), a refined microstructure of a CNP-reinforced composite tends to form a homogenous oxide layer during the tribological experiment, whereas this is not observed for the coarse grained, unreinforced Ni reference. When choosing the MMC processing parameters to produce CNP-reinforced MMC with the same mean grain size, irrespective of the CNP type and concentration, a frictional reduction is only possible for the CNT-reinforced composites. For the reference, ND and OLC reinforced samples, the same tribological behavior is observed under various experimental conditions. These findings underline the statement that the microstructure affects the frictional behavior of CNP-reinforced composites to a rather minor degree and only due to induced differences in the surface oxidation behavior.

PROTECTIVE COATINGS AND TAILORED SURFACE DESIGN

Aiming towards a more detailed understanding of the lubrication mechanism of CNP-containing surfaces, the influence of the surface roughness as well as deterministic surface designs on the lubrication activity of CNP is investigated in **PAPER V, VI, VII and IX**. For this purpose, the different surfaces are coated using EPD in order to create homogeneous coatings with a defined thickness, allowing for copying of the generated surface topographies.

- *Surface roughness:*

It is found in **PAPER VI**, that the high aspect ratio and flexibility of 1-D CNT particles is beneficial for a constant lubrication, irrespective of the given surface roughness, since the particles can be dragged into the direct tribological contact region thus efficiently separating the contacting surfaces. Even though 0-D particles can separate the contacting surfaces and lubricate the contact by sliding/rolling, they lose this ability when interacting with a surface roughness higher than the particle diameter. Hence, with a particle diameter of 10 nm (at maximum) for OLC, the lubrication of technical surfaces or wear-subjected composite surfaces is not possible, which is also confirmed in **PAPER VIII**. The intrinsic lubrication mechanism of CNT is further found to be a mixture of two mechanisms. For one part, CNT are found oriented perpendicular to the sliding direction of the surfaces, separating the surfaces and being able to perform a sliding/rolling movement. For the other part, degraded CNT are found oriented parallel to the sliding direction of the surfaces, forming a lubricating graphitic carbon layer.

- *Surface design:*

Since the surface topography plays an important role for the lubrication activity of the CNP, a deterministic surface topography is created on a steel surface by DLIP using a nanosecond laser or by DLW using a femtosecond laser, which is thoroughly analyzed in **PAPER V, VII and IX**. Because of the aforementioned reasons, the as-produced line-like surface structures are coated exclusively with CNT and not OLC or ND. Using EPD as a coating technique, it is shown by focused ion beam (FIB) cross-sections and SEM, that the laser patterning-induced surface topography is copied homogeneously by the CNT coating. The coating of these surfaces with CNT is done for two reasons: First, the possibility to create self-lubricating surfaces throughout versatile structuring and coating techniques using CNT should be evaluated. Second, the surface state of a composite-type surface should be imitated and simplified by a periodic surface design in order to allow for a more detailed understanding of the lubricating mechanism of CNP reinforced composites. In this regard, a large amount of CNT agglomerates in CNT-reinforced MMC feature a diameter of 1 µm or more (similar to the produced line-like surface structures with a depth of 1 µm). Furthermore, since the CNT are not chemically or physically bonded to the surrounding Ni matrix, the created laser-patterned, CNT-coated surfaces can be considered similar to the CNT-reinforced composite surfaces.

It is found, that the CNT coating and laser patterning act synergetically. Although bare patterning or coating fails in terms of continuous friction reduction, long-lasting lubrication is achieved by combining both approaches (frictional reduction of up to a factor of 4 compared to the reference). The CNT coating is further found to act as a tribo-chemical protection layer, efficiently separating the surfaces, hindering the surfaces from strong oxidation (by acting as an oxygen diffusion barrier) and reducing the formation of oxidic wear particles. Hence, wear of the laser patterning induced surface topography is slowed down due to the CNT coating. Nevertheless, oxidic wear particles do form, but they are trapped in the surface depressions of the laser structure and thus are transferred out of the tribological contact. Additionally, the created surface depressions of the laser patterns act as solid lubricant storage, supplying the surface continuously with pristine CNT (as in the case of CNT-MMC surfaces) thus prolonging the longevity of the lubrication effect significantly (more than five times compared to the CNT-coated, unpatterned surface).

In this regard, a schematic model of the lubrication mechanism of the surfaces is provided in **PAPER V**. The general lubrication mechanism of the surface is based on elastic compression and restoration of CNT bundles, stored inside of the surface depressions and being continuously dragged into the direct tribological contact due to their high aspect ratio and flexibility. Raman analysis of the CNT in the wear tracks provides further insights onto their degradation mechanism, which is correlated to a three-stage amorphization trajectory model (see section 2.1.4). According to this model, nanocrystalline graphite is formed when CNT are tribologically stressed. In **PAPER IX**, the lubrication effect of CNT is discussed further and is found to act on a mixture of rolling/sliding of

CNT and graphitic lubrication by degraded CNT, which is presented in detail in a schematic model within this paper. In this regard, the degradation process of CNT, forming nanocrystalline graphite is very important, since pristine CNT can slide/role on top of formed graphitic layers, reducing the friction to COF values lower than what would be expected for a pure graphite-based lubrication.

Comparing the surface structures achieved using a nanosecond or femtosecond laser, a different laser-material interaction is observed. The ablation process of the femtosecond laser translates into the creation of surfaces with a higher load-bearing capacity. Hence, surfaces can be produced, which resemble even more the surfaces of CNT reinforced composite. In order to investigate the effect of the stored solid lubricant volume on the longevity of the lubrication effect, two different structural depths (1µm and 3µm) are chosen. Unexpectedly, the surfaces with less deep structures provide longer lubrication compared to the surfaces with deeper structures. Despite other influencing aspects discussed in **PAPER VII**, the steeper slope of the surface depressions of the deeper structures is found to be too high to allow for an elastic compression and restoration of the CNT bundles and thus the efficient supply of the contact with the solid lubricant.

Since the CNT-coated surfaces are similar to the CNT-reinforced composite surfaces, the presented lubrication mechanism models of **PAPER V, VII and IX** can be transferred to composite-type surfaces as well.

SELF-LUBRICATING MMC, STRESS COLLECTIVE AND CONTACT SITUATION

For a detailed investigation of the tribological behavior of CNP-reinforced MMC, the composites are reinforced with different concentrations of CNP (5, 10 and 20 vol%) and exposed to different geometrical contact situations (conformal and non-conformal), different relative humidities (4% and 45%) and different loads (in order to achieve fully elastic or elasto-plastic contact conditions) in **PAPER IV, VIII and IX**.

- *CNP concentration:*

In **PAPER VIII**, it can be seen that effective lubrication is observed only for CNT. The lubrication effect is more pronounced for higher concentrations, which is in good agreement with the findings of **PAPER IV**. Neither for ND nor for OLC, is a significant lubrication effect observable, which is explained by the particles being too small to be successfully brought into the tribological contact in order to separate the surfaces.

- *Relative humidity:*

The composites are investigated under different relative humidity in **PAPER IV, VIII and IX**, actively avoiding (in low humidity) or allowing (in medium humidity) for a graphite-based (intercalation/delamination) lubrication, respectively. Exclusively for CNT-reinforced composites, effective and constant lubrication is given under all tested conditions and particle concentrations. This

is explained with the high versatility of the lubrication mechanism of CNT. In the case of low humidity, lubrication is based on sliding/rolling of CNT on top of graphitic layers (which were formed by degraded CNT). For higher relative humidity, the lubrication is a mixture between sliding/rolling of CNT and a graphite-based lubrication.

- *Geometrical contact situation:*

Both, non-conformal and conformal contact conditions are analyzed in **PAPER VIII and IX**, respectively. In both cases, an effective lubrication is given for CNT. The lubrication is even more pronounced for conformal contact conditions, since a higher amount of CNT is present, lower contact pressures are applied and the surfaces can be separated more easily by CNT.

- *Loading condition:*

The contact loading is chosen based on contact mechanics simulations using the Jackson-Green model (using an Al_2O_3 ball as counter material) in **PAPER VIII**. In this simulation, the mechanical properties as well as the measured surface topographies of the contacting surfaces are taken into account. For a normal load of 100 mN, the composite bulk material behaves fully elastic whereas an elasto-plastic contact regime is reached at 8 N normal load. For low loads and relative humidity, the presence of CNT decreases a tribologically-induced surface oxidation as it has already been shown for the CNT coatings in **PAPER IV, V and VII**, which is not given for OLC- or ND-reinforced MMC. The lubrication mechanism of CNT in these composites is found to be based on the same mechanisms as in the laser-structured, CNT-coated surfaces, whereas the lubrication mechanism of the surfaces exposed to higher loads slightly differs. This is due to the formation of a homogeneous tribo-layer in all the CNP-reinforced composites, consisting of homogeneously intermixed Ni, NiO and carbon, which is investigated using TEM and EDS analysis. It is further observed, that cracks are formed within this layer, leading to the formation of individual, loosely-bonded sheets, which can freely move on top of each other or the substrate surface. The lubricating effects for CNT-reinforced composites is explained with the high aspect ratio and the possibility of CNT to be dragged in between the formed surface sheets, allowing the sheets to slide upon each other or the substrate due to the already described, intrinsic lubrication mechanism of CNT.

- *Sliding speed:*

Different linear sliding speeds are used in **PAPER IV, V, VI, VII, VIII and IX** from 1 mm/s, over 1 cm/s up to 1 m/s. Regardless of whether the surfaces are coated with CNT or reinforced with CNT, effective lubrication is provided in all cases, rendering the general lubrication effect insensitive to sliding speeds within these ranges.

All this highlights CNT as a very versatile solid lubricant, which can be used under various contact situations and environmental conditions in order to successfully create self-lubricating surfaces.

Even though they have shown homogeneous distribution, a high mechanical reinforcement effect and also potential lubrication effects, ND and OLC are not suited for self-lubricating surfaces.

Summarizing, a continuous supply of CNP into the tribological contact is the most important thing to consider for CNP based self-lubricating surfaces, which can be achieved by CNP coated surfaces with a deterministic surface topography and/or CNP reinforced-MMC. Only for CNT, an effective lubrication is given irrespective of all tested loads, speeds, surfaces, materials, relative humidity or contact mechanics. This can be explained with the high aspect ratio of CNT, allowing them to be dragged into the tribological contact. Lubrication is achieved for all conditions due to the different possibilities of CNT to lubricate the contact (particle sliding/rolling and/or graphite-based lubrication).

OBJECTIVE 3

The findings of **ALL PREVIOUS PAPERS** are combined in this final objective in order to create application-oriented advanced self-lubricating surfaces based on CNP in **PAPER IX**. This is achieved by manufacturing CNT-reinforced composites with a volume concentration of 20% based on the performance shown in **PAPER VIII**, laser structuring the composite surfaces using the femtosecond laser with a structural depth of 1 µm found in **PAPER VII** and subsequently coating the surface structures homogeneously by EPD with CNT in order to protect the surface and to reduce surface oxidation, as developed in **PAPER V, VI and VII**. Based on this development, a prototypical self-lubricating material has been processed and machined to be tested in a macroscopically loaded (20 N) conformal contact situation (similar to real testing conditions of a technical journal-type bearing). Continuously self-lubricating surfaces are produced, allowing for a maximum permanent reduction in friction and wear by a factor of 4 and 115, respectively, compared to a pure Ni surface with the lubrication mechanisms being fully understood.

4. INCLUDED PAPERS

4.0 Outline

I

Colloidal mixing is found to be a suitable technique for the processing of CNP-reinforced Ni-MMC with the dispersion process and the distribution of CNP in MMC being extensively analyzed. A functionalization or degradation of CNP can be avoided, still allowing for homogeneous particle distributions within the MMC. 0-D CNP and an sp^3-hybridization allow for the most homogeneous distributions, the smallest mean grain size and highest mechanical reinforcement effect.

II

The homogeneous distribution of ND in **PAPER I** is transferred to OLC by first manufacturing ND reinforced Ni-MMC and subsequently transforming ND to OLC within the already sintered composite by annealing. It is the first time in literature that the transformation process of ND to OLC within an MMC has been investigated.

III

The influence of CNP concentration on their distribution as well as the grain refinement effect is analyzed based on the processing method of **PAPER I**. Using the acquired experimental data, a modified Zener-model is introduced, predicting the mean grain sizes of the composites as a function of the CNP type and concentration and allowing for full process control of CNP Ni-MMC manufacturing.

IV

With the findings of **PAPER I and III**, a tribological comparison of CNT reinforced Ni-MMC and CNT-coated Ni (by drop casting CNT on a pure Ni sample) is conducted. It is found that a refined microstructure plays only a minor role regarding its effect on a frictional reduction. Much more important is the general presence or absence of CNP in the tribological contact. A continuous supply of CNP into the tribological contact is the most important thing to consider for CNP-based self-lubricating surfaces.

V

Based on **PAPER IV**, a simplified surface situation, comparable to CNT-reinforced composites, is reproduced, allowing for a more detailed understanding of the lubrication mechanism. This is achieved by creating a deterministic surface topography on steel surfaces using DLIP, subsequently coating these surfaces by electrophoretic deposition with CNT, copying the surface topography by the CNT coating. A schematic model, describing the lubrication mechanism of these surfaces is presented and the longevity of the lubrication is significantly extended (factor of 5) compared to unpatterned surfaces.

VI

The influence of surface roughness on the lubrication activity of 0-D and 1-D CNP is investigated. It is found that the high aspect ratio of 1-D particles is beneficial for a constant lubrication irrespective of the given surface roughness, since the particles can be dragged into the direct tribological contact region thus efficiently separating the contacting surfaces. 0-D particles lose their ability to lubricate the contact if a surface roughness higher than the particle diameter is reached.

VII

Based on the findings of **PAPER V and VI**, different surface designs are created by DLW using a femtosecond pulsed laser system. The created surfaces provide a higher load bearing capability than the surface of **PAPER V**. However, only for a specific surface design an efficient lubrication and a further prolongation of the lubrication effect up to almost 100 000 sliding cycles under the given loading conditions is achieved.

VIII

Based on the findings of **PAPER I, III and IV**, CNP reinforced Ni-MMC are produced with different CNP concentrations, all having the same microstructure. Using contact mechanics simulations and taking into account the mechanical properties and the surface topographies of the composites, tribological measurements under fully elastic and elasto-plastic contact conditions are conducted. Additionally, the composites are investigated under different relative humidity, actively avoiding (in low humidity) or allowing (in medium humidity) for a graphite-based lubrication. Exclusively for CNT reinforced composites, effective and constant lubrication is given under all tested conditions and the lubrication and wear mechanisms of the individual composites are investigated and discussed in detail using various high-resolution characterization methods.

IX

The findings of **ALL PREVIOUS PAPERS** are combined in this final work in order to create advanced self-lubricating surfaces based on CNP. This is achieved by manufacturing the most promising CNT reinforced composites of **PAPER VIII**, laser structuring the composite surfaces using the surface design of **PAPER VII** and subsequently coating the surface structures by EPD with CNT, which was developed in **PAPER V, VI and VII**. This way, constantly self-lubricating surfaces are produced, allowing for a maximum reduction in friction and wear by a factor of 4 and 115, respectively, compared to a pure Ni surface. Additionally, the lubrication and degradation mechanism of CNT in a tribological contact is investigated and presented in detail by Raman analysis in a schematic model.

I Dispersion analysis of carbon nanotubes, carbon onions, and nanodiamonds for their application as reinforcement phase in nickel matrix composites

Leander Reinert[1], Marco Zeiger[2], Sebastian Suárez[1], Volker Presser[2] and Frank Mücklich[1]

[1] Department of Material Science and Engineering, Saarland University, 66123 Saarbrücken, Germany
[2] INM – Leibniz Institute for New Materials, 66123 Saarbrücken, Germany

*Published in **"RSC Advances" (Impact factor (2018): 3.108)***
Reproduced by permission of The Royal Society of Chemistry.
Accessible online at: https://doi.org/10.1039/C5RA14310A

Own contribution:

Sample processing including particle dispersion and sintering; Dynamic light scattering; Zeta Potential measurement; Raman spectroscopy analysis; Scanning electron microscopy and particle distribution analysis; Electron backscatter diffraction; Vickers micro-hardness measurement; Writing; Discussion; Planning.

Abstract:

Dispersions of multi-wall carbon nanotubes, onion-like carbon, and nanodiamonds in ethylene glycol are produced using a homogenizer and an ultrasonic bath, altering the treatment time. The dispersed particles are then used as reinforcement phase for nickel matrix composites. These nanoparticles are chosen to represent different carbon hybridization states (sp^2 vs. sp^3) or a different particle geometry (0D vs. 1D). This allows for a systematic investigation of the effect of named differences on the dispersibility in the solvent and in the composite, as well as the mechanical reinforcement effect. A comprehensive suite of complementary analytical methods are employed, including transmission electron microscopy, Raman spectroscopy, dynamic light scattering, sedimentation analysis, zeta-potential measurements, scanning electron microscopy, electron back scatter diffraction, and Vickers microhardness measurements. It can be concluded that the maximum achievable dispersion grade in the solvent is similar, not altering the structural integrity of the particles. However, nanodiamonds show the best dispersion stability, followed by onion-like carbon, and finally multi-walled carbon nanotubes. The distribution and agglomerate sizes of the particles within the composites are in good agreement with the dispersion analysis, which is finally correlated with a maximum grain refinement by a factor of 3 and a maximum mechanical reinforcement effect for nanodiamonds.

Cite this as:
L. Reinert, M. Zeiger, S. Suárez, V. Presser, F. Mücklich, Dispersion analysis of carbon nanotubes, carbon onions and nanodiamonds for their application as reinforcement phase in nickel matrix composites. *RSC Advances* **2015**, 5, 95149-95159. (*https://doi.org/10.1039/C5RA14310A*)

RSC Advances

PAPER

View Article Online
View Journal | View Issue

Cite this: *RSC Adv.*, 2015, **5**, 95149

Dispersion analysis of carbon nanotubes, carbon onions, and nanodiamonds for their application as reinforcement phase in nickel metal matrix composites

L. Reinert,*[a] M. Zeiger,[ab] S. Suárez,[a] V. Presser[ab] and F. Mücklich[a]

Dispersions of multi-wall carbon nanotubes, onion-like carbon, and nanodiamonds in ethylene glycol are produced using a homogenizer and an ultrasonic bath, altering the treatment time. The dispersed particles are then used as reinforcement phase for nickel matrix composites. These nanoparticles are chosen to represent different carbon hybridization states (sp^2 *vs.* sp^3) or a different particle geometry (0D *vs.* 1D). This allows for a systematic investigation of the effect of named differences on the dispersibility in the solvent and in the composite, as well as the mechanical reinforcement effect. A comprehensive suite of complementary analytical methods are employed, including transmission electron microscopy, Raman spectroscopy, dynamic light scattering, sedimentation analysis, zeta-potential measurements, scanning electron microscopy, electron back scatter diffraction, and Vickers microhardness measurements. It can be concluded that the maximum achievable dispersion grade in the solvent is similar, not altering the structural integrity of the particles. However, nanodiamonds show the best dispersion stability, followed by onion-like carbon, and finally multi-walled carbon nanotubes. The distribution and agglomerate sizes of the particles within the composites are in good agreement with the dispersion analysis, which is finally correlated with a maximum grain refinement by a factor of 3 and a maximum mechanical reinforcement effect for nanodiamonds.

Received 20th July 2015
Accepted 29th October 2015

DOI: 10.1039/c5ra14310a

www.rsc.org/advances

1. Introduction

Tailoring of the physical properties of composite materials has been an extensively studied topic over the last decades. Lately, carbon nanomaterials have been introduced as very promising reinforcement candidates in composites to increase strength,[1–3] hardness,[4–6] electrical and thermal conductivity,[5,7,8] thermo-mechanical stability,[9] and reduce friction and wear.[10–12] Carbon allotropes can be found in a wide range of morphologies and configurations; they are also attractive reinforcement phases mainly due to their outstanding properties and low density compared to other reinforcement materials.[13–15]

For our work, we focus on three types of carbon nanoparticles (CNPs), namely multi-wall carbon nanotubes (MWCNT),[16] nanodiamonds (ND),[15] and onion-like carbons (OLC).[17] CNTs can be described as helical hollow cylinders of graphitic carbon (sp^2-hybridized) having one or multiple shells and a high aspect ratio (*i.e.*, quasi one-dimensional).[16] ND are spherical diamond nanoparticles with a diamond lattice spacing of 0.21 nm and a primary particle diameter of around 5 nm (*i.e.*, quasi zero dimensional).[15] Due to the synthesis *via* detonation reaction, ND are covered with functional groups and amorphous carbon layers. ND particles also can form agglomerates with sizes up to hundreds of nanometers.[18] Thermal annealing in inert atmosphere or vacuum allows to transform ND to OLC.[19] The latter are also known as carbon onions and can be understood as multi-shell fullerene nanoparticles (*i.e.*, quasi zero dimensional) with a typical spacing of 0.34–0.36 nm between the outer shells.[20,21] Depending on the synthesis method and conditions, the ratio between sp^3- and sp^2-hybridized carbon can be tuned, as well as the degree of carbon ordering.[19,22,23]

We chose these three particular CNPs as they show either a different carbon hybridization state or a different particle geometry. This allows for a systematic investigation of the effect of those differences on the particle distribution and the properties in a composite material.

Since a fine and homogeneous distribution of the particles is required to achieve an optimum reinforcing effect,[8] the main drawback of working with CNPs is their notorious tendency to agglomerate due to intermolecular forces like dipole–dipole forces or van-der-Waals forces.[24–26] This behavior is highly dependent on the synthesis conditions.[18,19,22,23] CNP agglomerates tend to reduce the intrinsic properties of the CNP and also

[a]*Department of Materials Science and Engineering, Saarland University, 66123 Saarbrücken, Germany. E-mail: l.reinert@mx.uni-saarland.de*
[b]*INM-Leibniz Institute for New Materials, Saarland University, 66123 Saarbrücken, Germany*

the matrix–reinforcement interface.[8] Hence, finding a way to efficiently disaggregate and distribute CNPs within a matrix material without significantly altering their structure or properties is the key to fully exploit the potential of CNP composites.

There are two mayor strategies for facile CNP de-agglomeration: mechanical milling and dispersion in solvents. Focusing on sp^2-hybridized CNPs, mechanical milling (*e.g.*, ball milling) is known to unbundle agglomerates efficiently, but this process also affects the particle morphology and defect state, in particular for CNT and OLC.[27–29] The second possibility can be sub-classified into two alternatives: (1) the nanoparticles can be functionalized (covalently or non-covalently), or (2) be dispersed in a suitable solvent without prior functionalization.[30] The covalent functionalization implies the dissociation of a C–C bond or the utilization of dangling bonds to enable surface functionalization (*e.g.*, hydroxyl, carboxyl or carbonyl groups), rendering the particles dispersible. This treatment procedure involves the opening of the structure, generating a weak point where the particle might mechanically fail. Furthermore, it does not only affect the mechanical properties of the particle, but many physical properties of the CNPs are diminished as well.[31–33]

All of the CNPs in this study show a strong tendency to agglomerate in their native (as received) form. In case of CNTs, their high aspect ratio, high flexibility, and strong attractive forces lead to a strong tendency to form bundles.[24,25] During unbundling, to avoid a change of the graphitic structure, it is possible to functionalize the CNT non-covalently by physisorption of molecules. This implies the use of surfactants, polymers, or organic molecule wrapping.[34–37] In several studies, the optimum CNT/solvent ratio for different solvents has been studied and some solvent systems have been identified that do not require prior carbon functionalization.[30]

Detonation nanodiamonds also show a strong tendency to form agglomerates.[26] During the synthesis, the detonation wave during the synthesis may generate dangling bonds at the surface of the ND that react and form covalent interparticle bonds, graphitic shells or surface functional groups which interact *via* dipole–dipole or van-der-Waals forces leading to agglomerates.[26] Similar to CNT, one way to disperse NDs is by covalent functionalization; depending on the target solvent, one would adapt either hydrophobic or hydrophilic functional groups on the surface of ND particles.[38,39] This can for example be achieved by using organic molecules like polymer brushes of polystyrene and poly(*t*-butyl methacrylate)[40] or by an esterification reaction of carboxylic acid chlorides on hydroxylated nanodiamonds.[41] Also a non-covalent functionalization of ND is possible, using different kinds of surfactants combined with prior chemical or thermal oxidation.[39,42,43]

OLCs derived by thermal annealing of ND also tend to form agglomerates; depending on the applied synthesis conditions, agglomeration is a result of onsetting particle–particle sintering and strong intermolecular forces.[19,22,23] Covalent functionalization may strongly improve the solubility of carbon onions in suitable solvents; for example, Liu *et al.* successfully used fluorination to severely improve the solubility in organic solvents.[44] It is also possible to use a surfactant like polyacrylic acid to significantly reduce agglomeration of OLCs.[29]

Our work was motivated by the need to find improved ways to modify metal matrix composites by employing suitable CNP materials. We exemplify the potentials and limitations of CNT, OLC, or ND nanoparticles for nickel matrix composites. As a first step, we employed a homogenizer and ultrasonication to derive dispersions of CNT, OLC, or ND in ethylene glycol. We excluded chemical post-synthesis treatment since the latter prohibits a proper analysis of the influence of the hybridization state of carbon atoms and the particle geometry on the particles dispersion. Such post-synthesis treatments would also add an additional step to the process while our goal was to explore the facile production of composite materials. To the best of our knowledge, this is the first systematic comparison of the dispersion of CNTs, OLCs, or NDs in a metal matrix. Dynamic light scattering (DLS) was used to determine the particle agglomeration sizes in the solvent. Additionally, the stability of the dispersions was investigated by sedimentation analysis and zeta-potential measurements. The structural integrity of the particles was analyzed by Raman spectroscopy as a function of the processing time by the homogenizer or the ultrasonic bath.

After this step, we adapted the CNPs to a sintered nickel matrix composite. We correlated the results from the comprehensive particle characterization with the distribution of the particles within the nickel matrix, the obtained microstructure, and the resulting mechanical reinforcement effect analyzed by scanning electron microscopy (SEM), electron back scatter diffraction (EBSD), and Vickers microhardness measurements. Nickel was chosen as matrix material as it forms only metastable carbides under very specific conditions, therefore being suited for a reinforcement based on CNPs with the parasitic emergence of interphases.[45] Additionally, the distribution of reinforcing particles in a metal matrix composite as well as their properties strongly influences the development of the reinforcing effect.[46] Therefore, for their subsequent utilization as precursors in composite materials manufacturing, it is of utmost importance to understand the disaggregation and colloidal stability of different (non-functionalized) CNPs in solvents.

2. Experimental

2.1 Processing

In this work, dispersions of MWCNT (Baytubes C150P from Bayer, purity > 95%, individual particle diameter of 5–20 nm), ND (NaBond Technologies Co., purity > 98%, individual particle diameter 4–8 nm), and nanodiamond-derived OLC[19] in ethylene glycol were analyzed. OLC were synthesized from the same ND powder mentioned before by annealing the material in graphite crucibles (30 mm in diameter and 20 mm in height) in a vacuum furnace with tungsten heaters (model: 1100-3580-W1, Thermal Technology Inc.) using a heating and cooling rate of 15 °C min^{-1}. The chamber pressure is between 10 mPa and 100 mPa. OLC are synthesized at 1750 °C with a holding time of 3 h.

For the dispersion process, we used a homogenizer (WiseTis, Witeg) and an ultrasonic bath (Sonorex Super RK 514 BH by Bandelin, 860 W, 35 kHz). In case of ultrasonic treatment, the strong shear force that can exfoliate the agglomerates comes from cavitation, which leads to a process of bubble formation,

growth, and collapse. The efficiency of this process can be correlated to the solvent parameters like viscosity, vapor pressure and surface tension, as well as the time, sonication frequency, and intensity.[30] Some of the most promising solvents for stable dispersions, like dimethylformamide (DMF), are highly toxic, which is complicating cost effective large-scale applications.[30] The solvent ethylene glycol has already been used successfully in other works and is not toxic.[47] Furthermore, polyole like ethylene glycol allow for a subsequent functionalization of carbon nanoparticles or the deposition of metal particles onto the carbon nanoparticles, establishing the possibility of further research work on this topic.[47] Hence, ethylene glycol is a versatile solvent and was therefore chosen for the present work. The concentration was kept constant for all three different CNP materials at 0.006 vol%. This is calculated after having measured the densities by gas pycnometry with a Micromeritics AccuPyc 1330 gas pycnometer using helium (purity grade: 5.0). Before, the powders were dried in a furnace at 120 °C for 1 h to remove any amount of adsorbed water. After ten purges, each sample was analyzed by 20 separate measurements with a fill pressure of 134 Pa and an equilibration rate of 34 Pa min^{-1}. The measured skeletal densities were 1.92 ± 0.01 g cm^{-3} for CNT, 1.97 ± 0.03 g cm^{-3} for OLC, and 3.30 ± 0.01 g cm^{-3} for ND.

The obtained dispersions were used to manufacture nickel matrix composites with Ni dendritic powder (Alfa Aesar, −325 mesh) with a particle volume content of 6.5%. This volume content is equivalent to 1.48 mass% of CNT, 1.52 mass% of OLC and 2.51 mass% of ND. The importance of the utilization of the volume fraction lies in the fact that it is the most direct way to compare the behavior to other composites (other matrices). In order to allow for a proper comparison of different carbon nanoparticles in the same metal matrix system, the volume amount of particles in the system must be kept constant instead of the mass fraction. A maximum reasonable concentration of CNTs in the nickel matrix was found to be 3 mass%, which is equivalent to about 12.5 vol%.[45] With this concentration, a density of 98% could be reached and a the grain refinement effect was maximized using nickel matrix composites. Higher concentrations lead to a decrease of the reinforcement effect due to a more pronounced re-agglomeration of the CNTs.[45] Based on this fact, a medium amount of the reinforcing carbon nanoparticles was chosen in this study.

After evaporating the solvent of the dispersions in a furnace at 150 °C, the powder was pressed to green pellets (pressure of 990 MPa) which can be sintered in a hot uniaxial press (axial pressure of 264 MPa) in vacuum (2×10^{-6} mbar) at 750 °C for 2.5 h. More information on the synthesis process is provided elsewhere.[48]

2.2 Characterization

Samples were analyzed as a powder dispersed on lacey carbon grids using transmission electron microscopy (TEM) (JEOL 2100F) operated at 200 kV.

To characterize the dispersion in ethylene glycol, the hydrodynamic radius of the particle agglomerates in the solvent is measured using dynamic light scattering (ALV Compact Goniometer) with a wavelength of 532 nm as a function of the time spent in the homogenizer or the ultrasonic bath. All spectra were recorded directly after the dispersion process to represent the dispersion state at this time. These results were then correlated to the sedimentation characteristics of the particles, measured using a Lumisizer (LUM GmbH) with 200–4000 rpm and a wavelength of 470 nm, taking ~24 h until all particles had settled. The dispersion stability was investigated by zeta-potential measurements with a particle charge detector (Mütek PCD-03 pH, BTG). Five dispersions of each type with the same particle volume concentration and a treatment of five minutes in the homogenizer and 20 min in the ultrasonic bath were measured and the resulting data was averaged. A conducting salt (ammonium acetate, purity > 97%, Alfa Aesar) with a concentration of 10^{-3} mol dm^{-3} was added to increase the conductivity of the solvent ethylene glycol while keeping the pH constant at 7.6 thus allowing for the measurement.[49]

Raman spectra were recorded using an inVia Raman microscope (Renishaw) with an excitation wavelength of 532 nm (2.33 eV) for the examination of CNT and OLC, as this wavelength is more sensitive to coupled modes induced by sp^2-hybridization of carbon atoms.[23] The data was recorded using a grating with 2400 lines per mm, a 50×-objective (numeric aperture: 0.9), a spectral resolution of 1.2 cm^{-1}, and a laser power of 0.2 mW. For ND, an UV-Raman spectrometer (developed by the Institute Jean-Lamour in Nancy, France) with a 50×-objective (numeric aperture: 0.55), a grating of 1800 lines per mm, a spectral resolution of 1.2 cm^{-1}, an excitation wavelength of 325 nm (3.81 eV), and a laser power of 0.2 mW was used due to the higher sensitivity to sp^3-hybridization of the carbon atoms.[23] The reference spectrum is measured using the as-received agglomerated carbon nanoparticle powders. During the dispersion of the different carbon nanoparticles in the ultrasonic bath, an aliquot was taken out of the dispersions with a pipette at the particular times (10, 20, and 120 min) and deposited onto a silicon wafer. The solvent was subsequently evaporated at 150 °C in a furnace. Finally, the agglomerates on the silicon wafer were measured with Raman spectroscopy to obtain the provided spectra. All Raman spectra were recorded three times with an acquisition time of 10 s to eliminate cosmic rays and to improve the signal-to-noise ratio. Additionally, a linear baseline subtraction and intensity normalization were conducted for all spectra. To identify peak positions and full width at half maximum (FWHM) data, a Lorentz fit was performed for all data. Spectra of the powders after the dispersion treatment were enabled by drying a droplet casted on a silicon wafer in a furnace at 150 °C.

After the production of the nickel matrix composites, the samples were grinded and polished (the finest polish was done using a diamond slurry containing diamond particles of 1 μm in diameter) and the distribution of the particles in the matrix was analyzed using a dual beam focused ion beam/field emission scanning electron microscopy (FIB/FE-SEM) workstation (FEI Helios NanoLab 600). The obtained SEM pictures were binarized (a4i analysis software) with a resolution of 62 nm per pixel to allow for a quantitative distribution analysis of the particle

agglomerates. Two pixels are needed to define an agglomerate. The mean grain size of the matrix after sintering is measured by EBSD with an EDAX TSL detector attached to the dual beam microscope. The scanned area is of 250 × 250 μm^2 applying an accelerating voltage of 20 kV, a current of 22 nA, and a step size of 0.3 μm. For the analysis, a grain is defined as at least two adjacent points with a maximum misorientation of 5° beyond which a grain boundary is determined. The acquired raw data was post-processed using confidence index (CI) normalization, followed by the removal of points with CI below 0.1. The grains intersecting the scan window were excluded from the analysis. Vickers microhardness measurements were performed with a Vickers microindenter (Durascan, Struers) with an indenting force of 0.98 N (HV 0.1) and a holding time of 10 s. For each sample, 20 measurements at different spots were conducted and averaged.

3. Results and discussion

3.1 Agglomerate size distribution

The three different CNP materials were first characterized using TEM (Fig. 1). It can be seen that the particles show the characteristic morphology and atomic structure of MWCNT (Fig. 1a and d), OLC (Fig. 1b and e), and ND (Fig. 1c and f) as described in literature.[15,16,18,20,21] OLCs consist of several spherical shells with a spacing of 0.34–0.36 nm. The primary particles are connected to each other by local sintering and graphitic connections and show a diameter between 5 nm and 10 nm.[20,21] ND shows a diamond lattice spacing of 0.21 nm and ND particles are engulfed by amorphous carbon layers.[18] The average size of ND particles is comparable to that of OLC. The ND and OLC particles exhibit local formation of hard aggregates due to the synthesis process.[19,26] This feature complicates the dispersion process because of the covalent bonding and sintering of the particles. For CNTs, the high aspect ratio can lead to a mechanical interlocking, resulting in the formation of agglomerates that have to be disentangled.[24] TEM is a highly localized method to investigate the particle structures or agglomeration sizes in vacuum (*i.e.*, not in the solvent medium). To study the dispersion process of nanoparticles, methods have to be used which can be applied to characterize the particles in liquids, like DLS. As a starting point for the ultrasonic treatment ($t = 0$), the particle powders (CNT, OLC, or ND) were dispersed in ethylene glycol using the homogenizer for 5 min which breaks-up the initially large agglomerates (up to 1 mm). The results are exemplified in Fig. 2, showing the number fraction of particles as a function of the hydrodynamic radius for different treatment times in the ultrasonic bath.

Starting with a hydrodynamic radius of up to 250 nm after the treatment with the homogenizer ($t = 0$), the hydrodynamic radius of all particles decreases over the first 20 min of ultrasonication. However, longer sonication yields no significant further decrease of the radius, even if the particles are treated for up to 2 h. Therefore, a saturation of the hydrodynamic radius can be found for all kinds of particles at around 40–70 nm. Based on this fact, the dispersions used for the composite manufacturing were all treated for 5 min in the homogenizer and 20 min in the ultrasonic bath. This observation is in good agreement with the work of Krüger *et al.*[18] who developed a model classifying ND agglomerates in three different sizes, of which only the first two, namely large agglomerates (radius of 10–15 μm) and intermediate agglomerates (radius of 1–1.5 μm), could be broken up mechanically in a solvent using an ultrasonic bath. Yet, core aggregates (radius of 50–100 nm) could only be disaggregated by functionalizing the ND.[18]

The agglomerate sized derived from DLS data are complicated by the shape of CNPs. Commonly, DLS is used for analysis only of spherical shaped particles,[50] the latter being an acceptable approximation for ND and OLC. In contrast to that, the high aspect ratio of a single CNT prohibits the assumption of a spherical form, whereas a CNT agglomerate can be approximated to have an overall spherical shape. In principle, measuring the hydrodynamic radius of CNT agglomerates can be done by DLS.[51] However, even then, we have to consider that DLS only shows a snap shot of the maximum dispersion grade of the different particles. Therefore, we need to employ a complementary technique to analyze the dispersion stability by means not directly dependent on the shape of the particles. Thus, the next section is dedicated to dispersion stability testing by centrifugal sedimentation analysis.

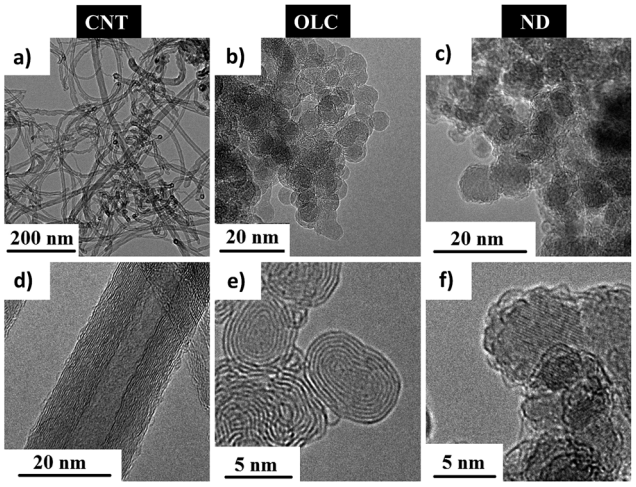

Fig. 1 TEM images of MWCNT (a, d), OLC (b, e), and ND (c, f) nanoparticles.

3.2 Stability of the dispersions

Fig. 3 shows the results for the velocity distributions from centrifugal sedimentation analysis of the dispersions treated 5 min in the homogenizer and 20 min of sonication. Both plots present the vol% of particles sedimenting with a specific velocity. The cumulative plot and the density distribution both show the same data but differ in the way of illustration. The density distribution (Fig. 3b) demonstrates all details of the distribution, for example the mean value, whereas the cumulative version (Fig. 3a) gives the area under the density function. This means the cumulative approach sums up all the volume percentages until a defined velocity. For example for CNT

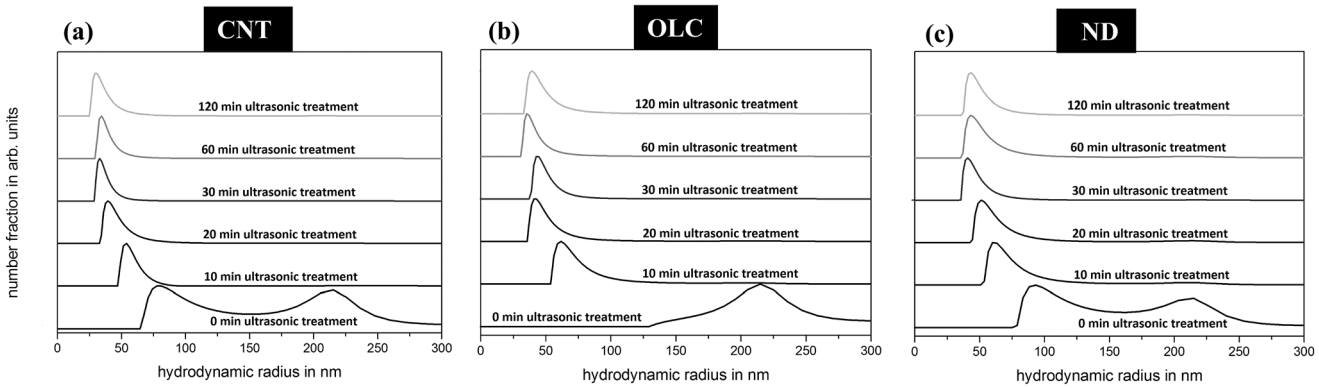

Fig. 2 DLS data of (a) CNT, (b) OLC, and (c) ND in ethylene glycol after different times of ultrasonic treatment. The spectrum of at 0 min is equal to a pre-treatment of 5 min in the homogenizer to break up the largest agglomerates.

roughly 40 vol% of the particles sediment with maximum 10 μm s^{-1}. This kind of distribution function makes it easier to compare between different datasets because less details are shown compared to the density distribution. Using this method, the dispersion stability and re-agglomeration behavior of the different particles can be analyzed. The data are strongly dependent on the particle densities. As CNT show the lowest density (similar to OLC) and the highest sedimentation velocity (Fig. 3a), they seem to re-agglomerate most quickly after the dispersion process, thus forming the largest agglomerates. Although the maximum sedimentation velocities of ND and OLC are identical, OLC show a slower sedimentation velocity for up to ~70% of the distribution than ND (Fig. 3a). However, as ND features a 1.7 times higher density than OLC, the OLC particles seemingly build up larger maximum agglomerates than ND and still sediment slower as their density is much smaller. Consequently, the tendency to re-agglomerate and the dispersion stability differ. The ND dispersion clearly shows the sharpest peak in Fig. 3b, indicating a more homogeneous agglomerate diameter distribution.

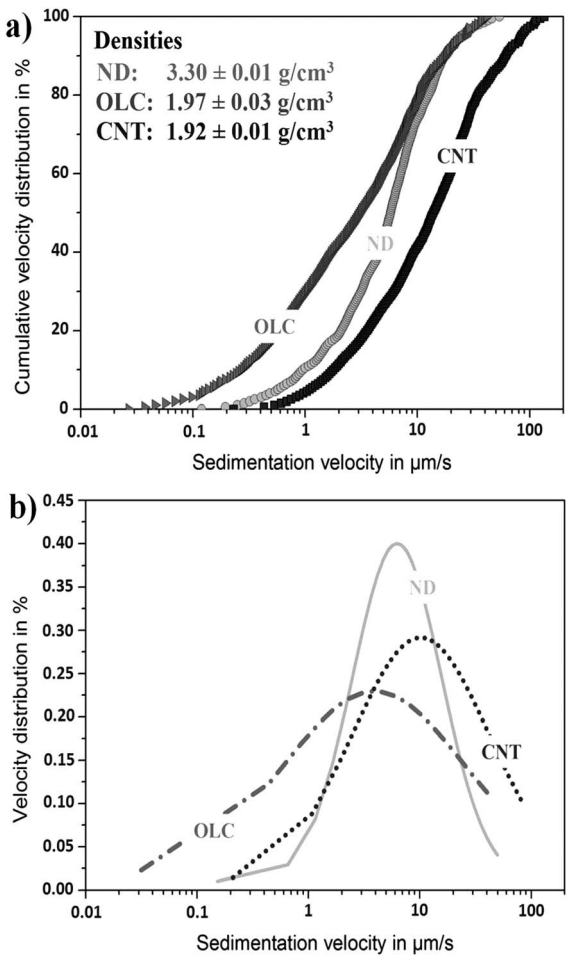

Fig. 3 Sedimentation analysis of CNT, OLC, and ND dispersion in ethylene glycol, showing (a) the sedimentation velocity of the particles as cumulative plot (including particle densities) and (b) the fitted data using a log-normal function.

In summary, the ND dispersion is the most stable dispersion and most suitable as precursor for a composite manufacturing, whereas the CNT dispersion tends to be the least stable one with the largest agglomerates. Zeta-potential measurements confirm this assumption, allowing for a quantitative evaluation of the dispersion stability. A dispersion showing an absolute value of the zeta-potential higher or lower than ±50 mV is considered to be stable.[52] The closer the zeta-potential approaches 0, the more unstable the dispersion becomes. In Table 1, the results of the zeta-potential measurements for the three different particle dispersions types are summarized. The ND dispersions show a slightly higher zeta-potential than CNT and OLC and the zeta-potential of OLC appears to be similar to the potential of the CNT dispersions within the scatter of the method. Therefore,

Table 1 Mean values and standard deviations of five zeta-potential measurements for each particle type in ethylene glycol with a concentration of 10^{-3} mol dm^{-3} of ammonium acetate

Particle	Zeta-potential in mV
CNT	−21.7 ± 1.4
OLC	−24 ± 1.9
ND	−31.6 ± 2.4

the dispersion of ND presents itself as the most stable one, which is in good agreement with the results of the sedimentation analysis.

The difference in the sedimentation characteristics between CNT and OLC cannot be explained only by a different zeta-potential. As the zeta-potential is similar and the main difference between CNT and OLC is based on their morphology, the different agglomeration behavior can be a consequence of the high aspect ratio of CNT as well as their larger dimension, resulting in a morphologically favored agglomeration effect.[24] In the case of ND, functional groups may be present on the surface due to the synthesis, resulting in a chemically more stabilized dispersion.[19]

3.3 Influence of the dispersion process on the structural integrity of the particles

Conventional processing, for example *via* ball milling, may yield a good dispersion, but is usually at the expense of structural CNP degradation, leading to a poor reinforcing effect and potential chemical degradation when used in metal matrix composites.[29,53] In our study, we therefore chose sonication as a gentler method for particle dispersing. To facilitate the de-aggregation, a homogenizer is previously used to break up larger agglomerates (up to *ca.* 1 mm), thus reducing the total time needed to disperse the particles in the ultrasonic bath and also reducing the total amount of stress on the particles. However, since the particles are still mechanically highly stressed, a change or variation of the structural state may still be possible and needs to be investigated.[51]

A well-established method to study the defect state of CNPs is Raman spectroscopy.[54,55] In Fig. 4(a and b), Raman spectra using visible light laser excitation of CNT and OLC can be seen after different ultrasonication treatment times. The first peak at around 1350 cm^{-1} corresponds to the D-mode, generated by the presence of defects in the CNT or OLC structure, for example a disruption of the aromatic system of π-electrons in the framework.[44,56] Close to 1600 cm^{-1}, the G-mode is detected which can be attributed to the tangential vibrations of carbon atoms with sp^2-hybridization and can be used to describe their crystalline state.[55–57] The shoulder at the G-mode at higher wavenumbers can be assigned to the different resonance types of the inner and outermost of the MWCNT.[58] Finally, the G′-mode is observed at around 2700 cm^{-1}, corresponding to an overtone of the defect-related D-mode, and its intensity is proportional to the sample purity level.[56]

A quantitative analysis of the Raman spectra can be accomplished by evaluating the normalized intensity ratios D/G and the G′/D, which are shown as a function of time in the ultrasonic bath for CNT (Table 2) and OLC (Table 3). Since the Raman signal is sensitive to the irradiated volume and in order to obtain a reliable comparison between spectra, it is generally accepted that the correlation should be carried out with intensity ratios. Specifically, the D/G ratio corresponds to the defect density whereas the G′/D ratio can be correlated with the purity level of graphitic material.[55] Tuinstra and Koenig[59] observed that the D/G ratio is inversely proportional to the mean domain size in graphitic structures, whereas the domain size is defined as the mean distance between two consecutive defects (*e.g.*, crystal boundary in polycrystalline graphite). Since then, this ratio has been extensively used as an indicator of the defect density in sp^2 carbons. DiLeo *et al.*[55] showed that the G′/D ratio is proportional to the purity of a MWCNT sample. The explanation is based on the fact that the G′ band is more sensitive than the D band to carbonaceous impurities, deriving in a very close correlation to average purity values obtained by thermogravimetry. The Raman full width at half maximum (FWHM, Γ) can be correlated with the degree of structural ordering.[60] Ideally, the defect density should be as low as possible, since defects can act as nucleation centers for failure propagation, leading to reduced mechanical properties.[61] Based on the data, neither CNT nor OLC show a significant variation of the initial D/G or G′/D ratio as well as the FWHM, even after 2 h of sonication. This leads to the assumption that both particle types are not significantly altered from the initial structural state during the dispersion process.

The structural integrity analysis of the ND dispersions has to be discussed separately, as the detected bands differ from the ones of CNT and OLC. It is noteworthy that Raman analysis of ND materials required UV-laser radiation in contrast to the use of visible light laser for sp^2-hybridized nanocarbons. For all ND

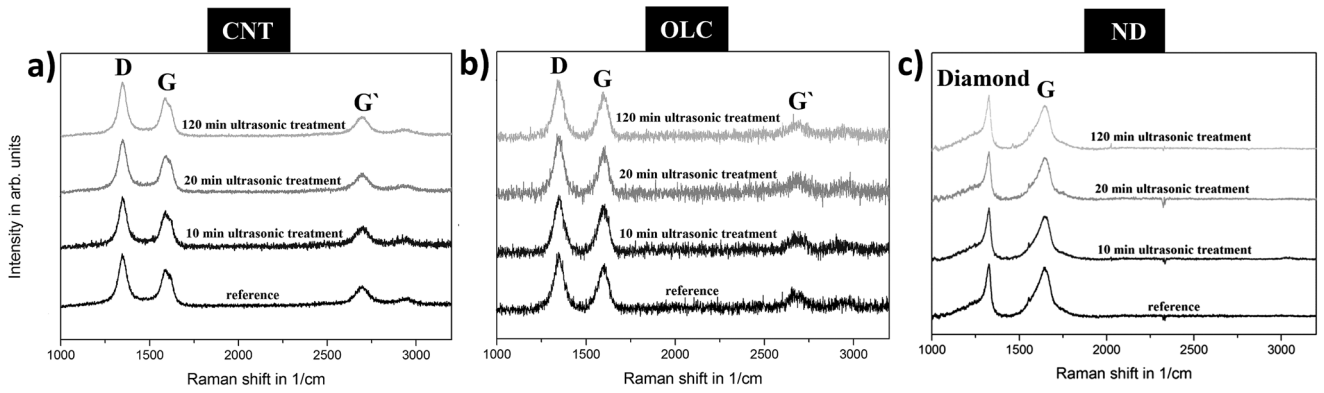

Fig. 4 Raman spectra of CNT (a), OLC (b) and ND (c) on a silicon wafer as a function of the time spent in the ultrasonic bath in the solvent ethylene glycol.

Table 2 Normalized Raman data of CNT as a function of time spent in the ultrasonic bath. A Lorentz fit was performed to identify the peak positions and the FWHM (Γ)

D ($1348\ cm^{-1}$)	G ($1593\ cm^{-1}$)	G′ ($2696\ cm^{-1}$)	Γ_D in cm^{-1}	Γ_G in cm^{-1}	$\Gamma_{G'}$ in cm^{-1}	D/G	G′/D	t in min
1	0.73	0.44	58.4	75.5	91.2	1.37	0.44	Ref
1	0.75	0.49	55.8	73.3	93.5	1.33	0.49	10
1	0.72	0.41	59.7	75.2	91.8	1.39	0.41	20
1	0.72	0.40	56.0	72.9	90.6	1.39	0.40	120

Table 3 Normalized Raman data of OLC as a function of time spent in the ultrasonic bath. A Lorentz fit was performed to identify the peak positions and the FWHM (Γ)

D ($1348\ cm^{-1}$)	G ($1597\ cm^{-1}$)	G′ ($2686\ cm^{-1}$)	Γ_D in cm^{-1}	Γ_G in cm^{-1}	$\Gamma_{G'}$ in cm^{-1}	D/G	G′/D	t in min
1	0.81	0.40	66.2	64.5	118.3	1.23	0.40	Ref
1	0.85	0.38	64.4	63.1	127.2	1.18	0.38	10
1	0.86	0.41	61.5	60.9	119.8	1.16	0.41	20
1	0.79	0.32	64.7	63.0	122.5	1.27	0.32	120

Table 4 Normalized Raman data of ND as a function of time spent in the ultrasonic bath. A Lorentz fit was performed to identify the peak positions and the FWHM (Γ)

Diamond ($1320\ cm^{-1}$)	G ($1629\ cm^{-1}$)	$\Gamma_{diamond}$ in cm^{-1}	Γ_G in cm^{-1}	Diamond/G	t in min
1	0.92	39.8	103.8	1.23	Ref
1	0.85	38.4	96.9	1.18	10
1	0.89	36.5	93.1	1.16	20
1	0.83	38.2	98.5	1.27	120

spectra, a down-shifted diamond band at ~1320 cm^{-1} (diamond) can be observed as well as a band at ~1630 cm^{-1}, often simply tagged as G-mode in analogy to sp^2-hybridized (graphitic) carbon (Fig. 4c). However, at least three separate peaks assigned to O–H bending vibrations (~1640 cm^{-1}), C=O stretching vibrations (1740 cm^{-1}), and finally sp^2-hybridized carbon band (1590 cm^{-1}) are superimposing to generate this band.[62] For the studied ND, we see very little variation of the Γ diamond and the diamond/G ratio (Table 4). In conclusion, just like for OLC and CNT, we also see no statistically significant variation of the sample's structural ordering after de-aggregation.

3.4 Microstructural investigation of the reinforced nickel matrix composites

In Fig. 5a–c, SEM pictures (backscattered electrons) of the three different composites are shown all containing 6.5 vol% of CNPs. The black areas are particle agglomerates, whereas the different shades of gray correspond to different grain orientations of the nickel matrix. Based on the binary pictures in Fig. 5d–f we see that the CNTs yield significantly later aggregates (up to 15 μm) in the nickel matrix composites (Ni CNT) compared to the other composites. The smallest maximum size of agglomerates can be detected for ND nickel matrix composites (Ni ND) and is about 3 μm. This is in excellent agreement with the results from sedimentation analysis. Not only the agglomerate sizes differ, but also the distribution homogeneity within the matrix as the small agglomerates in the case of Ni ND are most evenly distributed. The individual agglomerate area of the binary SEM pictures of Fig. 5d–f as a function of the total image area fraction of the agglomerates can be used for a quantitative analysis (Fig. 6). Using the binarized images, black pixels are assigned to agglomerates and white pixels to the metal matrix. The individual pixel size is 62 nm, agglomerates smaller than that cannot be detected, but as the minimum agglomerate diameter measured by DLS is 80 nm, an even higher resolution would not be reasonable. As seen, the agglomerate size distribution is the smallest for Ni ND composites and by far the largest for Ni CNT composites, aligning well with the sedimentation analysis. An evenly distribution of small agglomerates is the most promising reinforcement method for metal matrix composites, since it can homogeneously act on the grain boundaries during grain growth, and thus reduce recrystallization processes enhancing the microstructural thermal stability.[63] Forces can be homogeneously transferred by the particles as a larger interface between the particles and the matrix is available.[2,63]

Although a large interface area of particles and matrix is required for optimized properties, the formation of a brittle interphase (*e.g.*, carbide formation) at the interface may severely impact the mechanical properties. A brittle interphase could act as nucleation center for failure propagation, as it has the tendency to crack very easily.[8] To inhibit this, the carbon particles should show a low defect density and a matrix material should be chosen, which does not act as carbide creator.[8] As it is shown elsewhere, nickel is a reasonable candidate for a comparison of different carbon particles as it only forms

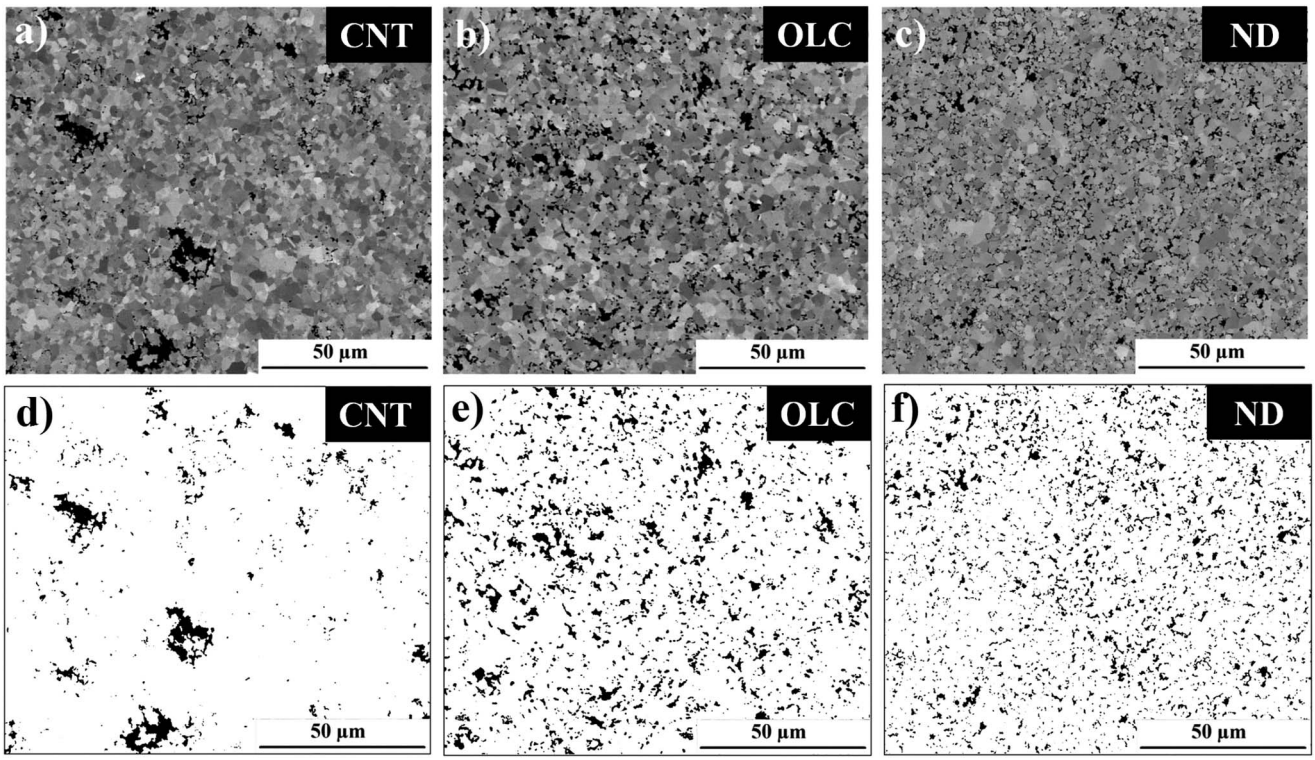

Fig. 5 SEM pictures of (a) CNT-, (b) OLC-, and (c) ND- nickel matrix composites after polishing at the top surface. The uniaxial pressure is applied at the bottom and top surface of the samples. The pictures are binarized for (d) CNT-, (e) OLC-, and (f) ND- nickel matrix composites to enable a better qualitative comparison. The agglomerate sizes decrease significantly and the distribution of the particles becomes more homogenous from (a) to (c) or rather (d) to (f).

metastable carbides; yet, no carbide phases are observed in the case of CNTs for the used conditions in our work.[45,64] The observed differences in agglomerate sizes and distribution patterns can be well correlated with the results from dispersion analysis. The sedimentation analysis and zeta-potential measurement demonstrated that ND present the most stable dispersion in ethylene glycol. The production of the nickel matrix composites starts with the evaporation of the solvent in a furnace at 150 °C for 5 h. During this time, the different CNP dispersions re-agglomerate in different ways, which can be explained by the different hybridization states of the carbon atoms and the different particle morphologies. Attractive forces occur between the particles due to the π-bonding of the sp^2-hybridization of carbon atoms in OLC and CNT particles. The large aspect ratio of CNT further leads to possible mechanical interlocking, enabling the emergence of even larger agglomerates than in the case of OLC. Despite the fact that ND show a similar morphology compared to OLC, their sp^3-hybridized carbon atoms are subjected to smaller attractive forces between each other as well as a stabilizing effect of the attached functional groups from the synthesis process. This translates into superior dispersion grade and stability than that of both, CNT or OLC dispersions.

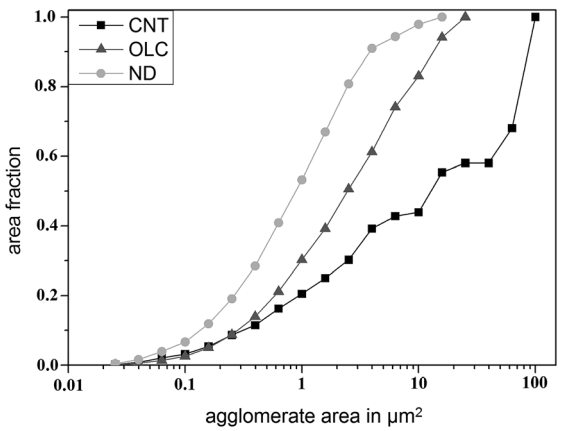

Fig. 6 Individual agglomerate area as a function of the total image agglomerate area (area fraction) in Fig. 5d–f with a resolution of 62 nm per pixel.

The possible grain refinement effect of the different particle types and distributions can be investigated by performing EBSD measurements on an unreinforced nickel reference and on the samples already investigated by SEM (Fig. 7). The mean grain size of the nickel matrix is significantly reduced by the addition of 6.5 vol% of CNPs up to a factor of 3 for ND and OLC. Furthermore, the Ni CNT composites show larger grains than Ni OLC or Ni ND composites. This can be explained by the agglomerate distribution, as seen from SEM. As the distribution of ND and OLC particles is much more homogenous than the CNT particle distribution, they can homogeneously act as obstacle for the grain boundaries during grain growth through

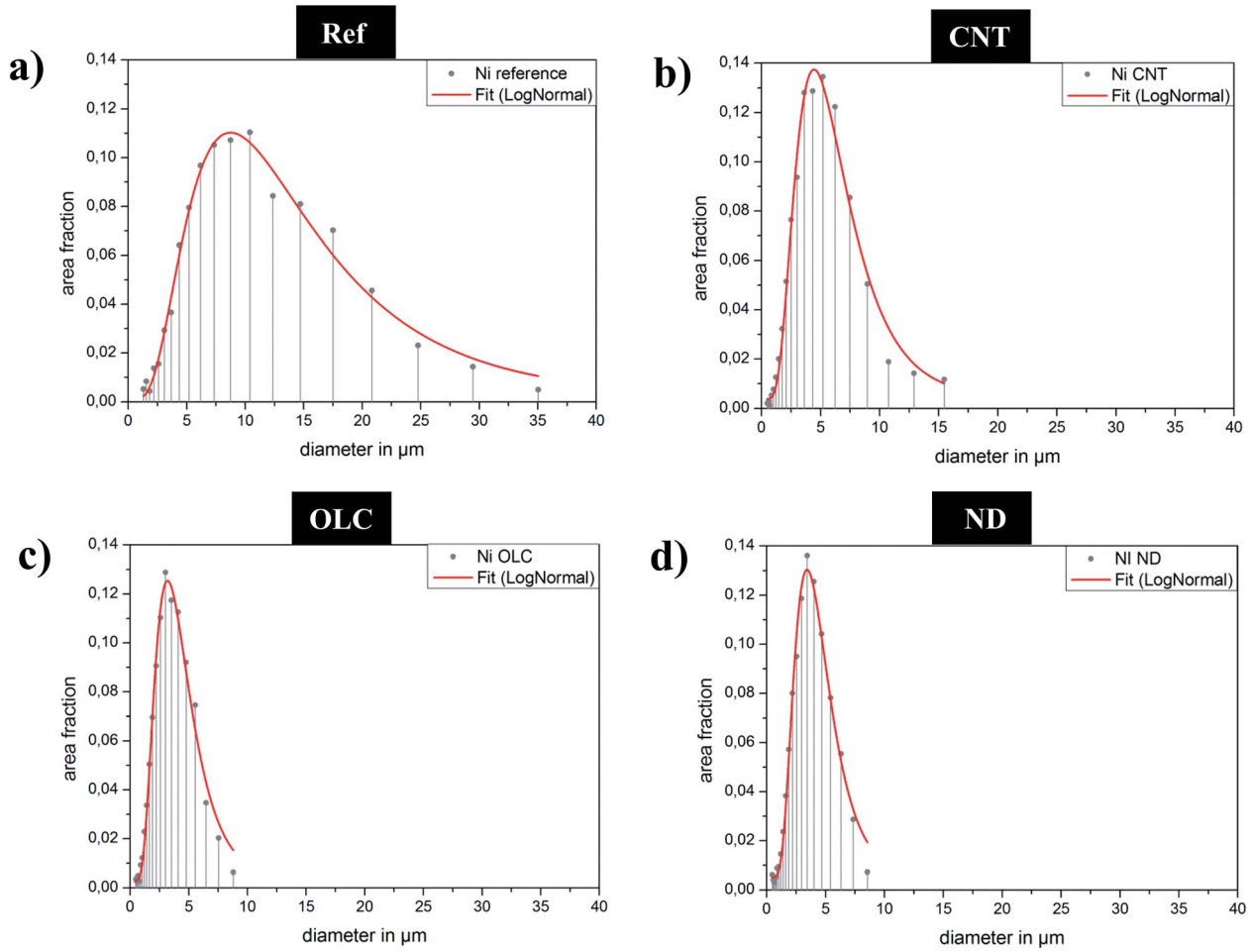

Fig. 7 Grain size distribution of (a) unreinforced nickel reference, (b) Ni CNT, (c) Ni OLC, and (d) Ni ND composites. A LogNormal fit is performed to calculate the mean grain size and the fitted curves are plotted as solid lines (red).

sintering, and thus leading to a finer grain size distribution.[45,63] Although Fig. 6 shows significant differences in the agglomerate size distribution of the Ni ND and Ni OLC composites, their similar grain size distribution is reasonable. This can be explained as the grain refinement effect is known to be more dependent on the agglomerate distribution within the matrix material rather than on the actual agglomerate size.[63]

Grain refinement directly influences the mechanical properties of the material (*e.g.*, hardness or strength).[45] We performed Vickers microhardness measurements on the composite samples to analyze this effect. The results can be correlated with the mean grain size, as seen in Table 5, and the microhardness has been increased when comparing the nickel reference with the CNP reinforced samples. In good correlation to the grain refinement, the Ni CNT sample shows the lowest hardness of the reinforced samples. This can be explained with the larger grain sizes in comparison to Ni OLC and Ni ND, due to the Hall–Petch effect.[63,65] Although the grain sizes of Ni OLC and Ni ND composites do not differ much, the microhardness of Ni ND is higher than for Ni OLC. This could be due to the smaller ND agglomerate size in Ni ND that allow for a larger interface between ND and the nickel matrix, being able to efficiently transfer the external forces to a higher amount than the Ni OLC composites.[2] Rather small agglomerates are known to enable the Orowan mechanism, thus leading to a reinforcing effect of the composite.[63] The difference in hardness of the composites could also be attributed to differences in the mechanical properties of the OLC and ND particles themselves.

In addition to that, if the particles are distributed unevenly, such as for the Ni CNT composites, depletion zones can exist, that are not reinforced at all. These areas lead to an abnormal grain growth during sintering, ending up with inhomogeneous composite properties. This induces weak spots in the composite

Table 5 Mean grain sizes and mean values of Vickers microhardness measurements of the unreinforced nickel reference and the samples reinforced with CNT, OLC or ND

Sample	Mean grain size in µm	HV 0.1
Ni reference	12.9 ± 0.5	109 ± 6
Ni CNT	5.7 ± 0.2	119 ± 8
Ni OLC	4.2 ± 0.1	125 ± 4
Ni ND	4.0 ± 0.1	135 ± 4

material, reducing the mechanical reinforcement effect and generating anisotropy in the properties as can be seen at the higher standard deviation for the hardness of the Ni CNT composites.[2,66]

Summarizing, a low aspect ratio and the sp^3-hybridization seems to benefit a small agglomerate size and homogenous distribution of CNPs within a metal matrix composite, thus leading to a strong grain refinement and beneficial mechanical reinforcement effect.

4. Conclusions

The dispersion process of non-functionalized MWCNT, OLC, and ND in ethylene glycol using a homogenizer and an ultrasonic bath was studied. The dispersions were used as precursor for the production of nickel matrix composites. In particular, using Raman spectroscopy we found that no damage was inflicted upon the CNPs due to the dispersion process. Yet, although the maximum dispersion grade in the solvent is similar, ND show the best dispersion stability, followed by OLC, and finally MWCNT. This observation is in good agreement with the distribution and agglomerate sizes of the particles in the composite as ND show the smallest and MWCNT the largest agglomerate sizes. In addition, a low aspect ratio and the sp^3 hybridization is found to be beneficial for both, a small agglomerate size in the dispersions as well as a homogeneous distribution of small agglomerates within the composite. Finally, a maximum grain refinement by a factor of 3 and a maximum mechanical reinforcement effect of around 25% (Vickers microhardness) are observed for Ni ND composites. This observation aligns perfectly with the results of the dispersion analysis.

Acknowledgements

The present work is supported by funding from the Deutsche Forschungsgemeinschaft (DFG, project: MU 959/38-1). L. R., S. S., and F. M. wish to acknowledge the EFRE Funds of the European Commission for support of activities within the AME-Lab project. This work was supported by the CREATe-Network Project, Horizon 2020 of the European Commission (RISE Project No. 644013). M. Z. and V. P. thank Prof. E. Arzt (INM) for his continuing support. Dr P. Miska is acknowledged for UV-Raman measurements at the Institute Jean Lamour (Nancy, France). Dr C. Gachot, Dr A. Rosenkranz, Dr M. Hans, B. Bax, and N. Souza are kindly acknowledged for valuable discussions.

References

1 J. Y. Hwang, B. K. Lim, J. Tiley, R. Banerjee and S. H. Hong, *Carbon*, 2013, **57**, 282–287.
2 S. R. Bakshi and A. Agarwal, *Carbon*, 2011, **49**, 533–544.
3 D. Nunes, M. Vilarigues, J. B. Correia and P. A. Carvalho, *Acta Mater.*, 2012, **60**, 737–747.
4 D. Nunes, J. B. Correia and P. A. Carvalho, *Microsc. Microanal.*, 2013, **19**, 2013.
5 V. Livramento, J. B. Correia, N. Shohoji and E. Ōsawa, *Diamond Relat. Mater.*, 2007, **16**, 202–204.
6 J. N. Boland and X. S. Li, *Materials*, 2010, **3**, 1390–1419.
7 L. Kumari, T. Zhang, G. Du, W. Li, Q. Wang, A. Datye and K. Wu, *Compos. Sci. Technol.*, 2008, **68**, 2178–2183.
8 A. Agarwal, S. Bakshi and D. Lahiri, *Carbon Nanotubes-Reinforced Metal Matrix Composites*, 2011.
9 D. Nunes, J. B. Correia and P. A. Carvalho, *Microsc. Microanal.*, 2012, **18**, 73–74.
10 Y. Li, B. X. Li and W. J. Zou, *Appl. Mech. Mater.*, 2011, **80–81**, 683–687.
11 A. Hirata, M. Igarashi and T. Kaito, *Tribol. Int.*, 2004, **37**, 899–905.
12 K. Miyoshi, K. W. S. Jr, R. L. Vander Wal, R. Andrews and A. Sayir, *Tribol. Lett.*, 2005, **19**, 191–201.
13 Y. Gogotsi and V. Presser, *Carbon Nanomater.*, 2014, 279–298.
14 S. R. Bakshi, D. Lahiri and A. Agarwal, *Int. Mater. Rev.*, 2010, **55**, 41–64.
15 V. N. Mochalin, O. Shenderova, D. Ho and Y. Gogotsi, *Nat. Nanotechnol.*, 2012, **7**, 11–23.
16 S. Iijima, *Nature*, 1991, **354**, 56–58.
17 J. Cebik, J. K. McDonough, F. Peerally, R. Medrano, I. Neitzel, Y. Gogotsi and S. Osswald, *Nanotechnology*, 2013, **24**, 1–10.
18 A. Krüger, F. Kataoka, M. Ozawa, T. Fujino, Y. Suzuki, a. E. Aleksenskii, a. Y. Vul' and E. Ōsawa, *Carbon*, 2005, **43**, 1722–1730.
19 M. Zeiger, N. Jäckel, M. Aslan, D. Weingarth and V. Presser, *Carbon*, 2015, **84**, 584–598.
20 H. W. Kroto, J. R. Heath, S. C. O'Brian, R. F. Curl and R. E. Smalley, *Nature*, 1985, **318**, 162–163.
21 D. Ugarte, *Nature*, 1992, **359**, 707–709.
22 K. Bogdanov, A. Fedorov, V. Osipov, T. Enoki, K. Takai, T. Hayashi, V. Ermakov, S. Moshkalev and A. Baranov, *Carbon*, 2014, **73**, 78–86.
23 O. O. Mykhaylyk, Y. M. Solonin, D. N. Batchelder and R. Brydson, *J. Appl. Phys.*, 2005, **97**, 1–16.
24 S. D. Bergin, Z. Sun, D. Rickard, P. V Streich, J. P. Hamilton and J. N. Coleman, *ACS Nano*, 2009, **3**, 2340–2350.
25 S. Castro, PhD Thesis, Saarland university, 2007.
26 A. Pentecost, S. Gour, V. Mochalin, I. Knoke and Y. Gogotsi, *ACS Appl. Mater. Interfaces*, 2010, **2**, 3289–3294.
27 N. Pierard, a. Fonseca, J.-F. Colomer, C. Bossuot, J.-M. Benoit, G. van Tendeloo, J.-P. Pirard and J. Nagy, *Carbon*, 2004, **42**, 1691–1697.
28 N. Pierard, A. Fonseca, Z. Konya, I. Willems and G. van Tendeloo, *Chem. Phys. Lett.*, 2001, **335**, 1–8.
29 J.-Y. Lee, K.-H. Cho, D.-P. Lim, Y.-B. Lee and D.-S. Lim, *Appl. Phys. A*, 2007, **88**, 693–697.
30 Q. Cheng, S. Debnath, E. Gregan and H. J. Byrne, *J. Phys. Chem. C*, 2010, **114**, 8821–8827.
31 F. Avilés, J. V. Cauich-Rodríguez, L. Moo-Tah, a. May-Pat and R. Vargas-Coronado, *Carbon*, 2009, **47**, 2970–2975.
32 N. Karousis, N. Tagmatarchis and D. Tasis, *Chem. Rev.*, 2010, **110**, 5366–5397.
33 C. A. Dyke and J. M. Tour, *J. Am. Chem. Soc.*, 2003, **125**, 1156–1157.

34 Y.-L. Zhao and J. F. Stoddart, *Acc. Chem. Res.*, 2009, **42**, 1161–1171.
35 L. Vaisman, H. D. Wagner and G. Marom, *Adv. Colloid Interface Sci.*, 2006, **128–130**, 37–46.
36 H. Wang, *Curr. Opin. Colloid Interface Sci.*, 2009, **14**, 364–371.
37 B. Munkhbayar, M. J. Nine, J. Jeoun, M. Bat-Erdene, H. Chung and H. Jeong, *Powder Technol.*, 2013, **234**, 132–140.
38 V. N. Mochalin and Y. Gogotsi, *J. Am. Chem. Soc.*, 2009, **131**, 4594–4595.
39 U. Maitra, A. Gomathi and C. N. R. Rao, *J. Exp. Nanosci.*, 2008, **3**, 271–278.
40 J. Cheng, J. He, C. Li and Y. Yang, *Chem. Mater.*, 2008, **20**, 4224–4230.
41 A. Krueger and T. Boedeker, *Diamond Relat. Mater.*, 2008, **17**, 1367–1370.
42 C.-C. Li and C.-L. Huang, *Colloids Surf., A*, 2010, **353**, 52–56.
43 Y. Zhu, X. Xu, B. Wang and Z. Feng, *China Particuol.*, 2004, **2**, 132–134.
44 Y. Liu, R. L. Vander Wal and V. N. Khabashesku, *Chem. Mater.*, 2007, **19**, 778–786.
45 S. Suarez, F. Lasserre and F. Mücklich, *Mater. Sci. Eng., A*, 2013, **587**, 381–386.
46 G. B. V. Kumar, C. S. P. Rao and N. Selvaraj, *J. Miner. Mater. Charact. Eng.*, 2011, **10**, 59–91.
47 M. F. Variava, T. L. Church, A. T. Harris and A. I. Minett, *J. Mater. Chem. A*, 2013, **1**, 8509.
48 S. Suárez, A. Rosenkranz, C. Gachot and F. Mücklich, *Carbon*, 2013, 1–8.
49 M. D. Chadwick, J. W. Goodwin, E. J. Lawson and P. D. A. Mills, *Colloids Surf., A*, 2002, **203**, 229–236.
50 W. I. Goldburg, *Am. J. Phys.*, 1999, **67**, 1152.
51 S. Badaire, P. Poulin, M. Maugey and C. Zakri, *Langmuir*, 2004, **20**, 10367–10370.
52 S. Vallar, D. Houivet, J. El Fallah, D. Kervadec and J. Haussonne, *J. Eur. Ceram. Soc.*, 1999, **19**, 1017–1021.
53 H. J. Choi, J. H. Shin and D. H. Bae, *Composites, Part A*, 2012, **43**, 1061–1072.
54 M. A. Pimenta, G. Dresselhaus, M. S. Dresselhaus, L. G. Cançado, A. Jorio and R. Saito, *Phys. Chem. Chem. Phys.*, 2007, **9**, 1276–1291.
55 R. A. DiLeo, B. J. Landi and R. P. Raffaelle, *J. Appl. Phys.*, 2007, **101**, 064307.
56 J. H. Lehman, M. Terrones, E. Mansfield, K. E. Hurst and V. Meunier, *Carbon*, 2011, **49**, 2581–2602.
57 S. Tomita, T. Sakurai, H. Ohta, M. Fujii and S. Hayashi, *J. Chem. Phys.*, 2001, **114**, 7477.
58 X. Zhao, Y. Ando, L.-C. Qin, H. Kataura, Y. Maniwa and R. Saito, *Appl. Phys. Lett.*, 2002, **81**, 2550.
59 F. Tuinstra and J. L. Koenig, *J. Chem. Phys.*, 1970, **53**, 1126–1130.
60 S. Suarez, F. Lasserre, O. Prat and F. Mücklich, *Phys. Status Solidi*, 2014, **211**, 1555–1561.
61 K. I. Tserpes and P. Papanikos, *Compos. Struct.*, 2007, **79**, 581–589.
62 V. Mochalin, S. Osswald and Y. Gogotsi, *Chem. Mater.*, 2009, **21**, 273–279.
63 A. Sanaty-Zadeh, *Mater. Sci. Eng., A*, 2012, **531**, 112–118.
64 J. Y. Hwang, A. R. P. Singh, M. Chaudhari, J. Tiley, Y. Zhu, J. Du and R. Banerjee, *J. Phys. Chem. C*, 2010, **114**, 10424–10429.
65 N. Hansen, *Scr. Mater.*, 2004, **51**, 801–806.
66 P. Rossi, S. Suarez, F. Soldera and F. Mücklich, *Adv. Eng. Mater.*, 2014, **17**, 1017–1021.

II In-situ nanodiamond to carbon onion transformation in metal matrix composites

Sebastian Suarez[1], **Leander Reinert[1]**, Marco Zeiger[2], Patrice Miska[3], Samuel Grandthyll[4], Frank Müller[4], Volker Presser[2] and Frank Mücklich[1]

[1] Department of Material Science and Engineering, Saarland University, 66123 Saarbrücken, Germany
[2] INM – Leibniz Institute for New Materials, 66123 Saarbrücken, Germany
[3] Institue Jean Lamour, CNRS UMR 7198, Université de Lorraine, Nancy, F-54000, France
[4] Experimental Physics, Saarland University, Campus E2 9, 66123 Saarbrücken, Germany

Published in ***"Carbon" (Impact factor (2018): 7,082)***
Accessible online at: *https://doi.org/10.1016/j.carbon.2017.12.072*

Own contribution:

Sample processing including particle dispersion and sintering; UV-Raman spectroscopy analysis; Scanning electron microscopy and particle distribution analysis; Writing; Discussion; Planning.

Abstract:

In the present study, nickel matrix composites reinforced with a fine distribution of nanodiamonds (6.5 vol%) as reinforcement phase are annealed in vacuum at different temperatures ranging from 750 °C to 1300 °C. This is carried out to evaluate the in-situ transformation of nanodiamonds to carbon onions within a previously densified composite. The resulting materials are thoroughly analyzed by complementary analytical methods, including Raman spectroscopy, transmission electron microscopy, scanning electron microscopy, energy dispersive X-ray spectroscopy and X-ray photoelectron spectroscopy. The proposed in-situ transformation method presents two main benefits. On one hand, since the particle distribution of a nanodiamond-reinforced composite is significantly more homogenous than in the case of the carbon onions, it is expected that the transformed particles will preserve the initial distribution features of nanodiamonds. On the other hand, the proposed process allows for the tuning of the sp^3/sp^2 carbon ratio by applying a single straightforward post-processing step.

Cite this as:
S. Suárez, L. Reinert, M. Zeiger, P. Miska, S. Grandthyll, F. Müller, V. Presser, F. Mücklich, In-situ nanodiamond to carbon onion transformation in metal matrix composites. *Carbon* **2017**, 129, 631-636. (*https://doi.org/10.1016/j.carbon.2017.12.072*)

Carbon 129 (2018) 631–636

Contents lists available at ScienceDirect

Carbon

journal homepage: www.elsevier.com/locate/carbon

In-situ nanodiamond to carbon onion transformation in metal matrix composites

Sebastian Suarez [a, *], Leander Reinert [a, b], Marco Zeiger [c, d], Patrice Miska [e], Samuel Grandthyll [f], Frank Müller [f], Volker Presser [c, d], Frank Mücklich [a, b, **]

[a] Functional Materials, Department of Materials Science and Engineering, Saarland University, Campus D3 3, 66123, Saarbrücken, Germany
[b] Materials Engineering Center Saarland (MECS), Campus D3 3, 66123, Saarbrücken, Germany
[c] Energy Materials, Department of Materials Science and Engineering, Saarland University, Campus D2 2, 66123 Saarbrücken, Germany
[d] INM - Leibniz Institute for New Materials, Campus D2 2, 66123 Saarbrücken, Germany
[e] Institute Jean Lamour, CNRS UMR 7198, Université de Lorraine, Nancy, F-54000, France
[f] Experimental Physics, Saarland University, Campus E2 9, 66123 Saarbrücken, Germany

ARTICLE INFO

Article history:
Received 16 November 2017
Received in revised form
15 December 2017
Accepted 18 December 2017
Available online 21 December 2017

ABSTRACT

In the present study, nickel matrix composites reinforced with a fine distribution of nanodiamonds (6.5 vol%) as reinforcement phase are annealed in vacuum at different temperatures ranging from 750 °C to 1300 °C. This is carried out to evaluate the in-situ transformation of nanodiamonds to carbon onions within a previously densified composite. The resulting materials are thoroughly analyzed by complementary analytical methods, including Raman spectroscopy, transmission electron microscopy, scanning electron microscopy, energy dispersive X-ray spectroscopy and X-ray photoelectron spectroscopy. The proposed in-situ transformation method presents two main benefits. On one hand, since the particle distribution of a nanodiamond-reinforced composite is significantly more homogenous than in case of the carbon onions, it is expected that the transformed particles will preserve the initial distribution features of nanodiamonds. On the other hand, the proposed process allows for the tuning of the sp^3/sp^2 carbon ratio by applying a single straightforward post-processing step.

1. Introduction

Carbon nanoparticles, in their wide variety, are found in numerous technological applications covering fields ranging from nanoelectronics to medicine, among several others. Specifically, sp^2-hybridized nanocarbons have been thoroughly investigated in the last three decades [1]. Two particularly interesting nanocarbons are nanodiamonds as well as carbon onions. Nanodiamonds are sp^3-hybridized carbon nanoparticles with a lattice spacing of about 0.21 nm and a primary particle diameter of around 5 nm (i.e., quasi zero dimensional) [2]. They have been synthesized by a variety of different methods like detonation technique, laser ablation, ultrasound cavitation and others [2]. Intrinsic properties such as superior hardness and Young's modulus, high thermal conductivity, electrical resistivity, and chemical stability demonstrate the high potential of this carbon nanomaterial [2,3]. Beside applications for example in the medical sector, nanodiamonds are promising to reinforce metallic composites. In this regard, nanodiamonds have shown high performances by increasing hardness as well as wear resistance [4–6].

Carbon onions (also called onion-like carbon, OLC) are multilayered fullerene-like polyhedral nanoparticles [7]. By varying the synthesis method and its parameters, both, the sp^3 to sp^2 carbon ratio and the atomic arrangement can be adjusted. Carbon onions provide a high electrical conductivity [3], large surface area because of their nanometer-size (typically 5–10 nm), and very good mechanical properties [7]. Thus, the particles are used as reinforcement phase for composite materials [8], for tribological lubrication [9], electrochemical energy storage [10], or water treatment [7].

Nanodiamonds obtained from a detonation process are often used as starting materials in the thermal synthesis of carbon onions. Thermal annealing in a temperature range above 700 °C under vacuum or inert gas atmosphere allows to tune the sp^2/sp^3 ratio

* Corresponding author. Functional Materials, Department of Materials Science and Engineering, Saarland University, Campus D3 3, 66123, Saarbrücken, Germany.
** Corresponding author. Functional Materials, Department of Materials Science and Engineering, Saarland University, Campus D3 3, 66123, Saarbrücken, Germany.
E-mail addresses: s.suarez@mx.uni-saarland.de (S. Suarez), muecke@matsci.uni-sb.de (F. Mücklich).

https://doi.org/10.1016/j.carbon.2017.12.072
0008-6223/

and modify, accordingly, properties like the electrical conductivity [7,11,12]. Regarding the mechanical and tribological properties, sp^3-hybridized carbons are rather known for its hardness and its resistance to wear [6,13], whereas sp^2-hybridized carbons are usually associated with lubricity and friction reduction [14,15]. For an extended overview of the physical properties of both nanoparticles, please refer to the work of Mochalin et al. [2] and Zeiger et al. [7] and references therein.

A way of capitalizing on the properties of these nanodiamonds and carbon onions with macroscopic materials is by using these carbon nanoparticles as reinforcement phase in metal matrix composites (MMC). One of the major challenges during the manufacturing of this type of MMC is the carbon nanoparticle agglomeration. Particularly, if the selected fabrication route is the solid state processing (i.e., sintering), the mass transport leads to densification and results in an increased agglomerate formation [16]. This may lead to a poor interface between matrix and reinforcement, decreasing the potential enhancement of the physical properties. To obtain an optimum reinforcing effect, microstructural tailoring can be applied to avoid or minimize nanoparticle agglomeration. This can be achieved by modifying the microstructure in several ways. First, during densification in solid-state routes, the homogeneous distribution of a reinforcement phase pins the grain boundaries, resulting in a smaller mean grain size and increased strength. Second, during application, the particle dispersion acts on the dislocation mobility, reducing it and increasing the thermal stability of the microstructure [17]. Third, in tribological applications, the homogeneous and continuous release of carbon nanoparticles from the MMC towards the contact region can be beneficial and may be optimized in materials with a homogeneous distribution of the reinforcement phase.

In previous studies, it has been shown that sp^2-hybridized carbon nanoparticles form agglomerates faster and to a higher degree than their sp^3-hybridized counterparts mainly due to van der Waals interactions [8]. Additionally, nanodiamonds have shown good colloidal stability in ethylene glycol, which serves as a precursor for MMC fabrication [8]. This further translates to an improved distribution homogeneity of nanodiamonds in the metal matrix, compared to carbon onion reinforced MMC processed by the same route [18]. Considering the different material properties of these two carbon nanoparticles, it is of high interest to produce carbon onion reinforced MMC with the same distribution homogeneity as nanodiamonds to enable wider application flexibility. One possibility to increase the dispersion and distribution of carbon nanoparticle is the chemical modification of surface functional groups (covalent or non-covalent) [19]. However, a covalent functionalization (e.g., with hydroxyl, carboxyl or carbonyl groups) implies the breaking of covalent carbon bonds; thus, compromising the structural integrity of the particles and affecting their intrinsic properties [20,21]. A non-covalent functionalization involves the use of surfactants, polymers, or molecule wrapping [22–25]. The main drawback of this route is that, after processing at high temperatures (e.g., sintering), these additional products remain degraded by-products at the reinforcement-matrix interface, significantly hindering the load/charge transfer capability of the composite.

The present study explores a straightforward technique to overcome the limitations in the dispersion and distribution homogeneity of carbon onions as reinforcement material in MMC, avoiding the use of any chemical functionalization. This is done by thermal treatment of already densified nanodiamond reinforced MMC to trigger in-situ the nanodiamond to carbon onion phase transformation. Furthermore, as the annealing temperature allows to tune the sp^2/sp^3-ratio, the material properties of the composite can be adapted to match the requirements for different applications. The analysis is supported by a wide span of advanced characterization methods, including Raman spectroscopy with ultraviolet laser radiation, transmission electron microscopy (TEM), scanning electron microscopy (SEM), energy dispersive X-ray spectroscopy (EDS), and X-ray photoelectron spectroscopy (XPS).

2. Materials and methods

Nanodiamond powder was purchased from NaBond Technologies Co., with a carbon purity 98–99% and individual particle diameter 4–6 nm. For the composite manufacturing, the nanodiamonds were dispersed in ethylene glycol (0.1 mg/mL) by shear mixing (5 min) and ultrasonication (20 min). For this process, a homogenizer UltraTurrax (IKA-Werke GmbH) and an ultrasonic bath from Bandelin (Sonorex Super RK 514 BH, 860 W, and 35 kHz) were used. After dispersion, Ni dendritic powder (AlfarAesar, −325 mesh) was added and mixed again by shear mixing for 5 min to achieve a mixture of 6.5 vol% of nanodiamonds in nickel powder. Subsequently, the solvent was evaporated at 150 °C and the obtained powder is pre-densified to green cylindrical pellets with a diameter of 8 mm using a uniaxial press (990 MPa pressure). This step was followed by hot uniaxial pressing in vacuum ($2 \cdot 10^{-4}$ Pa) at a temperature of 750 °C, using a pressure of 264 MPa for 2.5 h and a heating and cooling rate of 20 °C/min. Using these parameters, a final relative density of 98% was achieved. Only few materials qualify for the choice of the matrix material since metals that readily react with carbon (e.g., Al, Ti, Cr) might affect the evaluation. In this case, Ni was selected as the matrix material, since it does not form stable carbides (a consequence of the carbon nanoparticle degradation) under the studied range of conditions. The only carbide formed by Ni is of metastable nature in a wide temperature range. Ni_3C is, among all possible carbides, the one with the lowest formation energy (26.36 kJ/mol) [26].

The already densified nanodiamond-reinforced samples are then post-processed by an annealing step under vacuum (10^{-3} Pa) at 750 °C, 900 °C, 1100 °C, and 1300 °C, each for 3 h of holding time with a heating and cooling rate of 10 °C/min. It is not possible to investigate higher transformation temperatures (1700 °C, as reported in Ref. [27], where high graphitization is achieved) due to the limitation given by the melting temperature of the matrix material ($T_{m,\,Ni} = 1453$ °C).

Characterization of the samples was done by TEM using a JEOL 2100F transmission electron microscope operated at 200 kV. Small fractions of the samples were removed by scratching and dispersed in isopropanol. These fractions are deposited onto Cu grids coated with lacey carbon for their subsequent TEM analysis.

Raman spectroscopy was performed using a Horiba UV-Raman spectrometer, working with an excitation laser wavelength of 325 nm (3.81 eV). The choice was made since UV excitation is more sensitive to sp^3-hybridized carbons than visible light [28]. The laser power on the sample was 5 mW and the in-focus-plane spot size of approximately 5 μm. The used numerical aperture was 0.5 and we chose a grating of 2400 lines/mm, resulting in a spectral resolution of 1.2 cm^{-1}. For the analysis, the spectra were fitted with Lorentz functions. The reported peak parameters correspond to those of the fitted functions.

SEM and EDS analyses were performed using a dual beam focused ion beam/field emission scanning electron microscope workstation (FEI Helios NanoLab 600). SEM micrographs were recorded with an accelerating voltage of 5 kV and current of 1.4 nA.

The XPS measurements were performed with an ESCA MkII spectrometer (Vacuum Generators) in normal emission mode using Al-K_α excitation ($\hbar\omega = 1486.6$ eV) and a 150°-type hemispherical analyzer with a pass energy of 20 eV. The calibration was made to the Au-4f 7/2 line at 83.80 eV. The acquired C-1s spectra of the samples treated at 750 °C and 1300 °C were fitted with four

Gaussian distributions corresponding to sp^2, sp^3, C-O, and C=O bonded carbon. Both spectra were fitted simultaneously, meaning that for each carbon species, the binding energy as well as the width of the corresponding peak are the same in both spectra, that is, both spectra just differ in the distribution of peak heights.

3. Results and discussion

The UV-Raman characterization provides detailed insights into the transformation steps from nanodiamond to carbon onions within the composite [29]. Fig. 1 shows the evolution of the transformation of nanodiamond at different processing temperatures.

The initial state presents three peaks at 1097.8 cm^{-1}, 1325.8 cm^{-1}, and 1637.2 cm^{-1}, which correspond to pure nanodiamond powder. The first peak at low wavenumbers is assigned to the presence of partially crystalline diamond [30], whereas the second peak is typically identified as crystalline diamond. The third peak (higher wavenumber) is an upshifted G band, moved by the convolution of the peaks generated by C=C, O-H, and C=O bonds [31].

The reported temperatures for the sp^3/sp^2 transformation range from 670 °C to 1000 °C and depend strongly on the synthesis method and surface chemistry of the nanodiamonds [7,32,33]. The first selected temperature (750 °C) is usually applied to densify this type of composites by hot uniaxial pressing in vacuum [34] and is above the onset temperature for graphitization observed by differential scanning calorimetry by Xu et al. [35]. At this temperature, the low wavenumber peak observed at room temperature vanishes, and a new peak appears at 1236.8 cm^{-1} that can be related to the signal combination of large and small domain scattering [2]. Yushin et al. assign this peak to partially crystalline diamond, which does concur with a short-range order scattering type [30]. The other two observed peaks correspond to the diamond band (1328.3 cm^{-1}) and the upshifted G-band of sp^2-hybridized carbon (1624.1 cm^{-1}).

By increasing the temperature to 900 °C, the transformation from sp^3-to sp^2-hybridization becomes more evident in alignment with the work of Cebik et al. [36]. Three peaks are observed at 1326.4 cm^{-1}, 1395.4 cm^{-1}, and 1600.7 cm^{-1}, with the first band assigned to diamond, the second to the D-band and the last to the upshifted G-band of sp^2-hybridized carbon. Moreover, the intensity of the diamond band is clearly reduced. In this case, the position of the G-band is in agreement to what was reported by Ferrari and Robertson [28]; the latter work assigned the position of the G-band at 1600 cm^{-1} to a nanocrystalline-graphite. This upshift is actually a convolution of the G-mode of sp^2-hybridized carbon and the D′-mode which represents short range order. Therefore, the Raman spectrum shows the first indication of the coexistence of diamond and a graphitic phase.

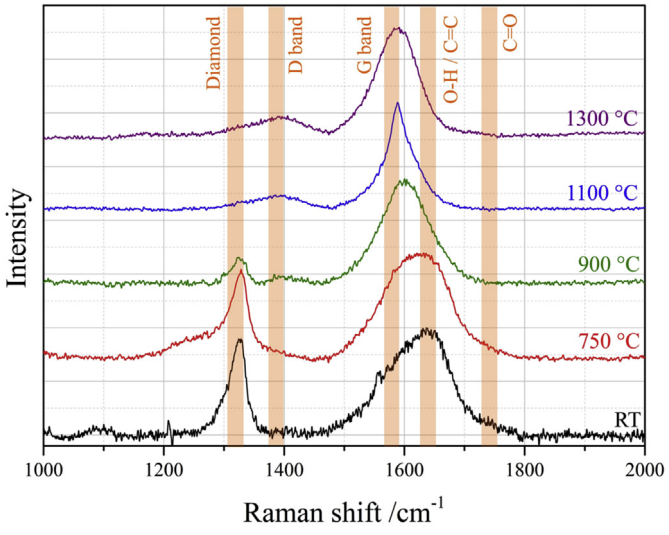

Fig. 1. Raman spectra of nanodiamond reinforced Ni composites at different post synthesis treatment temperatures. The characteristic bands are highlighted in orange. (A colour version of this figure can be viewed online.)

The following annealing temperature steps were set at 1100 °C and 1300 °C. In this range, the transformation noticeably continues, and the two characteristic bands of sp^2-hybridized carbon are clearly observed. The spectrum of the sample treated at 1100 °C has a D-band positioned at 1389.6 cm^{-1} and a G-band located at 1589.1 cm^{-1}, whereas the spectrum of the 1300 °C sample presents peaks at 1392.5 cm^{-1} and 1588.1 cm^{-1} of the D- and G band, respectively. In both cases, the extent of graphitization is significant. The full width at half maximum for the D- and G-bands are 124.5 cm^{-1} and 93.7 cm^{-1}, respectively. These values are in agreement with those reported by Zeiger et al. [11] and Cebik et al. [36], representing an increased long-range order of the sp^2 carbon.

An SEM/EDS analysis of the sample post-processed at 1300 °C is shown in Fig. 2. The distribution of the particles is homogeneous on a 100 μm length scale. The carbon nanoparticle distribution ranges from aggregates of 100 nm up to several micrometers, which may be caused by the initial agglomeration of the nanodiamond powder.

Because of the synthesis method of the detonation nanodiamonds, dangling bonds may form at their surface. The latter can react and form covalent interparticle bonds, resulting in the development of agglomerates [37]. Such agglomerates cannot be dispersed by shear mixing or ultrasonication. Yet, these agglomerates are developed to a much lower degree than in case of carbon onions. If the latter are used as powder during mixing, the particles interaction due to the π-bonds are much more pronounced, leading to a strong re-agglomeration behavior after the dispersion process and during densification. The consequence would be the formation of larger agglomerates with an inhomogeneous distribution [8].

A morphological evaluation of the samples treated at 1300 °C is shown in Fig. 3. It is clearly noticeable that there are still, at least, two different phases in the material (as observed in Fig. 3a). Carbon onions are identified by their characteristic multi-shell architecture, whereas there are also small nanodiamond domains. The lattice distance obtained by a grayscale profile analysis (Fig. 3b) coincides with the 0.34 nm spacing of graphitic structures ((002) plane). A third phase is identified as nickel with its characteristic lattice spacing matching the (111) plane (Fig. 3c).

Some defective layers can be found on the outer shells, and disorder is noticeable in the inner space of the carbon onions. The former has been already reported in other works on the thermal annealing of nanodiamonds at 1300 °C and can be assigned to the presence of amorphous carbon [7,11]. The latter may be related to the stress increment in the interior of the carbon onion, derived from the volume change in the particle during the transformation. Carbon onions synthesized in this temperature range (750–1300 °C) show a defective inner structure resulting from the shortage of sp^3-hybridized atoms at the sp^3-sp^2 interface [38]. There is also a strong connectivity of the individual carbon particles. This neck formation has been reported, among others, by Zeiger et al. [11] and leads to aggregation of the particles.

We used XPS to quantify the sp^2/sp^3 ratio for the samples which were treated at 750 °C and at 1300 °C (Fig. 4). Based on the fitting procedure explained in the experimental section, the difference in binding energy of sp^2-and sp^3-bonded carbon is about 600 meV, which is comparable to the values reported in literature (e.g., 800 meV in Ref. [39]). For the 750 °C sample (Fig. 4a), it is found that the particles contain sp^2 and sp^3 hybridized carbon atoms with a

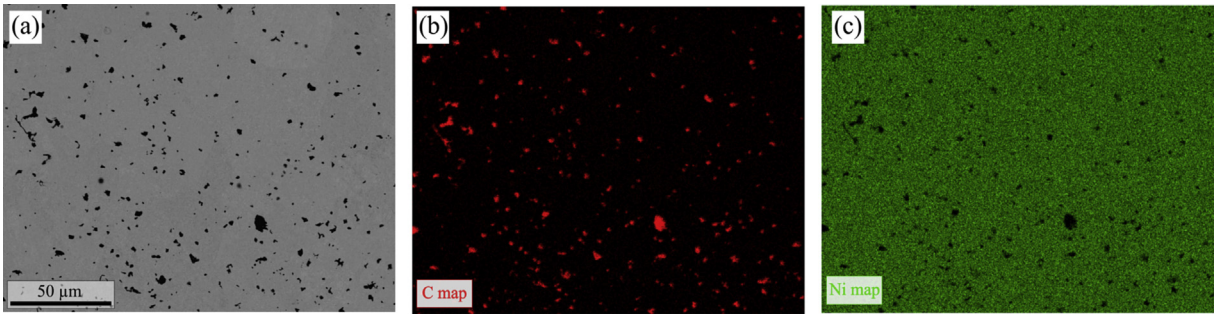

Fig. 2. (a) Secondary electron micrograph of the surface of the sample treated at 1300 °C. (b) EDS chemical map of the C distribution (in red) and (c) Ni distribution (in green). (A colour version of this figure can be viewed online.)

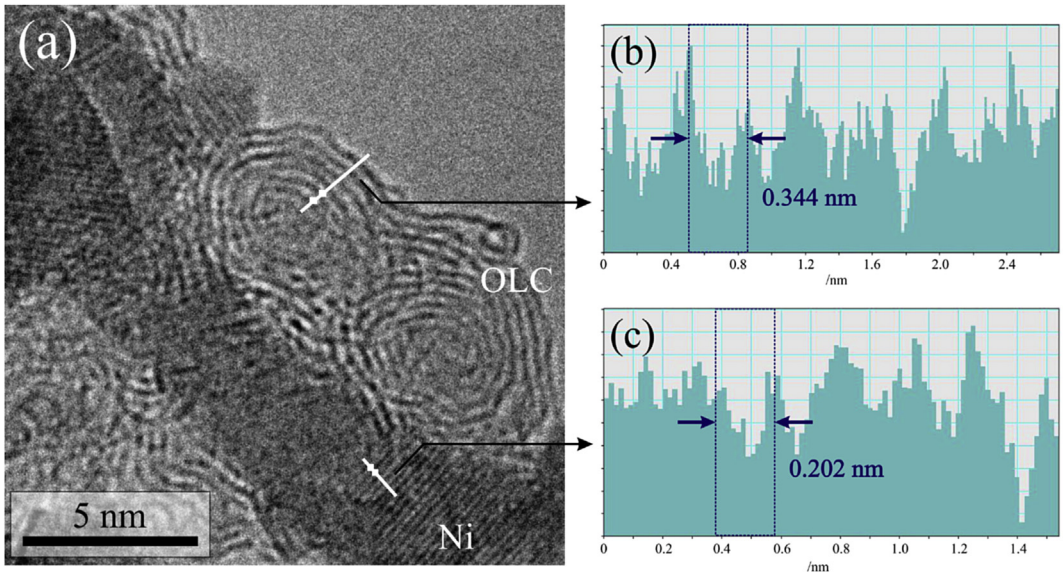

Fig. 3. (a) TEM image of the scratched material after thermal treatment at 1300 °C. (b) Grayscale line profile of a carbon onion, where the interplanar distance is in accordance to the (002) plane of graphitic carbon. (c) Grayscale line profile of a nickel domain, showing an interplanar distance corresponding to the (111) plane. (A colour version of this figure can be viewed online.)

significant amount of C-O occurrence. This can be traced back to the detonation synthesis method of the nD [37]. Moreover, the appearance of incompletely crystallized carbon as outer shell of the nanodiamonds is well-known in literature, therefore explaining the relatively large relative amount of sp^2-hybridized carbon atoms [11]. The C=O bonding is also detected by Raman spectroscopy as side shoulder at 1760 cm^{-1}. In case of the sample which was post processed at 1300 °C (Fig. 4b), a significant transformation can be observed.

With 84.2 at% of sp^2-hybridized carbon atoms, the particles seem to be largely graphitized, in agreement with the results from Raman spectroscopy and TEM analysis. A small fraction (1.7%) of sp^3 hybridized carbon is still detected. It must thus be mentioned that, by processing the composites with the conditions proposed in this study, it is possible to reduce significantly the nD fraction. However, there is still disordered domains within the carbon onions, which might need additional energy for their conversion, because of the stress generated by the volume expansion of the nanoparticle. Longer treatment times eventually result in larger transformation. However, transformation kinetics (conversion rates) in the analyzed temperature range are low and strongly dependent on the original nD particle size (smaller nD convert faster) [38]. Yet, once the outer layers are converted, they become more difficult to rearrange and relieve generated stresses, thus possibly stabilizing a structurally disordered core region [38]. This would hinder the proper conversion, irrespective of the treatment time. In addition, we see a significant de-functionalization of the carbon nanoparticles, as the number of functional groups like C-O and C=O clearly decreases.

4. Conclusions

The transformation process of nanodiamond to carbon onions in a pre-densified nanodiamond-reinforced nickel matrix composite is studied. This is done by pressure-less, thermal annealing of the sintered sample under vacuum with temperatures ranging from 750 °C to 1300 °C. Raman spectroscopy measurements reveal that the sp^3 to sp^2 carbon ratio can be tuned by the annealing temperature. These results are confirmed by TEM analysis, showing the presence of carbon onions (with a disordered nucleus) dispersed in the nickel matrix after the annealing step at 1300 °C. The XPS data of the samples with the lowest and highest selected treatment temperatures demonstrates that the sp^2 carbon content of the particles increased from 31.1% (750 °C) up to 84.2% (1300 °C). Hence, it is demonstrated that it is possible to modify the sp^2 to sp^3 ratio within the metal matrix composite, simply by selecting the

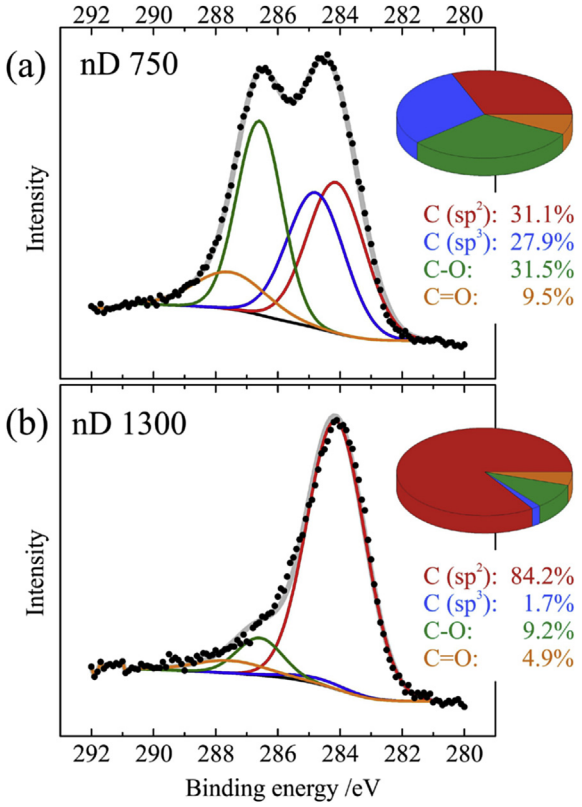

Fig. 4. (a) C-1s spectra of the sample treated at 750 °C and, (b) at 1300 °C with the corresponding distribution of carbon bonds on Shirley background. (A colour version of this figure can be viewed online.)

appropriate treatment temperature.

Acknowledgements

L. Reinert, S. Suarez, and F. Mücklich wish to acknowledge the EFRE Funds of the European Commission for support of activities within the AME- Lab project and the funding from the Deutsche Forschungsgemeinschaft (DFG, project: MU 959/38-1 and project: SU 911/1-1). This work was supported by the CREATe-Network Project, Horizon 2020 of the European Commission (RISE Project No. 644013). F. Müller and S. Grandthyll acknowledge funding from the German Research Foundation (DFG) via the Collaborative Research Center SFB 1027. V. Presser and M. Zeiger kindly thank Prof. Eduard Arzt for his continuing support.

References

[1] Y. Gogotsi, V. Presser, Carbon Nanomaterials, second ed., CRC Press, Boca Raton, FL, USA, 2013.
[2] V.N. Mochalin, O. Shenderova, D. Ho, Y. Gogotsi, The properties and applications of nanodiamonds, Nat. Nanotechnol. 7 (2012) 11–23, https://doi.org/10.1038/nnano.2011.209.
[3] V.L. Kuznetsov, Y.V. Butenko, A.L. Chuvilin, A.I. Romanenko, A.V. Okotrub, Electrical resistivity of graphitized ultra-disperse diamond and onion-like carbon, Chem. Phys. Lett. 336 (2001) 397–404, https://doi.org/10.1016/S0009-2614(01)00135-X.
[4] L. Wang, Y. Gao, Q. Xue, H. Liu, T. Xu, Effects of nano-diamond particles on the structure and tribological property of Ni-matrix nanocomposite coatings, Mater. Sci. Eng. A 390 (2005) 313–318, https://doi.org/10.1016/j.msea.2004.08.033.
[5] V.Y. Dolmatov, T. Fudzhimura, G.K. Burkat, E.A. Orlova, Preparation of wear-resistant chromium coatings using nanodiamonds of different nature, Powder Metall. Met Ceram. 42 (2003) 587–591, https://doi.org/10.1023/B:PMMC.0000022197.90234.f4.
[6] Y. Li, W.J. Zou, B.X. Li, Q.M. Dong, The frictional properties and mechanism of nano-diamond/Ni composite coatings by brush-plating, Adv. Mater. Res. 291–294 (2011) 197–200, https://doi.org/10.4028/www.scientific.net/AMR.291-294.197.
[7] M. Zeiger, N. Jäckel, V.N. Mochalin, V. Presser, Review: carbon onions for electrochemical energy storage, J. Mater. Chem. A 4 (2016) 3172–3196, https://doi.org/10.1039/C5TA08295A.
[8] L. Reinert, M. Zeiger, S. Suárez, V. Presser, F. Mücklich, Dispersion analysis of carbon nanotubes, carbon onions, and nanodiamonds for their application as reinforcement phase in nickel metal matrix composites, RSC Adv. 5 (2015) 95149–95159, https://doi.org/10.1039/C5RA14310A.
[9] A. Hirata, M. Igarashi, T. Kaito, Study on solid lubricant properties of carbon onions produced by heat treatment of diamond clusters or particles, Tribol. Int. 37 (2004) 899–905, https://doi.org/10.1016/j.triboint.2004.07.006.
[10] C. Portet, G. Yushin, Y. Gogotsi, Electrochemical performance of carbon onions, nanodiamonds, carbon black and multiwalled nanotubes in electrical double layer capacitors, Carbon 45 (2007) 2511–2518, https://doi.org/10.1016/j.carbon.2007.08.024.
[11] M. Zeiger, N. Jäckel, M. Aslan, D. Weingarth, V. Presser, Understanding structure and porosity of nanodiamond-derived carbon onions, Carbon N. Y. 84 (2015) 584–598, https://doi.org/10.1016/j.carbon.2014.12.050.
[12] Q. Zou, Y.G. Li, B. Lv, M.Z. Wang, L.H. Zou, Y.C. Zhao, Transformation of onion-like carbon from nanodiamond by annealing, Inorg. Mater. 46 (2010) 127–131, https://doi.org/10.1134/S002016851002007X.
[13] E. Falcao, F. Wudl, Review carbon allotropes: beyond graphite and diamond, J. Chem. Technol. Biotechnol. 82 (2007) 524–531, https://doi.org/10.1002/jctb.
[14] P.K. Rohatgi, S. Ray, Y. Liu, Tribological properties of metal matrix-graphite particle composites, Int. Mater. Rev. 37 (1992) 129–152, https://doi.org/10.1179/imr.1992.37.1.129.
[15] L. Ru-Tie, X. Xiang, C. Fu-Sheng, L. Jin-Zhong, H. Li-Ling, Z. Yi-Qing, Tribological performance of graphite containing tin lead bronzesteel bimetal under reciprocal sliding test, Tribol. Int. 44 (2011) 101–105, https://doi.org/10.1016/j.triboint.2010.09.012.
[16] P. Rossi, S. Suarez, F. Soldera, F. Mücklich, Quantitative assessment of the reinforcement distribution homogeneity in CNT/metal composites, Adv. Eng. Mater. 17 (2015) 1017–1021, https://doi.org/10.1002/adem.201400352.
[17] S. Suarez, F. Lasserre, F. Soldera, R. Pippan, F. Mücklich, Microstructural thermal stability of CNT-reinforced composites processed by severe plastic deformation, Mater. Sci. Eng. A 626 (2015) 122–127, https://doi.org/10.1016/j.msea.2014.12.065.
[18] L. Reinert, S. Suarez, T. Müller, F. Mücklich, Carbon nanoparticle-reinforced metal matrix composites: microstructural tailoring and predictive modeling, Adv. Eng. Mater. 19 (2017) 1600750, https://doi.org/10.1002/adem.201600750.
[19] Q. Cheng, S. Debnath, E. Gregan, H.J. Byrne, Ultrasound-Assisted swnts dispersion: effects of sonication parameters and solvent properties, J. Phys. Chem. C 114 (2010) 8821–8827, https://doi.org/10.1021/jp101431h.
[20] F. Avilés, J.V. Cauich-Rodríguez, L. Moo-Tah, A. May-Pat, R. Vargas-Coronado, Evaluation of mild acid oxidation treatments for MWCNT functionalization, Carbon 47 (2009) 2970–2975, https://doi.org/10.1016/j.carbon.2009.06.044.
[21] C.A. Dyke, J.M. Tour, Solvent-free functionalization of carbon nanotubes, J. Am. Chem. Soc. 125 (2003) 1156–1157, https://doi.org/10.1021/ja0289806.
[22] Y.-L. Zhao, J. Fraser Stoddart, Noncovalent functionalization of single-walled carbon nanotubes, Acc. Chem. Res. 42 (2009) 1161–1171, https://doi.org/10.1021/ar900056z.
[23] L. Vaisman, H.D. Wagner, G. Marom, The role of surfactants in dispersion of carbon nanotubes, Adv. Colloid Interface Sci. 128–130 (2006) 37–46, https://doi.org/10.1016/j.cis.2006.11.007.
[24] H. Wang, Dispersing carbon nanotubes using surfactants, Curr. Opin. Colloid Interface Sci. 14 (2009) 364–371, https://doi.org/10.1016/j.cocis.2009.06.004.
[25] B. Munkhbayar, M.J. Nine, J. Jeoun, M. Bat-Erdene, H. Chung, H. Jeong, Influence of dry and wet ball milling on dispersion characteristics of the multi-walled carbon nanotubes in aqueous solution with and without surfactant, Powder Technol. 234 (2013) 132–140, https://doi.org/10.1016/j.powtec.2012.09.045.
[26] J.S. Gibson, J. Uddin, T.R. Cundari, N.K. Bodiford, A.K. Wilson, First-principle study of structure and stability of nickel carbides, J. Phys. Condens. Matter 22 (2010) 445503, https://doi.org/10.1088/0953-8984/22/44/445503.
[27] M. Zeiger, N. Jäckel, D. Weingarth, V. Presser, Vacuum or flowing argon: what is the best synthesis atmosphere for nanodiamond-derived carbon onions for supercapacitor electrodes? Carbon 94 (2015) 507–517, https://doi.org/10.1016/j.carbon.2015.07.028.
[28] A. Ferrari, J. Robertson, Interpretation of Raman spectra of disordered and amorphous carbon, Phys. Rev. B 61 (2000) 14095–14107, https://doi.org/10.1103/PhysRevB.61.14095.
[29] S. Osswald, V.N. Mochalin, M. Havel, G. Yushin, Y. Gogotsi, Phonon confinement effects in the Raman spectrum of nanodiamond, Phys. Rev. B Condens. Matter 80 (2009), https://doi.org/10.1103/PhysRevB.80.075419.
[30] G.N. Yushin, S. Osswald, V.I. Padalko, G.P. Bogatyreva, Y. Gogotsi, Effect of sintering on structure of nanodiamond, Diam. Relat. Mater. 14 (2005) 1721–1729, https://doi.org/10.1016/j.diamond.2005.06.030.
[31] S. Osswald, G. Yushin, V. Mochalin, S.O. Kucheyev, Y. Gogotsi, Control of sp2/sp3 carbon ratio and surface chemistry of nanodiamond powders by selective oxidation in air, J. Am. Chem. Soc. 128 (2006) 11635–11642, https://doi.org/10.1021/ja063303n.
[32] V.L. Kuznetsov, Y. V Butenko, Diamond phase transitions at nanoscale, in:

Ultrananocrystalline Diam, second ed., Elsevier Inc., 2012, pp. 181–244, https://doi.org/10.1016/B978-1-4377-3465-2.00007-4.
[33] J.K. McDonough, A.I. Frolov, V. Presser, J. Niu, C.H. Miller, T. Ubieto, M.V. Fedorov, Y. Gogotsi, Influence of the structure of carbon onions on their electrochemical performance in supercapacitor electrodes, Carbon 50 (2012) 3298–3309, https://doi.org/10.1016/j.carbon.2011.12.022.
[34] S. Suarez, F. Lasserre, F. Mücklich, Mechanical properties of MWNT/Ni bulk composites: influence of the microstructural refinement on the hardness, Mater. Sci. Eng. A 587 (2013) 381–386, https://doi.org/10.1016/j.msea.2013.08.058.
[35] N.S. Xu, J. Chen, S.Z. Deng, Effect of heat treatment on the properties of nano-diamond under oxygen and argon ambient, Diam. Relat. Mater. 11 (2002) 249–256.
[36] J. Cebik, J.K. McDonough, F. Peerally, R. Medrano, I. Neitzel, Y. Gogotsi, S. Osswald, Raman spectroscopy study of the nanodiamond-to-carbon onion transformation, Nanotechnology 24 (2013) 205703, https://doi.org/10.1088/0957-4484/24/20/205703.
[37] A. Pentecost, S. Gour, V. Mochalin, I. Knoke, Y. Gogotsi, Deaggregation of nanodiamond powders using salt- and sugar-assisted milling, ACS Appl. Mater. Interfaces 2 (2010) 3289–3294, https://doi.org/10.1021/am100720n.
[38] O.A. Shenderova, D.M. Gruen (Eds.), Ultrananocrystalline Diamond: Synthesis, Properties, and Applications, first ed., William Andrew Publisher, Norwich, NY, USA, 2006.
[39] P. Mérel, M. Tabbal, M. Chaker, S. Moisa, J. Margot, Direct evaluation of the sp3 content in diamond-like-carbon films by XPS, Appl. Surf. Sci. 136 (1998) 105–110, https://doi.org/10.1016/S0169-4332(98)00319-5.

III Carbon Nanoparticle-Reinforced Metal Matrix Composites: Microstructural Tailoring and Predictive Modeling

Leander Reinert, Sebastian Suárez, Thomas Müller and Frank Mücklich

Department of Material Science and Engineering, Saarland University, 66123 Saarbrücken, Germany

*Published in **"Advanced Engineering Materials" (Impact factor (2017): 2.319)***
Accessible online at: https://doi.org/10.1002/adem.201600750

Own contribution:

Sample processing including particle dispersion and sintering; Scanning electron microscopy and particle distribution analysis; Electron backscatter diffraction; Writing; Discussion; Planning.

Abstract:

Nickel matrix composites are produced with concentrations of 0.5–10 vol% of carbon nanotubes (CNT), onion-like carbon (OLC), or nanodiamonds (nD) as reinforcement phase by hot pressing. The effect of the carbon nanoparticle (CNP) type and concentration on the microstructure is analyzed. Grain sizes are measured and a model is adapted to predict the observed grain refinement for all CNP. The individual saturation concentration and maximum achievable grain refinement differs (for CNT: 3 vol%, OLC: 6.5 vol% and nD: 10 vol%), which is correlated to the agglomerate diameter distribution. This can be traced back to different hybridization states and different particle geometries, therefore providing valuable information for CNP-reinforced Metal matrix composites to a general extent.

Cite this as:
L. Reinert, S. Suárez, T. Müller, F. Mücklich, Carbon Nanoparticle-Reinforced Metal Matrix Composites: Microstructural Tailoring and Predictive Modeling. *AEM* **2017**, 19, 1600750. (*https://doi.org/10.1002/adem.201600750*)

ADVANCED ENGINEERING MATERIALS

DOI: 10.1002/adem.201600750

Carbon Nanoparticle-Reinforced Metal Matrix Composites: Microstructural Tailoring and Predictive Modeling**

By *Leander Reinert, Sebastian Suarez,* Thomas Müller* and *Frank Mücklich*

Nickel matrix composites are produced with concentrations of 0.5–10 vol% of carbon nanotubes (CNT), onion-like carbon (OLC), or nanodiamonds (nD) as reinforcement phase by hot pressing. The effect of the carbon nanoparticle (CNP) type and concentration on the microstructure is analyzed. Grain sizes are measured and a model is adapted to predict the observed grain refinement for all CNP. The individual saturation concentration and maximum achievable grain refinement differs (for CNT: 3 vol%, OLC: 6.5 vol% and nD: 10 vol%), which is correlated to the agglomerate diameter distribution. This can be traced back to different hybridization states and different particle geometries, therefore providing valuable information for CNP-reinforced Metal matrix composites to a general extent.

1. Introduction

Composite materials provide the capability of tailoring their properties (mechanical, electrical, thermal, etc.), by managing simple variables, such as the chosen reinforcement material, the reinforcement volume fraction, or the processing parameters. For those reasons, they have been in the spotlight of materials research for the last few decades. At the same time, carbon nanomaterials have been foreseen as very promising candidates as reinforcement phase due to their outstanding intrinsic properties and low density,[1–3] which are essential features for composite materials. When used in composites, they can lead to increased strength,[4–6] hardness,[7–9] electrical and thermal conductance,[8,10,11] thermomechanical stability,[12] as well as a reduction in friction and wear,[13–15] just to enumerate some examples. In general, carbon nanomaterials can be found in many different morphologies and configurations. Specifically for this work, the focus is placed on three types of carbon nanoparticles (CNP), namely: carbon nanotubes (CNT),[16] nanodiamonds (nD),[3] and onion-like carbons (OLC).[17] These CNP were selected as they show either a specific carbon hybridization or particle geometry, therefore, covering a wide span of carbon nanomaterials and allowing a systematic analysis of the effect of those differences on the microstructure in a metal matrix composite (MMC). One of the advantages would be that all those CNP possess a certain degree of chemical inertness, and behave in the same way, when no interphases are formed with the matrix in MMC (e.g., Cu, Ag, etc.).

For CNP-reinforced metal matrix composites, the material strengthening due to grain refinement has been identified in several different matrices.[8,18–21] In general, the magnitude of the reinforcing effect generated by CNP in a metal matrix composite is strongly affected by their distribution,[5,22,23] which directly influences the mechanical properties of the material (e.g., hardness or strength) due to grain boundary strengthening.[21] Also, rather small agglomerates are known to enable the Orowan mechanism, thus, leading to a reinforcing effect of the composite.[24,25] Furthermore, a finer distribution of small agglomerates creates a larger amount of interface between reinforcement and matrix, efficiently, increasing the load transfer during stress.[5] Additionally, other factors, such as the generation of dislocations resulting from thermal mismatch between matrix and reinforcements can also contribute to an expected strengthening of the material.[26]

In this context, the main drawback of working with CNP is their tendency to form agglomerates due to intermolecular forces like dipole–dipole forces, van der Waals forces,[27–29] or

[*] *Dr. S. Suarez, L. Reinert, T. Müller, Prof. Dr. F. Mücklich*
Chair of Functional Materials, Deptartment of Materials Science and Engineering, Saarland University, Campus D3 3, Saarbrücken D-66123, Germany
E-mail: s.suarez@mx.uni-saarland.de

[**] *The present work is supported by funding from the Deutsche Forschungsgemeinschaft (DFG, project: MU959/38-1 and project: SU 911/1-1). The authors wish to acknowledge the EFRE Funds of the European Commission for support of activities within the AME-Lab project. This work was supported by the CREATe-Network Project, Horizon 2020 of the European Commission (RISE Project No. 644013). The authors would like to thank Prof. Dr. Volker Presser (INM, Saarbrücken) for providing the OLC and nD powder.*

as a consequence of the synthesis methods themselves.[30–33] In a previous study, an alternative processing route has been proposed,[23] which allows for the direct comparison of the aforementioned three CNP in terms of their distribution and the generated microstructure, when used as reinforcement phase in a nickel metal matrix composite. Nickel appears to be a suitable candidate as matrix material for a comparative study, since it only forms metastable carbides under very specific conditions, as shown in a previous study reported by Suarez et al.[21] Considering the possibility of a prediction of the resulting mean grain size of a biphasic material as a function of the amount of the secondary phase (that with lower volume fraction), Smith[34] presented a grain boundary pinning model (Zener model).[35] This model considers a grain boundary mobility hindering, when the driving force for grain growth is balanced with the counterforce exerted by the secondary phase distribution within the composite.[36] However, it has been extensively demonstrated that the general case considers certain features that are far from the real conditions and, thus, fail to effectively predict the resulting mean grain size. A clear example of this is thoroughly discussed by Manohar et al. in their review of the evolution of the Zener model throughout the past years.[35] It is then clear, that a general descriptive model would not be realistic and, therefore, each system should be modeled according to its particular set of processing parameters.

Based on a generalization of the Zener model, Suarez et al.[21] were further able to adapt it for the prediction of the mean grain size of a nickel metal matrix composite, reinforced with different volume fractions of MWCNT by considering a descriptive shape factor of the CNT. This approach fits perfectly with the experimental data but, as already stated, is specifically linked to the conditions, described in the report.

Considering this as a starting point, the present study is focused on the adaptation of a Zener model to predict the final obtained mean grain size as a function of the amount of the three types of CNP studied. As information regarding hybridization state and particle morphology of carbon nanoparticles is considered in this study, it provides valuable information for CNP-reinforced metal matrix composites to a more general extent.

2. Materials and Methods

2.1. Production

Nickel matrix composites reinforced with multiwall carbon nanotubes (Baytubes C150P, purity>95%, individual particle diameter of 5–20 nm), nanodiamonds (NaBond Technologies Co., purity>98%, individual particle diameter 4–8 nm), or onion-like carbon (obtained from nanodiamonds) are analyzed. To synthesize OLC, the nanodiamond powder is annealed in graphite crucibles in furnace with tungsten heaters (Model: 1100-3580-W1, Thermal Technology Inc.) under vacuum (1×10^{-5} mbar) using a heating and cooling rate of 15 °C min^{-1} and a maximum temperature of 1 750 °C (hold for 3 h). The particle agglomerates are dispersed in ethylene glycol using a homogenizer (WiseTis, Witeg) and an ultrasonic bath. The processing steps are described elsewhere.[23] The obtained dispersions are finally used as precursors to manufacture nickel matrix composites with Ni dendritic powder (Alfa Aesar, −325 mesh) with a particle volume fractions of 0.5, 1, 3, 6.5, and 10 vol%. A hot uniaxial press (axial pressure of 264 MPa) under vacuum (2×10^{-6} mbar) is used at 700 °C for 2.5 h to densify the powder mixture.[23] After densification, an additional annealing step (550 °C for 6 h under vacuum at 2×10^{-6} mbar) was added in order to allow for an extended grain growth.

2.2. Characterization

After the production of the composites, the samples are polished up to 1 μm polishing suspension, after which an oxide polishing suspension (OPS) is used as final preparation step. The samples are, then, characterized in a dual beam workstation FE-SEM/FIB Helios NanoLab 600™ (FEI). The mean grain size of the matrix after sintering is measured by electron backscattered diffraction (EBSD), with an EDAX TSL™ detector attached to the electron microscope. The scanned areas are at least of (250 × 250) μm applying an accelerating voltage of 20 kV, a current of 22 nA, and a step size of 0.3 μm. For the evaluation, a grain was defined as at least two adjacent points with a misorientation lower than 5°, beyond which a grain boundary is set. In order to have reliable and representative statistics, at least 10 000 grains are considered for each nanoparticle concentration. The acquired raw data is further post-processed using confidence index (CI) standardization, followed by the removal of points with CI below 0.09. All grains intersecting the scan window were removed from the analysis.

Furthermore, SEM was used to record micrographs of all different composites at three independent spots (always same magnification of 500 times with a resolution of 1 024 × 884) in order to correlate the mean grain size with the mean agglomerate diameter. For analysis, the three micrographs were each divided in four subsections, which were binarized and segmented using the a4i (Archive4Images) resulting in 12 sub-segments for each particle type and concentration. This allows determining the area of each individual agglomerate within the sub-segment. From the area, an equivalent agglomerate diameter was calculated assuming the agglomerates to be fairly round. The agglomerate diameter distribution for all segments was, then, classified into 20 equidistant sections to allow for a graphical illustration of the distribution.

Also, the analyzed areas were mapped by energy dispersive X-ray spectroscopy (EDX) in order to correlate areas with high carbon content to the SEM micrographs. An accelerating voltage of 5 kV and a current of 22 nA has been used.

3. Results and Discussion

3.1. Microstructure and Particle Distribution

The acquired grain size data has to be fitted, in order to calculate the mean grain size and the standard deviation. All

samples showed a log-normal type of grain size distribution. Table 1 shows the mean grain size values for each concentration (area weighed).

In all samples, there is a clear downward trend to a refinement saturation value, beyond which the mean grain size starts to increase. Reinert et al.[23] demonstrated that differences in the agglomerate sizes and the distribution of the three used CNP can be expected, with nD showing the lowest and CNT showing the highest tendency to form large agglomerates. Interestingly, this trend can be correlated to the, here, obtained saturation values for the grain refinement.[23] For smaller agglomerate sizes (nD-containing samples), a better distribution of the nanoparticles is expected, thus, enhancing their grain boundary pinning efficiency up to larger volume fractions. Samples that present a larger agglomerate size (CNT-containing samples), do not efficiently act on the moving boundaries during sintering. This has two main reasons: First, larger agglomerates mean that there is a lower amount of individually distributed particles at the grain boundaries, and second, large agglomerates usually present a poor interfacial cohesion to the matrix, which translates into an inefficient boundary drag and load transfer.[21]

Due to the nature of the powder blending and manufacturing process, all types of particles are placed at grain boundaries.[37] It is, therefore, rational to assume that all the refinement process would take place, only if a proper interfacial contact between reinforcement and matrix is provided. Furthermore, it is well known that Ni does not form any type of carbide phases when combined with C (under normal conditions).[38] The Ni–C phase diagram shows a single metastable carbide (Ni_3C), which is formed only under certain non-equilibrium conditions.[39] On one hand, the formation of this phase would be certainly beneficial for the interaction of the grain boundaries with the reinforcement by providing a seamless interfacial contact. However, it would be detrimental from the perspective of retaining the outstanding physical properties of the nanoparticles. Based on the resulting grain size values, reported in Table 1, it is valid to state that the particles present a very good interfacial contact to the matrix without chemically reacting with it, thus, highlighting the remarkable efficiency of the manufacturing process. This has been previously analyzed and discussed specifically for the Ni-CNT system,[40] but can be straightforwardly transferred to both, the Ni-OLC and Ni-nD systems.

Typical microstructures for the different reinforcement types are shown in Figure 1. Particularly, the shown scanning electron micrographs (a–c) belong to the 3 vol% samples, where the black regions are the particle agglomerates. All show a homogeneous distribution, and the particle agglomerates are placed at the grain boundaries. In order to prove that the black areas are CNPs, EDX-maps have been added below the corresponding SEM-micrograph. The Black areas in these EDX-maps represent the existence of elementary carbon. Thus, it can be seen, that the elementary carbon distribution correlates perfectly with the black areas from the SEM-micrographs.

Figure 2 shows the agglomerate size distribution histograms for each concentration.

It can be observed that in all cases, the nD samples show a narrower size distribution compared to those of CNT and OLC. This indicates a close to monomodal size distribution and is related to the weak agglomeration activity of nD, which is traced back mainly to their hybridization.[23] CNT and OLC show a widespread, multimodal agglomerate size distribution. This is also related to their sp^2 hybridization, in which the electron delocalization of the p-orbitals favors their interaction and subsequent agglomeration due to van der Waals interactions.

The histograms show a correlation, to a certain extent, to the saturation behavior identified in the mean grain size (Table 1). Thus, by increasing the particle fraction, the agglomerate size is also increased and the refinement efficiency is hindered. Specifically, the first three concentrations (0.5, 1, and 3 vol%) show no significant differences between the agglomerate sizes (Figure 2a–c), as they are all much smaller than a maximum value of almost 7 μm. At 6.5 vol%, the difference starts to be noticeable, showing a wider agglomerate distribution of the CNTs. Finally, the most critical case in which all samples show a spread distribution is for the highest evaluated concentration (i.e., 10 vol%). However, even for 10 vol%, nD still show by far the highest amount of small agglomerates, justifying their

Table 1. Mean grain sizes and their respective standard deviation for all the studied nanoparticles and volume fractions. The values were obtained from EBSD scans. The saturation value for each type of nanoparticle is highlighted in grey.

	CNT		OLC		nD	
Vol. fraction $\%^{-1}$	$<d>_{Area}\,\mu m^{-1}$	$\pm\sigma_{Area}\,\mu m^{-1}$	$<d>_{Area}\,\mu m^{-1}$	$\pm\sigma_{Area}\,\mu m^{-1}$	$<d>_{Area}\,\mu m^{-1}$	$\pm\sigma_{Area}\,\mu m^{-1}$
0	19.57	15.61	19.57	15.61	19.57	15.61
0.5	8.20	9.52	5.58	7.75	7.86	7.77
1	4.66	2.39	3.38	1.58	3.26	1.64
3	4.01	2.31	3.70	1.84	3.55	1.78
6.5	4.23	2.17	2.74	1.53	2.78	1.55
10	4.50	2.53	2.95	1.49	2.32	1.39

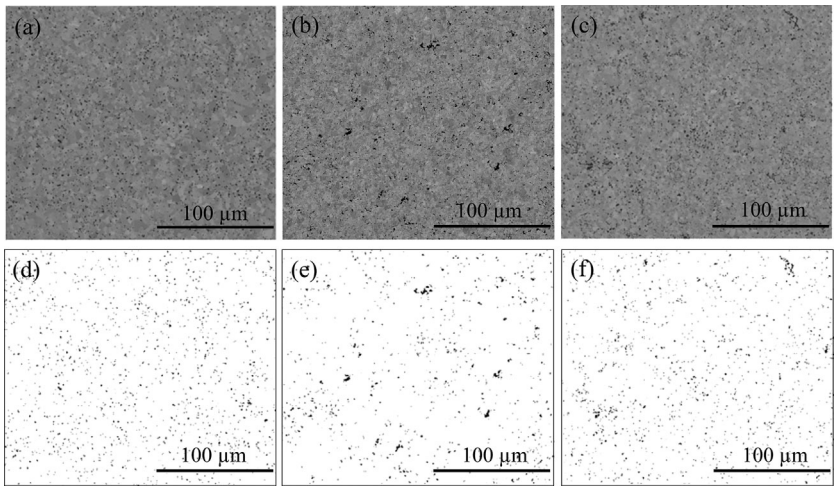

Fig. 1. Backscattered electron micrographs of the Ni-matrix composites with 3 vol% reinforcement fraction. of (a) CNT, (b) OLC, and (c) nD. The dark black regions are the different particle agglomerates. This is proven by EDX-mappings of the same areas for (d) CNT, (e) OLC, and (f) nD. The black regions in these EDX-maps show areas with elementary carbon content, which correlates perfectly with the black areas of the backscattered electron micrographs.

grain refinement effect for up to this concentration. When the mean grain sizes shown in Table 1 are contrasted to the pure Ni reference state (mean grain size of 19.5 µm), a maximum fivefold refinement for MWCNT, about 7-fold for OLC and about 8.5-fold for nD is accomplished. These resulting grain sizes correspond to 3 vol% of MWCNT, 6.5 vol% of OLC, and 10 vol% of nD.

3.2. Predictive Microstructural Modeling

It has been already shown that the conventional theoretical models fail to predict the final mean grain size in these types of composites.[21] This is further supported by the amount of available models reported throughout the years, which start from the same original equation, but render completely different outcomes.[35] Basically, the Zener model predicts the critical grain size, at which the grain boundary driving and drag forces are balanced and no further growth is possible.[35,36] There is extensive evidence that, in order to reliably model a biphasic system, each feature of the secondary phase must be considered. Specifically, in fiber-type reinforcements, it is of utmost relevance to precisely know how the contact and relative orientation between the fiber and matrix might be. This is a non-trivial task, which can be straightforwardly overcome by assuming a random distribution of the fiber and considering certain morphological parameters that would ensure the consideration of the different contact possibilities. Specifically, for the case of CNT reinforcements, Lahiri et al.[41] proposed a very interesting variation of the Zener drag model, in which the specific surface area of the CNT is considered. For our particular case, we further simplify the modeling by considering the mean agglomerate size of CNP after their dispersion, which would fundamentally interact with the grain boundaries as a single body. By starting from the theoretical model proposed by Smith,[42] a simpler equation can be derived by combining two known factors (particle radius and volume fraction):

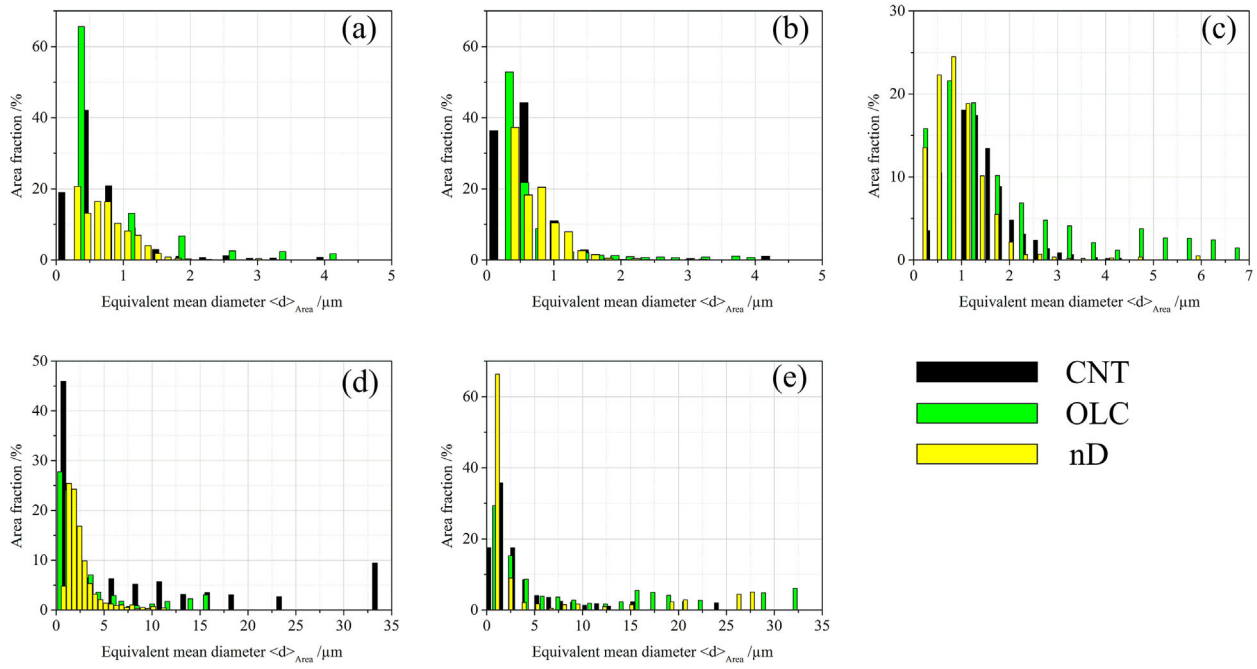

Fig. 2. Equivalent mean agglomerate diameter histograms of (a) 0.5 vol%, (b) 1 vol%, (c) 3 vol%, (d) 6.5 vol%, and (e) 10 vol%.

ADVANCED ENGINEERING MATERIALS

$$\overline{D} = \frac{K \cdot r}{f^n} \quad (1)$$

In Equation 1, D is the mean grain size, r the mean radius of the particle agglomerates after dispersion, f is the reinforcement volume fraction, and K and n are fitting constants that depend on the material system (matrix and reinforcement).

For the used dispersion process and parameters, it has been found that all three kinds of CNP behave in the same way, leading to a mean agglomerate radius of 40–70 nm.[23] Therefore, a mean agglomerate radius of 50 nm is assumed, here, as a first approximation. Furthermore, since the grain boundary pinning is more active at the onset of the grain growth (largest fraction of the energy is dissipated due to a larger grain boundary curvature[36]), the consideration of the initial agglomerate size is the most suitable way to approach the problem.

It has to be kept in mind, that the reagglomeration behavior of the different CNP differs, which will result in different final agglomerate sizes in the sintered composite as shown before in this report. However, as already mentioned, by assuming that all reinforcement types behave the same (different NP), it is reasonable to assume that the fundamental role in pinning is played by agglomerates and not individual NP. Additionally, no interfacial phases are expected to be formed. Under these circumstances, the equation can be expressed as follows:

$$\overline{D} = \frac{0.99 \pm 0.07}{f^{0.4}} \quad (2)$$

A n-coefficient of 0.4 can be found for systems, where the secondary particles are placed at the grain boundaries,[43] which is true in the case of the used composites.[22,23]

In general, the model is in good agreement to all the experimental data obtained for nD and OLC, except for 1 vol %, which might be related to the low concentration and, therefore, an inhomogeneous distribution of the reinforcement phase (Figure 3). However, the real mean grain size for CNT is twice as high as predicted by the model for concentrations higher than 3 vol%. This can be perfectly correlated to the CNT's saturation value for the grain refinement, as shown in Table 1. The CNT show a higher tendency to form agglomerates due to the high aspect ratio and sp^2-hybridization, leading to a saturation value of the volume concentration lower than for OLC and nD.[23] The larger agglomerate sizes lead to a less pronounced grain pinning effect and, therefore, the model is no longer valid for those concentrations.

Summarizing, it is observed that OLC and nD retain their agglomerate size at higher concentrations to a certain degree, resulting in a better distribution and, thus, a more efficient grain refinement. The CNT may show multiple interactions with the grain boundaries depending on how the grain boundaries come across the CNT. It is expected that the behavior of the CNT-containing samples are governed by the randomness of the CNT distribution and their increased agglomerate size.[44] Finally, it can be stated that the model proposed, in this report, is suitable for all three systems analyzed for a wide concentration range, except for larger CNT concentrations where the model provides a fair approximation, but with a certain deviancy resulting from the increased agglomeration activity.

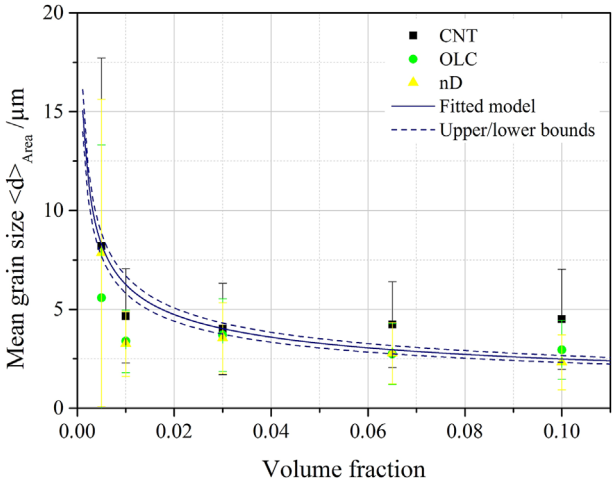

Fig. 3. Mean grain size for all different studied systems as a function of the CNP volume fraction. The blue solid curve represents the empirical Zener boundary pinning model and the dashed blue lines show its upper and lower bounds as analytically shown in Equation 2.

4. Concluding Remarks

After producing and measuring the mean grain size of CNT, OLC, and nD reinforced nickel matrix composites, a model based on the Zener equation is successfully adapted to fit and predict the observed grain refinement for all three kinds of carbon nanoparticles. It is shown, that the model is perfectly valid, as long as no saturation value of the grain refinement effect for the individual particle type is reached. However, the individual concentration, at which a saturation value is reached differs and can be correlated to the mean agglomerate size distribution within the composites. This difference can be correlated to different reagglomeration behaviors due to different carbon hybridization states (sp2 versus sp3) or particle geometries (0D versus 1D) for the three kinds of carbon nanoparticles. In this respect, CNTs show the highest tendency to build larger agglomerates, thus, reaching its grain refinement saturation value at lower concentrations than OLC and nD. Compared to the unreinforced reference with a mean grain size of 19.5 µm, a maximum grain refinement of a factor of 5 for MWCNT, about 7 for OLC and about 8.5 for nD is achieved. These values correspond to 3 vol% of MWCNT, 6.5 vol% of OLC, and 10 vol% of nD.

Article first published online: January 31, 2017
Manuscript Revised: January 11, 2017
Manuscript Received: November 4, 2016

[1] Y. Gogotsi, V. Presser, *Carbon Nanomaterials*, 2nd Ed., CRC Press, Boca Raton FL **2014**.
[2] S. R. Bakshi, D. Lahiri, A. Agarwal, *Int. Mater. Rev.* **2010**, *55*, 41.
[3] V. N. Mochalin, O. Shenderova, D. Ho, Y. Gogotsi, *Nat. Nanotechnol*. **2012**, *7*, 11.
[4] J. Y. Hwang, B. K. Lim, J. Tiley, R. Banerjee, S. H. Hong, *Carbon* **2013**, *57*, 282.
[5] S. R. Bakshi, A. Agarwal, *Carbon* **2011**, *49*, 533.
[6] D. Nunes, M. Vilarigues, J. B. Correia, P. A. Carvalho, *Acta Mater*. **2012**, *60*, 737.
[7] D. Nunes, J. B. Correia, P. A. Carvalho, *Microsc. Microanal*. **2013**, *19*, 2013.
[8] V. Livramento, J. B. Correia, N. Shohoji, E. Osawa, *Diamond Relat. Mater*. **2007**, *16*, 202.
[9] J. N. Boland, X. S. Li, *Materials* (Basel) **2010**, *3*, 1390.
[10] L. Kumari, T. Zhang, G. Du, W. Li, Q. Wang, A. Datye, K. Wu, *Compos. Sci. Technol*. **2008**, *68*, 2178.
[11] A. Agarwal, S. R. Bakshi, D. Lahiri, *Carbon Nanotubes reinforced Metal Matrix Composites* 1st ed. CRC Press, Boca Raton, FL, USA **2011**.
[12] D. Nunes, J. B. Correia, P. A. Carvalho, *Microsc. Microanal*. **2012**, *18*, 73.
[13] Y. Li, B. X. Li, W. J. Zou, *Appl. Mech. Mater*. **2011**, *80–81*, 683.
[14] A. Hirata, M. Igarashi, T. Kaito, *Tribol. Int*. **2004**, *37*, 899.
[15] K. Miyoshi, K. W. Street, R. L. Vander Wal, R. Andrews, A. Sayir, *Tribol. Lett*. **2005**, *19*, 191.
[16] S. Iijima, *Nature* **1991**, *354*, 56.
[17] H. W. Kroto, J. R. Heath, S. C. O'Brian, R. F. Curl, R. E. Smalley, *Nature* **1985**, *318*, 162.
[18] C. Guiderdoni, E. Pavlenko, V. Turq, A. Weibel, P. Puech, C. Estournès, A. Peigney, W. Bacsa, Ch. Laurent, *Carbon* **2013**, *58*, 185.
[19] H. Dieringa, *J. Mater. Sci*. **2010**, *46*, 289.
[20] H. J. Choi, J. H. Shin, D. H. Bae, *Compos. Sci. Technol*. **2011**, *71*, 1699.
[21] S. Suarez, F. Lasserre, F. Mücklich, *Mater. Sci. Eng. A* **2013**, *587*, 381.
[22] S. Suarez, E. Ramos-Moore, B. Lechthaler, F. Mücklich, S. Suárez, *Carbon* **2014**, *70*, 173.
[23] L. Reinert, M. Zeiger, S. Suárez, V. Presser, F. Mücklich, *RSC Adv.* **2015**, *5*, 95149.
[24] V. Mochalin, S. Osswald, Y. Gogotsi, *Chem. Mater*. **2009**, *21*, 273.
[25] A. Sanaty-Zadeh, *Mater. Sci. Eng. A* **2012**, *531*, 112.
[26] S. C. Tjong, *Mater. Sci. Eng. R Rep*. **2013**, *74*, 281.
[27] S. D. Bergin, Z. Sun, D. Rickard, P. V. Streich, J. P. Hamilton, J. N. Coleman, *ACS Nano* **2009**, *3*, 2340.
[28] M. R. S. Castro, *Alternative Conductive Coatings Based on Multi-Walled Carbon Nanotubes*, Ph.D. Thesis, Saarland University, **2007**.
[29] A. Pentecost, S. Gour, V. Mochalin, I. Knoke, Y. Gogotsi, *ACS Appl. Mater. Interfaces* **2010**, *2*, 3289.
[30] A. Krüger, F. Kataoka, M. Ozawa, T. Fujino, Y. Suzuki, A. E. Aleksenskii, A. Ya. Vul', E. Ōsawa, *Carbon* **2005**, *43*, 1722.
[31] M. Zeiger, N. Jäckel, M. Aslan, D. Weingarth, V. Presser, *Carbon* **2015**, *84*, 584.
[32] K. Bogdanov, A. Fedorov, V. Osipov, T. Enoki, K. Takai, T. Hayashi, V. Ermakov, S. Moshkalev, A. Baranov, *Carbon* **2014**, *73*, 78.
[33] O. O. Mykhaylyk, Y. M. Solonin, D. N. Batchelder, R. Brydson, *J. Appl. Phys*. **2005**, *97*, 074302.
[34] C. S. Smith, *Trans. Met. Soc. AIME* **1948**, *175*, 15.
[35] P. A. P. Manohar, M. Ferry, T. Chandra, *ISIJ Int*. **1998**, *38*, 913.
[36] D. A. Porter, K. E. Easterling, *Phase Transformations in Metals and Alloys*, 2nd ed., Chapman & Hall, London, UK **1992**.
[37] P. Rossi, S. Suarez, F. Soldera, F. Mücklich, *Adv. Eng. Mater*. **2014**, *17*, 1017.
[38] J. Y. Hwang, A. R. P. Singh, M. Chaudhari, J. Tiley, Y. Zhu, J. Du, R. Banerjee, *J. Phys. Chem. C* **2010**, *114*, 10424.
[39] M. Singleton, P. Nash, *Bull. Alloy Phase Diagrams* **1989**, *10*, 121.
[40] S. Suarez, F. Lasserre, O. Prat, F. Mücklich, *Phys. Status Solidi* **2014**, *211*, 1555.
[41] D. Lahiri, V. Singh, A. K. Keshri, S. Seal, A. Agarwal, *Carbon* **2010**, *48*, 3103.
[42] C. Smith, *Trans. AIME* **1948**, *175*, 15.
[43] G. Muralidharan, R. G. Thompson, *Scr. Mater*. **1997**, *36*, 755.
[44] N. Sun, B. Patterson, J. Suni, H. Weiland, L. Allard, *Acta Mater*. **2006**, *54*, 4091.

IV Tribo-Mechanisms of Carbon Nanotubes: Friction and Wear Behavior of CNT-Reinforced Nickel Matrix Composites and CNT-Coated Bulk Nickel

Leander Reinert[1], Sebastian Suárez[1] and Andreas Rosenkranz[1,2]

[1] Department of Material Science and Engineering, Saarland University, 66123 Saarbrücken, Germany
[2] Institute of Experimental Physics, Pontificia Universidad Católica de Chile, Santiago 7820436, Chile

*Published in **"Lubricants" (Impact factor: not applicable)***

Accessible online at: https://doi.org/10.3390/lubricants4020011

Own contribution:

Sample processing including particle dispersion and drop casting of particles; Tribological experiments and friction coefficient analysis; Scanning electron microscopy and wear track analysis; Raman Spectroscopy; Writing; Discussion; Planning.

Abstract:

In this study, nickel matrix composites reinforced by carbon nanotubes (CNTs) are compared to unreinforced CNT-coated (by drop-casting) bulk nickel samples in terms of their friction and wear behavior, thus gaining significant knowledge regarding the tribological influence of CNTs and the underlying tribo-mechanism. It has been shown that the frictional behavior is mainly influenced by the CNTs present in the contact zone, as just minor differences in the coefficient of friction between the examined samples can be observed during run-in. Consequently, the known effect of a refined microstructure, thus leading to an increased hardness of the CNT reinforced samples, seems to play a minor role in friction reduction compared to the solid lubrication effect induced by the CNTs. Additionally, a continuous supply of CNTs to the tribo-contact can be considered isolated for the reinforced composites, which provides a long-term friction reduction compared to the CNT-coated sample. Finally, it can be stated that CNTs can withstand the accumulated stress retaining to some extent their structural state for the given strain. A comprehensive study performed by complementary analytical methods is employed, including Raman spectroscopy and scanning electron microscopy tounderstand the involved friction and wear mechanisms.

Cite this as:
L. Reinert, S. Suárez, A. Rosenkranz, Tribo-Mechanisms of Carbon Nanotubes: Friction and Wear Behavior of CNT-Reinforced Nickel Matrix Composites and CNT-Coated Bulk Nickel. *Lubricants* **2016**, 4, 11. (*https://doi.org/10.3390/lubricants4020011*)

lubricants

MDPI

Article

Tribo-Mechanisms of Carbon Nanotubes: Friction and Wear Behavior of CNT-Reinforced Nickel Matrix Composites and CNT-Coated Bulk Nickel

Leander Reinert [1], Sebastian Suárez [1] and Andreas Rosenkranz [1,2,*]

[1] Department of Material Science and Engineering, Saarland University, Saarbrücken 66123, Germany; l.reinert@mx.uni-saarland.de (L.R.); s.suarez@mx.uni-saarland.de (S.S.)

[2] Institute of Experimental Physics, Pontificia Universidad Católica de Chile, Santiago 7820436, Chile

* Correspondence: a.rosenkranz@mx.uni-saarland.de; Tel.: +49-681-302-70554; Fax: +49-681-302-70502

Academic Editors: Werner Oesterle and Ga Zhang

Received: 1 March 2016; Accepted: 14 April 2016; Published: 19 April 2016

Abstract: In this study, nickel matrix composites reinforced by carbon nanotubes (CNTs) are compared to unreinforced CNT-coated (by drop-casting) bulk nickel samples in terms of their friction and wear behavior, thus gaining significant knowledge regarding the tribological influence of CNTs and the underlying tribo-mechanism. It has been shown that the frictional behavior is mainly influenced by the CNTs present in the contact zone, as just minor differences in the coefficient of friction between the examined samples can be observed during run-in. Consequently, the known effect of a refined microstructure, thus leading to an increased hardness of the CNT reinforced samples, seems to play a minor role in friction reduction compared to the solid lubrication effect induced by the CNTs. Additionally, a continuous supply of CNTs to the tribo-contact can be considered isolated for the reinforced composites, which provides a long-term friction reduction compared to the CNT-coated sample. Finally, it can be stated that CNTs can withstand the accumulated stress retaining to some extent their structural state for the given strain. A comprehensive study performed by complementary analytical methods is employed, including Raman spectroscopy and scanning electron microscopy to understand the involved friction and wear mechanisms.

Keywords: carbon nanotubes; metal matrix composites; drop casting; solid lubricant

1. Introduction

In recent years, carbon nanotubes (CNTs) have been receiving a lot of attention in the research community due to their outstanding intrinsic physical properties, particularly mechanical [1] and thermal [2]. In addition to that, their shape, high aspect ratio and high flexibility rendered them as a promising candidate for solid lubrication or as a lubricant additive in tribological applications. Several studies have proved the ability of CNTs to reduce friction and wear; for example, when used as the reinforcement phase in composites [3–9], as a protective film [10–13], solid lubricant [8–10,12,14,15], or lubricant additive [16–19]. Although all of these systems show improvements to a different extent, the tribo-mechanisms inducing these effects are clearly differing and not completely understood. The variation in testing parameters and tribological systems used make it rather difficult to correlate the measured effect to the underlying friction and/or wear mechanism. Therefore, the aim of the present work is to study the behavior of CNTs used as reinforcement phase or as a protective film, but keeping all the tribological testing parameters fairly constant. Thus, differences in the tribological behavior can be traced back more easily as a function of the purpose of use.

The main drawback of CNTs is their processing difficulty due to strong van der Waals interactions that generate agglomerates. This reduces all of the aforementioned properties, as well as the integration

as a second phase; for example, in composites [20]. One method for facile de-agglomeration of CNTs is the dispersion in solvents. The CNTs can be dispersed with [21–25] or without prior functionalization [26,27]. As a functionalization (covalently or non-covalently) changes the chemical composition and/or physical properties of the CNTs, this should be avoided if effects of CNTs on an experiment need to be considered in isolation [21–25]. Therefore, for the present research work, we resigned on functionalizing the CNTs. Based upon our experience in previous studies, ethylene glycol is chosen as the solvent due to its low toxicity and good dispersion results for CNTs [26,28,29]. Furthermore, polyols like ethylene glycol allow for a subsequent functionalization of CNTs or the deposition of metal particles onto their surface, establishing the possibility of further research work on this topic [28].

In order to study the tribological behavior of CNTs, it seems to be reasonable to start with experiments under dry conditions to avoid the influence of a lubricant such as oil or grease. Thus, there are two main possibilities: (1) the study of a CNT-film deposited on a surface; or (2) the investigation of a composite material. Regarding CNT-films on top of surfaces, friction- and wear-reducing effects are often correlated to the ability of CNTs to roll and, thus, separating the rubbing surfaces. In this context, the CNTs can act as ball bearings [5,9,30,31]. For example, Dickrell *et al.* [31] were able to prove differences in the frictional behavior of CNTs as a function of their orientation on top of a surface. Often, the friction reduction of CNTs is also explained by their degradation, thus forming a lubricating graphitic tribolayer [5,8,9,11]. In this case, simulations estimate a contact pressure between 1.5 to 2.5 GPa to deteriorate the CNTs [32].

When it comes to reinforced composites, several influences on friction and wear have to be added to the discussion. There are three groups of composite materials that have to be distinguished first. Polymer-matrix composites are mainly used in applications where light weight is desired, but no heat resistance is needed. Oppositely, ceramic matrices are used where inertness under high temperatures, as well as high mechanical properties, are required. Finally, metal matrix composites (MMC) lie between both application fields, presenting an intermediate research field that offers high ductility, high electrical conductivity, as well as good heat resistivity. Therefore, MMCs are selected in this work for the composite material. In the case of MMCs, besides the mentioned effects of CNTs, wear reduction is often referred to as a hindered plastic deformation of the material due to the restricted movement of dislocations induced by the presence of CNTs [30]. Furthermore, reduced wear can be correlated to the grain refinement effect, thus inducing an increased hardness (Hall-Petch relation) [29]. Furthermore, it is important to mention that not only changes in the microstructure affect the tribological properties, but also the formation of interphases between CNTs and matrix material needs to be considered. In the literature, it is controversially discussed if there is a formation of interphases in a CNT-reinforced metal matrix composite, or rather when using which metal matrix [33]. When using nickel as the matrix material, no chemical reaction between Ni and CNTs can be observed [34,35]. Furthermore, nickel forms only metastable carbides under very specific conditions, therefore being suitable for a reinforcement based on CNTs with the parasitic emergence of interphases [36,37]. Consequently, nickel is chosen as the matrix material in the present study.

2. Results and Discussion

2.1. Frictional Behavior

The different sample sets were first compared in terms of the temporal evolution of the coefficient of friction (COF) using a ball-on-disk tribometer under linear reciprocating motion and an Al_2O_3 ball as counter body. In Figure 1 the COF is plotted as a function of the number of sliding cycles (total sliding cycles of 200) for the sintered Ni reference, the CNT-coated sample and the CNT-reinforced sample.

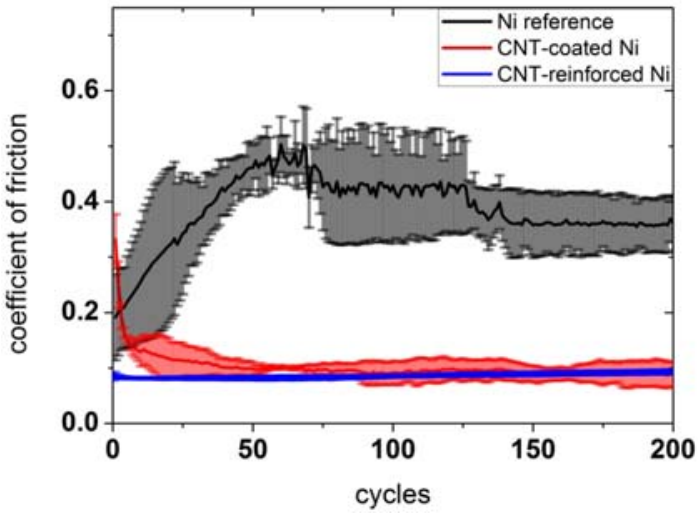

Figure 1. Temporal evolution of the COF plotted as a function of the number of sliding cycles for a sintered Ni reference, a CNT-coated, and a CNT-reinforced sample.

The COF of the Ni reference increases during the first 60 cycles from 0.2 to roughly 0.45. In the beginning of the experiment, only some single asperities of the ball and the substrate are in contact with each other, thus generating a small contact area. With time (increasing number of sliding cycles), the initial surface roughness is worn off and the indentation depth of the asperities increases which leads to an enlargement of the contact area. This is directly related to the increase in the COF as observed in Figure 1. Moreover, as Raman spectroscopy can show later in this work, the formation of an oxide layer contributes to the increasing COF, since Ni oxide is known to act as a high-shear strength layer [5]. Afterwards, the COF drops slightly down within the next 90 cycles to a value of 0.36 remaining stable for the rest of the measuring time. After a certain time, the substrate and the counter body undergo a transition from non-conformal to conformal contact conditions due to the smoothing of the surface roughness which results in a reduced COF. The behavior is typical for pure metals and has been already extensively investigated [38].

In case of the CNT-coated sample, the COF drops down within the first 50 cycles from 0.38 to 0.1, remaining stable at this value for the rest of the measurement. The high initial COF may be explained by shifting large amounts of entangled CNTs to the sides of the wear track within the first sliding cycles. The shifting and stacking of entangled CNTs requires a higher transversal force, thus resulting in a higher COF. Subsequently, the wear track can be continuously supplied with small amounts of CNTs that are transferred from the end of the wear tracks back to the contact area. In addition to that, entangled CNTs are also transferred to the ball, which can be seen in Figure 2. These transferred CNTs will also contribute to the continuous supply of CNTs to the contact area. In this case, the CNTs act as solid lubricant as there is no other difference to the nickel reference than the CNTs in the contact area [5,10,12,14,15]. Furthermore, it is noteworthy that no oxide formation is detected in this case.

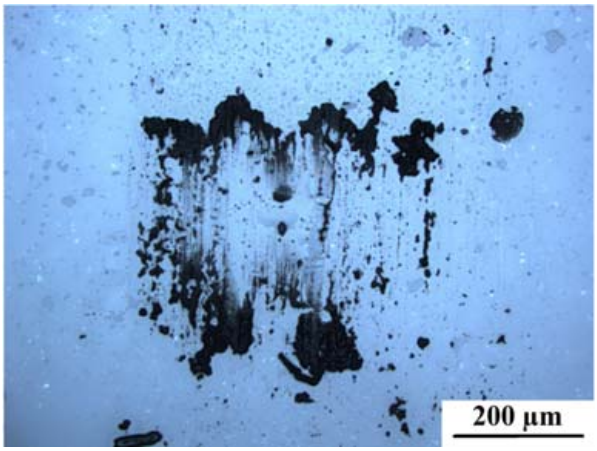

Figure 2. Light microscope picture of the Al_2O_3 counter body having rubbed against the CNT-coated sample for 200 sliding cycles.

Regarding the CNT-reinforced sample, the COF remains stable and at a low value of around 0.1 over the entire measuring time. Using the Hertzian contact model, the contact pressure for the given material pairing (Al_2O_3 against Ni) can be estimated to 1.56 GPa [29]. This value greatly exceeds the yield strength of the samples, which is 0.3 for pure Ni and 0.45 GPa for the CNT-reinforced Ni. Thus, a greater penetration depth and a subsequently increased real contact area is resulting for the Ni reference [29]. Additionally, a very similar COF can be noticed after the first 50 sliding cycles for the CNT-reinforced sample compared to the CNT-coated sample. This might be a consequence of the embedded CNT clusters that can act as a lubricant reservoir, supplying the rubbing surfaces continuously with CNTs [5]. As the COF of both samples is nearly identical, it is reasonable to assume that this behavior is mainly induced by CNTs present in the contact zones.

This being stated, it is of interest to examine the long-term behavior of these samples. In Figure 3 the temporal evolution of the COF of the three samples for 20,000 sliding cycles is depicted.

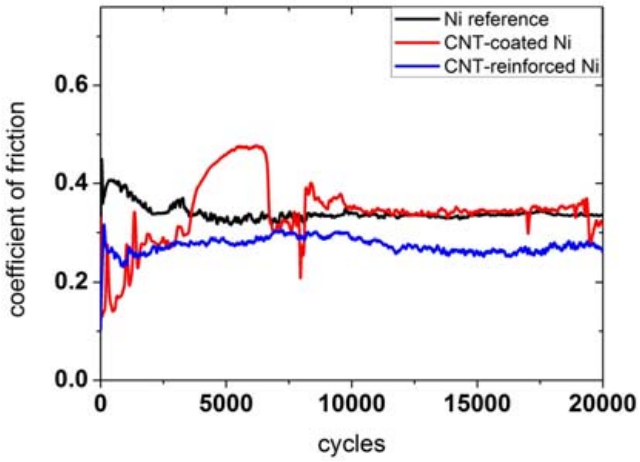

Figure 3. Temporal evolution of COF plotted against the number of sliding cycles for a Ni reference, a CNT-coated sample, and a CNT-reinforced sample.

For the Ni reference, it can be observed that the COF decreases within the first 2500 cycles from 0.4 to 0.35, henceforward remaining fairly constant. With time, the surface asperities are worn off, thus generating conformal contact conditions. This process ends after the first 2500 cycles, reaching an equilibrium and, thus, steady state conditions [38]. As could also be detected for the 200 sliding cycles, Ni oxide is formed during the run-in. As a consequence, the final COF is mainly influenced

by this oxide layer. The steady-state COF is also in good agreement with those values reported in the literature for microcrystalline Ni rubbed against Al_2O_3 [39].

In the case of CNT-coated Ni, it becomes clear that the COF is just reduced within the first 3000 cycles. During this time interval, the COF increases from 0.1 to 0.35 and also shows some sharp spikes. These spikes can be explained with the removal of the CNT layer. It is worth mentioning that this removal is just temporary because CNTs that have been shifted out of the wear track can be partially transferred back during the sliding movement. In between 3000 and 7000 sliding cycles, the COF increases from 0.35 to 0.47. This might be a consequence of several influences which act at the same time. On the one hand, this increase might be attributed to the occurrence of the ongoing direct contact of the Al_2O_3 ball with the Ni substrate (increasing contact area), thus showing a similar behavior as the reference within the first 1000 cycles. Furthermore, the generation of oxide particles contributes to the increasing COF as discussed for the reference. Finally, the CNTs are not acting as a lubricant anymore, as they are completely shifted out of the wear track. However, carbon can still be found in the middle of the wear track as shown by Raman spectroscopy and discussed later in this work. It is rather unclear, how the observed carbon configuration affects the COF. This topic is subject of ongoing research work and will be addressed in a follow-up paper. During the next 3000 cycles, the contacting surfaces undergo a transition from non-conformal to conformal contact conditions. Additionally, several spikes can be noticed which might be caused by a temporary appearance of "fresh" CNTs that have been transferred back again from the sides of the wear track to the contact zone. The observed spikes that show a higher COF can result from the generation of wear particle accumulations. After 10,000 cycles, the CNT-layer is completely removed and the COF remains stable for the rest of the measurement, as observed for the reference. This can be explained with the presence of an oxide layer and the complete absence of CNTs.

The CNT-reinforced sample shows a rather different behavior. For this sample, the COF increases from 0.1 to 0.3 within the first 500 cycles. During the next 1000 cycles, the COF decreases again to a value of 0.25. For the remaining testing time, the COF fluctuates between 0.25 and 0.3. The first increase can be explained by the increasing contact area, as asperities of the ball and the substrate are worn off with time and the surface is slightly indented by the counter body. Afterwards, the decrease of COF seems to be a consequence of CNTs that reach the contact area as they are released from the agglomerate clusters inside the nickel matrix due to wear. The fluctuation in the third part might be explained by the limited amount of CNTs that can be transferred to the contact area. In other words, while the surface is worn off, new CNTs will be continuously shifted to the contact area, thus supplying the contact zone with new solid lubricant. However, it is worth mentioning that the amount of CNTs transferred to the contact zone will differ with time due to the slightly inhomogeneous distribution of CNT clusters in the bulk material. Another reason for a fluctuation of the COF might be the mild and very irregular formation of oxides within the wear track. This can be explained by a partial protection against oxidation induced by the irregular presence of CNTs, as carbon can act as an oxygen diffusion barrier. This is because of the higher stability of carbon oxide compared to Ni oxide, which can be seen in the corresponding Ellingham diagram.

2.2. Wear Behavior

In general, it can be pointed out that different wear mechanisms are normally acting simultaneously during a tribological experiment. Therefore, only the dominating mechanisms are named and discussed in the following section. In Figure 4, SEM micrographs of the wear tracks observed on the Ni reference after 200 (a) and 20,000 sliding cycles (b) are depicted.

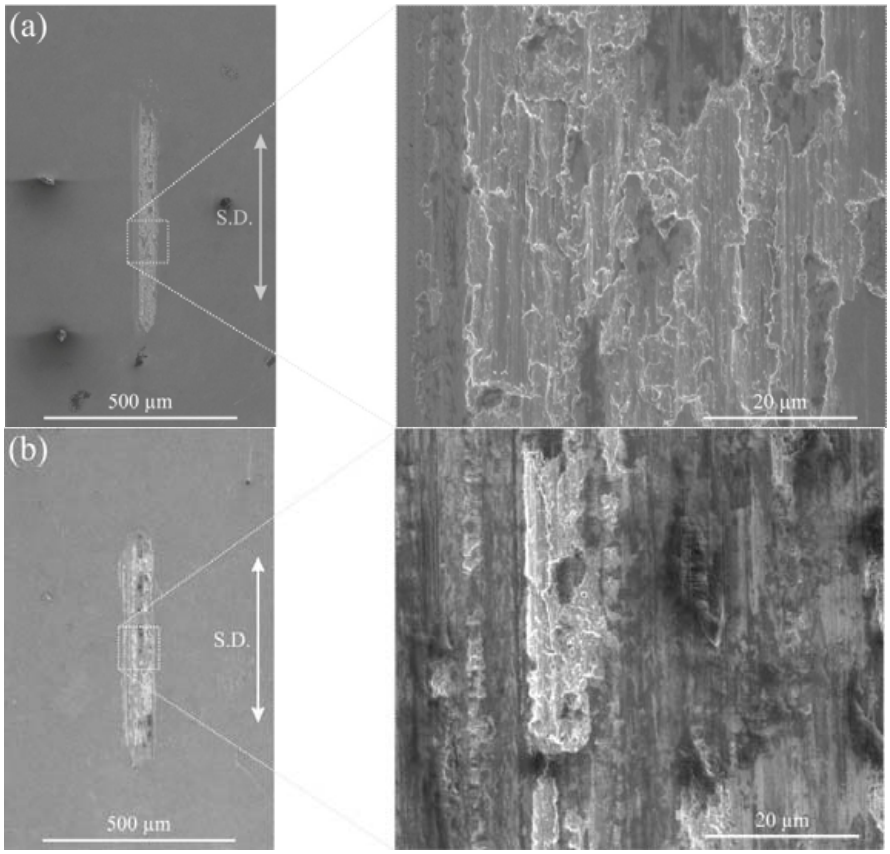

Figure 4. Wear tracks after 200 (**a**) and 20,000 (**b**) sliding cycles on the Ni reference. Detailed images of the middle of the wear tracks (highest sliding velocity) are given using a higher magnification.

It can be stated that the main wear mechanism for both wear tracks is plowing. This is evident as the hardness of the counter body (Al_2O_3 ball) greatly exceeds the hardness of the nickel reference. Furthermore, the formation of Ni oxide particles can additionally add an abrasive component. Particularly for NiO, it has also been proven that it acts as a high shear strength layer which increases the COF [5]. Together with the increasing contact area during the run-in process, this leads to an enlarged COF. The oxide formation was studied by Raman spectroscopy and will be further discussed in the next section of the present work.

Furthermore, an enlarged wear track width after 20,000 sliding cycles wear track compared to 200 cycles is clearly noticeable. This is a consequence of the ongoing indentation of the Al_2O_3 ball into the sample during the measurement, thus generating a larger contact area with the flanks of the ball and, thus, expanding the width of the wear track.

In Figure 5, the corresponding wear tracks for the CNT-coated sample are displayed.

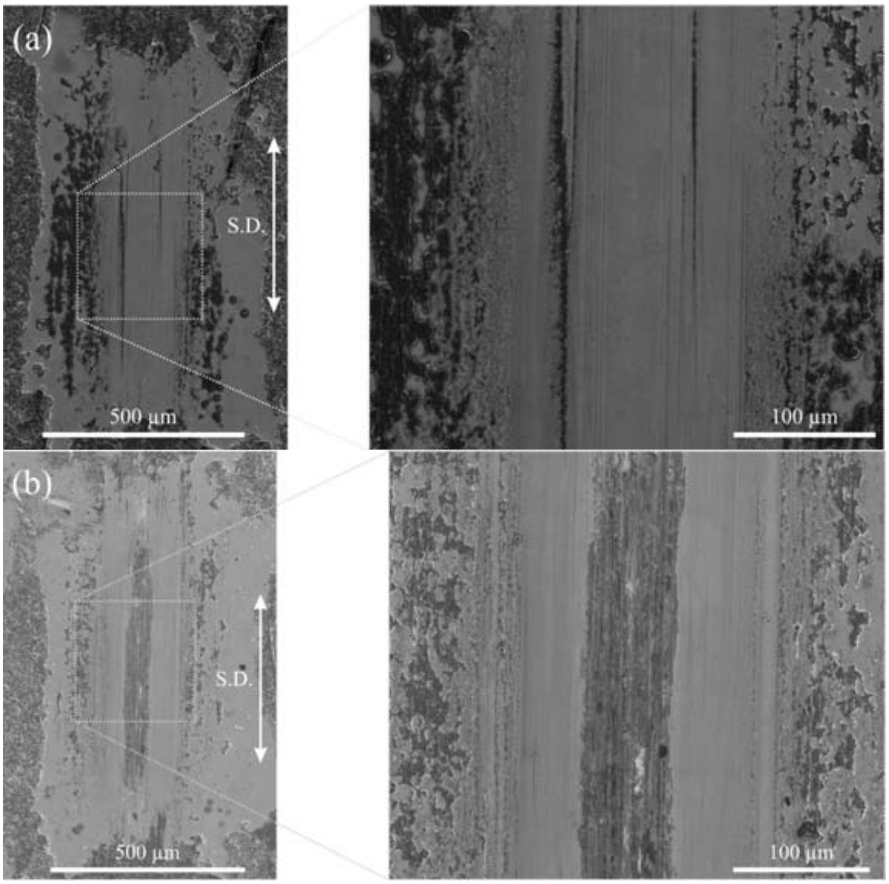

Figure 5. Wear tracks of the CNT-coated sample after 200 (**a**) and 20,000 sliding cycles (**b**). Detailed images of the middle of the wear tracks (highest sliding velocity) are given using a higher magnification.

In case of the 200 sliding cycles, no severe wear of the nickel substrate can be noticed. Apart from slight scratches that might have been generated by larger asperities of the ball the Ni surface is still polished. It is worth mentioning that even after the tribological experiment, individual grains can still be recognized, which is only possible for highly-polished surfaces. Inside of the mentioned scratches, CNTs can be found which is verified by Raman spectroscopy. These CNTs, as well as the CNTs from the wear track end, can lubricate the sample, thus preventing the occurrence of severe wear. In general, the absence of severe wear demonstrates that the temporal evolution of the COF for 200 cycles is mainly dominated by the contact of the CNT-coating with the counter body, acting as a protective layer for the Ni substrate. Furthermore, no oxide formation can be detected. This observation seems to be reasonable as there is almost no direct contact between the counter body and the Ni substrate. The lack of oxides might also contribute to the low COF observed for the 200 sliding cycles.

For 20,000 sliding cycles, two areas in the wear tracks can be distinguished. On the one hand, in the middle of the wear track, a small area (width between 60 and 70 µm) with severe wear and pronounced plowing as well as oxidation marks can be found. On the other hand, a wider wear track having some slight scratches and a similar appearance compared to the wear track observed after 200 sliding cycles is clearly visible. When comparing the wear track widths after 200 and 20,000, it is noticeable that the wear track width is more or less constant. The area, where severe wear occurs might be connected to the increasing COF after 3000 cycles, when the Al_2O_3 ball potentially gets in full contact to the Ni substrate. Thus, from this point on, the similar behavior of the COF compared to the Ni reference could be explained by this hypothesis. As for the reference, the dominating wear mechanism is most probably plowing. Additionally, similar to the reference, an oxide formation can be observed in the middle. Moreover, at the ends of the wear track, oxidic wear particles are deposited.

The formation of these particles mainly contributes to the increasing COF during run-in, thus showing a similar frictional behavior as the reference. However, in contrast to the Ni reference, the width of the area with severe wear occurrence is decreased which might be due to the CNTs that avoid the direct contact of the flanks of the ball with the Ni substrate.

In Figure 6, the wear track on the CNT-reinforced sample after 20,000 cycles is depicted.

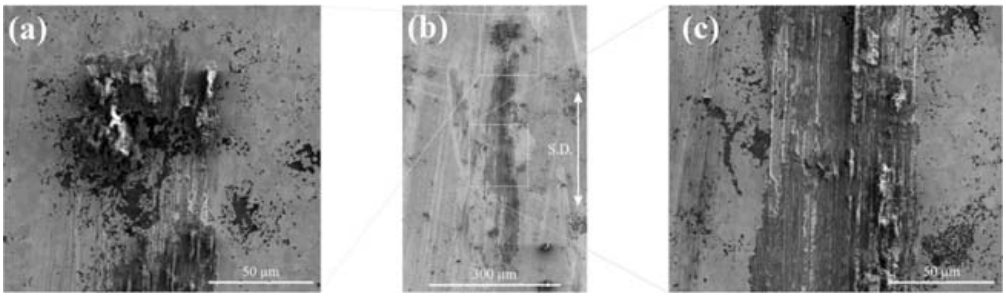

Figure 6. Wear track of the CNT-reinforced sample after 20,000 sliding cycles (**b**) imaged at different positions. The upper part of the wear track (**a**) as well as the middle (**c**) are shown in a higher magnification.

Although the dominating wear mechanism is, again, plowing, the wear track seems to be very inhomogeneous. In some areas, severe wear occurs, whereas other parts are nearly unaffected. Having a closer look at the areas with less wear, it can be observed that CNT clusters are present in these areas. As a consequence, the inhomogeneous wear track can be well correlated with the distribution of the CNT clusters within the composite. In addition to this, a large amount of oxidic wear particles can be found at the ends of the wear track, but less oxidic wear particles can be determined within the wear track. It might be reasonable to assume that these particles are shifted out of the contact zone, thus having a reduced influence of the resulting COF. Additionally, as there is a continuous supply of "fresh" CNTs during the tribological measurement, the sample is always lubricated. Noticing that the COF is not as low as in the beginning of the measurement of the CNT-coated sample, this mainly seems to be a function of the amount of CNTs involved in the process and present in the tribological contact zone. Consequently, a better distribution of CNT clusters, as well as a higher amount in the contact zone would probably lower the resulting COF to a larger extent and allows for improved wear protection of the composite material. This is currently subject of ongoing research work and will be published by the authors in a follow-up paper.

2.3. Structural and Chemical Analysis of the Wear Tracks

Raman spectroscopy is widely recognized as the most suitable technique to assess the structural state of sp^2 carbon materials. In the specific case of CNTs, this technique provides very useful information for the proper description of their defect and purity state [40]. Within the typical resonances in CNTs, the most relevant are the D (defect-related), G (graphitic lattice-related), and G′ (second order resonance, purity-related) bands [41]. Additionally, the analysis of the FWHM of the G band (Γ_G) depict the evolution of the crystallinity of the graphitic lattice [37]. Finally, it has been empirically shown that the distance between defects is related to the excitation wavelength (λ) of the spectrometer and the intensity ratio of the D and G band [42,43]. This distance can, thus, be calculated by [43]:

$$L_a = \left(2.4 \times 10^{-10}\right) \cdot \lambda_{laser}^4 \cdot \left(\frac{I_D}{I_G}\right)^{-1} \quad (1)$$

It is important to consider that, since Raman spectroscopy is a volume-sensitive technique, it is necessary to normalize the information (to the peak with the maximum intensity) and that only a comparison of intensity ratios provides reliable information.

For this study, we focused our analysis on the most relevant structural indicators obtained by Raman spectroscopy, namely: defect index (I_D/I_G), purity index ($I_{G'}/I_D$), G-band center position (X_{CG}), crystallinity (Γ_G), and mean inter-defect distance (L_a).

Figure 7 shows the spectra of different positions within and outside the wear track for the CNT-coated sample after 200 sliding cycles. Region A lies outside the contact zone, region B consists of distributed carbon phase within the track, region C contains distributed agglomerates inside the track, region D contains CNTs within a wear scratch and, finally, region E is at the center of the wear track. Generally, all spectra show a similar peak distribution except for that taken at spot E. In this case, there are no peaks whatsoever, representing a typical result of a pure metal. It is well known that metals with either fcc, hcp, or bcc crystal lattices present no first-order Raman spectra [44]. Interestingly, by considering the quantitative analysis of the Raman data presented in Table 1, several conclusions can be drawn. First, a clear degradation of the CNTs structural quality can be observed as we move towards the center of the wear track. This is supported by an increasing I_D/I_G ratio and certainly, by a reduction in the mean inter-defect distance. However, the crystallinity does not show a significant deviation within the measured values, thus withstanding a possible conclusion in this respect. Regarding the purity index, it follows a similar behavior as the crystallinity, being directly related to the deterioration of the graphitic structure into an amorphous-type sp^2 carbon phase.

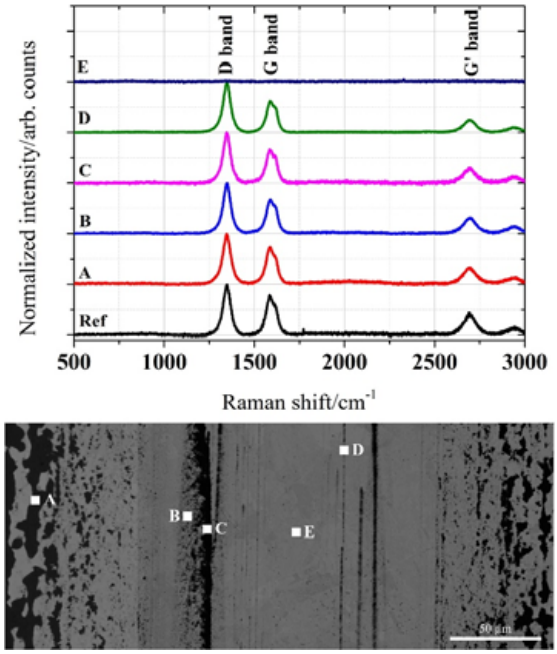

Figure 7. Raman spectra of different spots of the wear track taken from the CNT-coated sample after 200 sliding cycles.

Table 1. Descriptive parameters obtained by Raman spectroscopy of the CNT-coated sample after 200 sliding cycles.

Position	I_D/I_G	$I_{G'}/I_D$	X_{CG} (cm^{-1})	Γ_G (cm^{-1})	L_a (nm)
Reference	1.247	0.435	1593.0	73.9	15.4
A	1.360	0.319	1593.9	62.3	14.1
B	1.461	0.314	1594.4	79.1	13.2
C	1.511	0.313	1593.1	75.9	12.7
D	1.591	0.251	1594.8	75.6	12.1
E	—	—	—	—	—

The Raman spectra of the CNT-coated sample tested for 20,000 sliding cycles are shown in Figure 8. Here, three different regions are clearly noticeable. Region A is on the edge of the track, where apparently lightly modified CNTs are. Region B lies within the contact zone, where the CNTs seem to be embedded in the matrix. Finally, region C (light grey zone) is where the highest contact pressure was applied.

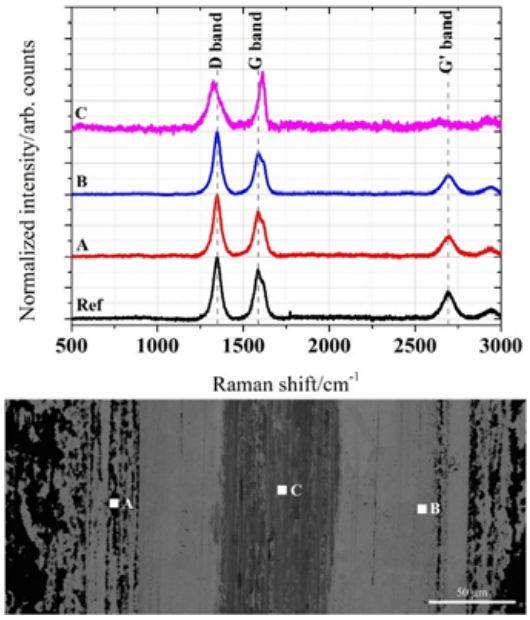

Figure 8. Raman spectra of different spots of the wear track taken from the CNT-coated sample after 20,000 sliding cycles.

The quantification of the Raman spectra (Table 2) provides similar results as those shown for 200 cycles regarding tendencies on the different intensity ratios analyzed. However, due to the longer measuring time, the effects become more evident. Specifically, there is a clear increment in the defect ratio (and subsequently, the inter-defect distance), related to the increased exposure time to the tribological contact. Furthermore, the quality indicators (purity index and crystallinity) show a strong degradation of the CNTs towards a different carbon configuration, namely amorphous nano-carbons. This is also strongly supported by the G-band shift towards a higher Raman shift [45].

Table 2. Descriptive parameters obtained by Raman spectroscopy of the CNT-coated sample after 20,000 sliding cycles.

Position	I_D/I_G	$I_{G'}/I_D$	X_{CG} (cm^{-1})	Γ_G (cm^{-1})	L_a (nm)
Reference	1.247	0.435	1593.0	73.9	15.4
A	1.373	0.303	1592.3	80.2	14.0
B	1.493	0.294	1594.2	93.8	12.9
C	—	—	1607.1	—	—

Regarding the surface chemistry after the tribological experiments, all studied cases showed the presence of Ni oxide (NiO) [46,47]. This is straightforwardly detected with Raman spectroscopy by observing the resonance at 550 and 1100 cm^{-1}.

Specifically, the peak at 550 cm^{-1} corresponds to a one-phonon (1P) scattering and the peak at 1100 cm^{-1} corresponds to a two-phonon (2P) scattering process [46,47]. Figure 9 shows the spectra of the samples in the range of interest. The 1P scattering is detected in all the samples, whereas 2P is observable only in the reference sample, even after only 200 cycles. This would indicate that the

oxidation activity was stronger in the absence of CNTs which is related to the capability of the CNTs to avoid the direct exposure of the metal to the environment. Particularly, in the case of the CNT-coated samples, the protection is evident. However, in the case of the CNT-reinforced Ni, the behavior is quite different. The protection is achieved only after a CNT-layer is formed after run-in, where the CNTs are provided by the agglomerates present within the matrix.

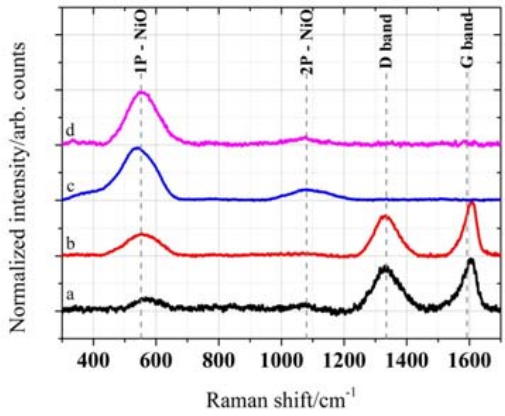

Figure 9. Raman spectra of the studied samples in the range from 300 to 1700 cm^{-1}. (**a**) CNT-reinforced Ni 20,000 cycles; (**b**) CNT-coated Ni 20,000 cycles; (**c**) Ni reference 200 cycles; and (**d**) Ni reference 20,000 cycles. The resonance bands for NiO (1P and 2P) and sp^2 carbon (D and G) are shown for comparison.

Finally, we analyzed the state of the CNTs that were transferred from the coating to the counter body during the experiment. The Raman spectra and its subsequent quantitative analysis are shown in Figure 10 and Table 3, respectively. As for the substrate, an increment in the defect ratio and the inter-defect distance can be observed which is proportional to the increasing exposure time of the CNTs in the tribological contact.

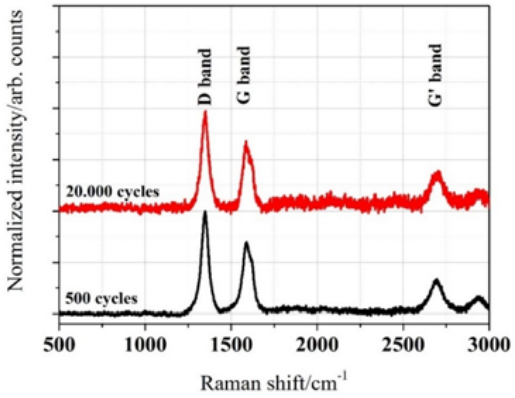

Figure 10. Raman spectra of the transferred CNTs from the coating to the counter body (alumina ball).

Table 3. Descriptive parameters obtained by Raman spectroscopy of the CNT-coated sample after 20,000 sliding cycles.

Position	I_D/I_G	$I_{G'}/I_D$	X_{CG} (cm^{-1})	Γ_G (cm^{-1})	L_a *(nm)*
Reference	1.247	0.435	1593.0	73.9	15.4
500	1.436	0.336	1594.1	73.8	13.4
20,000	1.521	0.387	1594.9	84.5	12.6

3. Experimental Section

3.1. Materials

Commercially available multi-walled CNTs (Baytubes C150P from Bayer (Leverkusen, Germany), purity >95%, individual particle diameter of 5–20 nm) and dendritic Ni powder (Alfa Aesar (Karlsruhe, Germany), maximum particle size of 44 µm, purity of 99.8%) were used as starting materials. They were blended by a colloidal mixing process using ethylene glycol as solvent. In order to ensure good dispersion, a homogenizer (WiseTis, Witeg) and an ultrasonic bath (Sonorex Super RK 514, Bandelin, 860 W, 35 kHz) were employed for five and 20 min, respectively. These processing parameters, as well as a concentration of 0.006 vol% of CNTs in the solvent were chosen according to previous studies [26]. In a previous study, the zeta-potential of this system was determined to be 21.7 $\pm$ 1.4 mV [26].

After the dispersion process, the solvent was evaporated in a furnace at 150 °C. The obtained powder mixtures were used to fabricate nickel matrix composites with 1 wt % MWCNTs. In order to do so, the powder was consolidated using an axial pressure of 990 MPa to generate cylindrical samples with a diameter of 8 mm. Afterwards, these samples were densified in a hot uniaxial press under vacuum (10^{-4} Pa) at 1023 K for 2.5 h.

The CNT-coated Ni samples were manufactured by drop-casting. The suspension consisted of a dispersion of the already-described CNTs in ethylene glycol with a concentration of 0.4 mg/mL. The deposition process was based on the pre-heating of the sample up to 150 °C and the sequential drop deposition up to an accumulated amount of 20 drops. The individual drop volume was 50 µL. After the first drying step (drop evaporation), the samples were dried in a ventilated furnace at 200 °C for 2 h, in order to fully remove the remaining solvent.

3.2. Chemical Characterization and Wear Track Analysis

After the fabrication of the nickel matrix composites, the samples were grinded and polished (ending with a 1 µm diamond polishing suspension) in order to guarantee a good surface quality with a root mean square roughness of 2.8 $\pm$ 0.5 *nm*.

Prior to and after the tribological experiments, Raman spectra were recorded using an inVia Raman microscope (Renishaw) with an excitation wavelength of 532 nm in order to study the quality of the CNTs and to investigate tribo-oxidational effects. The data was recorded using a grating with 2400 lines per mm, a 50x-objective (numeric aperture: 0.9) and a laser power of 0.2 mW. The optical elements of the Raman microscope used in this analysis produced a laser spot size of roughly 5 µm (full width at half maximum), a spectral resolution of about 1.2 cm^{-1} and a penetration depth of approximately 1 µm.

After the tribological measurements, the samples were imaged by light microscopy (BX 60, Olympus) or scanning electron microscopy (Helios Nanolab 600, FEI) in order to investigate the wear tracks which can get a hint to the underlying friction and wear mechanisms. For scanning electron microscopy, a voltage of 5 kV was applied using a working distance of 4 mm.

3.3. Tribological Experiments

Tribological experiments under dry sliding conditions were conducted using a ball-on-disk tribometer (CSM Instruments) in linear reciprocating sliding mode with a stroke length of 0.6 mm, a maximum sliding speed of 1 mm/s and a normal load of 100 mN. The number of cycles was set to be 200 and 20,000 cycles in order to study the run-in behavior and the long-term stability of the fabricated samples (CNT-composites and CNT-coated samples). The counter body was an Al_2O_3 ball with a diameter of 6 mm. This ball material was chosen to avoid any plastic deformation of the counter body. The ball is mounted on a cantilever with a stiffness of 0.7624 µN/µm in normal and 1.1447 µN/µm in tangential direction. During the experiment, the deflections of the cantilever in the horizontal and vertical direction are measured using optical fiber displacement sensors. Consequently, the normal and friction force can be calculated, thus, resulting in the continuous measurement of the COF with

a frequency of 100 Hz. A mean value for each sliding cycle was then calculated from the absolute measured raw values of one forward and backward motion, excluding the data obtained at the reversal points. Finally, the mean value of each sliding cycle was plotted as a function of the total sliding cycles. Temperature and relative humidity were kept constant at 20 $\pm$ 2 °C and 4% $\pm$ 1%, respectively.

4. Conclusions

In this work, we were able to compare (by fixing the testing parameters) the frictional behavior of CNT-reinforced and CNT-coated samples. With regard to the tribological short-term experiments (200 sliding cycles), both samples induce a significant friction reduction (roughly by a factor of four) under dry friction, compared to the polished reference. It can be stated that the frictional behavior is mainly influenced by the CNTs present in the contact zone, as no difference in the COF between both samples can be observed. As a consequence, the known effect of a refined microstructure, thus leading to an increased hardness of the CNT reinforced samples seems to play a minor role in friction reduction compared to the solid lubrication effect induced by the CNTs.

Regarding the tribological long-term experiments (20.000 sliding cycles), it could be observed that the friction reduction of the CNT-coated samples just lasts for the first 3000 cycles after which the COF approaches the value of the reference. This can be explained by the gradual removal of CNTs from the contact zone. In contrast to that, the CNT-reinforced sample demonstrates a pronounced friction reduction over the entire 20.000 sliding cycles, which can be attributed mainly to the continuous supply of CNTs to the contact zone. In conjunction to the mentioned points, the generation of wear particles and the formation of an oxide layer (high shear strength layer) have to be taken into consideration. In this context, CNTs proved to act as an efficient barrier to avoid the oxidation of the contact region during the experiments. The avoidance of the oxidation turns out very useful, since the generation of a superficial oxide would unavoidably increase the COF due to an increased shear strength.

Regarding the structural resistance of the CNTs during the tribological experiments, we were able to show that even for extended test duration, the CNTs can withstand the accumulated stress, retaining to some extent their structural state. The occurrence of amorphous nano-carbons within the wear track of the CNT-reinforced sample and their effect on the tribological properties of the composite is subject of ongoing research work and will be published by the authors in a follow-up paper.

Acknowledgments: The present work is supported by funding from the Deutsche Forschungsgemeinschaft (DFG, project: MU 959/38-1 and project: SU 911/1-1). The authors wish to acknowledge the EFRE Funds of the European Commission for support of activities within the AME-Lab project. This work was supported by the CREATe-Network Project, Horizon 2020 of the European Commission (RISE Project No. 644013).

Author Contributions: Leander Reinert and Andreas Rosenkranz manufactured the samples as well as designed, performed and analyzed the tribological experiments. Leander Reinert and Sebastian Suárez measured and analyzed the Raman spectroscopy data. All authors discussed and wrote the manuscript.

Conflicts of Interest: The authors declare no conflict of interest.

References

1. Lu, Y.; Liaw, P.K. The mechanical properties of nanostructured materials. *JOM* **2001**, *53*, 31–35. [CrossRef]
2. Kim, P.; Shi, L.; Majumdar, A.; McEuen, P. Thermal transport measurements of individual multiwalled nanotubes. *Phys. Rev. Lett.* **2001**, *87*, 215502. [CrossRef] [PubMed]
3. Chen, W.X.; Tu, J.P.; Wang, L.Y.; Gan, H.Y.; Xu, Z.D.; Zhang, X.B. Tribological application of carbon nanotubes in a metal-based composite coating and composites. *Carbon* **2003**, *41*, 215–222. [CrossRef]
4. Kim, K.T.; Cha, S.I.; Hong, S.H. Hardness and wear resistance of carbon nanotube reinforced Cu matrix nanocomposites. *Mater. Sci. Eng. A* **2007**, *449–451*, 46–50. [CrossRef]
5. Scharf, T.W.; Neira, A.; Hwang, J.Y.; Tiley, J.; Banerjee, R. Self-lubricating carbon nanotube reinforced nickel matrix composites. *J. Appl. Phys.* **2009**, *106*. [CrossRef]
6. Tan, J.; Yu, T.; Xu, B.; Yao, Q. Microstructure and wear resistance of nickel–carbon nanotube composite coating from brush plating technique. *Tribol. Lett.* **2006**, *21*, 107–111. [CrossRef]

7. Guiderdoni, C.; Estournès, C.; Peigney, A.; Weibel, A.; Turq, V.; Laurent, C. The preparation of double-walled carbon nanotube/Cu composites by spark plasma sintering, and their hardness and friction properties. *Carbon* **2011**, *49*, 4535–4543. [CrossRef]
8. Dorri Moghadam, A.; Omrani, E.; Menezes, P.L.; Rohatgi, P.K. Mechanical and tribological properties of self-lubricating metal matrix nanocomposites reinforced by carbon nanotubes (CNTs) and graphene—A review. *Compos. Part B Eng.* **2015**, *77*, 402–420. [CrossRef]
9. Omrani, E.; Moghadam, A.; Menezes, P.L.; Rohatgi, P.K. New emerging self-lubricating metal matrix composites for tribological applications. *Ecotribology* **2016**, 63–103. [CrossRef]
10. Hirata, A.; Yoshioka, N. Sliding friction properties of carbon nanotube coatings deposited by microwave plasma chemical vapor deposition. *Tribol. Int.* **2004**, *37*, 893–898. [CrossRef]
11. Hu, J.J.; Jo, S.H.; Ren, Z.F.; Voevodin, A.; Zabinski, J.S. Tribological behavior and graphitization of carbon nanotubes grown on 440C stainless steel. *Tribol. Lett.* **2005**, *19*, 119–125. [CrossRef]
12. Miyoshi, K.; Street, K.W., Jr.; Vander Wal, R.L.; Andrews, R.; Sayir, A. Solid lubrication by multiwalled carbon nanotubes in air and in vacuum. *Tribol. Lett.* **2005**, *19*, 191–201. [CrossRef]
13. Dickrell, P.L.; Pal, S.K.; Bourne, G.R.; Muratore, C.; Voevodin, A.; Ajayan, P.M.; Schadler, L.S.; Sawyer, W.G. Tunable friction behavior of oriented carbon nanotube films. *Tribol. Lett.* **2006**, *24*, 85–90. [CrossRef]
14. Zhang, X.; Luster, B.; Church, A.; Muratore, C.; Voevodin, A.; Kohli, P.; Aouadi, S.; Talapatra, S. Carbon nanotube-MoS2 composites as solid lubricants. *ACS Appl. Mater. Interfaces* **2009**, *1*, 735–739. [CrossRef] [PubMed]
15. Arai, S.; Fujimori, A.; Murai, M.; Endo, M. Excellent solid lubrication of electrodeposited nickel-multiwalled carbon nanotube composite films. *Mater. Lett.* **2008**, *62*, 3545–3548. [CrossRef]
16. Chen, C.S.; Chen, X.H.; Xu, L.S.; Yang, Z.; Li, W.H. Modification of multi-walled carbon nanotubes with fatty acid and their tribological properties as lubricant additive. *Carbon* **2005**, *43*, 1660–1666. [CrossRef]
17. Peng, Y.; Hu, Y.; Wang, H. Tribological behaviors of surfactant-functionalized carbon nanotubes as lubricant additive in water. *Tribol. Lett.* **2006**, *25*, 247–253. [CrossRef]
18. Lu, H.F.; Fei, B.; Xin, J.H.; Wang, R.H.; Li, L.; Guan, W.C. Synthesis and lubricating performance of a carbon nanotube seeded miniemulsion. *Carbon* **2007**, *45*, 936–942. [CrossRef]
19. Kristiansen, K.; Zeng, H.; Wang, P.; Israelachvili, J.N. Microtribology of Aqueous Carbon Nanotube Dispersions. *Adv. Funct. Mater.* **2011**, *21*, 4555–4564. [CrossRef]
20. Coleman, J.N. Liquid-Phase Exfoliation of Nanotubes and Graphene. *Adv. Funct. Mater.* **2009**, *19*, 3680–3695. [CrossRef]
21. Avilés, F.; Cauich-Rodríguez, J.V.; Moo-Tah, L.; May-Pat, A.; Vargas-Coronado, R. Evaluation of mild acid oxidation treatments for MWCNT functionalization. *Carbon* **2009**, *47*, 2970–2975. [CrossRef]
22. Karousis, N.; Tagmatarchis, N.; Tasis, D. Current progress on the chemical modification of carbon nanotubes. *Chem. Rev.* **2010**, *110*, 5366–5397. [CrossRef] [PubMed]
23. Dyke, C.A.; Tour, J.M. Solvent-free functionalization of carbon nanotubes. *J. Am. Chem. Soc.* **2003**, *125*, 1156–1157. [CrossRef] [PubMed]
24. Vaisman, L.; Wagner, H.D.; Marom, G. The role of surfactants in dispersion of carbon nanotubes. *Adv. Colloid Interface Sci.* **2006**, *128–130*, 37–46. [CrossRef] [PubMed]
25. Zhao, Y.-L.; Stoddart, J.F. Noncovalent Functionalization of Single-Walled Carbon Nanotubes. *Acc. Chem. Res.* **2009**, *42*, 1161–1171. [CrossRef] [PubMed]
26. Reinert, L.; Zeiger, M.; Suarez, S.; Presser, V.; Mücklich, F. Dispersion analysis of carbon nanotubes, carbon onions, and nanodiamonds for their application as reinforcement phase in nickel metal matrix composites. *RSC Adv.* **2015**, *5*, 95149–95159. [CrossRef]
27. Cheng, Q.; Debnath, S.; Gregan, E.; Byrne, H.J. Ultrasound-Assisted SWNTs Dispersion: Effects of Sonication Parameters and Solvent Properties. *J. Phys. Chem. C* **2010**, *114*, 8821–8827. [CrossRef]
28. Variava, M.F.; Church, T.L.; Harris, A.T.; Minett, A.I. Polyol-assisted functionalization of carbon nanotubes—A perspective. *J. Mater. Chem. A* **2013**, *1*, 8509. [CrossRef]
29. Suárez, S.; Rosenkranz, A.; Gachot, C.; Mücklich, F. Enhanced tribological properties of MWCNT/Ni bulk composites – Influence of processing on friction and wear behaviour. *Carbon* **2014**, *66*, 164–171. [CrossRef]
30. Chen, X.H.; Chen, C.S.; Xiao, H.N.; Liu, H.B.; Zhou, L.P.; Li, S.L.; Zhang, G. Dry friction and wear characteristics of nickel/carbon nanotube electroless composite deposits. *Tribol. Int.* **2006**, *39*, 22–28. [CrossRef]

31. Dickrell, P.L.; Sinnott, S.B.; Hahn, D.W.; Raravikar, N.R.; Schadler, L.S.; Ajayan, P.M.; Sawyer, W.G. Frictional anisotropy of oriented carbon nanotube surfaces. *Tribol. Lett.* **2005**, *18*, 59–62. [CrossRef]
32. Colonna, F.; Fasolino, A.; Meijer, E.J. Graphitization of single-wall nanotube bundles at extreme conditions: Collapse or coalescence route. *Phys. Rev. B* **2013**, *88*, 165416. [CrossRef]
33. Bakshi, S.R.; Agarwal, A. An analysis of the factors affecting strengthening in carbon nanotube reinforced aluminum composites. *Carbon* **2011**, *49*, 533–544. [CrossRef]
34. Hwang, J.Y.; Neira, A.; Scharf, T.W.; Tiley, J.; Banerjee, R. Laser-deposited carbon nanotube reinforced nickel matrix composites. *Scr. Mater.* **2008**, *59*, 487–490. [CrossRef]
35. Suarez, S.; Soldera, F.; González Oliver, C.; Acevedo, D.; Mücklich, F. Thermomechanical Behavior of Bulk Ni/MWNT Composites Produced via Powder Metallurgy. *Adv. Eng. Mater.* **2012**, *14*, 499–502. [CrossRef]
36. Suarez, S.; Lasserre, F.; Mücklich, F. Mechanical properties of MWNT/Ni bulk composites: Influence of the microstructural refinement on the hardness. *Mater. Sci. Eng. A* **2013**, *587*, 381–386. [CrossRef]
37. Suarez, S.; Lasserre, F.; Prat, O.; Mücklich, F. Processing and interfacial reaction evaluation in MWNT/Ni bulk composites. *Phys. Status Solidi* **2014**, *211*, 1555–1561. [CrossRef]
38. Blau, P.J. On the nature of running-in. *Tribol. Int.* **2005**, *38*, 1007–1012. [CrossRef]
39. Shafiei, M.; Alpas, A.T. Friction and Wear Mechanisms of Nanocrystalline Nickel in Ambient and Inert Atmospheres. *Metall. Mater. Trans. A* **2007**, *38*, 1621–1631. [CrossRef]
40. Lehman, J.H.; Terrones, M.; Mansfield, E.; Hurst, K.E.; Meunier, V. Evaluating the characteristics of multiwall carbon nanotubes. *Carbon* **2011**, *49*, 2581–2602. [CrossRef]
41. Jorio, A.; Dresselhaus, M.; Dresselhaus, G. *Carbon Nanotubes: Advanced Topics in the Synthesis, Structure, Properties and Applications*; Springer-Verlag: Heidelberg, Germany, 2008; p. 720.
42. Tuinstra, F.; Koenig, J.L. Raman Spectrum of Graphite. *J. Chem. Phys.* **1970**, *53*, 1126–1130. [CrossRef]
43. Pimenta, M.A.; Dresselhaus, G.; Dresselhaus, M.S.; Cançado, L.G.; Jorio, A.; Saito, R. Studying disorder in graphite-based systems by Raman spectroscopy. *Phys. Chem. Chem. Phys.* **2007**, *9*, 1276–1291. [CrossRef] [PubMed]
44. Creighton, J.A.; Withnall, R. The Raman spectrum of gallium metal. *Chem. Phys. Lett.* **2000**, *326*, 311–313. [CrossRef]
45. DiLeo, R.A.; Landi, B.J.; Raffaelle, R.P. Purity assessment of multiwalled carbon nanotubes by Raman spectroscopy. *J. Appl. Phys.* **2007**, *101*, 064307. [CrossRef]
46. Mironova-Ulmane, N.; Kuzmin, A.; Steins, I.; Grabis, J.; Sildos, I.; Pärs, M. Raman scattering in nanosized nickel oxide NiO. *J. Phys. Conf. Ser.* **2007**, *93*, 012039. [CrossRef]
47. Mironova-Ulmane, N.; Kuzmin, A.; Grabis, J.; Sildos, J.; Voronin, V.I.; Berger, I.F.; Kazantsev, V.A. Structural and Magnetic Properties of Nickel Oxide Nanopowders. *Solid State Phenom.* **2011**, *168–169*, 331–334. [CrossRef]

V Long-lasting solid lubrication by CNT-coated patterned surfaces

Leander Reinert, Federico Lasserre, Carsten Gachot, Philipp Grützmacher, Timothy MacLucas, Nicolas Souza, Frank Mücklich and Sebastian Suárez

Department of Material Science and Engineering, Saarland University, 66123 Saarbrücken, Germany

*Published in **"Nature – Scientific Reports" (Impact factor (2017): 4.609)***

Accessible online at: https://doi.org/10.1038/srep42873

Own contribution:

Laser texturing; Tribological experiments and friction coefficient analysis; Scanning electron microscopy and wear track analysis; Raman Spectroscopy; Writing; Discussion; Planning.

Abstract:

The use of lubricants (solid or liquid) is a well-known and suitable approach to reduce friction and wear of moving machine components. Another possibility to influence the tribological behaviour is the formation of well-defined surface topographies such as dimples, bumps or lattice-like pattern geometries by laser surface texturing. However, both methods are limited in their effect: surface textures may be gradually destroyed by plastic deformation and lubricants may be removed from the contact area, therefore no longer properly protecting the contacting surfaces. The present study focuses on the combination of both methods as an integral solution, overcoming individual limitations of each method. Multiwall carbon nanotubes (MWCNT), a known solid lubricant, are deposited onto laser surface textured samples by electrophoretic deposition. The frictional behaviour is recorded
by a tribometer and resulting wear tracks are analysed by scanning electron microscopy and Raman spectroscopy in order to reveal the acting tribological mechanisms. The combined approach shows an extended, minimum fivefold longevity of the lubrication and a significantly reduced degradation of the laser textures. Raman spectroscopy proves decelerated MWCNT degradation and oxide formation in the contact. Finally, a lubricant entrapping model based on surface texturing is proposed and demonstrated.

Cite this as:
L. Reinert, F. Lasserre, C. Gachot, P. Grützmacher, T. MacLucas, N. Souza, F. Mücklich, S. Suárez, Long-lasting solid lubrication by CNT-coated patterned surfaces. *Scientific Reports* **2017**, 7, 42873. (*https://doi.org/10.1038/srep42873*)

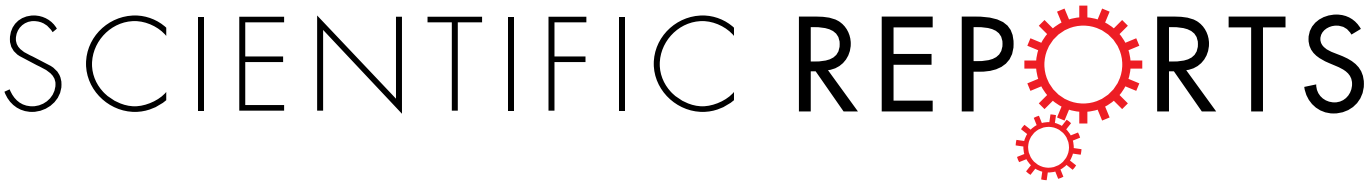

OPEN

Long-lasting solid lubrication by CNT-coated patterned surfaces

L. Reinert, F. Lasserre, C. Gachot, P. Grützmacher, T. MacLucas, N. Souza, F. Mücklich & S. Suarez

Received: 27 July 2016
Accepted: 16 January 2017
Published: 17 February 2017

The use of lubricants (solid or liquid) is a well-known and suitable approach to reduce friction and wear of moving machine components. Another possibility to influence the tribological behaviour is the formation of well-defined surface topographies such as dimples, bumps or lattice-like pattern geometries by laser surface texturing. However, both methods are limited in their effect: surface textures may be gradually destroyed by plastic deformation and lubricants may be removed from the contact area, therefore no longer properly protecting the contacting surfaces. The present study focuses on the combination of both methods as an integral solution, overcoming individual limitations of each method. Multiwall carbon nanotubes (MWCNT), a known solid lubricant, are deposited onto laser surface textured samples by electrophoretic deposition. The frictional behaviour is recorded by a tribometer and resulting wear tracks are analysed by scanning electron microscopy and Raman spectroscopy in order to reveal the acting tribological mechanisms. The combined approach shows an extended, minimum fivefold longevity of the lubrication and a significantly reduced degradation of the laser textures. Raman spectroscopy proves decelerated MWCNT degradation and oxide formation in the contact. Finally, a lubricant entrapping model based on surface texturing is proposed and demonstrated.

With the increasing demand for lower energy consumption and CO_2 emissions, the urge to reduce friction and wear to a minimal level, for example in automotive parts such as cylinder liners, piston rings or bearings in passenger cars, becomes increasingly important[1]. Introducing surface textures in materials has proven to be effective at lowering the coefficient of friction (COF) by reducing the real area of contact and by trapping wear debris and thus reducing the ploughing component of the COF[2,3].

Out of various techniques to create well-defined surface patterns such as honing, micro coining or lithography, laser surface texturing (LST) and in particular direct laser interference patterning (DLIP) are suitable approaches[4–6]. In case of DLIP, interference fields produced by several coherent high-power laser sub-beams melt and shift material according to temperature- and thus surface tension gradients. This produces periodic patterns composed of different interference geometries such as line-, dot- or even lattice-like textures with typical feature sizes in the order of microns- down to several sub-microns, depending on the material[4].

Studies on the tribological behaviour of DLIP-processed metallic surfaces have shown a significant reduction in friction and wear[2,3]. In addition to the effects caused by a reduced contact area and trapping of wear debris, the depressions of a textured surface may act as reservoirs for liquid or even solid lubricants, thus supplying the loaded contact with lubricants if necessary[7,8]. This mainly enhances the longevity of the lubrication and therefore avoids premature failure of machine components.

As far as solid lubricants or protective coatings are concerned, graphite, MoS_2, DLC or Carbon Nanotube (CNT) coatings, amongst others, are able to mitigate friction and wear in loaded contacts. CNTs have received special attention due to their shape, high aspect ratio, sp^2-carbon hybridisation state and high flexibility. Several studies have proved the ability of CNTs to reduce friction and wear, for example when used as reinforcement phase in composites[9–14], as protective film[15–18], solid lubricant[15,17,19,20] or lubricant additive[21–24]. Regarding their friction- and wear-reducing effects, CNTs are often linked to roller bearings[11,25,26], effectively rolling and separating the rubbing surfaces. Dickrell *et al.*[26] were able to prove differences in the frictional behaviour of CNTs as a function of their orientation on top of a surface. Often, the friction reduction of CNTs is also explained by their degradation, forming a lubricating carbonaceous tribolayer[11,16]. In this case, simulations estimate a contact pressure threshold between 1.5 to 2.5 GPa to deteriorate the CNTs[27].

Department of Material Science and Engineering, Chair of Functional Materials, Saarland University, 66123 Saarbrücken, Germany. Correspondence and requests for materials should be addressed to L.R. (email: l.reinert@mx.uni-saarland.de)

Despite the abovementioned advantages, laser surface texturing and solid lubricants/protective films also have some drawbacks. In particular, surface textures may be gradually destroyed by plastic deformation, especially at the asperities with high local contact pressures[2,3]. Furthermore, coatings may be removed from the contact area depending on the loading conditions, thereby diminishing surface protection[28].

The present study attempts to overcome these weaknesses by combining both approaches, namely, lubrication and its storage in textured depressions thus enhancing the endurance and efficiency of both, as well as reducing the COF. In order to do so, it is decisive to be able to copy an underlying texture (or in general complex geometries) with a homogeneous coating thickness.

Regarding the fabrication of CNT coatings, several techniques have been applied so far, including spray[29] and dip coating[30], CVD[31], drop casting[28] etc. Among those, electrophoretic deposition (EPD) has been successfully identified as a suitable, straightforward and easily scalable technique to deposit CNT films on different materials like metals or ceramics[32]. EPD is based on the electrophoresis principle: the motion of charged particles in an electric field and the subsequent adhesion/physisorption of these particles onto an electrode substrate in a fluid medium. It allows for short processing times, no shaping constraints, and homogeneous as well as controlled depositions, compared to drop casting or spin coating for example[32,33]. Decisively, EPD allows for copying complex geometries and textured surfaces resulting in an efficient deposition of coatings with homogeneous thicknesses[32]. For the given reasons, this study focuses on the combination of DLIP and EPD-deposited, multiwall CNT (MWCNT) coatings in order to study the tribological performance.

A commercially available steel (AISI 316) will be used as substrate material because of its technological relevance and due to the experience of our research group with this material in terms of laser patterning and the related effects on microstructural and chemical changes in the material[34]. The tribological results will be carefully analysed in terms of the coefficient of friction and the corresponding wear tracks. The wear tracks are analysed in light of microstructural and chemical findings by SEM/FIB and Raman spectroscopy, which also allows correlating the structural state of the MWCNTs with the tribological results. The tribological behaviour of the MWCNT-coated structures will be contrasted with that of bare (unlubricated) structures to isolate corresponding effects. Finally, a model will be presented which aims at explaining the mechanisms of entrapping the solid lubricant in the texture depressions.

Experimental Section

Materials. Commercially available MWCNTs (purchased at graphene supermarket, diameter 50–85 nm, length 10–15 μm) and steel (austenitic stainless steel AISI 316L) with a mirror-polished surface finish and a size of $20 \times 20 \times 1\,mm^3$ were used as starting materials.

Laser texturing. A pulsed Nd: YAG laser (Spectra Physics, Quanta Ray PRO 290) with a pulse duration of 10 ns and a repetition rate of 10 Hz was used for the laser structuring of the polished steel substrates. The primary laser beam was split into two sub-beams with equal intensity using suitable beam splitters. An overlap of these beams on the sample surface results in a line-like interference pattern. Due to the absorption characteristics of steel, the third harmonic of the laser system at 355 nm and a laser fluence of 400 mJ cm^{-2} were selected. Both, the laser fluence and a structural periodicity of the interference pattern (line spacing) of 9 μm were chosen based on previous studies that show the highest homogeneity of the structures using these parameters[2,3].

Roughness measurement. The roughness of the polished steel samples and the laser textured samples was measured using a white light interferometer (Zygo New View 7300) equipped with a 3-D imaging surface structure analyser. The root mean square roughness of the polished steel reference and the laser textured sample was 30 nm and 300 nm, respectively.

Fabrication of CNT films. *CNT functionalisation.* The main drawback in CNT processing is the strong van der Waals interactions that generate agglomerates. During EPD, for instance, larger (and heavier) particles need larger voltages to be deposited, due to an enhanced viscous drag. However, the use of larger voltages tends to further aggregate separated CNTs[35]. Deposition thus loses homogeneity and density and incorporates pores[35]. Furthermore, larger particles tend to flocculate and settle leading to gradient film thicknesses in vertical electrode configurations[33]. In the case of non-flat surfaces the deposited material cannot replicate the original surface, which may translate to an easier detachment of the coating.

For the given reasons and the fact that CNTs are quasi inert and therefore unreactive during EPD, a covalent functionalisation step has been performed as suggested elsewhere[36]. 3 g of CNTs were refluxed in 225 ml of mixed concentrated nitric (68%, 168.75 ml) and sulfuric (97%, 56.25 ml) acid at 130 °C for 30 minutes. This step leads to the creation of acidic sites on the surface of the nanotubes, improving CNT dispersion and stabilisation by conferring a negative charge to the surface of the nanotubes[36] and thus aiding the EPD process by reducing the presence of agglomerates. Afterwards, rinsing steps with deionised water were carried out with a 2 μm pore size filter. Finally, the CNTs were dried in a ventilated oven at 100 °C for 3 h to allow for the evaporation of water.

EPD process. For the deposition process, the mirror-polished reference and the laser-textured steel plates were used as electrodes. The plates were cleaned to remove possible contaminants, organic or other, that could interfere with the correct deposition of the CNTs. The cleaning consisted in a sequence of 10 min ultrasound steps, each in cyclohexane, acetone and isopropanol alternated with deionised water rinsing, except for the last step, immediately followed by drying in pressurised air.

A 0.25 mg ml^{-1} CNT solution was prepared by mixing the functionalised CNTs and acetone in a homogeniser (WiseTis HG-15, Witeg–Germany) for 5 min and ultrasonicating the solution for another 10 min in a bath (Bandelin sonorex super RK 514 BH, 35 kHz–860 W)[37]. Afterwards, 3 ml of triethylamine (TEA) were added in

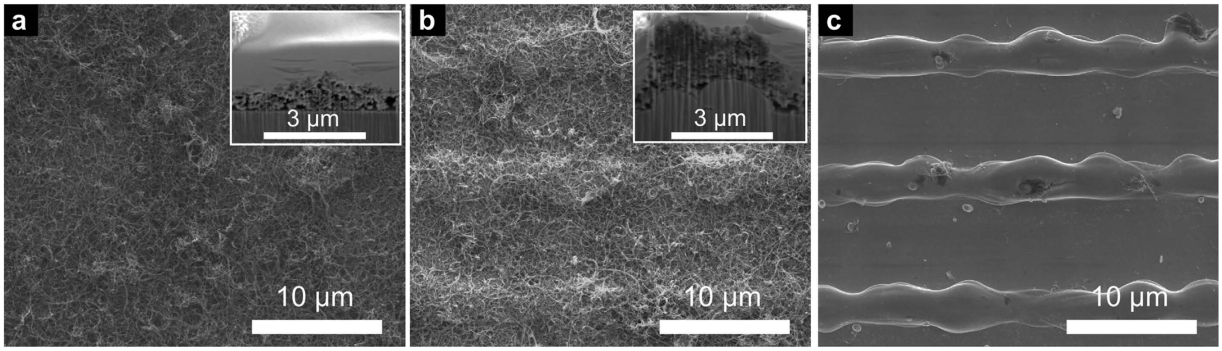

Figure 1. SEM micrographs of coated (**a**) untextured and (**b**) textured samples and (**c**) an as-textured sample. The structural periodicity of both laser textures is 9 µm. The insets in (**a**,**b**) show FIB-cross sections of the corresponding sample. There, the CNT-film can be seen between the steel substrate and the Pt protective film used for the cross section.

order to assist in the deprotonation of the CNT acidic groups[38]. Finally, the negatively charged CNTs could be deposited onto the anode (anodic deposition).

The electrophoretic depositions were performed in a deposition cell at a constant voltage of 20 V for 10 min, maintaining an electrode separation of 1.3 cm. After the deposition, the electrodes were taken out of the solution, keeping the voltage for 5 min. This assures that the film does not crack during the extraction of the electrodes from the liquid and also helps in the drying process[39].

Chemical characterisation and wear track analysis. After the deposition of the CNT layer on the steel substrate, tribological experiments were performed. Prior to and after the tribological experiments, Raman spectra were acquired using an inVia Raman microscope (Renishaw) with an excitation wavelength of 532 nm in order to study the quality of the CNTs and to investigate tribo-oxidational effects. The data was recorded using a grating of 2400 lines mm^{-1}, a 50x objective (numeric aperture: 0.9) and a laser power of 2 mW. The optical elements of the Raman microscope used in this analysis produced a laser spot size of roughly 5 µm (full width at half maximum) and a spectral resolution of about 1.2 cm^{-1}. Every area is measured at least three times at different spots for statistical back-up and the mean value including the standard deviation is plotted.

After the tribological measurements, the samples were imaged using scanning electron microscopy (Helios Nanolab 600, FEI) in order to investigate the wear tracks, so as to analyse the potential underlying friction and wear mechanisms.

Tribological Experiments. Tribological experiments under dry sliding conditions (no additional oil or grease) were conducted using a ball-on-disk tribometer (CSM Instruments) in linear reciprocating sliding mode with a stroke length of 0.6 mm, a maximum sliding speed of 1 mm/s and a normal load of 100 mN. The number of cycles was set to 500 and 10.000 cycles in order to study the run-in behaviour and the long-term stability of the fabricated samples. The counter body was an Al_2O_3 ball with a diameter of 6 mm. The stroke length was chosen short enough to allow for several measurements at different spots of one sample, but also long enough to cover 67 maximum positions of the laser texture per stroke, therefore providing sufficient statistics. The normal load produces a contact radius of about 12 µm and a contact pressure of 346 MPa for the given material pairing (alumina against steel), calculated with the Hertzian contact model[40,41] (used mechanical properties of the materials can be found in the supplementary information). This means, that at least two maximum positions of the laser texture are in direct contact with the ball at any time of the measurement. The choice of the ball material was made to avoid any plastic deformation of the counter body. The ball is mounted on a cantilever with a stiffness of 0.7624 µN μm^{-1} and 1.1447 µN μm^{-1} in normal and tangential directions, respectively. During the experiment, the deflections of the cantilever in the horizontal and vertical direction are measured using optical fibre displacement sensors. Consequently, the normal and friction forces can be calculated thus resulting in the coefficient of friction. Temperature and relative humidity were kept constant at 20 ± 2 °C and $4\% \pm 1\%$, respectively. All tribological experiments were conducted in perpendicular sliding direction in relation to the produced line-like laser-texture. This is because of previous studies showing the most pronounced friction and wear reducing effects when using this configuration[2,3]. For every sample, three measurements were conducted and the mean value including standard deviation was built and plotted against the number of sliding cycles.

Results and Discussion

EPD coating. After laser-texturing (Fig. 1c), the samples were coated with CNTs by EPD. As expected from the negative surface charge of the functionalised CNTs, the deposition occurs at the anode and without any detection of hydrogen evolution during the deposition. Both untextured and textured samples could be homogenously coated (Fig. 1a,b). The deposited thickness is 1–2 µm, measured at different spots of either sample type by FIB-cross sections. Furthermore, the cross-sections (insets of Fig. 1a,b) show that the CNT film follows the surface's profile. Finally, small CNT agglomerates are found within the coatings, possibly a consequence of the stated van der Waals interactions. Nonetheless, the entire surface is covered with disaggregated CNTs, providing a consistent surface coating.

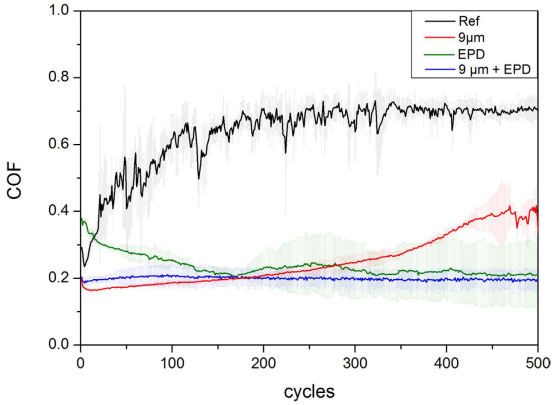

Figure 2. Temporal evolution of the dynamic COF (of one forward and backward sliding motion) plotted as a function of the number of sliding cycles (500 cycles) for the polished steel reference (Ref), textured, coated reference (Ref + coated) and textured + coated sample.

Frictional behaviour. The different sample sets were compared in terms of the temporal evolution of the coefficient of friction (COF), which can be seen in Fig. 2 for a maximum of 500 sliding cycles.

The COF of the reference increases during the first 200 sliding cycles from 0.25 to roughly 0.7. After 200 sliding cycles, the COF remains stable at 0.7, thus reaching steady state conditions. The described behaviour is typical for pure metals and has already been extensively investigated elsewhere[42]. In the beginning of the experiment, only few single asperities of the ball and the substrate are in contact with each other thus generating a small contact area and consequently, a small COF. The increasing COF can be explained by the increasing real contact area, which is generated by wearing off said asperities and also by increasing the indentation depth of the ball into the substrate. However, the development of the COF appears to be very unstable for the reference compared to the other samples. The formation and disintegration of wear particle agglomerates might be responsible for this. The nature of those wear particles and the possible formation of an oxidic layer will be examined later in this work by SEM and Raman spectroscopy. In general, the steady state COF of the used material pairing for the reference correlates well with the literature[43].

Regarding the textured sample, a continuous increase in the COF from 0.2 to 0.4 during the entire experiment can be noticed. It has already been shown, that the observed friction reduction is mainly attributed to a reduced real contact area[2,3]. This is reasonable, as the ball only gets in contact with the maximum position of the laser texture. The continuous increase of the COF during the experiment could be related to the steady increase in the real contact area due to a gradual removal of the surface texture. After 450 cycles, the COF fluctuates similarly to the reference, which might also be indicative of the destruction of the surface texture, therefore allowing the direct contact of the ball with wear particle agglomerates that are formed and broken up in a statistical manner. When regarding the COF of the ref + coated sample, a gradual decrease during 500 cycles from almost 0.4 to 0.2 is noted. Additionally, it is worth mentioning that the COF of the ref + coated sample is higher than the reference for the first 10 cycles. This may be explained by large amounts of entangled CNTs being shifted to the sides and ends of the wear track. The shifting and stacking of entangled CNTs requires a higher transversal force thus resulting in an even higher COF than the reference. Subsequently, a continuous supply of small amounts of CNTs seems to set in, acting as solid lubricant and reducing the COF[11,15,17,19,20]. Also, CNTs might be transformed to a lubricating carbon film[11,16]. Finally, the COF of the textured + coated sample appears constant and stable throughout the experiment at 0.2. This means that it shows influences of both friction reducing methods: laser-texturing at the beginning of the measurement and lubricant coating at the end of the measurement. Thus, this indicates a composite type behaviour of texture and solid lubrication. As for the other samples, a detailed wear track investigation and an investigation of the CNT lubrication activity might give a hint on the underlying friction mechanism, which will be discussed in detail later in the present study.

As the COF of the ref + coated- and the textured + coated samples is nearly identical after the first 150 cycles, it is reasonable to assume that this behaviour is mainly induced by CNTs present in the contact zones. This being stated, it is of interest to examine the long-term behaviour of these samples, as the textured + coated samples might provide CNTs to the contact area for a longer period of time.

The temporal evolution of the COF at 10000 cycles provides us with information about the lifespan behaviour (Fig. 3). As described for the 500 cycles measurement, the reference clearly shows steady state behaviour after the first 200 sliding cycles for the already discussed reasons, approaching a COF of roughly 0.65.

The textured sample reveals an evolution of the COF very similar to that of the reference, yet only reaching steady state conditions after 1000 cycles. As already mentioned for the 500 cycles measurement, this might be a consequence of the ongoing destruction of the laser-texture, finally leading to the same contact conditions as the reference.

Looking at the ref + coated sample, the COF drops within the first 750 cycles from 0.35 to 0.15, remaining at this value for the next 1500 cycles. Subsequently, the COF sharply increases to 0.4 within 100 cycles, followed by a gradual approach to the reference value during the next 3500 cycles. This sharp increase might be a consequence of the degradation or disappearance of CNTs in the contact area, as described in the wear and Raman sections

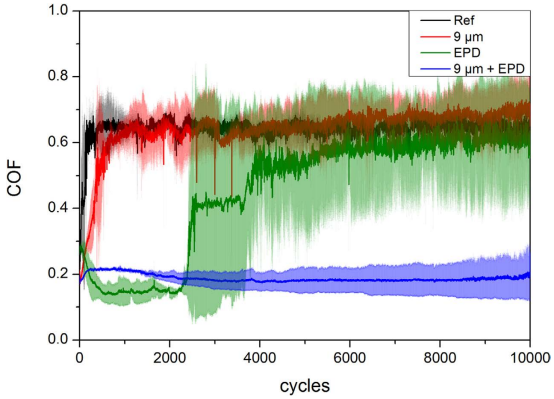

Figure 3. Temporal evolution of the COF plotted as a function of the number of sliding cycles (10000 cycles) for the polished steel reference (Ref), the textured, coated reference (Ref + coated) and textured + coated sample.

(3.3 and 3.4, respectively). It is noteworthy that the COF of the ref + coated sample shows a very high standard deviation after the first 2200 sliding cycles. This is due to individual measurements that have shown the observed sharp increase of the COF up to the reference value after different amounts of sliding cycles. All individual measurements have shown this sharp increase between 2200 and 4000 sliding cycles.

Finally, it should be pointed out that the textured + coated sample features the same low COF (0.2) for the entire 10000 sliding cycles. However, between 200 and 2200 cycles, the COF is higher than that of the ref + coated sample, which could be explained by the ability of CNTs to roll only on top of a flat, polished surface as already reported by Dickrell *et al.*[26]. This ability might be reduced in the case of the textured + coated sample, as the textured surface shows a much higher roughness of 300 nm compared to 30 nm of the reference (which is within the same order of magnitude as the CNT mean diameter), therefore hindering a rolling movement of the CNTs to a certain degree. However, the ongoing lubrication effect of the textured + coated sample for 10000 cycles is significant. A possible explanation for this would be the entrapping of solid lubricant (CNTs) by the laser-texture.

Wear track. In general, a better understanding of the frictional behaviour of a tribological contact pair can be achieved by analysing the dominating wear mechanisms. In this context, it should be noted that different wear mechanisms usually act simultaneously during a tribological experiment. Therefore, only the dominating mechanisms are named and discussed in the following section. The wear tracks of all samples after 500 sliding cycles are depicted in Fig. 4 to allow for further discussion.

For the reference wear track, the dominating wear mechanism is ploughing, as can be seen in Fig. 4a. This is evident as the hardness of the counter body (Al_2O_3 ball) greatly exceeds that of the steel substrate. Wear particles are observed within and around the wear track, which might add an abrasive component in this respect. Also, the formation of a steady-state oxide layer might occur and contribute to the stabilisation of the COF[44].

Regarding the textured sample after 500 cycles in Fig. 4b, the continuous increase of the COF during the experiment can be related to the steady increase in the real contact area due to a gradual removal of the surface texture. As in the reference wear track, the main acting wear mechanism is ploughing. However, it can be seen that the surface texture is not yet completely removed after 500 cycles and less severe wear is observed, compared to the reference. In general, less wear particles are found that are spread over the wear track. This might be a consequence of the reduced direct contact of the ball with wear particles as the minimum positions can trap wear debris, thus reducing the abrasive component[2,3]. As the laser-texture is still partially intact, the real contact area is still reduced compared to the reference and the COF is lower. The friction reducing effect within the first 500 cycles, induced by laser-textured steel surfaces has been published in previous studies[2,3].

Regarding the corresponding wear track of the ref + coated sample (Fig. 4c), a clear shift of the CNT coating towards the end of the wear track can be observed. This supports the assumption that the high initial COF could be explained by shifting large amounts of entangled CNTs to the sides and ends of the wear track within the first sliding cycles. Subsequently, the wear track can be continuously supplied with small amounts of CNTs that are transferred from the ends of the wear track back to the contact area (grey area in the middle of the wear track), acting as solid lubricant and therefore reducing the COF again[11,15,17,19,20]. The CNTs, responsible for this lubrication effect, can be observed at both ends of the grey area and will be analysed in more detail within the chemical analysis. Despite that, no severe wear or wear particles can be noticed within the wear track compared to those of the reference and the textured sample.

Finally, the wear track of the textured + coated sample shows a very different appearance. After 500 cycles, the maximum positions are still present, even though they are a flattened, and the minimum positions are filled with CNTs as can be seen in Fig. 4d. This observation strongly supports the hypothesis of a solid lubricant entrapping caused by the laser-texture.

The wear tracks of the long-term measurements (10000 cycles) must be considered to understand the observed sharp increase of the COF after 2200 cycles in the case of the ref + coated sample, as opposed to the stability observed in the textured + coated sample. Therefore, SEM micrographs of the wear tracks after 10000 sliding cycles are depicted in Fig. 5.

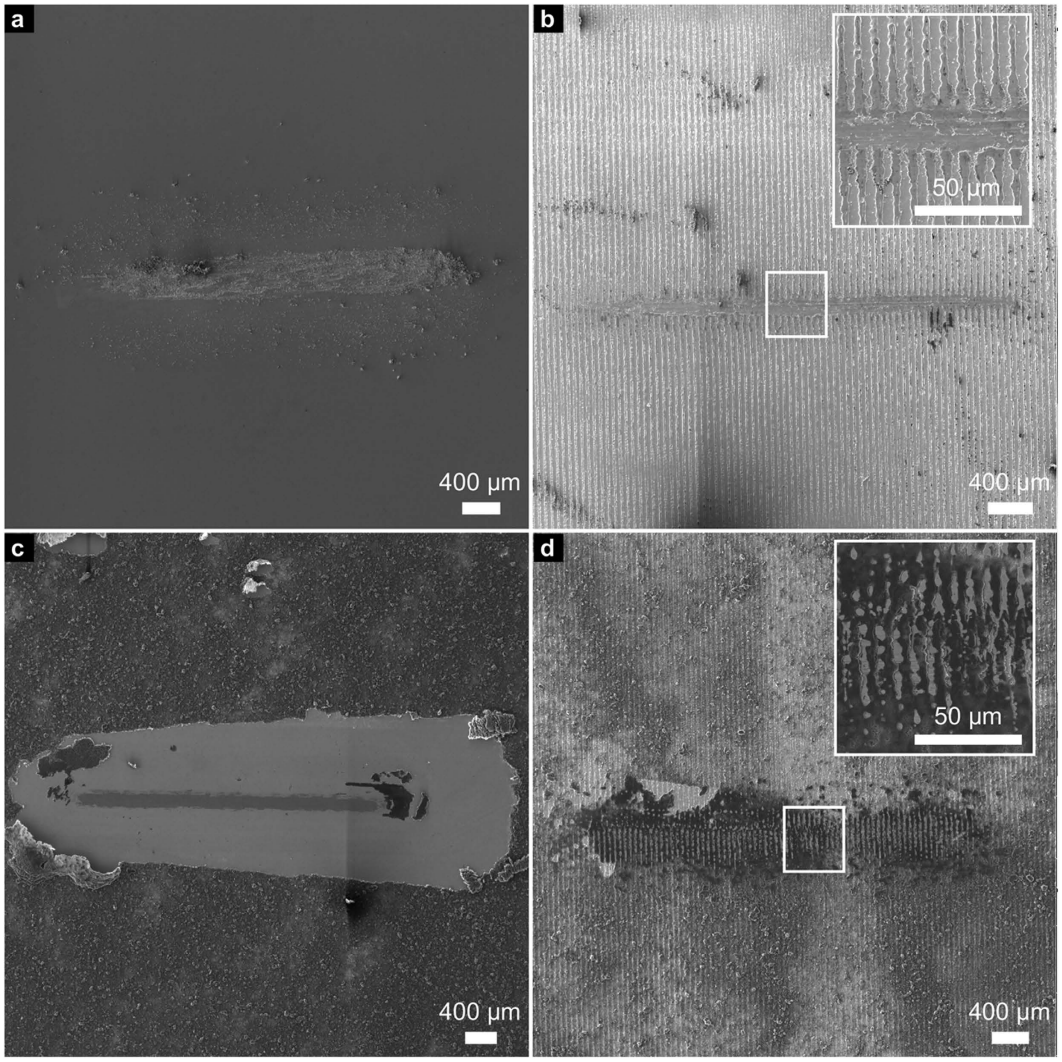

Figure 4. SEM micrographs of the wear tracks after 500 sliding cycles on (**a**) the reference, (**b**) the textured sample, (**c**) the ref + coated sample and (**d**) the textured + coated sample.

For the reference, the behaviour of the COF as well as the dominating wear mechanism are already well explained by the previously described 500 cycle measurements. The only difference is the occurrence of much more severe wear as can be seen in Fig. 5a.

Regarding the wear track of the textured sample (Fig. 5b), it can be stated that the laser-texture has been completely removed within the contact area by ploughing, throughout exhibiting severe wear. Hence, a reduction of the real contact area can no longer be achieved and the COF behaves very similarly to the reference after the first 1000 cycles.

Comparing the wear track of the ref + coated sample after 10000 cycles in Fig. 5c, to that after 500 cycles in Fig. 4c, the additional appearance of severe wear is clearly noticeable. A reasonable explanation for this observation is the disappearance of the lubricating CNTs within the contact zone. The continuous removal of CNTs by the ball out of the contact zone as well as their absence at the ends of the severe wear area might be the reason for that. Hence, a direct contact of ball and substrate material is very likely to happen after the first 2200 sliding cycles, when a sharp increase of the COF can be observed. The slow increase of the COF for the next 3500 cycles (until it reaches the reference value) can be explained with an increasing real contact area between ball and steel substrate as well as individual measurements that show the described sharp increase of the COF at a later or earlier stage of the measurement.

When analysing the wear track of the textured + coated sample (Fig. 5d), different regions can be distinguished. In the middle of the wear track width, severe wear is observed with ploughing being the dominant wear mechanism. This region is very similar to the reference wear track after 10000 cycles. However, regarding the flanks of the wear track, an almost unworn laser-texture can still be noticed, storing CNTs in the minimum positions. It is therefore reasonable, that even after 10000 sliding cycles, the wear track is still supplied with CNTs that lubricate the system and keep the COF at a low value of 0.2. In comparison to the ref + coated sample, the CNTs are stored within the contact zone and don't have to be applied from the surrounding area. Thus, the contacting

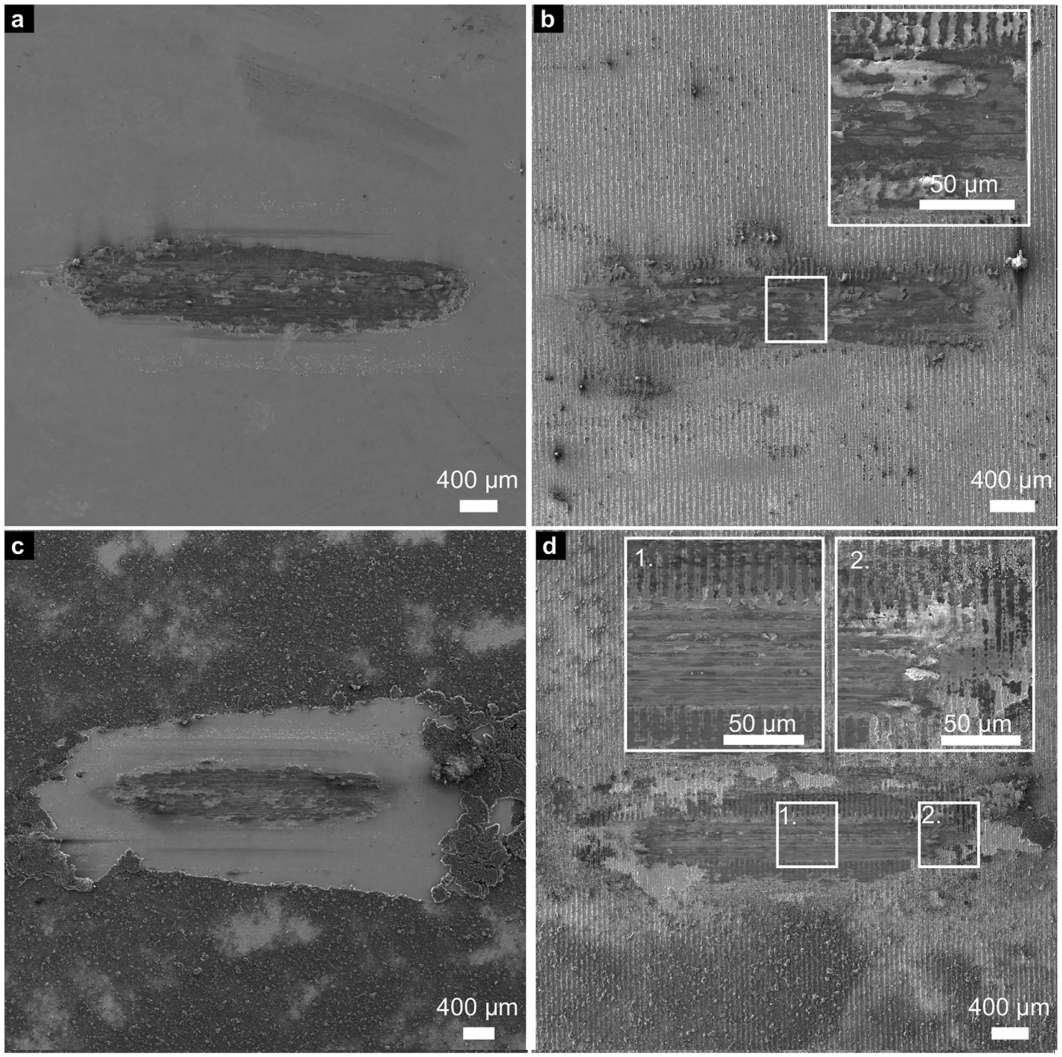

Figure 5. SEM micrographs of the wear tracks after 10000 sliding cycles on (**a**) the reference, (**b**) the laser textured sample, (**c**) the EPD coated sample and (**d**) the laser textured/EPD coated sample.

surfaces are provided with CNTs for a considerably prolonged period of time. A differentiated discussion about oxide formation and structural state of the CNTs within the wear tracks is done in the following part of this study.

Structural and chemical analysis. A deeper discussion of the COF evolution and the solid lubrication activity of the CNTs requires a detailed analysis of the tribochemistry as well as the structural integrity of the CNTs. In this study, the analysis is focused on the interpretation of the most relevant structural indicators obtained by Raman spectroscopy, namely: defect index (I_D/I_G), purity index ($I_{G'}/I_D$), and the G-band centre position (X_{CG}).

Figure 6 shows the electron micrographs and respective Raman spectra of the wear tracks after 500 and 10000 cycles for the reference and the laser-textured samples. In all the cases, regions of interest were defined based on their relevance to the study.

For the reference wear track after 500 cycles (Fig. 6a), the appearance of iron and chromium oxides (II) indicates that a tribologically-induced oxidation took place, due to the direct contact of the ball with the steel substrate under high local pressure[2,45]. The peak at 225 cm^{-1} corresponds to the α-Fe_2O_3 band, whereas the peak at 270 cm^{-1} is composed by a convolution of α-Fe_2O_3 and Cr_2O_3 peaks. The peaks at 380 cm^{-1} and 480 cm^{-1} are related to the occurrence of (Fe, Cr)O_3 and γ- Fe_2O_3, respectively[45–47]. Finally, the peak with its maximum intensity at 660 cm^{-1} and a large full width at half maximum (Γ) is a convolution of FeO, Fe_3O_4 and Fe_2O_3 vibrational modes[45]. This observation consists of two different phenomena, the formation of a layer of oxidic nature and the development of oxidic wear particles during the experiment, which add an abrasive component. The latter is strongly related to the former, since the high local contact pressure applied breaks the oxide layer, generating wear particles that are included in the contact. These particles are subsequently embedded within the wear track (composed of the softer base metal) during the sliding motion, inducing a composite-type effect and contributing to the stabilisation of the COF.

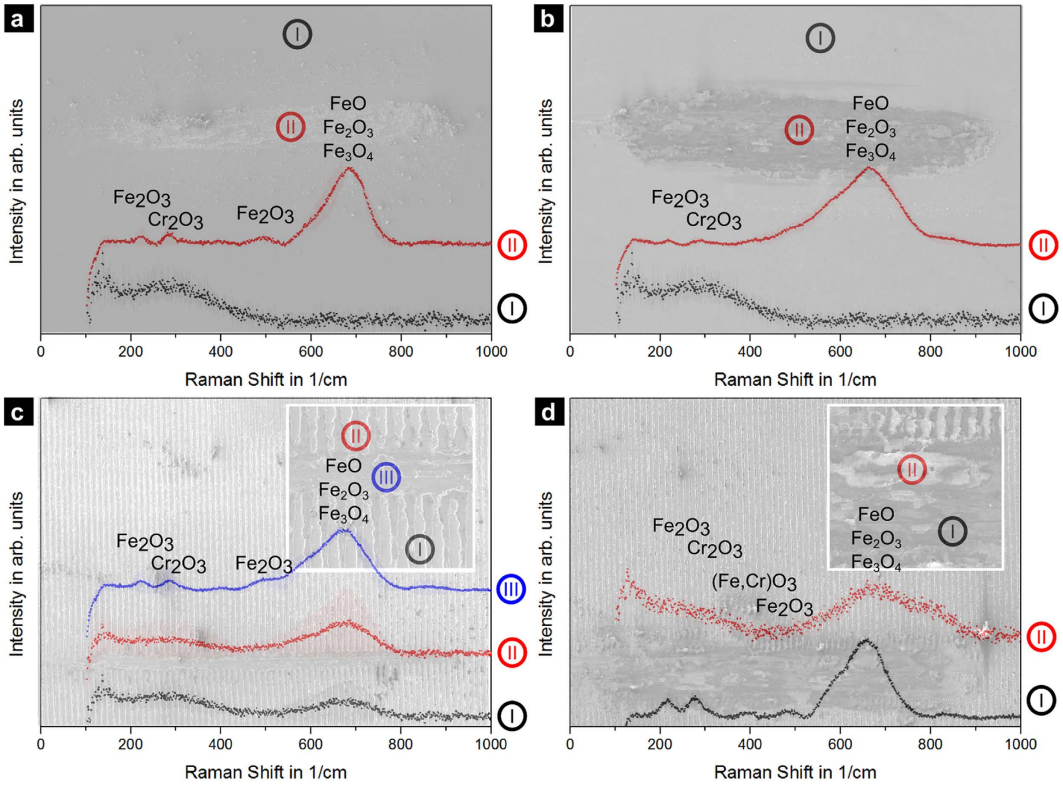

Figure 6. Raman spectra of the wear tracks at different spots of (**a**) the reference after 500 cycles and (**b**) 10000 cycles, and (**c**) the textured sample after 500 cycles and (**d**) 10000 cycles.

In the case of the reference wear track after 10000 cycles (Fig. 6b), iron oxide is predominantly observed. This is reasonable as the COF of the reference is already in a steady-state condition after the first 200 cycles. Therefore, a change in the tribochemistry is rather unexpected. However, in comparison to the wear track after 500 cycles, the observed compositional changes in the oxide formation are probably due to a lack of chromium oxide detection based on its low volume fraction (compared to iron).

In the case of the textured sample after 500 sliding cycles (Fig. 6c), metal oxides are also found in the maximum (II) and minimum (I) positions outside of the severe wear track. This is explained by the thermally induced melting process during laser texturing and the consequent formation of an oxide layer[34]. Within the area of severe wear (III), the oxide peaks are considerably more pronounced, accordingly indicating a similar tribo-oxidation effect as observed on the reference material. Finally, for the wear track of the textured sample after 10000 cycles (Fig. 6d), no significant change in the oxidation behaviour can be observed compared to the short-term measurement. This leads to the conclusion, that the change in the COF (at almost 1000 cycles) in the specific case of the textured sample is exclusively generated by the increment in the real contact area due to wear occurring at the maximum positions. Interestingly, certain areas (I) can be found with pronounced oxide formation, whereas other regions (II) show less oxide formation. This might be a consequence of the on going ploughing mechanism which reorders oxides and bare metal in a stochastic manner.

For the analysis of the CNT lubrication activity, electron micrographs and respective Raman spectra of the coated sample wear tracks after 500 and 10000 cycles are depicted in Fig. 7. In addition to the Raman analysis of the centre and the outside of the wear track, it is also important to analyse the shifted CNTs that pile-up at the end of the wear track since it may also play a role during the tribological experiment.

The EPD coated sample shows no formation of oxides after 500 cycles (Fig. 7a). This supports prior observations on similar systems, where the CNT coatings have been proposed as oxidation protective coatings for low-cycle friction conditions[28]. In this context, CNTs are able to efficiently separate the steel surface from the ball, acting as a roller bearing and thus reducing friction and wear[11,48]. However, in Fig. 7b, intense oxide peaks can be found within the centre (I) and the end of the wear track (II) after 10000 cycles. Their appearance can be straightforwardly correlated to the coating failing after around 2200 sliding cycles, where a sharp increase in the COF is noticeable. Specifically, as no surface separation is possible anymore, the oxidation protection induced by the interstitial CNTs ceases. This leads to the formation of an oxide scale that, due to the large contact pressure develops into oxidic wear particles that act as an abrasive third body component participating in the transition from mild to severe wear.

Raman spectra of the wear track of the textured + coated sample (Fig. 7c) show a weak oxide peak on the texture maximum positions (II) after 500 cycles. As already mentioned, this is an unavoidable feature of the laser texturing. On the other hand, as observed in the ref + coated sample, the structure within the wear track (I and III) does not show remarkable oxide peaks, likely due to the oxidation damping provided by the CNTs. When

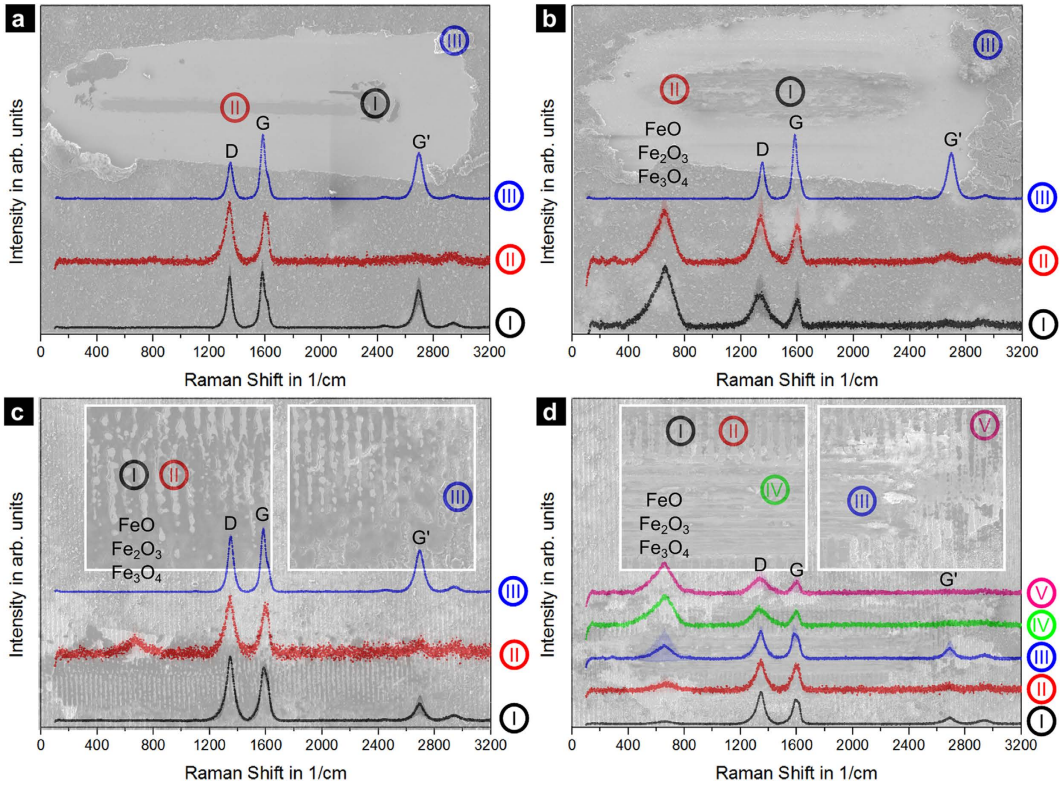

Figure 7. Raman spectra of the wear tracks at different spots of (**a**) the ref + coated sample after 500 cycles and (**b**) 10000 cycles and (**c**) the textured + coated sample after 500 cycles and (**d**) 10000 cycles.

analysing the wear track after 10000 cycles (Fig. 7d), it can be observed that, the intensity of the oxide peaks correlates to the extent of the effective contact area between counterpart and sample, being the minimum the position with the lowest amount (I), follow by the surface maximum (II), the end of the severe wear track (III) and finally within the severe wear track (IV); where the effective contact area between counterpart and sample is the highest. Interestingly, the strongest oxide peaks are detected at the very end of the wear track (V). This might be due to the fact that the generated oxidic wear particles of the severe wear track are shifted to the very end and there stored in the minima.

In the case of the ref + coated and the textured + coated samples, aside from the discussion of their oxidation behaviour, the focus of the analysis is also placed on the structural state of the CNTs. Table 1 shows the most relevant structural indicators to allow for a direct comparison.

The shifted CNTs (a III) have been transported out of the contact zone in the beginning of the measurement, showing almost identical defect and purity indexes as the reference state. Thus, they can be excluded from any tribological activity. Since these CNTs are out of the contact zone they do not exhibit any damage and retain their original structural integrity even after 10000 cycles (b III). CNTs found at the centre (a II) and end of the wear track (a I) show an increase in the I_D/I_G ratio and a decrease in the purity index, indicative of CNT degradation. Comparing both regions, degradation seems to be significantly more pronounced in the centre (a I). This is due to the fact that this zone is situated where the maximum relative velocity is reached between the sample and the counterpart and the most severe mechanical and thermal stresses are expected. Specifically, the centre (a II) is located within the direct tribological contact zone, whereas the end (a I) would act as supplementary CNT storage. Although the shifted CNTs (a III) and the CNTs at the end of the wear track (a I) maintain the position of their G band, those present at the centre (a II) show an up-shifting to roughly 1600 1/cm.

This up-shifting has been thoroughly discussed in the literature by Ferrari and co-workers[49] and corresponds to a transient state of the CNTs (clustering of the affected graphitic structure) towards nano-crystalline graphite. This is enclosed in a three-stage phenomenological model proposed by them, which analyses the transition from a graphitic-like to an amorphous-like structure (predominantly sp^3-hybridisation) as function of the G-band centre position (X_{CG}).

When observing the descriptive indexes for the ref + coated sample after 10000 cycles, an up-shift in the G band towards 1600 1 /cm is observed for CNTs within the centre (b I) and the end of the wear track (b II). The transient state is reached at the end of the wear track (b II) as well, inferring an accumulated CNT degradation towards a disordered state.

Regarding the textured + coated sample after 500 cycles, all measured regions show a degradation of the CNTs compared to the reference state CNTs. Particularly, those regions within the wear track (c I and II) have a defect index higher than at the end of the wear track (c III). However, the degradation in the interior regions is not as pronounced as in the centre (a II) of the ref + coated sample. This might be a consequence of the ongoing

Sample	Cycles	Position	I_D/I_G	$I_{G'}/I_D$	X_{CG} (1/cm)	Description
Initial CNT			0.595	1.294	1583.2	Reference state
Ref + coated	500	a I	0.918	0.735	1585.8	End of wear track
		a II	1.278	0.156	1602.8	Centre of wear track
		a III	0.563	1.273	1585.4	Shifted CNTs
	10000	b I	1.167	0.226	1598.4	Centre of wear track
		b II	1.266	0.222	1599.0	End of wear track
		b III	0.564	1.272	1587.4	Shifted CNTs
Textured + coated	500	c I	1.195	0.274	1591.7	Min–inside
		c II	1.121	0.292	1597.8	Max–inside
		c III	0.876	0.751	1586.7	End of wear track
	10000	d I	1.227	0.203	1598.9	Min–inside
		d II	1.129	0.255	1598.3	Max–inside
		d III	1.175	0.402	1592.1	End of severe wear
		d IV	1.202	0.311	1597.0	Centre of wear track
		d V	1.235	0.210	1598.3	Min–End of wear track

Table 1. Descriptive parameters obtained by Raman spectroscopy of the coated samples, measured at different positions in the wear track. (Min–inside) stands for minimum within wear track, (Max–inside) stands for maximum within wear track, and (Min–End of wear track) stands for minimum at the end of the wear track.

transfer of CNTs between maxima and minima during the experiment, thus exchanging the tribo-active CNTs more frequently. It should be kept in mind that the measured Raman spectra present a mean value of all the CNTs measured (for example degraded CNTs might be stacked upon intact CNTs in the minima). Interestingly, the G band position of the CNTs stored within the minima (c I) lies within the first stage of the amorphisation trajectory described in the Ferrari model. Then, it is reasonable to assume that those CNTs would sequentially be driven towards the contact zone as the experiment carries on. Thus, it becomes evident that the transition towards amorphous nanocarbons seems to be detrimental for the solid lubrication effect. However, the exchange between minima and maxima might lead to a general prolonged lifetime of the involved CNTs, as always just a small part of the involved CNTs is in a direct tribological contact. After the long term tests (d I–d V), all the analysed regions show similar Raman indices, each lying at the end of the first stage of amorphisation.

Mechanism of entrapping solid lubricant. As both the wear track and Raman analyses correlate perfectly with the idea of a solid lubricant entrapping by the laser texture, the following part is focused mainly on this trapping mechanism and provides a schematic model to understand the frictional behaviour of the system. In Fig. 8, a high magnification SEM micrograph of a FIB cross-section within the wear track of the textured + coated sample after 500 sliding cycles (a) is depicted and correlated to a schematic draft of the mechanisms acting during the sliding motion (b).

In b1, the intact, coated laser texture is depicted. As soon as the ball gets into contact with the coating, CNTs are partially transferred to the alumina ball by adhesion (b2). This leads to the shifting of the CNTs towards the minima. At the same time, pressure is applied to the maxima of the laser-texture throughout the coating, resulting in a plastic deformation and a shearing-off of metallic material (b3). Due to adhesion effects, some CNTs are dragged towards the contact area (b4), preventing the direct contact of the alumina-ball with the steel substrate and therefore reducing the COF. Furthermore, the laser-texture prevents the full transfer of CNTs by storing most of the particles within the minima (b4-b5). In addition to the CNT storage capabilities of the minima, also metallic or oxidic wear particles could be partially stored (b5), therefore reducing abrasive wear. Finally, a slight lift of the stored CNTs mainly on one side of the maxima can be noticed (a). This is due to the mentioned adhesion between the alumina ball and the stored CNT particles during the sliding motion (b6), and elastic recovery of the compressed CNT volume after the stroke (b7). In the FIB cross-section (a), the last sliding cycle direction of the experiment was from left to right. Due to this observation and the ongoing lubrication, it can be expected that the protruding CNTs in the minima (b7) will be redragged into the direct contact zone of the maxima as soon as the sliding direction is inverted. These mechanisms can be well correlated to the lower COF compared to the ref + coated sample within the first 150 sliding cycles, as no additional transversal force for the CNT shifting is generated. The CNTs of the textured + coated sample (that were stacked and transferred out of the wear track in the ref + coated sample) are now stored in the minima, thus acting as a lubricant reservoir. In addition to a reduction of the real contact area by laser-texturing, the maxima are lubricated by the CNTs derived from the minima. Apart from milder wear than the textured sample, a reduced oxide formation was also noticed by Raman spectroscopy.

Summarizing, the combination of both methods, laser texturing and EPD coating, is found to overcome individual limitations by complementing one another. While the laser-texture provides the system with a certain load carrying capacity and lubrication storage, the CNT coating prevents its degradation, oxidation and acts as a long lasting solid lubricant.

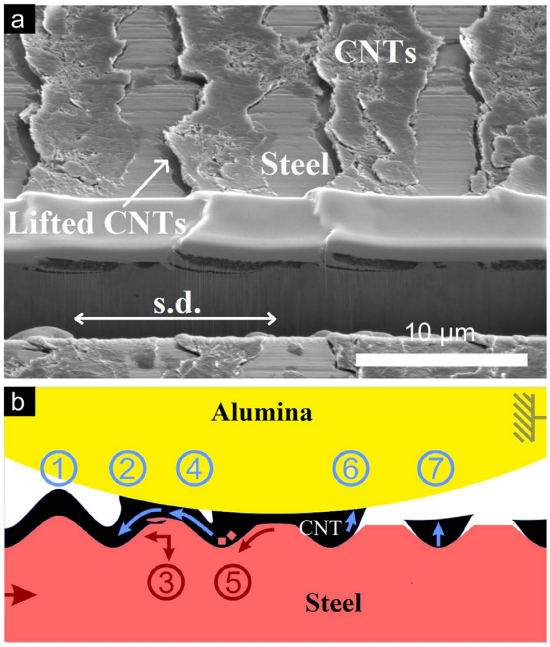

Figure 8. FIB cross-section of the wear track centre of (**a**) the textured + coated sample after 500 sliding cycles and (**b**) a schematic illustration, representing the acting mechanisms during the tribological experiment.

Conclusions

In the present work, CNT coating and laser texturing of steel surfaces are combined in order to act synergetically in terms of reducing friction and wear. The laser textures are perfectly copied by the CNT coating using EPD as coating technique. A tribological comparison to laser-textured/uncoated surfaces, untextured/CNT-coated surfaces and untextured/uncoated references is conducted. The following statements refer to a comparison with an untextured/uncoated reference:

1. $\leq$**1000 sliding cycles:** Frictional reduction in the case of a **textured/uncoated sample**, which is accompanied by a gradual degradation of the surface texture.
2. $\leq$**2200 sliding cycles:** Frictional reduction by a factor of four in the case of **untextured/coated sample** until the CNTs are dragged out of the contact zone and the COF increases.
3. $\geq$**10000 sliding cycles:** Stable frictional reduction by a factor of three in case of **textured/coated sample**.

The slightly less pronounced frictional reduction of point 3 compared to point 2 can be explained with a higher roughness of the textured/coated sample (rms of 300 nm compared to 30 nm), thus hindering the CNT rolling movement and reducing the dimension of the lubricating effect. Furthermore, a direct correlation of the CNT degradation in a tribological contact with an already known three-stage phenomenological model (transition from graphitic-like to amorphous-like structures) is established using Raman spectroscopy. It is found, that the combination of laser texturing and CNT-coating slows down the degradation process of the CNTs within a tribological contact and also the formation of oxidic wear particles. Finally, the significant extension of the lubricant longevity in point 3 is related to a synergistic effect of CNTs and laser textures and can be exemplified by a lubricant entrapping model, which is proposed and demonstrated.

References

1. Holmberg, K., Andersson, P. & Erdemir, A. Global energy consumption due to friction in passenger cars. *Tribol. Int.* **47,** 221–234 (2012).
2. Gachot, C. *et al.* Dry Friction Between Laser-Patterned Surfaces: Role of Alignment, Structural Wavelength and Surface Chemistry. *Tribol. Lett.* **9,** 193–202 (2013).
3. Rosenkranz, A., Reinert, L., Gachot, C. & Mücklich, F. Alignment and wear debris effects between laser-patterned steel surfaces under dry sliding conditions. *Wear* **318,** 49–61 (2014).
4. Mücklich, F., Lasagni, A. & Daniel, C. Laser Interference Metallurgy–using interference as a tool for micro / nano structuring. *Int. J. Mat. Res.* **97,** 1337–1344 (2006).
5. Xia, Y. Soft Lithography and the Art of Patterning—A Tribute to Professor George M. Whitesides. *Adv. Mater.* **16,** 1245–1246 (2004).
6. Etsion, I. State of the Art in Laser Surface Texturing. *J. Tribol. Trans. ASME* **127,** 248 (2005).
7. Rosenkranz, A., Heib, T., Gachot, C. & Mücklich, F. Oil film lifetime and wear particle analysis of laser-patterned stainless steel surfaces. *Wear* **334–335,** 1–12 (2015).
8. Grützmacher, P., Rosenkranz, A. & Gachot, C. How to guide lubricants–Tailored laser surface patterns on stainless steel. *Appl. Surf. Sci.* **370,** 59–66 (2016).
9. Chen, W. X. *et al.* T ribological application of carbon nanotubes in a metal-based composite coating and composites. *Carbon* **41,** 215–222 (2003).
10. Kim, K. T., Cha Il, S. & Hong, S. H. Hardness and wear resistance of carbon nanotube reinforced Cu matrix nanocomposites. *Mater. Sci. Eng. A* **449–451,** 46–50 (2007).

11. Scharf, T. W., Neira, A., Hwang, J. Y., Tiley, J. & Banerjee, R. Self-lubricating carbon nanotube reinforced nickel matrix composites. *J. Appl. Phys.* **106,** 013508 (2009).
12. Tan, J., Yu, T., Xu, B. & Yao, Q. Microstructure and wear resistance of nickel–carbon nanotube composite coating from brush plating technique. *Tribol. Lett.* **21,** 107–111 (2006).
13. Guiderdoni, C. *et al.* The preparation of double-walled carbon nanotube/Cu composites by spark plasma sintering, and their hardness and friction properties. *Carbon* **49,** 4535–4543 (2011).
14. Suárez, S., Rosenkranz, A., Gachot, C. & Mücklich, F. Enhanced tribological properties of MWCNT/Ni bulk composites–Influence of processing on friction and wear behaviour. *Carbon* **66,** 164–171 (2014).
15. Hirata, A. & Yoshioka, N. Sliding friction properties of carbon nanotube coatings deposited by microwave plasma chemical vapor deposition. *Tribol. Int.* **37,** 893–898 (2004).
16. Hu, J. J., Jo, S. H., Ren, Z. F., Voevodin, A. & Zabinski, J. S. Tribological behavior and graphitization of carbon nanotubes grown on 440C stainless steel. *Tribol. Lett.* **19,** 119–125 (2005).
17. Miyoshi, K. Jr., Wal, K. W. S., Vander, R. L., Andrews, R. & Sayir, A. Solid lubrication by multiwalled carbon nanotubes in air and in vacuum. *Tribol. Lett.* **19,** 191–201 (2005).
18. Dickrell, P. L. *et al.* Tunable friction behavior of oriented carbon nanotube films. *Tribol. Lett.* **24,** 85–90 (2006).
19. Zhang, X. *et al.* Carbon nanotube-MoS_2 composites as solid lubricants. *ACS Appl. Mater. Interfaces* **1,** 735–9 (2009).
20. Arai, S., Fujimori, A., Murai, M. & Endo, M. Excellent solid lubrication of electrodeposited nickel-multiwalled carbon nanotube composite films. *Mater. Lett.* **62,** 3545–3548 (2008).
21. Chen, C. S., Chen, X. H., Xu, L. S., Yang, Z. & Li, W. H. Modification of multi-walled carbon nanotubes with fatty acid and their tribological properties as lubricant additive. *Carbon* **43,** 1660–1666 (2005).
22. Peng, Y., Hu, Y. & Wang, H. Tribological behaviors of surfactant-functionalized carbon nanotubes as lubricant additive in water. *Tribol. Lett.* **25,** 247–253 (2006).
23. Lu, H. F. *et al.* Synthesis and lubricating performance of a carbon nanotube seeded miniemulsion. *Carbon* **45,** 936–942 (2007).
24. Kristiansen, K., Zeng, H., Wang, P. & Israelachvili, J. N. Microtribology of Aqueous Carbon Nanotube Dispersions. *Adv. Funct. Mater.* **21,** 4555–4564 (2011).
25. Chen, X. H. *et al.* Dry friction and wear characteristics of nickel/carbon nanotube electroless composite deposits. *Tribol. Int.* **39,** 22–28 (2006).
26. Dickrell, P. L. *et al.* Frictional anisotropy of oriented carbon nanotube surfaces. *Tribol. Lett.* **18,** 59–62 (2005).
27. Colonna, F., Fasolino, A. & Meijer, E. J. Graphitization of single-wall nanotube bundles at extreme conditions: Collapse or coalescence route. *Phys. Rev. B* **88,** 165416 (2013).
28. Reinert, L., Suárez, S. & Rosenkranz, A. Tribo-Mechanisms of Carbon Nanotubes: Friction and Wear Behavior of CNT-Reinforced Nickel Matrix Composites and CNT-Coated Bulk Nickel. *Lubricants* **4,** 11 (2016).
29. Majumder, M. *et al.* Insights into the physics of spray coating of SWNT films. *Chem. Eng. Sci.* **65,** 2000–2008 (2010).
30. Mirri, F. *et al.* High-Performance Carbon Nanotube Transparent Conductive Films by Scalable Dip Coating. 9737–9744 (2012).
31. De Nicola, F. *et al.* Super-hydrophobic multi-walled carbon nanotube coatings for stainless steel. *Nanotechnology* **26,** 145701 (2015).
32. Boccaccini, A. R. *et al.* Electrophoretic deposition of carbon nanotubes. *Carbon* **44,** 3149–3160 (2006).
33. Besra, L. & Liu, M. A review on fundamentals and applications of electrophoretic deposition (EPD). *Prog. Mater. Sci.* **52,** 1–61 (2007).
34. Rosenkranz, A. *et al.* Oxide Formation, Morphology, and Nanohardness of Laser-Patterned Steel Surfaces. *Adv. Eng. Mater.* 10.1002/adem.201400487 (2015).
35. Thomas, B. J. C. *et al.* Electrophoretic Deposition of Carbon Nanotubes on Metallic Surfaces. *Key Eng. Mater.* **314,** 141–146 (2006).
36. Esumi, K., Ishigami, M., Nakajima, A., Sawada, K. & Honda, H. Chemical treatment of carbon nanotubes. *Carbon* **34,** 279–281 (1995).
37. Reinert, L., Zeiger, M., Suarez, S., Presser, V. & Mücklich, F. Dispersion analysis of carbon nanotubes, carbon onions, and nanodiamonds for their application as reinforcement phase in nickel metal matrix composites. *RSC Adv.* **5,** 95149–95159 (2015).
38. De Riccardis, M. F., Carbone, D. & Rizzo, A. A novel method for preparing and characterizing alcoholic EPD suspensions. *J. Colloid Interface Sci.* **307,** 109–15 (2007).
39. Hasan, S. A., Kavich, D. W., Mahajan, S. V. & Dickerson, J. H. Electrophoretic deposition of CdSe nanocrystal films onto dielectric polymer thin films. *Thin Solid Films* **517,** 2665–2669 (2009).
40. Hertz, H. Über die Berührung von elastischen festen Körpern. *J. für die reine und Angew. Math.* **92** (1881).
41. Green, I. Poisson ratio effects and critical valus in spherical and cylindrical Hertzian contacts. *Int. J. Appl. Mech. Eng.* **10,** 451–462 (2005).
42. Blau, P. J. On the nature of running-in. *Tribol. Int.* **38,** 1007–1012 (2005).
43. Dogan, H., Findik, F. & Morgul, O. Friction and wear behaviour of implanted AISI 316L SS and comparison with a substrate. *Mater. Des.* **23,** 605–610 (2002).
44. Stott, F. H. & Wood, G. C. The influence of oxides on the friction and wear of alloys. *Tribol. Int.* 211–218 (1978).
45. Oh, S. J., Cook, D. C. & Townsend, H. E. Characterization of iron oxides commonly formed as corrosion products on steel. *Hyperfine Interact.* **112,** 59–66 (1998).
46. Mccarty, K. F. & Boehme, D. R. A Raman Study of the Systems Fe3xCrxO4 and Fe2xCrxO3. *J. Solid State Chem.* **79,** 19–27 (1989).
47. Farrow, R. L., Benner, R. E., Nagelberg, A. S. & Mattern, P. L. Characterization of surface oxides by raman spectroscopy. *Thin Solid films* **73,** 353–358 (1980).
48. Dorri Moghadam, A., Omrani, E., Menezes, P. L. & Rohatgi, P. K. Mechanical and tribological properties of self-lubricating metal matrix nanocomposites reinforced by carbon nanotubes (CNTs) and graphene–A review. *Compos. Part B Eng.* **77,** 402–420 (2015).
49. Ferrari, A. & Robertson, J. Interpretation of Raman spectra of disordered and amorphous carbon. *Phys. Rev. B* **61,** 14095–14107 (2000).

Acknowledgements

The present work is supported by funding from the Deutsche Forschungsgemeinschaft (DFG, project: MU 959/38-1 and project: SU 911/1-1). The authors wish to acknowledge the EFRE Funds of the European Commission for support of activities within the AME- Lab project. This work was supported by the CREATe-Network Project, Horizon 2020 of the European Commission (RISE Project No. 644013).

Author Contributions

L.R., F.L. and C.G. performed and discussed the laser texturing of the steel surfaces. F.L., P.G. and T.M. designed, performed and analysed the electrophoretic coating of the steel surfaces. L.R., N.S. and S.S. were responsible for Raman analysis and discussion. L.R., C.G. and P.G. designed, conducted and analysed the tribological experiments. L.R., S.S., C.G. and F.L. obtained and discussed the SEM micrographs of the wear tracks. F.M. contributed with valuable discussion in all points. All authors discussed and wrote the manuscript.

Additional Information

Supplementary information accompanies this paper at http://www.nature.com/srep

Competing financial interests: The authors declare no competing financial interests.

How to cite this article: Reinert, L. *et al.* Long-lasting solid lubrication by CNT-coated patterned surfaces. *Sci. Rep.* **7**, 42873; doi: 10.1038/srep42873 (2017).

Publisher's note: Springer Nature remains neutral with regard to jurisdictional claims in published maps and institutional affiliations.

VI Influence of surface roughness on the lubrication effect of carbon nanoparticle-coated steel surfaces

Leander Reinert, Silas Schütz, Sebastian Suárez and Frank Mücklich

Department of Material Science and Engineering, Saarland University, 66123 Saarbrücken, Germany

*Published in **"Tribology letters" (Impact factor (2018): 2.182)***
The final publication is available at link.springer.com
Accessible online at: https://doi.org/10.1007/s11249-018-1001-6

Own contribution:

Planning of tribological experiments; Friction coefficient analysis; Scanning electron microscopy and wear track analysis; Writing; Discussion; Planning.

Abstract:

In the present study, a systematic evaluation of the influence of the surface roughness on the lubrication activity of multiwall carbon nanotubes (MWCNT) and onion-like carbon (OLC) is performed. MWCNT and OLC are chosen as they both present an sp^2-hybridization of carbon atoms, show a similar layered atomic structure and exhibit the potential to roll on top of a surface. However, their morphology (size and aspect ratio) clearly differs, allowing for a methodical study of these differences on the lubrication effect on systematically varied surface roughness. Stainless steel platelets with different surface finishing were produced and coated by electrophoretic deposition with OLC or MWCNT. The frictional behavior is recorded using a ball-on-disc tribometer and the resulting wear tracks are analyzed by scanning electron microscopy in order to reveal the acting tribological mechanisms. It is found, that the lubrication mechanism of both types of particles is traced back to a mixture between a rolling motion on the surfaces and particle degradation, including the formation of nanocrystalline graphitic layers. This investigation further highlights, that choosing the suitable surface finish for a tribological application is crucial for achieving beneficial tribological effects of carbon nanoparticle lubricated surfaces.

Cite this as:
L. Reinert, S. Schütz, S. Suárez, F. Mücklich, Influence of surface roughness on the lubrication effect of carbon nanoparticle-coated steel surfaces. *Tribology letters* **2018**, 66 (*https://doi.org/10.1007/s11249-018-1001-6*)

Tribology Letters (2018) 66:45
https://doi.org/10.1007/s11249-018-1001-6

ORIGINAL PAPER

Influence of Surface Roughness on the Lubrication Effect of Carbon Nanoparticle-Coated Steel Surfaces

L. Reinert[1] · S. Schütz[1] · S. Suárez[1] · F. Mücklich[1]

Received: 6 December 2017 / Accepted: 6 February 2018

Abstract
In the present study, a systematic evaluation of the influence of the surface roughness on the lubrication activity of multi-wall carbon nanotubes (MWCNT) and onion-like carbon (OLC) is performed. MWCNT and OLC are chosen as they both present an sp^2-hybridization of carbon atoms, show a similar layered atomic structure, and exhibit the potential to roll on top of a surface. However, their morphology (size and aspect ratio) clearly differs, allowing for a methodical study of these differences on the lubrication effect on systematically varied surface roughness. Stainless steel platelets with different surface finishing were produced and coated by electrophoretic deposition with OLC or MWCNT. The frictional behavior is recorded using a ball-on-disk tribometer, and the resulting wear tracks are analyzed by scanning electron microscopy in order to reveal the acting tribological mechanisms. It is found that the lubrication mechanism of both types of particles is traced back to a mixture between a rolling motion on the surfaces and particle degradation, including the formation of nanocrystalline graphitic layers. This investigation further highlights that choosing the suitable surface finish for a tribological application is crucial for achieving beneficial tribological effects of carbon nanoparticle lubricated surfaces.

Keywords Solid lubrication · Carbon nanotubes · Onion-like carbon · Lubrication mechanisms · Surface roughness

1 Introduction

The tribological optimization of various technical systems is dictated by the demand for lower energy consumption and, in most cases, is directly linked to an efficient lubrication [1]. Certainly, the most established way to reduce friction and wear lies in the use of a suitable fluid lubrication medium. However, certain mechanical systems set the need to replace fluid with solid lubricants, as when the system runs under unfavorable environmental conditions such as high temperatures or vacuum [2, 3].

In this regard, along with classical solid lubricants (e.g., graphite or MoS_2), carbon nanomaterials have shown to be very promising candidates for these applications [4–7]. This fact is traced back to their intrinsic physical properties, morphology, and low density compared to other materials [8–10]. The focus of this work is on multi-wall carbon nanotubes (MWCNT) [11] and onion-like carbons (OLC) [12]. MWCNT can be described as multi-shell graphitic cylinders with large aspect ratio [11]. OLC show a similar multi-shell graphitic carbon structure. However, as OLC are fullerene-like nanoparticles with a polyhedral form and a typical diameter of only 4–10 nm, they are often ascribed to be "zero dimensional" [12, 13].

In case of MWCNTs, several works confirm their ability to reduce friction and wear when used as protective films [5, 6, 14, 15], solid lubricant [16–18], reinforcement phase in composites [19–21], or lubricant additive [22–24]. Some studies are based on the assumption that CNTs form a carbonaceous layer on the surface, which presents similar tribo-mechanisms to those of graphite [15, 21]. Others explain these beneficial effects with their ability to efficiently separate the sliding surfaces while acting as roller bearings [7, 16, 25]. In this regard and depending on the applied contact pressure, a so-called tank-belt effect has already been simulated and reported in literature, describing the deformation of rolling CNT between two contacting surfaces under shear [26, 27]. The deformation of the CNT and rolling movement could lead to delamination and the formation of flake-like graphitic structures. Further on, the possibility to reduce surface oxidation and thus hindering the formation of abrasive

✉ L. Reinert
l.reinert@mx.uni-saarland.de

[1] Department of Materials Science, Saarland University, Campus D3.3, 66123 Saarbrücken, Germany

Published online: 09 February 2018

third bodies in the tribological contact might also influence the observed tribological behavior [7, 14].

Considering the polyhedral form, low amount of dangling bonds on their surface, and also their potentially high mechanical strength, it is reasonable to assume that OLC might act as ball bearings in a tribological contact as well [8]. In the case of an nominally perfectly flat surface (silicon wafer), OLC coating showed a friction coefficient lower than 0.05 and also a wear reduction by 3–6 orders of magnitude compared to a graphite lubrication [28]. In this respect, with the curvature of OLCs being higher compared to MWCNTs, it is supposed that they show less intermolecular interactions to the surface and thus are able to freely move [29, 30]. This lubrication effect can also be maintained under vacuum conditions [28]. Despite these very promising statements of OLC as solid lubricant, there is a significant drawback. OLC lubrication decreases significantly when the normal contact pressure exceeds a certain threshold value [31]. It is also assumed that, depending on the OLC particle size, they might be trapped within the asperities of a given surface roughness and therefore no longer provide a lubricating effect [28]. However, this being a very important point, there is no systematic study comparing the effect of the surface roughness on the lubrication activity of CNP for the same tribological system yet.

Considering the surface roughness, it often defines the characteristic of a tribological system [32–35]. However, it is often linked to the final application, as this determines how much effort can be put in the design or processing of a surface. For example, surface roughness is rather low and well defined in microelecromechanical systems (MEMS) [36], whereas it is usually high in the case of large technical surfaces of machine elements [35]. With the initial work of Bowden and Tabor, the interaction between asperities of a rough surface with regard to the influence on the frictional behavior became a much discussed topic [37]. This interaction could be correlated with adhesion/welding and subsequent releasing (in case that a critical shear stress is applied) and depends upon several factors such as the electronic structure of the materials, free surface energies, interlayers, and ambient conditions [33, 38]. The friction behaviors of rough surfaces are further influenced by plastic deformation and consequently, on deformation energies, contact angles between asperities or the mechanical properties of the contacting materials [38]. Concerning these interactions, it was shown that very small shear stresses are possible between atomically flat surfaces with non-matching surface corrugations, allowing for vanishing friction [39, 40]. Several different models tried to explain the interaction of two contacting surfaces under dry conditions and different scales, starting at molecular level, like for example the Tomlinson or the Frenkel–Kontorova model [41, 42]. Based on the effects of macroscopic surface roughness on friction, numerous works successfully manipulated the stochastic surface roughness so as to create specifically designed surface geometries in order to control the coefficient of friction [14, 43–47]. Generally, adjusting a specific roughness for a given tribological application can be crucial, as it majorly determines contact mechanics and thus whether a contact situation is elastic or elasto-plastic and whether a real contact area is large or small [33]. Accordingly, different contact simulation models rely on surface descriptive parameters, for example, the Greenwood–Williamson, Jackson–Green or the Persson model [48–50].

However, when it comes to the use of nanoparticles as lubricants, surface roughness also plays an important role [27, 51, 52]. There are many studies about different kinds of nanoparticles (for example, MWCNT, MoS_2, nanodiamonds, OLC, alumina) used as lubricant additives [22, 30, 53–58]. Most of them refer to the shape, nanostructure, surface functionalization, concentration, or the size of the particles being the most important characteristics for an efficient lubrication. Considering nanoparticles as solid lubricant and not as lubricant additive, their shape and size compared to the surface roughness become even more important, as particles can be trapped, entirely be removed from the direct tribological contact or hindered in their rolling movement by surface asperities [14, 28]. Nonetheless, simulations or experiments regarding the solid lubrication activity of inorganic or organic nanoparticles so far concentrate on very low roughness surfaces like for example Si-wafer [31, 59].

Thus, the present study is motivated by the need to classify the lubrication effect of carbon nanoparticles (CNP) as solid lubricant for different surface roughness values. This could be beneficial as a stepping-stone for further research, as the size and morphology of CNPs could be selected in order to fit the tribological requirements.

For this purpose, a suitable technique must be found in order to coat surfaces with a pre-defined surface roughness in a reproducible and controllable way. There are different techniques available for carbon nanoparticle coating of metallic surfaces, including spray [60] and dip coating [61], CVD [62], drop casting [7]. One of the most suitable and straightforward techniques is electrophoretic deposition (EPD) [63]. In contrast to drop casting or spray coating, EPD provides the advantage of being easily scalable, very homogeneous, and reproducible [14, 63, 64]. Therefore, it is used in the present study.

Concerning the CNP coatings, MWCNT and OLC are chosen since they present similar atomic arrangement as well as possible lubrication mechanism (rolling mechanism). Their different morphology and particle size allow for a systematic investigation of the lubrication activity as a function of the initial surface roughness of a defined tribological system. Thus, stainless steel surfaces with different pre-defined surface roughness are coated with

OLC or MWCNT, respectively. Stainless steel is used as substrate material because of its technological relevance.

2 Experimental Section

2.1 Materials

Austenitic stainless steel (AISI 316L) platelets ($20 \times 20 \times 1$ mm^3) are used as substrate material for the tribological experiments. For the coatings, MWCNTs were purchased at graphene supermarket (diameter 20–85 nm, length 5–15 µm), and OLC were synthesized from detonation nanodiamond powder (purchased from NaBond Technologies Co., purity > 98%, individual particle diameter 4–8 nm). This is done by annealing at 1750 °C for 3 h in graphite crucibles in a vacuum furnace with tungsten heaters (model: 1100-3580-W1, Thermal Technology Inc.) applying a heating and cooling rate of 15 °C min^{-1}. The chamber pressure is between 10 and 100 mPa. The synthesized OLC show an individual particle diameter of 4–10 nm and almost full sp^2 carbon hybridization as can be seen in prior studies [13, 65].

2.2 Surface Preparation and Characterization

The stainless steel platelets are ground flat using a fully automated grinding and polishing device (TegraPol by Struers). The surfaces were then polished up to different end finishes. Two samples are polished using 2500 grit sandpaper from Leco corp. (MI, USA), which corresponds to a (8.5 ± 0.5) µm particle size. Furthermore, two samples of each kind are polished using 6-, 3-, and 1-µm diamond-polishing suspensions, respectively. Finally, also two samples are polished using a 0.5-µm oxide polishing suspension (OPS) to achieve the lowest surface roughness. In the following, the samples are designated as 8.5, 6, 3, 1, and 0.5 µm, respectively. Subsequently, these surfaces are characterized in terms of their resulting surface roughness (root-mean-squared roughness, R_{rms}) using a white light interferometer (WLI, Zygo NewView 7300) equipped with a 3D imaging surface structure analyzer. The micrographs were recorded using a 50× objective and providing a surface height resolution of < 0.1 nm. Each sample is measured 10 times at different spots from which the mean value and standard deviation is determined. Additionally, SEM micrographs of each surface were acquired using a FIB/FE-SEM dual beam station (FEI Helios NanoLab) using an acceleration voltage of 5 kV and a current of 1.4 nA.

2.3 EPD Process

For the deposition process, the as-prepared platelets were thoroughly cleaned in order to remove possible contaminants. This was carried out by 10 min of ultrasonication (Sonorex Super RK 514 BH by Bandelin, 860 W, 35 kHz), respectively, in cyclohexane, followed by acetone and finally isopropanol. Afterward, the platelets are used as electrodes. A dispersion with a concentration of 0.25 mg ml^{-1} CNT or OLC was prepared using acetone as solvent. In order to disperse the particles, a shear mixer (Ultra-turrax T-25 by IKA) was used for 5 min followed by ultrasonic treatment of the dispersion for another 20 min [65]. Subsequently, triethylamine (TEA) was added in order to add negatively charged COO^- surface groups [66]. Finally, the negatively charged CNPs are deposited in a deposition cell at a voltage of 20 V for 10 min, maintaining an electrode separation of 1.3 cm (anodic deposition). In order to measure the coating thickness, FIB cross sections were prepared with focused ion beam machining using 30 kV of bias.

2.4 Tribological Experiments

For the tribological experiments, a ball-on-disk tribometer (Nanotribometer from CSM Instruments) was used in a linear reciprocating sliding mode with a stroke length of 600 µm. The normal load of 50 mN was applied using an alumina ball (purchased from Anton Paar GmbH) with a diameter of 6 mm, mounted on a cantilever with a stiffness of 0.7624 µN µm^{-1} in normal and 1.1447 µN µm^{-1} in tangential direction. Alumina is chosen to avoid any plastic deformation of the counter-body. The surface roughness of the ball is not modified and used as delivered for all experiments. It is measured by WLI for 10 different ball surfaces, and a mean value of $R_{\mathrm{rms}} = 20 \pm 6$ nm is determined. This is the best surface finish of commercially available alumina balls with a diameter of 6 mm we could purchase. The number of sliding cycles was set to 500 with a maximum sliding speed of 1 mm/s. The low load and low amount of sliding cycles are chosen in order to prevent severe wear and thus not to change the surface roughness of the substrate material significantly during the experiment. Also, by applying low contact pressures, the particles are not hindered to freely move on the surfaces [31]. Temperature and relative humidity were kept constant at 20 ± 2 °C and 4 ± 1%, respectively. A very low relative humidity is chosen in order to reduce lubrication effects based on a simple graphitic lubrication, which would need a higher relative humidity to be effective [67–69]. Three measurements were performed for each type of sample, and the mean value of the coefficient of friction (COF) including standard deviation is plotted against the number of sliding cycles for each type of sample.

3 Results and Discussion

After grinding and polishing the surfaces of the stainless steel platelets, they are analyzed using WLI as well as SEM. In Fig. 1, the different obtained surfaces are shown, and the corresponding R_{rms} values including the standard deviations are given.

As expected, a clear decrease in the mean R_{rms} value is observed, from 42 nm in case of the preparation with sandpaper (8.5 µm) down to 3.9 nm for the oxide polishing suspension (0.5 µm). The SEM micrographs show large scratch marks and even plastically deformed material in case of the sandpaper preparation (Fig. 1a). For the higher-grade surface finishing, these scratches are gradually removed until the marks reach the detection limit of the used techniques (in case of the 0.5-µm polishing suspension) (Fig. 1f). During this surface preparation process, the samples were moved circularly over the rotating sandpaper or polishing cloth, keeping a constant pressure. This is done to avoid the formation of anisotropic scratch marks resulting in the formation of randomly oriented scratch marks on the steel surfaces.

Comparing these surfaces with the surface of the alumina ball ($R_{rms} = 20 \pm 6$ nm), the slightly larger standard deviation compared to the steel surfaces can be explained by 1–2-µm-sized, randomly appearing nicks in the alumina surface. However, the surface of each ball was studied by WLI before using it in the tribological experiment. Surfaces with marked nicks were consequently avoided.

The surfaces of the steel substrates are coated with CNT or OLC. The obtained coatings cover the surfaces homogeneously, as shown in Fig. 2a, b. However, there are clear differences between the two coatings. OLC form small agglomerates of a few 100 nm in diameter, which are stacked onto the metal surface. In case of CNT, a dense coating of intertwinned CNT is observed, forming large agglomerates on the surface.

In Fig. 2c, a FIB cross section of the OLC coating on a 3-µm polished steel surface is depicted. As exemplarily shown here, the thicknesses of the deposited coatings were measured. The achieved thicknesses are 3 ± 1 µm for the OLC coatings and 3 ± 2 µm for the CNT coatings. The CNT coatings show higher fluctuation in the coating thickness due to a higher tendency to form agglomerates, which has already been reported in previous studies [14, 65]. Furthermore, it is noticeable that the coating mainly consists of stacked small particle agglomerates, including a large quantity of pores in between the individual agglomerates (Fig. 2c). However, this is not considered as a debilitating factor for the tribological effects, as the coating will be compressed by the counterpart contacting the surface. Both types of coatings are not chemically bonded to the steel surface and show very low adhesion, being physisorption the only interdependency between coating and steel surface. This is done deliberately in order to allow a systematic study of the

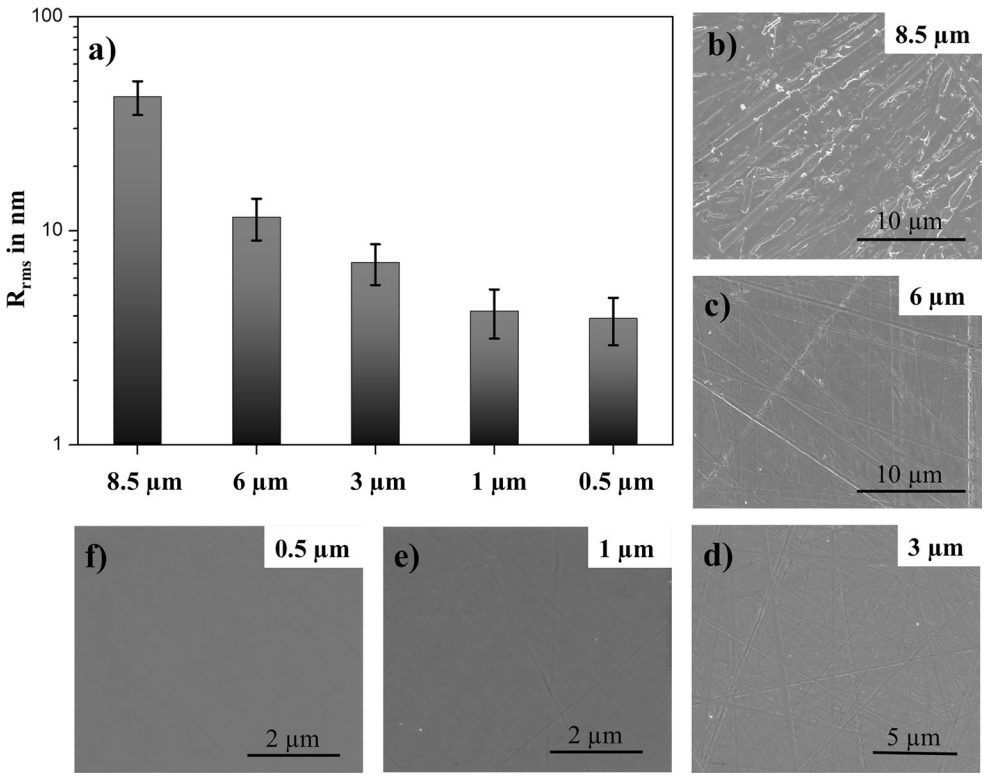

Fig. 1 **a** R_{rms} values of the prepared surfaces including the standard deviation before coating with CNT or OLC, respectively. The SEM micrographs correspond to **b** 8.5 µm, **c** 6 µm, **d** 3 µm, **e** 1 µm, and **f** 0.5 µm surface finishing

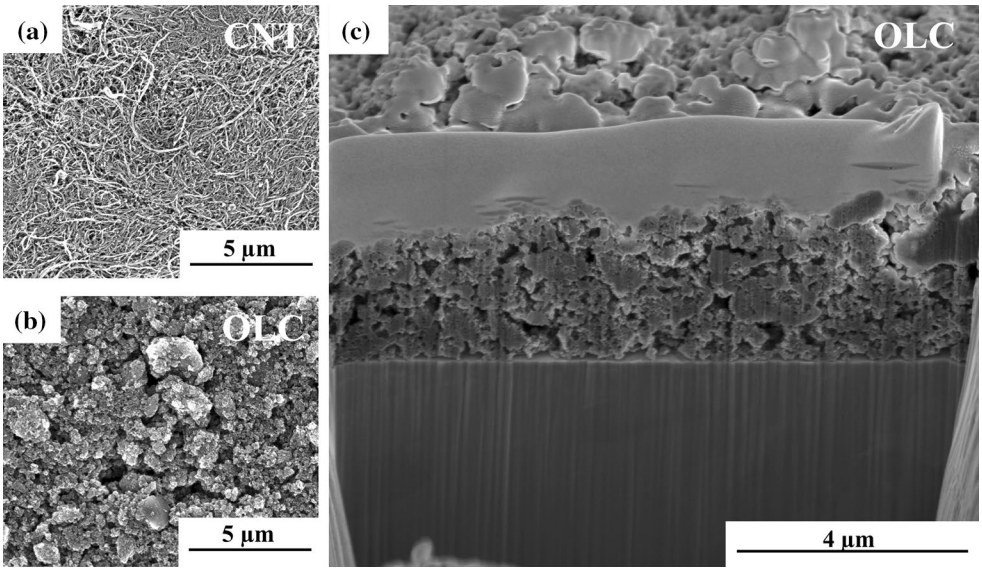

Fig. 2 SEM micrographs of **a** the CNT coating and **b** the OLC coating on the steel surface with a 3-µm finishing are shown. Also, the thickness of the OLC coating is demonstrated by a FIB cross section in **c**

lubrication mechanism of the particles without any chemical influence of the substrate by allowing the particles to move freely over the steel surface.

The different samples were then compared in terms of the temporal evolution of the COF for a maximum of 500 sliding cycles, which is shown in Fig. 3.

The reference COF corresponds to an uncoated steel surface with a finishing of 1 µm (R_{rms} = 4.2 ± 1.1 nm). It is observed, that the COF increases during the first 250 cycles from 0.25 to 0.7, finally reaching steady-state conditions. This behavior is well known for pure metal surfaces and is extensively discussed in other works, for example in Blau et al. [70]. It can be explained with an increasing real contact area as a consequence of the combination of two effects: the wearing off of intrinsic asperities and an increment of the indentation depth of the ball into the substrate. The rather unstable evolution of the COF is related to the formation and disintegration of wear particles, which was also already examined in previous studies [14]. The obtained steady-state reference COF of 0.7 is in agreement with the value reported in the literature [71].

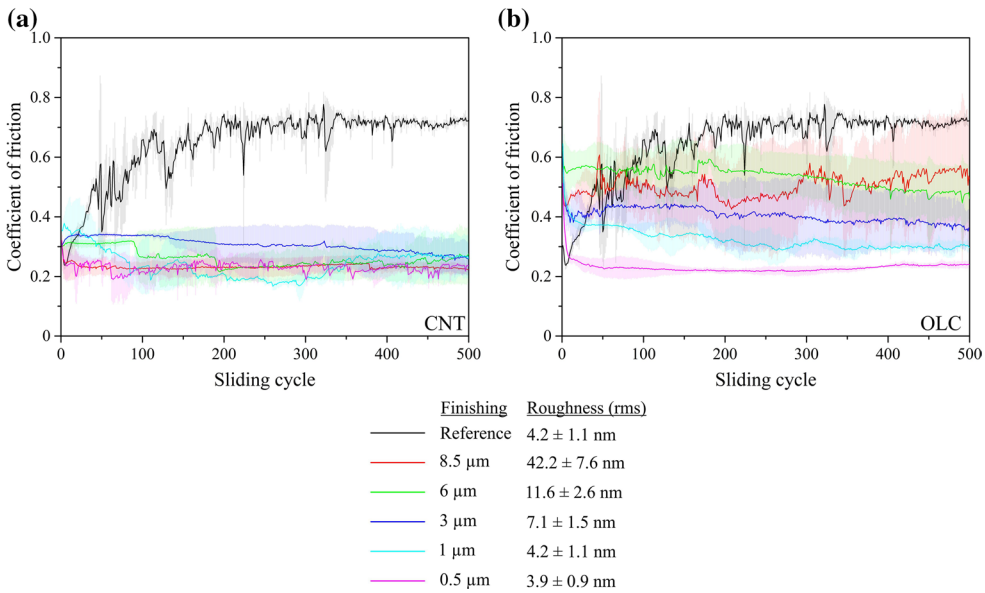

Fig. 3 Temporal evolution of the dynamic COF as a function of the number of sliding cycles for **a** CNT-coated surfaces and **b** OLC coated surfaces. The different colors correspond to different initial surfaces roughness as indicated below the graphs

Regarding the CNT-coated surfaces (Fig. 3a), a clear reduction in the COF can be observed. Furthermore, the impact of different surface roughness appears to be negligible as a COF of approximately 0.2 is sustained for all CNT-coated surfaces after 500 sliding cycles. This is explained by the size and morphology of the CNTs. As the used CNTs present an outer diameter of 20–85 nm and a length of 5–15 µm, they can effectively separate the two sliding surfaces with R_{rms} values between 3.9 and 42 nm. Although some of the surface scratches of the samples with higher roughness are larger than 85 nm in width, CNT could still be dragged out of these areas due to their high aspect ratio and their curved morphology with high flexibility. This allows CNTs to roll and/or to be degraded to nanocrystalline graphitic flakes and thus to lubricate the contact, as it was observed by Raman spectroscopy investigations in a previous study [14]. The slight variations in the frictional behavior of the different surfaces show no clear trend and provide a relatively large standard deviation. This is related to a varying thickness (3 ± 2 µm) of the CNT coating in the different measuring areas. Considering the applied normal force (50 mN) and the coating thickness range (from a maximum of 5 µm to a minimum of 1 µm), partially entangled CNT have to be pulled by the alumina ball during the initial sliding cycles, resulting in a varying tangential force until almost all the CNTs are shifted toward the end of the wear track. This will be further discussed in the wear track analysis.

Concerning the frictional behavior of the surfaces coated with OLC in Fig. 3b, a clear difference of the COF as a function of the pre-defined surface finishing is noticeable. For the COF evolution of the 8.5-µm (R_{rms} = 42 ± 7.5 nm) and 6-µm (R_{rms} = 11.5 ± 2.5 nm) samples, only a marginal frictional reduction can be observed after the first 100 sliding cycles until the end of the measurement. As the roughness of these surfaces are evidently larger than the diameter of the OLC particles (4–10 nm), it seems reasonable to state that the OLCs are trapped within the surface scratch marks and are being removed from the direct contact zone, as already reported by Hirata et al. [28]. Still, some of the particles remain in direct tribological contact, contributing to the slight reduction of the mean value of the COF. However, the high fluctuation of the COF in case of the 8.5-µm surface finishing is comparable with the behavior of the reference. Therefore, it becomes clear that the acting tribo-mechanisms of both samples are similar and most likely dominated by the direct contact of the alumina ball with the steel surface.

By analyzing the higher-grade surface finishes [3 µm (R_{rms} = 7.1 ± 1.5 nm), 1 µm (R_{rms} = 4.2 ± 1 nm) and 0.5 µm (R_{rms} = 3.9 ± 0.9 nm)], the COF is gradually decreasing and the standard deviations are clearly reduced. Considering that the R_{rms} values (7.1–3.9 nm) are now in the range of the particle diameter, a separation of the two sliding surfaces by OLC is conceivable. This leads to a stabilization of the COF evolution and thus explains the reduced standard deviation. As discussed in the introduction, the OLC morphology, low amount of dangling bonds, and their high strength make it reasonable to assume that they are acting as rolling elements, efficiently reducing the friction coefficient. However, the COF of the system is not reaching values below 0.2, as observed by Hirata et al. [28]. This might be a consequence of the counterpart roughness (R_{rms} of 20 nm), being able to trap OLC particles within the surface asperities. Nonetheless, an effect on the COF by surface roughness variation of the substrate material is clearly noticeable.

In order to achieve a better understanding of the acting tribo-mechanisms, the wear tracks have to be analyzed in more detail. Figure 4 shows two SEM micrographs of single MWCNT on the steel surface (3-µm surface finishing) after the tribological experiment with the given sliding direction (S.D.).

The SEM micrographs exemplify the dimensions of the scratch marks of a 3-µm sample surface compared to the used MWCNT. These micrographs support the assumption, that MWCNT cannot be trapped within the roughness of the prepared surfaces. Considering the structural integrity of the particles, the MWCNT oriented perpendicular to the sliding direction seem to be unmodified and only slightly

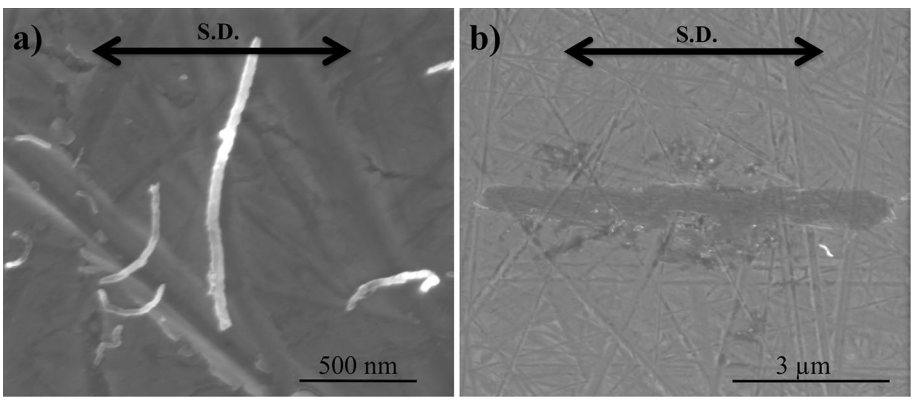

Fig. 4 SEM micrographs of **a** shortened MWCNT, oriented perpendicular to the sliding direction (S.D.) on a 3-µm surface and **b** one single damaged, delaminated MWCNT, oriented parallel to the sliding direction (S.D.) on a 3-µm surface

shorter than the initial length of 5–15 µm (Fig. 4a). This fact supports the assumption of MWCNT are able to roll on the surface. In contrast to that, the MWCNT which is aligned in parallel to the sliding direction appears to be fully degraded and delaminated (Fig. 4b). This observation is consistent with Raman spectroscopy studies of previous works, describing the transition of MWCNT toward nanocrystalline graphite in a tribological contact [14]. The demonstrated situations represent the extreme possible cases and, as the MWCNT coating consists of randomly oriented particles, the lubrication mechanism almost certainly consists of a mixture of both cases.

In Fig. 5, the wear tracks of (a) the 3-µm surface coated with CNT and (b) the 3-µm surface coated with OLC are shown. In both cases, besides the shifted coating toward the end of the wear tracks, no sign of severe wear of the substrate steel material is observed after 500 sliding cycles.

This fact also supports the assumption that both surfaces are effectively separated by the particles when their diameter is in the range of the surface roughness. Thus, it can be concluded that the tribological contact is dominated by the separation of the two surfaces by the carbon nanoparticles and not by a direct interaction of the substrate steel with the alumina ball. This observation correlates well with the reduction in the COF in Fig. 3 as energy losses due to plastic deformation or adhesion of the potentially contacting surfaces could be avoided. Furthermore, the shift of the carbon nanoparticle (CNP) coatings toward the end of the wear track takes place within the initial sliding cycles and therefore can be correlated with the initially high COF values. Considering the very low normal load of 50 mN, this is reasonable, as a slightly higher tangential force is needed in order to shift the agglomerated particle coatings toward the ends of the wear track, resulting in a higher COF. Particularly for the CNT-coated surfaces, this effect is more pronounced as the CNT form an entangled network on the substrate surface. Thus, mechanically entangled CNT are piled up at the left-hand side of the wear track. Although this shifting of the coating happens within the initial sliding cycles, the lubrication effect is present for the entire experiment, showing that only few CNPs need to be in direct tribological contact for an efficient lubrication as most of them are dragged out of the direct contact area.

Figure 6 presents the wear tracks of the 8.5-µm finished surfaces coated with CNT or OLC, respectively. It is noticeable that the direct tribological contact zone in the middle of the SEM micrographs is by far less wide than the area of the removed coating. This can be explained by two facts. First, if the alumina ball applies pressure to the surface, only the center and its vicinity are in direct contact to the substrate material. The flanks of the alumina ball are only in contact with the coating, which is shifted with the moving ball. Second, as the particles are agglomerated and entangled, coated areas that were not in direct contact to the alumina ball might be pulled by moving neighboring particles. Overall, this leads to the observed broad removal of the coating around the direct tribological contact zone. Furthermore, the wear track of the CNT coating (Fig. 6a) does not show any appearance of severe wear of the substrate material with the initially produced scratch marks of the surface preparation still being identifiable (Fig. 6c). However, the formation of a gray layer and filled scratch marks indicate the possibility of storing degraded MWCNT. Nevertheless, the lubrication effect of this system is still active, as shown in Fig. 3a. In contrast to that, Fig. 6b and d clearly exhibits signs of severe wear as anisotropic scratch marks parallel to the sliding direction are formed. This indicates that OLCs lose their ability to separate both surfaces, which is in agreement with the evolution of the COF. Furthermore, OLC particles are trapped within the as-prepared surface scratch marks, therefore not participating in the direct tribological contact to any further extent (Fig. 6d). For the 6-µm surfaces, similar observations were made.

Looking in detail at the wear tracks of the 3-µm finished surfaces (Fig. 7), differences between both coatings can be observed again. In case of the CNT-coated sample, the surface is in pristine condition after the tribological experiment (500 sliding cycles), and no particle trapping is noticed, even with higher magnification. For the OLC coating, although no severe wear is observed, particles are partially stored in the scratch marks of the surface. Thus, the contacting surfaces of ball and substrate can still be separated, but the possible

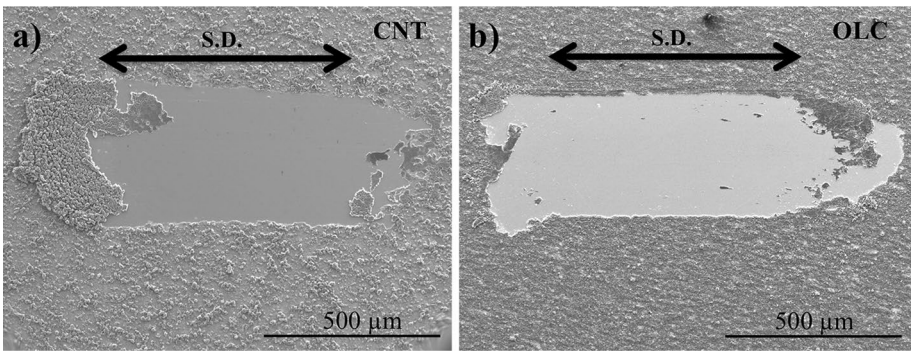

Fig. 5 SEM micrographs of the wear track after the tribological experiment of the 3-µm steel substrate coated wit **a** CNT and **b** OLC. In both cases, no severe wear of the substrate material is observed. The sliding direction (S.D.) is indicated with an arrow

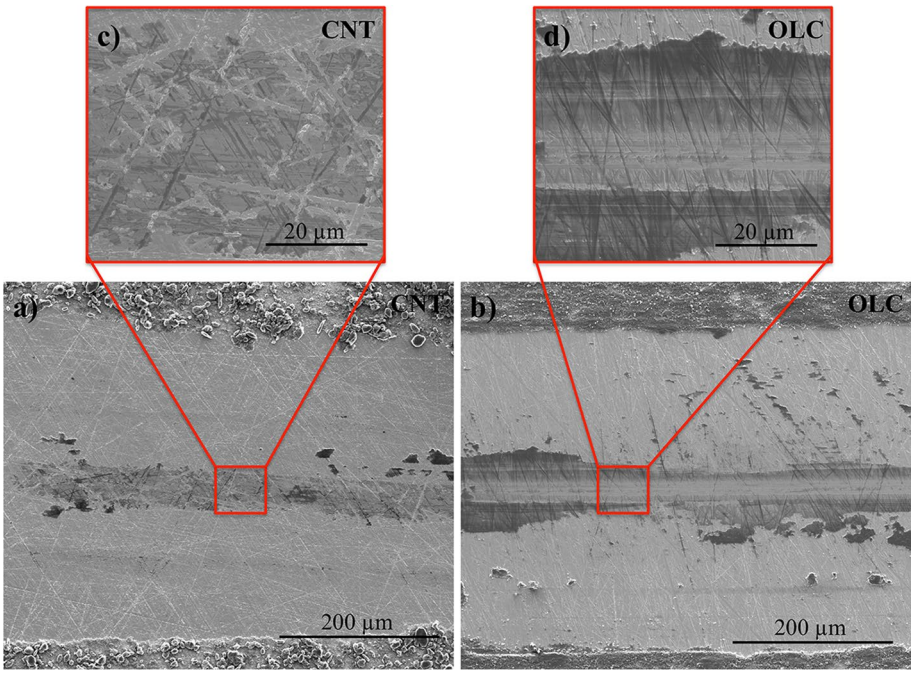

Fig. 6 SEM micrographs of the wear tracks after the tribological experiment on the 8.5-µm surfaces coated with **a** MWCNT and **b** OLC. Higher-magnification SEM micrographs show the scratch marks in more detail and are depicted in **c** for CNT and **d** for OLC. Severe wear is only observed for the OLC coated surface

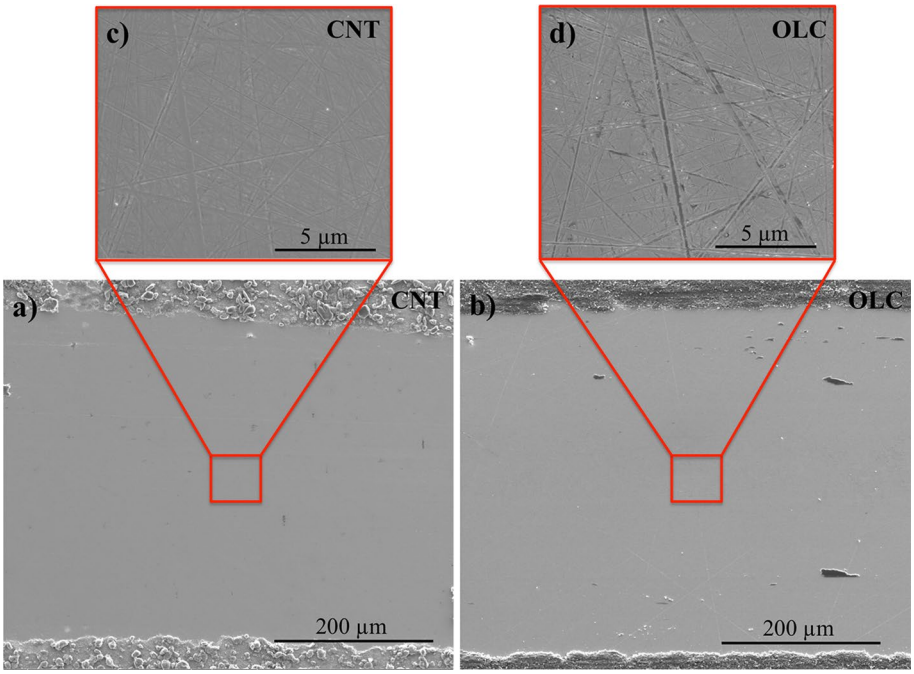

Fig. 7 SEM micrographs of the wear tracks after the tribological experiment on the 3-µm surfaces coated with **a** MWCNT and **b** OLC. Higher-magnification SEM micrographs show the scratch marks in more detail and are depicted in **c** for CNT and **d** for OLC

rolling mechanism of the OLC appears to be strongly hindered, as analyzed in the COF measurement in Fig. 3b.

In Fig. 8, a single scratch mark of the OLC wear track in Fig. 7b, d is shown under high magnification, marked with red lines. OLC particles are observed between the red lines, which are stored in the scratch mark thus severely restricting their ability to freely move or roll on the surface.

For the 1-µm and 0.5-µm finished surfaces, no particle trapping is found, neither in case of CNT nor in case of OLC coatings. This explains the decreasing COF in case of the OLC coatings, as less surface scratch marks can interfere with the potential rolling mechanism of the particles.

However, by observing at very high magnification in the SEM (Fig. 9), gray-shaded areas are detected in the wear tracks for both coatings. These areas might result from the degradation of the carbon particles in the direct tribological contact, thus forming nanocrystalline graphitic layers as already reported by Reinert et al. [14].

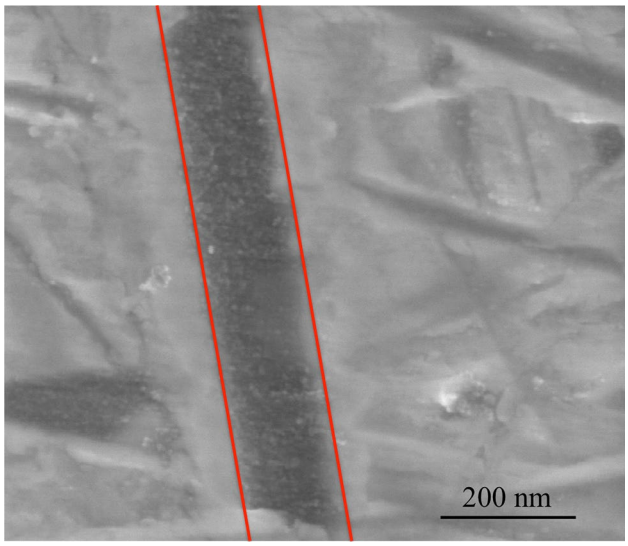

Fig. 8 High-magnification SEM micrograph of a scratch mark (marked in red) within the wear track of the 3-µm surface coated with OLC after the experiment. It can be seen, that the scratch mark is filled with trapped OLC particles that cannot efficiently roll on the surface therefore providing no pronounced lubrication effect (Color figure online)

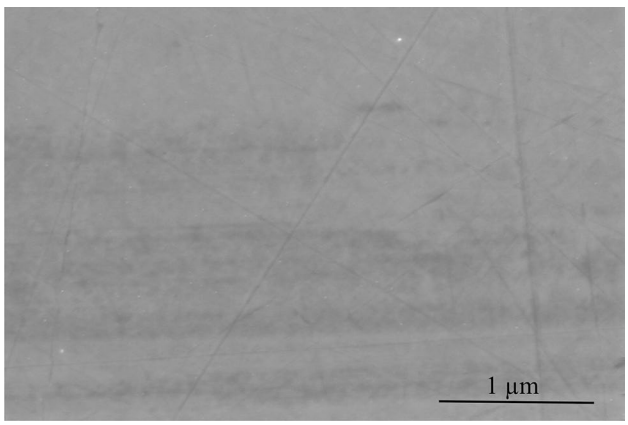

Fig. 9 High-magnification SEM micrograph of the wear track after the tribological experiment on the 1-µm surface coated with MWCNT. The surface is representative for the OLC coating as well

Thus, the lubrication mechanism of both types of particles is traced back to a mixture between a rolling motion on the surfaces and particle degradation, including the formation of nanocrystalline graphitic layers. Summarizing, this investigation highlights that choosing the suitable surface finish for a tribological application is crucial for achieving beneficial tribological effects of CNP-lubricated surfaces.

4 Conclusions

In the present study, a systematic evaluation of the influence of surface roughness on the lubrication activity of MWCNT and OLC has been carried out. It was observed that the friction coefficient of the steel surfaces (against alumina counterbodies) can be decreased considerably from 0.7 to 0.2 after applying an electrophoretically deposited OLC or MWCNT coating. The degree of frictional reduction in case of OLC is increasing with decreasing surface roughness. For a roughness higher than the diameter of the OLC particles (4–10 nm), only marginal lubrication is observed. This is explained by the particles being trapped within the initially induced surface scratch marks, therefore not being able to separate the contacting surfaces. When the surface roughness is in the range of the OLC particle diameter or below, efficient lubrication is observed. For MWCNT, no dependence of the lubrication activity on the surface roughness is observed. This is explained by their larger diameter (20–85 nm) and high aspect ratio (length of 5–15 µm), allowing them to be dragged inside of the direct tribological contact region. The lubrication mechanism of both types of particles is traced back to a mixture between a rolling motion on the surfaces and particle degradation, including the formation of nanocrystalline graphitic layers. However, it is assumed that the lubrication effect for both particles would be even more pronounced in case of a smoother surface of the ball ($R_{rms} = 20 \pm 6$ nm), as it might hinder the particles in their rolling mechanism. The aforementioned results emphasize that, in order to achieve beneficial tribological effects of carbon nanoparticle lubricated surfaces, the choice of a suitable surface finish for a tribological application is of utmost importance.

Acknowledgements The present work is supported by funding from the Deutsche Forschungsgemeinschaft (DFG, project: MU 959/38-1 and SU 911/1-1). L. R., S.S., and F. M. wish to acknowledge the EFRE Funds of the European Commission for support of activities within the AMELab project. This work was supported by the CREATe-Network Project, Horizon 2020 of the European Commission (RISE Project No. 644013).

References

1. Holmberg, K., Andersson, P., Erdemir, A.: Global energy consumption due to friction in passenger cars. Tribol. Int. **47**, 221–234 (2012). https://doi.org/10.1016/j.triboint.2011.11.022
2. Donnet, C., Erdemir, A.: Solid lubricant coatings: recent developments and future trends. Tribol. Lett. **17**, 389–397 (2004)
3. Aouadi, S.M., Gao, H., Martine, A., Scharf, T.W., Muratore, C.: Lubricious oxide coatings for extreme temperature applications: a review. Surf. Coat. Technol. **257**, 266–277 (2014)
4. Li, Y., Li, B.X., Zou, W.J.: The relationship between nanocrystalline structure and frictional properties of nanodiamond/Ni

composite coatings by brush plating. Appl. Mech. Mater. **80–81**, 683–687 (2011). https://doi.org/10.4028/www.scientific.net/AMM.80-81.683
5. Hirata, A., Yoshioka, N.: Sliding friction properties of carbon nanotube coatings deposited by microwave plasma chemical vapor deposition. Tribol. Int. **37**, 893–898 (2004). https://doi.org/10.1016/j.triboint.2004.07.005
6. Miyoshi, K., Street Jr., K.W., Vander Wal, R.L., Andrews, R., Sayir, A.: Solid lubrication by multiwalled carbon nanotubes in air and in vacuum. Tribol. Lett. **19**, 191–201 (2005). https://doi.org/10.1007/s11249-005-6146-4
7. Reinert, L., Suárez, S., Rosenkranz, A.: Tribo-mechanisms of carbon nanotubes: friction and wear behavior of CNT-reinforced nickel matrix composites and CNT-coated bulk nickel. Lubricants **4**, 11 (2016). https://doi.org/10.3390/lubricants4020011
8. Gogotsi, Y., Presser, V.: Carbon Nanomaterials. CRC Press, Boca Raton (2014). ISBN 9781138076815
9. Bakshi, S.R., Lahiri, D., Agarwal, A.: Carbon nanotube reinforced metal matrix composites—a review. Int. Mater. Rev. **55**, 41–64 (2010). https://doi.org/10.1179/095066009X12572530170543
10. Mochalin, V.N., Shenderova, O., Ho, D., Gogotsi, Y.: The properties and applications of nanodiamonds. Nat. Nanotechnol. **7**, 11–23 (2012). https://doi.org/10.1038/nnano.2011.209
11. Iijima, S.: Helical microtubules of graphitic carbon. Nature **354**, 56–58 (1991)
12. Cebik, J., McDonough, J.K., Peerally, F., Medrano, R., Neitzel, I., Gogotsi, Y., Osswald, S.: Raman spectroscopy study of the nanodiamond-to-carbon onion transformation. Nanotechnology **24**, 1–10 (2013). https://doi.org/10.1088/0957-4484/24/20/205703
13. Zeiger, M., Jäckel, N., Aslan, M., Weingarth, D., Presser, V.: Understanding structure and porosity of nanodiamond-derived carbon onions. Carbon **84**, 584–598 (2015). https://doi.org/10.1016/j.carbon.2014.12.050
14. Reinert, L., Lasserre, F., Gachot, C., Grützmacher, P., MacLucas, T., Souza, N., Mücklich, F., Suarez, S.: Long-lasting solid lubrication by CNT-coated patterned surfaces. Sci. Rep. (2017). https://doi.org/10.1038/srep42873
15. Hu, J.J., Jo, S.H., Ren, Z.F., Voevodin, A., Zabinski, J.S.: Tribological behavior and graphitization of carbon nanotubes grown on 440C stainless steel. Tribol. Lett. **19**, 119–125 (2005). https://doi.org/10.1007/s11249-005-5091-6
16. Tunable friction behavior of oriented carbon nanotube films: Dickrell, P.L., Pal, S.K., Bourne, G.R., Muratore, C., Voevodin, a. a., Ajayan, P.M., Schadler, L.S., Sawyer, W.G. Tribol. Lett. **24**, 85–90 (2006). https://doi.org/10.1007/s11249-006-9162-0
17. Zhang, X., Luster, B., Church, A., Muratore, C., Voevodin, A.A., Kohli, P., Aouadi, S., Talapatra, S.: Carbon nanotube-MoS_2 composites as solid lubricants. ACS Appl. Mater. Interfaces **1**, 735–739 (2009). https://doi.org/10.1021/am800240e
18. Arai, S., Fujimori, A., Murai, M., Endo, M.: Excellent solid lubrication of electrodeposited nickel-multiwalled carbon nanotube composite films. Mater. Lett. **62**, 3545–3548 (2008). https://doi.org/10.1016/j.matlet.2008.03.047
19. Chen, W.X., Tu, J.P., Wang, L.Y., Gan, H.Y., Xu, Z.D., Zhang, X.B.: T ribological application of carbon nanotubes in a metal-based composite coating and composites. Carbon **41**, 215–222 (2003)
20. Kim, K.T., Cha, S.I., Hong, S.H.: Hardness and wear resistance of carbon nanotube reinforced Cu matrix nanocomposites. Mater. Sci. Eng. A **449–451**, 46–50 (2007). https://doi.org/10.1016/j.msea.2006.02.310
21. Scharf, T.W., Neira, A., Hwang, J.Y., Tiley, J., Banerjee, R.: Self-lubricating carbon nanotube reinforced nickel matrix composites. J. Appl. Phys. **106**, 013508 (2009). https://doi.org/10.1063/1.3158360
22. Chen, C.S., Chen, X.H., Xu, L.S., Yang, Z., Li, W.H.: Modification of multi-walled carbon nanotubes with fatty acid and their tribological properties as lubricant additive. Carbon **43**, 1660–1666 (2005). https://doi.org/10.1016/j.carbon.2005.01.044
23. Peng, Y., Hu, Y., Wang, H.: Tribological behaviors of surfactant-functionalized carbon nanotubes as lubricant additive in water. Tribol. Lett. **25**, 247–253 (2006). https://doi.org/10.1007/s11249-006-9176-7
24. Lu, H.F., Fei, B., Xin, J.H., Wang, R.H., Li, L., Guan, W.C.: Synthesis and lubricating performance of a carbon nanotube seeded miniemulsion. Carbon **45**, 936–942 (2007). https://doi.org/10.1016/j.carbon.2007.01.001
25. Dickrell, P.L., Sinnott, S.B., Hahn, D.W., Raravikar, N.R., Schadler, L.S., Ajayan, P.M., Sawyer, W.G.: Frictional anisotropy of oriented carbon nanotube surfaces. Tribol. Lett. **18**, 59–62 (2005). https://doi.org/10.1007/s11249-004-1752-0
26. Ni, B., Sinnott, S.B.: Tribological properties of carbon nanotube bundles predicted from atomistic simulations. Surf. Sci. **487**, 87–96 (2001). https://doi.org/10.1016/S0039-6028(01)01073-1
27. Martin, J.M., Ohmae, N.: Nanolubricants. Wiley, New York (2008). ISBN 978-0-470-06552-5
28. Hirata, A., Igarashi, M., Kaito, T.: Study on solid lubricant properties of carbon onions produced by heat treatment of diamond clusters or particles. Tribol. Int. **37**, 899–905 (2004). https://doi.org/10.1016/j.triboint.2004.07.006
29. Park, S., Srivastava, D., Cho, K.: Generalized chemical reactivity of curved surfaces: carbon nanotubes. Nano Lett. **3**, 1273–1277 (2003). https://doi.org/10.1021/nl0342747
30. Street, K.W., Marchetti, M., Vander Wal, R.L., Tomasek, A.J.: Evaluation of the tribological behavior of nano-onions in Krytox 143AB. Tribol. Lett. **16**, 143–149 (2004)
31. Bucholz, E.W., Phillpot, S.R., Sinnott, S.B.: Molecular dynamics investigation of the lubrication mechanism of carbon nano-onions. Comput. Mater. Sci. **54**, 91–96 (2012). https://doi.org/10.1016/j.commatsci.2011.09.036
32. Menezes, P.L., Kishore, Kailas, S.V.: Effect of surface roughness parameters and surface texture on friction and transfer layer formation in tin–steel tribo-system. J. Mater. Process. Technol. **208**, 372–382 (2008). https://doi.org/10.1016/j.jmatprotec.2008.01.003
33. Persson, B.N.J., Albohr, O., Tartaglino, U., Volokitin, A.I., Tosatti, E.: On the nature of surface roughness with application to contact mechanics, sealing, rubber friction and adhesion. J. Phys. Condens. Matter. (2005). https://doi.org/10.1088/0953-8984/17/1/r01
34. Sahin, M., Çetinarslan, C.S., Akata, H.E.: Effect of surface roughness on friction coefficients during upsetting processes for different materials. Mater. Des. **28**, 633–640 (2007). https://doi.org/10.1016/j.matdes.2005.07.019
35. Svahn, F., Kassman-Rudolphi, Å., Wallén, E.: The influence of surface roughness on friction and wear of machine element coatings. Wear **254**, 1092–1098 (2003). https://doi.org/10.1016/S0043-1648(03)00341-7
36. Komvopoulos, K.: Adhesion and friction forces in microelectromechanical systems: mechanisms, measurement, surface modification techniques, and adhesion theory. J. Adhes. Sci. Technol. **17**, 477–517 (2003). https://doi.org/10.1163/15685610360554384
37. Bowden, F.P., Tabor, D.: Mechanism of metallic friction. Nature **3798**, 197–199 (1942). https://doi.org/10.1038/150197a0
38. Czichos, H., Habig, K.: Tribologie-Handbuch. Vieweg + Teubner, Wiesbaden (2010). ISBN 978-3-8348-0017-6
39. Hirano, M., Shinjo, K., Kaneko, R., Murata, Y.: Anisotropy of frictional forces in muscovite mica. Phys. Rev. Lett. **67**, 2642–2646 (1991)
40. Dienwiebel, M., Verhoeven, G., Pradeep, N., Frenken, J., Heimberg, J., Zandbergen, H.: Superlubricity of graphite. Phys. Rev.

Lett. **92**, 126101 (2004). https://doi.org/10.1103/PhysRevLett.92.126101
41. Tomlinson, G.A.: A molecular theory of friction. Lond. Edinb. Dublin Philos. Mag. J. Sci. **7**, 905–939 (1929). https://doi.org/10.1080/14786440608564819
42. Weiss, M., Elmer, F.: Dry friction in the Frenkel–Kontorova–Tomlinson model: static properties. Phys. Rev. B Condens. Matter **53**, 7539–7549 (1996)
43. Etsion, I.: State of the art in laser surface texturing. J. Tribol. Trans. ASME **127**, 248 (2005). https://doi.org/10.1115/1.1828070
44. Rapoport, L., Moshkovich, A., Perfilyev, V., Gedanken, A., Koltypin, Y., Sominski, E., Halperin, G., Etsion, I.: Wear life and adhesion of solid lubricant films on laser-textured steel surfaces. Wear **267**, 1203–1207 (2009). https://doi.org/10.1016/j.wear.2009.01.053
45. Gachot, C., Rosenkranz, A., Reinert, L., Ramos-Moore, E., Souza, N., Müser, M.H., Mücklich, F.: Dry friction between laser-patterned surfaces: role of alignment, structural wavelength and surface chemistry. Tribol. Lett. **9**, 193–202 (2013). https://doi.org/10.1007/s11249-012-0057-y
46. Rosenkranz, A., Reinert, L., Gachot, C., Mücklich, F.: Alignment and wear debris effects between laser-patterned steel surfaces under dry sliding conditions. Wear **318**, 49–61 (2014). https://doi.org/10.1016/j.wear.2014.06.016
47. Sondhauß, J., Fuchs, H., Schirmeisen, A.: Frictional properties of a mesoscopic contact with engineered surface roughness. Tribol. Lett. **42**, 319–324 (2011)
48. Persson, B.N.J.: Contact mechanics for randomly rough surfaces. Surf. Sci. Rep. **61**, 201–227 (2006). https://doi.org/10.1016/j.surfrep.2006.04.001
49. Greenwood, J., Williamson, J.: Contact of nominally flat surfaces. R. Soc. Publ. **295**, 300–319 (1966)
50. Jackson, R.L., Green, I.: A statistical model of elasto-plastic asperity contact between rough surfaces. Tribol. Int. **39**, 906–914 (2006). https://doi.org/10.1016/j.triboint.2005.09.001
51. Akbulut, M.: Nanoparticle-based lubrication systems. J. Powder Metall. Min. **1**, 377–411 (2012). https://doi.org/10.1002/9781118483961.ch17
52. Wu, Y.Y., Tsui, W.C., Liu, T.C.: Experimental analysis of tribological properties of lubricating oils with nanoparticle additives. Wear **262**, 819–825 (2007). https://doi.org/10.1016/j.wear.2006.08.021
53. Ivanov, M.G., Ivanov, D.M., Pavlyshko, S.V., Petrov, I., Vargas, A., McGuire, G., Shenderova, O.: Nanodiamond-based nanolubricants. Fuller. Nanotub. Carbon Nanostruct. **20**, 606–610 (2012). https://doi.org/10.1080/1536383x.2012.657010
54. Joly-Pottuz, L., Vacher, B., Ohmae, N., Martin, J.M., Epicier, T.: Anti-wear and friction reducing mechanisms of carbon nano-onions as lubricant additives. Tribol. Lett. **30**, 69–80 (2008). https://doi.org/10.1007/s11249-008-9316-3
55. Khalilpourazary, S., Meshkat, S.S.: Investigation of the effects of alumina nanoparticles on spur gear surface roughness and hob tool wear in hobbing process. Int. J. Adv. Manuf. Technol. **71**, 1599–1610 (2014). https://doi.org/10.1007/s00170-013-5591-8
56. Rahmati, B., Sarhan, A.A.D., Sayuti, M.: Investigating the optimum molybdenum disulfide (MoS_2) nanolubrication parameters in CNC milling of AL6061-T6 alloy. Int. J. Adv. Manuf. Technol. **70**, 1143–1155 (2014). https://doi.org/10.1007/s00170-013-5334-x
57. Hwang, Y., Lee, C., Choi, Y., Cheong, S., Kim, D., Lee, K., Lee, J., Kim, S.H.: Effect of the size and morphology of particles dispersed in nano-oil on friction performance between rotating discs. J. Mech. Sci. Technol. **25**, 2853–2857 (2011). https://doi.org/10.1007/s12206-011-0724-1
58. Kogovšek, J., Remškar, M., Mrzel, A., Kalin, M.: Influence of surface roughness and running-in on the lubrication of steel surfaces with oil containing MoS_2 nanotubes in all lubrication regimes. Tribol. Int. **61**, 40–47 (2013). https://doi.org/10.1016/j.triboint.2012.12.003
59. Tevet, O., Von-Huth, P., Popovitz-Biro, R., Rosentsveig, R., Wagner, H.D., Tenne, R.: Friction mechanism of individual multilayered nanoparticles. Proc. Natl. Acad. Sci. **108**, 19901–19906 (2011). https://doi.org/10.1073/pnas.1106553108
60. Majumder, M., Rendall, C., Li, M., Behabtu, N., Eukel, J.A., Hauge, R.H., Schmidt, H.K., Pasquali, M.: Insights into the physics of spray coating of SWNT films. Chem. Eng. Sci. **65**, 2000–2008 (2010). https://doi.org/10.1016/j.ces.2009.11.042
61. Mirri, F., Ma, A.W.K., Hsu, T.T., Behabtu, N., Eichmann, S.L., Young, C.C., Tsentalovich, D.E., Pasquali, M.: High-performance carbon nanotube transparent conductive films by scalable dip coating. ACS Nano **6**, 9737–9744 (2012)
62. De Nicola, F., Castrucci, P., Scarselli, M., Nanni, F., Cacciotti, I., De Crescenzi, M.: Super-hydrophobic multi-walled carbon nanotube coatings for stainless steel. Nanotechnology **26**, 145701 (2015). https://doi.org/10.1088/0957-4484/26/14/145701
63. Boccaccini, A.R., Cho, J., Roether, J.A., Thomas, B.J.C., Jane Minay, E., Shaffer, M.S.P.: Electrophoretic deposition of carbon nanotubes. Carbon **44**, 3149–3160 (2006). https://doi.org/10.1016/j.carbon.2006.06.021
64. Besra, L., Liu, M.: A review on fundamentals and applications of electrophoretic deposition (EPD). Prog. Mater Sci. **52**, 1–61 (2007). https://doi.org/10.1016/j.pmatsci.2006.07.001
65. Reinert, L., Zeiger, M., Suarez, S., Presser, V., Mücklich, F.: Dispersion analysis of carbon nanotubes, carbon onions, and nanodiamonds for their application as reinforcement phase in nickel metal matrix composites. RSC Adv. **5**, 95149–95159 (2015). https://doi.org/10.1039/C5RA14310A
66. De Riccardis, M.F., Carbone, D., Rizzo, A.: A novel method for preparing and characterizing alcoholic EPD suspensions. J. Colloid Interface Sci. **307**, 109–115 (2007). https://doi.org/10.1016/j.jcis.2006.10.037
67. Yen, B.K., Ishihara, T.: Effect of humidity on friction and wear of Al–Si eutectic alloy and Al–Si alloy-graphite composites. Wear **198**, 169–175 (1996)
68. Savage, R.H.: Graphite lubrication. J. Appl. Phys. **19**, 1 (1948). https://doi.org/10.1063/1.1697867
69. Berman, D., Erdemir, A., Sumant, A.V.: Graphene: a new emerging lubricant. Mater. Today **17**, 31–42 (2014). https://doi.org/10.1016/j.mattod.2013.12.003
70. Blau, P.J.: On the nature of running-in. Tribol. Int. **38**, 1007–1012 (2005). https://doi.org/10.1016/j.triboint.2005.07.020
71. Dogan, H., Findik, F., Morgul, O.: Friction and wear behaviour of implanted AISI 316L SS and comparison with a substrate. Mater. Des. **23**, 605–610 (2002). https://doi.org/10.1016/S0261-3069(02)00066-3

VII Influence of surface design on the solid lubricity of carbon nanotubes-coated steel surfaces

Christian Schäfer[1], **Leander Reinert[1]**, Timothy MacLucas[1], Philipp Grützmacher[1], Rolf Merz[2], Frank Mücklich[1] and Sebastian Suárez[1]

[1] Department of Material Science and Engineering, Saarland University, 66123 Saarbrücken, Germany
[2] Institut für Oberflächen-und Schichtanalytik GmbH, Trippstadter Straße 120, 67663 Kaiserslautern, Germany

Published in ***"Tribology letters" (Impact factor (2018): 2.182)***
The final publication is available at link.springer.com
Accessible online at: https://doi.org/10.1007/s11249-018-1044-8

Own contribution:

Planning and coordination of tribological experiments; Friction coefficient analysis; Scanning electron microscopy and wear track analysis; Raman spectroscopy analysis; Writing; Discussion; Planning.

Abstract:

Topographically designed surfaces are able to store solid lubricants, preventing their removal out of the tribological contact and thus significantly prolonging the lubrication lifetime of a surface. The present study provides a systematic evaluation of the influence of surface structure design on the solid lubrication effect of multi-walled carbon nanotubes (MWCNT) coated steel surfaces. For this purpose, direct laser writing using a femtosecond pulsed laser system is deployed to create surface structures, which are subsequently coated with MWCNT by electrophoretic deposition. The structural depth or aspect ratio of the structures and thus the lubricant storage volume of the solid lubricant is varied. The frictional behavior of the surfaces is recorded using a ball-on-disc tribometer and the surfaces are thoroughly characterized by complementary characterization techniques. Efficient lubrication is achieved for all MWCNT coated surfaces. However, and in contrast to what would be expected, it is shown that deeper structures with larger lubricant storage volume do not lead to an extended lubrication lifetime and behave almost equally to the coated unstructured surfaces. This can be attributed, among other things, to differences in the final surface roughness of the structures and the slope steepness of the structures, which prevent efficient lubricant supply into the contact.

Cite this as:
C. Schäfer, L. Reinert, T. MacLucas, P. Grützmacher, R. Merz, F. Mücklich and S. Suárez, Influence of surface design on the solid lubricity of carbon nanotubes-coated steel surfaces, *Tribology letters* **2018,** 66:89 (*https://doi.org/10.1007/s11249-018-1044-8*)

Tribology Letters (2018) 66:89
https://doi.org/10.1007/s11249-018-1044-8

ORIGINAL PAPER

Influence of Surface Design on the Solid Lubricity of Carbon Nanotubes-Coated Steel Surfaces

C. Schäfer[1] · L. Reinert[1] · T. MacLucas[1] · P. Grützmacher[1] · R. Merz[2] · F. Mücklich[1] · S. Suarez[1]

Received: 8 March 2018 / Accepted: 19 June 2018

Abstract
Topographically designed surfaces are able to store solid lubricants, preventing their removal out of the tribological contact and thus significantly prolonging the lubrication lifetime of a surface. The present study provides a systematic evaluation of the influence of surface structure design on the solid lubrication effect of multi-walled carbon nanotubes (MWCNT) coated steel surfaces. For this purpose, direct laser writing using a femtosecond pulsed laser system is deployed to create surface structures, which are subsequently coated with MWCNT by electrophoretic deposition. The structural depth or aspect ratio of the structures and thus the lubricant storage volume of the solid lubricant is varied. The frictional behavior of the surfaces is recorded using a ball-on-disk tribometer and the surfaces are thoroughly characterized by complementary characterization techniques. Efficient lubrication is achieved for all MWCNT-coated surfaces. However, and in contrast to what would be expected, it is shown that deeper structures with larger lubricant storage volume do not lead to an extended lubrication lifetime and behave almost equally to the coated unstructured surfaces. This can be attributed, among other things, to differences in the final surface roughness of the structures and the slope steepness of the structures, which prevent efficient lubricant supply into the contact.

Keywords Solid lubrication · Laser structuring · Carbon nanotubes · Coatings · Surface modification

1 Introduction

In the past years, it has been extensively reported, that precisely produced periodic surface structures positively influence friction and wear in mechanically loaded components for example by reducing the real contact area and trapping wear debris [1–3]. To create those surface structures, there is a great number of possible techniques available, such as micro coining [4], burnishing [5], lithography and anisotropic etching [6], honing [7], and laser surface texturing (LST) [1]. Regarding LST, a distinction can be made between direct laser writing (DLW) and direct laser interference patterning (DLIP). While DLIP is based on the interference of several laser beams, making high speed surface patterning possible [8, 9], DLW provides a greater flexibility of the created structures (e.g., higher aspect ratios) through successive surface processing.

Well defined depressions on a textured surface may also act as a reservoir for liquid and solid lubricants and are therefore able to continuously provide the loaded contact area with lubricant, resulting in a reduction of friction and wear and thus prolonging the duty life of the tribological stressed components [10–13].

Concerning solid lubricants, materials like graphite [14], MoS_2 [13, 14], WS_2 [15], and carbon nanotubes (CNTs) [16] turned out to be very effective in lowering the coefficient of friction (COF). Among those, particularly CNTs are exceedingly promising candidates due to their unique properties, such as their sp^2-hybridization state and the resulting binding conditions, their unique form, their high aspect ratio as well as their high flexibility. Numerous studies have shown, that CNTs can significantly contribute to reduce friction and wear in tribological applications, for example as a reinforcing second phase in composites [17–22], as a solid protective film [23–27], or as an additive in liquid lubricants [28–31]. Scharf et al. [19] were able to trace the self-lubricating properties of Ni/CNT-composites to the formation

✉ S. Suarez
s.suarez@mx.uni-saarland.de

[1] Department of Materials Science, Saarland University, Campus D 3.3, 66123 Saarbrücken, Germany

[2] Institut für Oberflächen- und Schichtanalytik GmbH, Trippstadter Straße 120, 67663 Kaiserlautern, Germany

Published online: 21 June 2018

of a lubricating film of graphitic nature, which protects the contacted surface against tribo-chemical reactions (e.g., oxidation) and leads to a low shear strength within the contact area. Furthermore, the lubricating effect of CNTs is often linked to their ability to roll and slide over surfaces [32] and to act as spacers between a contacting tribological pair [33]. Dickrell et al. [26, 34] pointed out differences in the tribological behavior of CNT films depending on their orientation on the substrate surface. The horizontally aligned nanotubes showed an immense lowering of COF in comparison to the vertically arranged CNTs due to their ability – in case of the horizontal alignment – to perform complex motions that combine sliding and rolling [32].

Regarding the manufacturing of CNT-coatings, there is a large variety of possible techniques, e.g., spray coating [35], dip coating [36], drop casting [22, 37], chemical vapor deposition (CVD) [38], or electrophoretic deposition (EPD) [39–41]. Out of those, EPD offers a variety of benefits, such as low costs, simple procedure, reproducibility, good control of the layer thickness, microstructural homogeneity of the coatings as well as the possibility to deposit on complex shapes [42–44].

Despite the above-mentioned advantages, both, laser-induced surface structures as well as coatings containing solid lubricants involve drawbacks related to friction and wear. Periodical structures may be gradually removed and solid lubricants may be transported out of the contact area by continuous removal, severely hindering their positive tribological effects [2, 3, 22]. However, a combination of both methods could lead to an overcoming of those drawbacks.

Recently, Reinert et al. [45] investigated the tribological behavior of DLIP-structured and CNT-coated steel substrates. They could show, that the combination of both techniques facilitates the storage of CNTs within the depressions of the periodic surface structure, whereby the CNTs are continuously fed into the contact area thus reducing friction and wear to a significant degree. Compared to the isolated used methods, the period, in which a noticeably reduced COF is present, can be prolonged many times. The line-like structures complete their task as reservoirs for solid lubricant until they are completely removed.

The results shown in [45] form the basis for the motivation of this study. The increase in aspect ratio of the structures by producing deeper structures and thus increasing the volume of the reservoirs could lead to a further improvement of the tribological system. However, with the nanosecond laser system used in [45], the achievable structural depths are limited to approximately 1 µm [11, 46]. With an ultra-short pulsed laser system, material is removed by ablation, preventing the formation of piled up, molten and re-solidified material, thus leading to surfaces with a higher load-bearing capacity and a larger lubricant storage reservoir at the same time [47, 48]. For the given reasons, this study investigates the influence of the lubrication reservoir volume on the tribological behavior of CNT-coated steel samples. For varying the structure depth, an ultra-short pulsed laser system with a pulse duration of 100 fs and a repetition rate of 1 kHz is used. Due to the above-mentioned advantages over the other techniques, EPD is used for producing the CNT-coatings.

2 Materials and Methods

2.1 Materials

MWCNTs synthesized by catalytic chemical vapor deposition (CCVD) were purchased from Graphene Supermarket (USA). Their diameter distribution ranged between 50 and 85 nm and their length between 10 and 15 µm. The as-received carbon content is over 94%. The substrates consisted of stainless steel plates (AISI 304 grade) with a thickness of 1 mm and a (20×20) mm^2 area. The surface is finished to a mirror polishing ($R_a = 16.3 \pm 5.2$ nm). Before structuring the platelets, the surfaces were cleaned rigorously to remove possible contaminants. The cleaning process consisted of three consecutive 10 min ultrasound baths (Bandelin Sonorex RK514BH) in cyclohexane, acetone, and isopropanol alternated with deionized water rinsing followed by drying with pressurized air.

2.2 Characterization Techniques

The steel surfaces were topographically characterized by confocal laser-scanning microscopy (LEXT OLS4100, Olympus) with a laser wavelength of 405 nm. The lateral and vertical resolution of the equipment is 120 and 10 nm, respectively. The measurements were carried out with a 50X objective (N.A. = 0.95). The coatings and wear tracks were morphologically characterized with a field emission scanning electron microscopy/ focused ion beam (FE-SEM/FIB) Helios NanoLab 600 dual beam workstation (FEI) equipped with an EDS detector (EDAX). The structural characteristics of the CNTs and the oxide development were observed by Raman spectroscopy on an inVia Raman microscope (Renishaw). The used laser wavelength was 532 nm. The laser power on the sample was 2 mW (50X objective, N. A. 0.9), resulting in a spot size of 5 µm. The spectral resolution is 1.2 cm^{-1}. All the acquired spectra are further post-processed by removing the experimental background and fitting the characteristic peaks with Lorentz functions [49].

Oxide layer thickness and chemistry were characterized by AES (Auger electron spectroscopy) on different areas of the micro structured steel platelets after laser irradiation. The analysis was done by sputter depth profiles. Here the 10 keV, 10 nA primary electron beam is scanned selectively over

micro regions, defined before in SEM micrographs, alternatingly followed by single sputter steps with a Ar + beam (beam energy 2 keV) scanned over 2 mm x 2 mm. With the same ion gun adjustments the oxide layer of a standard reference sample (60 nm Ta_2O_5 oxide layer on Ta) was sputtered through in 490 min.

2.3 Ultra-Short Pulsed Laser Surface Structuring

The surfaces of the steel platelets are structured by direct laser writing (DLW) using a femtosecond pulsed laser system (Spectra-Physics, Ti:Sapphire laser) with a pulse length of 100 fs, a wavelength of 800 nm and a pulsing frequency of 1 kHz. The laser is focused on the sample surface with an output power of 30 mW producing a spot size of 10–15 µm Line-like structures are created on the steel platelets by moving them with a two axis motorized stage in a meander-like pattern. Subsequently, the sample is rotated by 90° and the process is repeated, finally resulting in a cross-like structure. Cross-like structures are chosen instead of line-like structures as the tribological measurement is performed in a rotational mode. Thus, a line-like structure would behave highly anisotropic. According to the pulse frequency, the stage velocity is adapted so that the individual laser pulses overlap by 50% and an almost constant structural depth of 1 µm is obtained for one laser pass. In order to create a structure depth of 3 µm, the laser beam is moved four times in total over each line. The distance from line to line is chosen to be 50 µm.

2.4 Coating Production by Electrophoretic Deposition

Prior to the deposition, the CNTs were acid-functionalized following the procedure described in a previous paper by [50]. Subsequently, the functionalized CNTs (9 mg) were dispersed in ethanol (90 mL) with triethylamine (13 mL) as an additive. The function of the additive is to improve the deposition rate of the dispersed CNTs by increasing the degree of deprotonation of the carboxy groups on the particles' surface. During the first part of the dispersion process, the colloidal solution is homogenized in a shear mixer (Ultra-Turrax T25, IKA-Germany) at 8000 rpm for 5 min. Secondly, the solution is further dispersed in an ultrasonic bath (Bandelin Sonorex RK514BH) for 20 min. The deposition occurred at a voltage of 40 V over a period of 10 min on the anode. During deposition, the electrodes are arranged in parallel to ensure the formation of a uniform electric field between the electrodes and therefore a homogeneous coating. The separation of the electrodes remained constant at 1.3 cm. After the deposition, the coated substrate was immersed in ethanol in order to wash out the additive.

2.5 Tribological Experiments

The tribological characterization was performed using a ball-on-disk micro-tribometer (CSM Instruments) working in rotational mode. The tribometer is placed within an environmental chamber to control temperature and humidity during the experiments. The chosen track radius was 5 mm and the normal load was 1 N. According to the Hertz contact model, the initial effective maximum contact pressure is approximately 757 MPa. The linear velocity was set to 1 cm/s so as to allow the lubricant to be pressed into the surface depressions and not to be swept away from the surface. The friction force was measured by a linear variable differential transformer (LVDT). Every experiment was repeated four times so as to perform a statistically representative analysis of the behavior. During the experiments, the temperature and humidity were kept constant at 25 °C and 45%, respectively. The selected static counterpart was an Al_2O_3 ball (Anton Paar GmbH), with a 6 mm diameter and a surface roughness of R_a: 23.8 ± 1.8 nm. As the alumina ball is much harder than the steel surface, wear is expected to occur mainly on the steel surface.

3 Results and Discussion

3.1 Initial State Characterization

The fabricated surfaces and the corresponding cross sections are depicted using laser-scanning microscopy in Fig. 1.

The surfaces show a homogeneous surface structure with a reproducible structural depth of 1 µm or 3 µm, respectively. Particularly for the structural depth of 3 µm (Fig. 1 c, f), the formation of high profile deposits is observed at the edges of the surface depressions. These can be traced back to a displacement of the molten from the ablation zone as well as to a re-depositioning of ablated material [51]. The effect is also present for the structures with a depth of 1 µm, but to a much lesser degree, as can be seen in Fig. 1 b and e. Furthermore, it has to be mentioned, that the crossing points of the laser structures present surfaces depressions, which are twice as deep. This is a consequence of being exposed to the laser beam in case of the horizontal and vertical structuring process. In order to evaluate the load-bearing capacity of the surfaces, Abbott-Firestone curves [52] are plotted in Fig. 2 for the reference as well as for the laser-structured surfaces.

It is observed that the high profile deposits represent the first 5% of the material portion for the structured samples. However, in case of the 3 µm-curve, the slope within this section is much higher than for the 1 µm-curve, indicating the presence of a large amount of rather pointy asperities due to displacement of molten material and material re-depositioning at the edges of the surface depressions. For

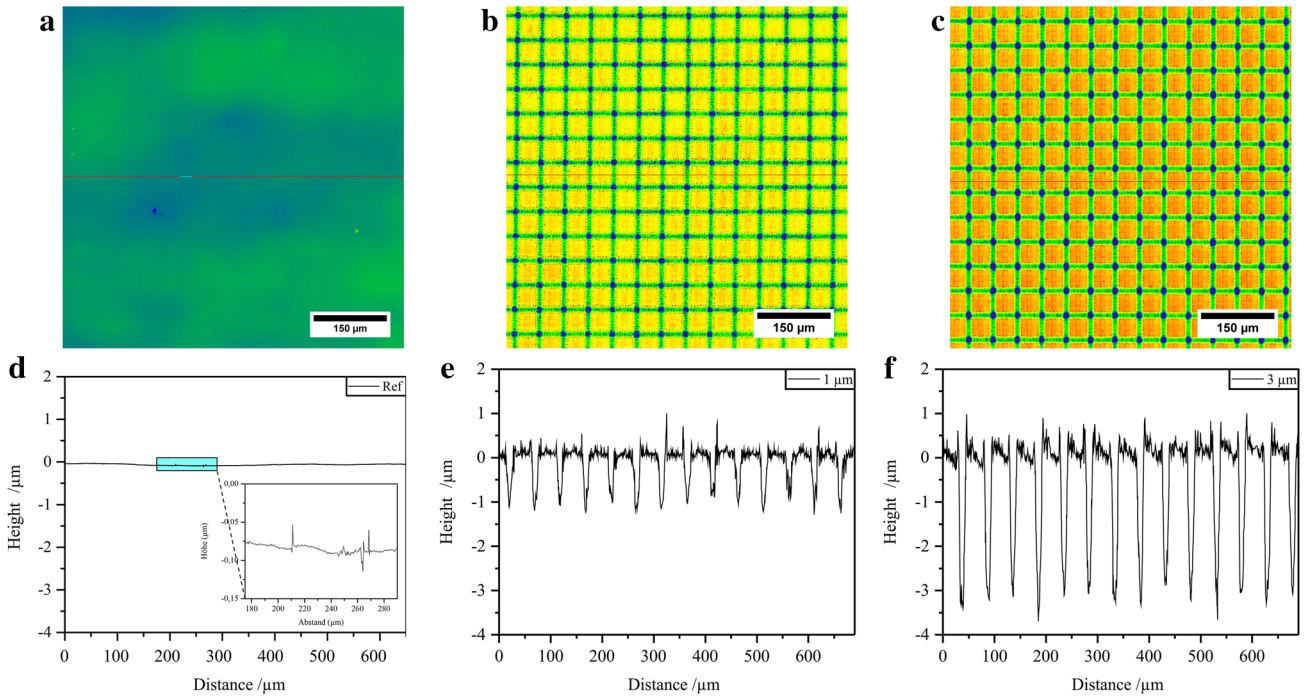

Fig. 1 Height profile color maps of **a** polished steel plate, **b** 1 µm DLW structure and **c** 3 µm DLW structure. **d–f** profile of the surfaces measured at the corresponding red lines of the color maps. (Color figure online)

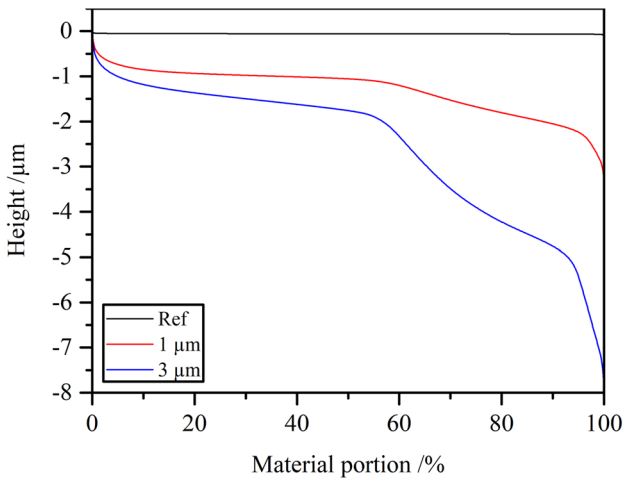

Fig. 2 Abbott-Firestone curves of the reference surface and the laser-structured surfaces with a depth of 1 and 3 µm, respectively. (Color figure online)

a material portion between 5 and 55%, the 1 µm-curve is almost in parallel to the reference curve, thus presenting a smooth surface with a high load-bearing capacity.

This is traced back to the almost unmodified large surface plateaus of 35×35 µm^2 in size. The 3 µm-curve drops twice as much in this section, which speaks for a surface with a higher roughness on the above-mentioned surface plateaus, possibly being a consequence of material re-depositioning and the generation of laser-induced periodic surface structures (LIPSS) [53]. The latter result from the interference between the incident and the already reflected laser beam. For strongly absorbing materials, like metals and semiconductors, low-spatial-frequency-LIPSS (LSFL) with periodicities in the range of the used laser wavelength and an orientation perpendicular to the polarization of the laser beam can be observed.. The next section (55–95%) is based on the generated surface depressions, which show a decrease in height of 1 µm or 3 µm, respectively. The last part of the curve (95–100%) corresponds to the intersecting points during the laser structuring process, consequently being twice as deep.

Subsequently, the surfaces were chemically characterized using Auger electron spectroscopy. For this purpose, the laser-structured surface (depth of 3 µm) and the unstructured steel reference are measured. The results can be found in Fig. 3.

In the case of the laser-structured surface, three areas are distinguished (1–3), with 1 representing the ablation area, 2 the edge of the surface depression where high profile deposits are found, and 3 the area that was not subjected to ablation. By comparing the graph of the unstructured reference with the graphs of the structured surface, it is obvious, that the concentration in oxygen is increased for the laser-structured surface. This could be explained with the ablated metal being highly reactive, and thus being oxidized during this process. Due to the re-deposition of ablated metal in area 2

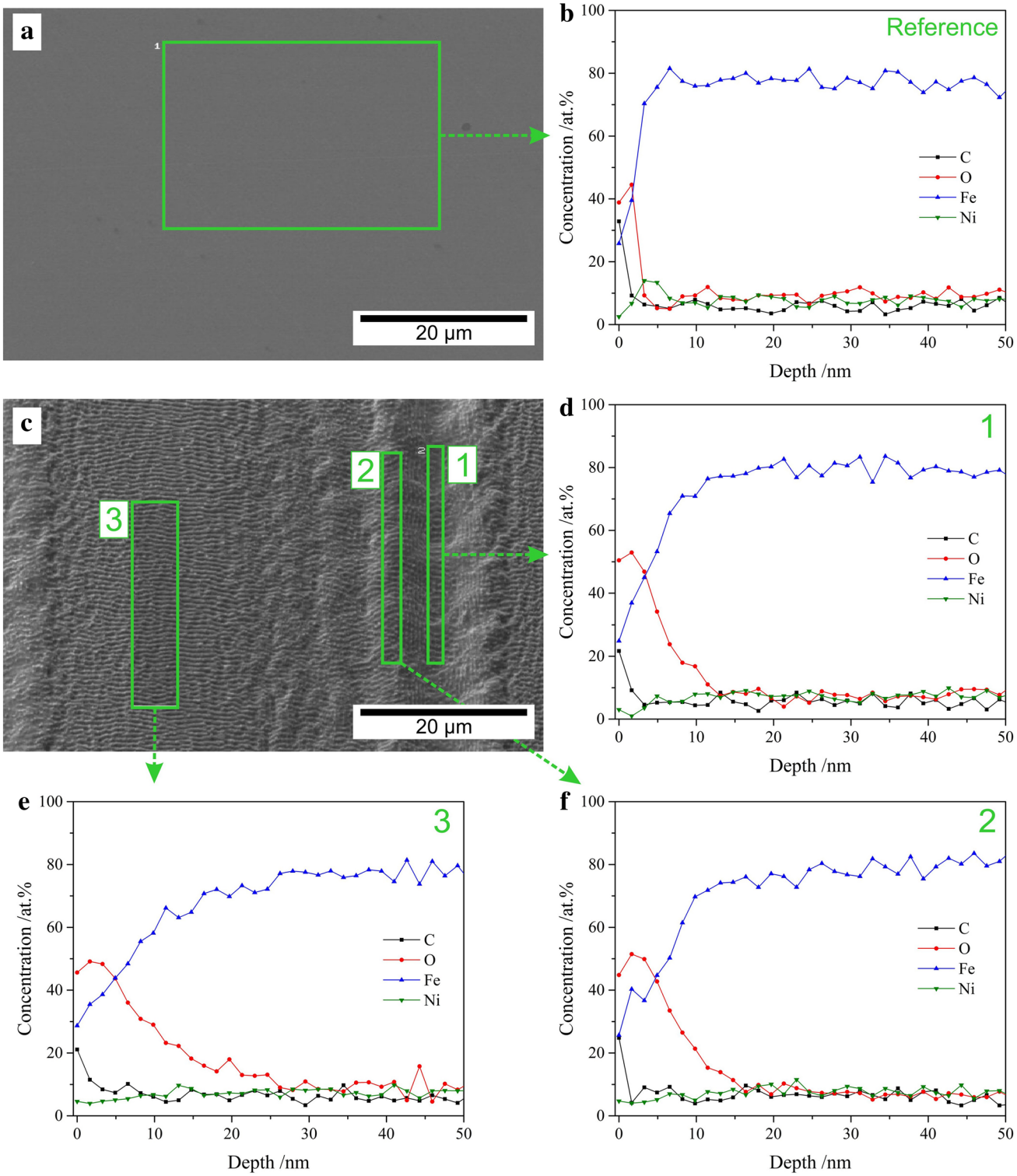

Fig. 3 SEM micrographs of **a** the unstructured steel reference and **c** the laser-structured surface with a structural depth of 3 µm. The marked regions 1–3 in c are measured by AES in (**d, e** and **f**), respectively. The corresponding AES characterization is also performed for the unstructured reference in (**b**). (Color figure online)

and 3, the areas are fully covered with metal oxides [54]. A quantitative comparison of oxidation between the different areas is not possible, since the areas provide different surface roughness. Thus, with the surfaces being measured after different sputtering times, oxides that were present between surface roughness asperities are possibly not removed and contribute to the AES signal even for higher depths. However, it can be concluded that light surface oxidation of the structured surfaces must be taken into account when discussing the tribological results. In addition, the above-mentioned LIPSS can be observed all over the sample.

Finally, the surfaces were coated with MWCNT using EPD. Figure 4 shows the obtained coated surfaces.

In all cases, CNT agglomerates are still observed on the surfaces. Furthermore, no evident uncovered areas or cracks in the coatings are identified. The SEM/FIB cross sections show a homogeneous thickness of approximately 1 µm in all cases. It is worth noting that in the 3 µm depth sample (Fig. 4f), some cavities in the coating at the topographical minimum are detected. All samples display a seamless interface between coating and substrate (insets of Fig. 4 b, d and f).

3.2 Frictional Behavior

The temporal evolution of the coefficient of friction is shown in Fig. 5. In the short-term tests (a), the COF of the uncoated samples (both, unstructured and structured) increases within the first 1000 cycles, finally reaching a steady state COF close to 0.9. This value is quite high for this tribological pair and could be related to a continuous growth of an oxide layer. Thus, the initially present higher surface oxidation of the laser-textured surfaces seems to play a minor role for the running in process of the uncoated surfaces. When observing the behavior of the coated samples, the difference in friction is quite significant. The unstructured, coated sample shows a significantly lower COF than the uncoated samples with an irregular evolution of the COF. This instability is related to the re-accommodation of solid lubricant with each rotating cycle, in which the CNTs are driven inhomogeneously towards the direct contact area. However, their lubrication capacity is still active during these cycles. Regarding the CNT-coated laser structures, both show a stable COF throughout the first 2000 cycles, with values around 0.2. Again, the stability in this case is related to how the CNTs are brought into contact during the test. This proves the reservoir-effect generated by the depressions storing and sequentially releasing lubricant.

If the focus is then placed on the long-term behavior of the surfaces, the analysis for the uncoated samples becomes inconsequential, since they have already reached their steady state at lower cycles. Hence, the long-term analysis only refers to the CNT-containing systems, which is shown in Fig. 5b.

After an initial slight drop, the Ref/CNT sample shows a continuous increase in COF until reaching steady state after approximately 45,000 cycles. It is noticeable that the COF standard deviation of this sample, which is already pronounced at the beginning, increases considerably from approx. 7000 cycles. This can be justified by the fact that individual measurements show an early or late sharp increase in COF and ultimately reach reference conditions earlier or later than the mean value. All individual measurements show this rapid increase between 7000 and almost 26,000 cycles. Furthermore, it can be observed that the curve shows several drops during the ascent, which might be correlated to fluctuations in concentration of CNT within the direct tribological contact area.

In the case of the structured and coated samples, both present an unexpected and counterintuitive development of the COF. The COF value of 3 µm/CNT surpasses that of 1 µm/CNT after about 3400 cycles. Contrary to the sample Ref/CNT, there are no leaps during the rise of the COF. The COF of the 3 µm/CNT sample continuously grows until the reference steady state COF value is reached at approx. 50,000 cycles, similar to the Ref/CNT sample. In contrast, the curve of 1 µm/CNT excels by a stable curve with a low COF and very low standard deviation. The standard deviation becomes significant only after about 40,000 cycles. Possible causes for this could be a degradation of the CNTs or their removal from tribological contact [45].

The considerably earlier increase in the COF of the sample 3 µm/CNT can be related to several causes. On one hand, the surface structures, characterized in Figs. 1 and 4, show a steeper profile of the structural flanks with increasing depth ($17 \pm 3°$ and $22 \pm 2°$ for 1 and 3 µm, respectively). As the lubrication mechanisms of the CNT coated laser structures were described to be based on compression and elastic restoration of the CNTs in the depressions in Reinert et al. [45], this effect might not be as pronounced for the 3 µm deep structures. Steeper profile flanks and also cavities within the CNT coating (see Fig. 4 f) are associated with a reduced elastic restoration effect, compared to the 1 µm deep structure thus making it more difficult to draw the CNTs from the structural cavities into tribological contact [45]. This means that the lubrication effect is lost at an early stage despite still having filled lubricant reservoirs available. Furthermore, the structures of this sample type are not completely filled to the level of the supporting surface with CNTs (see Fig. 4 e–f). During the first cycle of the Al_2O_3 counterpart, the CNTs are pressed into the cavities and thus the initial cavities are reduced. This further prevents the elastic restoration of CNTs after the alumina ball has passed. As a result, CNTs cannot further be removed from the depressions by adhesion to the ball during the following cycle of the counterpart. For

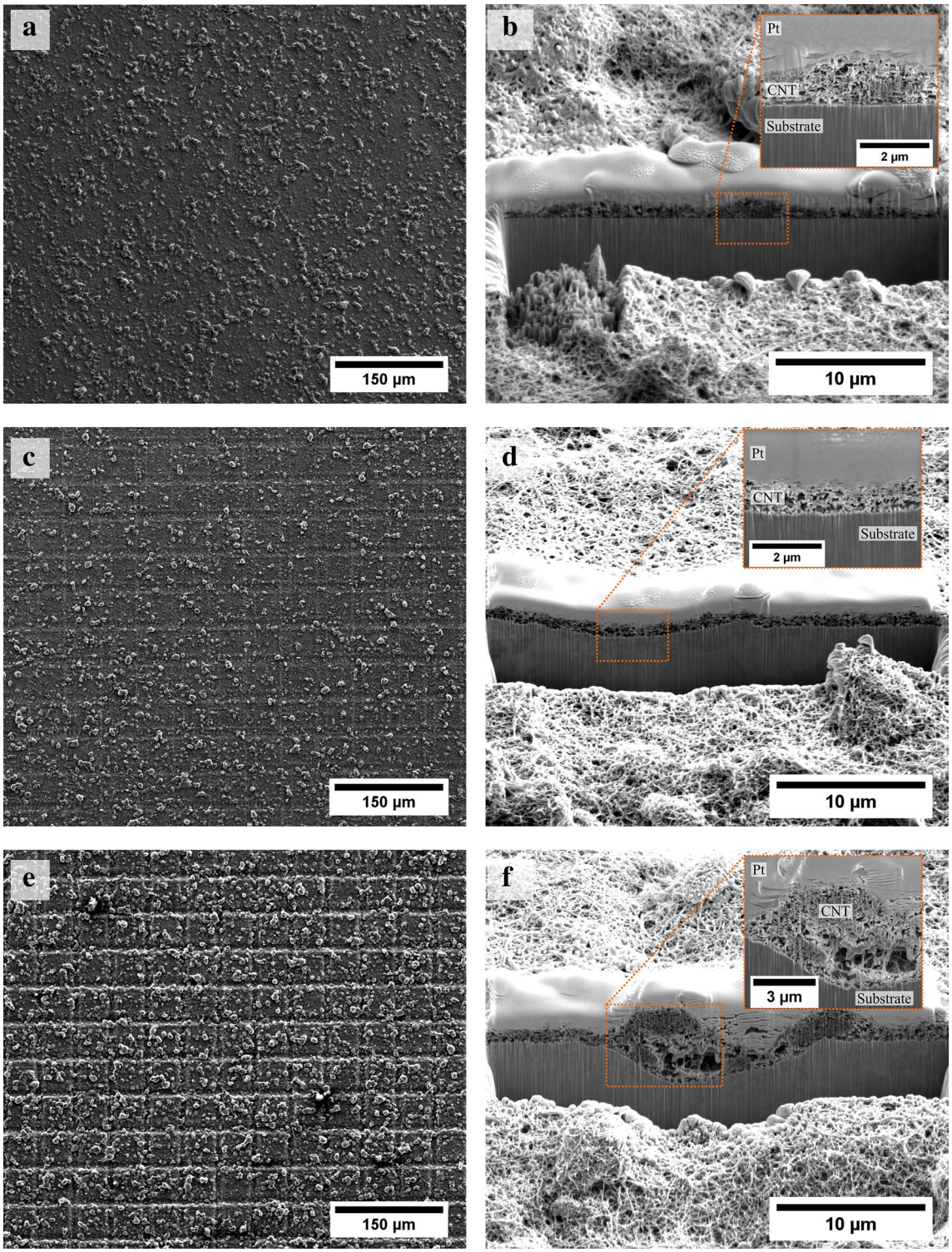

Fig. 4 Electron micrographs of the resulting EPD coatings for **a** coated reference, **c** 1 µm deep structure and **e** 3 µm deep structure. The images (**b, d** and **f**) show SEM/FIB cross sections of the corresponding coatings. The insets show a detailed view of the interfaces between the coating and the substrate for each case. (Color figure online)

this reason, the CNTs gradually disappear from the contact zone and direct contact between the substrate and counterpart occurs, causing the COF to rise and tend to the reference value. In addition, the larger number and height of oxidized material pilings at the edges of the cavities can also play a pivotal role. The high profile deposits (as observed in Fig. 1

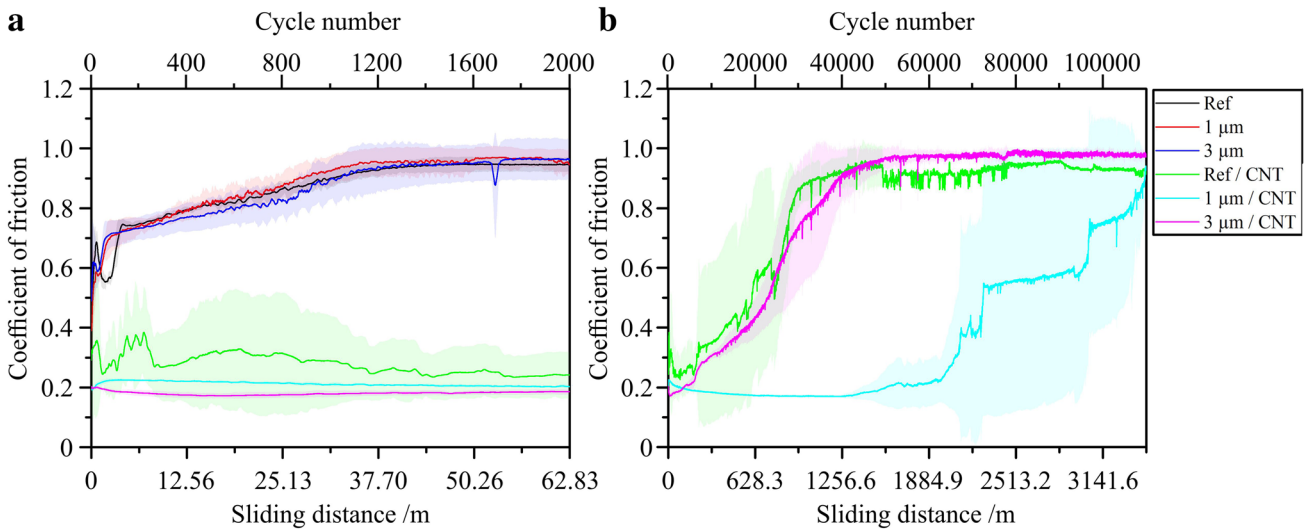

Fig. 5 **a** Short-term evolution of the coefficient of friction for the uncoated and coated samples. **b** Long-term development of the coefficient of friction for the coated samples. The shaded areas correspond to the standard deviation of the measurements. (Color figure online)

e–f) could be plastically deformed during the first passes, consequently leading to a partial hindering of a further lubricant supply. This effect could be fortified by premature abrasion of these asperities and the associated generation of oxidic wear particles, which could be stored on top of the CNTs in the depressions, hindering an efficient lubricant supply and additionally increasing the abrasive component of the tribological system.

Figure 5b further shows that the sample type 1 µm/CNT does not reach the steady state value of the reference sample (on average) until 110,000 cycles have been completed. The stepwise increments in the averaged COF curve and the large standard deviation result from the different points in time at which the tested samples experience a sudden increase from a very low COF to the reference steady state COF value. Possible causes for this observation are similar to the two other coated sample types (Ref/CNT and 3 µm/CNT), a degradation of the CNTs as well as the removal of the CNTs from the tribological contact. Due to wear, the laser-generated surface structures are completely removed after a certain time, so that there are no more lubricant reservoirs that could supply the contact with CNTs. All coated substrates show a similar lubricating effect as that reported in [45]. During tribological stress, the CNTs have large areas available on which they can roll/slide between the substrate and counterbody and thus reduce the COF before they are pressed into the nearest structural depression. When compared to the uncoated reference state, a significant COF reduction for the Ref/CNT is observed (factor of 4.5). With the degree of frictional reduction for the structured samples being even more pronounced (factor of 6), the lubrication lifetime of the 1 µm/CNT sample is prolonged (factor of 9).

3.3 Wear Track and Tribo-Chemical Analysis

In order to investigate the underlying lubrication mechanism, the structural state of the CNTs has to be examined. For this purpose, Raman spectroscopy analysis of the CNTs at both, the inside and outside of the wear tracks, is performed and compared to the spectra which were obtained by measuring pure CNT powder before the EPD coating process (black curve in the following figures). Despite the structural integrity analysis of the particles, also a tribo-chemical characterization is performed, focusing on the presence of oxides in the wear tracks. Raman analysis of the wear tracks was performed for all coated samples after 18,000 cycles and after reaching the reference steady state friction coefficient (end of lubrication lifetime). In this way, failure mechanisms can be accurately evaluated.

3.3.1 Ref/CNT Sample

For the sample type *Ref/CNT after 18,000 cycles*, the typical Raman bands of CNTs are observed in all measurement points (Fig. 6a). The measurements of the pure CNT powder (Fig. 6a, Ref spectrum) confirm the typical literature values for the D, G and G' bands [55, 56]. The D-peak of the studied MWCNTs is placed at a wavenumber of 1350.4 cm^{-1}, the G-peak at 1582.1 cm^{-1}, and the G'-peak at 2696.1 cm^{-1}. Furthermore, two additional peaks with low intensities can be identified immediately before and after the G' peak. The peak at 2450 cm^{-1} corresponds to a non-dispersive phonon mode [57] and that at a wavenumber of approx. 2900 cm^{-1} is due to a harmonic of the LO mode [58]. However, since these two resonances do not provide quantifiable information

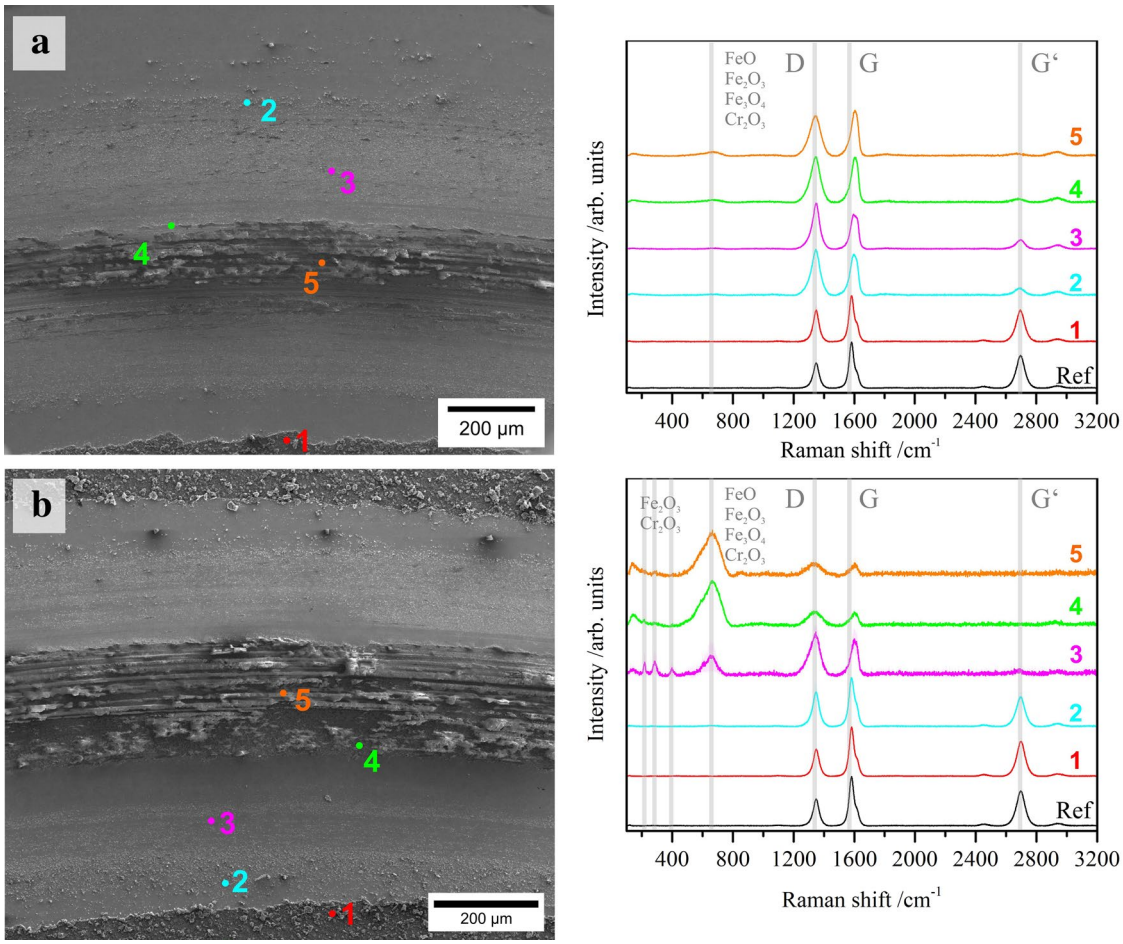

Fig. 6 Electron micrograph of a section of the wear track and Raman spectra acquired at specific sites after **a** 18,000 cycles and **b** after reaching the reference steady state friction coefficient (24,400 cycles). (Color figure online)

on the structural condition of the CNTs, they are neglected in the following for the interpretation of the tribochemistry. In contrast to that, the intensity ratio of the D- and the G-band (I_D/I_G) can be correlated to the defect index and thus, the crystalline domain size [56].

Interestingly, even at the center of the wear track (position of maximum contact pressure) CNTs with moderate I_D/I_G values are detected and only weak oxide peaks are recorded at 660 cm^{-1} (convolution of FeO, Fe_3O_4 and Fe_2O_3 vibrational modes) [59–61]. However, from position 2 inwards, the G-band is already shifted noticeably to higher wavenumbers (approx. 1600 cm^{-1}), as can be seen in Table 1. The aforementioned shift of the G-band was part of past investigations by Ferrari and Robertson [49], which subdivide the structural changes of graphitic materials into a phenomenological three-stage model. Depending on the position of the G-peak (X_{CG}) and based on the defect index (I_D/I_G), the model describes the transition

Table 1 Structural assessment of the CNTs at different stages of the tribological test

After 18,000 cycles				After reaching steady state reference COF			
Sample		I_D/I_G	X_{CG}	Sample		I_D/I_G	X_{CG}
	Ref	0.55	1582.1		Ref	0.55	1582.1
Ref/CNT	1	0.70	1583.1	Ref/CNT (24.4 k cycles)	1	0.56	1582.1
	2	1.12	1599.4		2	0.71	1582.1
	3	1.32	1594.0		3	1.18	1600.6
	4	1.02	1603.8		4	1.06	1598.4
	5	0.89	1603.8		5	1.03	1600.6

from a graphitic structure via nanocrystalline graphite to disordered carbon (mainly sp^3-hybridized). Since CNTs at their initial state are basically a highly crystalline graphitic modification, this model is suitable to track the structural integrity of the MWCNTs.

With the G-band upshifting and the increased defect index of over 1 (CNT reference: 0.55), a structural transition of the CNTs towards nanocrystalline graphite is established. The sharp increase in COF from 14,700 cycles onwards (0.71 after 18,000 cycles) is likely due to the failure of lubrication by the CNTs. With lubrication failing but nanocrystalline graphite being still present in the wear track, the lubrication mechanism of CNT seems not to be based on a pure graphite type lubrication - the shearing-off of individual graphene layers - but can be attributed also to an efficient separation of the surfaces and complex motions (sliding/rolling) of the CNTs. The degradation of the CNTs and thus lubrication failure is strongly related to the contact pressure gradient towards the center of the track. Consequently, a tribologically-induced oxide layer is formed with Raman peaks being observed at 225 cm^{-1} (α-Fe_2O_3 band), at 270 cm^{-1} (convolution of α-Fe_2O_3 and Cr_2O_3), at 380 cm^{-1} ((Fe, Cr)O_3 band) and finally at 660 cm^{-1} [59–61]. The oxide formation results from local heating derived from high contact pressures. This layer can be further disrupted, forming oxidic abrasive third bodies.

Figure 6b shows a wear track overview and the Raman spectra of the characteristic points in and around the wear track of the sample Ref/CNT after reaching steady state reference COF at 24,400 cycles. The general statement of this evaluation is similar to the analysis of the wear track after 18 000 cycles. However, the Raman spectra acquired in the interior region (measurement points 3–5) present even more significant changes. First, the formation of oxides is increasing towards the center of the wear track. In agreement with this observation, a steady decrease in the intensity of the CNT peaks and the increasing values of the defect index (I_D/I_G) show a further cumulative degradation of the CNTs towards the center of the wear track compared to the situation after 18,000 cycles. Moreover, the G'-band vanishes from the outer edge of the central wear track (position 4). In addition, a noticeable shift in the G-peak position up to a wavenumber of approx. 1600 cm^{-1} can be observed (Table 1).

It is thus evident that the CNTs are no longer (in sufficient quantity) in tribological contact, which means that they can no longer fulfill their function as spacers between the substrate and the counterpart. Thus, direct tribological contact of the two surfaces with a subsequent oxide formation occurs and lubrication vanishes.

3.3.2 1 µm/CNT Sample

The evaluation of the wear track of the *1 µm/CNT* sample after *18,000 cycles* is illustrated in Fig. 7a.

Contrary to what would be expected after a significant amount of cycles, no oxides can be detected in the entirety of the wear track. Even in the center of the track, CNTs can be detected in both, the topography maximum (2) and minimum (3, 4) of the laser structures. Accordingly and as the surfaces were already slightly oxidized in their initial state due to laser structuring, the acquisition depth of the Raman characterization can also be listed as a possible cause for the absence of oxidic resonances. However, a closer examination of the characteristic CNT peak positions and their intensity ratios (as listed in Table 2) in the spectra from the center of the wear track (2–4) reveals a structural degradation of the CNTs - similar to that on the *Ref/CNT sample*. The defect index has similarly high values (≥ 1) as *Ref/CNT*. The G-band upshift (approximately 1600 cm^{-1}) also indicates a structural state similar to nanocrystalline graphite.

Yet, *after 18,000 cycles*, the friction curves of this sample show a stable low COF (0.14) in the equilibrium state. Accordingly, the structural integrity of the CNTs seems to play only a minor role in maintaining the lubricating effect. Rather, the presence of a sufficient quantity of MWCNT in tribological contact and its continuous transport from the laser-induced lubricant reservoirs to the contact seems to be the dominant effect. In addition, the lubrication mechanism in the area of damaged CNTs can be based on their rolling/sliding ability on the one hand, but also on the lubricating behavior of graphite on the other hand.

The corresponding Raman evaluation of the sample type *1 µm/CNT after reaching steady state reference COF (110,000 cycles)* is shown in Fig. 7b. As already discussed before, only small amounts of oxidic substances are detected in the outer area of the wear track (measurement points 1 and 2). Based on the intensity ratios listed in Table 2, it is clear that the defect density of the MWCNTs in these ranges is higher than in the CNT initial state. In addition, the G-peak positions of the CNTs at both, the topography maxima and minima are again upshifted to 1599.5 cm^{-1} and 1595.1 cm^{-1}, respectively, indicating a structural degradation [49]. However, it should be noted that the detected peaks result from an averaging of all radiated CNTs. This means that in the minima, completely unaffected CNTs can still be stored, which to the moment have not had to bear any mechanical load. In the center of the wear track (Fig. 7b point 3), on the other hand, the intensity of the oxide peak at 670 cm^{-1} increases and that of the CNT peaks decrease significantly. The G'-band is no longer detected.

As already mentioned, the absence of the protective CNT layer leads to a tribo-chemical oxidation and the generation of third bodies, which results in the observed steep rise in

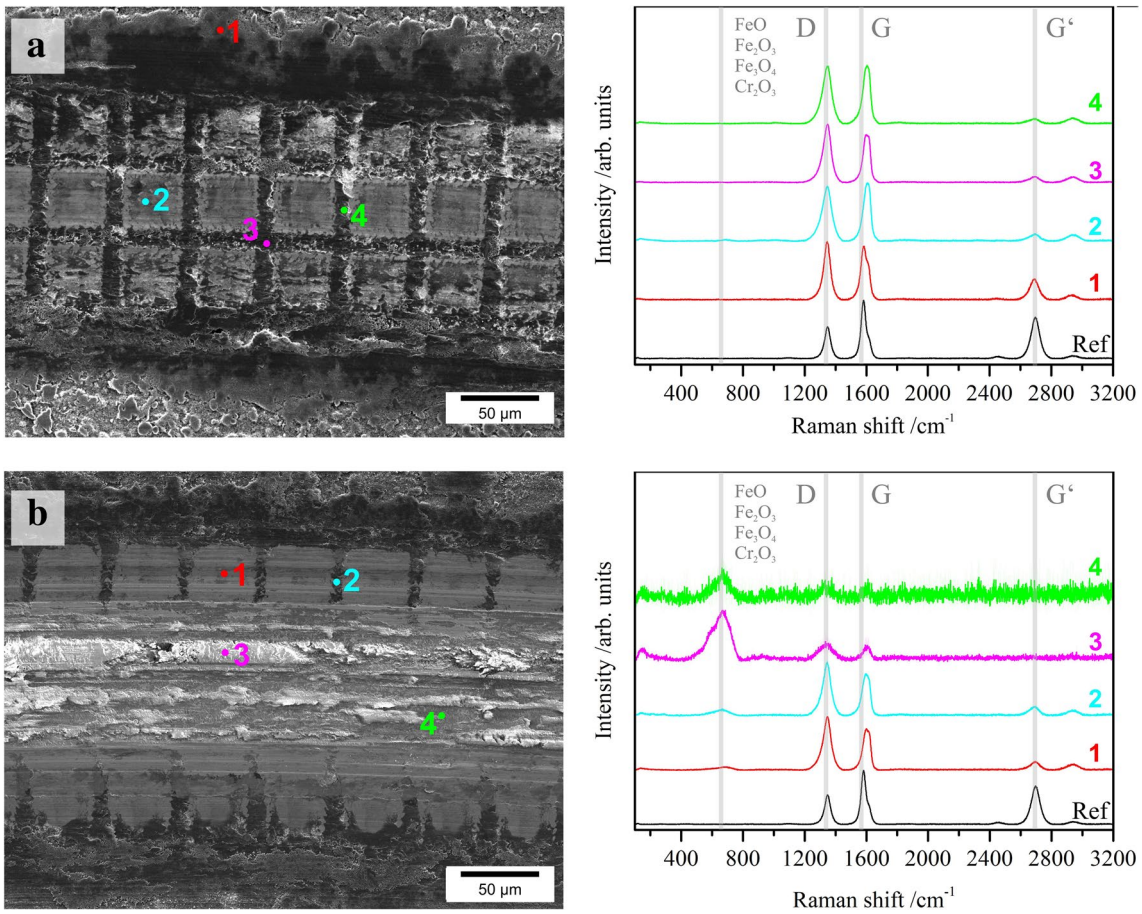

Fig. 7 1 µm/CNT sample after **a** 18,000 cycles and **b** after reaching the reference steady state friction coefficient (110,000 cycles). (Color figure online)

Table 2 Structural assessment of the CNTs at different stages of the tribological test

After 18,000 cycles				After reaching steady state reference COF			
Sample		I_D/I_G	X_{CG}	Sample		I_D/I_G	X_{CG}
	Ref	0.55	1582.1		Ref	0.55	1582.1
1 µm /CNT	1	1.08	1583.1	1 µm /CNT (110 k cycles)	1	1.30	1599.5
	2	0.93	1605.9		2	1.29	1595.1
	3	1.23	1600.5		3	1.23	1591.9
	4	0.99	1603.8		4	1.04	1600.8

COF. At the bright spots in the center of the track (4), the low intensity values are overlaid by a noisy signal typical for pure metallic substances. The presence of oxides and the characteristic CNT bands at these sites is due to the comparatively large laser spot size of the Raman microscope (approximately 5 µm).

3.3.3 3 µm/CNT Sample

For the sample *3 µm/CNT after 18,000 cycles*, the evaluated Raman spectra evidences CNTs everywhere in the wear track area (Fig. 8a), whereby a low intensity oxide peak can be detected in the region of the laser-induced structure minimum (4).

This is correlated with initially present surface oxidation due to the laser process and wear particles generated by previous abrasion of the initial, oxidized material pilings. These particles can be transported by the sphere into the minima positions of the surface structure, as discussed in [45]. Furthermore, the Raman spectrum at position 2 indicates that only small signals of the CNT bands are still acquired on the substrate within the wear track (Fig. 8a). In combination

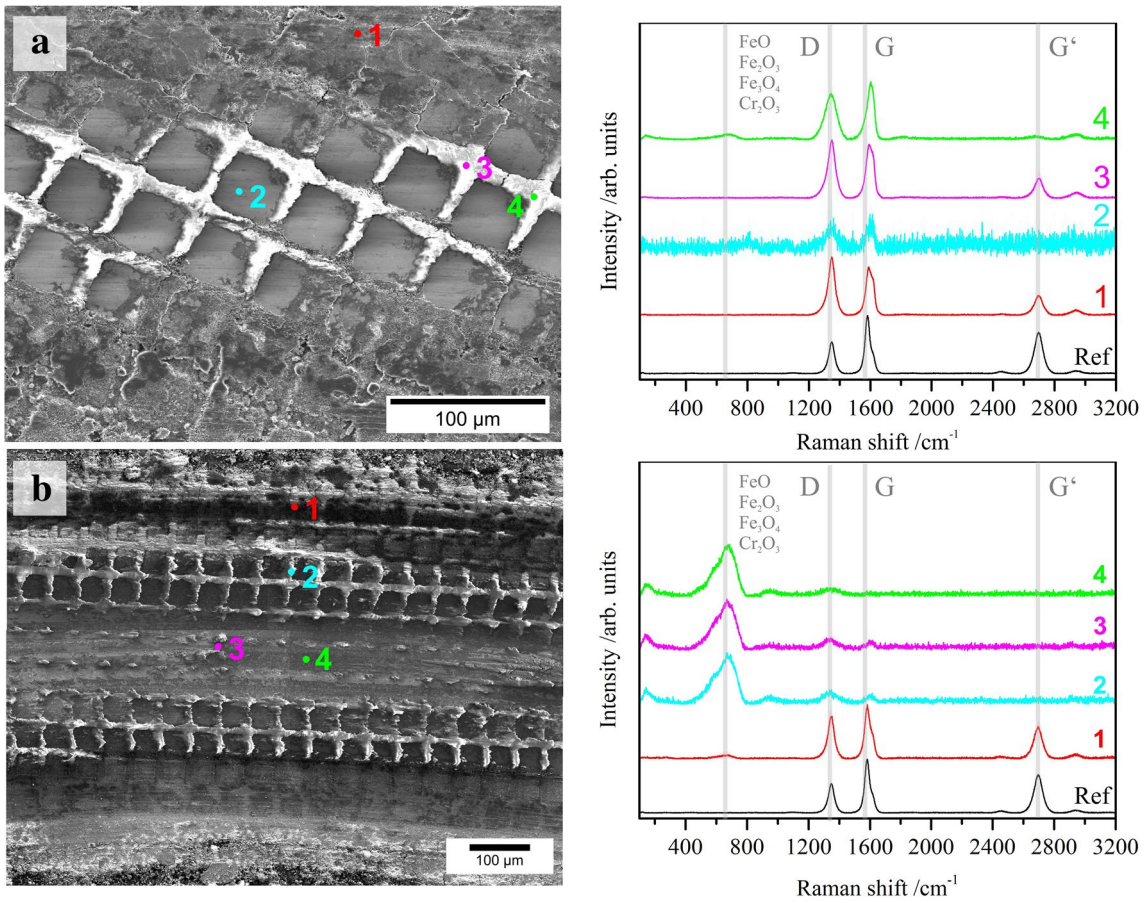

Fig. 8 3 µm/CNT sample after **a** 18,000 cycles and **b** after reaching the reference steady state friction coefficient (57,000 cycles). (Color figure online)

with the observed signal noise, it can be confirmed that in this sample type there is direct contact between the surfaces of the contact partners after only 18,000 cycles, which leads to an increase in friction and wear. The increase in COF (0.43), which has already occurred, confirms this observation. As with the other two coated samples, damage to the CNTs is observed to have already occurred on the basis of the values listed in Table 3.

The lack of lubricant in contact and the inadequate continuous feed into contact are the main factors affecting the lubrication process. Although small amounts of CNTs can be brought into contact, this is not enough to effectively separate the contacting surfaces from each other and hence, contribute to a continuous reduction of friction.

The Raman spectra of the characteristic areas of the wear track **after reaching the steady state COF of the reference at 57,000 cycles** are shown in Fig. 8b. Barely modified CNTs which were pulled out of the contact are observed only in the outer area (1) with only a small oxide peak at 670 cm^{-1} (see also Table 3). In contrast to the sample **1 µm/CNT**, even the laser-induced minima in the outer area of the track show a pronounced oxide peak and a G-peak shifted

Table 3 Structural assessment of the CNTs at different stages of the tribological test

After 18,000 cycles				After reaching steady state reference COF			
Sample		I_D/I_G	X_{CG}	Sample		I_D/I_G	X_{CG}
	Ref	0.55	1582.1		Ref	0.55	1582.1
3 µm /CNT	1	1.22	1590.7	3 µm /CNT (57 k cycles)	1	0.79	1582.1
	2	0.91	1613.5		2	1.31	1604.2
	3	1.08	1592.9		3	1.20	1606.5
	4	0.80	1602.7		4	–	–

to 1604.2 cm^{-1}. According to [49], such a wide upshifting of the G-peak beyond a wavenumber of 1600 cm^{-1} is not expected. This can be justified by the spectral resolution of the Raman microscope used (1.2 cm^{-1}) in combination with inaccuracies with the profile (Lorentz) fitting. Along with an increased defect density of 1.31 and the absence of the G' peak, it can be assumed that the CNTs are indeed degraded and again, transitioned into nanocrystalline graphite. At the same time, the largest shift of the G-peak (1606.5 cm^{-1}) can be seen there, whereas in the measuring range of point 4, this is no longer observed at all.

These findings confirm the assumptions made that there are no more noticeable amounts of CNTs in the entire wear track and that they disappear as the test evolves.

4 Conclusions

In the present study, a systematic evaluation of the influence of surface structure design on the solid lubrication effect of multi-walled carbon nanotubes (MWCNT) coated steel surfaces is provided. An efficient lubrication is achieved for all MWCNT coated surfaces with a maximum sixfold frictional reduction compared to the steel reference and friction coefficients as low as 0.14. In case of the cross-like surface pattern with a structural depth of 1 µm, a nine-fold extension of the lubrication lifetime compared to the MWCNT coated, unstructured sample is observed. However, and in contrast to what would be expected, it is shown that deeper structures (3 µm structural depth) with larger lubricant storage volume do not lead to an extended lubrication lifetime and behave almost equally to the coated unstructured surfaces. This can be attributed, among other things, to the formation of high profile deposits at the edges of the surface depressions due to displaced molten material and material re-depositioning as well as a higher slope steepness of the structures, which prevent efficient lubricant supply into the contact. The lubrication of MWCNT coatings is found to be based on the high aspect ratio of MWCNT allowing them to be dragged into the tribological contact as well as an elastic restoration of the coating after compaction during the tribological contact. The lubrication mechanism of the CNT is a mixture between graphite lubrication and their ability to perform complex motions and act as separating layer between the contacting surfaces. This study highlights the importance of a carefully selected surface design in order to achieve beneficial effects with regard to MWCNTs as solid lubricant coatings.

Acknowledgements The present work is supported by funding from the Deutsche Forschungsgemeinschaft (DFG, project: MU 959/38-1 and SU 911/1-1). The authors wish to acknowledge the EFRE Funds of the European Commission for support of activities within the AME-Lab project. This work was supported by the CREATe-Network Project, Horizon 2020 of the European Commission (RISE Project No. 644013). We thank Prof. Volker Presser (INM, Saarbrücken) for providing access to the Raman spectrometer and SFB 926 "Microscale Morphology of Component Surfaces" CRC 926 for measurements by Auger electron spectroscopy.

References

1. Etsion, I.: State of the art in laser surface texturing. J. Tribol. **127**, 248 (2005). https://doi.org/10.1115/1.1828070
2. Gachot, C., Rosenkranz, A., Reinert, L., Ramos-Moore, E., Souza, N., Müser, M.H., et al.: Dry friction between laser-patterned surfaces: Role of alignment, structural wavelength and surface chemistry. Tribol. Lett. **49**, 193–202 (2013). https://doi.org/10.1007/s11249-012-0057-y
3. Rosenkranz, A., Reinert, L., Gachot, C., Mücklich, F.: Alignment and wear debris effects between laser-patterned steel surfaces under dry sliding conditions. Wear. **318**, 49–61 (2014). https://doi.org/10.1016/j.wear.2014.06.016
4. Szurdak, A., Rosenkranz, A., Gachot, C., Hirt, G., Mücklich, F.: Manufacturing and tribological investigation of hot micro-coined lubrication pockets. Key Eng. Mater. **611–612**, 417–424 (2014). https://doi.org/10.4028/www.scientific.net/KEM.611-612.417
5. Koszela, W., Pawlus, P., Galda, L.: The effect of oil pockets size and distribution on wear in lubricated sliding. Wear. **263**, 1585–1592 (2007). https://doi.org/10.1016/j.wear.2007.01.108
6. Pettersson, U., Jacobson, S.: Influence of surface texture on boundary lubricated sliding contacts. Tribol. Int. **36**, 857–864 (2003). https://doi.org/10.1016/S0301-679X(03)00104-X
7. Pawlus, P.: Effects of honed cylinder surface topography on the wear of piston-piston ring-cylinder assemblies under artificially increased dustiness conditions. Tribol. Int. **26**, 49–55 (1993). https://doi.org/10.1016/0301-679X(93)90038-3
8. Lasagni, A., Roch, T., Bieda, M., Benke, D., Beyer, E.: High speed surface functionalization using direct laser interference patterning, towards 1 m 2 /min fabrication speed with sub-µm resolution. Proc. SPIE. **8968**, 89680A (2014). https://doi.org/10.1117/12.2041215
9. Mücklich, F., Lasagni, A., Daniel, C.: Laser Interference Metallurgy – using interference as a tool for micro/nano structuring. Zeitschrift. Für. Met. **97**, 1337–1344 (2006)
10. Rosenkranz, A., Heib, T., Gachot, C., Mücklich, F.: Oil film lifetime and wear particle analysis of laser-patterned stainless steel surfaces. Wear. **334–335**, 1–12 (2015). https://doi.org/10.1016/j.wear.2015.04.006
11. Rosenkranz, A., Krupp, F., Reinert, L., Mücklich, F., Sauer, B.: Tribological performance of laser-patterned chain links—Influence of pattern geometry and periodicity. Wear. **370–371**, 51–58 (2017). https://doi.org/10.1016/j.wear.2016.11.006
12. Grützmacher, P.G., Rosenkranz, A., Gachot, C.: How to guide lubricants—tailored laser surface patterns on stainless steel. Appl. Surf. Sci. **370**, 59–66 (2016). https://doi.org/10.1016/j.apsusc.2016.02.115
13. Rapoport, L., Moshkovich, A., Perfilyev, V., Lapsker, I., Halperin, G., Itovich, Y., et al.: Friction and wear of MoS2 films on laser textured steel surfaces. Surf. Coatings Technol. **202**, 3332–3340 (2008)
14. Cho, M.H., Ju, J., Kim, S.J., Jang, H.: Tribological properties of solid lubricants (graphite, Sb2S3, MoS2) for automotive brake friction materials. Wear. **260**, 855–860 (2006). https://doi.org/10.1016/j.wear.2005.04.003
15. Scharf, T.W., Prasad, S.V.: Solid lubricants: A review. J. Mater. Sci. **48**, 511–531 (2013). https://doi.org/10.1007/s10853-012-7038-2

16. Zhai, W., Srikanth, N., Kong, L.B., Zhou, K.: Carbon nanomaterials in tribology. Carbon N Y. **119**, 150–171 (2017). https://doi.org/10.1016/j.carbon.2017.04.027
17. Chen, W., Tu, J., Wang, L., Gan, H., Xu, Z.: Tribological application of carbon nanotubes in a metal-based composite coating and composites. Carbon N Y **41**, 215–222 (2003)
18. Kim, K.T., Cha, S., Hong, S.H.: Hardness and wear resistance of carbon nanotube reinforced Cu matrix nanocomposites. Mater. Sci. Eng. A. **449–451**, 46–50 (2007). https://doi.org/10.1016/j.msea.2006.02.310
19. Scharf, T., Neira, A., Hwang, J.Y., Tiley, J., Banerjee, R.: Self-lubricating carbon nanotube reinforced nickel matrix composites. J. Appl. Phys. **106**, 13508 (2009). https://doi.org/10.1063/1.3158360
20. Tan, J., Yu, T., Xu, B., Yao, Q.: Microstructure and wear resistance of nickel–carbon nanotube composite coating from brush plating technique. Tribol. Lett. **21**, 107–111 (2006). https://doi.org/10.1007/s11249-006-9025-8
21. Suárez, S., Rosenkranz, A., Gachot, C., Mücklich, F.: Enhanced tribological properties of MWCNT/Ni bulk composites - Influence of processing on friction and wear behaviour. Carbon N Y. **66**, 164–171 (2014). https://doi.org/10.1016/j.carbon.2013.08.054
22. Reinert, L., Suárez, S., Rosenkranz, A.: Tribo-Mechanisms of carbon nanotubes: friction and wear behavior of CNT-reinforced nickel matrix composites and cnt-coated bulk nickel. Lubricants. **4**, 1–15 (2016). https://doi.org/10.3390/lubricants4020011
23. Miyoshi, K., Street, K.W., Vander Wal, R.L., Andrews, R., Sayir, A.: Solid lubrication by multiwalled carbon nanotubes in air and in vacuum. Tribol. Lett. **19**, 191–201 (2005). https://doi.org/10.1007/s11249-005-6146-4
24. Hirata, A., Yoshioka, N.: Sliding friction properties of carbon nanotube coatings deposited by microwave plasma chemical vapor deposition. Tribol. Int. **37**, 893–898 (2004)
25. Hu, J.J., Jo, S.H., Ren, Z.F., Voevodin, A.A., Zabinski, J.S.: Tribological behavior and graphitization of carbon nanotubes grown on 440C stainless steel. Tribol. Lett. **19**, 119–125 (2005). https://doi.org/10.1007/s11249-005-5091-6
26. Dickrell, P.L., Pal, S.K., Bourne, G.R., Muratore, C., Voevodin, A.A., Ajayan, P.M., et al.: Tunable friction behavior of oriented carbon nanotube films. Tribol. Lett. **24**, 85–90 (2006). https://doi.org/10.1007/s11249-006-9162-0
27. Reinert, L., Schütz, S., Suárez, S., Mücklich, F.: Influence of surface roughness on the lubrication effect of carbon nanoparticle-coated steel surfaces. Tribol. Lett. **66**, 45 (2018). https://doi.org/10.1007/s11249-018-1001-6
28. Chen, C.S., Chen, X.H., Xu, L.S., Yang, Z., Li, W.H.: Modification of multi-walled carbon nanotubes with fatty acid and their tribological properties as lubricant additive. Carbon N Y. **43**, 1660–1666 (2005). https://doi.org/10.1016/j.carbon.2005.01.044
29. Peng, Y., Hu, Y., Wang, H.: Tribological behaviors of surfactant-functionalized carbon nanotubes as lubricant additive in water. Tribol. Lett. **25**, 247–253 (2007). https://doi.org/10.1007/s11249-006-9176-7
30. Lu, H.F., Fei, B., Xin, J.H., Wang, R.H., Li, L., Guan, W.C.: Synthesis and lubricating performance of a carbon nanotube seeded miniemulsion. Carbon N Y. **45**, 936–942 (2007). https://doi.org/10.1016/j.carbon.2007.01.001
31. Kristiansen, K., Zeng, H., Wang, P., Israelachvili, J.N.: Microtribology of aqueous carbon nanotube dispersions. Adv. Funct. Mater. **21**, 4555–4564 (2011). https://doi.org/10.1002/adfm.201101478
32. Falvo, M.R., Taylor, R.M., Helser, A., Chi, V., Brooks, F.P., Washburn, S., et al.: Nanometre-scale rolling and sliding of carbon nanotubes. Nature. **397**, 236–238 (1999). https://doi.org/10.1038/16662
33. Chen, X.H., Chen, C.S., Xiao, H.N., Liu, H.B., Zhou, L.P., Li, S.L., et al.: Dry friction and wear characteristics of nickel/carbon nanotube electroless composite deposits. Tribol. Int. **39**, 22–28 (2006). https://doi.org/10.1016/j.triboint.2004.11.008
34. Dickrell, P.L., Sinnott, S.B., Hahn, D.W., Raravikar, N.R., Schadler, L.S., Ajayan, P.M., et al.: Frictional anisotropy of oriented carbon nanotube surfaces. Tribol. Lett **18**, 59–62 (2005)
35. Majumder, M., Rendall, C., Li, M., Behabtu, N., Eukel, J.A., Hauge, R.H., et al.: Insights into the physics of spray coating of SWNT films. Chem. Eng. Sci. **65**, 2000–2008 (2010). https://doi.org/10.1016/j.ces.2009.11.042
36. Mirri, F., Ma, A.W.K., Hsu, T.T., Behabtu, N., Eichmann, S.L., Young, C.C., et al.: High-performance carbon nanotube transparent conductive films by scalable dip coating. ACS Nano. **6**, 9737–9744 (2012). https://doi.org/10.1021/nn303201g
37. Bardecker, J.A., Afzali, A., Tulevski, G.S., Graham, T., Hannon, J.B., Jen, A.K.Y.: Directed assembly of single-walled carbon nanotubes via drop-casting onto a UV-patterned photosensitive monolayer. J. Am. Chem. Soc. **130**, 7226–7227 (2008). https://doi.org/10.1021/ja802407f
38. De Nicola, F., Castrucci, P., Scarselli, M., Nanni, F., Cacciotti, I., De Crescenzi, M.: Super-hydrophobic multi-walled carbon nanotube coatings for stainless steel. Nanotechnology. **26**, 145701 (2015). https://doi.org/10.1088/0957-4484/26/14/145701
39. Boccaccini, A.R., Cho, J., Roether, J.A., Thomas, B.J.C., Jane Minay, E., Shaffer, M.S.P.: Electrophoretic deposition of carbon nanotubes. Carbon N Y. **44**, 3149–3160 (2006). https://doi.org/10.1016/j.carbon.2006.06.021
40. Thomas, B.J.C., Boccaccini, A.R., Shaffer, M.S.P.: Multi-walled carbon nanotube coatings using electrophoretic deposition (EPD). J. Am. Ceram. Soc. **88**, 980–982 (2005)
41. Cho, J., Konopka, K., Rozniatowski, K., Garcia-Lecina, E., Shaffer, M.S.P., Boccaccini, A.R.: Characterisation of carbon nanotube films deposited by electrophoretic deposition. Carbon N Y. **47**, 58–67 (2009). https://doi.org/10.1016/j.carbon.2008.08.028
42. Van der Biest, O.O., Vandeperre, L.J.: Electrophoretic deposition of materials. Annu. Rev. Mater. Sci. **29**, 327–352 (1999). https://doi.org/10.1146/annurev.matsci.29.1.327
43. Sarkar, P., Nicholson, P.S.: Electrophoretic deposition (EPD): Mechanisms, kinetics, and application to ceramics. J. Am. Ceram. Soc. **79**, 1987–2002 (1996). https://doi.org/10.1111/j.1151-2916.1996.tb08929.x
44. Boccaccini, A.R., Zhitomirsky, I.: Application of electrophoretic and electrolytic deposition techniques in ceramics processing. Curr. Opin. Solid State Mater. Sci. **6**, 251–260 (2002)
45. Reinert, L., Lasserre, F., Gachot, C., Grützmacher, P., MacLucas, T., Souza, N., et al.: Long-lasting solid lubrication by CNT-coated patterned surfaces. Sci. Rep. **7**, 42873 (2017). https://doi.org/10.1038/srep42873
46. Lasagni, A.: Advanced design of periodical structures by laser interference metallurgy in the micro / nano scale on macroscopic areas. Saarland University, Saarbrücken (2006)
47. Lasagni, A., D'Alessandria, M., Giovanelli, R., Mücklich, F.: Advanced design of periodical architectures in bulk metals by means of Laser Interference Metallurgy. Appl Surf Sci. **254**, 930–936 (2007). https://doi.org/10.1016/j.apsusc.2007.08.010
48. Leitz, K.-H., Redlingshöfer, B., Reg, Y., Otto, A., Schmidt, M.: Metal Ablation with Short and Ultrashort Laser Pulses. Phys Procedia. **12**, 230–238 (2011). https://doi.org/10.1016/j.phpro.2011.03.128
49. Ferrari, A., Robertson, J.: Interpretation of Raman spectra of disordered and amorphous carbon. Phys. Rev. B. **61**, 14095–14107 (2000). https://doi.org/10.1103/PhysRevB.61.14095
50. Thomas, B.J.C., Shaffer, M.S.P., Freeman, S., Koopman, M., Chawla, K.K., Boccaccini, A.R.: Electrophoretic Deposition of Carbon Nanotubes on Metallic Surfaces. Key Eng. Mater. **314**,

141–146 (2006). https://doi.org/10.4028/www.scientific.net/KEM.314.141
51. Le Harzic, R., Breitling, D., Weikert, M., Sommer, S., Föhl, C., Dausinger, F., et al.: Ablation comparison with low and high energy densities for Cu and Al with ultra-short laser pulses. Appl Phys A. **80**, 1589–1593 (2005). https://doi.org/10.1007/s00339-005-3206-4
52. Johnson, K.L.: Contact Mechanics, 1st edn. Cambridge University Press, New York (1985)
53. Bonse, J., Krüger, J., Höhm, S., Rosenfeld, A.: Femtosecond laser-induced periodic surface structures. J Laser Appl. **24**, 42006 (2012). https://doi.org/10.2351/1.4712658
54. Raillard, B., Gouton, L., Ramos-Moore, E., Grandthyll, S., Müller, F., Mücklich, F.: Ablation effects of femtosecond laser functionalization on steel surfaces. Surf Coatings Technol. **207**, 102–109 (2012). https://doi.org/10.1016/j.surfcoat.2012.06.023
55. Lehman, J.H., Terrones, M., Mansfield, E., Hurst, K.E., Meunier, V.: Evaluating the characteristics of multiwall carbon nanotubes. Carbon N Y. **49**, 2581–2602 (2011). https://doi.org/10.1016/j.carbon.2011.03.028
56. DiLeo, R.A., Landi, B.J., Raffaelle, R.P.: Purity assessment of multiwalled carbon nanotubes by Raman spectroscopy. J. Appl. Phys. 2007;101. https://doi.org/10.1063/1.2712152
57. Shimada, T., Sugai, T., Fantini, C., Souza, M., Cançado, L.G., Jorio, A., et al.: Origin of the 2450 cm-1 Raman bands in HOPG, single-wall and double-wall carbon nanotubes. Carbon N Y. **43**, 1049–1054 (2005). https://doi.org/10.1016/j.carbon.2004.11.044
58. Dresselhaus, M.S., Dresselhaus, G., Saito, R.: Jorio a. Raman spectroscopy of carbon nanotubes. Phys. Rep. **409**, 47–99 (2005). https://doi.org/10.1016/j.physrep.2004.10.006
59. Oh, S.J., Cook, D.C., Townsend, H.E.: Characterization of iron oxides commonly formed as corrosion products on steel. Hyperfine Interact **112**, 59–66 (1998)
60. McCarty, K.F., Boehme, D.R.: A Raman study of the systems Fe3 – xCrxO4 and Fe2 – xCrxO3. J Solid State Chem. **79**, 19–27 (1989). https://doi.org/10.1016/0022-4596(89)90245-4
61. Farrow, R., Benner, R., Nagelberg, A., Mattern, P.: Characterization of surface oxides by Raman spectroscopy. Thin Solid Films. **73**, 353–358 (1980). https://doi.org/10.1016/0040-6090(80)90499-X

VIII Tribological behavior of self-lubricating carbon nanoparticle reinforced metal matrix composites

Leander Reinert[1], Itzhak Green[2], Steffen Gimmler[1], Björn Lechthaler[1], Frank Mücklich[1] and Sebastian Suárez[1]

[1] Department of Material Science and Engineering, Saarland University, 66123 Saarbrücken, Germany
[2] George W. Woodruff-School of Mechanical Engineering, Georgia Institute of Technology, Atlanta, USA

Published in ***"Wear" (Impact factor (2018): 2.960)***
Accessible online at: https://doi.org/10.1016/j.wear.2018.05.003

Own contribution:

Planning and coordination of tribological experiments; Friction coefficient analysis; Surface analysis by laser scanning microscopy; Scanning electron microscopy and wear track analysis; Electron backscatter diffraction analysis; Electron dispersive spectroscopy analysis; Raman spectroscopy analysis; Writing; Discussion; Planning.

Abstract:

The present study focuses on investigating the dominant friction and wear mechanisms in the case of dry sliding of carbon nanoparticle reinforced nickel matrix composites under elastic and elasto-plastic contact conditions. For this purpose, multi-wall carbon nanotubes (CNT), onion-like carbon (OLC) and nanodiamonds (nD) were chosen to represent a large variety of carbon nanoparticles as they can be systematically distinguished regarding their carbon hybridization state (sp^2 vs. sp^3) as well as their morphology and size ("0D" vs. "1D"). Contact simulations based on the Greenwood-Williamson model are conducted in order to calculate the required contact loads. Friction and wear analysis is supported by complementary characterization techniques, including scanning electron microscopy, transmission electron microscopy, energy dispersive spectroscopy, Raman spectroscopy, light microscopy as well as laser scanning microscopy. It is found, that only CNT provide efficient lubrication as reinforcement phase in composites, presenting different lubrication mechanisms for the tested contact conditions. The high aspect ratio of CNT is found to be essential for the lubrication mechanisms, allowing the particles to be dragged into the direct tribological contact. The lubrication effect increases with increasing volume content of CNT, reaching a maximum steady state frictional reduction of 50% compared to the unreinforced nickel reference.

Cite this as:
L. Reinert, I. Green, S. Gimmler, B. Lechthaler, F. Mücklich and S. Suárez, Tribological behavior of self-lubricating carbon nanoparticle reinforced metal matrix composites. *Wear* **2018**, 408-409, 72-85 *(https://doi.org/10.1016/j.wear.2018.05.003)*

Wear 408–409 (2018) 72–85

Contents lists available at ScienceDirect

Wear

journal homepage: www.elsevier.com/locate/wear

Tribological behavior of self-lubricating carbon nanoparticle reinforced metal matrix composites

L. Reinert[a,*], I. Green[b], S. Gimmler[a], B. Lechthaler[a], F. Mücklich[a], S. Suárez[a]

[a] Department of Materials Science, Saarland University, Campus D3.3, D-66123 Saarbrücken, Germany
[b] George W. Woodruff School of Mechanical Engineering, Georgia Institute of Technology, Atlanta, USA

ARTICLE INFO

Keywords:
Carbon nanoparticles
Solid lubrication
Carbon nanotubes
Onion-like carbon
Nanodiamonds
Metal matrix composites

ABSTRACT

The present study focuses on investigating the dominant friction and wear mechanisms in case of dry sliding of carbon nanoparticle reinforced nickel matrix composites under elastic and elasto-plastic contact conditions. For this purpose, multi-wall carbon nanotubes (CNT), onion-like carbon (OLC) and nanodiamonds (nD) were chosen to represent a large variety of carbon nanoparticles as they can be systematically distinguished regarding their carbon hybridization state (sp^2 vs. sp^3) as well as their morphology and size ("0D" vs. "1D"). Contact simulations based on the Greenwood-Williamson model are conducted in order to calculate the required contact loads. Friction and wear analysis is supported by complementary characterization techniques, including scanning electron microscopy, transmission electron microscopy, energy dispersive spectroscopy, Raman spectroscopy, light microscopy as well as laser scanning microscopy. It is found, that only CNT provide efficient lubrication as reinforcement phase in composites, presenting different lubrication mechanisms for the tested contact conditions. The high aspect ratio of CNT is found to be essential for the lubrication mechanisms, allowing the particles to be dragged into the direct tribological contact. The lubrication effect increases with increasing volume content of CNT, reaching a maximum steady state frictional reduction of 50% compared to the unreinforced nickel reference.

1. Introduction

Nowadays, the increasing demand for lower energy consumption in nearly every technical application sets the need for the tribological optimization of various technical components, like for example automotive parts such as cylinder liners, piston rings or bearings in passenger cars [1]. One way of approaching these problems is to reduce friction and wear by lubricating these systems, in most cases with a suitable liquid lubricant. However, due to their potential impact on the environment and low evaporation point, there is a trend to replace liquid with solid lubricants in certain mechanical systems [2,3]. Also, problems often arise when a constant oil supply cannot be achieved, a low oil pressure appears or oil leakage occurs which can lead to catastrophic failure of the lubricated system. Thus, new approaches to create self-lubricating materials, which are insensitive about their atmospheric surrounding and external influences, have to be developed in order to fit the elevated requirements.

The possibility to tailor the physical and tribological properties of composite materials by variation of simple process parameters, the matrix or the reinforcement phase was extensively studied over the last decades. Beside of other reinforcement materials such as ceramics, MoS_2 or graphite, carbon nanomaterials are very promising reinforcement candidates in composites to increase strength [4–6], hardness [7–9], electrical and thermal conductivity [8,10,11] thermomechanical stability [12] and reduce friction and wear [13–17]. This is mainly due to their outstanding properties and low density compared to other reinforcement materials [18–20]. For our work, we focus on three types of carbon nanoparticles (CNPs), namely multi-wall carbon nanotubes (CNT) [21] nanodiamonds (ND) [20] and onion-like carbons (OLC) [22]. CNTs consist of helical hollow cylinders of graphitic carbon (sp^2-hybridized) having multiple shells and a high aspect ratio ("one-dimensional") [21]. The spherical diamond nanoparticles, named NDs, show a lattice spacing of 0.21 nm and feature a primary particle diameter of around 5 nm ("zero dimensional") [20]. NDs can be transformed to OLC by thermal annealing in inert atmosphere or vacuum. OLCs, which are also known as carbon onions, are multi-shell, graphitic, fullerene nanoparticles ("zero dimensional") with a typical spacing of 0.34–0.36 nm between the outer shells [22,23]. We chose these three particular CNPs as they show either a different carbon hybridization state or a different particle geometry/size, therefore

* Corresponding author. Permanent address: Saarland University, Campus D3.3, Saarbrücken D-66123, Germany.
E-mail address: l.reinert@mx.uni-saarland.de (L. Reinert).

https://doi.org/10.1016/j.wear.2018.05.003
Received 22 February 2018; Received in revised form 4 May 2018; Accepted 7 May 2018
Available online 09 May 2018
0043-1648/

representing a variety of carbon nanoparticles and allowing for a systematic investigation of the effect of those differences on the tribological properties of the composite material.

In case of CNTs, several works confirm the reduction in friction and/or wear when used as reinforcement phase in a metal matrix composite [16,24–27]. However, the tribo-mechanisms of the CNTs within these composites are still not fully understood. The effects might result from the influence of the CNTs on the microstructure of the composite. The particles could hinder the dislocation movement and therefore reduce plastic deformation of the surfaces. A higher strength, induced by a grain refinement effect (pinning effect) is also found to be a reason for a reduction in friction and wear. Typically, these effects are more pronounced for nanosized materials like for example CNT [28]. Furthermore, CNTs provide the ability to efficiently separate the sliding surfaces, slide or possibly act as roller bearings [29]. In this context, Dickrell et al. showed a frictional anisotropy effect of CNT coatings. Other studies have shown that the CNTs form a carbonaceous layer on the surface, which shows tribomechanisms similar to those of graphite [30,31]. Simulations at higher temperatures have shown, that there might be a pressure induced transformation of CNTs towards graphite when a pressure of about 1,5 – 2,5 GPa is applied [32]. However research works regarding this topic were conducted under different conditions and using different matrix materials, such as Cu, Al, Ni or the CNTs were applied as coating, for example on a SiO_2 substrate [5,24,27,33]. Thus, these findings leave it rather unclear how the lubrication mechanism in a composite type material reinforced with CNTs is working.

When it comes to NDs used as reinforcement phase in metal matrix composites, most of the research refers to a wear reducing effect instead of a frictional reduction [13,34–36]. A wear reduction can be traced back to an increased hardness of the composite by grain refinement. Furthermore, hindering of dislocation movement and also the hard particles themselves may contribute in a wear reduction of the composites [13,35]. However, NDs can also increase wear. An increased wear was ascribed to the breaking out of NDs from the matrix and consequently acting as abrasive third body within the tribological contact. On the other hand, NDs that are embedded in the matrix material could act as spacer between the two sliding surfaces and therefore prevent direct contact of the asperities [36]. The potential to act as roller bearing on top of a surface and thus to reduce friction is controversially discussed in literature [13,34].

Considering OLCs, there is yet no available literature, which investigates their effect as reinforcement phase in a metallic composite material on the tribological properties. However, there is research claiming for very beneficial tribological properties of OLCs. Because of their polyhedral form and also their high mechanical strength, it is reasonable to assume that they might act as a roller bearings in a tribological contact [18]. Furthermore, as the curvature of OLCs is smaller compared to CNTs, it is supposed that they show less intermolecular interactions to other materials and thus being able to freely move on top of a surface [37,38]. Research in this field has been conducted by Hirata et al. [39], showing that on a silicon wafer, a very low friction coefficient lower than 0.05 can be achieved and also wear can be significantly reduced by 3–6 orders of magnitude compared to using graphite as lubricant. Also, in contrast to a lubrication using graphite, the lubrication effect by OLCs is not affected using vacuum conditions. However, there is a change in the effect as a function of the surface roughness, as the particles can be trapped within the asperities and therefore no longer provide a lubricating effect as they are not in direct contact in between the surfaces anymore [39]. Furthermore, simulations show a dependence of the lubrication effect of the OLCs from the applied contact pressure. If the pressure exceeds a value of 5 GPa (in case of two contacting DLC coated surfaces, that are lubricated by OLC), the lubrication effect significantly decreases [40].

To sum up, the variation in testing parameters, materials and conditions in literature make it rather difficult to correlate the measured effects to the underlying friction and/or wear mechanism of carbon nanoparticles. In the present study, a tribological comparison between the described three different CNPs as reinforcement phase in a nickel matrix composite is provided for elastic and elasto-plastic contact conditions under low (4%) and medium (45%) relative humidity. This is to learn about the acting lubrication mechanisms of the individual particles in a composite material, which can only be achieved in case of investigating systematically distinguishable CNPs as reinforcement phase in the same matrix material and under the same conditions. To the best of our knowledge, this is the first systematic comparison of the tribological properties of CNTs, OLCs, or NDs in a metal matrix.

A dispersion analysis of these particular CNPs in the composite as well as a model to control and predict the final microstructure after sintering was published by our work group before [41,42]. Based on these works, it is possible to produce composite materials reinforced by these CNPs, which feature the same final microstructure and hardness. Thus, the influence of the microstructure and hardness on the tribological properties could be neglected. Nickel appears to be a suitable candidate as matrix material for a comparative study, since it only forms metastable carbides under very specific conditions, as shown in a previous study reported by Suarez et al. [43].

In order to test the composites under varying mechanical contact situations (fully elastic or elasto-plastic), contact mechanics simulations need to be performed to calculate the corresponding necessary normal loads. One of the earliest models of elastic asperity contact is that of Greenwood and Williamson (G-W) [44]. This model uses the solution of the contact of an elastic hemisphere and a rigid flat plane, otherwise known as the Hertz contact solution, to stochastically model an entire contacting surface of asperities with a postulated Gaussian height distribution. The G-W model also assumes that the asperities do not interfere with adjacent asperities and that the bulk material below the asperities does not deform. Supplementing the G-W model, many elasto-plastic asperity models have been devised [45–48]. The G-W model is a statistical method, and hinges upon obtaining statistical parameters like the radius of curvature (R), the areal asperity density (η) and the standard deviation of the surface heights (σ). A way of finding these parameters is given by McCool, using the spectral moments in order to calculate the aforementioned parameters [49]. In case of fully elastic contact conditions, the G-W model provides sufficiently accurate results for most of the engineering tasks and has gained wide acceptance. However, considering elasto-plastic contact conditions, the G-W model is not sufficient and it has to be extended. The contact conditions can be assessed by calculating the plasticity index ψ [44,48]. For cases where the plasticity index indicates elasto-plastic contact conditions, some early contact models have extended the venerable Greenwood-Williamson (G-W) model; these include, for example, the Kogut-Etsion (K-E) model [45], the Chang-Etsion-Bogy (CEB) model [46], or the Zhao-Maietta-Chang (ZMC) model [47]. A more recent model (that does not depend on limiting assumptions, e.g., material hardness) is developed by Jackson and Green (J-G model), producing predictions for contact area, contact force and surface separation [48,50]. Thus, in the present work, the J-G model is used in order to simulate the contact conditions in the given tribological system. The experimental work is done based on these simulations and various characterization methods are used with respect to the simulated contact regime.

In this regard, laser-scanning microscopy is used to generate the surface data on which the contact simulation is based upon. Furthermore, as a function of the given contact situation, the structural integrity of the particles is analyzed by Raman spectroscopy. Additionally, the obtained microstructure, and the resulting mechanical reinforcement effect are analyzed by scanning electron microscopy (SEM) and electron backscatter diffraction (EBSD). Finally, the generated wear tracks are analyzed by SEM and energy dispersive X-ray spectroscopy (EDS) in order to discuss the wear mechanisms as a function of the contact situation.

2. Materials and methods

2.1. Materials and manufacturing

Nickel matrix composites reinforced with CNT (Baytubes C150P from Bayer, purity > 95%, individual particle diameter of 5–20 nm, length of 2–10 μm), ND (NaBond Technologies Co., purity > 98%, individual particle diameter 4–8 nm), and nanodiamond-derived OLCs were produced by hot uniaxial pressing. To synthesize the OLCs, ND powder was annealed in graphite crucibles (30 mm in diameter and 20 mm in height) in a vacuum furnace with tungsten heaters (model: 1100–3580-W1, Thermal Technology Inc.) using a heating and cooling rate of 15 °C/min. The transformation temperature was 1750 °C with a holding time of 3 h. The chamber pressure was between 10 mPa and 100 mPa.

The particles were blended with the nickel powder (Alfa Aesar, 325 mesh) using a colloidal mixing method, using ethylene glycol as solvent [41,43]. For the particle dispersion, a shear mixer (Ultra-Turrax T-25 by IKA) and subsequently an ultrasonic bath (Sonorex Super RK 514 BH by Bandelin, 860 W, 35 kHz) were used for 5 and 20 min, respectively. Afterwards, Ni is added and blended with the dispersed particles (particle fraction: 5, 10 and 20 vol.-% for each type) in the shear mixer for another 5 min.

As shown in reference [42], the CNP concentration strongly affects the composites' microstructure if near-full densification (> 98%) is achieved. With the aim of obtaining a simplified system, the sintering parameters were chosen so as to avoid differences in the microstructure of the matrix, irrespective of the type and amount of CNP [42]. Nonetheless, the parameters are sufficient to achieve a good densification of the composite (at least 92%). Hence, the influence of the microstructure could be neglected when tribologically comparing the different composites.

The blends were pre-compacted in steel dies (diameter: 8 mm) with a pressure of 990 MPa. Then, the pellets are densified in a hot uniaxial press (with Al_2O_3 pistons) with an applied pressure of 264 MPa, temperature of 700 °C, a heating and cooling rate of 20 °C/min and a holding time of 2.5 h.

After densification, all samples were ground under water rinsing with successive sandpaper grit sizes of 320, 600, 1000, 2500 grit and then polished in a three-stage process using diamond polishing suspensions in the steps 6 μm, 3 μm and finally 1 μm.

2.2. Numerical modeling

Before tribological testing of the samples commences, it is desirable to estimate the contact conditions occurring under static loading. It is important to know whether the contact is fully elastic or elasto-plastic as it might influence the lubrication mechanism of the CNP. Therefore, it is important to determine which normal forces are needed for the given tribological system in order to provide reasonable contact situations. In order to find the statistical parameters for the simulation, real surface data had been obtained by laser scanning microscopy (LEXT OLS4100 by Olympus) with a lateral resolution of 120 nm and a height resolution of 10 nm using a 50× objective. For the simulation, the surface data of the unreinforced composite and the counterpart, consisting of an Al_2O_3 ball with a diameter of 6 mm, are used. To find the corresponding statistical surface parameters, the spectral moments can be employed:

$$m_0 = \frac{1}{N}\sum_{n=1}^{N}(z)_n^2 \tag{1}$$

$$m_2 = \frac{1}{N}\sum_{n=1}^{N}\left(\frac{dz}{dx}\right)_n^2 \tag{2}$$

$$m_4 = \frac{1}{N}\sum_{n=1}^{N}\left(\frac{d^2z}{dx^2}\right)_n^2 \tag{3}$$

where N is the total number of data points on a surface and z is the distance from the mean height of the surface to the asperity peak. The derivatives are calculated by a central finite difference scheme. In this work, both surfaces exhibit non-isotropic roughness and thus they are meshed into 2-D individual rows and columns. Along each of these directions, moments are averaged arithmetically (m_0) and harmonically (m_2 & m_4) in principal directions defined by where m_2 is maximum and minimum. The following procedure is then used:

1. Find *one* set of two orthogonal directions which give $m_{2(min)}$ and $m_{2(max)}$. Ignore all other values and directions. Calculate m_2 by harmonic mean from $m_{2(min)}$ and $m_{2(max)}$.
2. In that *specific* directions set above, calculate $m_{4(1)}$ and $m_{4(2)}$ (regardless of whether they are maximum or minimum). Calculate m_4 by harmonic mean from $m_{4(1)}$ and $m_{4(2)}$.
3. In that *specific* directions set above, calculate $m_{0(1)}$ and $m_{0(2)}$ (regardless of whether they are maximum or minimum). Calculate m_0 by arithmetic mean from $m_{0(1)}$ and $m_{0(2)}$.

The radius of curvature, R, the areal asperity density, η, and the root mean square, σ, are then calculated according to the work by McCool [49] using spectral moments obtained from the above procedure:

$$\sigma = \sqrt{m_0} \tag{4}$$

$$\eta = \left(\frac{m_4}{m_2}\right)\bullet\left(\frac{1}{6\pi\sqrt{3}}\right) \tag{5}$$

$$R = 0.375\bullet\left(\frac{\pi}{m_4}\right)^{0.5} \tag{6}$$

In addition, the standard deviation of the summit heights, σ_s, and the separation between the mean of the surface and summit surfaces, y_s, and the bandwidth parameter, α, are also calculated based upon:

$$\alpha = \frac{m_0\bullet m_4}{m_2^2} \tag{7}$$

$$\sigma_s^2 = \left(1-\frac{0.8968}{\alpha}\right)\bullet m_0 \tag{8}$$

$$y_s = \frac{4\bullet\sqrt{m_0}}{\sqrt{\pi\bullet\alpha}} \tag{9}$$

The model used is shown in Fig. 1. The model depicts an Al_2O_3 hemisphere that is brought into contact with a composite (CNT reinforced nickel) substrate. The surfaces, which have non-isotropic roughness, are set in a non-conformal contact. The contact is assumed to deform elasto-plastically, where bulk deformation is included.

The procedure for obtaining the clearance, h_0 (see Fig. 1**b**), and the final bulk deformation is outlined below:

I. Get the bulk deformation δ caused by the load, P, according to:
   (a) Obtain the critical load P_c that causes the onset of plasticity based on Green [51] (see Eq. 12 there);
   (b) If $P < P_c$ use the Hertzian contact solution for the bulk deformation in a "pure" elastic state [52];
   (c) If $P > P_c$ use the solution for the bulk deformation from [53] (see Fig. 5 there), and obtain the contact area from [56];
   (d) superimpose the bulk deformation to the geometry of the sphere (see step IV below).
II. Get the nominal pressure (p) and the real contact area (A_r) as a function of separation (h), as if the surfaces are both flat (conformal).
III. Make p and A_r functions of that separation, h.
IV. Assume (or "guess") a clearance h_0 and form a function $h = h(r)$

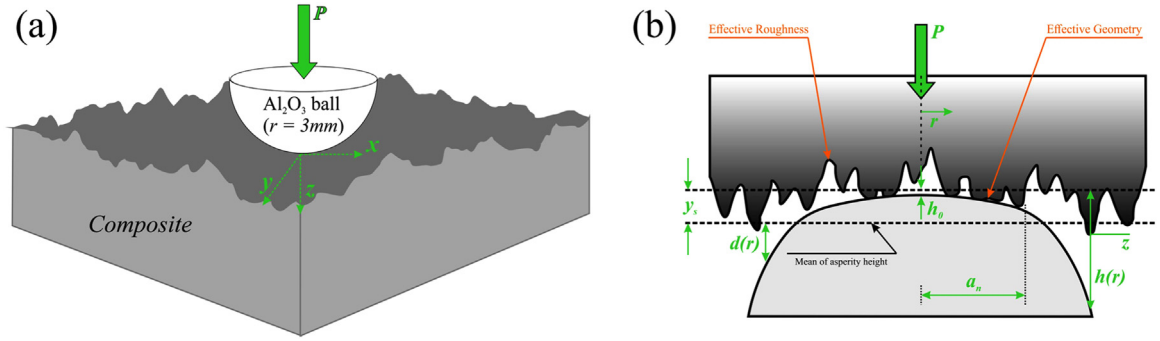

Fig. 1. (a) Schematic of contact between a rough hemisphere against a rough composite surface. (b) Contact model between an equivalent nominally flat rough surface against a smooth hemispherical-shaped counterpart.

that includes the bulk deformation.

V. Integrate (i.e., sum) p and A_r over "rings" at r with a differential width Δr to obtain the load P as a function of clearance h_0, and plot those results.

VI. Find that clearance h_0 that corresponds to the applied experimental load P (.1 or 8 N).

VII. For that clearance, calculate the real area of contact (post processing).

2.3. Characterization methods

2.3.1. Tribological characterization

The tribological experiments are performed with two ball-on-disc tribometers (a nano and a microtribometer from CSM instruments). This allows to measure under significantly different loads and environmental conditions. In both cases the static counterpart consisted of an Al_2O_3 ball with a diameter of *6 mm* (roughness $R_a = 22 \pm 7$ nm). The test parameters for both tribometers are summarized in Table 1.

The choice of two different tribometers (working under different normal loads) is made according to the calculated contact conditions, which should be elastic and elasto-plastic (see Section 3.1). Furthermore, the nanotribometer allows the systematic investigation of the lubrication activity at very low room humidity. Specifically, in the case of a full degradation of the CNPs towards graphite, it is expected that the lubricity will be severely hindered as a consequence of the shortage of water molecules that enhance the lubrication mechanism in graphite [54–56]. Thus, the reason for choosing two different relative humidities is to evaluate the lubrication behavior actively avoiding or allowing for a graphitic lubrication. All individual measurements have been repeated three times for statistical back-up. Consequently, the mean value including standard deviation is plotted for every investigated case. Al_2O_3 was selected as counterpart material because of its chemical inertness, low adhesion to the metallic matrix (compared to a metallic counterpart) and a much higher hardness compared to the composites. Due to these facts, wear of the alumina ball can be neglected and the focus can be put on the wear analysis of the composites.

2.3.2. Nanoparticle characterization

The structural state of the particles is surveyed by Raman spectroscopy. The data is acquired using an inVia Raman microscope (Renishaw) with an excitation wavelength of 532 nm (2.33 eV), a grating with 2400 lines per mm, a 50 × -objective (numerical aperture: 0.9), a spectral resolution of 1.2 1/cm, and a laser power of 0.2 mW. Visible excitation wavelengths in Raman spectroscopy are more sensitive (50–230 times for graphite and amorphous carbon, respectively) to coupled modes induced by sp^2-carbon atoms than for sp^3 [57,58]. Thus, NDs (sp^3-hybridization) Raman signal is weaker and might not be detected for the initial state. However, if a transformation of ND towards graphitic structures occurs, this could be easily observed as a consequence of the appearance of the sp^2 characteristic D and G bands. All Raman spectra were recorded three times with an acquisition time of 10 s to eliminate cosmic rays and to improve the signal-to-noise ratio. Additionally, a linear baseline subtraction and intensity normalization were performed for all spectra. To identify peak positions of the data, fitting with Lorentz functions was performed for all data [59]. The distribution of the particles in the matrix was analyzed using a light microscope (BX 60, Olympus).

2.3.3. Microstructural characterization

The mean grain size of the matrix after sintering determined by EBSD with an EDAX TSL detector incorporated in the dual beam microscope. The scanned area is of 250 × 250 μm^2 applying an accelerating voltage of 20 kV, a current of 22 nA, and a step size of 0.3 µm. For the analysis, a grain is defined as at least two adjacent points with a maximum misorientation of 5°, beyond which a grain boundary is determined. The acquired raw data was post-processed using confidence index (CI) standardization, followed by the removal of points with CI below 0.1. The grains intersecting the scan window were excluded from the analysis.

2.3.4. Wear track and surface roughness analysis

Before the tribological measurements, the surface roughness is determined for each sample using the laser scanning microscope. After the experiments, the wear tracks are analyzed using a dual beam focused ion beam/field emission scanning electron microscopy (FIB/FE-SEM) workstation (FEI Helios NanoLab 600) with a voltage of 5 kV and 1.4 nA of current. Finally, also energy dispersive X-ray spectroscopy (EDS) is performed for the wear tracks using a voltage of 5 kV and a current of 22 nA. The analysis of the sub-surface is performed on a transmission electron microscope (TEM) JEOL JEM 2010 working at 200 kV.

Table 1
Test parameters of the tribological experiments.

	Test load [N]	Maximum speed [mm/s]	Stroke length [mm]	Temperature [°C]	Humidity [%]	Sliding distance [m]	Mode
Nanotribometer	0.1	1	0.6	25	4	0.72	Linear reciprocating
Microtribometer	8	10	4	25	45	2.4	

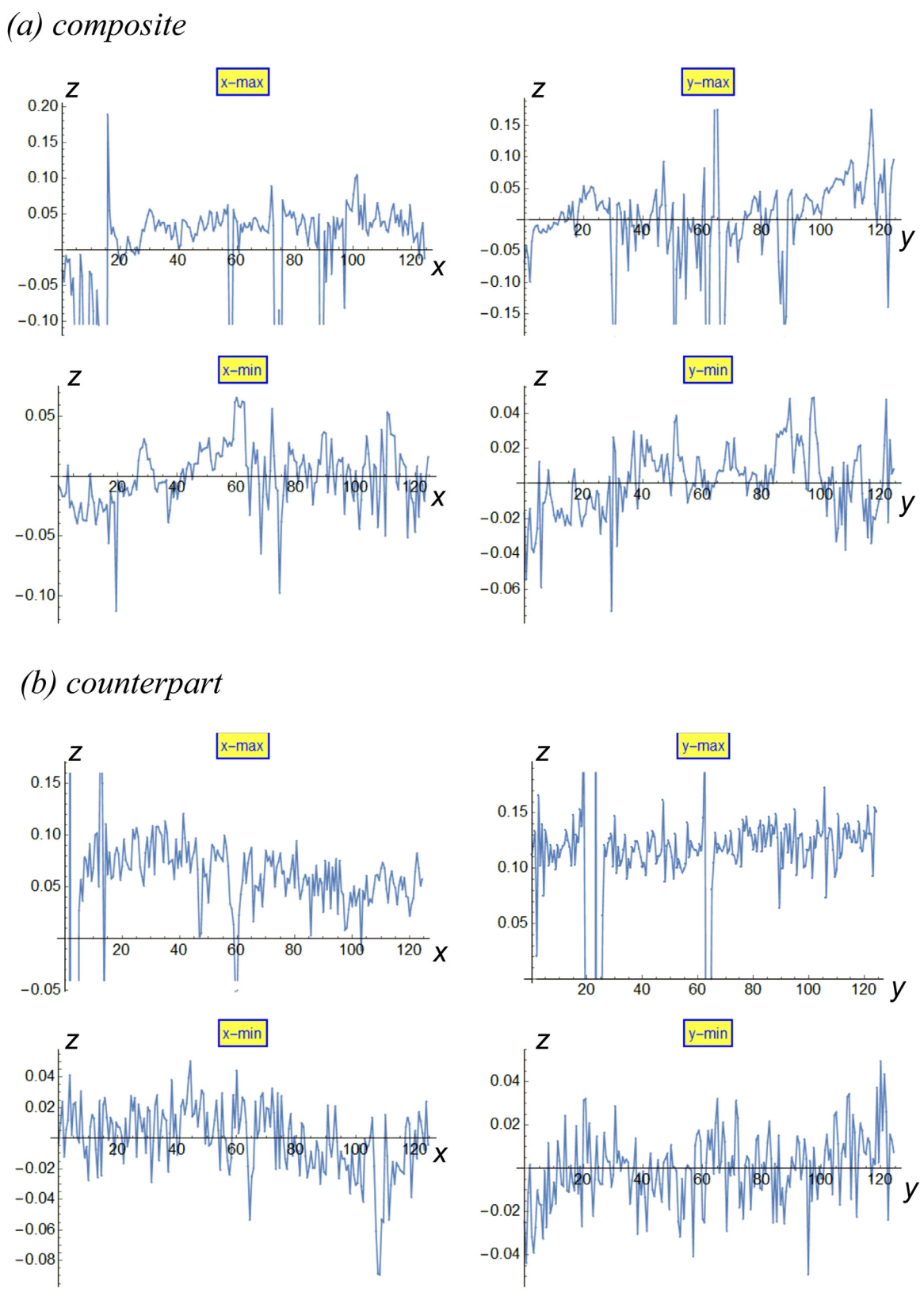

Fig. 2. Roughness line profiles in the maximum and minimum directions of (a) the composite, (b) the counterpart. All dimensions are in μm. The width shown corresponds in all cases to 120 μm.

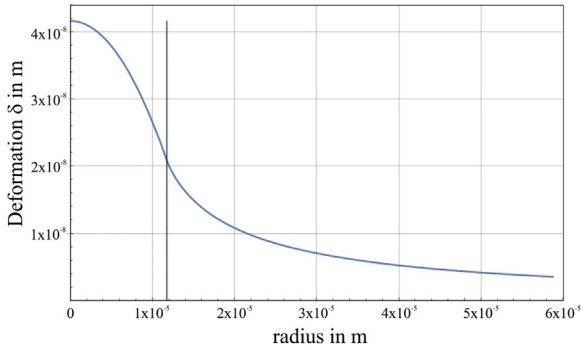

Fig. 3. Substrate deformation under a load of 0.1 N. The vertical line separates complete contact (left) and non-contact (right).

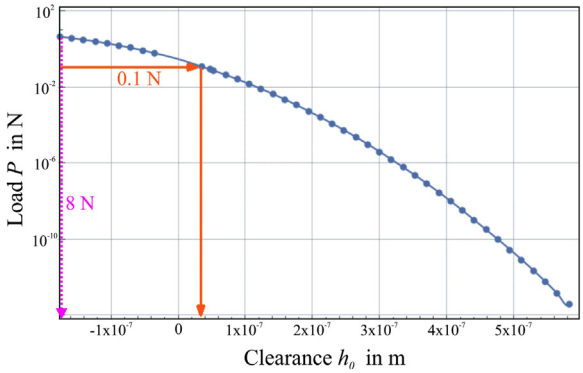

Fig. 5. Contact load as a function of the clearance h_0 between the contact pair. The arrows indicate both experimental loads investigated in this report.

3. Results and discussion

3.1. Contact mechanics modeling results

The roughness of the composite surface varies greatly in various radial directions, requiring the three-step special procedure to calculate the effective moments as detailed in Section 2.2. The surfaces roughness is digitized by a resolution of 0.125 μm. Fig. 2a shows the roughness of the composite while Fig. 2b shows the roughness of the ball in the corresponding $m_{2(min)}$ and $m_{2(max)}$ directions.

By the procedure outlined above and using Eqs. (1–9), the descriptive values of the surfaces are obtained. Following the definition given by Greenwood and Williamson [44] the plasticity index is:

$$\psi = \left(\frac{E'}{H}\right)\cdot\sqrt{\frac{\sigma}{R}} = 8.8 \tag{10}$$

That value indicates that surface asperities would clearly undergo plastic deformation. The next step is to determine whether the bulk remains elastic (see step I above). Using Hertzian theory as outlined by Johnson [60], the bulk deformation is shown in Fig. 3. The solution is obtained piecewise with the vertical line marking the radial position where to the left of it there is complete contact between the surfaces, while to the right the ball and the composite are separated. [Note that rough surfaces contact still takes place throughout, i.e., in both regions].

The maximum deformation under the action of the load of 0.1 N is at the origin giving $\delta = 46$ nm, whereas the critical value at the onset of plasticity is 152 nm [60]. Likewise, the critical value of the load that would cause plasticity in the bulk is 0.6 N (using [51]). Evidently, for that load the bulk deforms entirely elastically, whereas the asperities will deform in the elasto-plastic regime (because the plasticity index is 8.8). This fulfills step I above. Now the Jackson-Green (J-G) model [50,61] is employed for the elasto-plastic asperity contact. The results are shown in Fig. 4 a & b (the Greenwood-Williamson (G-W) and the corrected Kogut-Etsion (K-E) models are shown for reference only). This is in accordance with steps II and III above.

Steps IV and V above are subsequently performed. For brevity details are omitted but the outcome is shown in Fig. 5. Then, in step VI, the particular clearance h_0 that corresponds to the applied experimental load is found. Hence, entering Fig. 5 with a load of $0.1\,N$, the clearance is found to be $h_0 = 41\,nm$. Superimposing the asperities deformation along with the bulk deformation (attributing the entire latter deformation to the ball) gives the final flattened shape of the ball shown in Fig. 6a, while the pressure distribution at the contact is shown in Fig. 6b. It is evident that also the pressure distribution is flattened (compared to the Hertzian parabolic shape), where it is nearly constant in the full contact region, but it drops outside of that region.

The real area of contact is now finally evaluated in the two regions using the J-G model (with the information given in Fig. 3). In the region where the ball bulk is in contact with the composite (that is in the range $0 < r < a_0 = 11.74\,\mu m$, where a_0 is identified by the vertical lines in Figs. 3 and 6) the real contact area is $3.67 \times 10^{-11}\ m^2$, and the asperities contact outside that region (where $r > a_0 = 11.74\,nm$) result in a contact area of $5.57 \times 10^{-11}\ m^2$. The total real contact area is the sum of these, giving $9.25 \times 10^{-11}\ m^2$.

For the case when the load is $8\,N$, it is apparent from Fig. 5 that a negative value would be anticipated for h_0. That indicates that the contact is heavily loaded making rough surfaces analysis moot. In this case, it can be assumed that all asperities have been heavily and severely (plastically) deformed and the entire contact degenerates into a single elastoplastic spherical contact. The J-G model [50,61] is readily used to estimate the contact parameters. First the normalized load is calculated $P^* = P/P_c$, where P_c had already been obtained previously ($P_c = 0.6$ N). Using the load of $8\,N$, gives $P^* = 8/0.6 = 13.3$. Reverse-solving for the normalized interference (from J-G [50,61]), gives a non-dimensional interference $\omega^* = 6$. It is now straightforward to calculate the real area of contact from the said reference, where first the non-dimensional value is calculated, $A^* = A/A_c = 7.15$. Then, the critical area of contact is calculated, $A_c = 1.43 \times 10^{-9}\ m^2$, to finally obtain the

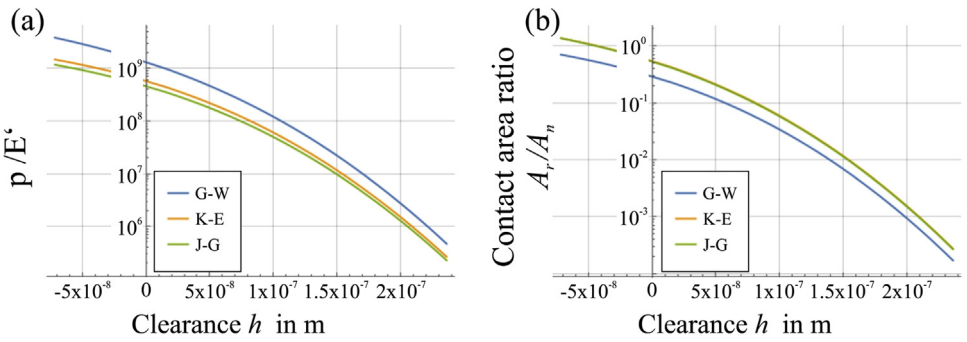

Fig. 4. (a) effective pressure p divided by reduced modulus E′ vs. the clearance, and (b) Contact area ratio vs. the clearance.

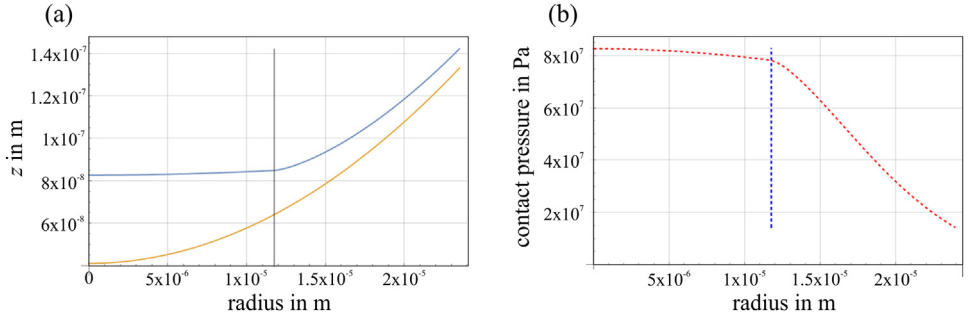

Fig. 6. (a) Deformation profile of the surface (blue) and the original surface profile (orange). (b) Contact pressure distribution throughout the counterpart radius.

real area of contact $A = 1.02 \times 10^{-8}\ m^2$. This value is two orders of magnitude larger than for that of the previous case (when the load is 0.1 N).

Based on these modeling results, the elastic and elasto-plastic contact regime is covered by choosing normal forces of 0.1 and 8 N. The lower load resides below the calculated critical elastic-plastic transition load, whereas the higher resides clearly well above it.

3.2. Initial state characterization

After surface preparation, the distribution of the reinforcement phases was analyzed by light microscopy. In Fig. 7, the distribution of the CNT agglomerates (dark regions) is shown as a function of the volume fraction in the composite. Earlier studies have shown, that the dark regions can directly be assigned to CNT agglomerates [42]. As expected, the amount of agglomerates is gradually increasing with higher volume concentration. However, the distribution of the particles seems to be unaffected by the amount of reinforcement phase, thus a homogeneous distribution of smaller and larger agglomerates within a constant size range is achieved in all cases. This is also the case for the composites reinforced with OLC and nD (the depicted micrographs are representative for all composites).

The surfaces were also evaluated with regards to their initial surface roughness after preparation by white light interferometry. In Table 2, the mean values and standard deviation of the surface roughness R_a for all composites is presented.

The surface roughness of the composites is gradually increasing with the amount of reinforcement phase even though the surface preparation was the same. In addition, the surface roughness of nD and OLC reinforced composites is significantly higher for 10 and 20 vol.-% compared to the CNT reinforced composites. For one part, this is a consequence of the different adhesion to a nickel matrix of both carbon hybridizations studied, where the adhesion of sp^2 carbon is higher than in case of sp^3 hybridized carbons [62]. Thus, the nD particles are removed easily from cavities of the surface during the sanding and polishing process. Naturally, higher particle concentrations result in a larger amount of cavities exposed to the surface, hence deriving in a higher resulting surface porosity and accordingly, a higher roughness. A higher porosity of the samples before surface preparation can be excluded as the relative densities of all composites are determined and reach a value of around 92%. Furthermore, CNT composites show lower surface roughness, as they are more likely to form mechanically interlocked agglomerates within the cavities due to their high aspect ratio. Thus, it is more difficult to remove them during the surface preparation process, as opposed to both, OLC or nD.

Table 2
Mean values and standard deviation of the surface roughness from the as-prepared surfaces of the composites with 5, 10 and 20 vol.-% concentrations of CNT, OLC or nD as reinforcement particles.

Sample		R_a (nm)
Unreinforced Ni		2.4 ± 0.1
CNT	5 vol.-%	13.6 ± 2.6
	10 vol.-%	19.1 ± 5.5
	20 vol.-%	38.6 ± 7.4
OLC	5 vol.-%	14.2 ± 6.0
	10 vol.-%	57.6 ± 3.7
	20 vol.-%	122.0 ± 39.5
nD	5 vol.-%	9.0 ± 5.5
	10 vol.-%	73.1 ± 16.2
	20 vol.-%	141.7 ± 19.5

The reference and the composites were further analyzed by EBSD in order to evaluate the resulting microstructure after densification. No change in the mean grain size or texture was observed as a function of the different particle volume contents or type. The observed behavior can be explained with the chosen sintering parameters, not allowing the

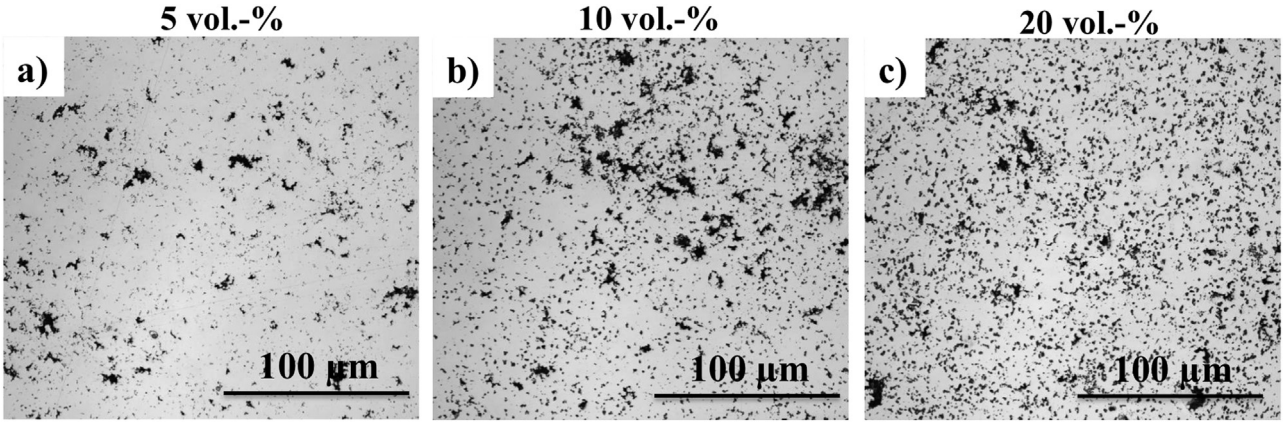

Fig. 7. CNT agglomerates (dark regions) distribution in the nickel matrix composites for a) 5 vol.-%, b) 10 vol.-% and c) 20 vol.-%. The distributions are also representative of the composites reinforced with OLC or nD.

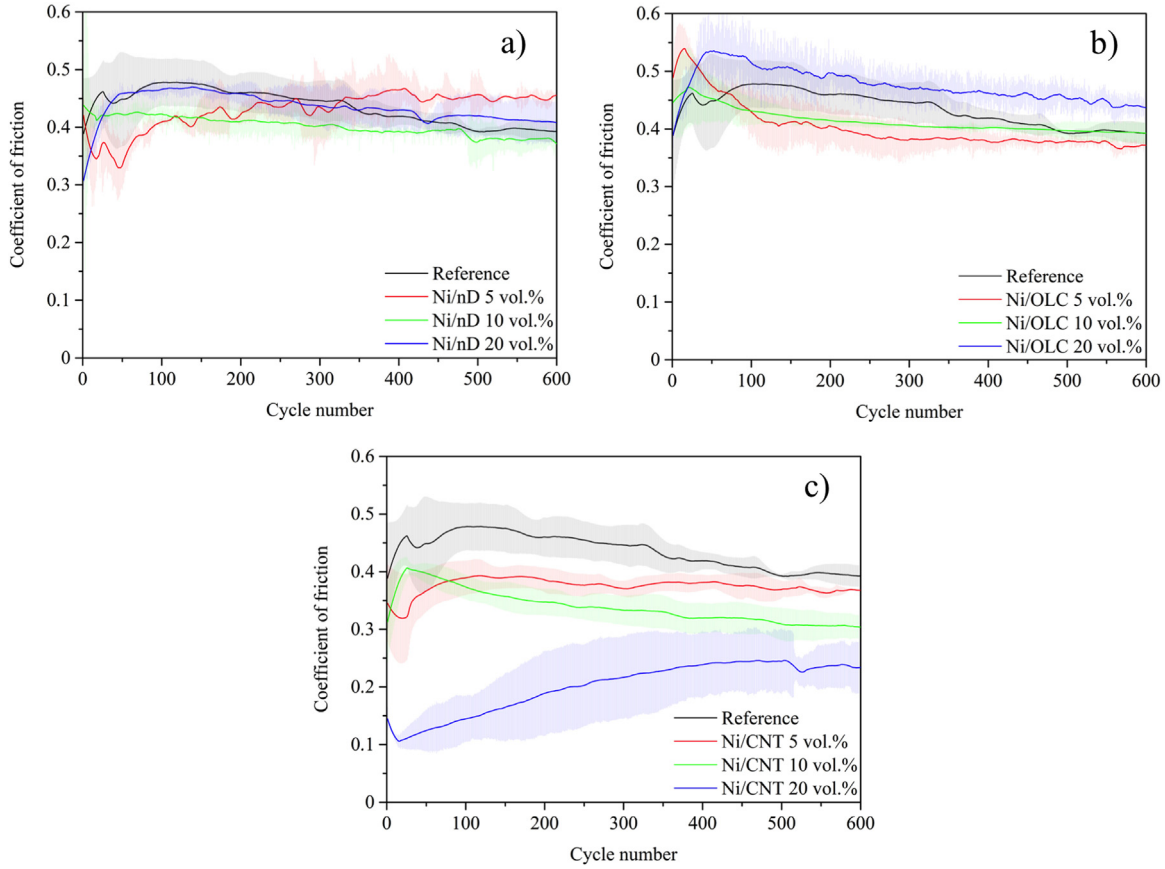

Fig. 8. Evolution of the COF for unreinforced nickel (Ref) and 5, 10 and 20 vol.-% of a) nD, b) OLC and c) CNT in a nickel matrix. The experiments were conducted using 0.1 N of normal load, a relative humidity of 4% and a temperature of 25 °C.

grains to efficiently grow. Thus, the boundary pinning generated by the particles is marginally developed. This becomes clear when comparing the mean grain size of the unreinforced nickel of 7 ± 2 µm with the mean grain size of all the composites of 3 ± 1 µm. Compared to a previous report, this reduction in mean grain size is not distinctive [42].

3.3. Frictional behavior

In Fig. 8 the measured evolution of the friction coefficients (COF) for 5, 10 and 20 vol.-% of nD, OLC and CNT are shown for 0.1 N of load and a relative humidity of 4%. The COF of the reference measurement increases during the first 100 cycles from 0.4 to 0.47 (plotted in Fig. 8 a, b and c for better clarity). From there on, the COF drops down to 0.39 during the next 500 sliding cycles, finally reaching steady state. This behavior is well-known for this contact situation and has been extensively discussed by Blau et al. [63]. The increasing COF for the first 100 cycles is explained with an increasing real contact area due to the wearing off of intrinsic asperities and an increment of the indentation depth of the ball into the substrate. Subsequently, the contact starts to reach a higher surface conformity and smoothening occurs, leading to a frictional reduction. The obtained steady-state reference COF of 0.39 is in agreement with the value reported in the literature [16,64]. Looking at the frictional behavior of the nD (Fig. 8a) or OLC (Fig. 8b) reinforced samples, a similar evolution of the COF to that of the reference can be observed. Considering the given curve dispersion, a change in volume fraction of both particle types leads to no significant change in the COF. This supports the assumption that the frictional behavior of these samples is dominated either by the direct contact of the counterpart with the nickel matrix or a tribologically generated oxide layer. This could be traced back to the fact that large quantities of the particles have been removed from the cavities of the surface during the surface finishing process. However, the mean COF value of the CNT reinforced samples (Fig. 8c) clearly decreases as a function of their volume fraction. This is also related to the different surface roughness and to the different particle size and morphology. As the roughness of nD and OLC containing samples highly exceeds the mean particle size of the spherical particles (4–10 nm), it is highly likely that the particles cannot separate the two contacting surfaces any longer, thus avoiding an efficient lubrication activity [39]. It is also likely that the formation of wear particles larger than the carbon nanoparticles or the formation of an oxide layer would explain the observed behavior.

In contrast to that, CNT provide a large aspect ratio (diameter of 5–20 nm with a length of 2–10 µm), which enables them to be dragged inside of the direct tribological contact zone thus lubricating the contact [30,65]. In previous studies, it was observed, that the tribological behavior of the composites is dominated by the presence or absence of CNT [16]. Thus, it is reasonable, that the COF is decreasing with increasing volume content of CNT. Furthermore, the COF for 20 vol.-% of CNT is increasing from 0.1 to 0.2 during running in. This could be explained with the formation of wear particles or oxide layers during the experiment, hindering CNT in their ability to slide or roll. Furthermore, although the contact pressure is chosen in order to avoid a structural delamination of the CNT towards graphite, it cannot be excluded. This is because higher contact pressures could be reached between individual asperities of the contacting surfaces. In this case, CNT would change its lubrication mechanism from a sliding or rolling movement at the beginning (COF = 0.1) to a more graphite like lubrication in the steady state regime (COF = 0.2). However, as the relative humidity of the experiment is only 4%, a straight graphitic lubrication can be excluded. Considering, that pristine CNT are included in the matrix material, it appears reasonable, that a mixture of pristine CNT and delaminated CNT dominates the frictional behavior under

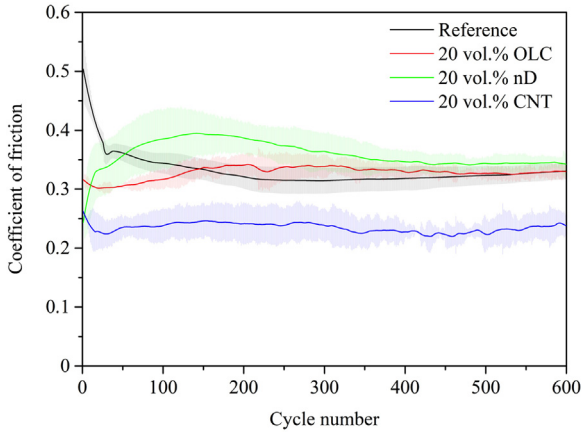

Fig. 9. Evolution of the COF for unreinforced nickel (Ref) and 20 vol.-% of OLC, nD and CNT in a nickel matrix. The experiments were conducted using 8 N of normal load, a relative humidity of 45% and a temperature of 25 °C.

steady state conditions. Additionally, a low relative humidity could slow down the running-in process due to a retarded formation of an oxide layer, which would explain a lower COF of CNT at the beginning of the measurement. However, this can be excluded as this effect should also be observed for all the other sample types, which is not the case. Therefore, a possible retarded surfaces oxidation could only be associated with the CNT particles or tribofilm and not the relative humidity. Raman spectroscopy, SEM and EDS analysis of the according wear tracks will investigate these assumptions further.

The investigation of the influence of the particle concentration on the friction coefficient has shown, that an enhanced lubrication can be reached with higher volume concentrations (for CNT). Thus, for the experiments with 8 N of normal load only the samples with 20 vol.-% of reinforcement phase were measured. In Fig. 9, the evolution of the COF for the reference and the three particle types is plotted.

For this contact situation, a similar behavior compared to the 0.1 N load is noticed. In case of the reference, The COF drops from 0.5 to 0.35 during the first 40 sliding cycles. After this, it stabilizes to a value of 0.35 and thus reaches steady-state condition. This type of COF evolution is also already well-known and typical for high contact pressures on metallic surfaces as reported by Blau et al. [63].

Although showing a slightly different run-in process, the OLC or nD reinforced samples stabilize towards the same COF value as the reference under steady state condition. The slight differences during the run-in process might arise from the initially high roughness of the composites, also resulting in a higher standard deviation. The standard deviation becomes smaller as soon as the system undergoes the transition towards steady-state condition, which could be explained with the removal of the initially present large surface asperities and thus the reach of surface conformity. No lubrication is observed for both types of particles. In contrast to the 0.1 N measurements, this cannot be explained with the absence of particles anymore. In case of higher contact pressures and a plastic deformation of the material, much higher wear is expected also revealing particle agglomerates that are encapsulated in the nickel matrix below the surface. Considering the behavior of the CNT reinforced samples, a constant lubrication effect is noticeable. However, the COF is not reaching values below 0.2 as it was observed for the 0.1 N load measurements. This might be because of a faster degradation process of the CNT due to a much higher contact pressure and a quicker running in process due to surface oxidation (which is promoted by the higher relative humidity) in combination with the much higher contact pressure. The formation of a lubricating absorbed water film can be excluded, since no lubrication is observed for nD or OLC reinforced composites. In contrast, lubrication does not vanish for CNT reinforced composites and is also present under steady state conditions.

3.4. Wear behavior at low load (0.1 N)

In order to achieve a better understanding of the acting tribo-mechanisms, the wear-tracks have to be analyzed in more detail. Fig. 10 depicts SEM micrographs of the wear tracks of the reference and of the samples reinforced with 20 vol.-% of CNP for the 0.1 N load measurements.

The reference clearly shows signs of abrasive wear with plowing being the dominant wear mechanism (Fig. 10a). A similar behavior is observed for the nD and OLC reinforced composites (Fig. 10 d and e). However, in case of the CNT reinforced samples, the wear mechanisms

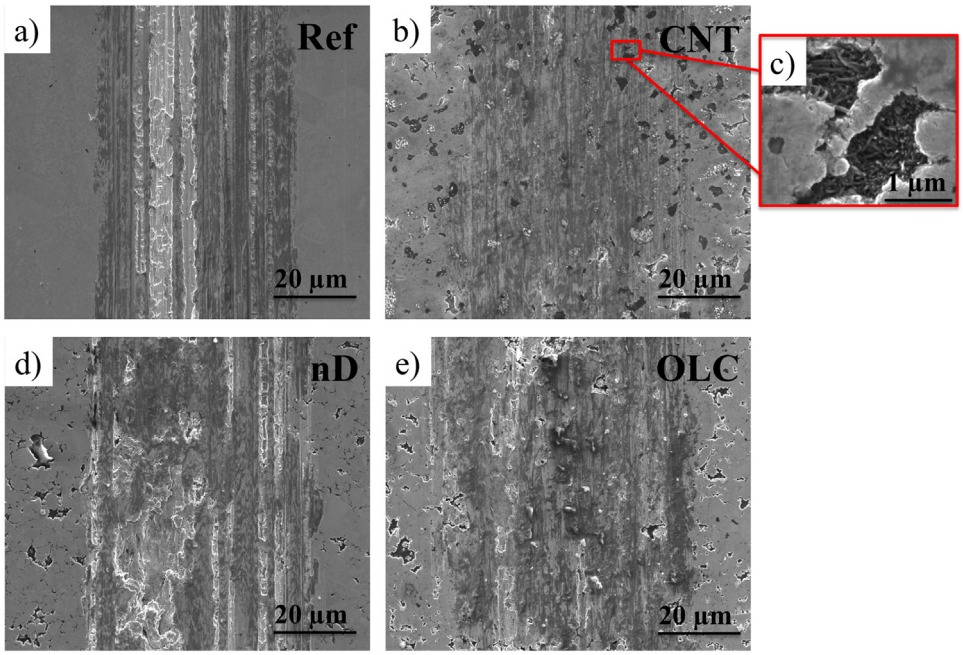

Fig. 10. Wear tracks for 0.1 N of normal load under 4% of relative humidity in case of a) the unreinforced reference and composites reinforced with 20 vol.-% of b) CNT, d) nD and e) OLC. A surface cavity of the CNT reinforced sample is depicted in c).

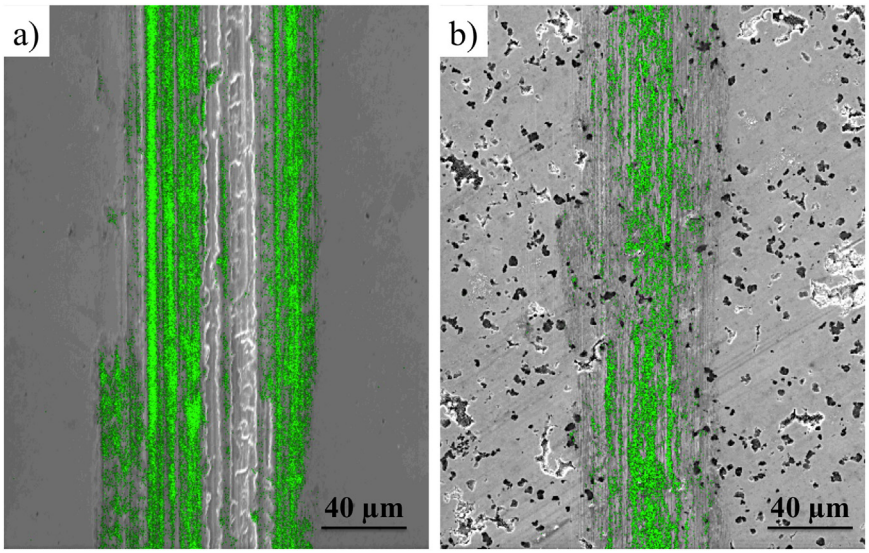

Fig. 11. EDS maps of oxygen (marked in the color green), superimposed with SEM images of the wear tracks for 0.1 N of normal load under 4% of relative humidity in case of a) the unreinforced reference and b) the composite reinforced with 20 vol.-% of CNT. (For interpretation of the references to color in this figure legend, the reader is referred to the web version of this article.)

seem to differ (Fig. 10 b). Although a direct contact between the two surfaces is not fully prohibited by the CNT, only mild wear is occurring. As already described in the discussion of the friction coefficient, this is explained with the large aspect ratio of CNT, which enables them to be dragged inside of the direct tribological contact zone thus reducing the direct contact of the alumina ball with the nickel matrix. In contrast to the nD and OLC reinforced samples, CNT agglomerates (dark regions) can still be observed within the wear track, demonstrating, that less plastic deformation or oxidation of the surrounding nickel matrix has occurred. Furthermore, in Fig. 10 c, CNT are found inside the surface cavities within the direct contact area. In this case, the formed tribolayer might consist out of nanocrystalline graphite layers, which were formed by delamination of CNT as they lubricate the contact. The oxidation behavior was further analyzed by EDS-mapping of oxygen in Fig. 11.

The wear track of the unreinforced reference (Fig. 11a) shows large areas with high oxygen content, which are randomly distributed within the wear track. This could be explained with the ongoing plowing mechanism, which stochastically reorders oxides and bare metal. With the wear mechanism of nD and OLC reinforced samples being similar to those of the reference, the depicted EDS-map is representative also for those samples. However, in case of CNT reinforced samples (Fig. 11b), the EDS-map clearly shows, that the wear track is less oxidized. These observation correlates well with the wear mechanism, as a stronger formation of an oxide layer and the development of oxidic wear particles during the experiment would result in a more pronounced abrasive component. Considering the evolution of the COF, the formation of a more pronounced oxide layer or oxidic wear particles that are embedded in the surface cavities in case of the reference, nD and OLC reinforced samples leads to the stabilization of the COF, finally reaching similar values in the steady state regime. With the CNT-reinforced samples showing less oxidation and a lower COF, it appears reasonable that the COF can still be dominated by the CNT instead of oxidic wear particles.

3.5. Wear behavior at high load (8 N)

Regarding the experiments with higher contact pressure (8 N), a different wear behavior is found, as can be seen in Fig. 12. As for the measurements with 0.1 N load, plowing can be identified as dominant wear mechanism for the reference. A slightly darker color of the wear track leads to the assumption that an oxide layer has formed during the experiment, which will be further evaluated by EDS mapping and Raman spectroscopy in the following sections (Fig. 12a).

The wear track of the CNT reinforced sample in Fig. 12b) is representative for nD and OLC reinforced samples as well. Beside the occurrence of abrasive wear, a distinctive formation of cracks all over the wear track is obvious. When looking at these cracks in more detail in Fig. 12c), it is found, that the cracks occur within a formed surface layer, resulting in the formation of independent surface sheets. The sheets are only loosely attached to the surface as large gaps between the surface and the sheets are present. Due to the high contact pressures, the surface layer might form by densification of wear particles, Ni and CNP. This is reasonable, as for the provided high contact pressure and the resulting wear of the surface, the CNP situated below the initial surface are brought into the tribological contact region. Finally, they are mixed with oxidic wear particles and Ni in a stochastic manner, all being compacted to form the observed surface layer. It can thus be concluded that, although the frictional behavior of the composites is obviously differing (see Fig. 9), the wear behavior under high contact pressure and medium relative humidity can be quite similar. The explanation on the formation of the observed surface sheets will be further verified using EDS mappings and TEM analysis in the following sections. In Fig. 13, the wear tracks are characterized by EDS-mapping in order to analyze the oxygen and carbon distribution.

The oxidation behavior of the reference wear track (Fig. 13a) has not significantly changed compared to the 0.1 N measurements. Still, the plowing mechanism reorders oxides and bare metal in a stochastic manner. In contrast to that, the formed layer, or individual sheets of the composite wear tracks show a homogeneous distribution of oxygen all over the wear track (Fig. 13b). This verifies that the formed sheets in fact consist of compacted oxidic wear particles. However, also carbon is homogeneously integrated into the surface sheets. Although the two originally contacting surfaces obviously cannot be separated anymore by CNP for high contact pressures (due to the formation of the surface layer), the lubrication effect is still active for CNT reinforced composites. Considering the gap between the sheets and the substrate in Fig. 12c, the cracking of the layer would allow the sheets to freely move during the tribological contact. Thus, it is reasonable, that the sheets could be separated from each other and from the substrate by the homogenously distributed CNP. In fact, a frictional reduction in case of CNT reinforced composites is observed in Fig. 9, which could be explained with the larger size and morphology of CNT, compared to nD or OLC [65]. Due to the large aspect ratio, CNT could be dragged into the direct tribological contact, providing a sliding and/or rolling movement or delaminate and form graphitic structures thus lubricating the system [30].

A material transfer from the composite surface to the alumina ball

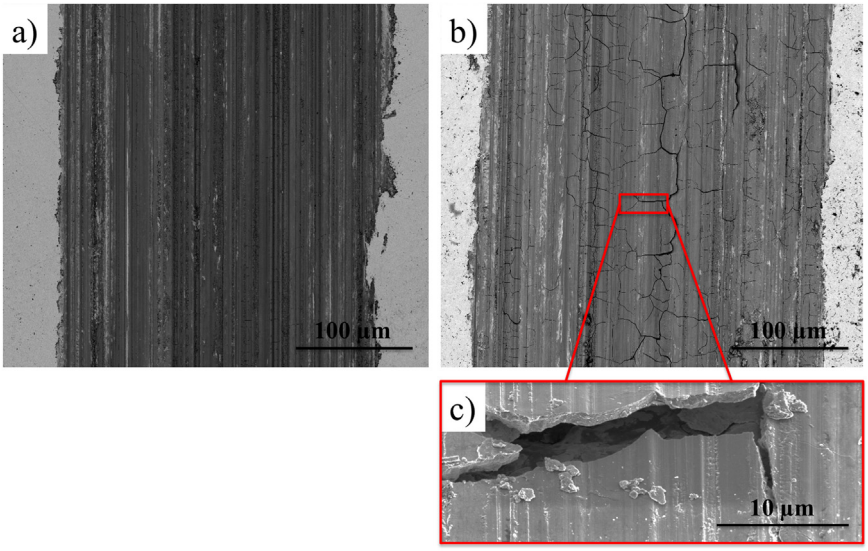

Fig. 12. Wear tracks for 8 N of normal load under 45% of relative humidity in case of a) the pure Ni reference and b) a composite reinforced with 20 vol.-% of CNT. The formation of loosely connected sheets on the surface of the wear track is depicted in a higher magnification in c).

has also been noticed for the high contact pressure experiments, vouching for a low adhesion of the surface sheets to the substrate. Thus, to extend the understanding of the composition of these sheets, a microstructural analysis with higher resolution is needed. Fig. 14 shows a TEM foil obtained from one of the sheets. It is observed that the sheet is of nanocrystalline nature and is composed of an intermixing of three different phases. It is predominantly composed of NiO, but traces of Ni and C are detected, verifying the explanations from above. As already mentioned, it can be interpreted that the ploughing mechanism acts as driving force for the formation of these multiphase plates. Furthermore, the high contact pressure applied would severely deform the microstructure of the sheet, inducing dynamic recrystallization and strongly reducing the grain size.

Regarding the carbon signal observed in Fig. 14b, it is not possible to precisely determine which morphology it would have. However, it can be unequivocally be related to carbon domains with a graphitic structure. A hypothesis for the formation of these sheets in case of the composite samples is the presence of carbon, which could act as a binder for the formed oxidic wear particles, allowing the formation of densified, but cracked sheets. However, an efficient lubrication is only given for CNT. The conclusion is therefore again fortified, that because of their larger size and high aspect ratio, CNT are able to separate the formed sheets and enable them to slide on each other and on the substrate. As nanocrystalline graphite is present in the sheets of all the CNP reinforced composites, it seems not to affect the COF significantly or the formed graphite flakes are too small to efficiently slide upon each other. Hence, lubrication is most likely based on sliding and/or rolling of CNT between the individual sheets.

3.6. Solid lubricant structural integrity assessment

The Raman spectra of the initial state CNP are shown in Fig. 15 and will be used as reference state in the analysis of the structural integrity of the solid lubricant.

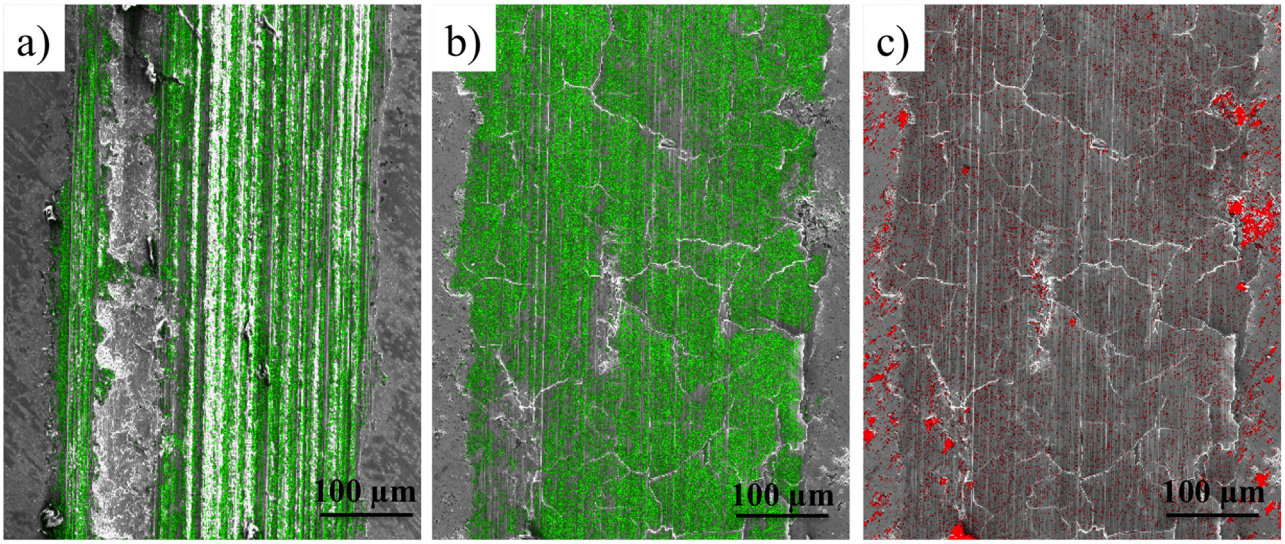

Fig. 13. EDS maps of oxygen (marked in the color green), superimposed with SEM images of the wear tracks for 8 N of normal load under 45% of relative humidity in case of a) the unreinforced reference and b) the composite reinforced with 20 vol.-% of CNT. In c), an EDS map of the carbon distribution (marked in the color red) of the wear track of the composite reinforced with 20 vol.-% of CNT is depicted. (For interpretation of the references to color in this figure legend, the reader is referred to the web version of this article.)

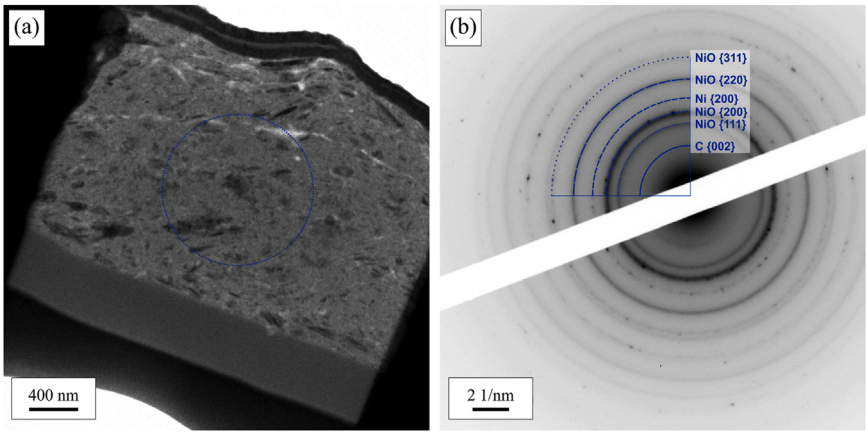

Fig. 14. (a) Transmission electron micrograph of a foil obtained from the sheet observed in the Ni/CNT 20 vol% samples tested with 8 N. The blue circle denotes the region where selected area electron diffraction was performed. (b) SAED pattern of the sample, where three different phases are identified (NiO, Ni and C). (For interpretation of the references to color in this figure legend, the reader is referred to the web version of this article.)

It is observed that all type of particles show a seemingly high structural quality in their initial state. It is worth noting that the homogeneity in the features is remarkable, as interpreted from the small standard deviation bars in the plots of the CNT and OLC particles. In the nD case, the signal-to-noise ratio is significant, as a result from the measurement of these particles with visible light excitation. Fig. 16 presents the Raman spectra acquired from the wear tracks for each sample type at different test loads and their corresponding relative humidity.

The reference sample shows the characteristic bands of NiO in both tested loads (Fig. 16a). Furthermore, the signal corresponding to Al_2O_3 is a consequence of material transfer from the counterpart during the experiment. As opposed to the reference case, all particle types show no detectable oxide peaks in the Raman characterization, likely as a consequence of the strong presence of carbon in the wear track, reducing to some extent the detection of oxides. However, as shown in the Section 3.4, oxide is indeed present in all cases. In the case of the CNT sample, there are no pronounced differences for both loads (Fig. 16b). When compared to the initial state of the CNTs (shown in Fig. 15a), the degradation is evident from the analysis of the intensity ratios and peak position, which is in agreement with the observations presented in Scharf et al. [30]. Specifically, the initial state CNTs have an I_D/I_G ratio of 0.68 and a G peak position of 1585.3 cm^{-1}, which correspond to CNTs with high degree of crystallinity. On the other hand, the post-test CNTs present an I_D/I_G ratio of 0.96 and 1.19 and a G peak position of 1603 and 1595 cm^{-1}, for 100 mN and 8 N respectively. The increment of the intensity ratio and the upshifting of the G band position vouch for a degradation of the CNTs [66] during the tribological contact, forming a lubricating nanocrystalline graphitic tribolayer, as already reported [30]. Regarding the OLC sample, the changes in the structural integrity of the particles is not as marked as in the CNT case (Fig. 16**c**), probably due to their inability to be effectively brought into contact during the test. This is supported by the values of the I_D/I_G ratio, which shows a change from 1.05 in the initial state (as observed from Fig. 15b) to 0.88 and 0.85 in the 100 mN and 8 N tests, respectively. Interestingly, the nD sample show strong resonance of the sp^2 carbon bands (Fig. 16d), which are theoretically present in very low volume fractions in the predominantly sp^3 nanodiamond (as a result of the synthesis by detonation) [23,67]. The observation of these bands is explained by the difference in the behavior of both hybridization states to the excitation with visible light. It has been reported that the sp^2 domains are up to 230 times more sensitive to visible light excitation than those with sp^3 hybridization, thus vanishing them in the background noise [57,58]. In any case, when compared to the initial state of the nD (Fig. 15c), the improvement in the sp^2 carbon crystallization becomes evident. It is still unclear and would be the subject of a report by itself, to which extent this sp^2 crystallization would influence the lubricity of this type of particles. However, as can be seen in Figs. 8 and 9, the COF is not affected by this fact.

Summarizing, the activity of the CNTs during lubrication is noticeable and more marked than the other nanoparticles studied. As already mentioned, this is a result of the different lubrication mechanisms shown by the particles, where only the CNTs could be straightforwardly dragged into the direct tribological contact during relative motion, as opposed to the case of the low aspect ratio particles (OLC and nD).

4. Conclusions

The present study investigates the dominant friction and wear mechanisms in case of dry sliding of carbon nanoparticle (CNT, OLC and nD) reinforced nickel matrix composites under elastic and elasto-plastic contact conditions. For the given materials and geometries and based on calculations using an extended Greenwood-Williamson model (Jackson-Green model), a critical normal load of 0.6 N is found below or above which the contact is either elastic or elasto-plastic. Measurements under elastic conditions were performed under 4% of relative humidity, thus excluding a graphite-based lubrication effect. It is shown that only CNT provide an efficient lubrication as

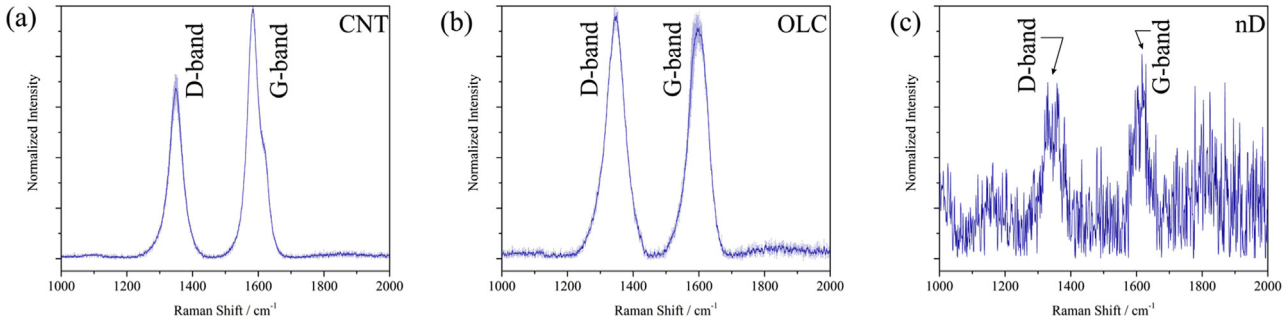

Fig. 15. Raman spectra of the initial state of (a) CNT, (b) OLC and (c) nD. The two main bands (G and D) of sp^2 carbon are identified in the figure.

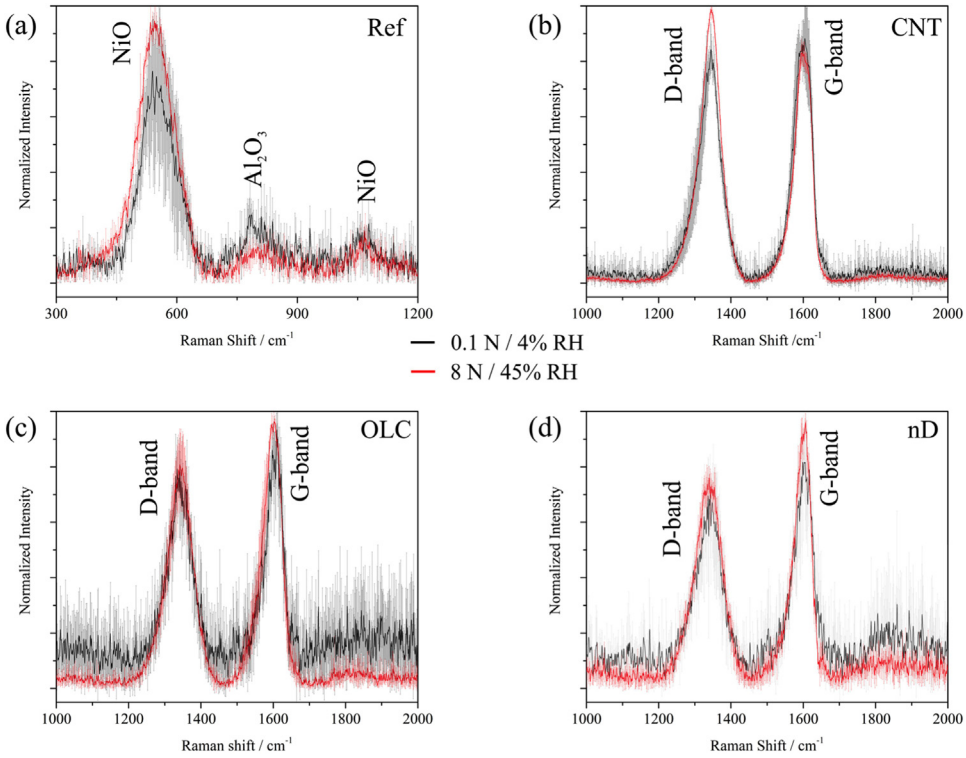

Fig. 16. Raman spectra of the wear tracks of (a) reference, (b) CNT, (c) OLC and (d) nD samples. All relevant indexed bands are identified in each figure. The red and black plots correspond in all cases to 100 mN/ 4% relative humidity and 8 N/ 45% relative humidity, respectively. (For interpretation of the references to color in this figure legend, the reader is referred to the web version of this article.)

reinforcement phase in composites with the lubrication mechanism being based on sliding and/or rolling of the tube-like particles. No lubrication is observed for "0D" particles, irrespective of their hybridization, thus the lubrication effect is further traced back to the large aspect ratio of CNT, allowing them to be dragged out of the surface cavities into the local direct tribological contact. For elasto-plastic contact conditions, the formation of dense, cracked, oxide-containing sheets is observed, which do not hinder CNT from efficiently lubricating the system. It is believed, that CNT are able to separate the sheets from each other and from the surface, hence allowing them to slide. The lubrication effect increases with increasing volume content of CNT, reaching a maximum steady state frictional reduction of 50% compared to the unreinforced nickel reference for elastic and elasto-plastic contact conditions for low and medium relative humidities. The present study highlights the potential of CNT as solid lubricant for self-lubricating metal matrix composites.

Acknowledgements

The present work is supported by funding from the Deutsche Forschungsgemeinschaft (DFG, project: MU 959/38-1 and SU 911/1-1). L. R., S.S., and F. M. wish to acknowledge the EFRE Funds of the European Commission for support of activities within the AME-Lab project. Prof. Dr. Volker Presser is acknowledged for providing the possibility to use Raman spectroscopy. This work was supported by the CREATe-Network Project, Horizon 2020 of the European Commission (RISE Project No. 644013).

Conflicts of Interest

The authors declare no conflict of interest.

References

[1] K. Holmberg, P. Andersson, A. Erdemir, Global energy consumption due to friction in passenger cars, Tribol. Int. 47 (2012) 221–234, http://dx.doi.org/10.1016/j.triboint.2011.11.022.

[2] C. Donnet, A. Erdemir, Solid lubricant coatings: recent developments and future trends, Tribol. Lett. 17 (2004) 389–397 (doi: 1023-8883/04/1000–0389/0).

[3] S.M. Aouadi, H. Gao, A. Martine, T.W. Scharf, C. Muratore, Lubricious oxide coatings for extreme temperature applications: a review, Surf. Coat. Technol. 257 (2014) 266–277, http://dx.doi.org/10.1016/j.surfcoat.2014.05.064.

[4] J.Y. Hwang, B.K. Lim, J. Tiley, R. Banerjee, S.H. Hong, Interface analysis of ultra-high strength carbon nanotube/nickel composites processed by molecular level mixing, Carbon 57 (2013) 282–287, http://dx.doi.org/10.1016/j.carbon.2013.01.075.

[5] S.R. Bakshi, A. Agarwal, An analysis of the factors affecting strengthening in carbon nanotube reinforced aluminum composites, Carbon 49 (2011) 533–544, http://dx.doi.org/10.1016/j.carbon.2010.09.054.

[6] D. Nunes, M. Vilarigues, J.B. Correia, P.A. Carvalho, Nickel–carbon nanocomposites: synthesis, structural changes and strengthening mechanisms, Acta Mater. 60 (2012) 737–747, http://dx.doi.org/10.1016/j.actamat.2011.10.012.

[7] D. Nunes, J.B. Correia, P.A. Carvalho, Nanodiamond dispersions in metallic matrices with different carbon affinity, Microsc. Microanal. 19 (2013) 2013, http://dx.doi.org/10.1017/S1431927613001220.

[8] V. Livramento, J.B. Correia, N. Shohoji, E. Ōsawa, Nanodiamond as an effective reinforcing component for nano-copper, Diam. Relat. Mater. 16 (2007) 202–204, http://dx.doi.org/10.1016/j.diamond.2006.05.008.

[9] J.N. Boland, X.S. Li, Microstructural characterisation and wear behaviour of diamond composite materials, Materials 3 (2010) 1390–1419, http://dx.doi.org/10.3390/ma3021390.

[10] L. Kumari, T. Zhang, G. Du, W. Li, Q. Wang, A. Datye, K. Wu, Thermal properties of CNT-Alumina nanocomposites, Compos. Sci. Technol. 68 (2008) 2178–2183, http://dx.doi.org/10.1016/j.compscitech.2008.04.001.

[11] A. Agarwal, S. Bakshi, D. Lahiri, Carbon Nanotubes - Reinforced Metal Matrix Composites, CRC press, 2011 (ISBN: 978-1-4398-1149-8).

[12] D. Nunes, J.B. Correia, P.A. Carvalho, Nanodiamond dispersions in nanostructured metals, Microsc. Microanal. 18 (2012) 73–74, http://dx.doi.org/10.1017/S1431927612013025.

[13] Y. Li, B.X. Li, W.J. Zou, The relationship between nanocrystalline structure and frictional properties of nanodiamond/ni composite coatings by brush plating, Appl. Mech. Mater. 80–81 (2011) 683–687, http://dx.doi.org/10.4028/www.scientific.net/AMM.80-81.683.

[14] A. Hirata, N. Yoshioka, Sliding friction properties of carbon nanotube coatings deposited by microwave plasma chemical vapor deposition, Tribol. Int. 37 (2004) 893–898, http://dx.doi.org/10.1016/j.triboint.2004.07.005.

[15] K. Miyoshi, K.W. Street Jr., R.L. Vander Wal, R. Andrews, A. Sayir, Solid lubrication by multiwalled carbon nanotubes in air and in vacuum, Tribol. Lett. 19 (2005) 191–201, http://dx.doi.org/10.1007/s11249-005-6146-4.

[16] L. Reinert, S. Suárez, A. Rosenkranz, Tribo-mechanisms of carbon nanotubes: friction and wear behavior of CNT-reinforced nickel matrix composites and CNT-coated bulk nickel, Lubricants 4 (2016) 11, http://dx.doi.org/10.3390/lubricants4020011.

[17] S. Suarez, L. Reinert, F. Mücklich, Carbon Nanotube (CNT)-Reinforced Metal Matrix Bulk Composites: Manufacturing and Evaluation, in: Diam. Carbon Compos. Nanocomposites, 2016. ⟨http://dx.doi.org/10.5772/63886⟩.

[18] Y. Gogotsi, V. Presser, Carbon Nanomaterials, CRC press, 2014 (ISBN: 13-978-1-4665-0242-0).
[19] S.R. Bakshi, D. Lahiri, A. Agarwal, Carbon nanotube reinforced metal matrix composites - a review, Int. Mater. Rev. 55 (2010) 41–64, http://dx.doi.org/10.1179/095066009×12572530170543.
[20] V.N. Mochalin, O. Shenderova, D. Ho, Y. Gogotsi, The properties and applications of nanodiamonds, Nat. Nanotechnol. 7 (2012) 11–23, http://dx.doi.org/10.1038/nnano.2011.209.
[21] S. Iijima, Helical microtubules of graphitic carbon, Nature 354 (1991) 56–58.
[22] J. Cebik, J.K. McDonough, F. Peerally, R. Medrano, I. Neitzel, Y. Gogotsi, S. Osswald, Raman spectroscopy study of the nanodiamond-to-carbon onion transformation, Nanotechnology 24 (2013) 1–10, http://dx.doi.org/10.1088/0957-4484/24/20/205703.
[23] M. Zeiger, N. Jäckel, M. Aslan, D. Weingarth, V. Presser, Understanding structure and porosity of nanodiamond-derived carbon onions, Carbon 84 (2015) 584–598, http://dx.doi.org/10.1016/j.carbon.2014.12.050.
[24] K.T. Kim, S. Il Cha, S.H. Hong, Hardness and wear resistance of carbon nanotube reinforced Cu matrix nanocomposites, Mater. Sci. Eng. A 449–451 (2007) 46–50, http://dx.doi.org/10.1016/j.msea.2006.02.310.
[25] X.H. Chen, J. Peng, F. Deng, J. Wang, W. Li, Tribological behavior of carbon nanotubes — reinforced nickel matrix composite coatings, J. Mater. Sci. Lett. 20 (2001) 2057–2060.
[26] X.H. Chen, C.S. Chen, H.N. Xiao, H.B. Liu, L.P. Zhou, S.L. Li, G. Zhang, Dry friction and wear characteristics of nickel/carbon nanotube electroless composite deposits, Tribol. Int. 39 (2006) 22–28, http://dx.doi.org/10.1016/j.triboint.2004.11.008.
[27] S. Arai, A. Fujimori, M. Murai, M. Endo, Excellent solid lubrication of electrodeposited nickel-multiwalled carbon nanotube composite films, Mater. Lett. 62 (2008) 3545–3548, http://dx.doi.org/10.1016/j.matlet.2008.03.047.
[28] A. Sanaty-Zadeh, Comparison between current models for the strength of particulate-reinforced metal matrix nanocomposites with emphasis on consideration of Hall–Petch effect, Mater. Sci. Eng. A 531 (2012) 112–118, http://dx.doi.org/10.1016/j.msea.2011.10.043.
[29] M.R. Falvo, R.M.T. Ii, A. Helser, V. Chi, Nanometre-scale rolling and sliding of carbon nanotubes, Nature 397 (1999) 1–3.
[30] T.W. Scharf, A. Neira, J.Y. Hwang, J. Tiley, R. Banerjee, Self-lubricating carbon nanotube reinforced nickel matrix composites, J. Appl. Phys. 106 (2009) 13508, http://dx.doi.org/10.1063/1.3158360.
[31] J.J. Hu, S.H. Jo, Z.F. Ren, A. Voevodin, J.S. Zabinski, Tribological behavior and graphitization of carbon nanotubes grown on 440C stainless steel, Tribol. Lett. 19 (2005) 119–125, http://dx.doi.org/10.1007/s11249-005-5091-6.
[32] F. Colonna, A. Fasolino, E.J. Meijer, Graphitization of single-wall nanotube bundles at extreme conditions: collapse or coalescence route, Phys. Rev. B 88 (2013) 165416, http://dx.doi.org/10.1103/PhysRevB.88.165416.
[33] P.L. Dickrell, S.K. Pal, G.R. Bourne, C. Muratore, a.a. Voevodin, P.M. Ajayan, L.S. Schadler, W.G. Sawyer, Tunable friction behavior of oriented carbon nanotube films, Tribol. Lett. 24 (2006) 85–90, http://dx.doi.org/10.1007/s11249-006-9162-0.
[34] C.-C. Chou, S.-H. Lee, Tribological behavior of nanodiamond-dispersed lubricants on carbon steels and aluminum alloy, Wear 269 (2010) 757–762, http://dx.doi.org/10.1016/j.wear.2010.08.001.
[35] L. Wang, Y. Gao, Q. Xue, H. Liu, T. Xu, Effects of nano-diamond particles on the structure and tribological property of Ni-matrix nanocomposite coatings, Mater. Sci. Eng. A 390 (2005) 313–318, http://dx.doi.org/10.1016/j.msea.2004.08.033.
[36] V.Y. Dolmatov, T. Fujimura, G.K. Burkat, E.A. Orlova, M.V. Veretennikova, Preparation of wear-resistant chromium coatings using different types of nanodiamonds, Powder Metall. Met. Ceram. 42 (2003) 55–59 (doi: 1068-1302/03/1112-0587).
[37] S. Park, D. Srivastava, K. Cho, Generalized chemical reactivity of curved surfaces: carbon nanotubes, Nano Lett. 3 (2003) 1273–1277, http://dx.doi.org/10.1021/nl0342747.
[38] K.W. Street, M. Marchetti, R.L. Vander Wal, A.J. Tomasek, Evaluation of the tribological behavior of nano-onions in Krytox 143AB, Tribol. Lett. 16 (2004) 143–149 (doi: 1023-8883/04/0200–0143/0).
[39] A. Hirata, M. Igarashi, T. Kaito, Study on solid lubricant properties of carbon onions produced by heat treatment of diamond clusters or particles, Tribol. Int. 37 (2004) 899–905, http://dx.doi.org/10.1016/j.triboint.2004.07.006.
[40] E.W. Bucholz, S.R. Phillpot, S.B. Sinnott, Molecular dynamics investigation of the lubrication mechanism of carbon nano-onions, Comput. Mater. Sci. 54 (2012) 91–96, http://dx.doi.org/10.1016/j.commatsci.2011.09.036.
[41] L. Reinert, M. Zeiger, S. Suarez, V. Presser, F. Mücklich, Dispersion analysis of carbon nanotubes, carbon onions, and nanodiamonds for their application as reinforcement phase in nickel metal matrix composites, RSC Adv. 5 (2015) 95149–95159, http://dx.doi.org/10.1039/C5RA14310A.
[42] L. Reinert, S. Suarez, T. Müller, F. Mücklich, Carbon nanoparticle-reinforced metal matrix composites: microstructural tailoring and predictive modeling, Adv. Eng. Mater. 19 (2017) 1–6, http://dx.doi.org/10.1002/adem.201600750.
[43] S. Suarez, F. Lasserre, F. Mücklich, Mechanical properties of MWNT/Ni bulk composites: influence of the microstructural refinement on the hardness, Mater. Sci. Eng. A 587 (2013) 381–386, http://dx.doi.org/10.1016/j.msea.2013.08.058.
[44] J. Greenwood, J. Williamson, Contact of nominally flat surfaces, Proc. R. Soc. Lond. 295 (1966) 300–319, http://dx.doi.org/10.1098/rspa.1966.0242.
[45] L. Kogut, I. Etsion, Elastic-plastic contact analysis of a sphere and a rigid flat, J. Appl. Mech. 69 (2002) 657–662.
[46] W.R. Chang, I. Etsion, D.B. Bogy, An elastic-plastic model for the contact of rough surfaces, J. Tribol. 109 (1987) 257–263.
[47] Y. Zhao, D.M. Maietta, L. Chang, An asperity microcontact model incorporating the transition From elastic deformation to fully plastic flow, J. Tribol. 122 (1999) 86–93.
[48] R.L. Jackson, I. Green, A statistical model of elasto-plastic asperity contact between rough surfaces, Tribol. Int. 39 (2006) 906–914, http://dx.doi.org/10.1016/j.triboint.2005.09.001.
[49] J.I. McCool, Relating profile instrument measurements to the functional performance of rough surfaces, Trans. ASME 109 (1987) 264–270.
[50] R. Jackson, I. Green, On the modeling of elastic contact between rough surfaces, Tribol. Trans. 54 (2011) 300–314, http://dx.doi.org/10.1080/10402004.2010.542277.
[51] I. Green, Poisson ratio effects and critical valus in spherical and cylindrical Hertzian contacts, Int. J. Appl. Mech. Eng. 10 (2005) 451–462.
[52] H. Hertz, Über die Berührung von elastischen festen Körpern, J. Für Die Reine Und Angew. Math. 92 (1881).
[53] R. Jackson, M. ASME, I. Chusoipin, I. Green, A finite element study of the residual sress and deformation in hemispherical contacts, J. Tribol. 127 (2005), http://dx.doi.org/10.1115/1.1843166.
[54] D. Berman, A. Erdemir, A.V. Sumant, Graphene: a new emerging lubricant, Mater. Today 17 (2014) 31–42, http://dx.doi.org/10.1016/j.mattod.2013.12.003.
[55] B.K. Yen, T. Ishihara, Effect of humidity on friction and wear of Al-Si eutectic alloy and Al-Si alloy-graphite composites, Wear 198 (1996) 169–175.
[56] R.H. Savage, Graphite lubrication, J. Appl. Phys. 19 (1948) 1, http://dx.doi.org/10.1063/1.1697867.
[57] S.R. Sails, D.J. Gardiner, M. Bowden, J. Savage, D. Rodway, Monitoring the quality of diamond films using Raman spectra excited at 514.5 nm and 633 nm, Diam. Relat. Mater. 5 (1996) 589–591, http://dx.doi.org/10.1016/0925-9635(96)90031-X.
[58] O.O. Mykhaylyk, Y.M. Solonin, D.N. Batchelder, R. Brydson, Transformation of nanodiamond into carbon onions: a comparative study by high-resolution transmission electron microscopy, electron energy-loss spectroscopy, x-ray diffraction, small-angle x-ray scattering, and ultraviolet Raman spectroscopy, J. Appl. Phys. 97 (2005) 1–16, http://dx.doi.org/10.1063/1.1868054.
[59] A. Ferrari, J. Robertson, Resonant Raman spectroscopy of disordered, amorphous, and diamondlike carbon, Phys. Rev. B 64 (2001) 75414, http://dx.doi.org/10.1103/PhysRevB.64.075414.
[60] K. Johnson, Contact Mechanics, Cambridge Univ. Press, 1985 (ISBN: 0-521-25576-7).
[61] R.L. Jackson, I. Green, A finite element study of elasto-plastic hemispherical contact against a rigid flat, J. Tribol. 127 (2005) 343–354.
[62] F. Banhart, Interactions between metals and carbon nanotubes: at the interface between old and new materials, Nanoscale 1 (2009) 201–213, http://dx.doi.org/10.1039/b9nr00127a.
[63] P.J. Blau, On the nature of running-in, Tribol. Int. 38 (2005) 1007–1012, http://dx.doi.org/10.1016/j.triboint.2005.07.020.
[64] M. Shafiei, A.T. Alpas, Friction and wear mechanisms of nanocrystalline nickel in ambient and inert atmospheres, Metall. Mater. Trans. A. 38 (2007) 1621–1631, http://dx.doi.org/10.1007/s11661-007-9157-y.
[65] L. Reinert, S. Schütz, S. Suarez, F. Mücklich, Influence of surface roughness on the lubrication effect of carbon nanoparticle-coated steel surfaces, Tribol. Lett. 66 (2018), http://dx.doi.org/10.1007/s11249-018-1001-6.
[66] A. Ferrari, J. Robertson, Interpretation of Raman spectra of disordered and amorphous carbon, Phys. Rev. B. 61 (2000) 14095–14107, http://dx.doi.org/10.1103/PhysRevB.61.14095.
[67] S. Suarez, L. Reinert, M. Zeiger, V. Presser, P. Miska, F. Müller, F. Mücklich, In-situ nanodiamond to onion-like carbon transformation in metal matrix composites, Carbon 129 (2017) 631–636, http://dx.doi.org/10.1016/j.carbon.2017.12.072.

IX Dry friction and wear of self-lubricating carbon nanotube-containing surfaces

Leander Reinert[1], Michael Varenberg[2], Frank Mücklich[1] and Sebastian Suárez[1]

[1] Department of Material Science and Engineering, Saarland University, 66123 Saarbrücken, Germany
[2] George W. Woodruff-School of Mechanical Engineering, Georgia Institute of Technology, Atlanta, USA

Published in ***"Wear" (Impact factor (2018): 2.960)***
Accessible online at: https://doi.org/10.1016/j.wear.2018.03.021

Own contribution:

Planning and coordination of sample processing, Surface analysis by laser scanning microscopy; Tribological experiments including friction coefficient and quantitative wear analysis; Scanning electron microscopy including particle distribution and wear track analysis; Raman spectroscopy; Electron backscatter diffraction analysis; Electron dispersive spectroscopy analysis; Writing; Discussion; Planning.

Abstract:

The unfavorable environmental conditions of certain tribological systems, such as operation at high temperatures or under vacuum, set the need to replace liquid with solid lubricants. Multi-Wall-Carbon Nanotubes (MWCNTs) have been emphasized as a very effective solid lubricant. The particles have been used to create self-lubricating materials by acting as reinforcement phase in composites or as solid-lubricant coating that works in conjunction with textured surfaces to prevent the removal of particles from the contact. However, both approaches are restricted to some extent. In the case of composites, the solid lubricant concentration is limited so as not to influence the mechanical stability of the final component. For coated surface structures, the textured surfaces can degrade during the experiment. The present study focuses on the combination of these approaches in order to create enhanced self-lubricating surfaces with MWCNTs as the solid lubricant. A custom-made ring on block tribometer is used to study the behavior of laser textured MWCNT-coated and MWCNT-reinforced nickel matrix composites under the conditions of unidirectional sliding in conformal contact. It is shown that the combination of both approaches allows for a maximum 4-fold reduction in friction and a 115-fold reduction in wear rate compared to the reference. Additionally, the lubrication mechanism of the MWCNTs is investigated in more detail and a structural degradation model of the mechanically stressed MWCNTs is proposed. Our results highlight the integrated solution as a suitable approach for self-lubricating surfaces subjected to unidirectional sliding

Cite this as:
L. Reinert, M. Varenberg, F. Mücklich, S. Suarez, Dry friction and wear of self-lubricating carbon nanotube-containing surfaces. *Wear* **2018**, 406-407, 33-42. (*https://doi.org/10.1016/j.wear.2018.03.021*)

Wear 406–407 (2018) 33–42

Contents lists available at ScienceDirect

Wear

journal homepage: www.elsevier.com/locate/wear

Dry friction and wear of self-lubricating carbon-nanotube-containing surfaces

Leander Reinert[a,*], Michael Varenberg[b], Frank Mücklich[a], Sebastian Suárez[a]

[a] Department of Materials Science, Saarland University, Campus D3.3, D-66123 Saarbrücken, Germany
[b] George W. Woodruff School of Mechanical Engineering, Georgia Institute of Technology, Atlanta, USA

ARTICLE INFO

Keywords:
Self-lubricating
Carbon nanotubes, Solid lubrication, Metal matrix composites
Laser texturing
Coating

ABSTRACT

The unfavorable environmental conditions of certain tribological systems, such as operation at high temperatures or under vacuum, set the need to replace liquid with solid lubricants. Multi-Wall-Carbon Nanotubes (MWCNTs) have been emphasized as a very effective solid lubricant. The particles have been used to create self-lubricating materials by acting as reinforcement phase in composites or as solid-lubricant coating that works in conjunction with textured surfaces to prevent the removal of particles from the contact. However, both approaches are restricted to some extent. In the case of composites, the solid lubricant concentration is limited so as not to influence the mechanical stability of the final component. For coated surface structures, the textured surfaces can degrade during the experiment. The present study focuses on the combination of these approaches in order to create enhanced self-lubricating surfaces with MWCNTs as the solid lubricant. A custom-made ring-on-block tribometer is used to study the behavior of laser textured MWCNT-coated and MWCNT-reinforced nickel matrix composites under the conditions of unidirectional sliding in conformal contact. It is shown that the combination of both approaches allows for a maximum 4-fold reduction in friction and a 115-fold reduction in wear rate compared to the reference. Additionally, the lubrication mechanism of the MWCNTs is investigated in more detail and a structural degradation model of the mechanically stressed MWCNTs is proposed. Our results highlight the integrated solution as a suitable approach for self-lubricating surfaces subjected to unidirectional sliding.

1. Introduction

In almost every technical system, motion is realized through various types of bearings. Their tribological optimization with respect to the material [1], the surface design [2,3] and the lubrication type [4] is an important task. The effective lubrication of a bearing is often achieved using a liquid lubricant. However, the use of solid instead of liquid lubricants can be advantageous in cases of unfavorable environmental conditions such as high temperatures or vacuum [5,6].

There is a wide variety of solid lubricants, such as MoS_2, WS_2 or graphite [5,6]. However, they also show restrictions with regard to their operational environment [5]. For example, MoS_2 is only used in applications working under vacuum or inert gas, since it can react with oxygen in an atmospheric environment and lose its lubrication abilities [5]. In contrast, graphite shows efficient lubrication exclusively under moderate to high relative humidity. In cases of low relative humidity or vacuum, a high coefficient of friction is observed because its lubrication mechanism relies on the intercalation of consecutive graphene layers by water molecules [7].

Recently, Multi-Wall Carbon Nanotubes (MWCNT) have been identified as very promising candidates to reduce friction and wear for a wide span of operational conditions, such as surface roughness, relative humidity, temperature, and environmental pressure [8–17]. Their ability to act as solid lubricant is based on their outstanding material properties and cylindrical shape built from multiple hollow graphitic shells with high aspect ratio [18–21].

There are different theories about the lubrication mechanism of MWCNT. Dickrell et al. showed a frictional anisotropy effect, particularly in case of CNT coatings [22,23]. CNT that are aligned horizontally to a surface show a much lower coefficient of friction than CNT aligned perpendicularly to the surface. It was concluded that CNT possess the ability to efficiently separate the sliding surfaces and are able to slide and/or roll on the surfaces. This theory is backed up by atomic force microscope experiments that measured the lateral forces involved in generating a sliding or a rolling motion of a single MWCNT on a graphitic surface [21]. In continuation of this work, a so called “tank-belt” model describing the CNT rolling motion as similar to that of a deformed chain rolling between two contacting surfaces under shear has

* Correspondence to: Saarland University, Campus D3.3, Saarbrücken D-66123, Germany.
E-mail address: l.reinert@mx.uni-saarland.de (L. Reinert).

https://doi.org/10.1016/j.wear.2018.03.021
Received 1 March 2018; Received in revised form 28 March 2018; Accepted 29 March 2018
Available online 03 April 2018

been also reported [24,25]. On the other hand, there is also work on fullerene-like nanoparticles used as oil additives, where the authors state that the nanoparticles cannot act as rolling bodies if the observed friction coefficient significantly exceeds that typical for rolling [26]. Interestingly, under high pressure and shear, the strong deformation of the CNT can result in the delamination of flake-like graphitic structures and the formation of carbonaceous layers on the surface, providing low shear strength similar to graphite lubrication [11,27,28]. Aside from experiments, simulations have shown that in the case of high temperatures, a pressure-induced transformation of CNT towards graphite may take place [29]. Due to the promising lubrication effects, CNTs have been used as coatings or reinforcement phases in composites [8,9,11,16,22,27,28,30].

In self-lubricating materials, metal matrix composites are of much interest due to their high technological relevance, the ability to tailor their microstructure and the possibility to incorporate solid lubricants as reinforcement phases [31–34]. For example, it is well known that the microstructures of composites, and thus their mechanical and tribological properties, can be adjusted by varying the type and amount of the reinforcement phase [35–37]. This is mainly attributed to a grain refinement control (pinning effect), which leads to higher strength of the composite. Furthermore, the particles might hinder the dislocation mobility, thus retarding the plastic deformation of the surfaces. Finally, a continuous supply of solid lubricant (i.e. CNT) can be ensured with ongoing wear of the surface, providing constant lubrication [9,11,30]. However, the amount of reinforcement phase is limited so as not to affect the mechanical integrity of the sintered composite.

An alternative to increase the amount of solid lubricant in a contact is to have a surface with regular depressions filled with the solid lubricant [10,38–41]. For CNT, this approach has been previously explored using direct laser interference patterning (DLIP) of steel surfaces in combination with a CNT coating produced by electrophoretic deposition (EPD) [10]. It was shown that the duration of the lubrication effect can be extended by a factor of at least five compared to a CNT-coated flat steel surface. This is due to the storage of CNTs in the surface depressions, preventing the removal of the CNTs from the contact and enabling a constant supply of solid lubricant.

The present study aims at combining both aforementioned approaches (CNT-reinforced metal matrix composites and laser-textured CNT-coated surfaces) in order to improve the self-lubricating ability of the surface. The study is also driven by the need to understand the lubrication mechanisms of CNTs, so that they can be used as solid lubricant in the most efficient way.

2. Materials and methods

2.1. Composite production

In this work, MWCNTs having a diameter of 20–85 nm and a length of 5–15 μm were purchased from Graphene Supermarket (USA). In their as-received form, the MWCNTs form agglomerates with a mean size of about 1 mm in diameter. In order to use the MWCNT as reinforcement phase in nickel matrix composites, they have to be disentangled, which is done using a colloidal dispersion and mixing process. For this process, ethylene glycol is used as a solvent, as it allows for fine and stable dispersions of MWCNTs [30,35,36,42]. Dispersing the nanoparticles in the solvent was done using a shear mixer (Ultra-turrax T-25 by IKA) for 5 min, followed by treatment in an ultrasonic bath (Sonorex Super RK 514 BH by Bandelin, 860 W, 35 kHz) for another 20 min. According to previous studies, this process allows for the best dispersion if particle surface functionalization is avoided and if it does not greatly influence the structural integrity of the particles [36]. Subsequently, Ni dendritic powder (Alfa Aesar, −325 mesh size) is added and mixed with the CNTs dispersed in the solvent using the shear mixer, so as to obtain a concentration of 20 vol.-% of MWCNTs in the Ni powder. Since Nickel only forms metastable carbides under very specific conditions, it

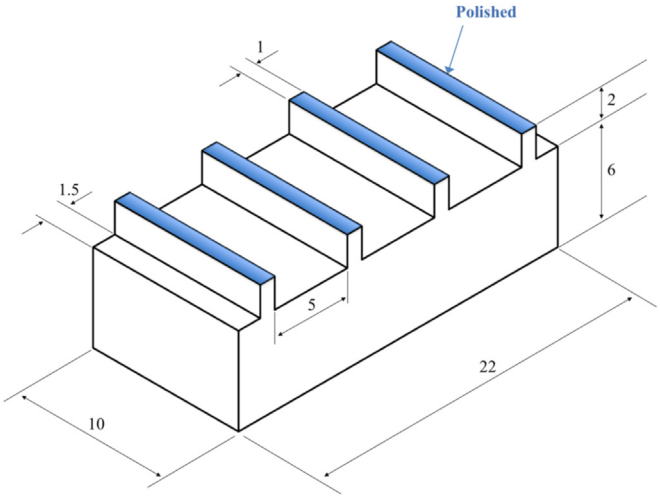

Fig. 1. Schematic of a machined sample. The sizes are in mm.

appears to be well suited for the presented study [42,43]. After evaporating the solvent in a furnace at 150 °C, the obtained powder is precompacted to green pellets with a diameter of 25.4 mm using a pressure of 420 MPa and sintered in a hot uniaxial press under vacuum and axial pressure of 40 MPa at 750 °C for 4 h. The heating and cooling rate is set to 10 °C/min. Additionally, an unreinforced pure Nickel reference is produced under the same conditions. With the given parameters, a densification of at least 95% is reached. The sintering parameters have been chosen based on a previously developed model predicting the final microstructure of these composites after sintering [35]. After the densification process, the cylindrical samples are ground flat on both sides and are polished using a diamond slurry containing diamond particles of 3 μm in diameter on one side. Subsequently, the polished composites are machined to the dimensions given in Fig. 1 and are cleaned with acetone and isopropanol in an ultrasonic bath in order to remove all surface contaminants. The geometrical shape of a block with teeth is needed in order to allow testing in the ring-on-block tribometer described in Section 2.4.

2.2. Laser texturing

Direct laser writing (DLW) using a femtosecond pulsed laser system is deployed to create surface depressions by ablation of the surface of CNT-reinforced metal matrix composites. Compared to DLIP, this process allows for the production of larger lubricant-storing surface depressions as well as higher load-bearing capacity. These effects are achieved by avoiding melting, bulging and resolidification of the surface, which can result in increased roughness [44–46]. Accordingly, the teeth of one of the machined 20 vol.-% of MWCNT-reinforced composite samples are laser textured using a femtosecond pulsed laser system (Spectra-Physics, Ti:Sapphire laser) with a pulse length of 100 fs and a wavelength of 800 nm. The beam (diameter of 8 mm) is focused on the sample surface by a lens in order to achieve a laser spot size of 15 μm. The sample is mounted on a motorized stage, which can perform a two-dimensional linear movement. The processed teeth of the block are moved through the laser beam in a meander-like pattern, thus creating a line-like structure oriented in parallel to the tooth's length. The distance from line-to-line (structural periodicity) is 50 μm providing a line width, according to the laser spot size, of 15 μm. With the laser pulse frequency being 1 kHz, the velocity of the stage is chosen to be 6.5 mm/s, so that the individual laser pulses overlap, and an almost constant structural depth of 1 μm can be obtained using a mean laser power of 35 mW. This structure is chosen intentionally, as it only slightly increases the value of the core roughness R_k of the surface compared to the reference surface, but still provides the possibility to store a large

amount of solid lubricant [45]. Furthermore, large polished areas (width of 35 μm) are provided between the line-like depressions, allowing MWCNTs to perform complex motions and/or to be destroyed at the interface while separating the contacting surfaces. On the other hand, the structural periodicity is chosen not to be too large, so that the tribological contact can be efficiently supplied with MWCNTs stored in the depressions and so that at least 20 line-like depressions get in contact for each individual tooth of the machined sample.

2.3. Electrophoretic deposition (EPD)

With regard to the CNT coatings, EPD has been found most suitable for the present study, being an easily scalable technique for depositing CNT films with a homogeneous thickness on different materials and complex textured surfaces [10,47]. It is based on the motion of charged particles in an electric field and the subsequent adhesion/physisorption of these particles onto an electrode substrate in a fluid medium. For the deposition process, the laser-textured block sample is used as anode and a steel block of the same dimensions is used as cathode. The blocks are cleaned stepwise using cyclohexane, acetone and isopropanol in the ultrasonic bath for 10 min, respectively. A dispersion of MWCNTs in acetone with a concentration of 0.25 mg ml^{-1} is prepared using the same dispersion method as described in Section 2.1. Hereupon, 3 ml of triethylamine (TEA) are added to the dispersion. This is done in order to add negatively charged COO^- surface groups to the outer layer of the MWCNTs, which allows for their deposition on the anode in an electric field [48]. Finally, using a constant voltage of 20 V for 10 min in a custom-built deposition cell, the sample is coated with MWCNTs. During this process, a distance of 1.3 cm between the teeth of the composites and the steel block is kept constant.

2.4. Tribological testing

Friction and wear tests were performed on a custom-built ring-on-block tribometer allowing for experiments under conditions of conformal contact with a constant contact area at the steady state regime (schematically presented in Fig. 2). The tribometer consists of a DC-motor-driven precise spindle and a loading frame that is able to rotate as well as to move radially with respect to the spindle's axis. A ring sample is fixed to the spindle's axis.

The ring, made out of mild steel SAE 1045, has an outer diameter of 38 mm, a Vickers hardness of HV 320 and is polished to a surface finish of R_a = 0.02 μm followed by a cleaning of the surface using acetone and isopropanol. The ring rotates with the speed ω = 250 rpm. Below the ring is the block sample that has four teeth of a cross sectional area S = 20 mm^2 each (Fig. 1). The block is fixed to the loading frame and is pressed against the rotating ring under a normal load of L = 20 N. The normal load is applied by a linear actuator that is controlled in a closed loop using the feedback received from a normal force transducer. The shape and the self-aligning ability of the block sample ensure that, after the running-in is finished, the area of contact between the samples does not change, and the wear volume can be calculated as V = Δd·S, where S is the cross sectional area of the tooth brought in contact with the ring, and Δd is the change in distance d measured by a proximity probe. A friction moment, M_f, that is produced due to the sliding between the ring and the block, pushes the loading frame around the spindle's axis, but its motion is stopped by a force transducer allowing the friction force, F, to be quantified. The effect of friction produced by a rotary bearing is cancelled by proper calibration of the friction force transducer. The experiments were conducted under conditions of 40% of relative humidity and a temperature of 25 °C.

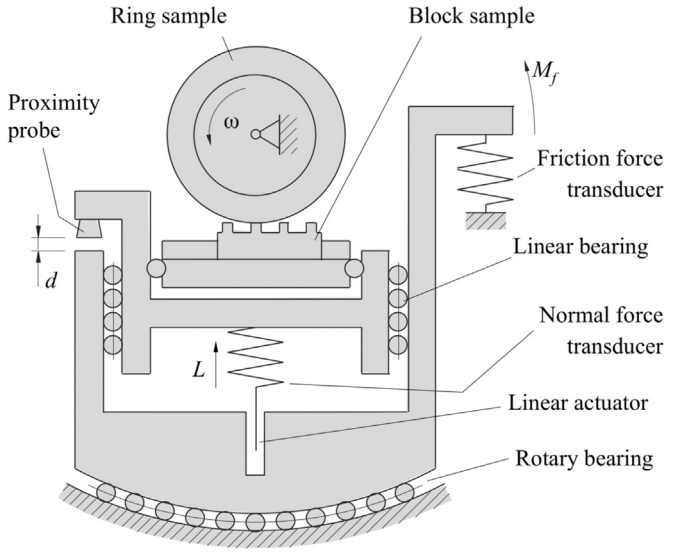

Fig. 2. Schematic of the ring-on-block tribometer, which illustrates the working principle of the device tribometer and the installation position of the block sample (depicted in Fig. 1). The individual teeth of the block sample have been laser structured and coated with MWCNT.

2.5. Characterization methods

The initial state characterization as well as the wear track analysis is performed using a focused ion beam/field emission (dual beam) SEM workstation (FEI Helios NanoLab 600). SEM micrographs and EDS maps are recorded with an accelerating voltage of 5 kV and current of 1.4 nA or 22 nA, respectively. The mean grain size and grain orientation of the composites is determined by EBSD with an EDAX TSL detector incorporated in the dual beam microscope. For the EBSD measurement, an accelerating voltage of 20 kV and a current of 22 nA is applied, scanning an area of 400 × 400 $μm^2$ with a step size of 0.3 μm. The acquired data is post-processed using confidence index (CI) standardization in addition to the removal of points with CI below 0.1. A grain is defined as at least two adjacent points with a maximum misorientation of 5°, beyond which a grain boundary is detected. The grains overlapping with the scan window are excluded from the analysis.

The structural integrity assessment of the MWCNTs is carried out by Raman spectroscopy analysis. For this purpose, an inVia Raman microscope (Renishaw) is used with an excitation wavelength of 532 nm (2.33 eV), a grating of 2400 lines mm^{-1}, a 50X-objective (numerical aperture: 0.9), a spectral resolution of 1.2 cm^{-1}, and a laser power of 0.2 mW. The data acquisition time is 10 s and each measurement is performed three times for statistical back up. The data is finally processed using a linear baseline subtraction and intensity normalization, followed by a fitting based on the Lorentz function in order to identify the peak positions [49]. Vickers microhardness is measured with a Vickers microindenter (Durascan, Struers) using an indentation force of 0.98 N ($HV_{0.1}$) and a holding time of 10 s. For each sample, 12 measurements at different spots were conducted and averaged.

3. Results and discussion

3.1. Initial state characterization

Before tribological testing, the samples were analyzed with regard to the MWCNT distribution in the composite and the microstructure of the Nickel matrix. In Fig. 3, EBSD maps of the unreinforced nickel reference and the reinforced composite, as well as an SEM micrograph of the composite surface, are shown. According to the color-coding of the grain orientations of the reference sample as well as the reinforced composite sample, no preferred grain orientation is found in either case.

Furthermore, it is clearly noticeable that the grain size is drastically reduced from a mean grain size of 29 ± 19 μm of the unreinforced reference to a mean grain size of 4.5 ± 2 μm in the case of the reinforced composite. This effect is well-known and is attributed to the

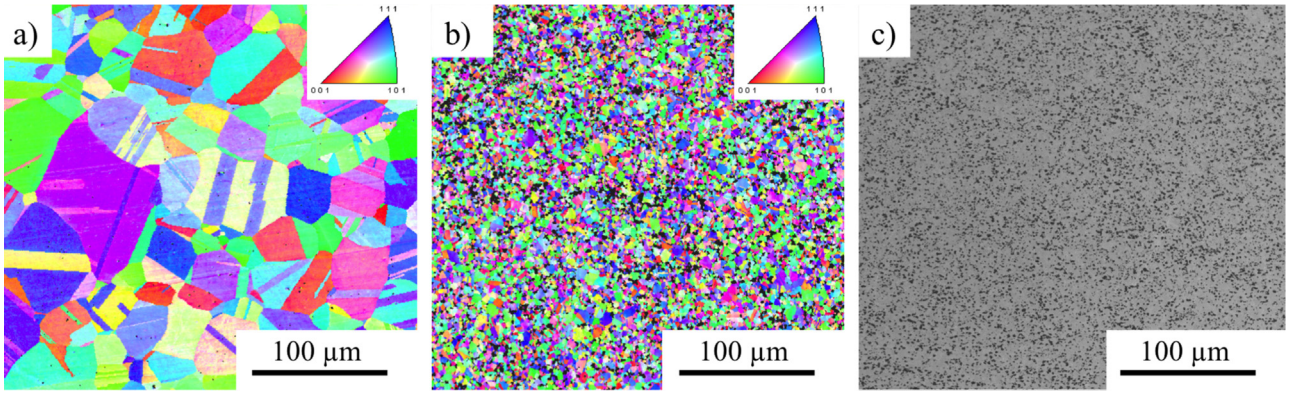

Fig. 3. EBSD maps of a) the unreinforced pure Nickel reference and b) the 20 vol.-% of MWCNT-reinforced composite. The fine and homogeneous distribution of MWCNT agglomerates (black dots) in the nickel matrix (grey) is depicted in c).

Zener pinning effect of CNTs in a metal matrix, resulting in a hindered grain boundary movement during sintering [50]. Due to the hindered grain boundary mobility, the grains are not able to freely grow; thus the mean grain size after sintering is reduced to a significant degree compared to the unreinforced reference. This fact also results in a higher hardness of the reinforced sample due to the Hall-Petch effect of 118 ± 2 HV of the composite compared to 108 ± 4 HV of the unreinforced reference [51,52]. As was already reported for CNT-reinforced Cu matrix composites, with a higher hardness of the composite a lower wear rate is expected [12].

Additionally, one of the MWCNT-reinforced composites is laser textured using DLW with a femtosecond pulsed laser system and subsequently coated with MWCNTs using EPD. The surface of the laser-textured composite surface before and after coating with MWCNT agglomerates is depicted in Fig. 4**a** and **b**.

From the cross-section shown in Fig. 4**c**, it can be seen that the applied laser texturing provides a structural periodicity of 50 µm with a width of 15 µm for the line-like depressions. The depth of the depressions is 1 µm. The coating thickness of 5–10 µm is measured using a FIB cross-section in Fig. 4**d**. It is evident that the laser-machined depressions are completely covered with the CNT coating.

For tribological experiments, it has to be kept in mind that a DLW process may induce a slightly higher surface oxidation within the irradiated areas [45]. No microstructure changes or phase transformations are expected, as the laser-material interaction in a femtosecond laser system is not long enough to induce thermalization, resulting only in the material ablation. Hence, recrystallization of the surface is excluded [46].

3.2. Friction and wear

The unreinforced Ni reference sample (Ref), the MWCNT-reinforced composite sample (Composite) as well as the laser-textured MWCNT-coated reinforced composite (Coated composite) were rubbed under the same conditions. The measurements of coefficient of friction (COF) are shown in Fig. 5. Each curve represents the mean value including the standard deviation of three measurements. The individual experiments were conducted until steady state was reached. The unreinforced reference was only measured for 400 s due to fast wearing off of the teeth. However, the final COF value of 0.6 correlates well with the steady state COF value reported in the literature for coarse grained Nickel sliding against steel at a relative humidity of 40% [53]. The running-in of the reference sample is typical for a non-lubricated metal-to-metal contact that has already been analyzed elsewhere [54]. The initial raise of the COF from 0.2 to 0.8 can be explained by an increase of the contact area during running-in. As the ring further removes material from the tooth, wear debris accumulates at the interface, leading to formation of a third-body layer that reduces adhesive interaction between the rubbing surfaces and leads to friction reduction. The steady state conditions are reached when the formation of the third-body layer is balanced with escape of wear debris from the interface.

For the composite sample, the COF curve starts with the same value as for the reference, but it only increases to a maximum value of 0.37 and decreases rapidly within the first 150 s to a value of 0.22. After this, it further decreases during the next 2500 s, reaching minimal values of as low as 0.13 at the steady state condition. In the beginning of the experiment, the MWCNTs are embedded in the Nickel matrix, and their contribution to friction is limited, so the COF value is close to that of the reference surface. With the steel ring starting to wear off the block material and to develop a conformal contact with the tooth, the embedded MWCNTs are gradually brought into the contact and start lubricating the system.

A previous study has already shown that the COF of MWCNT-reinforced composites is mainly influenced by the presence of MWCNTs in the contact zone and not by the differences in the composite microstructure [9]. It is assumed that the MWCNTs can easily be dragged out of the surface cavities due to their high aspect ratio [10,11]. With on-going wear, more and more MWCNTs are progressively brought into the contact, which further decreases the COF until it reaches the minimal value at the steady state condition. This constant value may be a consequence of the balance between the MWCNTs that are already present in or have just been dragged into the contact from the surface cavities and the MWCNTs that are pushed out of the contact with the wear debris. The lubricating effect of the MWCNTs is attributed to the presence of delaminated/degraded graphitic flakes and the pristine MWCNTs, which are able to slide or roll on the surface. Compared to other studies of the lubricating effect of MWCNTs under the non-conformal contact conditions with the steady state COF of around 0.2 [9–11], the presented COF results are significantly lower. It is believed that the conformal contact conditions support the MWCNTs' ability to separate the surfaces, thus providing higher efficiency in lubricating the system. Since the minimum COF is about 0.13, while rolling would result in friction coefficients of significantly lower values, sliding is considered to be the main type of relative motion [55]. Nonetheless, a partial rolling of the particles cannot be fully excluded.

The laser-textured MWCNT-coated reinforced sample (Coated Composite) also demonstrated a friction reduction compared to the reference surface. However, in contrast to the composite sample, the friction reduction is already seen in the beginning of the experiment with a COF value of 0.25–0.35. An explanation for this behavior is that MWCNTs are present in the contact zone as free particles right from the start. The COF slightly fluctuates for the first 1000 s, after which it continuously decreases and finally reaches the steady state conditions after 3500 s with the same COF as the composite sample. Interestingly, although the concentration of MWCNTs on the surface is much higher compared to the composite sample, the friction reduction is less

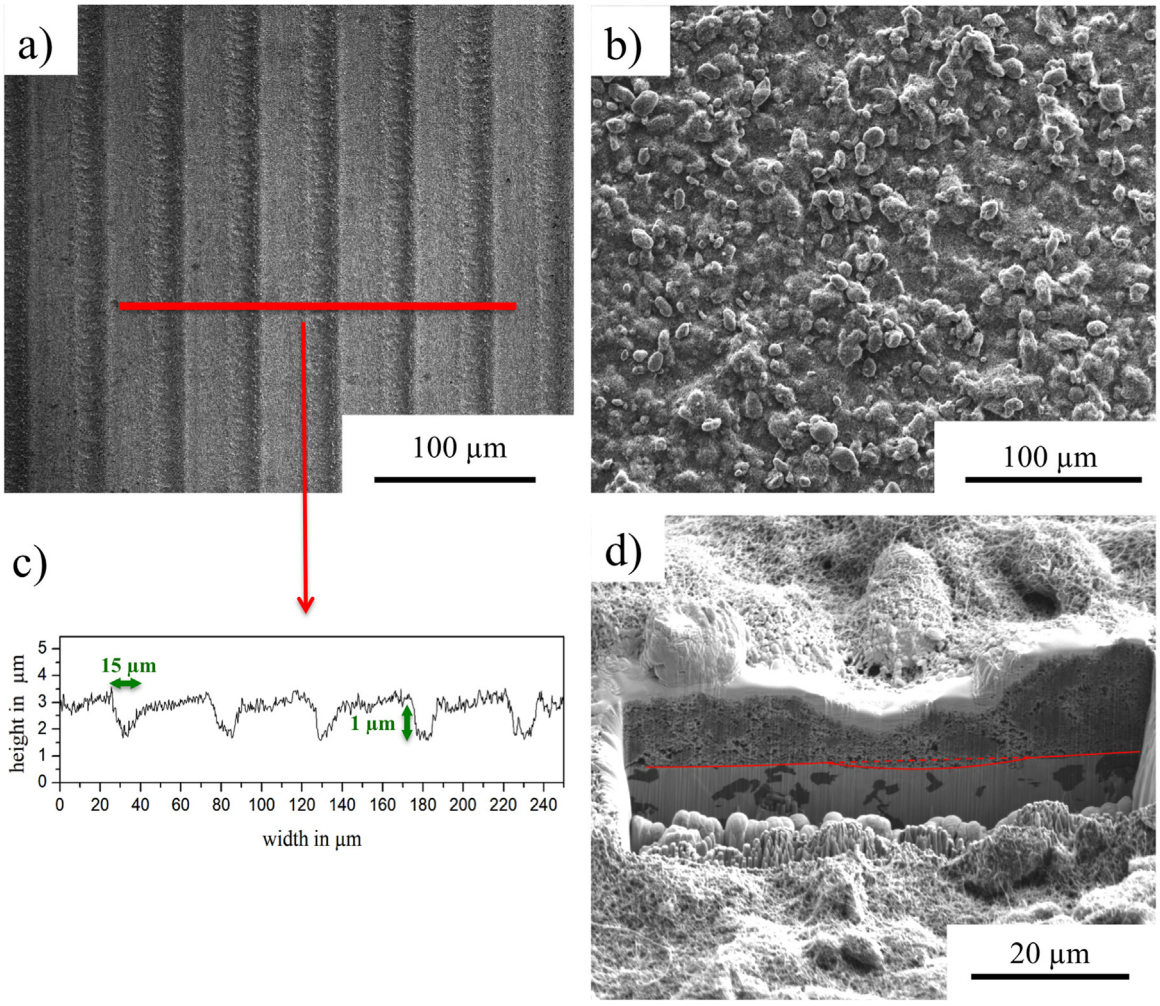

Fig. 4. SEM micrograph of the laser-textured composite sample a) before and b) after coating with MWCNTs. In c) a cross-section of the laser-textured surface (marked in red in a)) is depicted by laser scanning microscopy. A SEM micrograph of a FIB cross-section of the laser textured and coated composite is illustrated in d). The surface depression is marked in red for better visibility. (For interpretation of the references to color in this figure legend, the reader is referred to the web version of this article.).

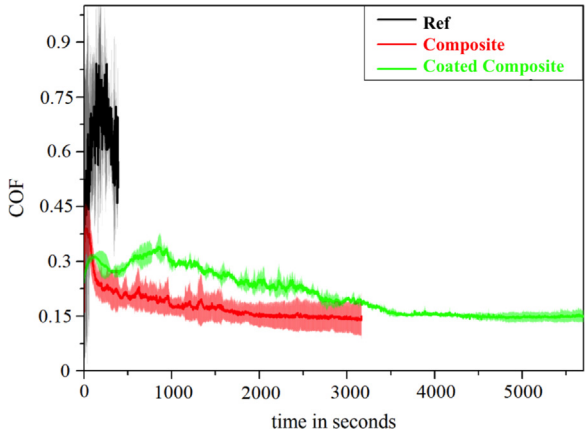

Fig. 5. Evolution of the COF of the unreinforced Nickel reference (Ref), the MWCNT-reinforced composite (Composite) and the MWCNT-reinforced composite after laser texturing and MWCNT coating (Coated Composite). Each curve represents the mean value including standard deviation of three measurements.

pronounced and is unstable. Most likely, this can be traced back to wear particles, which cannot be efficiently removed from the contact but are stored in the surface depressions. Wear particle agglomerations are thus formed and broken up in a stochastic manner, leading to a slight increase and destabilization of the friction coefficient. Additionally, the initially present thick MWCNT coating is not strong enough to support the load, so the ring sample penetrates it until the block sample is met, only being separated by a very thin layer of MWCNT. The thick coating creates a larger contact area, consequently leading to higher friction. However, with on-going wear, both effects are getting less pronounced. A higher COF due to a phase transformation or a change in mechanical properties of the surfaces induced by laser processing can be excluded, as the laser-material interaction of a femtosecond laser system is based on ablation and not on melting [46]. At the steady state, the laser structures and the MWCNT coating seem to be worn off completely, because the same frictional behavior as for the composite sample is observed. However, in order to get a better understanding of the mechanisms involved, a detailed analysis of wear and the oxidation behavior as well as the evaluation of the structural state of the MWCNT has to be performed.

The tooth wear Δd (see Fig. 2) is given as a function of time in Fig. 6, which also includes the curve slopes representing the wear rate.

It is clearly seen that the reference sample is worn much faster than the composite or the coated composite sample. Based on the curve

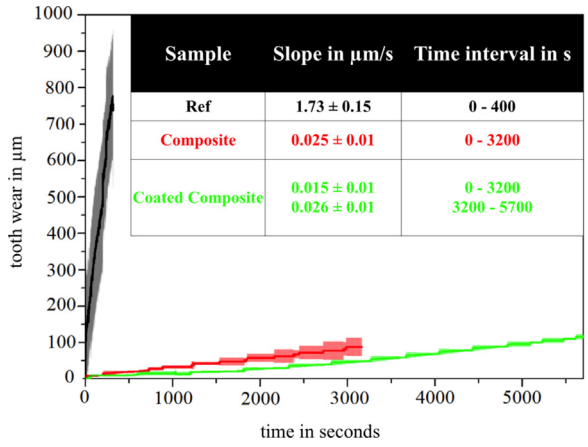

Fig. 6. The tooth wear Δd as a function of time. The slope of each individual curve represents the wear rate and is included in the graph. Each curve represents the mean value including standard deviation of three measurements.

slopes, the wear rate of the composite (0.025 ± 0.01 µm/s) is 70 times slower than that of the reference (1.73 ± 0.15 µm/s). For one part, this can be explained with the slightly higher hardness of the composite compared to the reference material. Additionally, the lower mean grain size of the composite material can lead to a more pronounced oxidation, as the grain boundaries would act as diffusion paths for oxygen [56,57]. The formation of a protective oxide layer can lead to a change in wear mechanism and thus to a lower wear rate. Furthermore, the MWCNTs are continuously dragged into the contact, efficiently reducing frictional stress and separating the surfaces, which also contributes to the wear reduction.

In case of the coated composite, two time intervals have to be analyzed separately, as the wear rate changes after 3200 s of the runtime. For the first 3200 s, the wear rate is 0.015 ± 0.01 µm/s, which corresponds to the reduction of wear by a factor of 115 compared to the reference. After 3200 s, the wear rate slightly increases, meeting the same value as in the composite sample. A straightforward reason for this behavior is the removal of the MWCNT-coated laser structures during the first 3200 s. With the wear rate being almost identical to that of the uncoated composite sample, the behavior of the coated sample is clearly dominated by the substrate material. This also appears reasonable when looking at the COF of the coated composite sample after 3200 s (Fig. 5), which is similar to the COF of the uncoated composite sample. However, although the COF of the coated composite sample is higher for the first 3200 s, the wear is lower. This can be explained by the fact that the contacting surfaces are more efficiently separated by the higher amount of MWCNTs homogeneously covering the composite surface. With on-going wear, the two contacting surfaces slowly undergo a transition towards a conformal contact. This means that with an increasing wear depth, the laser-induced surface depressions are gradually removed until the tooth contact surface replicates the ring shape. After 3200 s, the supply of the MWCNTs decreases, thus resulting in a higher wear rate. In the following sections, an extensive surface analysis is performed in order to back-up and discuss the above hypotheses in more detail.

3.3. Characterization of wear

In Fig. 7, SEM micrographs as well as EDS maps showing the middle of the worn teeth of the reference and composite samples are depicted. From the SEM micrographs, it is evident that the wear mechanisms of the two samples differ significantly.

The reference surface (Fig. 7**a, c**) exhibits clear signs of rupture and material transfer with formation of plate-like composite plastically-deformed fragments. Large areas of pure Nickel are exposed due to insufficient regeneration of a disrupted protective NiO surface layer, resulting in the formation and breaking of micro-welds during the experiment and creating a rough surface with a flake-like morphology. A random formation of oxides, which are mostly associated with transferred particles, is observed. Thus, the dominant wear mechanism for the reference sample is the pathological (severe) adhesive wear [58].

In contrast to that, the worn tooth of the composite sample (Fig. 7**b, d**) exhibits a rather smooth, fully oxidized surface with anisotropic scratch-marks in the sliding direction. The formation of a uniform oxide layer can be explained with the lower grain size in the case of the composite [56,57]. This oxide layer may work as a protective coating, as NiO is known to act as a high shear strength layer, which is hard to remove [11]. This clearly indicates normal (mild) tribo-chemical wear [58]. Interestingly, the formation of a high shear strength layer would typically result in a higher COF, which is not the case as can be seen in Fig. 5 [11]. This supports the above conclusion that the frictional behavior is dominated by the MWCNTs, which are transferred to the contact area from cavities and slide/roll on the smooth oxidized surface of the composite, efficiently reducing the COF.

3.4. Structural integrity of solid lubricant

Fig. 8 shows a partially worn tooth of the coated composite sample, where the measurement has been stopped during run-in at 1000 s. Three different areas can be noticed.

Area 1 corresponds to the pristine laser-textured and MWCNT-coated surface, which has not yet been in contact. Area 3 is long in a sliding contact, and, with the laser structures and MWCNT coating being completely removed, it matches the surface appearance of the uncoated composite sample, in which the tribological behavior is determined exclusively by the composite material. For area 2, the darker color of the MWCNT coating indicates that an initial contact has been established. However, the surface is still covered by MWCNTs and the MWCNT-filled line-like laser structures are still observed. Obviously, the tribological system is still in the process of running-in because the contact area does not completely cover the top surface of the tooth. This fact allows for a more detailed analysis of the lubrication mechanism of the particles. Additionally, wear particles are found in area 2, aligning with the remaining laser structures, which supports the statement of an increased and unstable friction coefficient due to wear debris trapping and the subsequent forming and breaking of wear particle agglomerations during running in.

Keeping in mind, that the tribological system undergoes a transition towards a conformal contact condition, it is reasonable to assume a contact pressure gradient, with the pressure increasing from area 1 to area 3 as indicated in Fig. 8. Raman spectroscopy was conducted for these areas. The spots marked as a-d in Fig. 8 are analyzed and the characteristic bands of MWCNTs are compared in order to identify the degradation process of the particles. In Fig. 9, the corresponding Raman spectra are plotted and the characteristic bands are given as D, G and G'. Additionally, schematic illustrations are added to the spectra to present the structural degradation model of the MWCNTs found in each contact situation (a-d).

The first peak at 1350 cm^{-1} belongs to the D-band, which is formed due to the presence of defects in the MWCNT structure. For example, a defect can be a crystal boundary in polycrystalline graphite or simply dangling covalent bonds of the aromatic system [59,60]. At around 1580–1600 cm^{-1}, the G-band is detected. The G-band describes the crystalline state of sp^2-hybridized carbon structures [61]. Its center position (X_{CG}) is used in a three-stage phenomenological model developed by Ferrari et al. [49], which analyses the transition from an ordered graphitic-like to an amorphous-like structure, thus quantifying the degradation process of such a highly crystalline structure as MWCNT. Finally, at around 2700 cm^{-1}, the G'-band corresponding to an overtone of the D-band is observed. The G'-band is very sensitive to carbonaceous impurities, providing a very close correlation to average

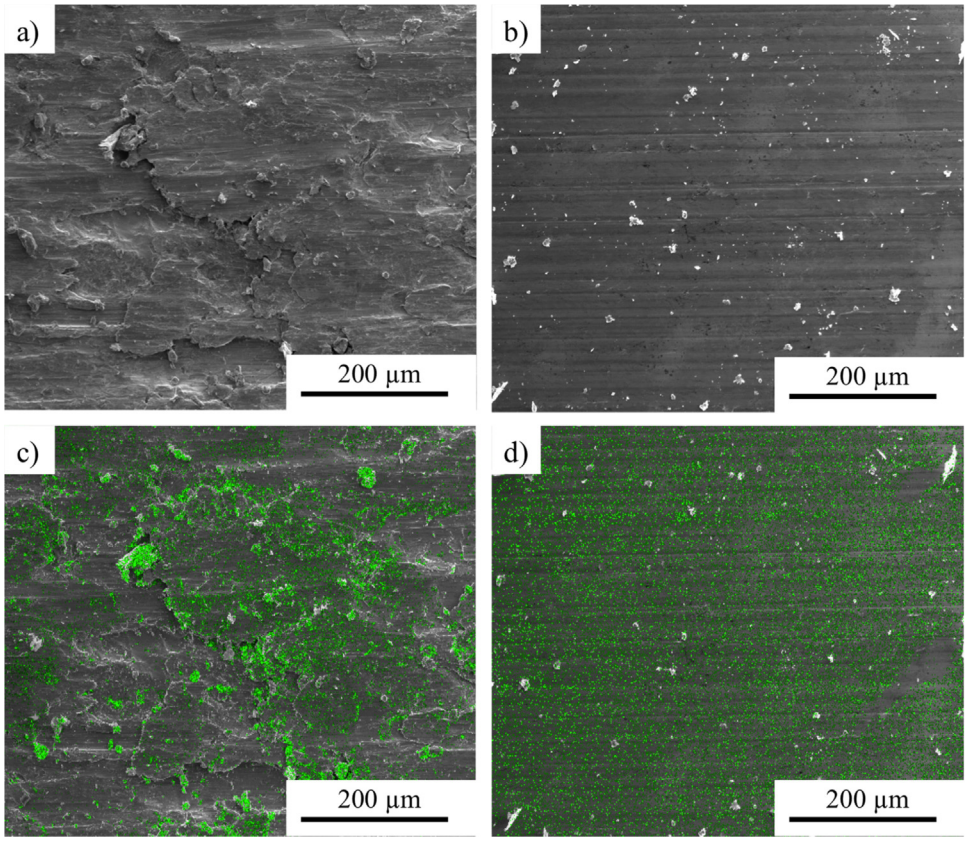

Fig. 7. SEM micrographs of the wear tracks in the middle of the tooth for a) the reference and b) the composite surfaces. EDS-maps of oxygen (color green) are superimposed with the SEM micrographs of c) the reference and d) the composite surfaces. (For interpretation of the references to color in this figure legend, the reader is referred to the web version of this article.).

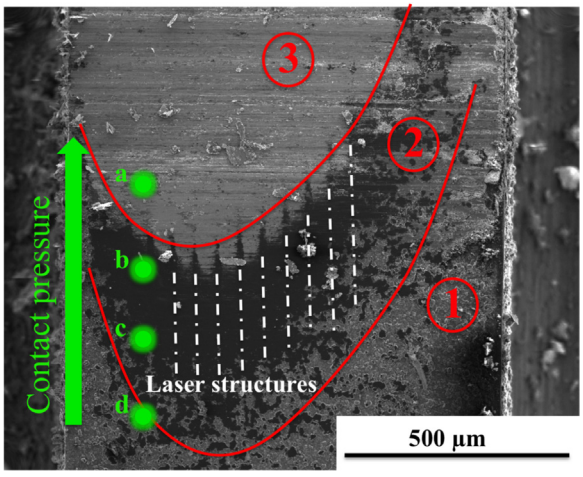

Fig. 8. SEM micrograph of a tooth of the coated composite sample after stopping the test at 1000 s. Three different areas of wear, which are separated by red lines for clarity, can be distinguished. Area 1 shows the initial laser-structured and MWCNT-coated surface, whereas area 3 shows the final stage of complete removal of laser structures and CNT coating. Area 2 corresponds to transition between area 1 and area 3, with the laser structures and MWCNT coating still being visible. (For interpretation of the references to color in this figure legend, the reader is referred to the web version of this article.).

purity values obtained by thermogravimetry [60].

From the first look at the spectra, it is obvious that, according to the measured spots on the worn tooth, the X_{CG} is shifting from lower to higher wavenumbers as a function of the contact pressure growing from (d) to (a) in Fig. 8. This upshifting corresponds to a transient state of the MWCNTs (clustering of the affected graphitic structure) towards a nano-crystalline graphite [49]. In addition, the band intensities clearly change as a function of the measured spot (contact pressure). Raman spectra can be quantitatively evaluated by the normalized intensity ratios D/G and G'/D. Specifically, the D/G ratio corresponds to the defect density and thus to the crystalline domain size, whereas the G'/D ratio can be correlated with the purity level of a graphitic material and is defined as the purity index [61,62].

The corresponding intensity ratios of the recorded spectra as well as the G-band position can be found in Table 1. However, it should be kept in mind that these data present mean values of all MWCNTs measured at individual spots, where degraded MWCNTs can be blended with intact MWCNTs, generating an integral of structural state information.

Comparing the data in Table 1, it is clearly seen that the defect density increases from (d) to (b) from 0.55 to 1.23 and slightly decreases again for (a). The purity index significantly drops from (d) to (a) with the X_{CG} wavenumber increasing from 1584 cm^{-1} to 1601 cm^{-1}. According to the amorphisation trajectory model by Ferrari et al. [49], this corresponds to the structural amorphisation of the MWCNTs in the sliding contact. For spot (d), the MWCNTs are in pristine, highly ordered and graphitic condition, which also indicates that they are practically not stressed and can move freely. With increasing contact pressure, the MWCNTs are deformed, creating high stresses at the outer shells of the MWCNT structure, which can result in breaking of individual covalent bonds and thus higher defect density (see Table 1(c) and Fig. 9(c, b)). Moving towards the main contact zone, the MWCNT structures start to delaminate and nanocrystalline graphitic flakes are formed, as the X_{CG} wavenumber reaches almost 1600 cm^{-1}. The third body layer here consists of a mixture between the damaged MWCNTs and stacked graphene layers. Finally, at spot (a), the remaining MWCNT coating is fully degraded to nanocrystalline graphitic flakes and nearly no intact MWCNTs can be found anymore. The defect density index decreases again, which can be correlated with the second stage of amorphisation due to the further decreasing purity index [49].

When the MWCNT agglomerates found in the cavities of the worn composite material are analyzed within area 3, the spectrum in Fig. 10 is obtained.

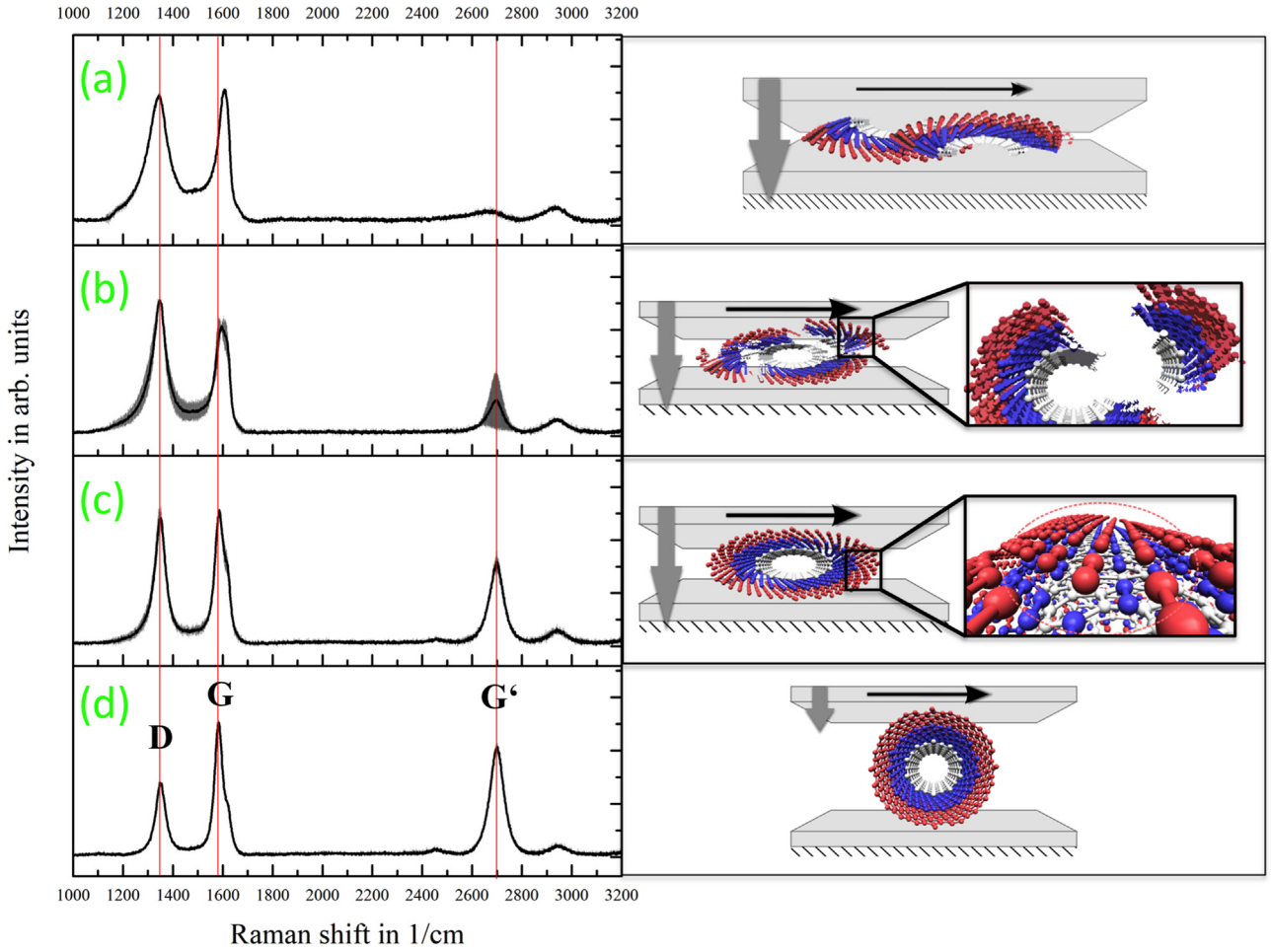

Fig. 9. Raman spectroscopy analysis of the spots a-d in Fig. 8 indicating the characteristic bands for MWCNT. Each spectrum was recorded three times, and the mean value with the standard deviation are plotted. For each spectrum, a schematic is added in order to visualize the interpretation of the Raman signal and to demonstrate the corresponding contact situation.

Table 1
Intensity ratios of the D, G and G' band as well as the G-band center position (X_{CG}) as a function of the measurement location on the worn tooth according to Fig. 8.

Position	I_D/I_G	$I_{G'}/I_D$	X_{CG} in cm^{-1}
(a)	0.96	0.11	1601
(b)	1.23	0.26	1589
(c)	0.94	0.65	1586
(d)	0.55	1.48	1584

The spectrum and thus the defect density, the purity index as well as the X_{CG} wavenumber of the MWCNTs found in the surface cavities in area 3 are very similar to these found in spot (c) (see Fig. 9 and Table 1). This means that the MWCNTs in the cavities are only slightly degraded and can be dragged into the contact to enhance lubrication. Taking into account that the Raman signal consists of the superposition of the signal generated by the MWCNTs that have already been in contact and the MWCNTs that are still stored in the cavities of the composite, it is reasonable to assume that the stored MWCNTs are still close to their pristine condition. Additionally, as the crystalline graphite has already been formed in the contact by the degraded MWCNTs, the pristine MWCNTs can slide or roll over these graphite layers depending on the individual contact situation. This possibility has been discussed in the work of Falvo et al. [21] studying the rolling and sliding mechanisms of MWCNTs on graphite using an atomic force microscope. However, based on the recorded COF, the dominant lubrication

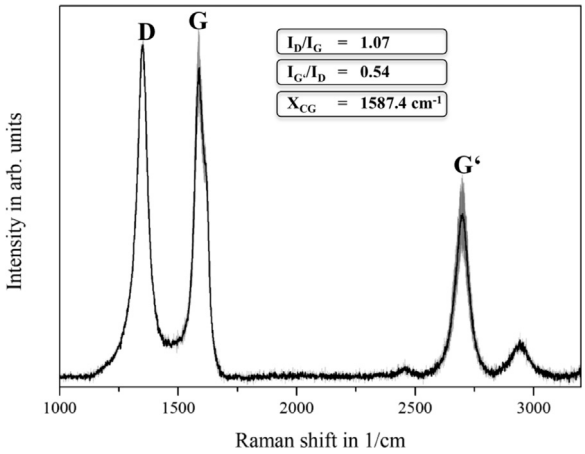

Fig. 10. Raman spectrum of the MWCNTs found in the surface cavities within the worn area of the composite material in area 3 (according to Fig. 9). The intensity ratios as well as the X_{CG} wavenumber are included.

mechanism of the presented system is certainly a mixture of the sliding MWCNTs and a graphite-based lubrication.

Finally, it is summarized that the MWCNTs from the cavities of the composite material are gradually brought into the contact, thus permanently lubricating the system. The steady state frictional behavior of the composite as well as the coated composite is dominated by the

constant supply of the MWCNTs stored in the cavities of the composite material. However, a surface coating combined with laser texturing is capable to reduce the wear rate during the running-in of the system by a factor of 1.6 compared to the uncoated composite material. This can be explained by a more efficient surface separation by the MWCNTs in the coated case and by the capability of the surface depressions to supply the contact area with a larger amount of solid lubricant compared to the composite cavities. The wear reduction reaches similar values as for the uncoated composite as soon as all of the coating and laser structures are removed. Only by combining the MWCNT coating with the MWCNT-reinforced composite, could the lubrication mechanism of the MWCNTs be understood in detail.

4. Conclusions

Here we report on the tribological behavior of an integral self-lubricating system under conformal contact conditions. The tests were carried out in a custom-built ring-on-block tribometer. We show that when combining a self-lubricating composite with an optimized solid-lubricant coating and a regular topography, improved self-lubricating effects are obtained. This system shows a maximum 4-fold reduction in the coefficient of friction and a 115-fold reduction in the wear rate compared to the reference state. Additionally, by performing a Raman spectroscopic characterization, we were able to evaluate the structural state of the solid lubricant throughout the generated pressure gradient, presenting a four-stage degradation model. Derived from this, it is possible to understand the lubrication mechanism of the MWCNTs and relate it to a transition from highly crystalline MWCNTs towards graphitic nano-clusters. The MWCNTs found in the cavities of the reinforced composite are close to their pristine state and are gradually brought into the contact, providing efficient lubrication throughout the lifetime of the composite material. The dominant lubrication mechanism is a mixture between the sliding MWCNTs and a graphite-based lubrication. Our results highlight the suitability of the proposed integrated solution as a promising approach for self-lubricating surfaces subjected to unidirectional sliding.

Acknowledgements

The present work is supported by funding from the Deutsche Forschungsgemeinschaft (DFG, project: MU 959/38-1 and SU 911/1-1). L. R., S.S., and F. M. wish to acknowledge the EFRE Funds (C/4-EFRE-13/2009/Br) of the European Commission for support of activities within the AME-Lab project. Prof. Dr. Volker Presser is acknowledged for providing the possibility to use Raman spectroscopy. This work was supported by the CREATe-Network Project, Horizon 2020 of the European Commission (RISE Project No. 644013). The authors further would like to thank Prof. Claudia A. Carrasco and Christopher Salvo for their help in processing the composite samples.

Competing interests

The authors declare no competing interests.

References

[1] H.K.D.H. Bhadeshia, Steels for bearings, Prog. Mater. Sci. 57 (2012) 268–435, http://dx.doi.org/10.1016/j.pmatsci.2011.06.002.
[2] C. Gachot, A. Rosenkranz, L. Reinert, E. Ramos-Moore, N. Souza, M.H. Müser, F. Mücklich, Dry friction between laser-patterned surfaces: role of alignment, structural wavelength and surface chemistry, Tribol. Lett. 9 (2013) 193–202, http://dx.doi.org/10.1007/s11249-012-0057-y.
[3] A. Rosenkranz, L. Reinert, C. Gachot, F. Mücklich, Alignment and wear debris effects between laser-patterned steel surfaces under dry sliding conditions, Wear (2014), http://dx.doi.org/10.1016/j.wear.2014.06.016.
[4] M.M. Khonsari, E.R. Booser, Applied Tribology – Bearing Design and Lubrication, 2017.
[5] C. Donnet, A. Erdemir, Solid Lubricant Coatings: recent developments and future trends, Tribol. Lett. 17 (2004) 389–397 (doi:1023-8883/04/1000–0389/0).
[6] S.M. Aouadi, H. Gao, A. Martine, T.W. Scharf, C. Muratore, Lubricious oxide coatings for extreme temperature applications: a review, Surf. Coat. Technol. 257 (2014) 266–277, http://dx.doi.org/10.1016/j.surfcoat.2014.05.064.
[7] D. Berman, A. Erdemir, A.V. Sumant, Graphene: a new emerging lubricant, Mater. Today 17 (2014) 31–42, http://dx.doi.org/10.1016/j.mattod.2013.12.003.
[8] A. Hirata, N. Yoshioka, Sliding friction properties of carbon nanotube coatings deposited by microwave plasma chemical vapor deposition, Tribol. Int. 37 (2004) 893–898, http://dx.doi.org/10.1016/j.triboint.2004.07.005.
[9] L. Reinert, S. Suárez, A. Rosenkranz, Tribo-mechanisms of carbon nanotubes: friction and wear behavior of CNT-reinforced nickel matrix composites and CNT-coated bulk nickel, Lubricants 4 (2016) 11, http://dx.doi.org/10.3390/lubricants4020011.
[10] L. Reinert, F. Lasserre, C. Gachot, P. Grützmacher, T. MacLucas, N. Souza, F. Mücklich, S. Suarez, Long-lasting solid lubrication by CNT-coated patterned surfaces, Sci. Rep. 7 (2017), http://dx.doi.org/10.1038/srep42873.
[11] T.W. Scharf, A. Neira, J.Y. Hwang, J. Tiley, R. Banerjee, Self-lubricating carbon nanotube reinforced nickel matrix composites, J. Appl. Phys. 106 (2009), http://dx.doi.org/10.1063/1.3158360.
[12] K.T. Kim, S. Il Cha, S.H. Hong, Hardness and wear resistance of carbon nanotube reinforced Cu matrix nanocomposites, Mater. Sci. Eng. A 449–451 (2007) 46–50, http://dx.doi.org/10.1016/j.msea.2006.02.310.
[13] X.H. Chen, J. Peng, F. Deng, J. Wang, W. Li, Tribological behavior of carbon nanotubes — reinforced nickel matrix composite coatings, J. Mater. Sci. Lett. 20 (2001) 2057–2060.
[14] X.H. Chen, C.S. Chen, H.N. Xiao, H.B. Liu, L.P. Zhou, S.L. Li, G. Zhang, Dry friction and wear characteristics of nickel/carbon nanotube electroless composite deposits, Tribol. Int. 39 (2006) 22–28, http://dx.doi.org/10.1016/j.triboint.2004.11.008.
[15] D.K. Singh, P.K. Iyer, P.K. Giri, Diameter dependence of oxidative stability in multiwalled carbon nanotubes: role of defects and effect of vacuum annealing, J. Appl. Phys. 108 (2010), http://dx.doi.org/10.1063/1.3491022.
[16] K. Miyoshi, K.W.S. Jr, R.L. Vander Wal, R. Andrews, A. Sayir, Solid lubrication by multiwalled carbon nanotubes in air and in vacuum, Tribol. Lett. 19 (2005) 191–201, http://dx.doi.org/10.1007/s11249-005-6146-4.
[17] L. Reinert, S. Schütz, S. Suarez, F. Mücklich, Influence of surface roughness on the lubrication effect of carbon nanoparticle-coated steel surfaces, Tribol. Lett. 66 (2018), http://dx.doi.org/10.1007/s11249-018-1001-6.
[18] S. Iijima, Helical microtubules of graphitic carbon, Nature 354 (1991) 56–58, http://dx.doi.org/10.1038/354056a0.
[19] Y. Gogotsi, V. Presser, Carbon Nanomaterials, CRC Press, 2014 (ISBN: 978-1-4665-0242-0).
[20] M.F.L. De Volder, S.H. Tawfick, R.H. Baughman, A.J. Hart, Carbon nanotubes: present and future commercial applications, Science 339 (2013) 535–539, http://dx.doi.org/10.1126/science.1222453.
[21] M.R. Falvo, R.M.T. Ii, A. Helser, V. Chi, Nanometre-scale rolling and sliding of carbon nanotubes, Nature 397 (1999) 1–3, http://dx.doi.org/10.1038/16662.
[22] P.L. Dickrell, S.B. Sinnott, D.W. Hahn, N.R. Raravikar, L.S. Schadler, P.M. Ajayan, W.G. Sawyer, Frictional anisotropy of oriented carbon nanotube surfaces, Tribol. Lett. 18 (2005) 59–62, http://dx.doi.org/10.1007/s11249-004-1752-0.
[23] P.L. Dickrell, S.K. Pal, G.R. Bourne, C. Muratore, A.A. Voevodin, P.M. Ajayan, L.S. Schadler, W.G. Sawyer, Tunable friction behavior of oriented carbon nanotube films, Tribol. Lett. 24 (2006) 85–90, http://dx.doi.org/10.1007/s11249-006-9162-0.
[24] B. Ni, S.B. Sinnott, Tribological properties of carbon nanotube bundles predicted from atomistic simulations, Surf. Sci. 487 (2001) 87–96, http://dx.doi.org/10.1016/S0039-6028(01)01073-1.
[25] J.M. Martin, N. Ohmae, Nanolubricants, John Wiley & Sons Ltd, 2008 (ISBN: 978-0-470-06552-5).
[26] R. Greenberg, G. Halperin, I. Etsion, R. Tenne, The effect of WS2 nanoparticles on friction reduction in various lubrication regimes, Tribol. Lett. 17 (2004) 179–186, http://dx.doi.org/10.1023/B:TRIL.0000032443.95697.1d.
[27] J.J. Hu, S.H. Jo, Z.F. Ren, A. Voevodin, J.S. Zabinski, Tribological behavior and graphitization of carbon nanotubes grown on 440C stainless steel, Tribol. Lett. 19 (2005) 119–125, http://dx.doi.org/10.1007/s11249-005-5091-6.
[28] A. Dorri Moghadam, E. Omrani, P.L. Menezes, P.K. Rohatgi, Mechanical and tribological properties of self-lubricating metal matrix nanocomposites reinforced by carbon nanotubes (CNTs) and graphene – a review, Compos. Part B Eng. 77 (2015) 402–420, http://dx.doi.org/10.1016/j.compositesb.2015.03.014.
[29] F. Colonna, A. Fasolino, E.J. Meijer, Graphitization of single-wall nanotube bundles at extreme conditions: collapse or coalescence route, Phys. Rev. B 88 (2013) 165416, http://dx.doi.org/10.1103/PhysRevB.88.165416.
[30] S. Suárez, A. Rosenkranz, C. Gachot, F. Mücklich, Enhanced tribological properties of MWCNT/Ni bulk composites – influence of processing on friction and wear behaviour, Carbon 66 (2014) 164–171, http://dx.doi.org/10.1016/j.carbon.2013.08.054.
[31] S.V. Prasad, R. Asthana, Aluminum metal–matrix composites for automotive applications: tribological considerations, Tribol. Lett. 17 (2004) 445–453, http://dx.doi.org/10.1023/B:TRIL.0000044492.91991.f3.
[32] M. Rosso, Ceramic and metal matrix composites: routes and properties, J. Mater. Process. Technol. 175 (2006) 364–375, http://dx.doi.org/10.1016/j.jmatprotec.2005.04.038.
[33] D. Miracle, Metal matrix composites – from science to technological significance, Compos. Sci. Technol. 65 (2005) 2526–2540, http://dx.doi.org/10.1016/j.compscitech.2005.05.027.
[34] I.M. Hutchings, Tribological properties of metal matrix composites, Mater. Sci. Technol. 10 (1994), http://dx.doi.org/10.1179/mst.1994.10.6.513.
[35] L. Reinert, S. Suarez, T. Müller, F. Mücklich, Carbon nanoparticle-reinforced metal

matrix composites: microstructural tailoring and predictive modeling, Adv. Eng. Mater. 19 (2017) 1–6, http://dx.doi.org/10.1002/adem.201600750.
[36] L. Reinert, M. Zeiger, S. Suarez, V. Presser, F. Mücklich, Dispersion analysis of carbon nanotubes, carbon onions, and nanodiamonds for their application as reinforcement phase in nickel metal matrix composites, RSC Adv. 5 (2015) 95149–95159, http://dx.doi.org/10.1039/C5RA14310A.
[37] R.A. Shahani, T.W. Clyne, Recrystallization in fibrous and particulate metal matrix composites, Mater. Sci. Eng. A 135 (1991) 281–285, http://dx.doi.org/10.1016/0921-5093(91)90576-9.
[38] L. Rapoport, A. Moshkovich, V. Perfilyev, I. Lapsker, G. Halperin, Y. Itovich, I. Etsion, Friction and wear of MoS2 films on laser textured steel surfaces, Surf. Coat. Technol. 202 (2008) 3332–3340, http://dx.doi.org/10.1016/j.surfcoat.2007.12.009.
[39] A.A. Voevodin, J.S. Zabinski, Laser surface texturing for adaptive solid lubrication, Wear 261 (2006) 1285–1292, http://dx.doi.org/10.1016/j.wear.2006.03.013.
[40] L. Rapoport, A. Moshkovich, V. Perfilyev, A. Gedanken, Y. Koltypin, E. Sominski, G. Halperin, I. Etsion, Wear life and adhesion of solid lubricant films on laser-textured steel surfaces, Wear 267 (2009) 1203–1207, http://dx.doi.org/10.1016/j.wear.2009.01.053.
[41] J. Deng, Y. Lian, Z. Wu, Y. Xing, Performance of femtosecond laser-textured cutting tools deposited with WS2 solid lubricant coatings, Surf. Coat. Technol. 222 (2013) 135–143, http://dx.doi.org/10.1016/j.surfcoat.2013.02.015.
[42] S. Suarez, L. Reinert, M. Zeiger, V. Presser, P. Miska, F. Müller, F. Mücklich, In-situ nanodiamond to onion-like carbon transformation in metal matrix composites, Carbon 129 (2018) 631–636, http://dx.doi.org/10.1016/j.carbon.2017.12.072.
[43] S. Suarez, F. Lasserre, F. Mücklich, Mechanical properties of MWNT/Ni bulk composites: influence of the microstructural refinement on the hardness, Mater. Sci. Eng. A 587 (2013) 381–386, http://dx.doi.org/10.1016/j.msea.2013.08.058.
[44] A. Lasagni, M. D'Alessandria, R. Giovanelli, F. Mücklich, Advanced design of periodical architectures in bulk metals by means of laser interference metallurgy, Appl. Surf. Sci. 254 (2007) 930–936, http://dx.doi.org/10.1016/j.apsusc.2007.08.010.
[45] B. Raillard, F. Mücklich, Ablation effects of femtosecond laser functionalization on surfaces, Laser Surf. Eng. Process. Appl. 207 (2014) 565–581, http://dx.doi.org/10.1016/B978-1-78242-074-3.00024-6.
[46] K.H. Leitz, B. Redlingshöer, Y. Reg, A. Otto, M. Schmidt, Metal ablation with short and ultrashort laser pulses, Phys. Procedia 12 (2011) 230–238, http://dx.doi.org/10.1016/j.phpro.2011.03.128.
[47] A.R. Boccaccini, J. Cho, J.A. Roether, B.J.C. Thomas, E. Jane Minay, M.S.P. Shaffer, Electrophoretic deposition of carbon nanotubes, Carbon 44 (2006) 3149–3160, http://dx.doi.org/10.1016/j.carbon.2006.06.021.
[48] M.F. De Riccardis, D. Carbone, A. Rizzo, A novel method for preparing and characterizing alcoholic EPD suspensions, J. Colloid Interface Sci. 307 (2007) 109–115, http://dx.doi.org/10.1016/j.jcis.2006.10.037.
[49] A. Ferrari, J. Robertson, Resonant Raman spectroscopy of disordered, amorphous, and diamondlike carbon, Phys. Rev. B 64 (2001) 75414, http://dx.doi.org/10.1103/PhysRevB.64.075414.
[50] P.A. Manohar, M. Ferry, T. Chandra, Five Decades of the Zener Equation, ISIJ Int. 38 (1998) 913–924, http://dx.doi.org/10.2355/isijinternational.38.913.
[51] N. Hansen, Hall–Petch relation and boundary strengthening, Scr. Mater. 51 (2004) 801–806, http://dx.doi.org/10.1016/j.scriptamat.2004.06.002.
[52] A. Sanaty-Zadeh, Comparison between current models for the strength of particulate-reinforced metal matrix nanocomposites with emphasis on consideration of Hall–Petch effect, Mater. Sci. Eng. A 531 (2012) 112–118, http://dx.doi.org/10.1016/j.msea.2011.10.043.
[53] R. Mishra, B. Basu, R. Balasubramaniam, Effect of grain size on the tribological behavior of nanocrystalline nickel, Mater. Sci. Eng. A 373 (2004) 370–373, http://dx.doi.org/10.1016/j.msea.2003.09.107.
[54] P.J. Blau, On the nature of running-in, Tribol. Int. 38 (2005) 1007–1012, http://dx.doi.org/10.1016/j.triboint.2005.07.020.
[55] I. Hutchings, P. Shipway, Tribology: Friction and Wear of Engineering Materials, Butterworth-Heinemann, Elsevier, 2017 (ISBN: 978-0-08-100910-9).
[56] M. Shafiei, A.T. Alpas, Friction and wear mechanisms of nanocrystalline nickel in ambient and inert atmospheres, Metall. Mater. Trans. A. 38 (2007) 1621–1631, http://dx.doi.org/10.1007/s11661-007-9157-y.
[57] R.K. Singh Raman, A.S. Khanna, R.K. Tiwari, J.B. Gnanamoorthy, Influence of grain size on the oxidation resistance of 2 1/4 Cr-1Mo steel, Oxid. Met. 37 (1992) 1–12, http://dx.doi.org/10.1007/BF00665627.
[58] M. Varenberg, Towards a unified classification of wear, Friction 1 (2013) 333–340, http://dx.doi.org/10.1007/s40544-013-0027-x.
[59] Y. Liu, R.L. Vander Wal, V.N. Khabashesku, Functionalization of carbon nano-onions by direct fluorination, Chem. Mater. 19 (2007) 778–786, http://dx.doi.org/10.1021/cm062177j.
[60] J.H. Lehman, M. Terrones, E. Mansfield, K.E. Hurst, V. Meunier, Evaluating the characteristics of multiwall carbon nanotubes, Carbon 49 (2011) 2581–2602, http://dx.doi.org/10.1016/j.carbon.2011.03.028.
[61] R.A. DiLeo, B.J. Landi, R.P. Raffaelle, Purity assessment of multiwalled carbon nanotubes by Raman spectroscopy, J. Appl. Phys. 101 (2007), http://dx.doi.org/10.1063/1.2712152.
[62] F. Tuinstra, J.L. Koenig, Raman spectrum of graphite, J. Chem. Phys. 53 (1970) 1126–1130, http://dx.doi.org/10.1063/1.1674108.

5. CONCLUSIONS AND OUTLOOK

The dissertation addresses the development of self-lubricating surfaces using a new and emerging field of solid lubricants (CNP). Hence, a method must be found, providing full process control and allowing for a comparable and reproducible way to produce CNP-containing surfaces without changing the CNP properties (**Objective 1**). Secondly, the lubrication activity and mechanism of the chosen CNP, providing systematically distinguishable morphology and carbon hybridization, must be evaluated and understood under varying stress collective, surface designs and contact situations (**Objective 2**). Based on these findings, a prototypical, constantly self-lubricating surface should be manufactured, combining the most efficient approaches (**Objective 3**). In the following, the most important findings of the dissertation are briefly summarized.

OBJECTIVE 1

CNP containing surfaces can be produced through CNP reinforcement of MMC. Regarding its processing, colloidal mixing followed by hot uniaxial pressing is chosen, since a functionalization or degradation of the CNP is avoided, still allowing for homogeneous particle distributions within the MMC. It is found that 0-D CNP and an sp^3-hybridization present the most homogeneous distributions, the smallest mean grain size and highest mechanical reinforcement effect. The best achievable particle distribution for sp^3-hybridized particles (ND) was successfully transferred to sp^2-hybridized particles (OLC) by annealing a pre-sintered ND-reinforced MMC. Even though the transformation process of ND to OLC is well known, it is the first time that it has been successfully conducted and characterized within a pre-sintered composite. Additionally, a model, based on the Zener-boundary drag effect, has been adapted, predicting the final mean grain size as a function of the type and concentration of the used CNP when the proposed optimum processing parameters are used. However, the processing parameters can also be chosen so as to produce CNP-reinforced MMC with various concentrations, all providing the same microstructure and thus allowing for a tribological comparison. Considering all these points, it can be stated that all challenges regarding the development of a reproducible and fully controllable processing method have been met.

OBJECTIVE 2

A continuous supply of CNP into the direct tribological contact is the most important thing to consider for CNP-based self-lubricating surfaces. A high aspect ratio and flexibility of the particles are beneficial to achieve a permanent lubrication, regardless of the given surface roughness, since the particles can be pulled into the direct tribological contact region thus efficiently separating the contacting surfaces. These conditions are met for 1-D CNT particles. Even though 0-D particles can separate the contacting surfaces and lubricate the contact by sliding/rolling, they lose this ability when interacting with a surface roughness higher than the particle diameter, which is given for most technical surfaces. A specifically designed deterministic surface (using DLIP or DLW) has been

introduced and is subsequently coated with CNT. It is found that the surface design and CNT coating interact synergetically with CNT being stored within the created surface depressions, which continuously supply the surface with the solid lubricant, achieving a 9-fold extension in the longevity of the lubrication effect. The surface lubrication mechanism acts on compression and elastic restoration of CNT bundles and the ability of CNT to be dragged inside of the contact region irrespective of the given topographical contact situation. Since the designed surface is comparable to a CNT-reinforced MMC surface, the lubrication mechanism can be transferred to CNP-reinforced MMC as well.

Particle degradation is observed for all CNP in a tribological contact. However, specifically for CNT, the degradation is directly related to its intrinsic lubrication mechanism. It is the first time that a tribologically induced CNT degradation has been quantified and correlated to an amorphization trajectory model. With on-going CNT degradation, nanocrystalline graphite is formed. This is very important so as to allow pristine CNT to perform a sliding/rolling movement on top of these graphitic surfaces, reducing the COF to values below what would be expected for a pure graphite-based lubrication. Based on contact mechanics simulations (using the Jackson-Green model), the composites are also tested under elastic or elaso-plastic contact situations, with only CNT reinforced MMC presenting constant lubrication. For low loads and low relative humidity, surface oxidation is reduced with CNT acting as an oxidation barrier, effectively separating the contacting surfaces and diminishing the occurrence of wear. Since graphite-based lubrication can be excluded for low relative humidity, lubrication is mainly associated with sliding/rolling of pristine CNT on top of the formed graphitic layer. For higher loads and relative humidity, strong oxidation is observed. However, the formed carbonaceous oxidic layer breaks into sheets, which can freely move on the surface being lubricated by CNT. In this case, lubrication acts on a mixture of sliding/rolling of CNT and shearing based graphite lubrication. Regarding conformal or non-conformal contact situations or different sliding speeds (1 mm/s – 1 m/s) for CNT coated or reinforced composites, efficient and constant lubrication is always given. This qualifies CNT as a versatile solid lubricant, adapting to the given contact situations and environmental conditions by effectively combining different solid lubricant working principles, namely: rolling, sliding and shearing.

OBJECTIVE 3

The combination of CNT-reinforced MMC, specific surface designing by laser structuring and subsequent CNT coating finally results in the production of advanced self-lubricating surfaces. A prototypical self-lubricating surface has been successfully manufactured and is tested in a macroscopically loaded (20 N) conformal contact situation (similar to real testing conditions of a journal-type bearing component), allowing for a maximum reduction in friction and wear by a factor of 4 and 115, respectively (compared to a pure Ni surface) with the lubrication mechanisms being fully understood.

Summarizing, out of the three studied CNP types, CNT are identified as a nano-scale, multi-purpose solid lubricant, which can be effectively applied to create self-lubricating surfaces. Being stored in a nickel matrix or a specifically designed surface, CNT are continuously transferred into the contact and are thus easy to replenish. The effectiveness of the lubrication is comparable to other currently used solid lubricants but is more robust regarding the stress collective or environmental conditions. With sp^2-hybridized graphitic carbon being the most stable carbon configuration under standard pressure and temperature, CNT are expected to provide a very good aging stability. CNT are further known to be thermally stable under atmospheric conditions at temperatures of up to 600-700°C, rendering CNT a promising solid lubricant candidate for higher temperature applications [354]. Additionally, CNT are able to carry away generated heat due to their high thermal conductivity and also provide a high electrical conductivity, rendering them an interesting reinforcement material for tribo-electrical applications (for example plug connectors or contact brushes). Due to their nano-scale size, low density and high mechanical strength, CNT further offer the possibility to mechanically reinforce structural components, which are subjected to friction and wear, thus also being usable for lightweight construction of machine elements. Finally, and together with all the mentioned points, the suitability of CNT as a lubricant under vacuum as well as under atmospheric conditions proves its advantage in terms of applicability and robustness compared to other solid lubricants.

OUTLOOK

The identification of the requirements needed to create self-lubricating surfaces based on CNT and the detailed understanding of their lubrication mechanism are a stepping-stone in the state of the art of this research field. The choice of laser patterning as a very versatile and flexible tool allows for the transfer of the chosen surface design to nearly any material surface. Additionally, the chosen coating technique (electrophoretic deposition) is suited for every electrically conductive substrate material. Hence, the findings presented in this dissertation could be easily transferred to almost any metallic surface, which highlights its wide span of applicability.

The utilization of CNT as solid lubricant in MMC requires the chemical inertness of the matrix material with regards to a potential carbide formation. Thus, with elements such as Cu and Sn showing no tendency to form carbides, the presented method could be transferred to sintered bronze slider bearings, which already find application in almost every sector of tribological importance (general mechanical engineering, automotive, power tools, sports and leisure equipment, office-, textile- or agricultural machinery, etc.). So far, these sintered slider bearings are soaked with a liquid lubricant (e.g. oil) or other solid lubricants such as MoS_2 are embedded. However, regarding the processing of CNT-reinforced sintered bronze slider bearings, research still needs to be carried out.

Regarding other technically applicable materials, such as steel or other alloys, they typically contain elements like Cr, Al, Ti or V, all showing a strong tendency to form thermodynamically-stable

carbides. Hence, when sintering a CNT powder mixture including these elements, CNT would be fully dissolved in the metal phase forming carbides and no lubrication can be expected. One way to overcome this limitation could be a protective coating of the CNT before sintering the composite material, with the coating acting as a diffusion barrier between the metal matrix and the CNT. In this regard, a full CNT encapsulation using the molecular level mixing method could be an interesting approach, although the CNT would be covalently functionalized and thus degraded to some extent. An alternative could be a galvanic coating of the CNT (e.g. with Ni). However, since the coating would form a metallic bond to the matrix material, the mobility of the encapsulated CNT could be reduced, diminishing the lubrication effect. Hence, further research should be carried out in this area.

Another promising approach to expand the field of application of CNT-reinforced Ni-MMC is its use as surface coating using electroless or electro deposition, which is currently studied in literature. These techniques allow applying the self-lubricating MMC onto technically more relevant alloys acting as a friction- and wear-reducing surface protection layer. Also, additive manufacturing, e.g. using laser-cladding, could be very promising in order to coat technically usable components. In this regard, the presented CNT Ni powder processing method could be used to manufacture a precursor powder for this processing route. However, both mentioned coating methods would involve a new process development and full material characterization, since the involved temperatures, microstructure or phase formations could differ significantly from the system presented in this dissertation. Therefore, it would be a complete study in itself.

6. NOT INCLUDED PAPERS

Within the framework of the present dissertation, further research sectors were addressed which are not directly correlated to the topic of the dissertation. Nonetheless, several papers have been published, which are mentioned in the following:

[1] C. Gachot, A. Rosenkranz, **L. Reinert**, E. Ramos-Moore, N. Souza, M. H. Müser, and F. Mücklich, "Dry Friction Between Laser-Patterned Surfaces: Role of Alignment, Structural Wavelength and Surface Chemistry," Tribol. Lett., vol. 9, 2013, doi: 10.1007/s11249-012-0057-y

[2] A. Rosenkranz, **L. Reinert**, C. Gachot, and F. Mücklich, "Alignment and wear debris effects between laser-patterned steel surfaces under dry sliding conditions," Wear, vol. 318, 2014, doi: 10.1016/j.wear.2014.06.016

[3] A. Rosenkranz, **L. Reinert**, C. Gachot, H. Aboufadl, S. Grandthyll, K. Jacobs, F. Müller, and F. Mücklich, "Oxide Formation, Morphology, and Nanohardness of Laser-Patterned Steel Surfaces," Adv. Eng. Mater., 2015, doi 10.1002/adem.201400487

[4] A. Rosenkranz, F. Krupp, **L. Reinert**, F. Mücklich, and B. Sauer, "Tribological performance of laser-patterned chain links – Influence of pattern geometry and periodicity," Wear, vol. 370, 2016, doi: 10.1016/j.wear.2016.11.006

[5] S. Suarez, **L. Reinert**, and F. Mücklich, "Carbon Nanotube (CNT)-Reinforced Metal Matrix Bulk Composites: Manufacturing and Evaluation," in Diamond and Carbon Composites and Nanocomposites, 2016. doi: 10.5772/63886

[6] M. Leidner, S. Thoss, H. Schmidt, **L. Reinert**, K. Trinh, C. Schäfer and F. Mücklich, "Verbesserung der tribologischen und elektrischen Eigenschaften von Zinn-Kontaktoberflächen durch Partikel/Schmierstoff-Einbettung mittels Laser-Texturierung" , 6th Symposium Connectors, 2017, pp. 59-67, Lemgo, Germany

[7] M. Leidner, S. Thoss, H. Schmidt, J. C. Poliseno, **L. Reinert**, C. Schäfer and F. Mücklich, "Verbesserung der tribologischen und elektrischen Eigenschaften von zinnbeschichteten Steckverbindern mittels Laser-Texturierung" , Albert-Keil Seminar of Connectors, 2017, Karlsruhe, Germany

REFERENCES

[1] B. Bhushan, *Principles and Applications of Tribology*, John Wiley & Sons, **1999**.

[2] A. Kamali, in *McMinn D.J.W. Mod. Hip Resurfacing*, Springer, **2009**, pp. 79–89.

[3] K. Holmberg, P. Andersson, A. Erdemir, *Tribol. Int.* **2012**, *47*, 221.

[4] M. Urbakh, J. Klafter, D. Gourdon, J. Israelachvili, *Nature* **2004**, *430*, 525.

[5] C. M. Taylor, *Wear* **1998**, *221*, 1.

[6] B. Zhmud, *Tribol. Lubr. Technol.* **2011**, *67*, 42.

[7] M. Eriksson, F. Bergman, S. Jacobson, *Wear* **2002**, *252*, 26.

[8] A. Khamlichi, M. Bezzazi, A. Jabbouri, R. P., J. P. Davim, *Int. J. Phys. Sci.* **2008**, *3*, 65.

[9] M. M. Khonsari, E. R. Booser, *Applied Tribology: Bearing Design and Lubrication*, John Wiley & Sons Ltd., **2008**.

[10] I. Etsion, *J. Tribol. Trans. ASME* **2005**, *127*, 248.

[11] H. K. D. H. Bhadeshia, *Prog. Mater. Sci.* **2012**, *57*, 268.

[12] M. Woydt, R. Wäsche, *Wear* **2010**, *268*, 1542.

[13] C.Donnet, Ali Erdemir, *Tribol. Lett.* **2004**, *17*, 389.

[14] S. M. Aouadi, H. Gao, A. Martine, T. W. Scharf, C. Muratore, *Surf. Coatings Technol.* **2014**, *257*, 266.

[15] J. R. Jones, M. J. Jansen, *Proc. Inst. Mech. Eng. Part J J. Eng. Tribol.* **2008**, *222*, 997.

[16] A. Dorri Moghadam, E. Omrani, P. L. Menezes, P. K. Rohatgi, *Compos. Part B Eng.* **2015**, *77*, 402.

[17] D. Berman, A. Erdemir, A. V. Sumant, *Mater. Today* **2014**, *17*, 31.

[18] T. W. Scharf, P. G. Kotula, S. V. Prasad, *Acta Mata.* **2010**, *58*, 4100.

[19] C. Muratore, A. A. Voevodin, *Annu. Rev. Mater. Res.* **2009**, *39*, 297.

[20] T. W. Scharf, S. V. Prasad, *J. Mater. Sci.* **2013**, *48*, 511.

[21] B. Bhushan, *Modern Tribology Handook*, CRC Press LLC, **2001**.

[22] S. V. Prasad, R. Asthana, *Tribol. Lett.* **2004**, *17*, 445.

[23] K. U. Kainer, in *Met. Matrix Compos. Cust. Mater. Automot. Aerosp. Eng.*, Wiley-VCH Verlag GmbH, **2006**.

[24] D. Miracle, *Compos. Sci. Technol.* **2005**, *65*, 2526.

[25] P. K. Rohatgi, M. Tabandeh-Khorshid, E. Omrani, M. R. Lovell, P. L. Menezes, in *Tribol. Sci. Eng. From Basics to Adv. Concepts*, Springer New York, **2013**, pp. 233–268.

[26] E. Omrani, A. Moghadam, P. L. Menezes, P. K. Rohatgi, in *Mater. Forming, Mach. Tribol.*, **2016**, pp. 63–103.

[27] G. Hatipoglu, M. Kartal, M. Uysal, T. Cetinkaya, H. Akbulut, *Tribol. Int.* **2016**, *98*, 59.

[28] W. X. Chen, J. P. Tu, L. Y. Wang, H. Y. Gan, Z. D. Xu, X. B. Zhang, *Carbon* **2003**, *41*, 215.

[29] X. H. Chen, J. Peng, F. Deng, J. Wang, W. Li, *J. Mater. Sci. Lett.* **2001**, *20*, 2057.

[30] J. Tan, T. Yu, B. Xu, Q. Yao, *Tribol. Lett.* **2006**, *21*, 107.

[31] Y. Gogotsi, V. Presser, *Carbon Nanomaterials*, CRC Press, **2014**.

[32] S. R. Bakshi, D. Lahiri, A. Agarwal, *Int. Mater. Rev.* **2010**, *55*, 41.

[33] V. N. Mochalin, O. Shenderova, D. Ho, Y. Gogotsi, *Nat. Nanotechnol.* **2012**, *7*, 11.

[34] M. R. Falvo, R. M. T. Ii, A. Helser, V. Chi, *Nature* **1999**, *397*, 1.

[35] P. L. Dickrell, S. B. Sinnott, D. W. Hahn, N. R. Raravikar, L. S. Schadler, P. M. Ajayan, W. G.

Sawyer, *Tribol. Lett.* **2005**, *18*, 59.

[36] A. Hirata, M. Igarashi, T. Kaito, *Tribol. Int.* **2004**, *37*, 899.

[37] K. T. Kim, S. Il Cha, S. H. Hong, *Mater. Sci. Eng. A* **2007**, *449–451*, 46.

[38] X. H. Chen, C. S. Chen, H. N. Xiao, H. B. Liu, L. P. Zhou, S. L. Li, G. Zhang, *Tribol. Int.* **2006**, *39*, 22.

[39] S. Arai, A. Fujimori, M. Murai, M. Endo, *Mater. Lett.* **2008**, *62*, 3545.

[40] S. Suárez, A. Rosenkranz, C. Gachot, F. Mücklich, *Carbon* **2014**, *66*, 164.

[41] Y. Li, B. X. Li, W. J. Zou, *Appl. Mech. Mater.* **2011**, *80–81*, 683.

[42] L. Wang, Y. Gao, Q. Xue, H. Liu, T. Xu, *Mater. Sci. Eng. A* **2005**, *390*, 313.

[43] V. Y. Dolmatov, T. Fujimura, G. K. Burkat, E. A. Orlova, M. V Veretennikova, *Powder Metall. Met. Ceram.* **2003**, *42*, 55.

[44] T. W. Scharf, A. Neira, J. Y. Hwang, J. Tiley, R. Banerjee, *J. Appl. Phys.* **2009**, *106*, 13508.

[45] J. M. Martin, N. Ohmae, *Nanolubricants*, John Wiley & Sons Ltd., **2008**.

[46] L. Joly-Pottuz, E. W. Bucholz, N. Matsumoto, S. R. Phillpot, S. B. Sinnott, N. Ohmae, J. M. Martin, *Tribol. Lett.* **2010**, *37*, 75.

[47] B. Ni, S. B. Sinnott, *Surf. Sci.* **2001**, *487*, 87.

[48] S. Iijima, *Nature* **1991**, *354*, 56.

[49] M. F. L. De Volder, S. H. Tawfick, R. H. Baughman, A. J. Hart, *Science* **2013**, *339*, 535.

[50] J. Cebik, J. K. McDonough, F. Peerally, R. Medrano, I. Neitzel, Y. Gogotsi, S. Osswald, *Nanotechnology* **2013**, *24*, 1.

[51] F. Mücklich, A. Lasagni, C. Daniel, *Int. J. Mat. Res.* **2006**, *97*, 1337.

[52] T. Hu, Y. Zhang, L. Hu, *Wear* **2012**, *278–279*, 77.

[53] A. Rosenkranz, T. Heib, C. Gachot, F. Mücklich, *Wear* **2015**, *334–335*, 1.

[54] H. O. Pierson, *Handbook of Carbon, Graphite, Diamonds and Fullerenes*, Noyes Publications, **1994**.

[55] M. S. Dresselhaus, G. Dresselhaus, P. Avouris, *Carbon Nanotubes*, Springer Verlag, **2003**.

[56] C. Buzea, I. I. Pacheco, K. Robbie, *Biointerphases* **2007**, *2*, 17.

[57] M. Terrones, A. R. Botello-Méndez, J. Campos-Delgado, F. López-Urías, Y. I. Vega-Cantú, F. J. Rodríguez-Macías, A. L. Elías, E. Muñoz-Sandoval, A. G. Cano-Márquez, J. C. Charlier, H. Terrones, *Nano Today* **2010**, *5*, 351.

[58] J. H. Lehman, M. Terrones, E. Mansfield, K. E. Hurst, V. Meunier, *Carbon* **2011**, *49*, 2581.

[59] I. Suarez-Martinez, N. Grobert, C. P. Ewels, *Carbon* **2012**, *50*, 741.

[60] L. Joly-pottuz, N. Matsumoto, H. Kinoshita, B. Vacher, M. Belin, G. Montagnac, *Tribol. Int.* **2008**, *41*, 69.

[61] V. V. Danilenko, *Phys. Solid State* **2004**, *46*, 595.

[62] C.-C. Chou, S.-H. Lee, *Wear* **2010**, *269*, 757.

[63] K. V. Purtov, A. I. Petunin, A. E. Burov, A. P. Puzyr, V. S. Bondar, *Nanoscale Res. Lett.* **2010**, *5*, 631.

[64] Y. R. Chang, H. Y. Lee, K. Chen, C. C. Chang, D. S. Tsai, C. C. Fu, T. S. Lim, Y. K. Tzeng, C. Y. Fang, C. C. Han, H. C. Chang, W. Fann, *Nat. Nanotechnol.* **2008**, *3*, 284.

[65] Q. Zhang, V. N. Mochalin, I. Neitzel, I. Y. Knoke, J. Han, C. A. Klug, J. G. Zhou, P. I. Lelkes, Y. Gogotsi, *Biomaterials* **2011**, *32*, 87.

[66] G.-W. Yang, J.-B. Wang, Q.-X. Liu, *J. Phys. Condens. Matter* **1998**, *10*, 7923.

[67] J.-P. Boudou, P. a Curmi, F. Jelezko, J. Wrachtrup, P. Aubert, M. Sennour, G. Balasubramanian, R. Reuter, A. Thorel, E. Gaffet, *Nanotechnology* **2009**, *20*, 1.

[68] N. R. Greiner, D. S. Phillips, J. D. Johnson, F. Volk, *Nature* **1988**, *333*, 440.

[69] D. M. Gruen, O. A. Shenderova, A. Y. Vul, *Synthesis, Properties and Applications of Ultrananocrystalline Diamond*, Springer Verlag, **2005**.

[70] S. Osswald, G. Yushin, V. Mochalin, S. O. Kucheyev, Y. Gogotsi, *J. Am. Chem. Soc.* **2006**, *128*, 11635.

[71] S. V Kidalov, F. M. Shakhov, A. Y. Vul, *Diam. Relat. Mater.* **2007**, *16*, 2063.

[72] K. M. El-Say, *J. Appl. Pharm. Sci.* **2011**, *1*, 29.

[73] M. Zeiger, N. Jäckel, V. N. Mochalin, V. Presser, *J. Mater. Chem. A* **2016**, *4*, 3172.

[74] A. Camisasca, S. Giordani, *Inorganica Chim. Acta* **2017**, *468*, 67.

[75] J. Bartelmess, S. Giordani, *Beilstein J. Nanotechnol.* **2014**, *5*, 1980.

[76] S. Iijima, *J. Cryst. Growth* **1980**, *50*, 675.

[77] D. Ugarte, *Nature* **1992**, *359*, 707.

[78] M. Ghosh, S. K. Sonkar, M. Saxena, S. Sarkar, *Small* **2011**, *7*, 3170.

[79] F. D. Han, B. Yao, Y. J. Bai, *J. Phys. Chem. C* **2011**, *115*, 8923.

[80] I. Alexandrou, H. Wang, N. Sano, G. A. J. Amaratunga, *J. Chem. Phys.* **2004**, *120*, 1055.

[81] M. Choucair, J. A. Stride, *Carbon* **2012**, *50*, 1109.

[82] L. Echegoyen, A. Ortiz, M. N. Chaur, A. J. Palkar, in *Chem. Nanocarbons*, **2010**, pp. 463–483.

[83] B. J. M. Etzold, I. Neitzel, M. Kett, F. Strobl, V. N. Mochalin, Y. Gogotsi, *Chem. Mater.* **2014**, *26*, 3479.

[84] P. Ganesh, P. R. C. Kent, V. Mochalin, *J. Appl. Phys.* **2011**, *110*, DOI 10.1063/1.3641984.

[85] M. Zeiger, N. Jäckel, M. Aslan, D. Weingarth, V. Presser, *Carbon* **2015**, *84*, 584.

[86] A. Rosenkranz, L. Freeman, S. Fleischmann, F. Lasserre, Y. Fainman, F. E. Talke, *Carbon* **2018**, *132*, 495.

[87] T. Belin, F. Epron, *Mater. Sci. Eng. B Solid-State Mater. Adv. Technol.* **2005**, *119*, 105.

[88] H. Dai, *Surf. Sci.* **2002**, *500*, 218.

[89] I. Kang, Y. Y. Heung, J. H. Kim, J. W. Lee, R. Gollapudi, S. Subramaniam, S. Narasimhadevara, D. Hurd, G. R. Kirikera, V. Shanov, M. J. Schulz, D. Shi, J. Boerio, S. Mall, M. Ruggles-Wren, *Compos. Part B Eng.* **2006**, *37*, 382.

[90] J. P. Salvetat-Delmotte, A. Rubio, *Carbon* **2002**, *40*, 1729.

[91] P. L. Dickrell, S. K. Pal, G. R. Bourne, C. Muratore, A. A. Voevodin, P. M. Ajayan, L. S. Schadler, W. G. Sawyer, *Tribol. Lett.* **2006**, *24*, 85.

[92] N. Souza, Laser and Carbon : Nanotube Synthesis and Annealing, Saarland university, **2017**.

[93] Y. Gogotsi, *Nanotubes and Nanofibers*, CRC Press, Taylor And Francis Group, **2006**.

[94] S. Reich, C. Thomsen, J. Maultzsch, *Carbon Nanotubes: Basic Concepts and Physical Properties*, Wiley-VCH Verlag GmbH, **2004**.

[95] R. Saito, M. Fujita, G. Dresselhaus, M. S. Dresselhaus, *Phys. Rev. B* **1992**, *46*, 1804.

[96] M. Yu, *Science (80-.).* **2000**, *287*, 637.

[97] P. Kim, L. Shi, A. Majumdar, P. McEuen, *Phys. Rev. Lett.* **2001**, *87*, 215502.

[98] S. Berber, Y. Kwon, D. Tomanek, *Phys. Rev. Lett.* **2000**, *84*, 4613.

[99] B. G. Demczyk, Y. M. Wang, J. Cumings, M. Hetman, W. Han, A. Zettl, R. O. Ritchie, *Mater. Sci. Eng. A* **2002**, *334*, 173.

[100] F. Li, H. M. Cheng, S. Bai, G. Su, M. S. Dresselhaus, *Appl. Phys. Lett.* **2000**, *77*, 3161.

[101] Y. Lu, P. K. Liaw, *JOM* **2001**, 31.

[102] M. R. Falvo, G. J. Clary, R. M. Taylor, V. Chi, F. P. Brooks, S. Washburn, R. Superfine, *Nature* **1997**, *389*, 582.

[103] S. Suarez, L. Reinert, F. Mücklich, in *Diam. Carbon Compos. Nanocomposites*, IntechOpen, **2016**.

[104] M. M. A. Rafique, J. Iqbal, *J. Encapsulation Adsorpt. Sci.* **2011**, *1*, 29.

[105] M. Paradise, T. Goswami, *Mater. Des.* **2007**, *28*, 1477.

[106] M. Kumar, Y. Ando, *J. Nanosci. Nanotechnol.* **2010**, *10*, 3739.

[107] K. E. Kim, K. J. Kim, W. S. Jung, S. Y. Bae, J. Park, J. Choi, J. Choo, *Chem. Phys. Lett.* **2005**, *401*, 459.

[108] H. Hou, A. K. Schaper, F. Weller, A. Greiner, *Chem. Mater.* **2002**, *14*, 3990.

[109] C. H. See, A. T. Harris, *Ind. Eng. Chem. Res.* **2007**, *46*, 997.

[110] N. M. Mubarak, E. C. Abdullah, N. S. Jayakumar, J. N. Sahu, *J. Ind. Eng. Chem.* **2014**, *20*, 1186.

[111] C. V. Raman, K. S. Krishan, *Nature* **1928**, *121*, 501.

[112] D. J. Gardiner, P. R. Graves, *Practical Raman Spectroscopy*, Springer Verlag Berlin Heidelberg, **1989**.

[113] S. R. Sails, D. J. Gardiner, M. Bowden, J. Savage, D. Rodway, *Diam. Relat. Mater.* **1996**, *5*, 589.

[114] O. O. Mykhaylyk, Y. M. Solonin, D. N. Batchelder, R. Brydson, *J. Appl. Phys.* **2005**, *97*, 1.

[115] A. Ferrari, J. Robertson, *Phys. Rev. B* **2000**, *61*, 14095.

[116] R. Loudon, in *Adv. Phys.*, **1964**, pp. 423–482.

[117] M. a Pimenta, G. Dresselhaus, M. S. Dresselhaus, L. G. Cançado, A. Jorio, R. Saito, *Phys. Chem. Chem. Phys.* **2007**, *9*, 1276.

[118] A. C. Ferrari, *Solid State Commun.* **2007**, *143*, 47.

[119] M. S. Dresselhaus, G. Dresselhaus, R. Saito, A. Jorio, *Phys. Rep.* **2005**, *409*, 47.

[120] R. A. DiLeo, B. J. Landi, R. P. Raffaelle, *J. Appl. Phys.* **2007**, *101*, DOI 10.1063/1.2712152.

[121] S. Suarez, F. Lasserre, O. Prat, F. Mücklich, *Phys. Status Solidi* **2014**, *211*, 1555.

[122] F. Tuinstra, *J. Chem. Phys.* **1970**, *53*, 1126.

[123] L. G. Caṇado, K. Takai, T. Enoki, M. Endo, Y. A. Kim, H. Mizusaki, A. Jorio, L. N. Coelho, R. Magalhães-Paniago, M. A. Pimenta, *Appl. Phys. Lett.* **2006**, *88*, 2.

[124] S. Prawer, K. W. Nugent, D. N. Jamieson, J. O. Orwa, L. A. Bursill, J. L. Peng, *Chem. Phys. Leters* **2000**, *332*, 93.

[125] G. N. Yushin, S. Osswald, V. I. Padalko, G. P. Bogatyreva, Y. Gogotsi, *Diam. Relat. Mater.* **2005**, *14*, 1721.

[126] G. Morell, O. Quifiones, Y. Diaz, I. M. Vargas, B. R. Weiner, R. S. Katiyar, *Diam. Relat. Mater.* **1998**, *7*, 1029.

[127] L. C. Nistor, V. Landuyt, V. G. Ralchenko, E. D. Obraztsova, A. A. Smolin, *Diam. Carbon Compos. Nanocomposites* **1997**, *6*, 159.

[128] V. Mochalin, S. Osswald, Y. Gogotsi, *Chem. Mater* **2009**, *21*, 273.

[129] D. B. Miracle, S. L. Donaldson, V. Chairs, S. D. Henry, P. Editor, C. Moosbrugger, T. Editor, G. J. Anton, E. Assistant, B. R. Sanders, M. Production, N. Hrivnak, C. Terman, C. Editors, J. Brown, E. J.

Kubel, M. Park, *ASM Handbook - Composites*, ASM International, **2001**.

[130] A. D. Moghadam, B. F. Schultz, J. B. Ferguson, E. Omrani, P. K. Rohatgi, N. Gupta, *Jom* **2014**, *66*, 872.

[131] T. Kuzumaki, K. Miyazawa, H. Ichinose, k. Ito, *J. Mater. Res.* **1998**, *13*, 2445.

[132] H. Kwon, M. Takamichi, A. Kawasaki, M. Leparoux, *Mater. Chem. Phys.* **2013**, *138*, 787.

[133] T. Borkar, J. Hwang, J. Y. Hwang, T. W. Scharf, J. Tiley, S. H. Hong, R. Banerjee, *J. Mater. Res.* **2014**, *29*, 761.

[134] B. Lim, C. Kim, B. Kim, U. Shim, S. Oh, B. Sung, J. Choi, S. Baik, *Nanotechnology* **2006**, *17*, 5759.

[135] Q. Liu, L. Ke, F. Liu, C. Huang, L. Xing, *Mater. Des.* **2013**, *45*, 343.

[136] C. A. Isaza Merino, J. M. Meza Meza, G. A. Sierra Gallego, *J. Manuf. Sci. Eng.* **2016**, *138*, 1.

[137] W. Xu, R. Hu, J. Li, H. Fu, *Trans. Nonferrous Met. Soc. China* **2011**, *21*, 2237.

[138] H. Imai, K. Kondoh, S. Li, J. Umeda, B. Fugetsu, M. Takahashi, *Mater. Trans.* **2014**, *55*, 522.

[139] J. Y. Hwang, A. Neira, T. W. Scharf, J. Tiley, R. Banerjee, *Scr. Mater.* **2008**, *59*, 487.

[140] A. Agarwal, S. Bakshi, D. Lahiri, *Carbon Nanotubes - Reinforced Metal Matrix Composites*, CRC Press, Taylor And Francis Group, **2011**.

[141] F. Avilés, J. V. Cauich-Rodríguez, L. Moo-Tah, A. May-Pat, R. Vargas-Coronado, *Carbon* **2009**, *47*, 2970.

[142] D. H. Nam, Y. K. Kim, S. I. Cha, S. H. Hong, *Carbon* **2012**, *50*, 4809.

[143] K. T. Kim, J. Eckert, G. Liu, J. M. Park, B. K. Limd, S. H. Hong, *Scr. Mater.* **2011**, *64*, 181.

[144] M. Lal, S. K. Singhal, I. Sharma, R. B. Mathur, *Appl. Nanosci.* **2012**, *3*, 29.

[145] P.-C. Tsai, Y.-R. Jeng, *Compos. Sci. Technol.* **2013**, *79*, 28.

[146] J. Y. Hwang, B. K. Lim, J. Tiley, R. Banerjee, S. H. Hong, *Carbon* **2013**, *57*, 282.

[147] H. J. Choi, J. H. Shin, D. H. Bae, *Compos. Part A Appl. Sci. Manuf.* **2012**, *43*, 1061.

[148] H. J. Choi, B. H. Min, J. H. Shin, D. H. Bae, *Compos. Part A Appl. Sci. Manuf.* **2011**, *42*, 1438.

[149] H. J. Choi, J. H. Shin, D. H. Bae, *Compos. Sci. Technol.* **2011**, *71*, 1699.

[150] H. Asgharzadeh, S.-H. Joo, H. S. Kim, *Metall. Mater. Trans. A* **2014**, *45*, 4129.

[151] O. Carvalho, G. Miranda, D. Soares, F. S. Silva, *Mech. Adv. Mater. Struct.* **2016**, *23*, 66.

[152] J. P. Tu, Y. Z. Yang, L. Y. Wang, X. C. Ma, X. B. Zhang, *Tribol. Lett.* **2001**, *10*, 225.

[153] Z. W. Xue, L. D. Wang, P. T. Zhao, S. C. Xu, J. L. Qi, W. D. Fei, *Mater. Des.* **2012**, *34*, 298.

[154] Q. Cheng, S. Debnath, E. Gregan, H. J. Byrne, *J. Phys. Chem. C* **2010**, *114*, 8821.

[155] J. Hilding, E. A. Grulke, Z. George Zhang, F. Lockwood, *J. Dispers. Sci. Technol.* **2003**, *24*, 1.

[156] C. Guiderdoni, E. Pavlenko, V. Turq, A. Weibel, P. Puech, C. Estournès, A. Peigney, W. Bacsa, C. Laurent, *Carbon* **2013**, *58*, 185.

[157] R. Sule, P. A. Olubambi, I. Sigalas, J. K. O. Asante, J. C. Garrett, W. D. Roos, *Synth. Met.* **2015**, *202*, 123.

[158] T. Tokunaga, K. Kaneko, Z. Horita, *Mater. Sci. Eng. A* **2008**, *490*, 300.

[159] S. Cho, K. Kikuchi, T. Miyazaki, K. Takagi, A. Kawasaki, T. Tsukada, *Scr. Mater.* **2010**, *63*, 375.

[160] K. Rajkumar, S. Aravindan, *Wear* **2011**, *270*, 613.

[161] C. Guiderdoni, C. Estournès, A. Peigney, A. Weibel, V. Turq, C. Laurent, *Carbon* **2011**, *49*, 4535.

[162] D. D. Phuong, P. Van Trinh, N. Van An, N. Van Luan, P. N. Minh, R. K. Khisamov, K. S. Nazarov, L. R. Zubairov, R. R. Mulyukov, A. A. Nazarov, *J. Alloys Compd.* **2014**, *613*, 68.

[163] U. Maitra, A. Gomathi, C. N. R. Rao, *J. Exp. Nanosci.* **2008**, *3*, 271.

[164] Suk-Joong L.Kang, *Sintering, Densification,Grain Growth,and Microstructure*, Elsevier Butterworth Heinemann, **2005**.

[165] C. Li, X. Liu, J. Yi, L. Teng, R. Bao, J. Tan, C. Yang, Z. Zou, *J. Mater. Res.* **2016**, *31*, 3757.

[166] Q. Huang, L. Gao, Y. Liu, J. Sun, *J. Mater. Chem.* **2005**, *15*, 1995.

[167] V. Livramento, J. B. Correia, N. Shohoji, E. Ōsawa, *Diam. Relat. Mater.* **2007**, *16*, 202.

[168] G.-D. Zhan, J. D. Kuntz, J. Wan, A. K. Mukherjee, *Nat. Mater.* **2003**, *2*, 38.

[169] S. Suárez, E. Ramos-Moore, B. Lechthaler, F. Mücklich, *Carbon* **2014**, *70*, 173.

[170] N. Hansen, *Scr. Mater.* **2004**, *51*, 801.

[171] P. A. Manohar, M. Ferry, T. Chandra, *ISIJ Int.* **1998**, *38*, 913.

[172] A. Sanaty-Zadeh, *Mater. Sci. Eng. A* **2012**, *531*, 112.

[173] S. R. Bakshi, A. Agarwal, *Carbon* **2011**, *49*, 533.

[174] M. Paramsothy, J. Chan, R. Kwok, M. Gupta, *Compos. Part A Appl. Sci. Manuf.* **2011**, *42*, 180.

[175] S. M. Uddin, T. Mahmud, C. Wolf, C. Glanz, I. Kolaric, C. Volkmer, H. Höller, U. Wienecke, S. Roth, H.-J. Fecht, *Compos. Sci. Technol.* **2010**, *70*, 2253.

[176] K. S. Munir, P. Kingshott, C. Wen, *Crit. Rev. Solid State Mater. Sci.* **2015**, *40*, 38.

[177] A. M. K. Esawi, K. Morsi, A. Sayed, M. Taher, S. Lanka, *Compos. Sci. Technol.* **2010**, *70*, 2237.

[178] R. George, K. T. Kashyap, R. Rahul, S. Yamdagni, *Scr. Mater.* **2005**, *53*, 1159.

[179] N. Hu, B. Jia, M. Arai, C. Yan, J. Li, Y. Liu, S. Atobe, H. Fukunaga, *Comput. Mater. Sci.* **2012**, *54*, 249.

[180] Y.-K. Kwon, S. Berber, D. Tománek, *Phys. Rev. Lett.* **2004**, *92*, 15901.

[181] N. Karousis, N. Tagmatarchis, D. Tasis, *Chem. Rev.* **2010**, *110*, 5366.

[182] Y.-L. Zhao, J. F. Stoddart, *Acc. Chem. Res.* **2009**, *42*, 1161.

[183] L. Vaisman, H. D. Wagner, G. Marom, *Adv. Colloid Interface Sci.* **2006**, *128–130*, 37.

[184] N. Pierard, a Fonseca, J.-F. Colomer, C. Bossuot, J.-M. Benoit, G. Van Tendeloo, J.-P. Pirard, J. . Nagy, *Carbon* **2004**, *42*, 1691.

[185] S. C. Tjong, *Mater. Sci. Eng. R Reports* **2013**, *74*, 281.

[186] R. Pérez-Bustamante, I. Estrada-Guel, W. Antúnez-Flores, M. Miki-Yoshida, P. J. Ferreira, R. Martínez-Sánchez, *J. Alloys Compd.* **2008**, *450*, 323.

[187] M. . Vidal-Sétif, M. Lancin, C. Marhic, R. Valle, J.-L. Raviart, J.-C. Daux, M. Rabinovitch, *Mater. Sci. Eng. A* **1999**, *272*, 321.

[188] L. M. Tham, L. Cheng, *Acta Mata.* **2001**, *49*, 3243.

[189] P. Poncharal, C. Berger, Y. Yi, Z. Wang, W. de Heer, *J. Phys. Chem. B* **2002**, *106*, 12104.

[190] I. Firkowska, A. Boden, A.-M. Vogt, S. Reich, *J. Mater. Chem.* **2011**, *21*, 17541.

[191] J. Hone, M. C. Llaguno, N. M. Nemes, A. T. Johnson, J. E. Fischer, D. A. Walters, M. J. Casavant, J. Schmidt, R. E. Smalley, J. Hone, M. C. Llaguno, N. M. Nemes, A. T. Johnson, *Appl. Phys. Lett.* **2004**, *77*, 666.

[192] S. Yamanaka, R. Gonda, A. Kawasaki, H. Sakamoto, Y. Mekuchi, M. Kun, T. Tsukada, *Mater. Trans.* **2007**, *48*, 2506.

[193] J. S. Gibson, J. Uddin, T. R. Cundari, N. K. Bodiford, A. K. Wilson, *J. Phys. Condens. Matter* **2010**, *22*, 445503.

[194] S. Suarez, F. Lasserre, F. Mücklich, *Mater. Sci. Eng. A* **2013**, *587*, 381.

[195] S. C. Tjong, *Carbon Nanotube Reinforced Composites*, Wiley-VCH Verlag GmbH, **2009**.

[196] V. A. Popov, E. V Vershinina, *Eur. J. Inorg. Chem.* **2016**, 2122.

[197] V. A. Popov, in *Nanocomposites*, Nova Science Publishers, Inc., **2013**, pp. 369–401.

[198] V. Popov, *Surf. Interface Anal.* **2018**, 1.

[199] H. Kwon, G. Lee, S. Kim, B. Lee, W. Seo, M. Leparoux, *Mater. Sci. Eng. A* **2015**, *632*, 72.

[200] F. Zhang, S. Liu, P. Zhao, T. Liu, J. Sun, *Mater. Des.* **2017**, *131*, 144.

[201] D. Nunes, V. Livramento, J. B. Correia, K. Hanada, *Mater. Sci. Forum* **2010**, *636–637*, 682.

[202] D. Nunes, M. Vilarigues, J. B. Correia, P. A. Carvalho, *Acta Mata.* **2012**, *60*, 737.

[203] M. Yu, C. George, Y. Cao, *J Mater Sci* **2014**, *49*, 3629.

[204] S. Yin, Y. Xie, J. Cizek, E. J. Ekoi, T. Hussain, D. P. Dowling, R. Lupoi, *Compos. Part B* **2017**, *113*, 44.

[205] D. J. Woo, B. Sneed, F. Peerally, F. C. Heer, L. N. Brewer, J. P. Hooper, S. Osswald, *Carbon* **2013**, *63*, 404.

[206] V. P. Isakov, A. I. Lyamkin, D. N. Nikitin, A. S. Shalimova, A. V Solntsev, *Prot. Met. Phys. Chem. surfaces* **2010**, *46*, 578.

[207] H. Czichos, K. Habig, *Tribologie-Handbuch*, Vieweg+Teubner, **2010**.

[208] C. Donnet, A. Erdemir, *Tribol. Lett.* **2004**, *17*, 389.

[209] A. Rosenkranz, L. Reinert, C. Gachot, H. Aboufadl, S. Grandthyll, K. Jacobs, F. Müller, F. Mücklich, *Adv. Eng. Mater.* **2015**, *17*, 1234.

[210] A. J. Gellman, N. D. Spencer, *J. Eng. Tribol.* **2002**, *216*, 443.

[211] P. J. Blau, in *Encycl. Tribol.*, Springer, Boston, **2013**.

[212] E. J. Abbott, F. A. Firestone, *Mech. Eng.* **1933**, *55*, 569.

[213] H. Hertz, *J. für die reine und Angew. Math. 92* **1881**.

[214] J. Greenwood, J. Williamson, *Proc. R. Soc. London* **1966**, *295*, 300.

[215] L. Kogut, I. Etsion, *J. Tribol.* **2004**, *126*, 34.

[216] W. R. Chang, I. Etsion, D. B. Bogy, *J. Tribol.* **1987**, *109*, 257.

[217] R. Jackson, I. Green, *Tribol. Trans.* **2011**, *54*, 300.

[218] B. N. J. Persson, *Surf. Sci. Rep.* **2006**, *61*, 201.

[219] W. Grabon, P. Pawlus, J. Sep, *Tribiology Int.* **2010**, *43*, 1882.

[220] A. Rosenkranz, A. Szurdak, C. Gachot, G. Hirt, F. Mücklich, *Tribiology Int.* **2016**, *95*, 290.

[221] R. A. Singh, E.-S. Yoon, H. J. Kim, H. Kong, S. Park, H. E. Jeong, K. Y. Suh, *Surf. Eng.* **2007**, *23*, 161.

[222] I. Etsion, *Tribol. Lett.* **2004**, *17*, 733.

[223] R. L. Jackson, I. Green, *Tribol. Int.* **2006**, *39*, 906.

[224] F. P. Bowden, D. Tabor, *The Friction and Lubrication of Solids*, Clarendon Press - Oxford, **2001**.

[225] R. Mishra, B. Basu, R. Balasubramaniam, *Mater. Sci. Eng. A* **2004**, *373*, 370.

[226] A. Kruglova, M. Engstler, G. Gaiselmann, O. Stenzel, V. Schmidt, M. Roland, S. Diebels, F. Mücklich, *Comput. Mater. Sci.* **2016**, *120*, 99.

[227] F. H. Stott, G. C. Wood, *Tribol. Int.* **1978**, 211.

[228] R. K. Singh Raman, A. S. Khanna, R. K. Tiwari, J. B. Gnanamoorthy, *Oxid. Met.* **1992**, *37*, 1.

[229] N. Argibay, M. Chandross, S. Cheng, J. R. Michael, *J. Mater. Sci.* **2017**, *52*, 2780.

[230] M. Hirano, K. Shinjo, R. Kaneko, Y. Murata, *Phys. Rev. Lett.* **1991**, *67*, 2642.

[231] W. F. Hosford, *Textures Microstruct.* **1996**, *26*, 479.

[232] G. Gottstein, *Physical Foundations of Materials Science*, Springer Verlag, **2004**.

[233] F. P. Bowden, D. Tabor, *Br. J. Appl. Phys.* **1966**, *17*, 1521.

[234] D. H. Buckley, W. A. Brainard, *Carbon* **1975**, *13*, 501.

[235] R. Sengupta, M. Bhattacharya, S. Bandyopadhyay, A. K. Bhowmick, *Prog. Polym. Sci.* **2011**, *36*, 638.

[236] J. S. Bunch, S. S. Verbridge, J. S. Alden, A. M. Van Der, J. M. Parpia, H. G. Craighead, P. L. Mceuen, J. S. Bunch, S. S. Verbridge, J. S. Alden, A. M. Van Der Zande, J. M. Parpia, H. G. Craighead, P. L. Mceuen, *Nano Lett.* **2008**, *8*, 2458.

[237] C. Lee, Q. Li, W. Kalb, X. Z. Liu, H. Berger, R. W. Carpick, J. Hone, *Science (80-.).* **2010**, *328*, 76.

[238] D. Berman, A. Erdemir, A. V. Sumant, *Carbon* **2013**, *54*, 454.

[239] D. Berman, A. Erdemir, A. V. Sumant, *Carbon* **2013**, *59*, 167.

[240] W. Zhai, N. Srikanth, L. B. Kong, K. Zhou, *Carbon* **2017**, *119*, 150.

[241] J. Robertson, *Mater. Sci. Eng. Reports* **2002**, *37*, 129.

[242] C. Donnet, A. Erdemir, *Tribology of Diamond-Like Carbon Films*, Springer, **2007**.

[243] A. Erdemir, O. L. Eryilmaz, G. Frenske, *J. Vac. Sci. Technol. A Vacuum, Surfaces, Film.* **2000**, *18*, 1982.

[244] T. W. Scharf, J. A. Ohlhausen, D. R. Tallant, S. V. Prasad, *J. Appl. Phys.* **2007**, *101*, DOI 10.1063/1.2711147.

[245] A. R. Konicek, D. S. Grierson, P. U. P. A. Gilbert, W. G. Sawyer, A. V. Sumant, R. W. Carpick, *Phys. Rev. Lett.* **2008**, *100*, 1.

[246] A. Savan, E. Pflüger, P. Voumard, A. Schröer, M. S. Paul, *Lubr. Sci.* **2000**, *12*, 185.

[247] L. Cizaire, B. Vacher, T. Le Mogne, J. M. Martin, L. Rapoport, A. Margolin, R. Tenne, *Surf. coatings Technol.* **2002**, *160*, 282.

[248] L. Rapoport, N. Fleischer, R. Tenne, *Adv. Mater.* **2003**, *15*, 651.

[249] H. E. Sliney, *Tribol. Int.* **1982**, *15*, 303.

[250] S. V. Prasad, J. S. Zabinski, *J. Mater. Sci. Lett.* **1993**, *12*, 1413.

[251] B. C. Windom, W. G. Sawyer, D. W. Hahn, *Tribol. Lett.* **2011**, *42*, 301.

[252] J. S. Zabinski, M. S. Donley, S. D. Walck, T. R. Schneider, N. T. McDevitt, *Tribol. Trans.* **1995**, *38*, 894.

[253] T. Polcar, A. Cavaleiro, *Surf. Coatings Technol.* **2011**, *206*, 686.

[254] B. J. Briscoe, D. Tabor, *Wear* **1975**, *34*, 29.

[255] A. Erdemir, *Tribol. Lett.* **2000**, *8*, 97.

[256] T. Aizawa, A. Mitsuo, S. Yamamoto, T. Sumitomo, S. Muraishi, *Wear* **2005**, *259*, 708.

[257] F. P. Bowden, D. Tabor, *Nature* **1942**, *150*, 197.

[258] J. Kogovšek, M. Remškar, A. Mrzel, M. Kalin, *Tribol. Int.* **2013**, *61*, 40.

[259] B. N. J. Persson, O. Albohr, U. Tartaglino, A. I. Volokitin, E. Tosatti, *J. Phys. Condens. Matter* **2005**, *17*, DOI 10.1088/0953-8984/17/1/R01.

[260] H. Lee, B. Bhushan, *J. Colloid Interface Sci.* **2011**, *353*, 574.

[261] M. Sahin, C. S. Çetinarslan, H. E. Akata, *Mater. Des.* **2007**, *28*, 633.

[262] F. Svahn, Å. Kassman-Rudolphi, E. Wallén, *Wear* **2003**, *254*, 1092.

[263] K. Komvopoulos, *J. Adhes. Sci. Technol.* **2003**, *17*, 477.

[264] J. Sondhauß, H. Fuchs, A. Schirmeisen, *Tribol. Lett.* **2011**, *42*, 319.

[265] S. Yuan, W. Huang, X. Wang, *Tribol. Int.* **2011**, *44*, 1047.

[266] A. Rosenkranz, L. Reinert, C. Gachot, F. Mücklich, *Wear* **2014**, *318*, 49.

[267] A. A. Voevodin, J. S. Zabinski, *Wear* **2006**, *261*, 1285.

[268] K. H. Leitz, B. Redlingshöer, Y. Reg, A. Otto, M. Schmidt, *Phys. Procedia* **2011**, *12*, 230.

[269] A. Lasagni, Advanced Design of Periodical Structures by Laser Interference Metallurgy in the Micro/nano Scale on Macroscopic Areas, Saarland university, **2006**.

[270] P. Grützmacher, A. Rosenkranz, C. Gachot, *Appl. Surf. Sci.* **2016**, *370*, 59.

[271] A. Rosenkranz, Tribologie an Oberflächen Mit Maßgeschneidertem Topographischem Design, Saarland university, **2014**.

[272] C. Gachot, A. Rosenkranz, L. Reinert, E. Ramos-Moore, N. Souza, M. H. Müser, F. Mücklich, *Tribol. Lett.* **2013**, *9*, 193.

[273] J. Li, D. Xiong, J. Dai, Z. Huang, R. Tyagi, *Tribol. Int.* **2010**, *43*, 1193.

[274] J. Kałużny, A. Merkisz-Guranowska, M. Giersig, K. Kempa, *Int. J. Automot. Technol.* **2017**, *18*, 1047.

[275] Y. Peng, Y. Hu, H. Wang, *Tribol. Lett.* **2006**, *25*, 247.

[276] Y. Yao, X. Wang, J. Guo, X. Yang, B. Xu, *Mater. Lett.* **2008**, *62*, 2524.

[277] M. G. Ivanov, D. M. Ivanov, S. V. Pavlyshko, I. Petrov, A. Vargas, G. McGuire, O. Shenderova, *Fullerenes, Nanotub. Carbon Nanostructures* **2012**, *20*, 606.

[278] A. P. Puzyr, A. E. Burov, G. E. Selyutin, V. Voroshilov, V. S. Bondar, *Tribol. Trans.* **2012**, *55*, 149.

[279] V. Y. Dolmatov, *J. Superhard Mater.* **2010**, *32*, 14.

[280] K. W. Street, M. Marchetti, R. L. Vander Wal, A. J. Tomasek, *Tribol. Lett.* **2004**, *16*, 143.

[281] K. Miyoshi, K. W. S. Jr., R. L. Vander Wal, R. Andrews, A. Sayir, *Tribol. Lett.* **2005**, *19*, 191.

[282] X. Zhang, B. Luster, A. Church, C. Muratore, A. a Voevodin, P. Kohli, S. Aouadi, S. Talapatra, *ACS Appl. Mater. Interfaces* **2009**, *1*, 735.

[283] J. J. Hu, S. H. Jo, Z. F. Ren, A. Voevodin, J. S. Zabinski, *Tribol. Lett.* **2005**, *19*, 119.

[284] S. Park, D. Srivastava, K. Cho, *Nano Lett.* **2003**, *3*, 1273.

[285] S. Heo, S. B. Sinnott, *J. Appl. Phys.* **2007**, *102*, DOI 10.1063/1.2784007.

[286] K. Mylvaganam, L. C. Zhang, K. Q. Xiao, *Carbon* **2009**, *47*, 1693.

[287] F. Colonna, A. Fasolino, E. J. Meijer, *Phys. Rev. B* **2013**, *88*, 165416.

[288] L. Rui, *AIP Adv.* **2014**, *4*, DOI 10.1063/1.4867087.

[289] Q. Ouyang, K. Okada, *Appl. Surf. Sci.* **1994**, *78*, 309.

[290] A. V. Gubarevich, S. Usuba, Y. Kakudate, A. Tanaka, O. Odawara, *Diam. Relat. Mater.* **2005**, *14*, 1549.

[291] D. Berman, S. A. Deshmukh, S. K. R. S. Sankaranarayanan, A. Erdemir, A. V. Sumant, *Science (80-.).* **2015**, *348*, 1118.

[292] J. Hone, R. W. Carpick, *Science (80-.).* **2015**, *348*, 1087.

[293] C. C. Chou, S. H. Lee, *J. Mater. Process. Technol.* **2008**, *201*, 542.

[294] O. Elomaa, T. J. Hakala, V. Myllymäki, J. Oksanen, H. Ronkainen, V. K. Singh, J. Koskinen, *Diam. Relat. Mater.* **2013**, *34*, 89.

[295] N. Matsumoto, L. Joly-Pottuz, H. Kinoshita, N. Ohmae, *Diam. Relat. Mater.* **2007**, *16*, 1227.

[296] E. W. Bucholz, S. R. Phillpot, S. B. Sinnott, *Comput. Mater. Sci.* **2012**, *54*, 91.

[297] M. Zhang, S. Fang, A. A. Zakhidov, S. B. Lee, R. H. Baughman, *Science (80-.).* **2005**, *309*, 1215.

[298] C. Feng, K. Liu, J. S. Wu, L. Liu, J. S. Cheng, Y. Zhang, Y. Sun, Q. Li, S. Fan, K. Jiang, *Adv. Funct. Mater.* **2010**, *20*, 885.

[299] M. E. Spotnitz, D. Ryan, H. A. Stone, *J. Mater. Chem.* **2004**, *14*, 1299.

[300] F. Mirri, A. W. K. Ma, T. T. Hsu, N. Behabtu, S. L. Eichmann, C. C. Young, D. E. Tsentalovich, M. Pasquali, *ACS Nano* **2012**, *6*, 9737.

[301] E. Y. Jang, T. J. Kang, H. W. Im, D. W. Kim, Y. H. Kim, *Small* **2008**, *4*, 2255.

[302] M. Majumder, C. Rendall, M. Li, N. Behabtu, J. A. Eukel, R. H. Hauge, H. K. Schmidt, M. Pasquali, *Chem. Eng. Sci.* **2010**, *65*, 2000.

[303] B. Dan, G. Irvin, M. Pasquali, *ACS Nano* **2009**, *3*, 835.

[304] T. V. Sreekumar, T. Liu, S. Kumar, L. M. Ericson, R. H. Hauge, R. E. Smalley, *Chem. Mater.* **2003**, *15*, 175.

[305] M. A. Meitl, Y. Zhou, A. Gaur, S. Jeon, M. L. Usrey, M. S. Strano, J. A. Rogers, *Nano Lett.* **2004**, *4*, 1643.

[306] L. Hu, D. S. Hecht, G. Gruner, *Nano Lett.* **2004**, *4*, 2513.

[307] F. De Nicola, P. Castrucci, M. Scarselli, F. Nanni, I. Cacciotti, M. De Crescenzi, *Nanotechnology* **2015**, *26*, 145701.

[308] A. Hirata, N. Yoshioka, *Tribol. Int.* **2004**, *37*, 893.

[309] M. D. Abad, J. C. Sánchez-López, A. Berenguer-Murcia, V. B. Golovko, M. Cantoro, A. E. H. Wheatley, A. Fernández, B. F. G. Johnson, J. Robertson, *Diam. Relat. Mater.* **2008**, *17*, 1853.

[310] A. R. Boccaccini, J. Cho, J. A. Roether, B. J. C. Thomas, E. Jane Minay, M. S. P. Shaffer, *Carbon* **2006**, *44*, 3149.

[311] B. J. C. Thomas, M. S. P. Shaffer, S. Freeman, M. Koopman, K. K. Chawla, A. R. Boccaccini, *Key Eng. Mater.* **2006**, *314*, 141.

[312] B. J. C. Thomas, A. R. Boccaccini, M. S. P. Shaffer, *J. Am. Ceram. Soc.* **2005**, *88*, 980.

[313] J. Cho, S. Schaab, J. A. Roether, A. R. Boccaccini, *J. Nanoparticle Res.* **2008**, *10*, 99.

[314] Y. Ma, J. Han, M. Wang, X. Chen, S. Jia, *J. Mater.* **2018**, *4*, 108.

[315] L. Besra, M. Liu, *Prog. Mater. Sci.* **2007**, *52*, 1.

[316] Y. Zhu, Y. Chen, C. Zhu, X. Shen, **2010**, *23*, 409.

[317] K. Balani, Y. Chen, S. P. Harimkar, N. B. Dahotre, A. Agarwal, *Acta Biomater.* **2007**, *3*, 944.

[318] M. Alishahi, S. M. Monirvaghefi, A. Saatchi, S. M. Hosseini, *Appl. Surf. Sci.* **2012**, *258*, 2439.

[319] W. X. Chen, F. Li, G. Han, J. B. Xia, L. Y. Wang, J. P. Tu, Z. D. Xu, *Tribol. Lett.* **2003**, *15*, 275.

[320] W. X. Chen, J. P. Tu, Z. D. Xu, W. L. Chen, X. B. Zhang, D. H. Cheng, *Mater. Lett.* **2003**, *57*, 1256.

[321] H. D. Lee, O. V. Penkov, D. E. Kim, *Thin Solid Films* **2013**, *534*, 410.

[322] W. Zhang, G. J. Ma, C. W. Wu, *Rev. Adv. Mater. Sci* **2014**, *36*, 75.

[323] R. Velázquez, V. Neto, K. Uppireddi, B. Weiner, G. Morell, *Coatings* **2013**, *3*, 243.

[324] K. Tsugawa, C. Technologies, A. Indu, A. Indu, *New Diam. Front. Carbon Technol.* **2006**, *16*, 337.

[325] N. Sharma, N. Kumar, B. Sundaravel, K. Panda, W. David, M. Kamarrudin, S. Dash, B. K. Panigrahi, A. K. Tyagi, I. N. Lin, B. Raj, *Tribol. Int.* **2011**, *44*, 980.

[326] A. M. Affoune, B. L. V. Prasad, H. Sato, T. Enoki, *Langmuir* **2001**, *17*, 547.

[327] L. La Torre Riveros, D. A. Tryk, C. R. Cabrera, *Rev. Adv. Mater. Sci.* **2005**, *10*, 256.

[328] L. La-Torre-Riveros, K. Soto, M. A. Scibioh, C. R. Cabrera, *J. Electrochem. Soc.* **2010**, *157*, B831.

[329] L. Schmidlin, V. Pichot, S. Josset, R. Pawlak, T. Glatzel, S. Kawai, E. Meyer, D. Spitzer, *Appl. Phys. Lett.* **2012**, *101*, DOI 10.1063/1.4772983.

[330] G. L. Bilbro, *Diam. Relat. Mater.* **2002**, *11*, 1572.

[331] D. Katyanasundaran, P. Molian, *Micro Nano Lett.* **2008**, *3*, 110.

[332] E. Maillard-Schaller, O. M. Kuettel, L. Diederich, L. Schlapbach, V. V. Zhirnov, P. I. Belobrov, *Diam. Relat. Mater.* **1999**, *8*, 805.

[333] I. Petrov, P. Detkov, A. Drovosekov, M. V. Ivanov, T. Tyler, O. Shenderova, N. P. Voznecova, Y. P. Toporov, D. Schulz, *Diam. Relat. Mater.* **2006**, *15*, 2035.

[334] H. Mazaheri, S. R. Allahkaram, *Appl. Surf. Sci.* **2012**, *258*, 4574.

[335] A. Valeryevna, J. Kitamura, S. Usuba, H. Yokoi, *Carbon* **2003**, *41*, 2601.

[336] T. Cabioc'h, E. Thune, M. Jaouen, *Chem. Phys. Lett.* **2000**, *320*, 202.

[337] D. Pech, M. Brunet, H. Durou, P. Huang, V. Mochalin, Y. Gogotsi, P.-L. Taberna, P. Simon, *Nat. Nanotechnol.* **2010**, *5*, 651.

[338] M. M. H. Bastwros, A. M. K. Esawi, A. Wifi, *Wear* **2013**, *307*, 164.

[339] B. Liu, Z. Zeng, Y. Lin, *Surf. Coatings Technol.* **2009**, *203*, 3610.

[340] S. T. Selvamani, S. Premkumar, M. Vigneshwar, P. Hariprasath, K. Palanikumar, *J. Magnes. Alloy.* **2017**, *5*, 326.

[341] M. Mansoor, M. Shahid, *Adv. Mater. Res.* **2015**, *1101*, 62.

[342] J.-W. An, D.-H. You, D.-S. Lim, *Wear* **2003**, *255*, 677.

[343] U. Abdullahi, M. A. Maleque, U. Nirmal, *Procedia Eng.* **2013**, *68*, 736.

[344] D. G. Liu, J. Sun, Z. X. Gui, K. J. Song, L. M. Luo, Y. C. Wu, *Diam. Relat. Mater.* **2017**, *74*, 229.

[345] W. X. Chen, J. P. Tu, L. Y. Wang, H. Y. Gan, Z. D. Xu, X. B. Zhang, *Carbon* **2003**, *41*, 215.

[346] Z. H. Li, X. Q. Wang, M. Wang, F. F. Wang, H. L. Ge, *Tribol. Int.* **2006**, *39*, 953.

[347] L. Zhang, Q. Wang, G. Liu, W. Guo, B. Ye, W. Li, H. Jiang, W. Ding, *Tribol. Lett.* **2018**, *66*, 1.

[348] Y. Li, B. X. Li, W. J. Zou, *Appl. Mech. Mater.* **2011**, *80–81*, 683.

[349] A. L. D. Skury, G. S. Bobrovinichii, S. N. Monteiro, *Mater. Sci. Forum* **2012**, *727–728*, 320.

[350] M. Bao, C. Zhang, D. Lahiri, A. Agarwal, *Jom* **2012**, *64*, 702.

[351] H. Kaftelen, M. L. Öveçoğlu, *J. Compos. Mater.* **2012**, *46*, 1521.

[352] A. Nieto, L. Jiang, J. Kim, D. E. Kim, J. M. Schoenung, *Sci. Rep.* **2017**, *7*, 1.

[353] A. Nieto, J. Kim, O. V. Penkov, D. E. Kim, J. M. Schoenung, *Surf. Coatings Technol.* **2017**, *315*, 283.

[354] L. S. K. Pang, J. D. Saxby, S. P. Chatfield, *J. Phys. Chem.* **1993**, *97*, 6941.

FIGURES